LATEST DEVELOPMENTS IN THE FIELD OF MAGNESIUM ALLOYS AND THEIR APPLICATIONS

EDITED BY: Hajo Dieringa, David StJohn, Maria Teresa Pérez and Karl Ulrich Kainer
PUBLISHED IN: Frontiers in Materials

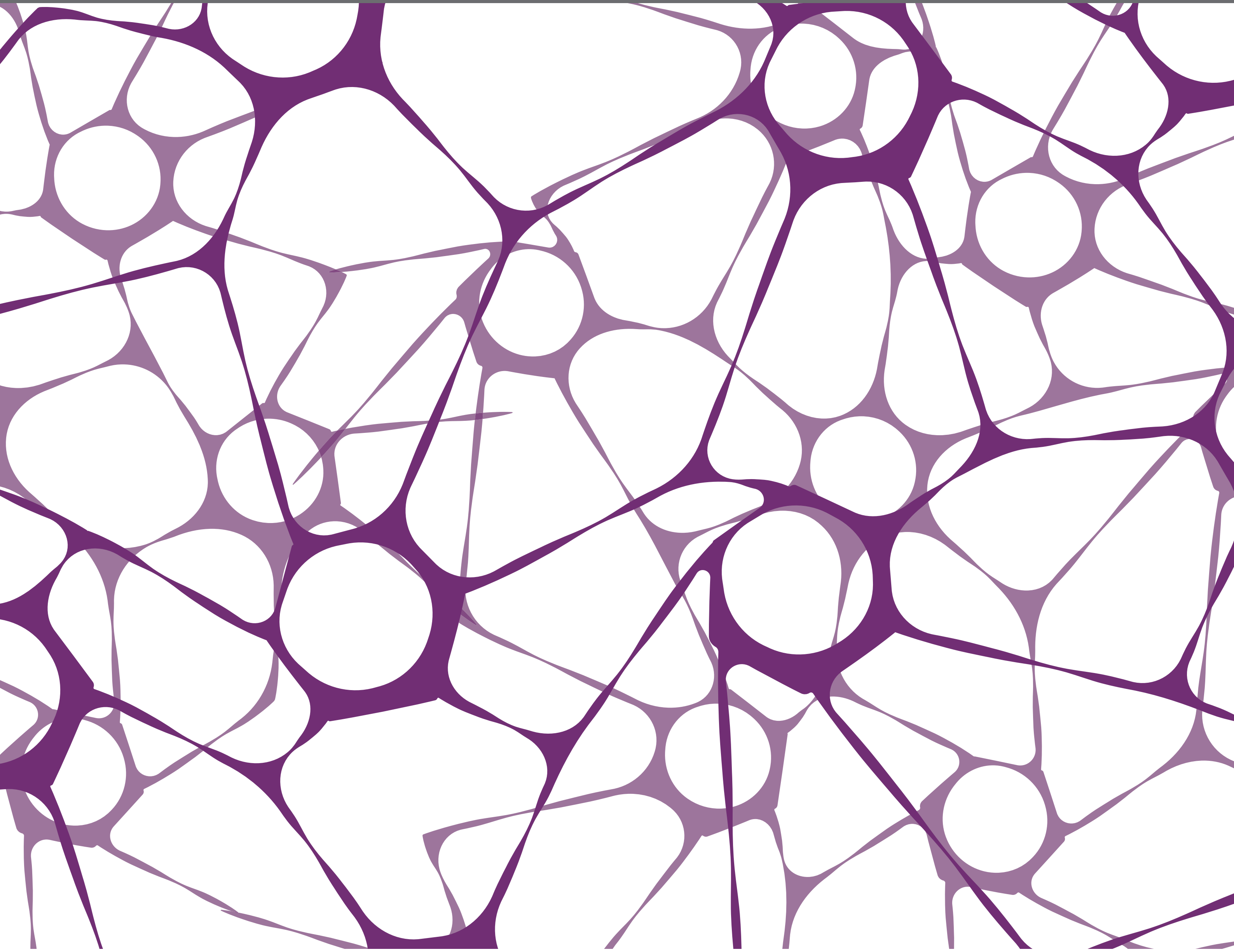

frontiers Research Topics

ISSN 1664-8714
ISBN 978-2-88971-284-7
DOI 10.3389/978-2-88971-284-7

About Frontiers

Frontiers is more than just an open-access publisher of scholarly articles: it is a pioneering approach to the world of academia, radically improving the way scholarly research is managed. The grand vision of Frontiers is a world where all people have an equal opportunity to seek, share and generate knowledge. Frontiers provides immediate and permanent online open access to all its publications, but this alone is not enough to realize our grand goals.

Frontiers Journal Series

The Frontiers Journal Series is a multi-tier and interdisciplinary set of open-access, online journals, promising a paradigm shift from the current review, selection and dissemination processes in academic publishing. All Frontiers journals are driven by researchers for researchers; therefore, they constitute a service to the scholarly community. At the same time, the Frontiers Journal Series operates on a revolutionary invention, the tiered publishing system, initially addressing specific communities of scholars, and gradually climbing up to broader public understanding, thus serving the interests of the lay society, too.

Dedication to Quality

Each Frontiers article is a landmark of the highest quality, thanks to genuinely collaborative interactions between authors and review editors, who include some of the world's best academicians. Research must be certified by peers before entering a stream of knowledge that may eventually reach the public - and shape society; therefore, Frontiers only applies the most rigorous and unbiased reviews.
Frontiers revolutionizes research publishing by freely delivering the most outstanding research, evaluated with no bias from both the academic and social point of view.
By applying the most advanced information technologies, Frontiers is catapulting scholarly publishing into a new generation.

What are Frontiers Research Topics?

Frontiers Research Topics are very popular trademarks of the Frontiers Journals Series: they are collections of at least ten articles, all centered on a particular subject. With their unique mix of varied contributions from Original Research to Review Articles, Frontiers Research Topics unify the most influential researchers, the latest key findings and historical advances in a hot research area! Find out more on how to host your own Frontiers Research Topic or contribute to one as an author by contacting the Frontiers Editorial Office: frontiersin.org/about/contact

LATEST DEVELOPMENTS IN THE FIELD OF MAGNESIUM ALLOYS AND THEIR APPLICATIONS

Topic Editors:
Hajo Dieringa, Helmholtz Centre Hereon, Germany
David StJohn, The University of Queensland, Australia
Maria Teresa Pérez, Instituto IMDEA Materiales, Spain
Karl Ulrich Kainer, Wrocław University of Technology, Poland

Citation: Dieringa, H., StJohn, D., Pérez, M. T., Kainer, K. U., eds. (2021). Latest Developments in the Field of Magnesium Alloys and their Applications. Lausanne: Frontiers Media SA. doi: 10.3389/978-2-88971-284-7

Table of Contents

frontiers
in Materials

EDITORIAL
published: 08 July 2021
doi: 10.3389/fmats.2021.726297

Editorial: Latest Developments in the Field of Magnesium Alloys and Their Applications

Hajo Dieringa[1]*, *David StJohn*[2], *María Teresa Pérez Prado*[3] *and Karl Ulrich Kainer*[4]

[1] *Helmholtz-Zentrum Hereon, Institute of Materials and Process Design, Department Hybrid Materials and Processes, Geesthacht, Germany,* [2] *School of Mechanical and Mining Engineering, The University of Queensland, Brisbane, QLD, Australia,* [3] *IMDEA Materials Institute, Madrid, Spain,* [4] *Wrocław University of Science and Technology, Wrocław, Poland*

Keywords: lightweight, cast and wrought alloys, biodegradability, corrosion protection, creep resistance, hybrid materials, functionalization

Editorial on the Research Topic

Latest Developments in the Field of Magnesium Alloys and their Applications

Magnesium-based alloys and composites as structural materials as well as functionalized magnesium materials have been experiencing a steady increase in interest in the demand for new applications as well as in the scientific community for many years. To give an expression and visibility for this high demand, the authors initiated this Research Topic to provide interested stakeholders with an overview of current developments in research in this sector. A total of 16 articles were published by 56 authors from 29 institutional affiliations in nine countries. 12 of these articles are original research, and two of each are mini-reviews and reviews. Of the original research articles, eight address wrought alloys, two cast materials, and two fundamentals of metallurgical principles of magnesium alloys. This certainly meets the current need for optimization of wrought Mg materials for sheet applications or extruded profiles. In the list of applications targeted by the authors, it is noticeable that biodegradable magnesium materials are now a major focus. This is partly due to the fact that this research field experienced an acceleration in interest a few years ago and partly due to the massive interest of the medical industry in new, cost-effective solutions in implant materials to enable transfer to, for example, surgical procedures. The two mini-reviews deal firstly with the suitability assessment of magnesium materials for new applications in drone design and secondly with the deformation properties of friction-stir-welded magnesium alloys. The two reviews target fundamental issues of alloy development in magnesium alloys, as well as the suitability of magnesium materials as hydrogen storage materials.

In the first mini-review (Ren et al.), an overview of the microstructural characteristics and resulting texture development of magnesium alloys that were welded using the Friction-Stir process is presented. This process is a solid-phase joining process that does not suffer solidification problems as in other welding processes. EBSD data, among other data, are used for the analysis, and the localised plastic deformation mechanisms are described. In addition to these analyses, process modifications are also presented that serve to increase the strength of the welded zone.

The second mini-review addresses the suitability of magnesium-based materials as construction materials for drones (Höche et al.). The main drivers for this are low density and good castability, but also good damping properties. However, critical characteristics are also highlighted and ways to avoid them are presented. With the help of Ashby maps, which plot the Young's modulus or strength against the material's density, the fields of possible application are identified and some new monolithic but also hybrid magnesium materials are presented for further developments, which can be used in manned or unmanned aerial vehicles in the future.

Edited and reviewed by:
John L. Provis,
The University of Sheffield,
United Kingdom

****Correspondence:***
Hajo Dieringa
hajo.dieringa@hereon.de

Specialty section:
This article was submitted to
Structural Materials,
a section of the journal
Frontiers in Materials

Received: *16 June 2021*
Accepted: *25 June 2021*
Published: *08 July 2021*

Citation:
Dieringa H, StJohn D, Pérez Prado MT and Kainer KU (2021) Editorial: Latest Developments in the Field of Magnesium Alloys and Their Applications.
Front. Mater. 8:726297.
doi: 10.3389/fmats.2021.726297

The first review (Rabkin et al.) deals with the hydrogen storage capability of extremely fine-grained magnesium alloys, one of the innovative topics in magnesium technology that fall under the category of functionalization. The fine grain size is achieved with the equal channel angular processing process (ECAP) and grain sizes below 1 μm are achieved. Also, other severe plastic deformation processes (SPD) such as high pressure torsion (HPT) result in grain sizes that significantly improve the kinetics of hydrogen loading and deloading. The authors argue that the best way to optimize the thermodynamics of the Mg-H system is to combine SPD with the selection of light alloying elements, which can be supported with computer-aided thermodynamic simulations (Campos et al.). Magnesium-based nanocomposites reinforced with carbon homologues, such as graphene or nanotubes, also show potential for suitability as hydrogen storage materials. More scientific studies are needed to better understand the detailed mechanisms of absorption and desorption and the influence of lattice defects.

The second review summarizes the basic principles of magnesium alloying (Kaya). In doing so, Miedema's model becomes the center of attention along with the assumptions according to Hume-Rothery. This Miedema assumption relates the electron density and the difference in electronegativity of two elements to the stacking fault energy generated thereby. In the simulation approaches, the short-range order (SRO) formation of atoms is considered and not only the uniform homogeneous distribution of atoms in solid solution. Furthermore, the author would like to see this Miedema approach extended to multicomponent systems. As examples, oxygen and Ca or CaO are presented here as alloying additions. This review article describes in detail the possibilities for modelling magnesium alloy systems and attempts to derive property predictions from the results. It will be a good basis for future alloy developments and alloy innovations.

In an original research article, Tun et al. developed and tested a high-entropy alloy (HEA) with composition Mg-xAl-xCu-xMn-xZn with $x = 5$ at% (Tun et al.). This material was extruded and Al6Mn and Al2CuMg phases appear in the microstructure, resulting in the high hardness combined with high compressive strength of 616 MPa also achieving good ductility of 16.9%. The tensile strength and ductility in the tensile test are found to be good at 318 MPa and 8.2%, respectively. Regarding the yield strength, the ratio between compression and tensile tests is 0.9, which is almost symmetrical and thus quite untypical for magnesium alloys.

In an original research article, the microstructure, texture, as well as the forming behaviour and mechanical characteristics of two magnesium alloys (Mg-Zn-RE and Mg-Zn-Ca) produced by twin roll casting process were investigated (Victoria-Hernández et al.). Both alloys were hot rolled and annealed. They both show a fine-grained microstructure, a good ductility higher than 30%, and a similar texture with a split in the transverse direction. However, the difference in yield strength in and perpendicular to the rolling direction is relatively large. The Erichsen Index (IE) of the Mg-Zn-RE is 8.4 after cold rolling, while the Mg-Zn-Ca alloy shows good stretch formability while having a lower Erichsen Index. The alloy containing calcium does not show exceptional hot formability. The crack-inducing effect of the Mg_2Ca phases is probably responsible for this. In conclusion, the suppression of the split texture is an effective way to suppress the anisotropy of the mechanical properties.

The effect of the addition of an Al-Be master alloy on the grain refining of a Mg-Zr alloy is studied in an original research article (Balasubramani et al.). It was originally assumed that the grain coarsening effect of this addition was due to a reaction of Be with Zr, thereby reducing the grain refining potential of the zirconium. In this work, however, it was shown that a reaction of the Al with Zr leads to intermetallic phases and thus reduces the absolute concentration of dissolved Zr. Consequently, this leads to a reduction of the grain refining effect by Zr. Furthermore, the grain refining effect of ultrasonic treatment of the melt was demonstrated and it was shown that beryllium is linked to oxides formed at the surface. The results of this study show that Be additions can lead to a reduction of ignitibility in grain refined cast alloys.

Creep resistance under compressive stress is investigated in an original research article on seven commercial and newly developed creep-resistant magnesium alloys processed in high-pressure die casting (Gavras et al.). These are the commercial AE42 and AE44, as well as a modified AE44, a commercial MRI230D, and three newly developed DieMag alloys that contain aluminium as well as barium and calcium in a 2:1:1 ratio in varying concentrations. In tensile tests at room temperature (RT), DieMag633 showed the highest yield strength of more than 200 MPa, but at the expense of ductility. MRI230D exhibited the second highest yield strength at RT with 180 MPa, followed by DieMag422 with 173 MPa. In tensile tests at 150°C, DieMag633 was also convincing with 160 MPa followed by MRI230D and DieMag422 with around 140 MPa. Thus, the yield strength of this most creep-resistant magnesium alloy at RT and at 150°C is higher than those of the aluminium alloy A380. The creep resistance at 200°C and different stresses between 60 and 100 MPa was best in the lower stress range for AE44 and at higher stresses for DieMag633.

The corrosion rate and mechanical properties of Mg-xAg alloys with x between 2 and 10 wt%, which may be suitable as biodegradable materials, are investigated in an original research article (Jessen et al.). These are thin films prepared by the magnetron sputtering technique and are as thin as 20 μm. They are compared with samples of pure magnesium produced in an identical manner. It was found that a Mg-10Ag alloy exhibits a tensile strength of 371 MPa with, however, moderate ductility. At a content of 6 wt% silver, the material shows a yield strength of 310 MPa with an elongation of 6%. The simultaneous investigation of the corrosion rates in combination with the mechanical properties suggest that the Mg-6Ag material is a promising material for degradable implants because the silver can also exhibit therapeutic effects.

Another original research paper addresses the biodegradable magnesium materials Mg-xGd with $X = 2$, 5 and 10, which can be used as implant materials (Harmuth et al.). The alloys were cast, solution treated and then extruded at different temperatures and speeds and the obtained profiles were investigated for their properties. It is shown that the mechanical properties can be varied over a wide range by the appropriate choice of parameters. Thus, the yield strengths in the tensile test range from 90 to 200 MPa and the ultimate tensile strengths from 180 to 280 MPa. In compression, yield strengths are between 80 and 220 MPa and ultimate compressive strengths between 300 and 450 MPa. Degradation rates are low at about 0.2 mm/year for all alloys and are not affected by process parameters. Mg-Gd alloys are therefore suitable for use as degradable implant materials.

Compression tests on a rolled and annealed Mg-1Zn-1Gd-0.6Zr alloy (ZEK110), which were performed in the sheet plane in the rolling direction, showed the following characteristics after analysis of the microstructure and texture of the deformed specimens (Basu and Al-Samman). Microstructure after annealing showed a large number of compression twins but also tension twins, which furthermore included second and third order twins. However, the growth of the twins is strongly hindered by Zr-rich precipitates and stress fields around other particles. <c+a> slip incorporates local plastic shear across the twin boundaries, while basal slip accumulates at interfaces in local dislocation pileup, contributing to grain boundary strengthening. Recrystallization and grain growth takes place. The importance of understanding twin deformation for the overall deformation process in magnesium materials has been demonstrated.

Another original research paper, which deals with the property optimisation of a Mg-3Zn-0.2Ca alloy by adding manganese (between 0.3 and 0.9 wt%), sees biomedicine as an application area for these alloys and, in particular, their use as degradable implant materials (Han et al.). With the increase of manganese, the grain size of the cast material first decreases and then increases again. This effect is attributed to the influence of manganese on supercooling during the solidification process. After extrusion of the materials, it is shown that with a content of 0.5 wt% manganese, a maximum yield strength of 302 MPa and a ultimate tensile strength of 327 MPa can be achieved. This is attributed to the influence of manganese on the recrystallization behaviour, which in turn influences the grain size. Investigations of the degradation rate and the corrosion potential show that the addition of manganese improves the properties and achieves optimum values at a manganese content of 0.5 wt%.

The property profile of extruded flat products is investigated in an original research article, and it is shown that microstructure, texture and mechanical behaviour differ significantly from rolled semi-finished products (Nienaber et al.). Three Zn-containing magnesium alloys were extruded with different process parameters, namely ZN10, ZX10 and AZ31, and the texture, microstructure and mechanical properties were studied on the strips formed. As expected, an increase in extrusion speed results in a higher deformation temperature, which leads to an increase in dynamic recrystallization. Differences in texture were also found in the three alloys. The AZ31 showed a strong basal texture, while the ZN10 and ZX10 showed more of a tilting of the basal plane towards the extrusion direction. This is similar in round extruded profiles. Soft textures allow better formability of the flat products. It was further found that retarding the dynamic recrystallization by choosing suitable alloying elements or by varying the process parameters leads to flat products with excellent forming properties, which could also be confirmed in Erichsen tests.

A research subject that has been a focus of interest for some years now is the long-period-stacking-ordered phases (LPSO) in magnesium alloys, which are held responsible for exceptional properties of some alloys. An original research article therefore deals with short range order (SRO) clusters in a Mg97Zn1Gd2 alloy (at%) that forms LPSO phases (Egusa et al.). Gadolinium-SRO clusters were identified with high-angle annular dark-field scanning transmission electron microscopy (HAADF-STEM) and zinc atoms were detected that are constituents of these clusters. First Principle Calculations supported the identification of the atomic distribution of Gd and Zn in STEM. These investigations on atomic scales show the possibilities of electron microscopy in correlating microstructure and properties.

Another original research article dealing with LPSO phases uses a combination of *in-situ* neutron diffraction and acoustic emission to investigate the deformation behaviour of two Mg-Zn-Y alloys (Máthis et al.). The alloys Mg-3Y-1.5Zn and Mg-7Y-6Zn (at%) show 32 and 85% LPSO phases in their microstructure, respectively. The investigations reveal that in both alloys the decrease in mechanical properties with an increase in temperature is only slight and that the load transfer from the magnesium matrix to the LPSO phases is the determining factor for these properties. This is particularly evident in the higher yield strength of the alloy with the higher content of LPSO phases. It turns out that twinning is the determining deformation mechanism in the alloy with low content of LPSO phases, while kinking is the determining mechanism in the other alloy. In this article, a contribution has been made to the understanding of the deformation mechanisms in LPSO alloys.

In summary, it can be stated that magnesium and its alloys are of great importance in all its variations, whether as a functionalised application (biodegradable implant material, hydrogen storage, post-Li battery, etc.), as a cast or wrought lightweight material or as a metallic matrix for hybrid materials, such as nanocomposites, laminates, etc. The wide range of papers submitted is proof of this trend, which will continue to make magnesium interesting for many applications in the future.

AUTHOR CONTRIBUTIONS

The Editorial was jointly written by the co-authors HD, DS, MP, and KK who also served as Guest Editors for the Research Topic. All authors contributed to the article and approved the submitted version.

Conflict of Interest: The authors declare that the research was conducted in the absence of any commercial or financial relationships that could be construed as a potential conflict of interest.

frontiers in Materials

ORIGINAL RESEARCH
published: 06 August 2019
doi: 10.3389/fmats.2019.00187

Hierarchical Twinning Induced Texture Weakening in Lean Magnesium Alloys

Indranil Basu[1]* *and Talal Al-Samman*[2]

[1] Laboratory of Metal Physics and Technology, Department of Materials, ETH Zürich, Zurich, Switzerland, [2] Institut für Metallkunde und Metallphysik, RWTH Aachen University, Aachen, Germany

Rolled and annealed Mg-1wt. %Zn-1wt. %Gd-0.6wt. %Zr (ZEK110) alloys were subjected to room temperature in-plane compression along the rolling direction, followed by isochronal annealing treatments for 1 h. Despite a starting orientation favoring c-axis extension, the as-deformed microstructure revealed a hierarchical network of twins with profuse quantities of second and third generation twinning appearing within primary tension and compression twins. Complex twin-twin and twin–particle interactions were accompanied by the activation of both basal and non-basal dislocation slip in the neighborhood. While the population density of twins nucleated was significantly high, twin growth was severely retarded due to the presence of secondary phases. In terms of the overall distribution of grain orientations, the as-deformed texture displayed a rather weak basal component with a large portion of the basal poles aligned toward the longitudinal direction with an angular spread of ± 30°. Recrystallization commenced within twins, at twin-twin intersections at lower annealing temperatures and occurred additionally near secondary phases at higher annealing temperatures, giving rise to diverse orientations of both basal and off-basal character. Subsequent growth led to favorable coarsening of the off-basal orientations resulting in an overall texture weakening. The findings provide critical insights with respect to engineering high-strength, high-ductility lean magnesium alloys, comprising hierarchical microstructures that are not only associated with favorable crystallographic textures but additionally display a multi-scale strengthening behavior.

Keywords: magnesium, twinning, twin-particle interactions, hierarchical microstructures, twin-twin interactions

OPEN ACCESS

Edited by:
Hajo Dieringa,
Helmholtz Centre for Materials and Coastal Research (HZG), Germany

Reviewed by:
Jing Su,
Max-Planck-Institut für Eisenforschung GmbH, Germany
Kristian Mathis,
Charles University, Czechia
Dong Jie,
Shanghai Jiao Tong University, China

****Correspondence:***
Indranil Basu
indranil.basu@mat.ethz.ch

Specialty section:
This article was submitted to Structural Materials, a section of the journal Frontiers in Materials

Received: *23 May 2019*
Accepted: *22 July 2019*
Published: *06 August 2019*

Citation:
Basu I and Al-Samman T (2019) Hierarchical Twinning Induced Texture Weakening in Lean Magnesium Alloys. Front. Mater. 6:187. doi: 10.3389/fmats.2019.00187

INTRODUCTION

Designing high-strength and high-cold-formability magnesium alloys remains a considerable challenge owing to the inherent anisotropy in the hexagonal crystal structure, wherein strain accommodation along the longer c-axis is difficult owing to significantly larger critical resolved shear stresses in this direction (Yoo, 1981; Mordike and Ebert, 2001; Hirsch and Al-Samman, 2013; Wu and Curtin, 2015; Wang et al., 2018). Present magnesium alloys thus show limited plasticity at ambient temperatures, primarily due to: (i) an insufficient number of active deformation mechanisms, which are unable to fulfill the von Mises criterion for homogeneous plastic deformation, and (ii) the consequent development of strong crystallographic textures during deformation giving rise to highly anisotropic plastic flow behavior (Yoo, 1981; Hirsch and Al-Samman, 2013; Wu and Curtin, 2015).

Over the past decade, there has been a focused emphasis laid upon utilizing a combination of intelligent alloying such as micro-additions of rare earth (RE) elements and optimizing microstructural design in order to obtain simultaneous strength—ductility enhancement (Bohlen et al., 2010; Al-Samman and Li, 2011; Noble, 2012; Peng et al., 2012). In this regard, the authors have previously shown the beneficial impact of combined additions of RE and non-RE elements on shear banding and, subsequent recrystallization and grain growth behavior in Mg alloys (Basu and Al-Samman, 2014). They reported that tailored microstructures displaying large ductility without any strength loss could be fabricated by appropriate thermo mechanical processing. They also inferred that the presence of non-RE elements such as Zn and Zr significantly augment the RE effects in the alloy (Basu and Al-Samman, 2014). In a similar line, the authors performed exhaustive investigations on the deformation twinning behavior in binary magnesium-rare earth alloys, wherein it was shown that the addition of solute rare earth elements modify the overall twinning response with comparable nucleation probabilities of both extension and compression twins. The impact of such twinning characteristics was evident on the annealing response that resulted in soft deformable textures devoid of the unfavorable basal texture component for industrial processing, such as sheet metal forming (Basu and Al-Samman, 2015).

Despite the significant progress made in the previous studies, there is a current lack of understanding of twinning in these systems in the presence of combined additions of RE and non-RE elements, wherein simultaneous solute as well as precipitate effects on the deformation twinning response can be exploited for an enhanced knowledge of these alloy systems. The current work thus extends our understanding of twinning characteristics in Mg-RE alloys with additional contribution from non-RE elements i.e., Zn and Zr and whether such RE—non-RE combinations can be utilized to design high strength-high ductility twinned microstructures.

BACKGROUND

Room temperature deformation of conventional Mg alloys typically offers only four independent slip deformation modes i.e., two each from the basal: (0001) <11$\bar{2}$0>, and prismatic: (10$\bar{1}$0) <11$\bar{2}$0> slip systems. However, since the aforementioned deformation modes only provide strain accommodation along the basal plane, magnesium tends to exhibit abundant deformation twinning activity as a strain accommodation mechanism along the <0001> c-axis (Yoo, 1981). However, unlike slip that is spatially more homogeneous with gradual lattice rotations, twinning results in drastic reorientation of the crystal by a significantly large misorientation angle (Yoo, 1981; Yoo and Lee, 1991; Aydiner et al., 2009). Such crystallographic rotation leads to formation of well-defined twin boundaries. While the presence of twin boundaries promote strengthening through dynamic grain refinement as well as lead to substantial latent hardening inside the twins; their role in terms of ductility is often seen as unfavorable (El Kadiri and Oppedal, 2010; Qiao et al., 2017). This is owing to the fact that twinning can either give rise to regions of severe shear incompatibility near the twin-parent interface (such as for compression twins) or generate crystallographically hard orientations (in case of extension twins) that adversely affect the overall elongation response (Aydiner et al., 2009; Molodov et al., 2014, 2017; Basu and Al-Samman, 2015). In this regard, promoting twin formation is often avoided when it comes to designing ductile Mg alloys, resulting in employing alternative routes such as designing fine-grained microstructures thereby abating twinning activity and increasing slip contribution (Yamashita et al., 2001; Hofstetter et al., 2015; Lin et al., 2016; Trang et al., 2018).

However, it must be understood that the aforementioned shear incompatibility and generation of non-deformable orientations during twinning is primarily as a result of the highly anisotropic dislocation slip prevalent in pure Mg, wherein pyramidal <c+a> slip modes require extremely high stresses (nearly 100 times the critical resolved shear stress of basal <a> slip) to activate (Yoo, 1981; Tonda and Ando, 2002; Wu and Curtin, 2015; Wu et al., 2018). In other words, the main reason behind the poor ductility response of twinned Mg alloys is the lack of homogeneity of slip deformation. A closer look into the origins of such poor formability indicates that the degree of anisotropy in stacking fault energies of the basal and non-basal planes plays a critical role in determining the overall plasticity response. Theoretically, the generalized stacking fault energy (γ_{GSFE}) for a crystallographic plane varies over the relative shear induced displacement that corresponds to displacing a plane of atoms by a magnitude equal to the Burgers vector. The resultant γ_{GSFE} curve along the slip direction of a crystallographic plane is described by a local maximum viz. '$\gamma_{unstable}$' and a local minimum referred to as 'γ_{stable}'. Physically, the value of $\gamma_{unstable}$ relates to the ease of generation of stacking faults on the plane i.e., dislocation nucleation and the value of γ_{stable} gives a measure of the mobility of the nucleated dislocations on the particular plane. The lower the γ_{GSFE} values, the easier is the strain accommodation on a particular crystallographic plane. In pure Mg and conventional Mg alloys, it has been shown that the stacking fault energy values of the pyramidal planes ($\gamma_{GSFE(Pyr.)}$) are larger than those for the basal planes ($\gamma_{GSFE(Bas.)}$), whereby dislocation nucleation on pyramidal planes becomes energetically unfavorable (Wu and Curtin, 2015; Wu et al., 2018). Moreover, even if they nucleate the high γ_{stable} values ensures that the glissile pyramidal dislocations immediately cross-slip to the basal planes thereby dissociating into a sessile <c> and <a>-type dislocations (Ahmad et al., 2018, 2019). By means of molecular dynamics simulations, it has been shown that the cross-slip barrier for pyramidal to basal transition is extremely low i.e., of the order of 0.3–0.5 eV (Wu and Curtin, 2015), in comparison to the cross-slip energy barrier between pyramidal planes that is calculated in the range of 0.6–0.9 eV (Ahmad et al., 2018), thereby explaining the favorability of such a transformation. In a later study, it was shown by means of atomistic simulations that addition of solute REs can contribute toward reducing the cross-slip energy barrier differential between pyramidal-pyramidal and pyramidal-basal planes by simultaneous strengthening of basal dislocations and lowering the stacking fault energies for non-basal planes. It was further predicted that the RE-effect on ductility would be enhanced in the presence of lean additions (within 1 wt. %) of solute Zn. This ensures a more homogeneous deformation response of RE containing Mg alloys (Wu et al., 2018).

In light of these theories, it becomes interesting to probe deformation twinning in lean magnesium-rare earth alloys as a parameter for designing microstructures that benefit from twin induced strengthening without suffering in terms of reduced ductility, owing to a more isotropic slip behavior. In particular, the impact of RE additions in the presence of additional non-RE elements on the twinning response as well as the slip behavior needs to be investigated.

EXPERIMENTAL METHODS

Mg-1Gd-1Zn-0.6Zr (wt.%) alloy (ZEK110) was cast as per ref. (Basu and Al-Samman, 2014) and hot-rolled to a final thickness reduction of 50% over multiple passes. In between each pass, the alloy was subjected to intermediate annealing treatments at 450°C for a duration of 10 min. Rolling resulted in preferential alignment of the basal planes parallel to the rolling direction, giving rise to a well-defined sheet texture. The alloy was subsequently subjected to a short recrystallization annealing treatment at 400°C for only 12 min in order to relieve the stored residual stresses in the microstructure, yet retain the rolling texture for the subsequent in-plane compression experiments. The annealing treatment resulted in an average grain size of 16.7 μm ± 2.9 μm.

Specially oriented specimens of dimensions 12 mm (Longitudinal Direction; LD) × 10 mm (Transverse Direction; TD) × 4 mm (Compression Direction; CD) were machined from the rolled and heat treated sheet and utilized for in-plane compression tests, such that the compression axis is aligned with the rolling direction. Plane strain deformation conditions were implemented by means of a channel-die setup integrated into a conventional screw-driven ZWICK testing machine. Frictional shear between the specimen and the channel-die walls was mitigated by using hexagonal boron nitride (hBN) powder as a lubricant. Since the primary motivation behind such a deformation set-up was to activate deformation twinning in the material, the final compressive strain was limited to a value: $\varepsilon_{logarithmic}$~6%, which typically corresponds to the value where twinning is known to exhaust and further deformation ensues primarily by dislocation slip. In order to assess the recrystallization and grain growth related texture and microstructural evolution, the deformed microstructures were subjected to isochronal annealing treatments for 60 min at 350 and 450°C.

Microstructural characterization was performed using visible light microscopy and electron backscatter diffraction (EBSD) analysis. Specimen surface was prepared by mechanical grinding and polishing techniques, followed by final step electro-polishing, giving rise to a damage free surface. Metallographic etching was performed using acetic picral. X-ray diffraction (XRD) measurements were performed to characterize the macro texture. For this, a Bruker D8 Advance diffractometer, equipped with a high-resolution area detector, operating at 30 kV and 25 mA, using filtered iron radiation and polycapillary focusing optics was used. The measurements were performed on the specimen mid-plane to obtain the bulk texture and avoid any surface effects. The quantitative texture analysis toolbox MTEX (Hielscher and Schaeben, 2008) was employed to calculate the orientation distribution function (ODF) and visualize the data from the pole figure measurements. EBSD measurements performed on electro-polished specimens were analyzed using commercially available EBSD analysis software and the MTEX toolbox. A step size of 0.3 μm and a camera binning of 4 × 4 was employed for the measurements.

RESULTS AND DISCUSSION

Flow Behavior Under In-plane Compression

Plane-strain compression (PSC) experiments in the present work was ideally designed to generate extension along the c-axis, since it is well-known that pure Mg undergoes $\{10\bar{1}2\}$ extension twinning under such circumstances. **Figure 1** displays the averaged stress-strain curve recorded for six individual in-plane compression tests on ZEK110 alloy. The error bars indicate the range of deviation in the stress values corresponding to the imposed strain. An inset image near the top left indicates flow curves recorded for higher strains clearly elucidating the twinning onset and exhaustion regimes. The bottom right inset image in **Figure 1** indicates the (0002) basal pole figure corresponding to the starting orientation. As depicted, the basal poles though preferentially aligned toward the LD, exhibit a large angular spread around the longitudinal axis of approx. ± 15° from the CD toward the TD. This is indicated by a rather weak rolling texture of the order of ~3 MRD (multiples of a random distribution).

The loading curve displays a "concave-up" shape that is often associated with twinning dominated deformation (Kelley and Hosford, 1968; Nave and Barnett, 2004). The initial "non-linearity" observed in the flow curves is often seen in PSC stress-strain curves and is possibly a result of compliance effects between the plunger of the channel-die and the sample. Twinning initiation is indicated with the onset of plateau and the subsequent rise in the applied stress most likely corresponds to exhaustion of twinning deformation and the corresponding twin boundary induced hardening effects (c.f. arrows shown in **Figure 1**).

Microstructure and Texture Evolution

Figures 2A,B show the optical microstructures and XRD bulk textures for ZEK110 after 6% PSC deformation and annealing at 350 and 450°C for 60 min, respectively. Despite the imposed c-axis extension, the contribution of {1012} extension twins seemed severely abated with respect to the XRD pole figure shown for the as-deformed ZEK110 alloy. Theoretically, twinning under c-axis extension is associated with an 86° reorientation of the basal poles such that they align with the

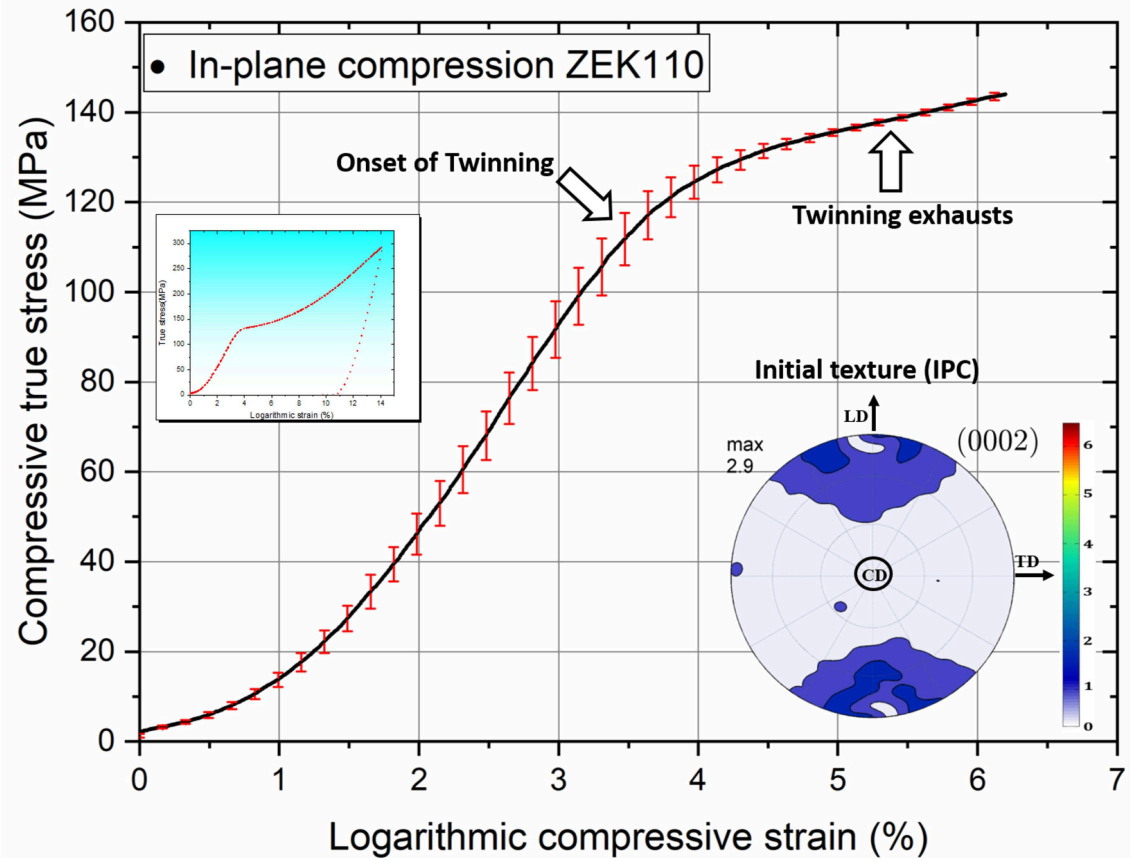

FIGURE 1 | Flow curves during in-plane compression of Mg-1wt.%Zn-1wt.%Gd-0.6wt.%Zr (ZEK110) alloy. White arrows indicate the onset of twinning and the strain at which twinning exhausts. Inset image on the lower right showing the starting texture of the specimen. Error bars indicate the stress variation across flow curves recorded for six independent deformation tests.

direction of loading i.e., CD. However, the as-deformed texture of ZEK110 displays a concentration of the basal poles lying between CD and LD, within an angular distance of ∼15 – 30° away from the LD. Annealing treatment at 350°C results in large orientation spread between the LD and CD, weakening the overall texture intensity from 6 MRD in the as-deformed state to 4 MRD in the annealed one. Further increase in the annealing temperature to 450°C, results in complete disappearance of the basal texture component that was visible in the as deformed and lower annealing temperature conditions. The orientations mostly lay within LD and CD with an angular spread of ± 30°. The texture intensity was further weakened with the maximum value dropping to 3 MRD.

Light microscopy investigations indicated heavily twinned microstructures in the as-deformed condition. Annealing at 350°C led to a partially recrystallized microstructure comprising of equiaxed grains as well as twinned regions. At higher annealing temperatures, a combination of large and small grain clusters describe the whole grain topology. Secondary phases, identified in earlier works as Zr-rich clusters (Basu and Al-Samman, 2014), are additionally observed as heterogeneously distributed all throughout the microstructure (c.f. **Figures 2B**, **3**). It must be noted that Gd was existing entirely in solid solution in the microstructure. The size ranges vary from particles being larger than 1 µm (ideal for stimulating recrystallization) to small ones that are < 1 µm (contribute toward grain boundary pinning; Humphreys and Hatherly, 2004).

Hierarchical Twinning and Non-basal Slip

In order to assess the characteristics and nature of deformation twins as well as the associated dislocation sub-structure generation, in depth EBSD analysis was employed to obtain simultaneously topological, orientation and strain information. **Figure 4A** shows the overall strain distribution in the as-deformed ZEK110 alloy by means of a kernel average misorientation (KAM) map. The black regions correspond to the unindexed areas and they systematically correspond to the Zr rich secondary phases present in the microstructure. The KAM physically describes the misorientation of a reference pixel i.e., kernel center, with respect to the nearest neighbor pixels lying in the defined kernel size. Since the degree of location crystal lattice rotation is directly proportional to the local shear strain, the KAM map also represents the local strain distribution in the microstructure. In the present case, a threshold KAM value of 2°

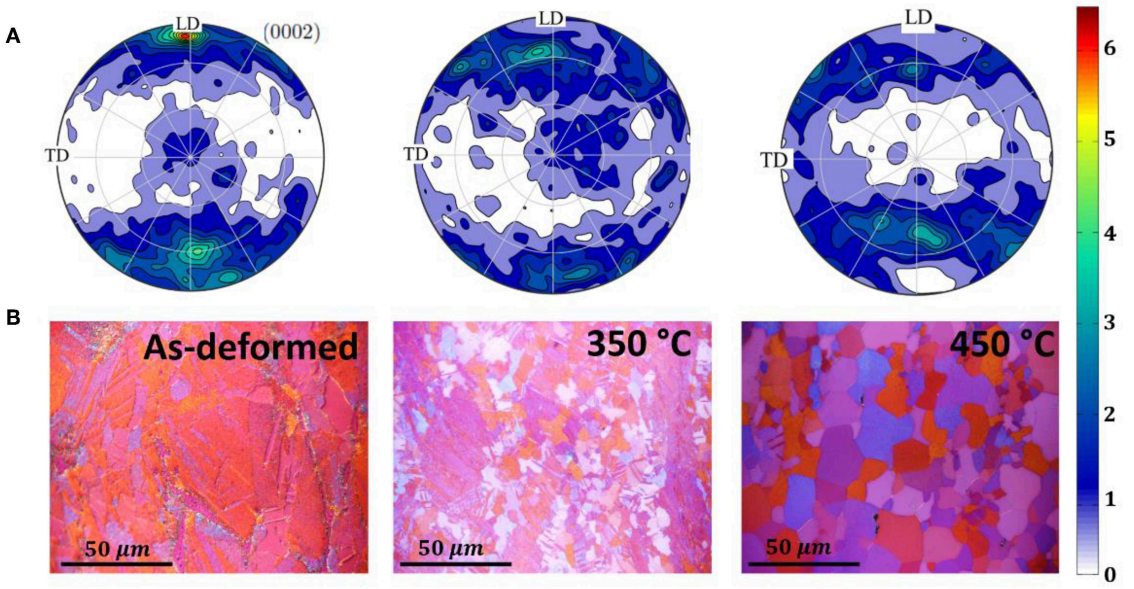

FIGURE 2 | (0002) recalculated pole figures from XRD **(A)**, and optical microstructures **(B)** after plane strain compression to 6% true strain, and static annealing treatments for 60 min at 350 and 450°C for ZEK110.

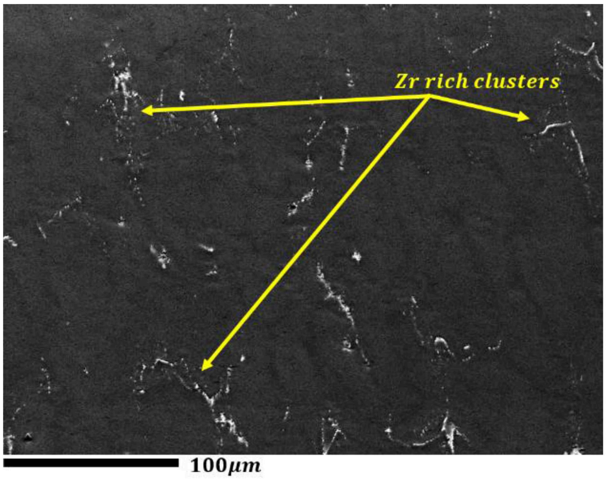

FIGURE 3 | Precipitate characterization and distribution in the ZEK110 alloy in the as-deformed state; the precipitates compositionally confer with Zr-rich phases that have been previously identified in Basu and Al-Samman (2014).

was implemented for a kernel size upto the 2nd nearest neighbor (Basu et al., 2017). **Figure 4B** displays the image quality map with grain boundaries overlaid with the definite twin axis/angle misorientation relationships. In this respect, the indexed twin boundaries in different colors revealed $\{10\bar{1}2\}$ extension twins (highlighted in red), $\{10\bar{1}1\}$ compression twins (blue) as well as $\{10\bar{1}1\} - \{10\bar{1}2\}$ double twins (yellow). An angular deviation of ±6° in the misorientation was accounted for. **Figure 4C** provides a magnified KAM map for the highlighted region in **Figure 4A**, depicting a strong KAM contrast. The local strain appears to systematically accumulate along slip bands (colored bright green) that correspond to $\{11\bar{2}2\}$ pyramidal <c+a> slip traces as corroborated by the image quality map shown as an inset image on the top left corner of **Figure 4C**. **Figure 4C** also reveals that the observed slip bands originate primarily near the detected $\{10\bar{1}1\} - \{10\bar{1}2\}$ double twin. The other inset of an inverse pole figure (IPF) map, with the viewing axis along the CD, indicates in-grain orientation gradients involving rotation of the $\{11\bar{2}2\}$ plane parallel to the plane of compression (c.f. yellow colored matrix in the IPF map in **Figure 4C**), thereby corroborating the existence of pyramidal <c+a> dislocation activity.

While grain boundaries play a critical role in terms of defect nucleation sites, there contribution as obstacles to dislocation motion directly influences the ease of plasticity and the degree of material strengthening that has been frequently addressed as the Hall-Petch effect. However, it must be understood that the strengthening potential of a grain boundary is strongly dependent upon the nature of dislocation-grain boundary interaction, whereby the grain boundary can (i) either act as an impenetrable barrier to dislocation motion (no transfer) leading to dislocation pile-ups and localized rotations or (ii) facilitate complete transfer of slip between two neighboring grains. This aspect is strongly influenced by the dislocation character as well as the grain boundary crystallography. A geometrical assessment of the feasibility of dislocation transfer across grain boundaries can be described via the slip transfer parameter (m') value, given as: $m' = (\mathbf{n_1} \cdot \mathbf{n_2}) \times (\mathbf{b_1} \cdot \mathbf{b_2})$, where $\boldsymbol{n_1}$ and $\boldsymbol{n_2}$ are the normalized intersection lines common to the active slip planes and the boundary plane, and $\boldsymbol{b_1}$ and $\boldsymbol{b_2}$ are the normalized slip directions in the pile-up and emission grains (Shen et al., 1988; Clark et al., 1992). While the first expression on the right hand side corresponds to the alignment of the slip planes, the

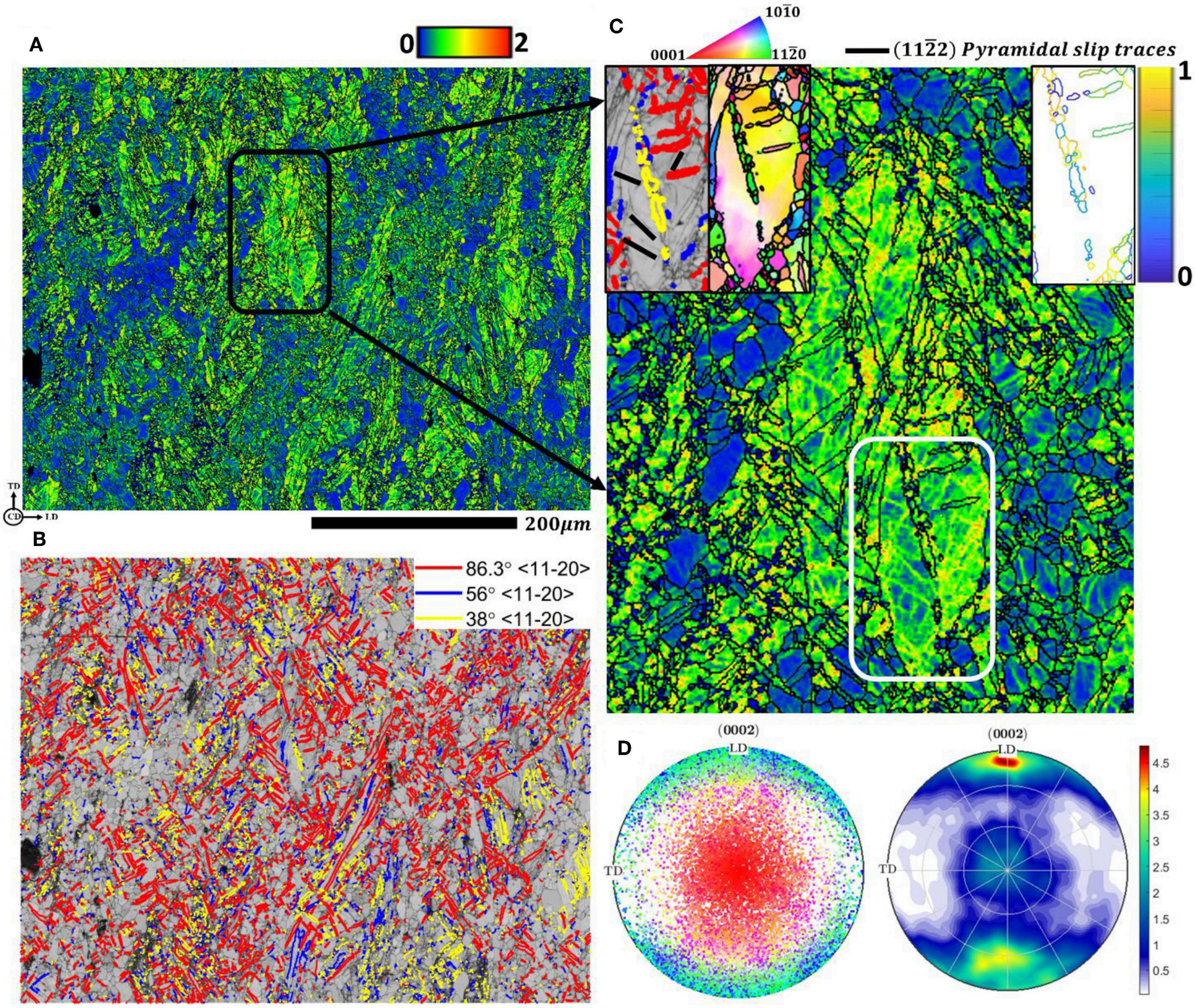

FIGURE 4 | (A) Kernel average misorientation map corresponding to ZEK110 deformed to 6% strain under plane strain compression, **(B)** corresponding image quality map with twin boundaries as {10$\bar{1}$2} extension twins (highlighted in red), {10$\bar{1}$1} compression twins (blue) as well as {10$\bar{1}$1} – {10$\bar{1}$2} double twins (yellow); **(C)** magnified image of the area highlighted in this figure. Corresponding inverse pole figure map as inset on the top left corner and the map showing the grain boundaries colored with respect to the degree of transparency to (11$\bar{2}$2 < 11$\bar{2}$3 > pyramidal slip transmission. Red lines overlaid on the map confer with (11$\bar{2}$2) pyramidal slip traces. Grain boundaries larger than 3° are shown in black. **(D)** (0002) single orientation scatter data and recalculated pole figures for the EBSD map shown in **(A)**.

second expression is related to the alignment of the incoming and outgoing slip directions. The higher the m' value, the easier is the slip transfer, and obviously, the lower is the stress concentration and dislocation pile-up at the boundary. The inset map on the top right corner in **Figure 4C** displays grain boundaries colored with respect to the corresponding m' values calculated for {11$\bar{2}$2} pyramidal <c+a> slip system as the active slip mode. Bright yellow and greenish yellow colors indicate easier slip transmission, while dark blue colored boundaries resist slip transfer i.e., block dislocation motion across the boundary. Large segments of the double-twin/parent interface in **Figure 4C** being primarily highlighted by green-yellow and yellow colors indicate that slip transfer of <c+a> dislocations across the twin boundary is geometrically favorable. The implications of such observations on the plasticity behavior in lean magnesium-rare earth alloys will be discussed later.

Apart from the presence of extension twins, in-plane compression also resulted in considerable amounts of compression twinning and higher order twin structures appearing throughout the microstructure. The likelihood of appearance of compression twins can be attributed to the larger spread of orientations about the LD, whereby certain grain orientations can experience c-axis compression arising from the lateral compressive stresses due to the die walls (Basu and Al-Samman, 2015, 2017). Moreover, the presence of pyramidal slip (as seen in **Figure 4C**) could also lead to dynamic reorientation of the parent grains during straining, whereby parts of the grains in due course start experiencing a compressive stress component along c-axis from the loading direction. The second aspect regarding the ease of nucleation of compression twins is attributed to the presence of Gd and Zn as solutes. On one hand, addition of solute REs facilitate the reduction of overall stacking fault energies of higher order planes such that nucleation of compression twin faults becomes relatively easier (Li and Ma, 2009; Sandlöbes et al., 2012), whereas on the other side the co-segregation and formation of Zn-Gd dimers (Nie et al., 2013) could effectively increase the activation energy of atomic shuffling processes that dictate tensile twin formation. Infact, similar observations were reported for Mg-Y alloys, wherein retarded atomic shuffling in $\{10\bar{1}2\}$ extension twins was attributed to the larger shuffling energies owing to the bigger Y atoms in the matrix (Stanford et al., 2015). Both these factors have been seen to result in competitive nucleation stresses for both $\{10\bar{1}2\}$ extension and $\{10\bar{1}1\}$ compression twin formation.

A more peculiar aspect that is evident during deformation of the current alloy is the appearance of higher order twinned structures i.e., hierarchical twin formation, whereby numerous instances of 3rd generation twins are observed. **Figure 5** illustrates different cases of such hierarchical twinning observed in the as deformed ZEK110. The parent grain in **Figure 5A** exhibits all three twin types i.e., extension, compression, and double twins. The double twins additionally undergo $\{10\bar{1}2\}$ extension twinning giving rise to two different twin variants shown in red ($\mathrm{TT1_{DT_{1P}}}$) and green ($\mathrm{TT2_{DT_{1P}}}$). In conventional Mg alloys, the red twin corresponds to the high Schmid factor variant and the green twin is associated with the low Schmid factor variant. The former shows a higher chance of nucleating primarily due to anisotropy in slip behavior in pure Mg, wherein strain accommodation is easier for the red twins in comparison to the green twins (Basu and Al-Samman, 2015). However, the appearance of both twin variants in rather equal proportions evinces to a non-Schmid twinning behavior prevalent in the present alloy that most likely arises from more homogeneous deformation behavior. In case of **Figure 5B**, a large compression twin ($\mathrm{CT_P}$) is shown to undergo both extension ($\mathrm{TT_{CT_P}}$) as well as compression twinning ($\mathrm{CT_{CT_P}}$). The broad non-twin like morphology of the primary compression twin ($\mathrm{CT_P}$) in **Figure 5B** develops from slip-induced coalescence of large number of individual compression twins nucleating adjacent to each other, indicated by the white arrows in the image on the left (c.f. **Figure 5B**). The 2nd generation compression twin ($\mathrm{CT_{CT_P}}$) further twins under a non-zero tensile stress component along the c-axis to give rise to a double twin relationship with the parent compression twin ($\mathrm{DT_{CT_P}}$).

Figure 6 shows another region comprising 3rd generation twins, wherein a compression twin $'\mathrm{CT}'_{\mathrm{DT_P}}$ forms inside a double twin $'\mathrm{DT}'_{\mathrm{P}}$ (c.f. **Figure 6A**). Interestingly, since the twins rotate the crystal about the same $< 11\bar{2}0>$ axis, the formation of compression twin inside a double twin results in creation of a new interface that is misoriented with respect to the original parent grain (P) by 13 about the $<11\bar{2}0>$ axis (c.f. misorientation profile along AB in **Figures 6B,E**). **Figure 6C** shows the grain-reference orientation- deviation (GROD) map corresponding to the same region, indicating large orientation gradients next the grain boundary from where the higher order compression twin seems to nucleate. **Figure 6D** displays the single orientation scatter data indicating the appearance of diverse orientations due to the formation of complex twinning structures within the same parent grain.

Using the kernel average misorientation data, the local geometrically necessary dislocation density values corresponding to the primary slip can be calculated using the strain gradient approach (Kubin and Mortensen, 2003; Konijnenberg et al., 2015) given as: $\rho_{\boldsymbol{GND}} = \frac{2\theta}{n\lambda}|\boldsymbol{b_d}|$, where, θ is the experimentally measured KAM value, λ is the step size (in the present case 300 nm), n is the number of nearest neighbors averaged in the KAM calculation (in the current case 2nd nearest neighbor) and $\boldsymbol{b_d}$ is the Burgers vector corresponding to the primary slip direction, which in the current case is attributed to basal <a> slip. The GND values corresponding to <c+a> slip are estimated by performing a crystallographic decomposition of the Nye tensor obtained from the local lattice curvature values extracted from EBSD (Nye, 1953; Field et al., 2005; Ruggles and Fullwood, 2013; Konijnenberg et al., 2015). The Nye tensor ($\propto_{ij}$) describes the contribution to geometrically necessary dislocation content from multiple slip systems that are needed to accommodate a given rotation in the crystal lattice and is mathematically expressed as, $\propto_{ij} = \sum_m \rho^m \boldsymbol{b}_i^m \boldsymbol{z}_j^m$, $\boldsymbol{b}_i^m$ and $\boldsymbol{z}_j^m$ are Burgers vector and slip plane normal for slip system m and ρ^m is dislocation content for the slip system m. The variation of the 2D–GND values for both <a> and <c+a> slip are represented in **Figure 6F**. Corresponding GND maps for both basal and pyramidal slip are indicated to the right of the plot in **Figure 6F**. The values indicate only an order of magnitude difference in dislocation density values between basal <a> and pyramidal <c+a> slip near the grain boundary (c.f. calculated GND density gradient along line $'\mathbf{1-2}'$ shown in **Figure 6C** and bottom image in **Figure 6F**). It is worthwhile to mention that the GND values from the strain gradient and lattice curvature approaches provide a lower bound estimate since it incorporates the contributions of only non-paired edge dislocation segments and dislocation walls, which result in an effective unclosed burgers circuit giving rise to a net non-zero misorientation. Moreover, experimental 2D EBSD data can provide only 5 terms of the Nye tensor viz. $\propto_{ij}$. This implies that dislocation densities from a maximum of five independent dislocation systems can be resolved, whereas the effective set size of available slip systems in a hexagonal close packed material is 21, indicating that above approach underdetermines the complete dislocation content from individual slip systems. It is expected that a more accurate estimate of GND values feasible from 3D data sets would therefore lead to much higher densities that directly correlate to large local internal stresses that contribute to twin nucleation. However, the current values provide a qualitative estimate of the dislocation density contributions from basal and non-basal slip modes. The ease of non-basal <c+a> slip further elucidates the preferred nucleation of compression type

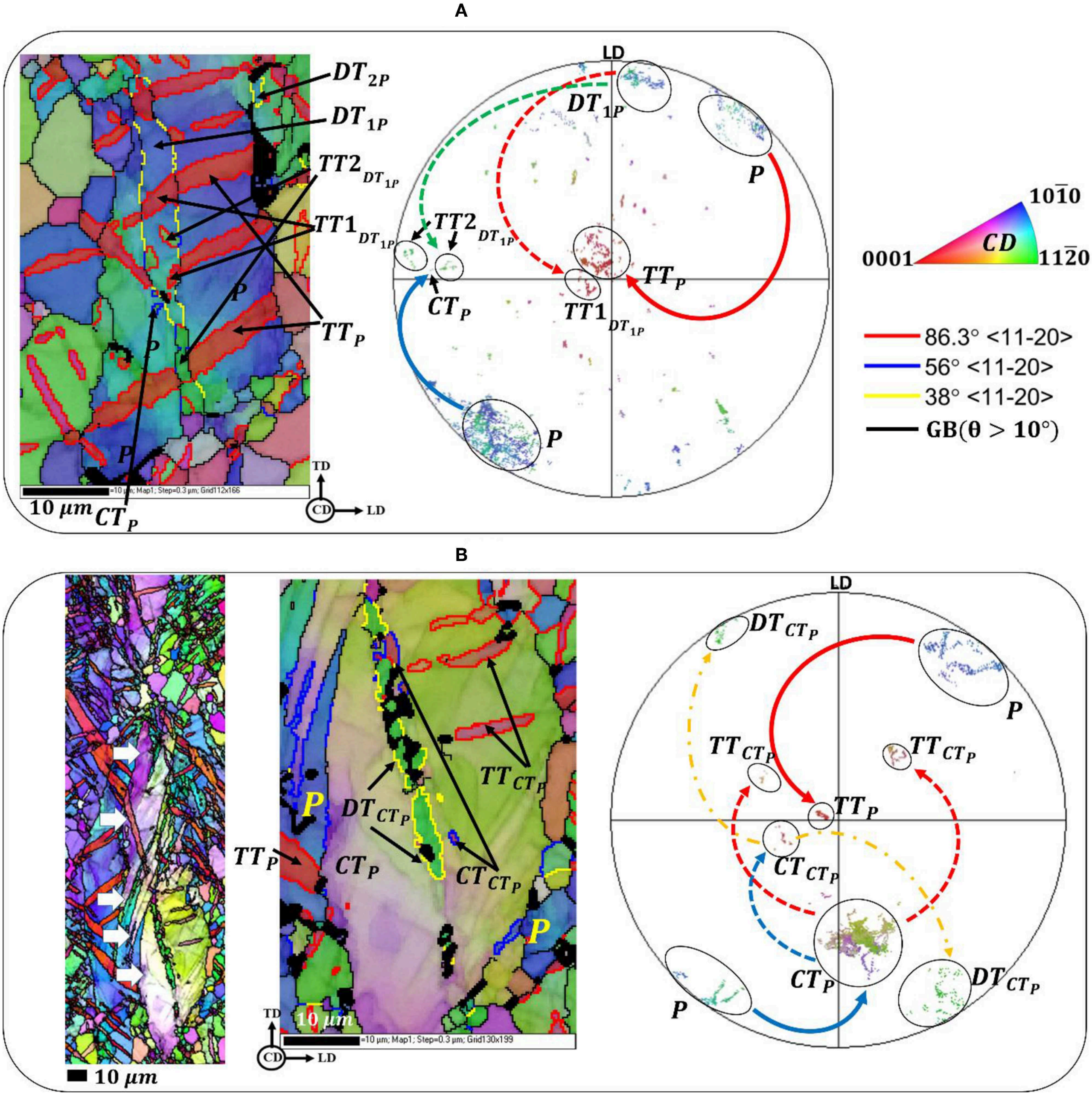

FIGURE 5 | Inverse pole figure maps and corresponding single orientation scatter data indicating different instances of hierarchically twinned structures comprising nested twins in ZEK110. The colored arrows in the single orientation scatter plots indicate the crystallographic rotation of the parent grains because of twinning. Grain boundaries larger than 10 are highlighted in black. Twin boundaries are shown as $\{10\bar{1}2\}$ extension twins (highlighted in red), $\{10\bar{1}1\}$ compression twins (blue) as well as $\{10\bar{1}1\} - \{10\bar{1}2\}$ double twins (yellow). White arrows in left most image in **(B)** indicate the remnant sections of individual compression twins that nucleated next to each other and coalesce through dislocation slip to form a broad compression twinned region.

twinning rather than formation of extension twins, which are typically the most favored twin type in pure Mg. In terms of microstructural design, it is proposed that such hierarchically twinned microstructures are extremely beneficial in terms of designing high strength-high ductility microstructures, wherein twin induced grain fragmentation results in simultaneous grain refinement, and generation of new and diverse orientations (c.f. as shown in the single orientation scatter plots and the IPF maps in **Figure 5**).

The existence and stability of such higher order twins in the current alloy are attributed to: (i) interaction of second phase particles with twins and (ii) local dislocation activity.

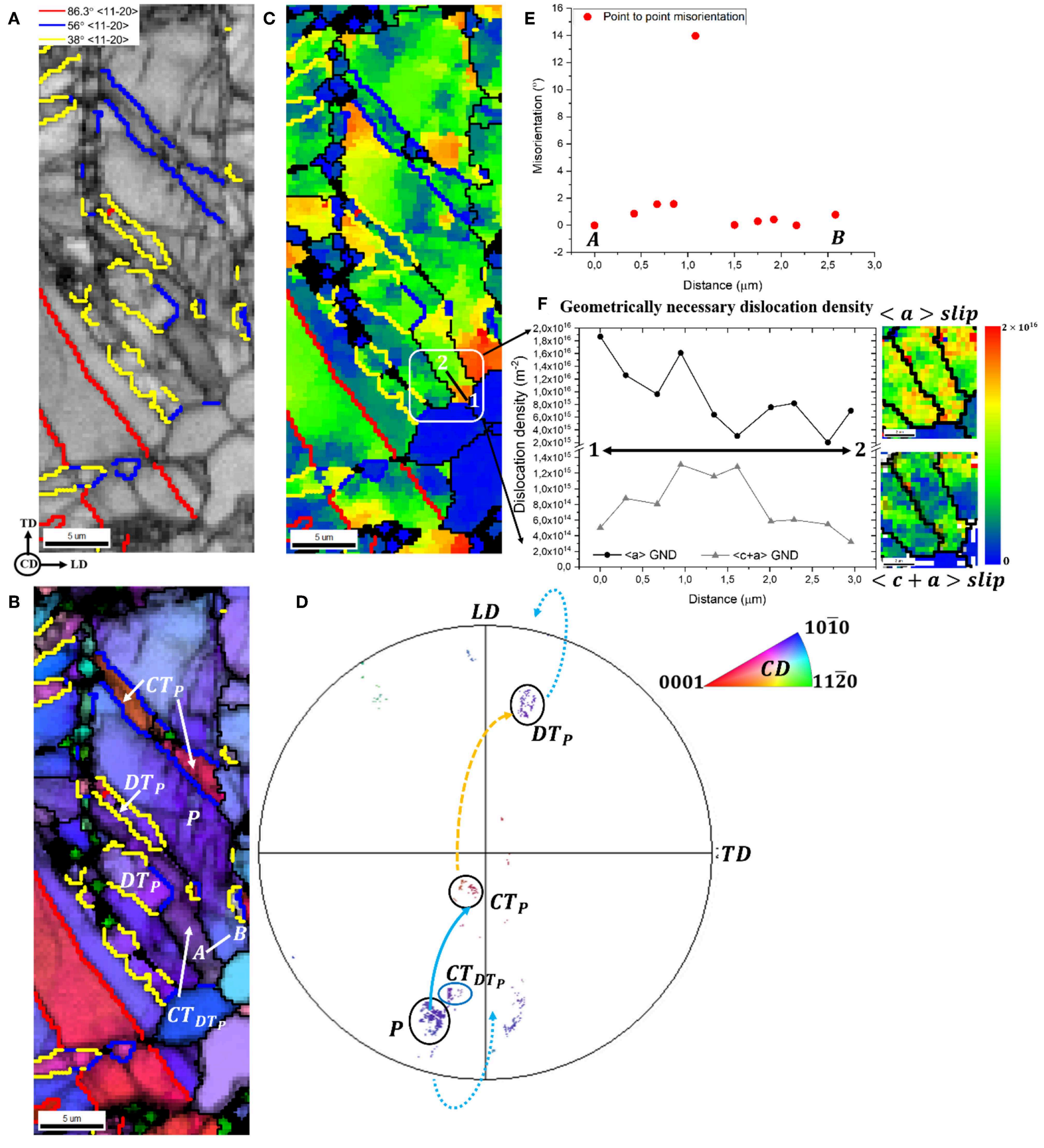

FIGURE 6 | **(A)** Image quality, **(B)** inverse pole figure, and **(C)** grain reference orientation deviation maps, showing formation of hierarchically twinned structures described by a $\{10\bar{1}1\}$ compression twin nucleating inside $\{10\bar{1}1\} - \{10\bar{1}2\}$ double twin. **(D)** Single orientation scatter data indicating the twin induced reorientations; **(E)** misorientation profile across the boundary (line AB) between the 3rd generation compression twin and the original parent grain; **(F)** geometrically necessary dislocation density gradients for <a>-type and <c+a> type slip near the grain boundary along line *1–2* are plotted as a function of distance; basal and pyramidal dislocation density maps are additionally shown to the right of the plot.

While Zr rich particles can retard twin growth severely, they also generate very high local stress states that can facilitate twin nucleation (Basu and Al-Samman, 2015). Quite contrarily, such high local stresses in pure Mg would typically result in crack nucleation rather than twins, primarily due to the large anisotropy in slip behavior. **Figure 7** shows the number of

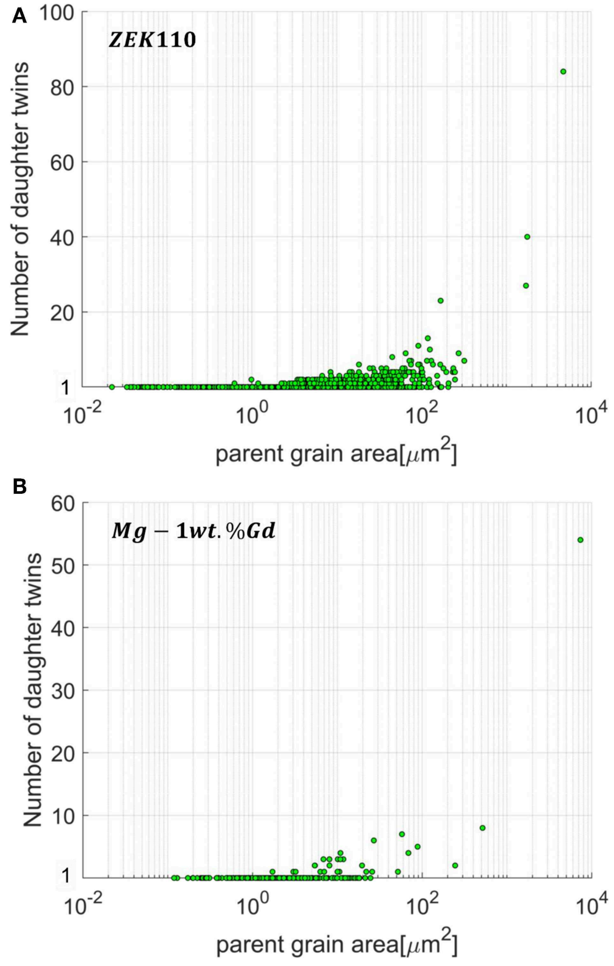

FIGURE 7 | Number of first generation twins per parent as a function of grain size for **(A)** ZEK110 and **(B)** Mg-1Gd from Basu and Al-Samman (2017).

daughter twins per grain as a function of the grain size for the ZEK110 alloy vis-a-vis solid solution Mg-1Gd alloy under the same deformation conditions. The trends indicate much higher overall twin number densities in the quaternary alloy with the number of twins nucleated in the largest grains being 1.5 higher than in the binary counterpart. The plot further indicates that the majority of the grains measured in the ZEK110 alloy nucleated multiple twins as opposed to most grains in the binary Mg-1Gd alloy comprising of only one daughter twin. It must be noted that the number of twins detected per grain in **Figure 7** only accounts for first generation twins, wherein the parent and twinned region can be distinctly identified. It is expected that the presence of more complex higher order twin structures would indicate that the realistic values of twin number density would be much higher than that measured. Nevertheless, the findings clearly address the dominance of twin nucleation in the quaternary alloy.

In order to accommodate the local strains around the twinned regions in the ZEK 110 alloy the role of dislocation slip is critical, wherein anisotropic slip behavior dominated by basal <a> slip can adversely affect local plasticity by creating regions of large strain incompatibility in and around such hierarchical twinned structures that would typically promote failure. However, the presence of non-basal dislocation activity in the present alloy can overcome this issue and effectively sustain material ductility. **Figures 8A,B** indicate microstructural regions in the as-deformed state showing abundant non-basal slip activity. In order to simultaneously visualize local orientation as well as strain distribution, EBSD maps are depicted as inverse pole figure maps overlaid upon image quality maps. The regions of lower image quality correspond to formation of slip bands inside the grains. Regions comprising such slip bands are separately identified in **Figure 8A** and magnified to reveal the character of dislocation slip active in the as-deformed state (c.f. Reg. I, Reg. II, and Reg. III in **Figure 8A**). The slip traces corresponding to $\{11\bar{2}2\}$ pyramidal planes are overlaid on the images in black lines indicating that the slip band orientations marked by black arrows are associated with 2nd order pyramidal <c+a> slip. Since pyramidal slip possesses five independent deformation modes as opposed to basal <a> slip that offers only two independent slip systems, the overall grain and twin co-deformation becomes much more homogeneous in the presence of <c+a> slip activity. This is validated by the large fraction of yellow and green colored grain boundaries, favoring pyramidal slip transfer across parent-twin interfaces (c.f. **Figures 8A,B**). On the other hand grain boundary strain transfer map for basal slip transfer indicates more blue colored boundaries (as shown in the basal <a> slip transfer map for the parent-twin interface enclosed in **Figure 8B**), thereby indicating that the same parent-twin interface can act as a strong barrier to the motion of basal <a> dislocations, shown by purple arrows. The corresponding local strain distribution (KAM map) shows larger local misorientations (higher strains) at the parent-twin interface (see lower right inset image in **Figure 8B**) that most likely corresponds to pile-up of basal dislocations at the twin boundary. The findings further indicate that while non-basal <c+a> slip contributes to enhanced plasticity, the activation of basal slip facilitates strengthening by piling-up at the newly formed parent-twin interfaces, thereby giving rise to a twinning induced dynamic Hall-Petch effect.

Recrystallization and Grain Growth Behavior

Figure 9 presents the EBSD analysis for annealing microstructure corresponding to heat treatment at 350°C for 60 min. **Figure 9A** indicates that the microstructure is partially recrystallized, highlighted by a distribution of recrystallized grains as well as still deformed regions comprising of non-recrystallized tension twins (boundaries highlighted in red). **Figure 9B** displays the corresponding (0002) pole figure. The EBSD texture indicates good agreement with the macro texture measured using XRD. In order to assess the contributions of the recrystallized and non-recrystallized grains to the overall orientation distribution, the EBSD map was classified into recrystallized (RXed) and un-recrystallized (un-RXed) areas.

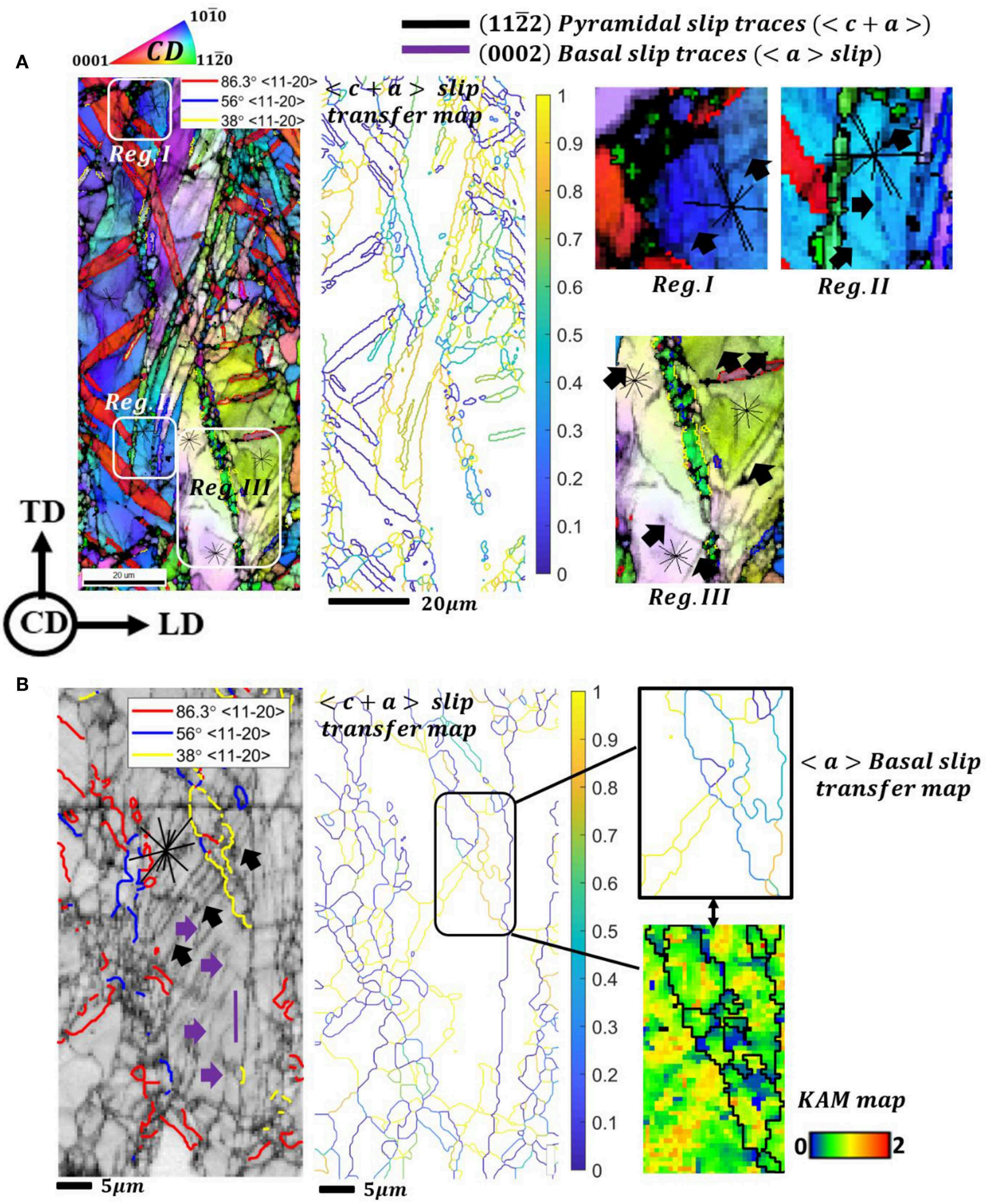

FIGURE 8 | Microstructural regions shown as inverse pole figure maps and grain boundary slip transmission map, **(A,B)** in the as-deformed ZEK110 alloy showing profuse $(11\bar{2}2) < 11\bar{2}3 >$ pyramidal slip (indicated by black slip traces) and secondary $(0001) < 11\bar{2}0 >$ basal slip (shown in purple slip traces) both inside the parent as well as twinned areas. Regions in **(A)** are magnified, indicating a good agreement of the observed slip traces in matrix and twinned regions with $(11\bar{2}2) <11\bar{2}3>$ pyramidal slip. The grain-boundary slip transfer maps in **(A,B)** correspond to $(11\bar{2}2) <11\bar{2}3 >$ pyramidal slip. The slip transmission map on the right hand side in **(B)**, describes the favorability of transfer of $(0001) <11\bar{2}0 >$ basal dislocations across the twin/grain boundaries in the region of interest highlighted by the black window. The bottom right image in **(B)** depicts the kernel average misorientation (KAM) map of the area of interest.

Figure 9C displays the recrystallized and non-recrystallized regions of the microstructure. RXed grains were characterized with a grain orientation spread (GOS) value within 2 and simultaneously possessing a grain boundary misorientation larger than 10°. The corresponding single orientation scatter plots for the RXed and un-RXed subsets are shown as inset on the top-left corner. The orientation spread indicates a higher density of orientations lying between the LD and CD for the recrystallized subset. These orientations typically correspond to those generated by compression twins and higher order twins,

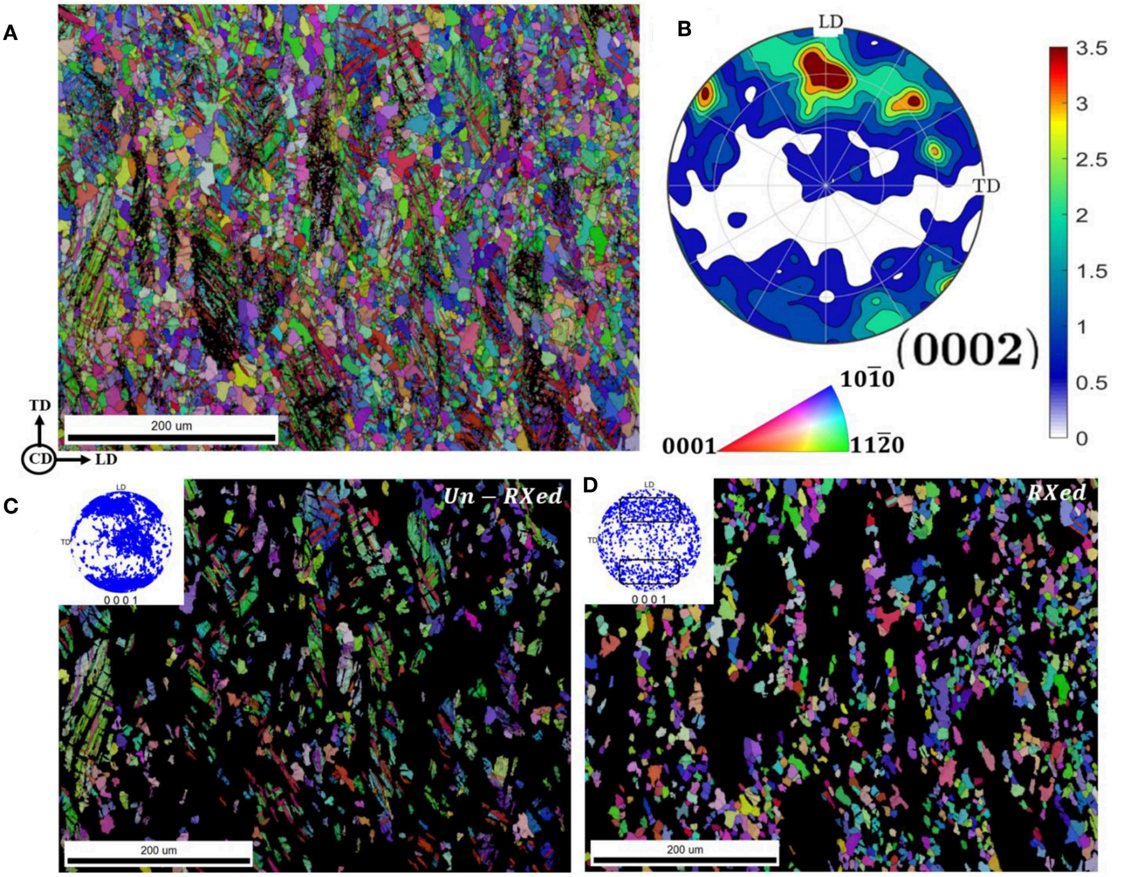

FIGURE 9 | EBSD map at 350°C (60 min annealing time) indicating a partially recrystallized microstructure, **(A)** inverse pole figure map, **(B)** recalculated (0002) pole figure, **(C,D)** show the recrystallized and un-recrystallized subsets. Corresponding single orientation scatter for recrystallized and un-recrystallized regions are shown as inset plots on the top left corner.

indicating that the compression and higher generation twins recrystallize earlier owing to larger local stored energy. This is quite likely attributed to more active <c+a> slip in the regions that are required to accommodate local strains arising from twin formation. Pyramidal slip activity near twins is critical for nucleation of compression twinning as its formation is shear dominated i.e., twin formation is driven by glide of twinning disconnections, in comparison to extension twins, where twin propagation and growth occurs primarily by atomic shuffling (Li and Zhang, 2014; Basu and Al-Samman, 2015). Presence of <c+a> slip with a Burgers vector $'\boldsymbol{b}'$ much larger than those of basal deformation modes not only increases the local stored dislocation energy ($E_{dis} \propto G\boldsymbol{b}^2$) but also provides a non-planar dislocation network that is necessary for generation of recrystallized nuclei/grains.

In case of the deformed subset, the orientations mostly conformed with the initial parent grains and extension twins that were still resistant to recrystallization. This is attributed to the tendency of the extension twins during deformation to grow via. atomic shuffling rather than deform by slip under applied stress, whereby dislocation activity is abated and subsequently leading to an absence of well-defined deformation substructure inside the twins that can potentially recrystallize under thermal activation. Moreover, the tendency of Zn-Gd dimers to segregate at the boundaries under thermal activation further drags the recrystallization process, whereby the twin boundaries are unable to recrystallize nor grow during annealing (Basu and Al-Samman, 2015). Apart from the extension-twinned regions, the vicinity of particles also did not show traces of recrystallization owing to insufficient thermal activation at 350°C.

Figure 10 indicates the microstructure after annealing for 60 min at 450°C. The microstructure indicates a clear bimodal grain size distribution with the presence of large grains and clusters of very small grains (c.f. **Figure 10A**) in the vicinity of certain unindexed areas that systematically correspond to the Zr-rich phases (c.f. yellow arrows in **Figure 10B**). The calculated texture from the EBSD data indicates an absence of basal orientations and majority of the grains with their c-axis aligned between the LD and CD along with a lateral spread of orientations along the TD. As mentioned previously, these orientations correspond to compression twins and higher generation twins. The findings indicate that the orientations

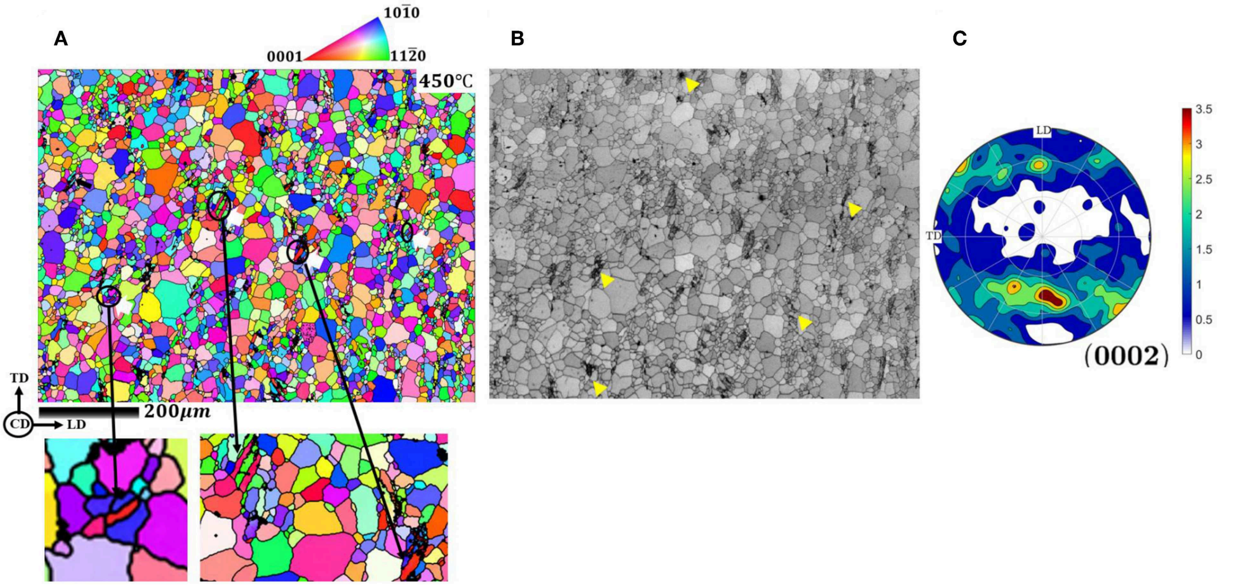

FIGURE 10 | EBSD map (at 450°C for 60 min) in inverse pole figure coloring **(A)** and image quality **(B)** color coding. Recalculated (0002) pole figure shown in **(C)**. Portions in **(A)** are zoomed in to shown the still un-recrystallized twins, marked by white arrows in **(A)**. Yellow markers in **(B)** indicate the fine grains recrystallizing near Zr-rich particle clusters.

nucleating inside the compression and higher order twins preferably undergo recrystallization and grain growth at higher annealing temperatures, thereby consuming the un-recrystallized parent grains and the majority of extension twins. Few extension twins are still visible after annealing at 450°C that seem to neither grow nor recrystallize (indicated by white arrows in **Figure 10A**). The particles generate recrystallized grains in their vicinity that give rise to the smaller grain clusters, however they seem to lack sufficient driving force to grow. The selective growth behavior in the current ZEK110 alloy is known to be an outcome of the dual effect of solute drag due to Gd-Zn solute pairs as well as Zener pinning from the finer Zr rich phases present in the microstructure (Basu and Al-Samman, 2014). The presence of such grain boundary pinning agents leads to a clear demarcation in grain sizes, wherein the smaller grains from particle stimulated recrystallization as well as extension twins possess insufficient energy to overcome the impending solute drag and particle pinning effects. On the other hand, the orientations from regions of higher stored energies are able break free of such drag effects and grow larger, subsequently dominating the overall orientation spectrum.

Implications in Terms of Microstructural Design of Lean Magnesium Alloys

The current observations are critical with respect to exploiting twinning in magnesium in order to tailor high strength-high ductility microstructures. The generic perception regarding twinning deformation in conventional Mg alloys is always associated with poor ductility response, owing to the large shear incompatibility generated near twin-parent interfaces. However, the current work reveals that through appropriate alloying strategies twinning as a deformation mode can be effectively utilized to not only accommodate imposed strain but also impart dynamic Hall-Petch strengthening.

With the means of RE-additions in conjunction with Zn and Zr, the influence of solutes as well as secondary phases on twinning behavior are favorably triggered to engineer failure resistant microstructures. From the literature, the presence of solute Zn and RE atoms contribute in intrinsically modifying basal and non-basal stacking fault energies, thereby promoting pyramidal slip as a dislocation mode as well as giving rise to a more competitive twin nucleation behavior in terms of extension and compression type twins. Simultaneously the role of Zr rich secondary phases becomes critical in severely restricting twin growth on one side and on the other hand contributing toward increasing the local stresses in the matrix to facilitate nucleation of compression twins. The superposition of both these factors contributes toward generating hierarchically twinned microstructures that not only give rise to a large orientation spread i.e., weak and deformable textures that are sustained during recrystallization and grain growth, but also promote dynamic grain fragmentation that imparts additional grain boundary hardening via. dynamic Hall-Petch mechanism.

CONCLUSIONS

Twinning induced deformation and subsequent annealing response is investigated for Mg-1wt.% Zn-1wt.% Gd-0.6wt.% Zr rolled alloy under plane strain compression perpendicular to the c-axis. It is shown that the role of non-REs can not only augment RE-solute effects on the overall deformation and annealing response but also play a significant role as secondary phases on impacting twinning behavior. Microstructures with hierarchical twins and profuse non-basal slip are observed. The following key conclusions are derived at,

a) Plane strain compression, despite normal to the c-axis, resulted in profuse amounts of both compression and extension type twins. Large amounts of 2nd and 3rd generation twins with a hierarchical morphology are present throughout the microstructure, giving rise to simultaneous grain fragmentation and large orientation spreads.
b) Twin growth is severely restricted by the Zr rich secondary phases and on the other hand local stress states near particles and grain boundaries promote twin nucleation.
c) Nested twin structures are supplemented with abundant $\{11\bar{2}2\}$ pyramidal <c+a> slip in and around the twin-parent interfaces. While <c+a> slip accommodates the local plastic shear across the newly formed twin boundaries, basal slip tends to accumulate at the interfaces resulting in local dislocation pile-up and contributing to the overall grain boundary strengthening.
d) Recrystallization and grain growth preferentially occur inside the compression and higher order twin structures that overcome solute and particle pinning effects, whereas the recrystallized grains nucleating around particles and recovered extension twins remain pinned even at higher annealing temperatures.
e) The implications of the current study are critical with respect to exploiting twinning to design high strength-high ductility lean Mg alloys.

DATA AVAILABILITY

The datasets generated for this study are available on request to the corresponding author.

AUTHOR CONTRIBUTIONS

IB designed the study, performed the experiments, and wrote the manuscript. IB and TA-S performed the data analysis and scientific interpretation of the work and made critical revisions to the article.

ACKNOWLEDGMENTS

The financial support of the Deutsche Forschungsgemeinschaft (DFG) (AL 1343/1-2) is gratefully acknowledged. The authors are grateful for Aniruddha Dutta for his assistance in the experiments.

REFERENCES

Ahmad, R., Wu, Z., Groh, S., and Curtin, W. A. (2018). Pyramidal II to basal transformation of $\langle c + a\rangle$ edge dislocations in Mg-Y alloys. *Scripta Mater.* 155, 114–118. doi: 10.1016/j.scriptamat.2018.06.026

Ahmad, R., Yin, B., Wu, Z., and Curtin, W. A. (2019). Designing high ductility in magnesium alloys. *Acta Mater.* 172, 161–184. doi: 10.1016/j.actamat.2019.04.019

Al-Samman, T., and Li, X. (2011). Sheet texture modification in magnesium-based alloys by selective rare earth alloying. *Mater. Sci. Eng. A* 528, 3809–3822. doi: 10.1016/j.msea.2011.01.080

Aydiner, C. C., Bernier, J. V., Clausen, B., Lienert, U., Tomé, C. N., and Brown, D. W. (2009). Evolution of stress in individual grains and twins in a magnesium alloy aggregate. *Phys. Rev. B* 80:024113. doi: 10.1103/PhysRevB.80.024113

Basu, I., and Al-Samman, T. (2014). Triggering rare earth texture modification in magnesium alloys by addition of zinc and zirconium. *Acta Mater.* 67, 116–133. doi: 10.1016/j.actamat.2013.12.015

Basu, I., and Al-Samman, T. (2015). Twin recrystallization mechanisms in magnesium-rare earth alloys. *Acta Mater.* 96, 111–132. doi: 10.1016/j.actamat.2015.05.044

Basu, I., and Al-Samman, T. (2017). Competitive twinning behavior in magnesium and its impact on recrystallization and texture formation. *Mater. Sci. Eng. A* 707, 232–244. doi: 10.1016/j.msea.2017.09.053

Basu, I., Ocelík, V., and De Hosson, J. T. M. (2017). Measurement of spatial stress gradients near grain boundaries. *Scripta Mater.* 136, 11–14. doi: 10.1016/j.scriptamat.2017.03.036

Bohlen, J., Yi, S., Letzig, D., and Kainer, K. U. (2010). Effect of rare earth elements on the microstructure and texture development in magnesium–manganese alloys during extrusion. *Mater. Sci. Eng. A* 527, 7092–7098. doi: 10.1016/j.msea.2010.07.081

Clark, W. A. T., Wagoner, R. H., Shen, Z. Y., Lee, T. C., Robertson, I. M., and Birnbaum, H. K. (1992). On the criteria for slip transmission across interfaces in polycrystals. *Scripta Metal. Mater.* 26, 203–206. doi: 10.1016/0956-716X(92)90173-C

El Kadiri, H., and Oppedal, A. L. (2010). A crystal plasticity theory for latent hardening by glide twinning through dislocation transmutation and twin accommodation effects. *J. Mech. Phys. Solids* 58, 613–624. doi: 10.1016/j.jmps.2009.12.004

Field, D. P., Trivedi, P. B., Wright, S. I., and Kumar, M. (2005). Analysis of local orientation gradients in deformed single crystals. *Ultramicroscopy* 103, 33–39. doi: 10.1016/j.ultramic.2004.11.016

Hielscher, R., and Schaeben, H. (2008). A novel pole figure inversion method: specification of the MTEX algorithm. *J. Appl. Crystallogr.* 41, 1024–1037. doi: 10.1107/S0021889808030112

Hirsch, J., and Al-Samman, T. (2013). Superior light metals by texture engineering: optimized aluminum and magnesium alloys for automotive applications. *Acta Mater.* 61, 818–843. doi: 10.1016/j.actamat.2012.10.044

Hofstetter, J., Rüedi, S., Baumgartner, I., Kilian, H., Mingler, B., Povoden-Karadeniz, E., et al. (2015). Processing and microstructure–property relations of high-strength low-alloy (HSLA) Mg–Zn–Ca alloys. *Acta Mater.* 98, 423–432. doi: 10.1016/j.actamat.2015.07.021

Humphreys, F. J., and Hatherly, M. (2004). *Recrystallization and Related Annealing Phenomena.* Oxford, UK: Pergamon Press.

Kelley, E., and Hosford, W. (1968). Plane-strain compression of magnesium and magnesium alloy crystals. *Trans. Met. Soc. AIME* 242, 5–13.

Konijnenberg, P. J., Zaefferer, S., and Raabe, D. (2015). Assessment of geometrically necessary dislocation levels derived by 3D EBSD. *Acta Mater.* 99, 402–414. doi: 10.1016/j.actamat.2015.06.051

Kubin, L. P., and Mortensen, A. (2003). Geometrically necessary dislocations and strain-gradient plasticity: a few critical issues. *Scripta Mater.* 48, 119–125. doi: 10.1016/S1359-6462(02)00335-4

Li, B., and Ma, E. (2009). Pyramidal slip in magnesium: Dislocations and stacking fault on the {1011} plane. *Philos. Magaz.* 89, 1223–1235. doi: 10.1080/14786430902936707

Li, B., and Zhang, X. Y. (2014). Global strain generated by shuffling-dominated {1012}<1011> twinning. *Scripta Mater.* 71, 45–48. doi: 10.1016/j.scriptamat.2013.10.002

Lin, J., Wang, X., Ren, W., Yang, X., and Wang, Q. (2016). Enhanced strength and ductility due to microstructure refinement and texture weakening of the

GW102K alloy by cyclic extrusion compression. *J. Mater. Sci. Technol.* 32, 783–789. doi: 10.1016/j.jmst.2016.01.004

Molodov, K. D., Al-Samman, T., and Molodov, D. A. (2017). Profuse slip transmission across twin boundaries in magnesium. *Acta Mater.* 124, 397–409. doi: 10.1016/j.actamat.2016.11.022

Molodov, K. D., Al-Samman, T., Molodov, D. A., and Gottstein, G. (2014). Mechanisms of exceptional ductility of magnesium single crystal during deformation at room temperature: multiple twinning and dynamic recrystallization. *Acta Mater.* 76, 314–330. doi: 10.1016/j.actamat.2014.04.066

Mordike, B. L., and Ebert, T. (2001). Magnesium: properties — applications — potential. *Mater. Sci. Eng. A* 302, 37–45. doi: 10.1016/S0921-5093(00)01351-4

Nave, M. D., and Barnett, M. R. (2004). Microstructures and textures of pure magnesium deformed in plane-strain compression. *Scripta Mater.* 51, 881–885. doi: 10.1016/j.scriptamat.2004.07.002

Nie, J. F., Zhu, Y. M., Liu, J. Z., and Fang, X. Y. (2013). Periodic segregation of solute atoms in fully coherent twin boundaries. *Science* 340:957. doi: 10.1126/science.1229369

Noble, K. R. (2012). *Origins of strength and ductility in Mg-RE binary alloys*. (Doctoral dissertation). Available online at: http://hdl.handle.net/11375/11839

Nye, J. F. (1953). Some geometrical relations in dislocated crystals. *Acta Metall.* 1, 153–162. doi: 10.1016/0001-6160(53)90054-6

Peng, Q., Huang, Y., Kainer, K. U., and Hort, N. (2012). High ductile as-cast Mg–RE based alloys at room temperature. *Mater. Lett.* 83, 209–212. doi: 10.1016/j.matlet.2011.08.009

Qiao, H., Guo, X. Q., Oppedal, A. L., El Kadiri, H., Wu, P. D., and Agnew, S. R. (2017). Twin-induced hardening in extruded Mg alloy AM30. *Mater. Sci. Eng. A* 687, 17–27. doi: 10.1016/j.msea.2016.12.123

Ruggles, T. J., and Fullwood, D. T. (2013). Estimations of bulk geometrically necessary dislocation density using high resolution EBSD. *Ultramicroscopy* 133, 8–15. doi: 10.1016/j.ultramic.2013.04.011

Sandlöbes, S., Friák, M., Zaefferer, S., Dick, A., Yi, S., Letzig, D., et al. (2012). The relation between ductility and stacking fault energies in Mg and Mg–Y alloys. *Acta Mater.* 60, 3011–3021. doi: 10.1016/j.actamat.2012.02.006

Shen, Z., Wagoner, R. H., and Clark, W. A. T. (1988). Dislocation and grain boundary interactions in metals. *Acta Metal.* 36, 3231–3242. doi: 10.1016/0001-6160(88)90058-2

Stanford, N., Marceau, R. K. W., and Barnett, M. R. (2015). The effect of high yttrium solute concentration on the twinning behaviour of magnesium alloys. *Acta Mater.* 82, 447–456. doi: 10.1016/j.actamat.2014.09.022

Tonda, H., and Ando, S. (2002). Effect of temperature and shear direction on yield stress by 11$$bar 2$$2<$$overline 11 $$23> slip in HCP metals23> slip in HCP metals. *Metal. Mater. Trans. A* 33, 831–836. doi: 10.1007/s11661-002-0152-z

Trang, T. T. T., Zhang, J. H., Kim, J. H., Zargaran, A., Hwang, J. H., Suh, B. C., et al. (2018). Designing a magnesium alloy with high strength and high formability. *Nat. Commun.* 9:2522. doi: 10.1038/s41467-018-04981-4

Wang, X. J., Xu, D. K., Wu, R. Z., Chen, X. B., Peng, Q. M., Jin, L., et al. (2018). What is going on in magnesium alloys? *J. Mater. Sci. Technol.* 34, 245–247. doi: 10.1016/j.jmst.2017.07.019

Wu, Z., Ahmad, R., Yin, B., Sandlöbes, S., and Curtin, W. A. (2018). Mechanistic origin and prediction of enhanced ductility in magnesium alloys. *Science* 359:447. doi: 10.1126/science.aap8716

Wu, Z., and Curtin, W. A. (2015). The origins of high hardening and low ductility in magnesium. *Nature* 526:62. doi: 10.1038/nature15364

Yamashita, A., Horita, Z., and Langdon, T. G. (2001). Improving the mechanical properties of magnesium and a magnesium alloy through severe plastic deformation. *Mater. Sci. Eng. A* 300, 142–147. doi: 10.1016/S0921-5093(00)01660-9

Yoo, M. H. (1981). Slip, twinning, and fracture in hexagonal close-packed metals. *Metallurg. Trans. A* 12, 409–418. doi: 10.1007/bf02648537

Yoo, M. H., and Lee, J. K. (1991). Deformation twinning in h.c.p. metals and alloys. *Philos. Magaz. A* 63, 987–1000. doi: 10.1080/01418619108213931

Conflict of Interest Statement: The authors declare that the research was conducted in the absence of any commercial or financial relationships that could be construed as a potential conflict of interest.

frontiers in Materials

ORIGINAL RESEARCH
published: 20 August 2019
doi: 10.3389/fmats.2019.00201

Wide Range Mechanical Customization of Mg-Gd Alloys With Low Degradation Rates by Extrusion

Jochen Harmuth[1]*, *Björn Wiese*[1]*, *Jan Bohlen*[2], *Thomas Ebel*[1] and *Regine Willumeit-Römer*[1]

[1] Metallic Biomaterials, Institute of Materials Research, Helmholtz-Zentrum Geesthacht, Geesthacht, Germany, [2] Magnesium Innovation Centre MagIC, Institute of Materials Research, Helmholtz-Zentrum Geesthacht, Geesthacht, Germany

Currently, only a few magnesium alloys have been approved for implant applications. For biomedical purposes, the choice of the alloying elements is a critical parameter and rare earth elements have been proven to be mechanically suitable and biologically tolerable. In this comprehensive study, tailoring the mechanical properties of binary Mg-Gd alloys by indirect extrusion is shown to obtain a property profile that is applicable to different biomedical applications. Mg-2Gd, Mg-5Gd, and Mg-10Gd were solid solution treated before extrusion. For each alloy various combinations of extrusion temperature and speed were applied. Resulting effects of alloy composition and processing on microstructure development, texture evolution, mechanical properties, and degradation behavior were investigated. Grain sizes and corresponding textures were adjusted by the extrusion parameters. Despite changes in the texture, grain boundary strengthening effects were confirmed for all alloys in accordance with the Hall-Petch relationship. The alloy composition contributed to the mechanical properties by solid solution strengthening and a combination of texture changes and slip activities. Consequently, mechanical properties can be tailored within a wide range resulting in tensile yield strengths of 90 to 200 MPa (ultimate tensile strengths 180–280 MPa) and compressive yield strengths of 80 to 220 MPa (ultimate compressive strengths 300–450 MPa) with elongations of 10–45%. Low degradation rates in the range of 0.2 mm/year were determined for all alloys. Degradation was only slightly influenced by the alloy composition but not affected by processing. Overall, the properties of Mg-Gd determined in this work appear to be suitable to future implant applications.

Keywords: extrusion, biomaterial, mechanical properties, degradation, gadolinium, rare earth elements, yield asymmetry, texture

Edited by:
Maria Teresa Pérez,
Instituto IMDEA Materiales, Spain

Reviewed by:
Antonio Riveiro Rodriguez,
University of Vigo, Spain
Dikai Guan,
University of Sheffield,
United Kingdom

***Correspondence:**
Jochen Harmuth
jochen.harmuth@hzg.de
Björn Wiese
bjoern.wiese@hzg.de

Specialty section:
This article was submitted to
Structural Materials,
a section of the journal
Frontiers in Materials

Received: *24 May 2019*
Accepted: *05 August 2019*
Published: *20 August 2019*

Citation:
Harmuth J, Wiese B, Bohlen J, Ebel T and Willumeit-Römer R (2019) Wide Range Mechanical Customization of Mg-Gd Alloys With Low Degradation Rates by Extrusion.
Front. Mater. 6:201.
doi: 10.3389/fmats.2019.00201

INTRODUCTION

As constant mineral element in the human body and contributing to a variety of metabolic processes magnesium features excellent biocompatibility (Eder, 2009). Furthermore, mechanical properties and degradation behavior of Mg outperform biodegradable polymers. However, in pure form Mg has insufficient mechanical strength for most implant applications, e.g., osteosyntheses. Alloying of pure Mg might overcome this drawback by varying modes of strengthening and by changing the deformation behavior and texture. However, excellent biocompatibility and slow degradation of alloying elements needs to be ensured. Due to the existing concerns related to the potential neurotoxicity of aluminum different alloying elements are under investigation (El-Rahman, 2003).

The application of aluminum-free magnesium alloys for biomedical implants is highly dependent on specific material properties such as good biocompatibility, robust degradation behavior, and relevant mechanical properties. Regarding these properties, rare earth based alloys have been proven to be suitable, for example in two different CE (European Conformity) approved implant applications: Magnezix alloy for screws and pins (company Syntellix)[1] (Wetterlöv Charyeva, 2015) and SynerMag® alloy for Magmaris magnesium scaffold (company Biotronik)[2] (Marukawa et al., 2016). In accordance with these approvals, also Mg-Gd alloys have shown promising potential in mechanical properties (Rokhlin, 2003; Hort et al., 2010) and *in vitro* and *in vivo* biocompatibility testing (Feyerabend et al., 2010; Myrissa et al., 2016).

The influence of rare earth elements on the mechanical properties of Mg alloys has been reported to be beneficial (Rokhlin, 2003; Tekumalla et al., 2014). Mechanisms such as grain size strengthening and solid solution strengthening have been addressed for Mg-Gd (Gao et al., 2009; Xu et al., 2016, 2018). The beneficial influence of rare earth elements in general (Imandoust et al., 2017) and in particular for Mg-Gd (Stanford and Barnett, 2008; Stanford et al., 2010; Kim et al., 2017) is also attributed to texture weakening and enhanced slip activation that results in improved ductility and reduced anisotropy. In addition, tailoring of mechanical properties is critical for implant design but the underlying mechanisms have to be fully understood, particularly for Mg-Gd. Regarding the degradation behavior, an absence of intermetallic phases, and dendritic segregation favors slow and homogeneous degradation. Here, degradation rates of rare earth based magnesium alloys can be influenced by heat treatments during processing (Dvorský et al., 2018), if required. Also, tailored surface treatments show potential for adjustments (Gawlik et al., 2017).

Thus, besides alloy composition, the influence of processing parameters on Mg-Gd alloys for biomedical applications needs to be addressed. In order to develop customized alloys, the aim of this work is to reveal the relation between the Gd content and the processing parameters to the property profile of as-extruded Mg-Gd alloys without deteriorating the low degradation behavior. As a result, reliable correlations between processing parameters and alloy properties were established in this study. Compared to previous works where mostly single material conditions or alloys have been described, findings in this work describe the overall capabilities of the Mg-Gd system for implant applications within a defined set of processing parameters for indirect extrusion. Results can be potentially transferred to other rare earth based Mg alloys and also applied as quality measures to verify reproducibility.

EXPERIMENTAL

Alloys with 2, 5, and 10 wt.% Gd were prepared by permanent direct chill casting in a resistance furnace. Pure magnesium (99.97%, Dead Sea Magnesium Ltd.) was melted in the furnace at 710°C, followed by the addition of pure Gd (99.9%, Dr. Ihme GmbH). The melt was stirred at 250 rpm for 15 min and poured into preheated molds. After placing the mold in a holding furnace at 650°C for 2 min the mold was slowly immersed into a water bath for a fast solidification of the ingot. The ingots were machined to cylinders of 150 mm length and 49 mm diameter and T4 treated (solid solution) at 525°C for 8 h. Before extrusion ingots were pre-heated to the respective extrusion temperatures for 1 h to establish a constant and homogeneous temperature distribution. Finally, round bars with a diameter of 10 mm were obtained by indirect extrusion (extrusion ratio 1:25). For each alloy different combinations of extrusion parameters were applied, varying the extrusion temperature (350, 400, and 450°C) and the profile exit speed (0.75, 1.50, and 3.00 m/min), referred to as the extrusion speed. The chemical composition of all alloys is presented in **Table 1**.

Material characterization was conducted in the as extruded condition. Microstructural analysis was carried out on longitudinal sections of the round profiles using optical microscopy. Samples were ground by SiC paper down to 2,500 grit, polished by 1 µm OPS^{TM} suspension (Cloeren Technology GmbH) with diamond 0.25 µm and etched by picric acid solution (Kree et al., 2004). Corresponding grain sizes were determined by counting line intersections with grain boundaries on three longitudinal sections (0.058 mm² each). Recrystallized areas were measured on three images of three longitudinal sections (5.8 mm² each) per sample and the corresponding mean value is expressed as degree of recrystallization (fraction of recrystallized area of overall area). SEM analysis was performed at an acceleration voltage of 15 kV and a working distance of 15 mm using a scanning electron microscope (TESCAN VEGA3-SB, Brno, Czech Republic) equipped with energy-dispersive X-ray spectroscopy (EDS).

Vickers hardness was determined on cross sections with a load of 5 kg (HV 5) and a dwell time of 30 s. An average of 10 measurements per sample were carried out on M1C 010 testing machine (Emco-Test GmbH). The tensile and compressive

TABLE 1 | Gd concentrations were measured by X-ray fluorescence spectroscopy.

Alloy	wt.% Gd	at.% Gd	Fe [ppm]	Cu [ppm]	Ni [ppm]	Mg
Mg-2Gd	1.97	0.29	20	<7	<13	bal.
Mg-5Gd	4.82	0.78	49	<7	<13	bal.
Mg-10Gd	9.62	1.62	119	<7	<13	bal.

Fe, Cu, and Ni were determined by atomic absorption spectroscopy.

---

[1] Syntellix. *Magnezix Alloy*. Available online at: http://www.syntellix.de/home.html (accessed November 15, 2018).

[2] Magnesium Elektron. *SynerMag Alloy Specifications*. Available online at: https://www.magnesium-elektron.com/markets/biomaterials/synermag/ (accessed November 15, 2018).

properties were determined by testing 5 samples per condition. Tensile test specimens were machined to a diameter of 5 mm and a gauge length of 25 mm corresponding to DIN 50125 form B. Samples for compression tests were machined to a diameter of 8 mm and a length of 12 mm. All tests were performed on a universal testing machine Zwick Z050 (ZwickRoell GmbH & Co. KG) at a constant strain rate of 10^{-3} s^{-1} at room temperature. Six pole figures were measured using X-ray diffraction on polished cross sections of the extruded bars. Cu Kα radiation with a beam size of 1.5 mm x 1 mm and tilt angles from 0 to 70° was used. An open source code MTEX (Bachmann et al., 2010) was applied to recalculate inverse pole figures in extrusion direction for texture presentation.

Degradation properties were determined by performing semi static weight loss tests under cell culture conditions (37°C, 5% CO_2, 20% O_2, 95% relative humidity). Prior to immersion samples were ground with 2,500 SiC paper, cleaned (20 min in hexane, 20 min in acetone, 5 min 100% ethanol all in ultrasonic bath, Merck KGaA) and sterilized (5 min in 70% ethanol). Initial weights were determined after cleaning, using an electronic balance (SBA 32, accuracy 0.1 mg, Scaltec). For each condition, three samples were immersed in Dulbecco's Modified Eagle's Medium (DMEM, Fisher Scientific) + Glutamax (Life Technologies^{TM}, Gibco) + 10% fetal bovine serum (FBS, PAA Laboratories) for 7 days with medium changes after 2 and 4 days. Corrosion products were removed by immersion in chromic acid (180 g/L in distilled water, Sigma-Aldrich) for 20 min. Samples were cleaned with 100% ethanol and distilled water and dried at ambient temperature. The weight after removal of corrosion products was recorded using the electronic balance.

RESULTS

Microstructure and Hardness

Microstructure profiles from longitudinal sections of the as extruded Mg-10Gd with corresponding extrusion parameters are presented in **Figure 1** serving as an example also for Mg-2Gd and Mg-5Gd that show similar results. Overall, homogeneous distributions of equiaxed fine grains are present in all conditions. At lower extrusion speeds and temperatures some non-recrystallized areas are also visible. Cubic particles are present in all microstructures and aligned in extrusion direction. Exemplarily, an SEM image of Mg-10Gd is shown in **Figure 2**. EDS spot measurements (see **Supplementary Figure 1**) revealed high Gd concentrations of 75 to 85 wt.% for these cubic particles. The surrounding matrix (black area) showed Gd concentrations of around 9 wt.% which is in line with the overall alloy composition of Mg-10Gd in this study. Next to Gd,

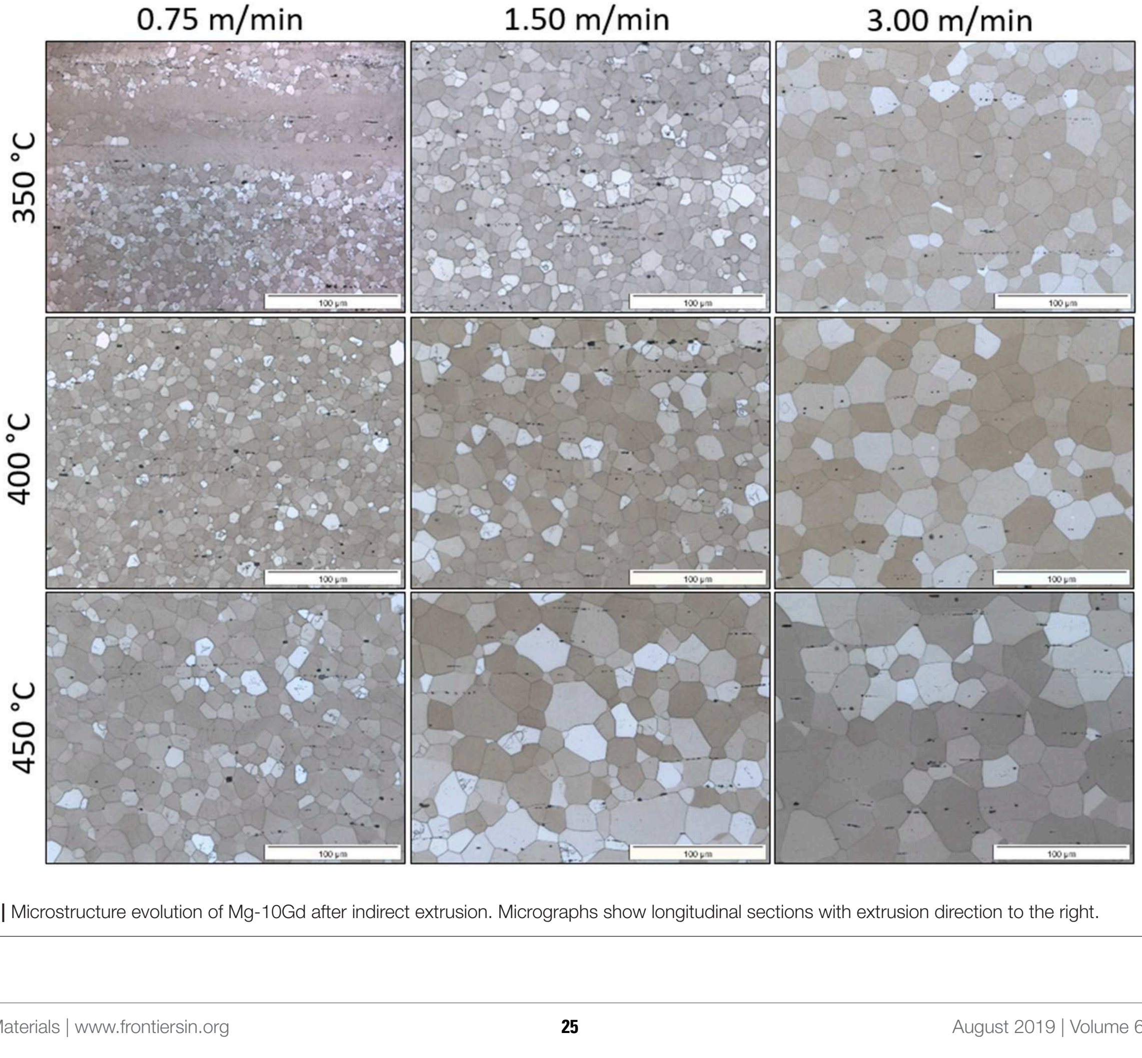

FIGURE 1 | Microstructure evolution of Mg-10Gd after indirect extrusion. Micrographs show longitudinal sections with extrusion direction to the right.

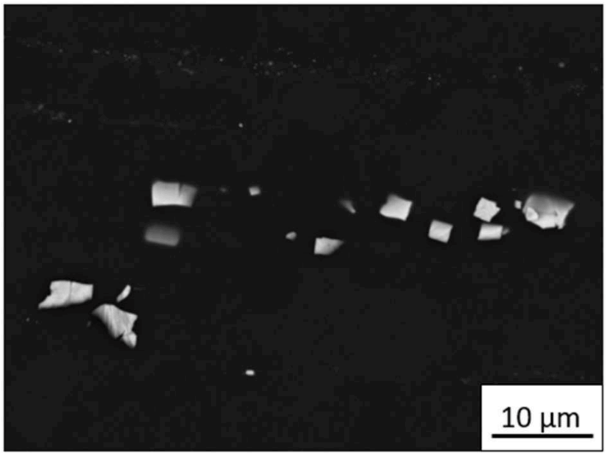

FIGURE 2 | SEM image (BSE) with GdH_2 particles aligned in extrusion direction.

measurements revealed the presence of magnesium. Low signals for silicon and oxygen are attributed to residues of polishing and minimal surface oxidation and can be neglected. Compared to former investigations these results indicate the presence of Gd hydrides (GdH_2) (Vlček et al., 2017). As a side note, when investigating samples by SEM, the amount/number of GdH_2 particles appeared to be similar for all alloys and conditions but was not further quantified.

The influence of the extrusion parameters on grain size and hardness is shown in **Figure 3**. For all alloys, grain sizes are similar at identical extrusion conditions indicating no influence of alloy composition. *Minor differences are of no significance and might be due to slight parameter variation during extrusion.* Increasing grain sizes are observed when the extrusion speed and/or the extrusion temperature is increased. This is due to an impact of deformation heat which increases with the extrusion speed as reported in earlier work (Bohlen et al., 2010). For all alloys, the average grain sizes range from 3 µm at 350°C and 0.75 m/min up to 25 µm at 450°C and 3.00 m/min. Both, increasing extrusion speed and extrusion temperature result in lower hardness values, as also shown in **Figure 3**. In addition, the effect of alloy composition on the hardness is visualized. Contrary to grain size evolution, hardness values are significantly affected by the alloy composition.

Furthermore, the microstructures are characterized by the degree of recrystallization after extrusion. Non-recrystallized areas are present in conditions after slow extrusion and at low temperatures and can be easily identified by their elongated band-like structure with significantly larger dimensions compared to the surrounding recrystallized fine grains (see top left micrograph in **Figure 1**). The degree of recrystallization for all alloys with respect to extrusion parameters is shown in **Figure 4**. Extrusion conditions representing speeds of 1.50 m/min or 3.00 m/min feature degrees of recrystallization of more than 95% for all three alloys and temperatures which is considered to be fully recrystallized. Only the slowest speed of 0.75 m/min is accompanied by not fully recrystallized microstructures in the three alloys. However, an increase in extrusion temperature leads to a higher degree of recrystallization in all alloys. The increase of Gd content visibly also leads to higher degrees of recrystallization.

Texture

Inverse pole figures are presented in **Figure 5**. For each alloy, four combinations of extrusion parameters are shown to analyze the influence of extrusion parameters and alloy composition. For 0.75 m/min and 350°C, all alloys show a similar strong texture dominated by intensities at the $\langle 10\bar{1}0\rangle$ pole (see **Figures 5A–C**). In part, this component of texture is characteristic of a not fully recrystallized microstructure and corresponds well to uniaxial deformation of hcp metals (Dillamore and Roberts, 1965; Bohlen et al., 2010). However, for Mg-10Gd the maximum intensity is significantly lower and a weak component at the $\langle 0001\rangle$ pole is present. Increasing the extrusion temperature to 450°C (**Figures 5D,E**) the textures for Mg-2Gd and Mg-5Gd are comparable. Again, Mg-10Gd shows further reduced intensities that are also shifted toward the $\langle 11\bar{2}0\rangle$ pole (**Figure 5F**). The component at the $\langle 0001\rangle$ pole vanished. When increasing the extrusion speed at constant temperatures maximum intensities in all alloys are significantly lowered and steadily shifted toward the $\langle 11\bar{2}0\rangle$ pole (see **Figures 5G–L**). This texture development correlates well with observations in microstructure evolution as non-recrystallized areas disappear and recrystallization takes place when extrusion speed and temperature are increased. Contrary to the microstructures, there is a larger effect of the extrusion speed to the weakening of textures whereas the influence of extrusion temperature is of minor importance. Additionally, the alloy composition is influencing the texture development as intensities are significantly lowered with increasing amount of Gd. In all alloys a "rare earth component" (Stanford and Barnett, 2008) is visible, characterized by intensities with tilt out of the arc between the $\langle 10\bar{1}0\rangle$ and $\langle 11\bar{2}0\rangle$ poles toward the $\langle 0001\rangle$ pole. Thus, a tilt of basal planes out of the extrusion direction results. This is more pronounced at higher Gd contents as well as at higher extrusion temperatures.

Tension and Compression Properties

Results of tension and compression testing in correlation to the respective extrusion parameters are summarized in **Figure 6**. Results of tensile yield strengths (TYS) and compressive yield strengths (CYS) are displayed in **Figure 6A**. *TYS and CYS decrease with increasing extrusion parameters. However, this effect is minimalized for the highest extrusion speed and with increasing Gd content*. The tensile and compressive yield strengths increase with increasing Gd content. Furthermore, a tension/compression (t/c) yield asymmetry can be observed. It is obtained by dividing corresponding TYS by CYS for identical extrusion conditions. For Mg-2Gd, CYS is lower than TYS leading to a t/c ratio of ≥ 1 for all conditions. This is partially reversed for Mg-5Gd that shows t/c ratios of 0.84–1.11. For Mg-10Gd, the yield asymmetry is completely reversed with t/c ratios of ≤ 1 for all conditions. Results of ultimate tensile strengths (UTS) and ultimate compressive strengths (UCS) are displayed in **Figure 6B**. In all conditions and for all alloys, UCS > UTS. Overall, ultimate

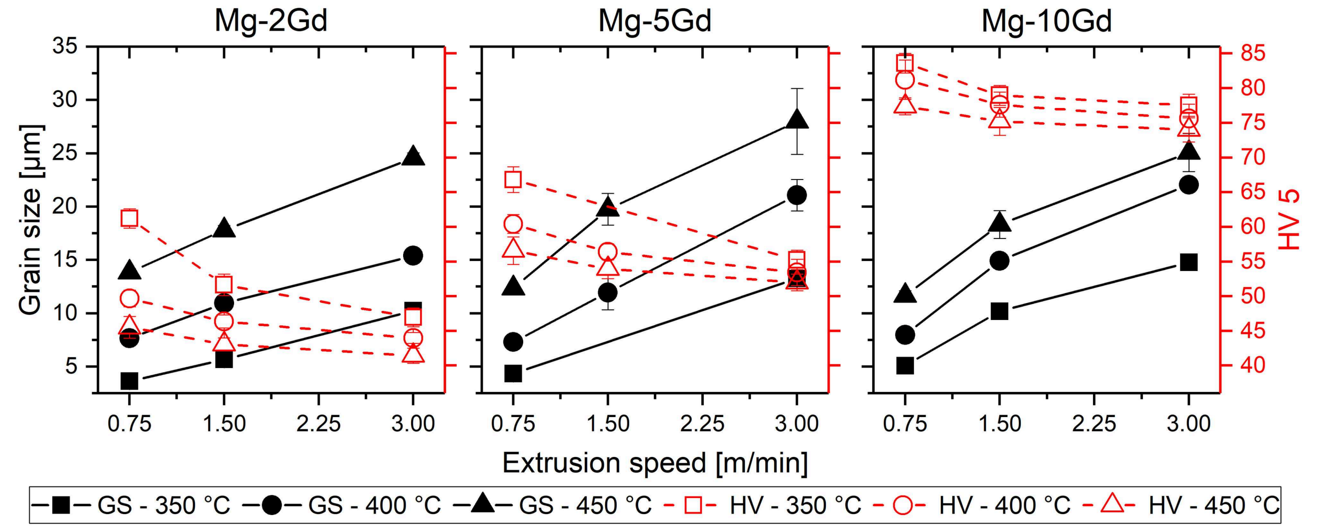

FIGURE 3 | Grain sizes (solid) and hardness (empty) for all alloys with respect to individual extrusion conditions. With increasing extrusion parameters, grain sizes trend higher, hardness values trend lower. Alloy composition is not affecting grain sizes but hardness values are significantly increased with higher Gd additions. Error bars are standard deviations.

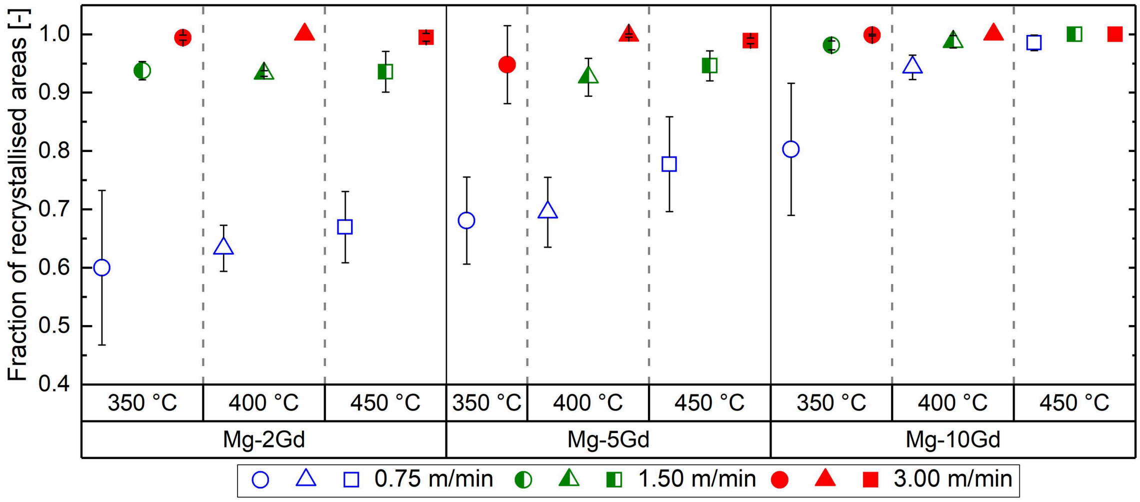

FIGURE 4 | Degree of recrystallization for all alloys with respect to extrusion parameters. Identical symbols refer to identical extrusion conditions and degree of recrystallization is comparable in between all alloys (i.e., blue circles represent 350°C and 0.75 m/min for each alloy). Error bars are standard deviations.

strengths decrease with increasing extrusion temperatures and speeds with the exception for UCS in Mg-2Gd at 400°C and Mg-5Gd at 400 C and 450°C. Ultimate strengths increase with increasing Gd content.

Results of elongation to fracture (A_{tt}) and compression to fracture (A_{tc}) are displayed in **Figure 6C**. The influence of extrusion parameters is first explained using data of Mg-2Gd. An increase in speed results in an increase in A_{tt} whereas an increase in temperature reduces A_{tt}. This trend can be seen also in Mg-5Gd and is valid for all conditions in Mg-10Gd except at 450°C. A_{tt} ranges from 10 to 48% for Mg-2Gd and from 14 to 35% for Mg-5Gd. Contrary, Mg-10Gd shows minimal variations from 27 to 33%. Same trends are visible for compressive deformation as an increase in extrusion speed also results in an increase in A_{tc}. Interestingly, changes in the extrusion temperature do not result in such a general trend. However, for Mg-10Gd an almost linear increase in A_{tc} can be observed when increasing speed and temperature that results in a range of 13–21%. For Mg-2Gd A_{tc} ranges from 11 to 29% and from 15 to 28% for Mg-5Gd. A wide range of A_{tt} and A_{tc} can be observed for low amounts of Gd in relationship with the parameter variation. These variations in A_{tt} and A_{tc} are narrowed, when Gd levels are increased.

Degradation Properties

Degradation rates (DR) after immersion for 7 days were calculated by Equation 1 with change in weight Δm [g], density ρ [g/cm^3] (measured based on Archimedes principle), surface

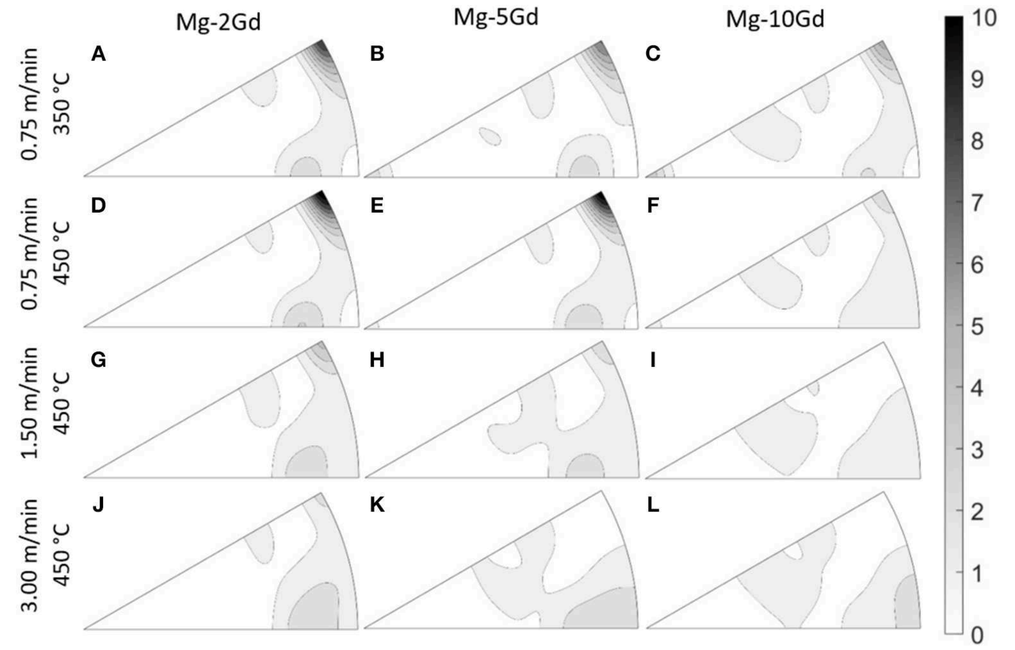

FIGURE 5 | Texture development of as extruded conditions. Bottom left $\langle 0001\rangle$ pole, bottom right $\langle 11\bar{2}0\rangle$ pole and top right $\langle 10\bar{1}0\rangle$ pole with intensities ranging from 0 to 10. **(A–C)** Extrusion at 0.75 m/min and 350°C; **(D–F)** extrusion at 0.75 m/min and 450°C; **(G–I)** extrusion at 1.50 m/min and 450°C; **(J–L)** extrusion at 3.00 m/min and 450°C.

area A [cm^2] and time t [h]. Results are presented in **Figure 7** and show similar and low values of around 0.15–0.25 mm/year with no statistical significant differences. DR are not affected by extrusion parameters. However, higher Gd contents tend to lower overall DRs. These degradation rates are perfectly suitable for further investigation by cell culture and *in vivo* studies.

$$\text{DR [mm/year]} = \left(8.76^{*}10^{4*}\Delta \text{m}\right) / (\rho^{*}\text{A}^{*}\text{t}) \qquad (1)$$

DISCUSSION

Microstructure and Texture Evolution

As described in previous studies, the development of microstructures and textures in rare earth containing Mg alloys is based on several mechanisms: in some parts by changes in grain nucleation and grain growth during recrystallization as a result of extrusion. In other parts by texture changes because of the activation of deformation mechanisms like slip and twinning (Yu et al., 2013; Kim et al., 2017; Harmuth et al., 2018).

First, contributions of grain nucleation and grain growth are discussed. Results show no significant difference in the grain size between different Gd contents for the same extrusion conditions. However, an increase of the Gd content also increases the fraction of recrystallized microstructure in those conditions where such behavior can be judged (e.g., at 350°C). As solid solution treatment prior to extrusion is also applicable to increasing contents of Gd it is hypothesized that intermetallic particles as nucleation sites of recrystallized grains (i.e., a particle stimulation of recrystallization) or particles as obstacles for grain boundary mobility (i.e., a particles related mobility drag) are not to be considered as important mechanisms in this regard. While in other alloys (see e.g., Mg-RE-Mn alloys, Vlček et al., 2017) the same microstructure development features have been discussed in the context of particle effects, it is suggested that another solute related source of grain nucleation is active with increasing Gd content. This also includes the deformation characteristics such as dislocations or twins leading to stress pile-ups and therefore sources of recrystallization. Contrary, the grain size is not changing with increasing Gd content which contradicts an enhanced grain growth ability. It is therefore hypothesized that the nucleation rate of recrystallized grains is increased by adding Gd whereas grain growth is somewhat restricted. Similar discussions have been presented for other Mg alloys including rare earth elements (Bohlen et al., 2010).

Concurrently, the texture evolution is affected by the extrusion conditions and the amount of Gd. Strong {10-10} fiber textures are present in materials processed at slow extrusion speeds that also feature non-recrystallized areas in the microstructure. As reported before, this deformation texture is a result of partial recrystallization known in Mg alloys in general, regardless of the addition of Gd (Bohlen et al., 2010; Yu et al., 2013; Kim et al., 2017). As described before, the increase in extrusion temperature appears to be of higher significance to the recrystallization and weakening of the textures. Again, a higher content of Gd is associated with less significant intensity at the <10-10> pole and concurrently the fraction of un-recrystallized microstructure.

Furthermore, a distinct texture development known as "rare earth texture" is addressed (Stanford and Barnett, 2008). It describes the orientation of basal planes with a tilt out of the extrusion direction. This component is present in all samples and is beneficial for deformation processes as it enables basal slip. Due to its low critical resolved shear stress of as low as 0.7 MPa it

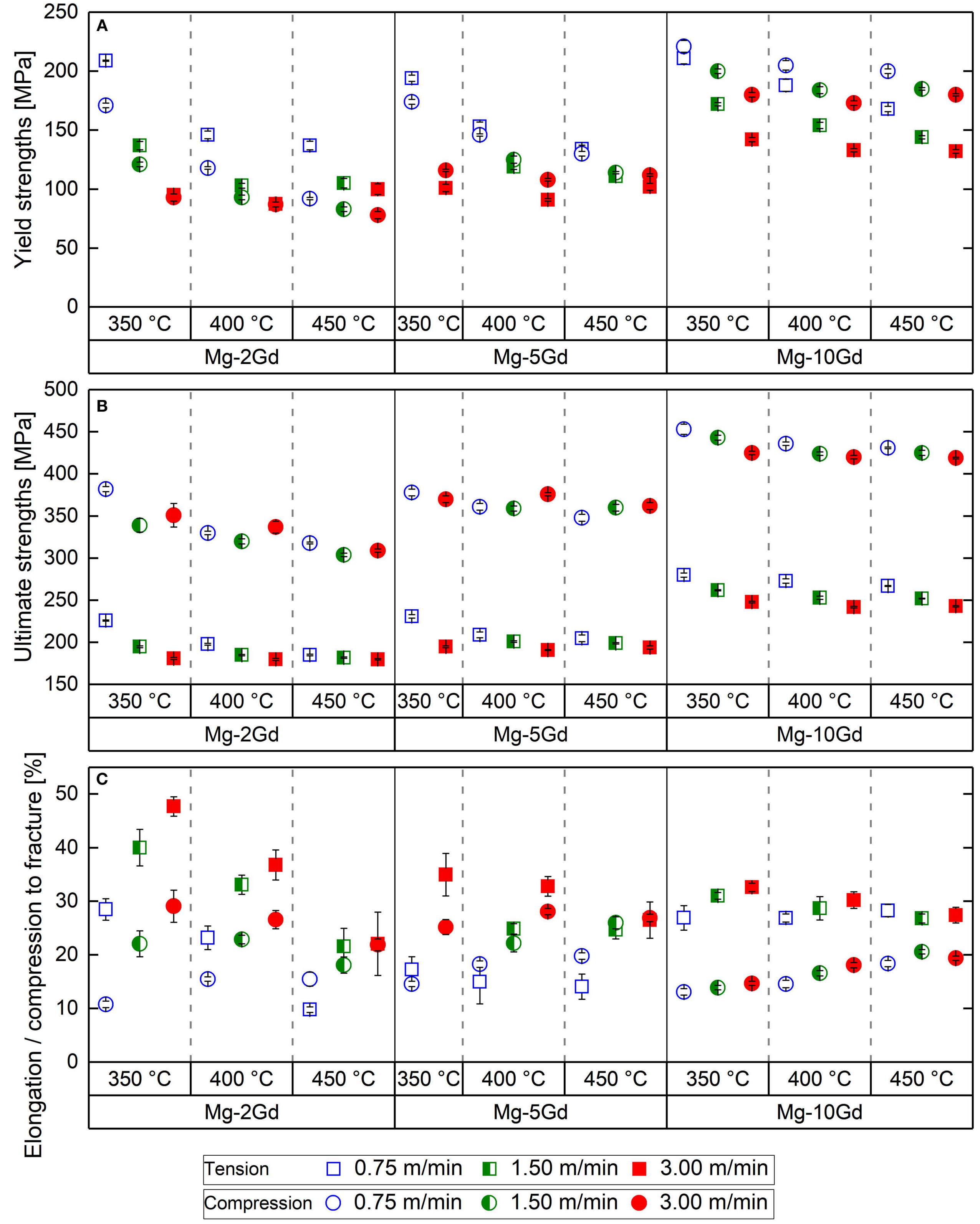

FIGURE 6 | Mechanical properties from tension and compression with respect to extrusion parameters. **(A)** Yield strengths, **(B)** ultimate strengths, and **(C)** elongation and compression to fracture.

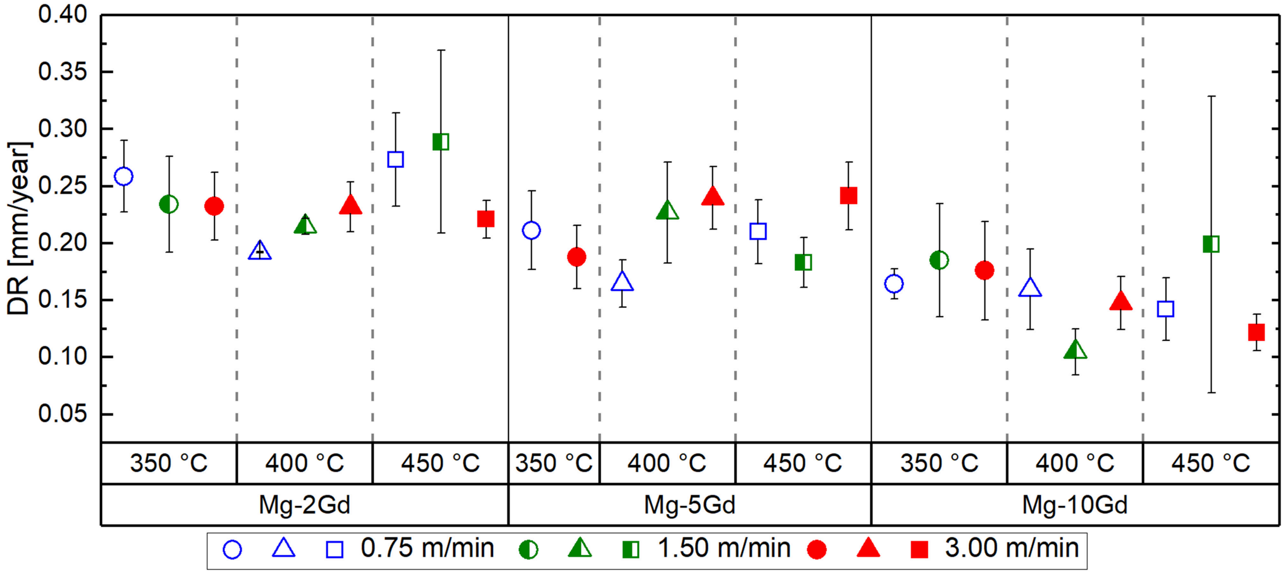

FIGURE 7 | Mean degradation rates after 7 days immersion. Error bars are standard deviations.

serves as the main deformation mechanism in magnesium alloys (Kammer, 2000; Fukuda et al., 2016).

In samples with low extrusion speeds and low extrusion temperatures, increasing Gd content weakens deformation textures and also develops texture components at the <0001> pole. This represents an orientation of basal planes perpendicular to the extrusion direction. A proposed explanation for this texture evolution can be found in a combination of shear band recrystallization and the solute drag effect as well as non-basal slip activation (Grey and Higgins, 1973; Kim et al., 2017). With increasing extrusion parameters and therefore coarser grains, the influence of Gd addition is reduced.

Grain Size Strengthening Effect

Results of tensile yield strengths (TYS) and compressive yield strengths (CYS) with respect to the average grain size, D, are plotted in **Figure 8**. Following the Hall-Petch relation (Equation 2) the inverse square root of the grain size is used to visualize potential grain boundary strengthening effects, with YS being the TYS or CYS, K_y [MPa μm$^{1/2}$] the strengthening coefficient associated with grain boundary strengthening and σ_0 [MPa] the friction stress for dislocation movement. Note, that a required statistical orientation relation between neighboring grains may not be fulfilled in the framework of the study as the samples exhibit a weak but non-random texture in all cases. Strengthening coefficients and friction stress are summarized in **Table 2**. As the textures remain weak in most cases, a potential contribution to these coefficients may be low.

$$YS\,[MPa] = K_y^{*}\ D^{-\frac{1}{2}}\ +\ \sigma_0 \qquad (2)$$

A linear behavior of grain size to yield strengths for tension and compression with high coefficients of determination is confirmed for all alloys. Furthermore, a reversed t/c asymmetry becomes visible with increasing Gd content, which also corresponds to higher degrees of recrystallization and weaker textures. Xu et al. (2018) determined a similar Hall-Petch relation and yield asymmetries for small grains within their analysis of a wide range of grain sizes. Minor differences in values might be attributed to

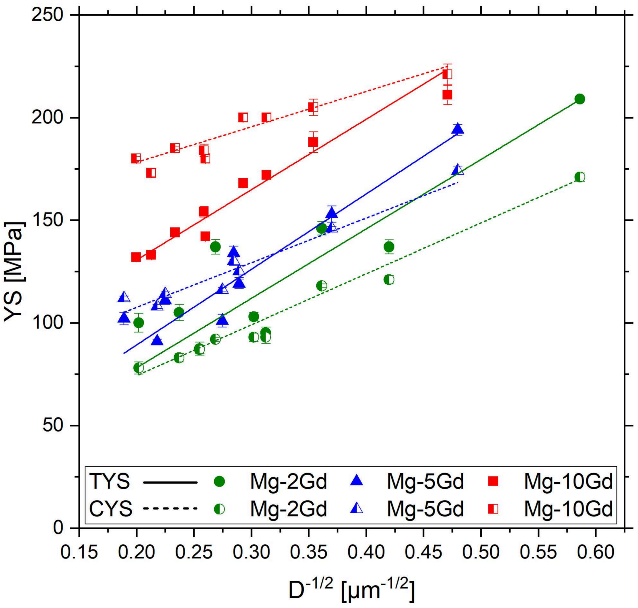

FIGURE 8 | Hall-Petch relation for all alloys. TYS denoted by solid lines and symbols. CYS denoted by halved symbols and dashed lines. Error bars are standard deviations.

the fact that a combination of heat treated and extruded material conditions with a large range in grain sizes (30 to more than 1,500 μm) were investigated. Similar results were also previously reported for Mg-0.49 at.% Gd (3.09 wt.% Gd) with K_y of 188 MPa $\mu m^{1/2}$ and σ_0 of 46.5 MPa for tension tests (Gao et al., 2009).

In hcp metals, yield strengths are affected by crystallographic orientation with respect to loading direction and alloy composition. Tension-compression yield asymmetries have been investigated before in as-extruded pure Mg with $t/c > 1$ (Sukedai and Yokoyama, 2010) and, reversed, for Mg-10Gd with $t/c < 1$ (Maier et al., 2012). This indicates that a shift in yield asymmetry is due to increasing Gd contents and is supported by the results of this work. This effect is most likely caused by an activation of {10-11} compression twins at the expense of {10-12} tension twins (Nagarajan et al., 2016).

The friction stress is increased with increasing Gd content for tension and compression (**Table 2**). Low friction stress for Mg-2Gd is due to the softening of prismatic slip and hardening of the basal plane by solute Gd atoms in dilute Mg alloys (Akhtar and Teghtsoonian, 1969). With higher concentrations of Gd atoms in solid solution, the hardening effect is increased. Furthermore, short range order is likely to contribute to hardening of slip and twinning in Gd alloys (Gencheva et al., 1981). Compared to previous works (Nagarajan et al., 2016), results for friction stress in this study are similar. Slight differences for Mg-10Gd are attributed to texture effects, i.e., higher CYS due to tensile twinning when <0001> pole intensity is present.

The strengthening coefficients in **Table 2** are not significantly different for all three alloys if the error margins are considered. However, the values for the compression tests remain visibly lower compared to those in tension. In recent work, it was proposed that this behavior is due to changes in twinning deformation (Harmuth et al., 2018). For increasing Gd contents {10-12} extension twinning is more and more inhibited by short range order whereas {10-11} compression twinning remains available for higher Gd contents in solid solution (Nagarajan et al., 2016). Consequently, the asymmetry between tension and compression is reversed as it is shown for Mg-10Gd.

A different analysis proposes the theory of a change in deformation mechanics with increased Gd content (Cepeda-Jiménez et al., 2018). This is supported by **Figure 9** showing the deformation behavior for Mg-2Gd and Mg-10Gd in tensile and compression testing. As expected, materials with smaller grain sizes show higher strengths during tension and compression no matter of the amount of Gd. As it can be seen in **Figure 9A**, in tension similar deformation behavior is visible for Mg-2Gd and Mg-10Gd. In compression (**Figure 9B**) Mg-2Gd shows a typical S-shape curve for small grains that is flattened with increasing grain size representing active twinning deformation. However, the distinct difference in the curves of Mg-10Gd support the theory that twinning is active in compression of Mg-2Gd but suppressed in compression of Mg-10Gd. This is attributed to increased Gd contents and an increase in extrusion speed accompanied by a higher degree of recrystallization and weaker textures. As a result t/c is already reversed for smaller grains when Gd contents are higher.

TABLE 2 | Hall-Petch coefficients for tension and compression including standard deviations (Harmuth et al., 2018).

	Tension			Compression		
Alloy	**K_y [MPa $\mu m^{1/2}$]**	**σ_0 [MPa]**	**R^2**	**K_y [MPa $\mu m^{1/2}$]**	**σ_0 [MPa]**	**R^2**
Mg-2Gd	338 ± 25	10 ± 13	0.96	248 ± 16	25 ± 5	0.97
Mg-5Gd	368 ± 45	16 ± 12	0.92	218 ± 26	64 ± 7	0.92
Mg-10Gd	343 ± 33	62 ± 9	0.94	173 ± 32	144 ± 8	0.81

Overall, grain size strengthening effects are easily observed in tension and compression yield strengths (**Figure 8**). TYS and CYS are linearly increased with decreasing grains sizes in the Hall-Petch plot. Also, a solid solution strengthening effect is visible. For identical grain sizes the increase in yield strengths is attributed to the increase of Gd atoms in solid solution.

Hardness Effects

Grain Sizes

The alloys in this study also exhibit a linear relationship of hardness to grain size that follows the Hall-Petch relationship (see **Figure 10**) and was reported before for aluminum alloys (Taha and Hammad, 1990). It can be described with reasonable security by Equation 3 with K_{HV} and H_0 being constants that were determined experimentally (see **Table 3**). Overall, smaller grains, represented by low extrusion parameters, feature higher hardness values than coarse grains, represented by higher extrusion parameters. Furthermore, an increase in hardness with increasing Gd content becomes visible that is independent of grain size. In contrast to these findings, Xu et al. (2016) reported independence of grain size and hardness. This is attributed to the large range of grain sizes (30 to more than 1,500 μm) that was investigated. The present work is focused on grain sizes ranging from 3 to 25 μm and clearly indicate a strengthening effect of grain size on hardness values.

$$HV5 = K^{*}_{HV}\ D^{-\frac{1}{2}} + H_0 \tag{3}$$

Ultimate Strengths

Results indicate that there is a direct relation between ultimate strengths and hardness values that is shown in **Figure 11**. Technically, a direct relationship between tensile/compressive strength and hardness is not to be expected as mechanisms of deformation and failure are different. However, as both measurements require loading the empirical relationship that is observed in this work appears to be viable. A similar relationship between UTS and hardness has been reported for steel (Pavlina and Van Tyne, 2008) and Cu alloys (Zhang et al., 2011). It can be described with reasonable security by Equation 4 with K_{US} and US_0 being constants that were determined experimentally (see **Table 4**). Limited availability of slip systems in Mg alloys and the already mentioned different CRSS for compressive and tensile twinning as well as the t/c asymmetry in yields strengths illustrate that this phenomenon is in need of further analysis. Nonetheless, both relations are applied to an accurate estimation of ultimate strengths from hardness measurements

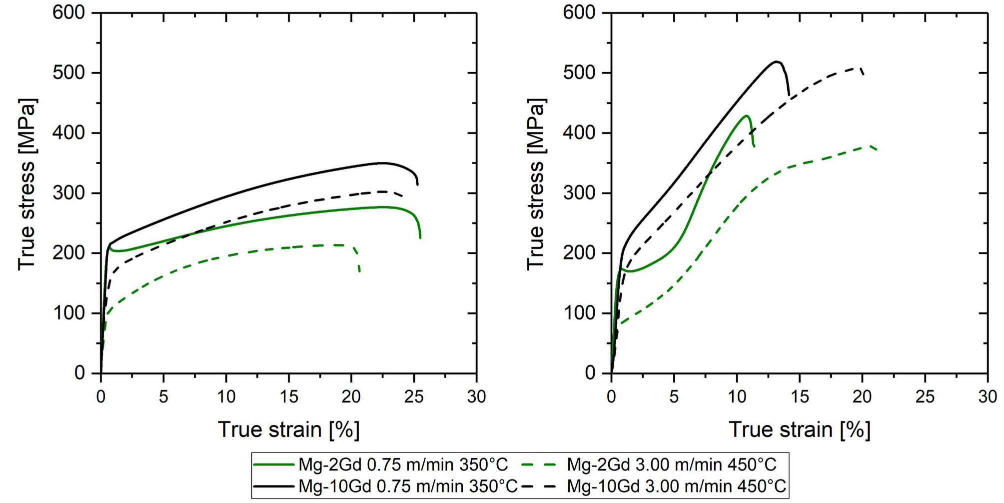

FIGURE 9 | True stress-strain curves for smallest (0.75 m/min and 350°C) and most coarse grains (3.00 m/min and 450°C) and lowest and highest Gd content. **(A)** Tension, **(B)** compression.

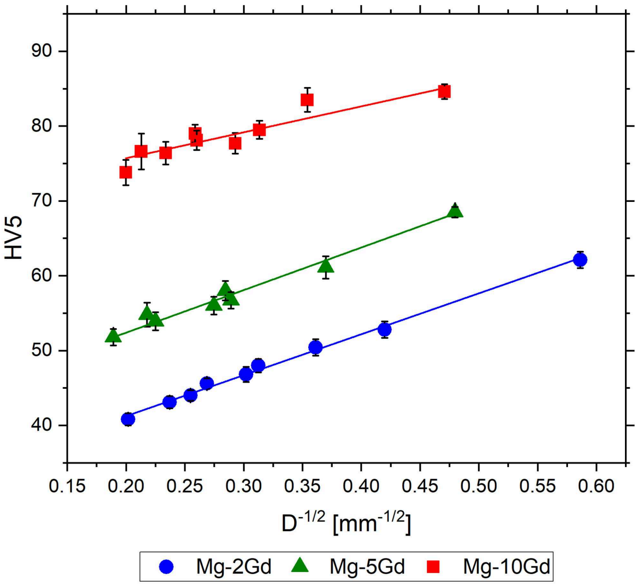

FIGURE 10 | Effect of grain size on hardness. Error bars are standard deviations.

without facilitating expensive and time consuming tensile and compression test. In addition to the Hall-Petch relationship, the most important mechanical properties can be derived from simple microstructure analysis and hardness measurement.

$$US\ [MPa] = \mathrm{K}^{*}_{\mathrm{US}}\ \mathrm{HV5} + US_0 \tag{4}$$

Fracture Strains

Fracture strains in tension exceed those in compression in most cases. In general, the fracture strains remain high in comparison to other magnesium extrusions. Interestingly, an increase in fracture strain with increasing speed is associated with an increase of the fraction of recrystallized microstructure. On the other hand, a decrease of fracture strains with increasing extrusion temperature is concurrent to larger grained microstructures. The higher the Gd content and the lower the differences in grain size or fraction of recrystallized microstructure the more similar are the fracture strains as visible in the case of Mg-10Gd. In compression this tendency is less strongly developed compared to tension. Furthermore, the texture component at the ⟨0001⟩ pole and a change in deformation mechanism as mentioned before might be contributing to the limitation of fracture strains for high Gd contents.

TABLE 3 | Coefficients for relation of hardness to grain size including standard deviations.

Alloy	K_{HV}	H_0	R^2
Mg-2Gd	54.3 ± 1.4	30.4 ± 0.5	0.99
Mg-5Gd	54.6 ± 3.4	41.7 ± 1.0	0.97
Mg-10Gd	37.8 ± 5.7	67.9 ± 1.7	0.86

Degradation Characteristics

The overall degradation behavior is low and appears applicable to biomedical applications despite significantly high levels of Fe contamination especially for Mg-10Gd. Degradation rates are not influenced by processing parameters, grain sizes or microstructural features. No conclusions can be drawn to put degradation rates in relation to the degree of recrystallization or the mechanical properties. A significant impact or correlation is not revealed. Overall, higher amounts of Gd up to 10 wt.% tend to lower degradation rates. This is in accordance

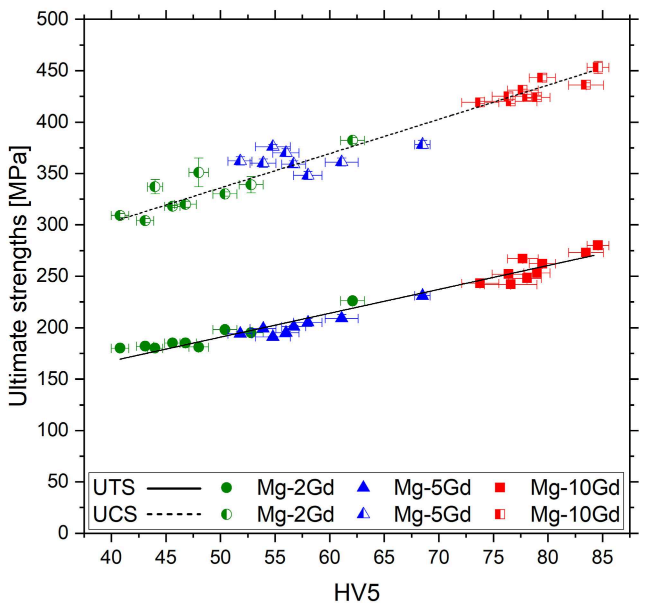

FIGURE 11 | Correlation between UTS/UCS and Vickers hardness. UTS denoted by solid lines and symbols. UCS denoted by halvedsymbols and dashed lines. Error bars are standard deviations.

TABLE 4 | Coefficients for relation of ultimate strengths to hardness including standard deviations.

US [MPa]	K_{US} [MPa]	US_0 [MPa]	R^2
UTS	2.3 ± 0.1	75 ± 7	0.98
UCS	3.3 ± 0.1	169 ± 7	0.97

with findings of Rokhlin (2003). It was also confirmed by Hort et al. (2010) in earlier studies. However, these results were obtained from as cast conditions only and showed significantly higher DRs. In this work, due to the fact that all materials have been solid solution heat treated and also after extrusion Gd remained in solid solution, potential local galvanic effects have been reduced to a minimum as reported previously (Dvorský et al., 2018). Similar DRs for as extruded Mg-5Gd have been reported by Gawlik et al. (2017). Further surface treatment by HAc etching is effective in reducing DRs and improving reproducibility. According to Gawlik et al. (2019) the acetic acid etching of Mg-xGd alloys is able to remove harmful surface bound Fe contaminants (e.g., from manufacturing) which in turn improve the reproducibility of the degradation behavior. Overall, degradation behavior in this study was assessed by short term tests only and requires further investigation.

Applicability and Transferability

In terms of applicability, a comparison of mechanical properties of Mg-10Gd at 350°C and 0.75 m/min to as extruded SynerMag® alloy system, that is used for an available implant, is favorable. Properties of SynerMag® featuring YS of 190–220 MPa (210 MPa for Mg-10Gd), UTS of 260–320 MPa (280 MPa), and A_{tt} of 20–35% (27%) (Magnesium Elektron).

Due to similar behavior of rare earth elements in Mg alloys in general (Rokhlin, 2003), application of these finding to different systems might be possible in the future in order to further improve properties by extrusion. Furthermore, findings can be transferred to production and quality control due to inexpensive and time saving analysis of properties.

CONCLUSIONS

Overall, several relationships between alloy composition, microstructures and mechanical properties have been derived that aid in further development of degradable implants based on rare earth Mg alloys. Furthermore, these findings can be applied to increase overall understanding of underlying mechanism in Mg alloys in general. The major findings are:

1) As extruded Mg-Gd system features homogeneous microstructures accompanied by weak textures that can be tailored by indirect extrusion.
2) The tension/compression yield asymmetry is inverted with increasing Gd content based on a change in deformation mechanism.
3) Higher Gd content is reducing the variation in the texture and increasing the recrystallization without an effect on the grain growth in the absence of nucleation particles.
4) The following relationships are confirmed in this work:
    a. Grain size strengthening effects on TYS/CYS and on hardness
    b. Hardness and ultimate strengths
5) Degradation of all materials is slow and not affected by processing or alloy composition. Mechanical properties can be varied in a wide range without deteriorating the superior degradation rate.
6) Within this frame of processing and alloy composition, customization of mechanical properties is feasible to meet standards of an already approved Mg alloy.

DATA AVAILABILITY

All datasets generated for this study are included in the manuscript/**Supplementary Files**.

AUTHOR CONTRIBUTIONS

JH, BW, and JB conceived, analyzed data, and designed experiments. JH and JB performed extrusion. JH performed characterization with assistance of BW and JB. JB, TE, and RW-R contributed materials, analysis tools. JH wrote initial manuscript and prepared the final manuscript. BW, JB, TE, and RW-R revised manuscript and assisted with valuable feedback and discussions.

FUNDING

The presented work was funded in parts by the Helmholtz Association: Project Virtual Institute MetBioMat (VH-VI 523 MetBioMat).

ACKNOWLEDGMENTS

The presented work follows a collaborative approach between the Institute for Metallic Biomaterials and the Magnesium Innovation Center. The help of and discussions with Prof. Karl Ulrich Kainer, Dr. Norbert Hort, and Dr. Dietmar Letzig is highly acknowledged. The authors appreciate the help of Mr. Günter Meister during casting the material and the advice of Mr. Gert Wiese for metallography in this work.

SUPPLEMENTARY MATERIAL

The Supplementary Material for this article can be found online at: https://www.frontiersin.org/articles/10.3389/fmats.2019.00201/full#supplementary-material

Supplementary Figure 1 | EDS spot measurements and corresponding spectra of magnesium matrix (1) and Gd rich particle (2).

REFERENCES

Akhtar, A., and Teghtsoonian, E. (1969). Solid solution strengthening of magnesium single crystals-I alloying behaviour in basal slip. *Acta Metall.* 17, 1339–1349. doi: 10.1016/0001-6160(69)90151-5

Bachmann, F., Hielscher, R., and Schaeben, H. (2010). Texture analysis with MTEX—free and open source software toolbox. *Solid State Phenom.* 160, 63–68. doi: 10.4028/www.scientific.net/SSP.160.63

Bohlen, J., Yi, S., Letzig, D., and Kainer, K. U. (2010). Effect of rare earth elements on the microstructure and texture development in magnesium-manganese alloys during extrusion. *Mater. Sci. Eng. A.* 527, 7092–7098. doi: 10.1016/j.msea.2010.07.081

Cepeda-Jiménez, C. M., Prado-Martínez, C., and Pérez-Prado, M. T. (2018). Understanding the high temperature reversed yield asymmetry in a Mg-rare earth alloy by slip trace analysis. *Acta Mater.* 145, 264–277. doi: 10.1016/j.actamat.2017.12.021

Dillamore, I. L., and Roberts, W. T. (1965). Preferred orientation in wrought in annealed metals. *Metall. Rev.* 10, 271–380. doi: 10.1179/095066065790138348

Dvorský, D., Kubásek, J., Vojtìch, D., Cavojský, M., and Minárik, P. (2018). Effect of heat pre-treatment and extrusion on the structure and mechanical properties of WZ21 magnesium alloy. *Mater. Tehnol.* 52, 499–505. doi: 10.17222/mit.2017.214

Eder, K. (2009). Magnesium-verbindungen - aufnahme, funktionen und therapeutische aspekte. *Pharm. Unserer Zeit.* 38, 262–267. doi: 10.1002/pauz.200800316

El-Rahman, S. S. A. (2003). Neuropathology of aluminum toxicity in rats (glutamate and GABA impairment). *Pharmacol. Res.* 47, 189–194. doi: 10.1016/S1043-6618(02)00336-5

Feyerabend, F., Fischer, J., Holtz, J., Witte, F., Willumeit, R., Drücker, H., et al. (2010). Evaluation of short-term effects of rare earth and other elements used in magnesium alloys on primary cells and cell lines. *Acta Biomater*. 6, 1834–1842. doi: 10.1016/j.actbio.2009.09.024

Fukuda, K., Koyanagi, Y., Tsushida, M., Kitahara, H., Mayama, T., and Ando, S. (2016). Activation stress for slip systems of pure magnesium single crystals in pure shear test. *J Japan Inst. Met.* 80, 334–339. doi: 10.2320/jinstmet.J2015062

Gao, L., Chen, R. S., and Han, E. H. (2009). Effects of rare-earth elements Gd and Y on the solid solution strengthening of Mg alloys. *J. Alloys Compd*. 481, 379–384. doi: 10.1016/j.jallcom.2009.02.131

Gawlik, M. M., Steiner, M., Wiese, B., González, J., Feyerabend, F., Dahms, M., et al (2017). The effects of HAc etching on the degradation behavior of Mg-5Gd. *J. Med. Mater. Technol. Spec. Issue Proc. 4th Euro BioMAT*. 1, 22–25. doi: 10.24354/medmat.v1i2.17

Gawlik, M. M., Wiese, B., Welle, A., Gonzalez, J., Desharnais, V., Harmuth, J., et al (2019). Acetic acid etching of Mg-xGd alloys. *Metals* 9:117. doi: 10.3390/met9020117

Gencheva, D. S., Katsnelson, A. A., Rokhlin, L. L., Silonov, V. M., and Khavadzha, F. A. (1981). Short order study in erbium and gadolinium containing magnesium-base alloys. *Fiz. Met. Metalloved.* 51, 788–793.

Grey, E. A., and Higgins, G. T. (1973). Solute limited grain boundary migration: a rationalisation of grain growth. *Acta Metall.* 21, 309–321. doi: 10.1016/0001-6160(73)90186-7

Harmuth, J., Wiese, B., Bohlen, J., Ebel, T., and Geesthacht, H. (2018). "Tailoring of material properties of Mg-Gd alloys for biomedical applications," in *Proceedings of the 11th International Conference on Magnesium Alloys and Their Applications* (Old Windsor), 376–381.

Hort, N., Huang, Y., Fechner, D., Störmer, M., Blawert, C., Witte, F., et al (2010). Magnesium alloys as implant materials-Principles of property design for Mg-RE alloys. *Acta Biomater*. 6, 1714–1725. doi: 10.1016/j.actbio.2009.09.010

Imandoust, A., Barrett, C. D., Al-Samman, T., Inal, K. A., and El Kadiri, H. (2017). A review on the effect of rare-earth elements on texture evolution during processing of magnesium alloys, *J. Mater. Sci.* 52, 1–29. doi: 10.1007/s10853-016-0371-0

Kammer, C. (2000). *Magnesium Taschenbuch, 1. Auflage*. Düsseldorf: Aluminium-Zentrale Düsseldorf.

Kim, S. H., Jung, J. G., You, B. S., and Park, S. H. (2017). Microstructure and texture variation with Gd addition in extruded magnesium. *J. Alloys Compd.* 695, 344–350. doi: 10.1016/j.jallcom.2016.10.179

Kree, V., Bohlen, J., Letzig, D., and Kainer, K. U. (2004). Metallographische gefügeuntersuchungen von magnesiumlegierungen. *Prakt. Metallogr. Metallogr.* 41, 233–246.

Maier, P., Müller, S., Dieringa, H., and Hort, N. (2012). "Mechanical and corrosion properties of as-cast and extruded MG10GD alloy for biomedical application," in *Magnesium Technology*, eds S. N. Mathaudhu, W. H. Sillekens, N. R. Neelameggham, and N. Hort (Cham: Springer), 253–259.

Marukawa, E., Tamai, M., Takahashi, Y., Hatakeyama, I., Sato, M., Higuchi, Y., et al. (2016). Comparison of magnesium alloys and poly-l-lactide screws as degradable implants in a canine fracture model. *J. Biomed. Mater. Res. Part B Appl. Biomater*. 104, 1282–1289. doi: 10.1002/jbm.b.33470

Myrissa, A., Martinelli, E., Szakács, G., Berger, L., Eichler, J., Fischerauer, S. F., et al. (2016). *In vivo* degradation of binary magnesium alloys - A long-term study. *Bio. Nano Mater.* 17, 121–130. doi: 10.1515/bnm-2016-0006

Nagarajan, D., CÃ¡ceres, C. H., and Griffiths, J. R. (2016). Grain size hardening effects in Mg-Gd solid solutions. *Metall. Mater. Trans. A* 47, 5401–5408. doi: 10.1007/s11661-016-3686-1

Pavlina, E. J., and Van Tyne, C. J. (2008). Correlation of yield strength and tensile strength with hardness for steels. *J. Mater. Eng. Perform.* 17,888–893. doi: 10.1007/s11665-008-9225-5

Rokhlin, L. L. (2003). *Magnesium Alloys Containing Rare Earth Metals: Structure and Properties, 1st Edn*. London: Taylor & Francis.

Stanford, N., Atwell, D., and Barnett, M. R. (2010). The effect of Gd on the recrystallisation, texture and deformation behaviour of magnesium-based alloys. *Acta Mater*. 58, 6773–6783. doi: 10.1016/j.actamat.2010.09.003

Stanford, N., and Barnett, M. R. (2008). The origin of "rare earth" texture development in extruded Mg-based alloys and its effect on tensile ductility. *Mater. Sci. Eng. A*. 496, 399–408. doi: 10.1016/j.msea.2008.05.045

Sukedai, E., and Yokoyama, T. (2010). Investigation of tensile-compressive yield asymmetry and the role of deformation twin in extruded pure magnesium. *Int. J. Mater. Res*. 101, 736–740. doi: 10.3139/146.110332

Taha, A. S., and Hammad, F. H. (1990). Application of the hall-petch relation to microhardness measurements on Al, Cu, Al-MD 105, and Al-Cu Alloys. *Phys. Status Solidi* 119, 455–462. doi: 10.1002/pssa.2211190207

Tekumalla, S., Seetharaman, S., Almajid, A., and Gupta, M. (2014). Mechanical properties of magnesium-rare earth alloy systems: a review. *Metals* 5, 1–39. doi: 10.3390/met5010001

Vlček, M., CíŽek, J., Lukáč., F., Hruška, P., Smola, B., Stulíková, I., et al. (2017). Hydrogen absorption in Mg-Gd alloy. *Int. Hydrogen Energy J.* 42, 22598–22604. doi: 10.1016/j.ijhydene.2017.04.012

Wetterlöv Charyeva, O. (2015). *Bioresorbable Magnesium Implants for Bone Applications*. Giessen: University Giessen.

Xu, Y., Gensch, F., Ren, Z., Kainer, K. U., and Hort, N. (2018). Effects of Gd solutes on hardness and yield strength of Mg alloys. *Prog. Nat. Sci. Mater. Int.* 28, 1–7. doi: 10.1016/j.pnsc.2018.10.002

Xu, Y., Ren, Z., Huang, Y., Kainer, K., and Hort, N. (2016). Solid solution strengthening in Mg-Gd. *Mag Technol.* 2016, 135–139. doi: 10.1002/9781119274803.ch27

Yu, H., Kim, Y. M., You, B. S., Yu, H. S., and Park, S. H. (2013). Effects of cerium addition on the microstructure, mechanical properties and hot workability of ZK60 alloy. *Mater. Sci. Eng. A.* 559, 798–807. doi: 10.1016/j.msea.2012.09.026

Zhang, P., Li, S. X., and Zhang, Z. F. (2011). General relationship between strength and hardness. *Mater. Sci. Eng.* A. 529, 62–73. doi: 10.1016/j.msea.2011.08.061

Conflict of Interest Statement: The authors declare that the research was conducted in the absence of any commercial or financial relationships that could be construed as a potential conflict of interest.

frontiers in Materials

ORIGINAL RESEARCH
published: 06 September 2019
doi: 10.3389/fmats.2019.00215

Introducing a High Performance Mg-Based Multicomponent Alloy as an Alternative to Al-Alloys

Khin Sandar Tun, Amit Kumar and Manoj Gupta*

Department of Mechanical Engineering, National University of Singapore, Singapore, Singapore

In this study, the design and development of a new Mg-based multicomponent alloy ($\rho_{th} = 2.33$ g/cc; $\rho_{ex} = 2.15$ g/cc) has been presented which exhibits excellent mechanical properties in hot extruded condition. $Mg_{80}Al_5Cu_5Mn_5Zn_5$ alloy was designed and synthesized using disintegrated melt deposition technique followed by hot extrusion. The alloy was designed in such a way that the concentration of each alloying element remained ≥5 at % with Mg (80 at %) as base metal. Significantly high hardness (196 HV) was realized in $Mg_{80}Al_5Cu_5Mn_5Zn_5$ alloy. Compression results showed substantially high ultimate compressive strength (UCS) 616 MPa of this alloy with a reasonably high ductility of 16.9%. This alloy also exhibited superior combination of tensile strengths (TYS- 211 MPa, UTS- 318 MPa) and ductility (8.2%). Overall combination of hardness, tensile and compression properties showed the current new lightweight alloy system as an alternative to most of the commercially used Al-based alloys.

Keywords: multicomponent alloy, magnesium, microstructure, mechanical properties, yield asymmetry

Edited by:
Hajo Dieringa,
Helmholtz Centre for Materials and Coastal Research (HZG), Germany

Reviewed by:
Wenxiang Xu,
Hohai University, China
Subodh Kumar,
Indian Institute of Science (IISc), India

***Correspondence:**
Manoj Gupta
mpegm@nus.edu.sg

Specialty section:
This article was submitted to Structural Materials, a section of the journal Frontiers in Materials

Received: 02 July 2019
Accepted: 20 August 2019
Published: 06 September 2019

Citation:
Tun KS, Kumar A and Gupta M (2019) Introducing a High Performance Mg-Based Multicomponent Alloy as an Alternative to Al-Alloys. Front. Mater. 6:215. doi: 10.3389/fmats.2019.00215

INTRODUCTION

High-performance materials are the key drivers to boost the safety and performance of devices in multiple engineering sectors. Lightweight materials assist in enhancing the efficiency of a vehicle by reducing the vehicle weight, thus reducing the energy requirements for operations. In general, 10% reduction in weight of a vehicle can reduce 6–8% fuel requirement, which is an important aspect of reducing the existing problem of carbon footprint (Cheah, 2010). The main drawback of the existing lightweight materials is either their limited properties or high manufacturing cost. Thus, continuous efforts have been made by researchers to develop new types of lightweight alloys, which are low in cost and capable to meet properties requirements (Miller et al., 2000). Over past three decades, efforts have been made to replace steel and iron with aluminum (Al) and magnesium (Mg) based materials.

In general, the basic principles of designing an alloy involves the application of the fundamental principles of chemistry and thermodynamic parameters (enthalpy, entropy, free energy, and so on), to decide whether certain elements are suitable for alloying or not. According to the entropy of mixing or Configurational Entropy, alloys can be classified as low, medium, and high entropy alloys (Yeh, 2013; Gao et al., 2016). If the CE of an alloy is <1.0 R (8.314 J/mol.K) then it is considered as a low-entropy alloy (LEA) and most of the conventional Fe-, Al-, Cu-, Mg-base alloys belongs to this category. If an alloy is having Configurational Entropy ≥1.0 R and ≤1.5 R then this is considered as a medium-entropy alloy (MEA) and bulk metallic glasses (BMGs) belong to this category. If for an alloy, Configurational Entropy is ≥1.5 R then it is considered as a high-entropy alloy (HEA). HEAs contains at least five principle elements, each having atomic percentage between 5 and 35%, to maximize the configurational entropy. This results in a simple solid solution structure with excellent properties (Cantor et al., 2004; Yeh et al., 2004; Varalakshmi et al., 2010; Senkov et al., 2011; Gao et al., 2016).

Most of the conventional alloys or LEAs have one dominant principal element as the amount of other alloying elements are in small quantity. Therefore, most of the lightweight conventional alloys possess good ductility but poor strength, which is not desirable for many structural applications. For example, Mg (density 1.74 g/cc) is lightest structural material and termed as "next generation material." However, the utilization of Mg and its alloys in critical engineering applications is still limited due to its low absolute strength, ductility, and creep resistance (Friedrich, 2006; King, 2007; Alam et al., 2011; Kumar et al., 2017). Although a variety of Mg and Al-base lightweight alloys have already been developed, alloys with better structural properties are still required to fulfill the current and future material requirements. On the other side, BMGs (MEAs) and recently develop HEAs possess very high compressive strength and hardness but no significant tensile response and poor ductility for their use in wide spectrum of structural applications. Thus, it requires a new strategy to design lightweight alloys, which overcome this barrier of strength and ductility.

Therefore, in this work, we have adopted an approach of multicomponent alloy (MCA) to design Mg-based $Mg_{80}Al_5Cu_5Mn_5Zn_5$ alloy. The reason for selecting this approach was to create a more disordered structure compared to conventional Mg alloy by using a higher amount of alloying elements (Al, Cu, Mn, Zn each 5 at %). This disordered structure is targeted to increase the overall entropy of the alloy leading eventually to formation of high strength phases embedded in a comparatively ductile phase. This combination of hard and soft phases is expected to exhibit a good combination of high strength and ductility. So the main objective of this work is to develop a new light weight multicomponent alloy system with better structural properties than the commonly used lightweight Mg alloys and Al alloys.

MATERIALS AND PROCESSING

In this work, $Mg_{80}Al_5Cu_5Mn_5Zn_5$ alloy was synthesized by using disintegrated melt deposition (DMD) technique, which is already established and ensures good microstructural and mechanical properties of Al-based and Mg-based alloys and their composites (Gupta and Wong, 2005; Nguyen and Gupta, 2008; Paramsothy et al., 2009; Meenashisundaram et al., 2014). This solidification-based technique is followed by hot extrusion to homogenize the microstructure for relatively superior mechanical performance.

Magnesium turnings (99.9% purity) (Acros Organics, USA), Al & Zn granules (99% purity) (Sigma Aldrich, USA), and Cu (99% purity) & Mn (99.95% purity) powders ($\sim 40\,\mu m$) (Alfa Aesar, USA) were used as starting material. Initially, all the elements in predetermined composition were superheated to 850°C in an inert argon gas atmosphere in a graphite crucible using electrical resistance furnace. The superheated melt was then stirred at 500 rpm for 10 min using a stainless steel impeller with twin blade (pitch 45°). The molten melt was poured through a nozzle of 10 mm diameter at the bottom of the crucible to the mold below the crucible. Two jets of argon gas, oriented normal to the melt stream were used to disintegrate the molten metal before it enters the mold to assist in realizing refined cast microstructure. The disintegrated melt was then deposited in the cylindrical mold of 40 mm diameter. This ingot was later machined to 36 mm diameter and 45 mm length for the secondary processing. Secondary processing involved the homogenization of ingot at 400°C for 1 h in a constant temperature furnace followed by hot extrusion at 350°C temperature using 150-ton hydraulic extrusion press. The extrusion ratio of 20.25:1 was set to obtain rods of diameter 8 mm.

CHARACTERIZATION

The microstructure of alloy was characterized using, scanning electron microscopes (JEOL JSM-6010 and Hitachi FESEM-S4300) equipped with energy dispersive spectrometric analysis (EDS). X-Ray diffraction analysis was conducted using an automated Shimadzu LAB-XRD- 6000 (Cu Kα: $\lambda = 1.54056$ A°) spectrometer with a scan speed of 2°/min. The density of extruded samples was measured using Archimedes principle. Microhardness of samples was measured using a Shimadzu HMV automatic digital microhardness tester (Kyoto, Japan) with a Vickers indenter (pyramidal shaped diamond indenter with a phase angle of 136°). An indenting load of 25 gf was used for a dwell time of 15 s. The test was performed as per ASTM E384-11e1. At least three samples were tested with minimum 10 repeatable values. The tensile properties were measured at ambient temperature in accordance with ASTM E8/E8M-15a. A fully automated servo-hydraulic mechanical testing machine, MTS-810 was used to test tensile specimens of diameter 5 mm and gauge length 25 mm using a strain rate of 1.693×10^{-4} s^{-1}. Clip type, Instron 2630-100 series extensometer was used to measure the tensile fracture strain. The compression properties were also measured using the same equipment at an ambient temperature in accordance with ASTM E9-09 using a strain rate of 8.334×10^{-5} s^{-1}. The specimens of 8 mm diameter, with length to diameter ratio of one were used. At least five different samples were tested to ensure repeatability of results. Fractured surfaces of all samples (under tensile and compressive load) were analyzed using Hitachi S-4300 FESEM.

RESULTS AND DISCUSSION

Figure 1 shows the results for microstructural characterization of extruded $Mg_{80}Al_5Cu_5Mn_5Zn_5$ alloy using SEM, XRD, and EDS analysis techniques. It is clear from the SEM micrograph (**Figure 1A**) that the alloy demonstrates a multiphase structure. Three different types of phase morphology were observed, the base matrix (dark gray), polyhedron shape phases (light gray) and scattered, and irregular shape phases. From the XRD results (**Figure 1B**), the matching peaks are identified as that of Mg (dominating hcp base structure) and the secondary phases of Al_6Mn phase and Al_2CuMg phase. EDS analysis (**Figures 1C–E**)

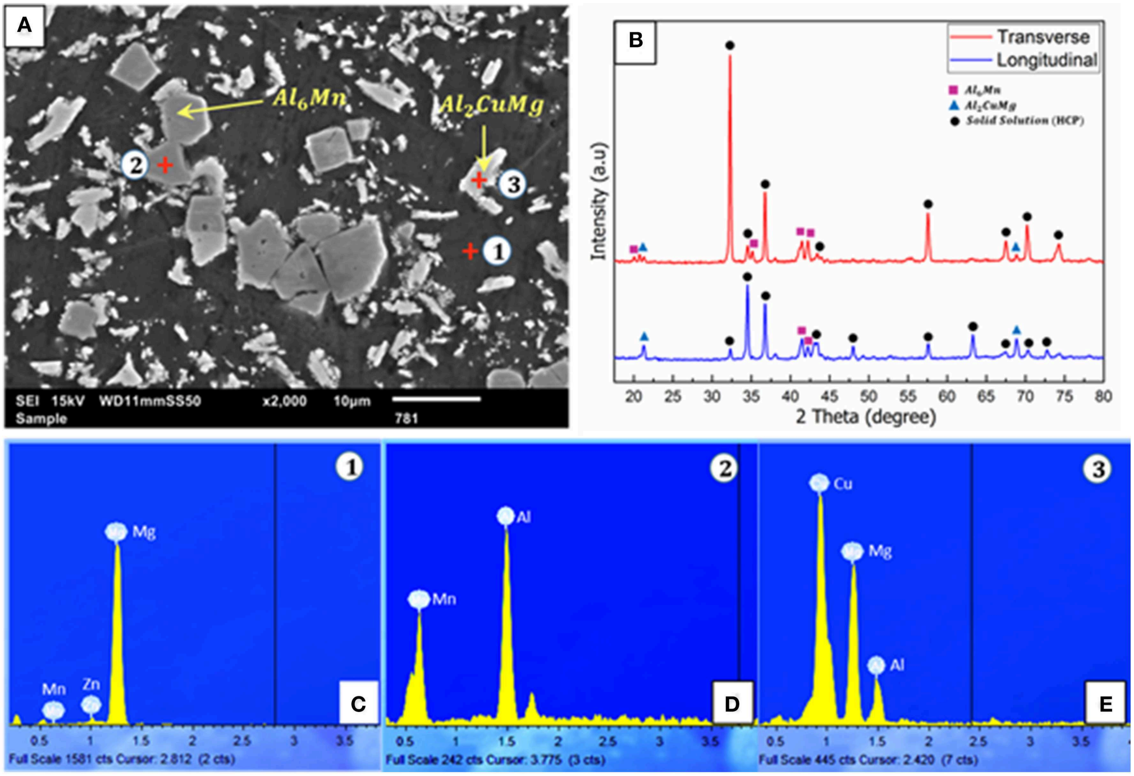

FIGURE 1 | SEM, XRD, and EDS results of $Mg_{80}Al_5Cu_5Mn_5Zn_5$ MCA. **(A)** SEM micrograph reveals the presence of three phases, base matrix, polyhedron phase, and smaller scattered precipitates. **(B)** XRD results revealing the presence of Mg hcp structure as a dominating phase together with the presence of Al_6Mn and Al_2CuMg phase. **(C–E)** EDS spectrums taken on three different phase location (1, 2, and 3) in SEM micrograph **(A)**, further verified the presence of Mg-base solid solution matrix with Al_6Mn and Al_2CuMg as embedded phases.

TABLE 1 | Mechanical properties of $Mg_{80}Al_5Cu_5Mn_5Zn_5$ alloy and other Mg-base and Al-base alloys.

Type of alloy	Composition	Compression			Tensile			Density (g/cc)	Microhardness (HV)
		CYS (MPa)	UCS (MPa)	ε (%)	TYS (MPa)	UTS (MPa)	ε (%)		
This work	$Mg_{80}Al_5Cu_5Mn_5Zn_5$	192 ± 0	616 ± 9	16.9 ± 0.8	211 ± 3	318 ± 5	8.2 ± 0.8	2.15	196 ± 41
Mg and alloys	Pure Mg	87 ± 4	240 ± 9	19.2 ± 0.7	125 ± 9	169 ± 11	6.2 ± 0.7	1.74	48 ± 1
	AZ31	93 ± 9	486 ± 4	19.7 ± 7.2	172 ± 15	263 ± 12	10.4 ± 3.9	1.77	64 ± 4
	ZK60	93 ± 8	498 ± 16	23.2 ± 4.6	182 ± 4	271 ± 1	6.7 ± 1	1.83	117 ± 6
Al alloys	Al6061 (Extruded)	NR	NR	NR	131	205	16.5	2.70	57.4 ± 1.1
	Al 2024-(O)	NR	NR	NR	130	240	12	2.78	50
	Al 7075-(O)	110	NR	NR	103	228	10	2.81	65

conducted on the phases (see 1, 2, and 3 marked locations in SEM micrograph, **Figure 1A**) revealed the presence of Mg, Zn, and Mn in base matrix (location 1), Al and Mn at polyhedral phase (location 2) and Al, Cu, and Mg at scattered phase (location 3), confirming further the results of XRD.

Table 1 summarizes the results of the mechanical characterization studies of $Mg_{80}Al_5Cu_5Mn_5Zn_5$ alloy under compression and tensile loading, hardness, and density measurement. The hardness results of $Mg_{80}Al_5Cu_5Mn_5Zn_5$ MCA show significantly high hardness value of the alloy when compared to Mg based (Paramsothy et al., 2012) and Al based alloys (Committee, 1990; Knowles et al., 2014; **Table 1**). It is understandable that both solid solution phase and intermetallic phases contributed to high hardness. These results also suggest that these materials are likely to exhibit superior tribological response (sliding wear) as per Archard's law. Further work is continuing in this area.

Based on the density of current Mg MCA (2.15 g/cc), comparison of tensile properties was made with Al alloys with density, 2.7–2.8 g/cc. As there was no heat treatment performed on this alloy, all the alloys chosen for the comparison point of view are taken in extruded conditions, without any heat treatment. Mg MCA developed in this study exhibited high tensile yield strength (211 MPa) and ultimate tensile strength (318 MPa) with a fracture strain of 8.2%. The tensile strengths of this Mg MCA are superior to Al-base alloys (see **Table 1**) reported in literature while maintaining the reasonable fracture strain value.

When compared to as-extruded Mg and Mg based alloys which were processed using the same fabrication technique (Sankaranarayanan et al., 2011; Paramsothy et al., 2012), the current Mg based MCA showed higher yield and ultimate tensile strengths with comparable failure strain considering the standard deviation. The compression results of $Mg_{80}Al_5Cu_5Mn_5Zn_5$ alloy showed substantially high ultimate compressive strength (UCS) 616 MPa, which is 61, 21 and 19% higher than the strength of pure Mg, AZ31, and ZK60 with a marginally lower ductility.

Figure 2 shows the mechanical behavior of $Mg_{80}Al_5Cu_5Mn_5Zn_5$ alloy. Engineering stress and strain response in compression and tension are shown in **Figure 2A**. Compression response of alloy shows evidence of significant strain hardening prior to fracture. Here, yield strength was calculated using 0.2% offset strain criterion in both compression and tensile testing. To further compare the compression response of $Mg_{80}Al_5Cu_5Mn_5Zn_5$ alloy over previously reported Mg alloys, ultimate compression strength and strain data are plotted in **Figure 2B**. The present MCA stands far above the reported Mg-based alloys in terms of strength while maintaining appreciable ductility (∼17%). **Figures 2C,D** shows the fractured sample during the tensile and compression testing, respectively. Tensile sample fractured in a near cup and cone mode revealing a relatively ductile character, while the compression failure occurred at 45° to compression axis resembling a ductile shear failure. To understand the failure mechanisms in tension and compression, fractography using SEM was performed on fractured surfaces. **Figure 3** shows the SEM fractography for samples failed under compressive and tensile loadings. The shear bands observed in compression fractograph clearly indicate the ductile failure under compression stress (**Figure 3A**). Tensile fractography also shows the dimple shaped features similar to common ductile fracture, except the presence of cleavage fracture at few locations. Cracking of hard icosahedral Al_6Mn phase was also observed (**Figure 3B**).

The large improvement in the mechanical properties of $Mg_{80}Al_5Cu_5Mn_5Zn_5$ MCA arises from the plastic deformation and strain hardening processes. By observing the SEM micrograph (**Figure 1A**) it is clear that the alloy contains a base hcp crystalline structure (Mg-rich solid solution) and two other dispersed hard phases Al_6Mn and Al_2CuMg. During compression, when load is applied on material good amount of plasticity was observed due to continuous solid solution base matrix. On the other hand, in tension, when material is subjected to stress, comparatively less amount of plastic deformation was observed due to less number of possible slip systems available in hcp structure. Due to the presence of secondary phases, high yield and ultimate tensile strength was achieved effectively but material failed at a fracture strain of ∼8.2%.

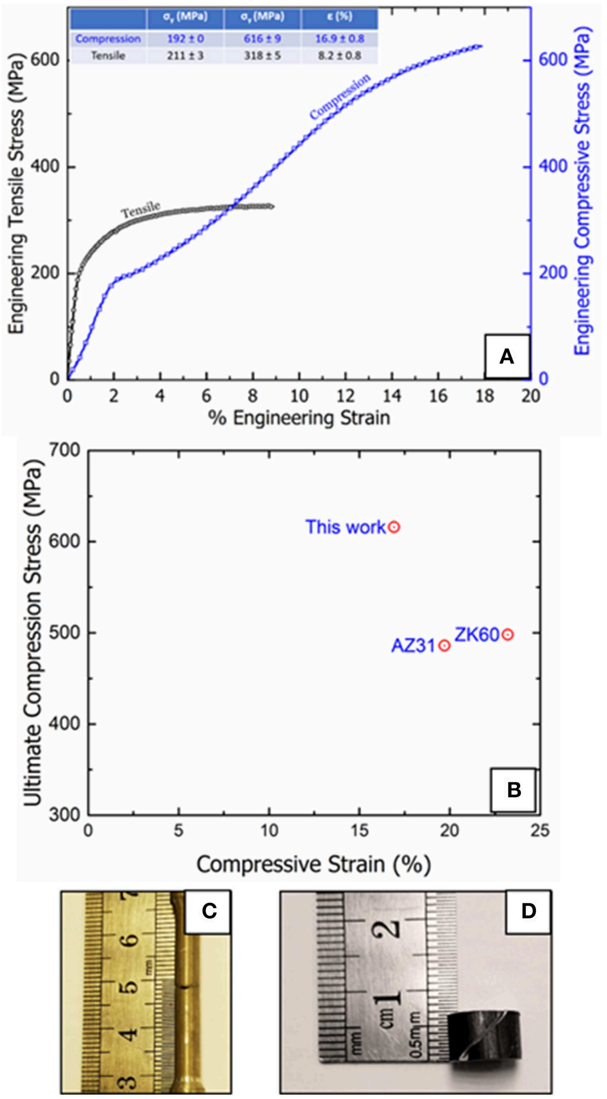

FIGURE 2 | Mechanical behavior of $Mg_{80}Al_5Cu_5Mn_5Zn_5$ alloy. **(A)** Engineering stress vs. strain graphs. Table (Inset) contains the engineering stress and strain values observed in compression and tension. Standard deviation results indicate the consistency and reliability of material. **(B)** Comparison of stress and strain with other Mg alloys reveals the superiority of $Mg_{80}Al_5Cu_5Mn_5Zn_5$ MCA. **(C,D)** Fractured samples during tensile and compression tests.

If overall properties, hardness, tensile, and compression are compared with other alloys, this alloy possesses a much better overall combination of structural properties. One important aspect of the weight critical industries such as automotive industry is that the material should exhibit almost symmetric tensile/compressive behavior (∼1). It is well-known that Mg and conventional wrought Mg alloys exhibit strong basal texture through secondary processing such as extrusion and rolling which leads to severe yield asymmetry (Kim et al., 2005; del Valle and Ruano, 2009; Yin et al., 2009; Gupta and Ling, 2011). The compression to tension yield asymmetry

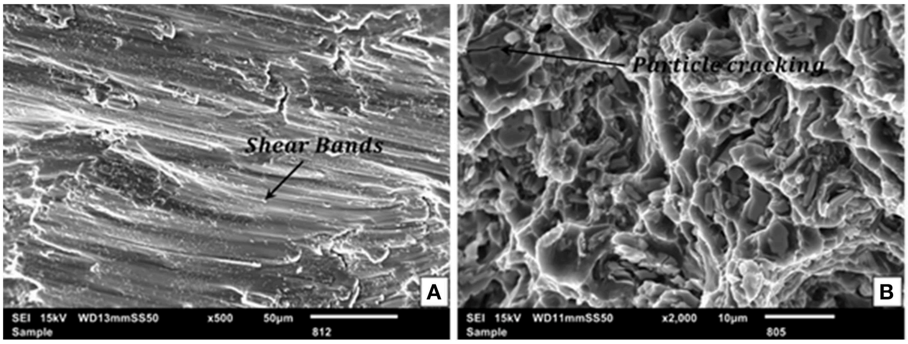

FIGURE 3 | SEM fractographs of $Mg_{80}Al_5Cu_5Mn_5Zn_5$ alloy in compression and tension. **(A)** Reveals the dominating shear failure in compression. **(B)** Shows ductile failure of the matrix under tension and cracked hard phase (Al_6Mn).

TABLE 2 | List of wrought Mg and alloys with their respective compression to tension asymmetry (C/T) ratio.

Materials	Compressive yield strength	Tensile yield strength	C/T ratio
$Mg_{80}Al_5Cu_5Mn_5Zn_5$	192	211	0.9
Pure Mg	87	125	0.69
AZ31	93	172	0.54
ZK60	93	182	0.51
AZ31B	95	200	0.475
AZ61A	130	230	0.56
AZ80A	140	250	0.56
ZK21A	135	195	0.69
ZK60A	185	250	0.74

ratio (C/T ratio) of current MCA, pure Mg, and various wrought Mg alloys are listed in **Table 2** (Gupta and Ling, 2011; Sankaranarayanan et al., 2011; Paramsothy et al., 2012). The C/T ratio in Mg MCA was measured to be 0.9 (∼1) (**Table 2** and **Figure 2A**) exhibiting nearly symmetric yield strength under tension and compression as compared to Mg and wrought Mg alloys with C/T ratio between 0.5 and 0.7 showing asymmetric yield strengths. A minimal yield asymmetry is often looked for material selection in transportation sector.

The XRD pattern of Mg MCA taken along transverse and longitudinal to the extrusion direction is shown in **Figure 1B**. It can be seen from the XRD pattern under longitudinal condition that there was relatively strong basal texture showing highest intensity of the peak related to basal plane. Under this condition, compressive stress parallel to the basal plane favors {1 0 1 2} twinning and this induces yielding at low stress level under compression. However, as seen in **Figure 2A**, yielding was not initiated at a lower stress showing the difficulty of plastic deformation induced by twinning in the current alloy system. Twinning for initial yielding was inhibited by the presence of different types of second phases. This phenomenon led to the realization of yield asymmetry ratio of 0.9 which is closer to 1, in Mg MCA showing the similar strength level under both tension and compression. In a related study (Hidalgo-Manrique et al., 2017), it was reported that the creation of precipitates through heat treatment prevent twin initiation and thereby reduce the yielding asymmetry by increasing the compressive yield strength. In the current study, the compressive yield strength was increased through the presence of second phases due to the addition of multiple alloying elements in Mg matrix without the additional step of heat treatment.

CONCLUSIONS

In this work, the effects of multicomponent alloying (Al, Cu, Mn, Zn, each 5 at %) on microstructural and mechanical properties of Mg were investigated. Following conclusions can be drawn:

Microstructural characterization concluded that Al_6Mn and Al_2CuMg dispersed hard phases are embedded in the soft Mg base hcp solid solution phase to give rise to superior combination of strength and ductility.

Significantly high hardness (196 HV) was realized in $Mg_{80}Al_5Cu_5Mn_5Zn_5$ alloy that is two to four times higher when compared to commercially used alloys.

Compression characterization results concluded that the $Mg_{80}Al_5Cu_5Mn_5Zn_5$ alloy shows superior combination of compressive strength (616 MPa) and ductility (16.9%) when compared to conventional Mg alloys.

Tensile characterization results showed that $Mg_{80}Al_5Cu_5Mn_5Zn_5$ alloy exhibits higher ultimate tensile strength (318 MPa) with a reasonable ductility (8.2%) when compared to conventional Mg and Al base alloys in as-extruded condition.

The current alloy system showed a symmetric tensile/compression yielding behavior which is an important aspect of the weight critical industrial application. This yield symmetry was achieved in the current as-extruded alloy without performing additional heat treatment.

DATA AVAILABILITY

All datasets generated for this study are included in the manuscript/supplementary files.

AUTHOR CONTRIBUTIONS

AK and MG designed the experiments. AK conducted the all necessary experiments under MG guidance. KT and AK wrote the manuscript. All authors commented on the manuscript.

FUNDING

The authors would like to acknowledge Ministry of Education Academic Research Funding (WBS# R-265-000-586-114) Singapore for the financial support in carrying out this research work.

REFERENCES

Alam, M. E., Han, S., Nguyen, Q. B., Salem Hamouda, A. M., and Gupta, M. (2011). Development of new magnesium based alloys and their nanocomposites. *J. Alloys Compd.* 509, 8522–8529. doi: 10.1016/j.jallcom.2011.06.020

Cantor, B., Chang, I. T. H., Knight, P., and Vincent, A. J. B. (2004). Microstructural development in equiatomic multicomponent alloys. *Mater. Sci. Eng. A* 375–−377, 213–218. doi: 10.1016/j.msea.2003.10.257

Cheah, L.W. (2010). *Cars on a* Diet: *The Material and Energy Impacts of Passenger Vehicle Weight Reduction in the US.* Massachusetts Institute of Technology (MIT).

Committee, A. I. H. (1990). *Properties and Selection: Nonferrous Alloys and Special-Purpose Materials*. Ohio: ASM International.

del Valle, J. A., and Ruano, O. A. (2009). Effect of annealing treatments on the anisotropy of a magnesium alloy sheet processed by severe rolling. *Mater. Lett.* 63, 1551–1554. doi: 10.1016/j.matlet.2009.04.014

Friedrich, H. E, and Mordike, B.L. (2006). *Magnesium Technology: Metallurgy, Design Data, Applications.* Heidelberg: Springer, Berlin.

Gao, M. C., Yeh, J. W., Liaw, P. K., and Zhang, Y. (2016). *High-Entropy Alloys: Fundamentals and Applications*. Cham: Springer International Publishing. doi: 10.1007/978-3-319-27013-5

Gupta, M., and Ling, S. N. M. (2011). *Magnesium, Magnesium Alloys, and Magnesium Composites*. Hoboken, NJ: Wiley. doi: 10.1002/9780470905098

Gupta, M., and Wong, W. (2005). Enhancing overall mechanical performance of metallic materials using two-directional microwave assisted rapid sintering. *Scr. Mater.* 52, 479–483. doi: 10.1016/j.scriptamat.2004.11.006

Hidalgo-Manrique, P., Robson, J. D., and Pérez-Prado, M. T. (2017). Precipitation strengthening and reversed yield stress asymmetry in Mg alloys containing rare-earth elements: a quantitative study. *Acta Mater.* 124, 456–467. doi: 10.1016/j.actamat.2016.11.019

Kim, S.-H., You, B.-S., Dong Yim, C., and Seo, Y.-M. (2005). Texture and microstructure changes in asymmetrically hot rolled AZ31 magnesium alloy sheets. *Mater. Lett.* 59, 3876–3880. doi: 10.1016/j.matlet.2005.07.024

King, J. F. (2007). Magnesium: commodity or exotic? *Mater. Sci. Technol.* 23, 1–14. doi: 10.1179/174328407X154374

Knowles, A. J., Jiang, X., Galano, M., and Audebert, F. (2014). Microstructure and mechanical properties of 6061 Al alloy based composites with SiC nanoparticles. *J. Alloys Compd.* 615, S401–S405. doi: 10.1016/j.jallcom.2014.01.134

Kumar, A., Meenashisundaram, G. K., Manakari, V., Parande, G., and Gupta, M. (2017). Lanthanum effect on improving CTE, damping, hardness and tensile response of Mg-3Al alloy. *J. Alloys Compd.* 695, 3612–3620. doi: 10.1016/j.jallcom.2016.11.400

Meenashisundaram, G. K., Seetharaman, S., and Gupta, M. (2014). Enhancing overall tensile and compressive response of pure Mg using nano-TiB_2 particulates. *Mater. Charact.* 94, 178–188. doi: 10.1016/j.matchar.2014.05.021

Miller, W. S., Zhuang, L., Bottema, J., Wittebrood, A. J., De Smet, P., Haszler, A., et al. (2000). Recent development in aluminium alloys for the automotive industry. *Mater. Sci. Eng. A* 280, 37–49. doi: 10.1016/S0921-5093(99)00653-X

Nguyen, Q. B., and Gupta, M. (2008). Enhancing compressive response of AZ31B magnesium alloy using alumina nanoparticulates. *Compos. Sci. Technol.* 68, 2185–2192. doi: 10.1016/j.compscitech.2008.04.020

Paramsothy, M., Chan, J., Kwok, R., and Gupta, M. (2012). Al2O3 nanoparticle addition to commercial magnesium alloys: multiple beneficial effects. *Nanomaterials* 2, 147–162. doi: 10.3390/nano2020147

Paramsothy, M., Hassan, S. F., Srikanth, N., and Gupta, M. (2009). Enhancing tensile/compressive response of magnesium alloy AZ31 by integrating with Al_2O_3 nanoparticles. *Mater. Sci. Eng. A* 527, 162–168. doi: 10.1016/j.msea.2009.07.054

Sankaranarayanan, S., Jayalakshmi, S., and Gupta, M. (2011). Effect of ball milling the hybrid reinforcements on the microstructure and mechanical properties of $Mg–(Ti + n\text{-}Al_2O_3)$ composites. *J. Alloys Compd.* 509, 7229–7237. doi: 10.1016/j.jallcom.2011.04.083

Senkov, O., Wilks, G., Scott, J., and Miracle, D. (2011). Mechanical properties of Nb 25 Mo 25 Ta 25 W 25 and V 20 Nb 20 Mo 20 Ta 20 W 20 refractory high entropy alloys. *Intermetallics* 19, 698–706. doi: 10.1016/j.intermet.2011.01.004

Varalakshmi, S., Kamaraj, M., and Murty, B. S. (2010). Processing and properties of nanocrystalline CuNiCoZnAlTi high entropy alloys by mechanical alloying. *Mater. Sci. Eng. A.* 527, 1027–1030. doi: 10.1016/j.msea.2009.09.019

Yeh, J.-W. (2013). Alloy design strategies and future trends in high-entropy alloys. *JOM* 65, 1759–1771. doi: 10.1007/s11837-013-0761-6

Yeh, J.-W., Chen, S.-K., Lin, S.-J., Gan, J.-Y., Chin, T.-S., Shun, T.-T., et al. (2004). Nanostructured high-entropy alloys with multiple principal elements: novel alloy design concepts and outcomes. *Adv. Eng. Mater.* 6, 299–303. doi: 10.1002/adem.200300567

Yin, D. L., Wang, J. T., Liu, J. Q., and Zhao, X. (2009). On tension–compression yield asymmetry in an extruded Mg−3Al−1Zn alloy. *J. Alloys Compd.* 478, 789–795. doi: 10.1016/j.jallcom.2008.12.033

Conflict of Interest Statement: The authors declare that the research was conducted in the absence of any commercial or financial relationships that could be construed as a potential conflict of interest.

frontiers
in Materials

ORIGINAL RESEARCH
published: 25 September 2019
doi: 10.3389/fmats.2019.00236

Mechanical Properties of Magnetron Sputtered Free Standing Mg-Ag Alloy Films

*Lea K. Jessen, Christiane Zamponi and Eckhard Quandt**

Chair of Inorganic Functional Materials, Institute for Materials Science, Faculty of Engineering, Kiel University, Kiel, Germany

Magnesium based alloys gained great interest for medical biodegradable applications. Limitations arise from high corrosion rates and mechanical properties of the Mg based alloys. In recent work it was shown that the corrosion rate of a precipitate free Mg-6Ag thin film can be reduced by a factor of three compared to pure sputtered Mg. As Mg-6Ag combines the very promising corrosion results with a potential therapeutically use of Ag ions, the investigation of their mechanical properties is needed for a full characterization of Mg-Ag alloys as biodegradable material. In this work the Ag content was varied from 2 to 10 wt%. The investigated thin film samples were dog-bone shaped samples with a thickness of 20 µm. The samples were fabricated by a combination of UV lithography, sacrificial layer technique and magnetron sputtering. The mechanical properties were determined using uniaxial tensile test. Compared to pure Mg samples fabricated by the same processing route the yield strength is approximately doubled for Ag containing samples. For films with a Ag concentration up to 8 wt% the elongation at fracture reaches a value of ~7%. Further increase of the Ag concentration leads to lower elongation at fracture. Thus, especially due to the low corrosion rate, Mg-6Ag shows the optimum of all investigated alloys, with a yield strength of ~310 MPa and an elongation at fracture of ~6%.

Keywords: magnetron sputtered thin films, Mg-Ag alloys, biodegradable, mechanical properties, microstructure

Edited by:
Hajo Dieringa,
Helmholtz Centre for Materials and Coastal Research (HZG), Germany

Reviewed by:
Jindrich Musil,
University of West Bohemia, Czechia
Thomas Ebel,
Helmholtz Centre for Materials and Coastal Research (HZG), Germany

****Correspondence:***
Eckhard Quandt
eq@tf.uni-kiel.de

Specialty section:
This article was submitted to Structural Materials, a section of the journal Frontiers in Materials

Received: *24 May 2019*
Accepted: *10 September 2019*
Published: *25 September 2019*

Citation:
Jessen LK, Zamponi C and Quandt E (2019) Mechanical Properties of Magnetron Sputtered Free Standing Mg-Ag Alloy Films. Front. Mater. 6:236. doi: 10.3389/fmats.2019.00236

INTRODUCTION

The research in the field of biodegradable materials is increased over the last decade (Zheng et al., 2014). Magnesium (Mg) and Mg based alloys are attractive candidates for biodegradable metallic implants (Li et al., 2004; Song, 2007). A limitation of these materials is a high corrosion rate. This limits the functional stability and thus the intended medical purpose of the implant (Hermawan et al., 2010; Zheng et al., 2014). Mg based alloys are used to tailor the corrosion rate as well as the mechanical properties. Commonly used alloying elements are for example Zn, Ca, or rare earths such as Y, Gd, Nd (Song, 2007; Witte et al., 2008; Hermawan, 2012; Zheng et al., 2014).

In the case of bulk materials an additional solution heat treatment with quenching (T4 heat treatment) (ASM International, 1992a) is needed because otherwise precipitates are formed. The temperatures and times differ depending on the alloy composition and sample size.

For the sputtered thin films, no additional heat treatment is necessary because magnetron sputtering is a non-equilibrium process which allows the fabrication of metastable supersaturated materials in certain compositional ranges exceeding the stable conditions (ASM International, 1992a; Li et al., 2004; Song, 2007; Witte et al., 2008; Hermawan et al., 2010; Hermawan, 2012; Schlüter et al., 2014; Zheng et al., 2014). Additionally, this leads to a high defect density in the fabricated films. The special microstructure of sputtered films compared to bulk material has an influence on the mechanical properties.

Mechanical tests on sputtered thin films were performed earlier on Mg-rare earth alloys (Schlüter et al., 2014). These alloys are known for their good mechanical properties, respectively, its high strength (Gao et al., 2009a,b; Hort et al., 2010). The mechanical and corrosion behavior of as deposited magnetron sputtered binary and ternary Mg-rare earth alloys were investigated. Mg-5Y and Mg-5Gd showed an elongation at fracture of ∼20% and a yield strength of ∼240 MPa. Even higher yield strength could be obtained for Mg-20Y with ∼400 MPa however the elongation at fracture was reduced to ∼6% (Schlüter et al., 2014). Mg-4Y-3Gd and Mg-4Y-3Nd was tested as well. The yield strength of the materials was in the range of 220–260 MPa and the elongation at fracture varied between 0 and 20% dependent on the sputter pressure (Schluter et al., 2011; Schlüter et al., 2013). The sputtered Mg-rare earth alloys showed promising mechanical properties. However, there is research necessary to find biocompatible alloys, which show even a lower corrosion rate compared to Mg-rare earth alloys.

The alloys of the Mg-Ag system are interesting for the use as an implant material because in this system, the biodegradable properties of Mg are combined with the antibacterial properties of Ag (Lansdown, 2002; Mijnendonckx et al., 2013; Tie et al., 2013; Liu et al., 2017). The Mg-Ag films could be for example used to avoid inflammations caused by the implantation. It was shown for bulk materials that it is possible to achieve a single phase material with an additional T4 solution heat treatment up to 6 wt% Ag (Tie et al., 2013; Liu et al., 2017; Maier et al., 2018). A solubility of low concentration of Ag ($<$ 15 wt% Ag@ 745 K) in Mg is theoretically achievable according to the Mg-Ag phase diagram (ASM International, 1992b). The Mg-Ag bulk alloys with up to 6 wt% showed a decrease in the corrosion rate compared to Mg and Mg-Ag alloys without any solution heat treatment (Maier et al., 2015, 2018; Liu et al., 2017). The lowest corrosion rate for *in vitro* test was obtained for Mg-2Ag measured in Dulbecco's modified Eagle's medium (DMEM) (Tie et al., 2013). At higher concentrations of Ag, precipitates were formed which led to an increased corrosion rate (Liu et al., 2017). The multi-phase microstructure was formed in the bulk material if no solution heat treatment was applied. Magnetron sputtered Mg-Ag films showed even lower corrosion rates compared to the bulk (Jessen et al., 2019). This is most probably the result of the special microstructure which is obtained by sputtering as well as the small grain diameter smaller than 1 μm. It was shown that the crystallographic orientation within the sample plays a role as well as the grain size (Liu et al., 2008; Jiang et al., 2017). For the sputtered films it was possible to achieve a precipitate free material up to 6 wt% Ag without an additional heat treatment. When the concentration was increased to 8 wt% Ag the formation of precipitates started but no influence on the corrosion rate was found. In the case of Mg-10Ag more and larger precipitates were detected which led to the formation of a galvanic cell and results in an increased corrosion rate. The lowest corrosion rate with 0.04 ± 0.01 mm/year was achieved for Mg-6Ag which is by a factor of approximately three lower than Mg (Jessen et al., 2019).

Another important criterium for biodegradable metallic implants are their mechanical properties namely the strength as well as the elongation at fracture. The Young's modulus of Mg alloys is about 45 GPa (ASM International, 1992a), which is compared to other metals e.g., Fe with a Young's modulus of 200 GPa, close to that of bone (3–20 GPa). For this reason, Mg is a welcome material for orthopedic applications, because the likelihood of stress shielding is minimized (Staiger et al., 2006; Hermawan, 2012). For bulk materials, the mechanical properties of Mg-Ag alloys were investigated on cylindrical specimens and wires. The test of the cylindrical samples of Mg-6Ag showed an increase of tensile strength by a factor two compared to Mg (Tie et al., 2014). Furthermore, wires of Mg-6Ag were tested, they showed an ultimate strength of ∼350 MPa and an elongation at fracture of ∼5%. A solution heat treatment reduced the strength to ∼240 MPa but increased the elongation at fracture by a factor of two to ∼10% (Maier et al., 2015, 2018).

For a detailed material analysis, a characterization of the mechanical properties is important. This is the reason why in this study the mechanical properties of as deposited sputtered Mg-Ag alloys free standing films showing very promising corrosion rates are investigated. Only the as deposited samples are investigated, because any additional heat treatment will lead to larger grains or precipitates, which will increase the corrosion rate again (Ralston et al., 2010). For the mechanical testing uniaxial tensile test on 20 μm thick samples were performed. Due to the fact of having free standing sputtered films it is possible to perform tensile tests to determine the mechanical properties. If the films were used as a coating, indentation measurements are needed to determine the hardness and Young's modulus which allows the estimation of crack formation (Musil, 2012, 2015). The influence of varying Ag content between 2 and 10 wt% on the mechanical properties will be determined. The obtained results will be compared to pure Mg free standing films fabricated by the same processing route.

EXPERIMENTAL

Fabrication

A combination of UV lithography and magnetron sputtering was used to fabricate the 20 μm thick free standing film samples. For tensile test dog-bone shaped samples were used, see **Figure 1**. The overall length of the dog-bone shaped sample is 14 mm. The strut has a length of 7 mm, a parallel length of 5.5 mm and a width of 0.5 mm. A mask aligner MA6-8 (Süss MicroTec, Germany) was used for UV lithography. The sputtering was performed in a cluster magnetron sputtering machine Von Ardenne CS730S (VON ARDENNE, Germany). For the fabrication process silicon (Si) wafers with a diameter of 100 mm were used as a substrate material. First the Si substrate was structured by UV lithography, then aluminum (Al), which served as a hard mask for the following Bosch process (Laermer and Schilp, 1996), was deposited on the structured wafer. The deep etching process is necessary to achieve the free standing dog-bone shaped samples. Aluminum nitride (AlN) as a sacrificial layer is deposited on the dry etched substrate, followed by the sputtering of the Mg-Ag alloy. Potassium hydroxide (KOH) (20%) was used to etch selectively the sacrificial AlN layer to achieve the free standing

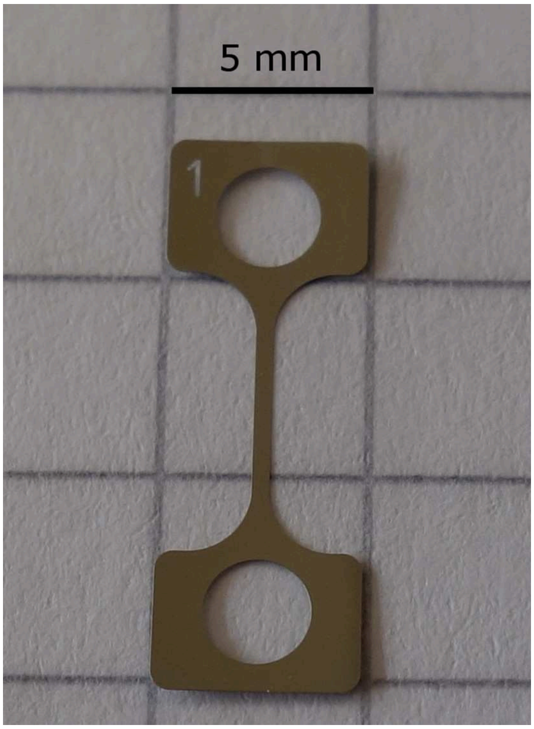

FIGURE 1 | Image of a dog-bone shaped sample.

dog-bone shaped samples. Further details on the fabrication process can be found in (Haffner et al., 2015).

The following targets were used for the different materials: pure Mg, pre alloyed targets of: Mg-2Ag, Mg-6Ag, Mg-8Ag, Mg-10Ag (FHR, Germany) the compositions of the alloys are given in wt%. The achieved composition of the sputtered films is equal to the target composition (Jessen et al., 2019). The sputtering power was set to 200 W for Mg (200 mm diameter) and to 50 W for all the Mg-Ag alloy targets (each 100 mm diameter). The argon (Ar) gas flow was set to 25 sccm for all sputter depositions. The sputtering pressures of the different materials were varied between $1.8 \cdot 10^{-3}$ mbar and $3.0 \cdot 10^{-3}$ mbar in order to minimize the film stress of the different materials. The substrate temperature was measured by temperature stripes which indicated a range between 71°C and 77°C for all depositions. **Table 1** summarizes the sputter parameters.

Analysis of Microstructure

To evaluate the microstructures of the different as deposited samples, cross sections were prepared by focused ion beam (FIB). Using a Helios NanoLab 600 (FEI, Germany) associated with a scanning transmission electron microscopy (STEM) detector. A transmission electron microscope (TEM) [F30 G2-STwin (Tecnai, FEI, Germany)] was employed to analyze the microstructure of the prepared cross sections in more detail.

Mechanical Properties

To determine the mechanical properties uniaxial tensile tests were performed using the above described dog-bone shaped samples. A tensile test machine of the type BETA 5–5/6 × 10 (Messphysik, Austria), with a special sample holder for thin samples was used. A strain rate of 0.4 %/min was applied and as fracture criterion, a force reduction of 60% relative to the maximum applied force was used. For each type, at least eight samples were measured to assess the statistic reliability. From these measurements the average values and standard deviation of the yield strength ($R_{p0.2}$) and elongation at fracture were determined.

Analysis of Fracture

After tensile testing the fractured surface and the surrounding area was investigated using a scanning electron microscope (SEM) (Zeiss Ultra Plus, Germany). X-ray diffraction (XRD) (SmartLab 9 kW, Rigaku, Japan) was used to identify the orientation of the columnar grains in a deformed state and a non-deformed state. Therefore, rocking curves were measured at different positions on the sample after tensile test. One measurement was performed on the head of the dog-bone; this is the reference measurement in a non-deformed area of the dog-bone (head). Another measurement was done at the strut near the head of the dog-bone, this is an area with only slight deformation [strut (head)]. The last measurement was performed next to the fractured surface in a high deformed area (strut (fracture). All measurements were done using Cu K_{α} radiation. The rocking curve was performed in a ω range of ± 8° around the (0002) peak ($\omega = 17.23°$) with a step size of 0.02° and scan speed of 8°/min.

RESULTS

Analysis of Microstructure

An overview of a cross section of a sputtered film (~10 μm thick) is shown in **Figure 2a**. The typical columnar growth of sputtered Mg based alloys is observable. The growth direction of the film is indicated as well as the direction of tensile force during the tensile test which is perpendicular to the growth direction. On the left side smaller grains are visible, where the film growth started. The grain diameter close to the surface of the sputtered samples is smaller than 1 μm. The preferential orientation of the film was determined by XRD. Due to the lowest surface energy of the (0001) plane of the hexagonal close packed structure the growth direction in [0001] is favored. (Thompson, 1990; ASM International, 1999; Gottstein, 2004; Mahieu, 2006; Jessen et al., 2019). **Figure 2b** shows a cross section of Mg at higher magnification. **Figure 2c** shows a cross section of Mg-6Ag at higher magnification that exhibits a special microstructure which resembles feather-like, so in the following it is referred to as feather-like microstructure. This microstructure will form due to agglomeration of Ag richer areas within a Mg based matrix. In the case of Mg-10Ag (also higher magnification) binary MgAg precipitates are formed, see **Figure 2d** (Jessen et al., 2019). The Mg-Ag precipitates could be not clearly assigned to the possible intermetallic phases like $Mg_{54}Ag_{17}$, Mg_7Ag_3, or Mg_3Ag (Tie et al., 2014; Liu et al., 2015a,b; Ren et al., 2018).

TABLE 1 | Sputter parameters of the different materials.

Material	Sputtering pressure (10^{-3} mbar)	Gas flow (Ar sccm)	Power (W)	Target diameter (mm)	Substrate deposition temperature (°C)	Deposition rate (nm/s)
Mg	2.1	25	200	200	71–77	1.85
Mg-2Ag	2.3	25	50	100	71–77	2.55
Mg-6Ag	3.0	25	50	100	71–77	2.58
Mg-8Ag	2.6	25	50	100	71–77	2.52
Mg-10Ag	1.8	25	50	100	71–77	2.27

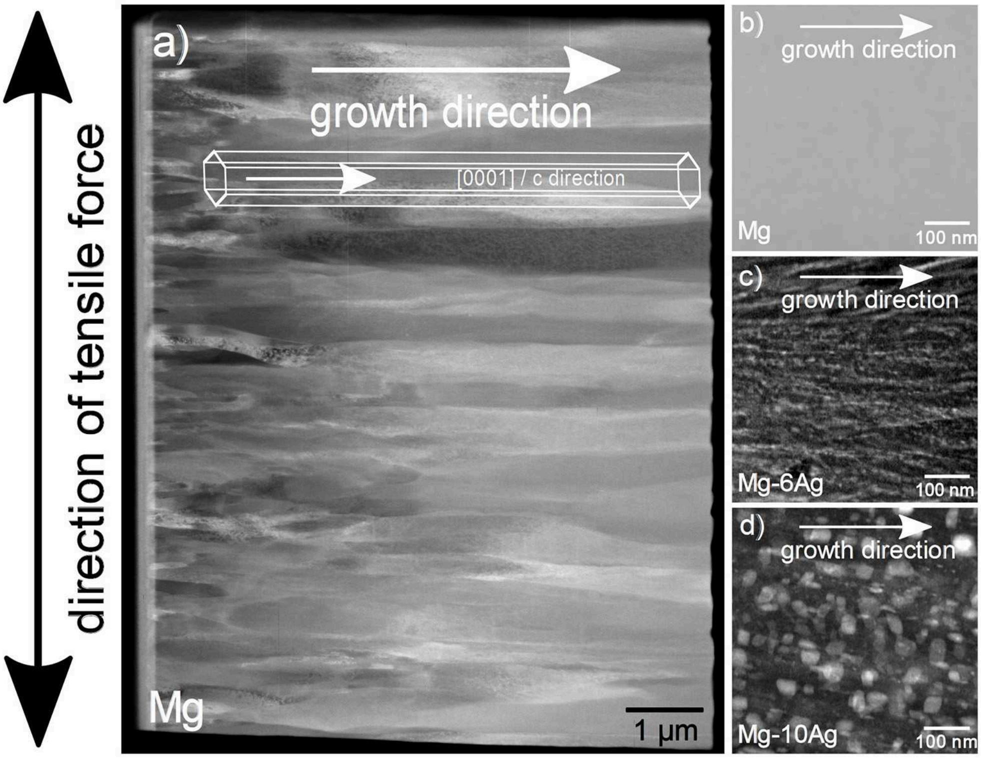

FIGURE 2 | STEM images of cross sections **(a)** Overview image of magnetron sputtered Mg based material, showing a columnar growth, furthermore is the growth direction of the film indicated which is perpendicular to the direction of applied tensile force. **(b)** Enlarged image of the microstructure of Mg. **(c)** Enlarged image of the microstructure of Mg-6Ag which shows a feather-like structure. **(d)** Enlarged image of the microstructure of Mg-10Ag, MgAg precipitates can be seen.

Mechanical Properties

The pulling direction during the tensile test is perpendicular to the growth direction of the samples. Some exemplary stress strain curves are shown in **Figure 3**. Furthermore, the average values and the calculated standard deviation of the yield strength ($R_{p0.2}$) and the elongation at fracture are shown. Mg shows the lowest yield strength with ∼150 MPa. The yield strength is increased with an increasing concentration of Ag. Mg-10Ag shows the highest yield strength with ∼371 MPa but also the lowest elongation at fracture with ∼4%.

Analysis of Fracture

The fractured surfaces were examined by SEM. In **Figure 4** exemplary images taken form an angle of the fractured surfaces of Mg-6Ag (a) and an enlargement of the fractured surface (b) are shown. Mg-6Ag was chosen because it showed the lowest corrosion rate (Jessen et al., 2019) and an increased yield strength compared to pure Mg, but the elongation at fracture was in the same range as Mg. The fractured surface of Mg-6Ag looked alike compared to Mg and all the Mg-Ag alloys. The fractured surface is rough indicating a moderately ductile fracture. This goes along with the results from the tensile test in which the elongation at fracture is about 7% for alloys up to 8 wt% Ag. Even Mg-10Ag showed the same fractured surface although this alloy exhibits the lowest elongation at fracture of the investigated materials with about 4%.

Figure 5 shows three normalized rocking curves for Mg-6Ag after tensile test at different positions on the dog-bone shaped

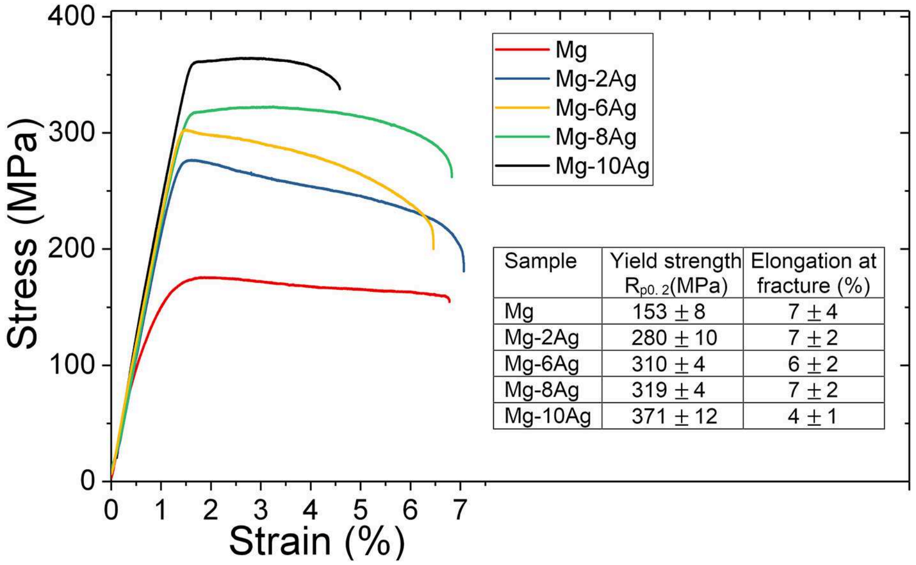

Sample	Yield strength $R_{p0.2}$(MPa)	Elongation at fracture (%)
Mg	153 ± 8	7 ± 4
Mg-2Ag	280 ± 10	7 ± 2
Mg-6Ag	310 ± 4	6 ± 2
Mg-8Ag	319 ± 4	7 ± 2
Mg-10Ag	371 ± 12	4 ± 1

FIGURE 3 | Exemplary stress strain curves of Mg, Mg-2Ag, Mg-6Ag, Mg-8Ag, and Mg-10Ag. With increasing amount of Ag the yield strength increases. From ∼153 MPa for pure Mg to ∼371 MPa for Mg-10Ag. Up to 8 wt% Ag the elongation at break is in the same range as Mg but for Mg-10Ag the elongation at break is decreased to ∼4%. The table shows the average values and calculated standard deviation of yield strength (MPa) and elongation at break (%).

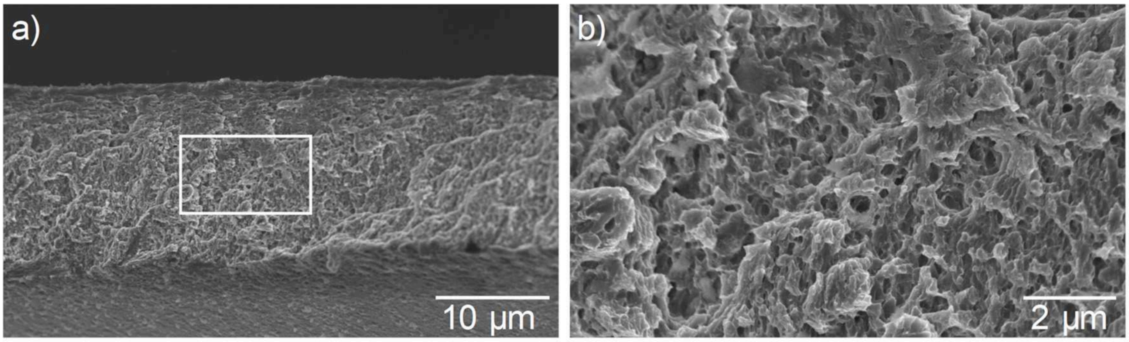

FIGURE 4 | Image taken from an angle of the fractured surface **(a)** Mg-6Ag, **(b)** Enlargement of fractured surface. The Images show a rough fractured surface, indicating a moderate ductile fracture.

sample to determine the change in full width half maximum (FWHM). The exemplary rocking curves of Mg-6Ag were chosen, because of the promising corrosion results and that the elongation at fracture of ∼6%. The FWHM was determined by Gaussian fit. Additionally, the standard error of the fit is given. Furthermore, a dog-bone shaped sample is shown and the different positions for the measurements. The rocking curve measured on the head of the dog-bone exhibits the smallest FWHM. There should be no deformation at the head of the dog-bone. The measurement on the strut next to the head shows an increase in the FWHM. The highest FWHM is detected for the measurement on the strut next to the fracture, which is the area with the highest deformation. This curve shows also an asymmetric behavior. Furthermore, a shift of the non-deformed measurement and the deformed measurement can be seen.

DISCUSSION

Mg based alloys have a hexagonal close packed structure. These materials have less gliding systems compared to cubic metals which results in a lower deformability at room temperature (RT). The dominant deformation mechanism at temperature below 225°C will be slip on the basal {0001} planes in the $<11\bar{2}0>$ directions. But also on the pyramidal planes $\{10\bar{1}1\}$ and $\{11\bar{2}2\}$ deformation can occur as well as the prismatic slip planes can be activated (Beck, 1939; Ion et al., 1982; Numakura and Koiwa, 1998; Kammer, 2000; Staroselsky, 2003; Schlüter et al., 2013). Twinning on the $\{10\bar{1}2\}$ planes in the $< \bar{1}011>$ direction is theoretically possible but here no hints of twinning were found. Due to the preferential orientated microstructure of the sputtered films it is most likely that the deformation will occur on the pyramidal plane at RT because these slip systems

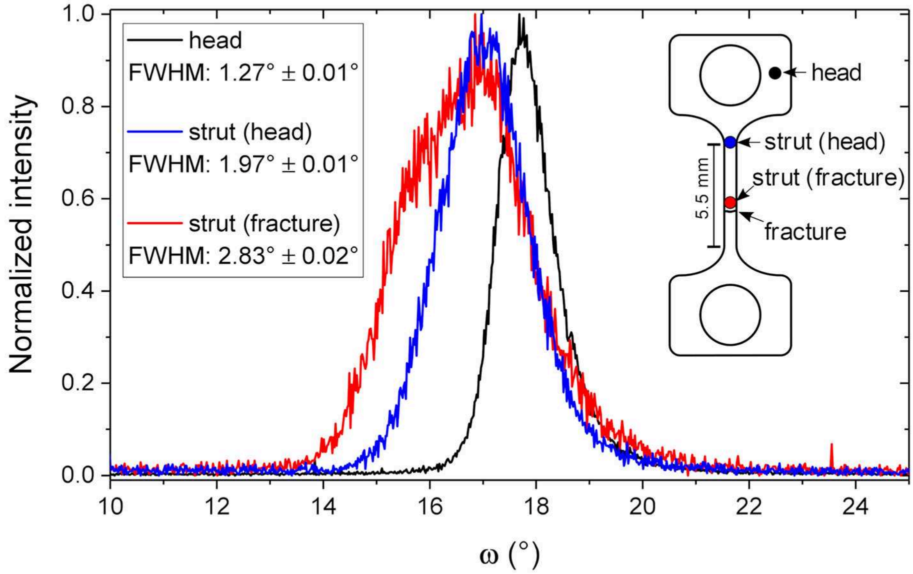

FIGURE 5 | Three different normalized rocking curves of Mg-6Ag measured at different positions on the dog-bone after tensile test are shown. Furthermore, a dog-bone shaped sample is shown and the different measurement points. Head: measurement on the head of the dog-bone; nearly non-deformed area; strut (head): measurement on the strut near the head of the dog-bone, less deformed area; strut (fracture): measurement near the fractured surface, high deformation area. A shift of the non-deformed and deformed curve can be seen. Furthermore, shows the curve of the deformed state an asymmetric behavior. The FWHM was obtained from the rocking curves by Gaussian fit furthermore the standard error of the fit is given. With increasing deformation, the FWHM is increased.

have the highest possibility to be activated due to Schmid's law. A shift of the maximum and the asymmetry of the peak during the rocking curve measurements of the (0002) plane, indicates the movement along these slip plane directions. Furthermore, the comparison of the FWHM shows that it increases from the non-deformed state at the head of the dog-bone shaped sample via a less deformed state to the high deformed state close to the fracture. This indicates that the defect density is increased at the facture. The different alloys up to 8 wt% Ag showed a moderate ductility. The results of the tensile tests showed an elongation at fracture of ∼7% and the SEM images of the fractured surfaces showed a rough surface which is an indication of a moderate ductile behavior. This is also in accordance with the results of the FWHM measurements, which showed that there is a plastic deformation within the materials which leads to an increase in the FWHM. Only Mg-10Ag showed a lower value for the elongation at fracture with ∼4% however, it exhibits the highest yield strength.

The investigated sputtered free standing films in this study show a high mechanical strength in the tensile tests. The high strength of sputtered films results from a high defect density in the films and from small grains. Compared to Mg film (thickness of 20 μm) the strength of Mg-Ag alloys is even doubled. Different hardening mechanism play a role for the different sputtered films. Due to the fabrication process of magnetron sputtering the films have a high initial defect density (Thornton, 2003). These defects in the films act as obstacles and lead to the higher strength of the sputtered films. Another effect for the strength of the materials is the grain diameter. The grain diameter of the different sputtered materials is similar and smaller than 1 μm (Jessen et al., 2019). In agreement with the Hall-Petch relation the small grain diameter leads to a higher strength (Hall, 1951; Gottstein, 2004). Due to similar grain diameters of the different alloys, the increased strength is a result of the higher Ag content. The increasing strength with Ag content can be explained by different hardening mechanisms. In accordance with the Mg-Ag phase diagram the solubility of Ag in Mg is up to 15 wt% at higher temperatures (745 K) given, at RT only maximum 2 wt% can be dissolved (ASM International, 1992b). The strength of Mg-2Ag can be explained by solid solution hardening (Gottstein, 2004). The feather-like microstructure of the Mg-6Ag sample, shows agglomeration of Ag without the formation of a second intermetallic phase. This potentially leads to a higher solid solution hardening compared Mg-2Ag. In the case of Mg-10Ag precipitates are formed ranging from 10 to 50 nm (**Figure 2d**). The maximum ultimate strength in these alloy system is obtained by a combination of solution hardening and additionally precipitation hardening (Gottstein, 2004).

In principle one should note that a comparison of the mechanical properties obtained by different authors might be misleading due to different sample geometries, microstructures and measurement systems. The as cast Mg-6Ag wires are in a similar range as the investigated thin film samples here. The wires of Mg-6Ag had an ultimate strength of ∼350 MPa and an elongation at fracture of 5% (Maier et al., 2018). The sputtered Mg-6Ag samples are in the range of 310 MPa and exhibited an elongation at fracture of ∼6%. But the thin films show a lower corrosion rate compared to the bulk materials, which can be a result of the smaller grain size and the columnar microstructure of the sputtered thin films (Liu et al., 2008; Jiang et al., 2017). It is well-established that the mechanical properties can be influenced by an additional heat treatment which will result in a higher elongation at fracture but will decrease the ultimate strength. Additionally, the corrosion properties will be changed, due to larger grain diameters and possible the formation of precipitates, the corrosion rate will be increased (Ralston et al., 2010).

CONCLUSION

It was shown that magnetron sputtering is a suitable method for the fabrication of 20 μm thick Mg-Ag films which show a moderate ductile behavior. Mg-Ag samples in the range of 2–8 wt% Ag showed similar ductility as Mg with an elongation at fracture of ∼7%. Furthermore, it was shown that it is possible to influence the yield strength with the addition of Ag. For 10 wt% Ag samples the ductility was decreased, but this alloy showed the highest strength of ∼371 MPa. For Mg-6Ag the yield strength could be increased by a factor of two from ∼150 MPa of Mg to ∼310 MPa with an elongation at fracture of ∼6%. These results in combination with the low corrosion rate of Mg-6Ag (Jessen et al., 2019) makes this material to a very promising candidate for future biodegradable medical implants.

DATA AVAILABILITY STATEMENT

The datasets generated for this study are available on request to the corresponding author.

AUTHOR CONTRIBUTIONS

The work was completed by cooperation of all authors. LJ, CZ, and EQ contributed on the concept and design of the project. LJ and CZ performed the experiments. LJ wrote the first draft of the manuscript. CZ and EQ revised the first draft of the manuscript. All authors read and approved the submitted version.

FUNDING

Funding by the DFG was gratefully acknowledged. This work was developed in the framework of the research training group GRK 2154 Materials for Brain.

ACKNOWLEDGMENTS

The authors thank Dr. Ulrich Schürmann from the Chair of Synthesis and Real Structure from the CAU Kiel for conducting the TEM investigations.

REFERENCES

ASM International (1992a). *ASM Handbook Volume 2: Properties and Selection: Nonferrous Alloys and Special-Purpose Materials.* Materials Park, OH: ASM International.

ASM International (1992b). *Volume 3-Alloy Phase Diagrams, 10th Edn.* Materials Park, OH: ASM International.

ASM International (1999). *ASM Specialty Handbook-Magnesium and Magnesium-Alloys.* Materials Park, OH: ASM International.

Beck, A. (1939). *Magnesium und Seine Legierungen.* Berlin; Heidelberg: Springer-Verlag GmbH.

Gao, L., Chen, R. S., and Han, E. H. (2009a). Solid solution strengthening behaviors in binary Mg-Y single phase alloys. *J. Alloys Compd*. 472, 234–240. doi: 10.1016/j.jallcom.2008.04.049

Gao, L., Chen, R. S., and Han, E. H. (2009b). Effects of rare-earth elements Gd and Y on the solid solution strengthening of Mg alloys. *J. Alloys Compd*. 481, 379–384. doi: 10.1016/j.jallcom.2009.02.131

Gottstein, G. (2004). *Physical Foundation of Material Science,* 1st Edn. Berlin; Heidelberg: Springer-Verlag GmbH.

Haffner, D., Zamponi, C., De Miranda, R. L., and Quandt, E. (2015). Micropatterned freestanding magnetron sputtered Mg-alloy scaffolds, *BioNanoMater*. 16, 19–22. doi: 10.1515/bnm-2015-0007

Hall, E. O. (1951). The deformation and ageing of mild steel III Discussion of results. *Proc. Phys. Soc. Sect.* 64:747. doi: 10.1088/0370-1301/64/9/303

Hermawan, H. (2012). *Biodegradable Metals: From Concept to Applications*. Springer Science & Business Media. doi: 10.1007/978-3-642-31170-3

Hermawan, H., Dubé, D., and Mantovani, D. (2010). Developments in metallic biodegradable stents. *Acta Biomater*. 6, 1693–1697. doi: 10.1016/j.actbio.2009.10.006

Hort, N., Huang, Y., Fechner, D., Störmer, M., Blawert, C., Witte, F., et al. (2010). Magnesium alloys as implant materials-Principles of property design for Mg-RE alloys. *Acta Biomater*. 6, 1714–1725. doi: 10.1016/j.actbio.2009.09.010

Ion, S. E., Humphreys, F. J., and White, S. H. (1982). Dynamic recrystallisation and the development of microstructure during the high temperature deformation of magnesium. *Acta Metall*. 30, 1909–1919. doi: 10.1016/0001-6160(82)90031-1

Jessen, L. K., Zamponi, C., Willumeit-Römer, R., and Quandt, E. (2019). Magnetron sputtered freestanding mgag films with ultra-low corrosion rate. *Acta Biomater*. doi: 10.1016/j.actbio.2019.05.060. [Epub ahead of print].

Jiang, B., Xiang, Q., Atrens, A., Song, J., and Pan, F. (2017). Influence of crystallographic texture and grain size on the corrosion behaviour of as-extruded Mg alloy AZ31 sheets. *Corros. Sci*. 126, 374–380. doi: 10.1016/j.corsci.2017.08.004

Kammer, C. (2000). *Magnesium Taschenbuch.* Düsseldorf: Aluminium-Verlag.

Laermer, F., and Schilp, A. (1996). *Method of Anistropically Etching Silicon, US patent* No. 5501893.

Lansdown, A. B. G. (2002). Silver I: its antibacterial properties and mechanism of action. *J. Wound Care*. 11, 125–130. doi: 10.12968/jowc.2002.11.4.26389

Li, L., Gao, J., and Wang, Y. (2004). Evaluation of cyto-toxicity and corrosion behavior of alkali-heat-treated magnesium in simulated body fluid. *Surf. Coatings Technol*. 185, 92–98. doi: 10.1016/j.surfcoat.2004.01.004

Liu, D., Dai, X., Wen, X., Qin, G., and Meng, X. (2015a). Crystallographic information of intermediate phases in binary Mg-X (X=Sn, Y, Sc, Ag) alloys. *Data Br*. 4, 190–192. doi: 10.1016/j.dib.2015.05.011

Liu, D., Dai, X., Wen, X., Qin, G., and Meng, X. (2015b). Predictions on the compositions, structures, and mechanical properties of intermediate phases in binary Mg-X (X = Sn, Y, Sc, Ag) alloys. *Comput. Mater. Sci*. 106, 180–187. doi: 10.1016/j.commatsci.2015.04.038

Liu, M., Qiu, D., Zhao, M. C., Song, G., and Atrens, A. (2008). The effect of crystallographic orientation on the active corrosion of pure magnesium. *Scr. Mater*. 58, 421–424. doi: 10.1016/j.scriptamat.2007.10.027

Liu, Z., Schade, R., Luthringer, B., Hort, N., Rothe, H., Müller, S., et al. (2017). Influence of the microstructure and silver content on degradation, cytocompatibility, and antibacterial properties of magnesium-silver alloys *in vitro*. *Oxid. Med. Cell. Longev*. 2017:8091265. doi: 10.1155/2017/8091265

Mahieu, S. (2006). Biaxial alignment in sputter deposited thin films. *Thin Solid Films* 515, 1229–1249. doi: 10.1016/j.tsf.2006.06.027

Maier, P., Szakács, G., Wala, M., and Hort, N. (2015). "Mechanical and corrosive properties of two magnesium wires: Mg4Gd and Mg6Ag," in *Magnesium Technology* (Cham: Springer), 393–398.

Maier, P., Zimmermann, F., Rinne, M., Szakács, G., Hort, N., and Vogt, C. (2018). Solid solution treatment on strength and corrosion of biodegradable Mg6Ag wires, mater. *Corros* 69, 178–190. doi: 10.1002/maco.201709502

Mijnendonckx, K., Leys, N., Mahillon, J., Silver, S., and Van Houdt, R. (2013). Antimicrobial silver: Uses, toxicity and potential for resistance. *BioMetals*. 26, 609–621. doi: 10.1007/s10534-013-9645-z

Musil, J. (2012). Hard nanocomposite coatings: thermal stability, oxidation resistance and toughness. *Surf. Coat. Technol*. 207, 50–65. doi: 10.1016/j.surfcoat.2012.05.073

Musil, J. (2015). Flexible hard nanocomposite coatings. *RSC Adv*. 5, 60482–60495. doi: 10.1039/C5RA09586G

Numakura, H., and Koiwa, M. (1998). Dislocations in metals and alloys with the hexagonal close-packed structure. *Metall. Sci. Tecnol.* 16, 4–19.

Ralston, K. D., Birbilis, N., and Davies, C. H. J. (2010). Revealing the relationship between grain size and corrosion rate of metals. *Scr. Mater*. 63, 1201–1204. doi: 10.1016/j.scriptamat.2010.08.035

Ren, Y., Zhao, H., Wang, L., Yang, B., Li, H., Sun, S., et al. (2018). Evidence of a novel intermetallic Mg7Ag3 phase in Mg–ag binary alloy system. *J. Appl. Crystallogr*. 51, 844–848. doi: 10.1107/S160057671800599X

Schluter, K., Reverey, J., Hort, N., Zamponi, C., and Quandt, E. (2011). Mechanical behaviour and corrosion performance of thin film magnesium WE alloys. *Light Met. Technol.* 690, 286–289. doi: 10.4028/www.scientific.net/MSF.690.286

Schlüter, K., Shi, Z., Zamponi, C., Cao, F., Quandt, E., and Atrens, A. (2014). Corrosion performance and mechanical properties of sputter-deposited MgY and MgGd alloys. *Corros. Sci*. 78, 43–54. doi: 10.1016/j.corsci.2013.08.027

Schlüter, K., Zamponi, C., Hapke, J., Hort, N., Kainer, K. U., and Quandt, E. (2013). Mechanical properties and corrosion behaviour of freestanding, precipitate-free magnesium WE43 thin films. *Int. J. Mater. Res*. 104, 286–292. doi: 10.3139/146.110860

Song, G. (2007). Control of biodegradation of biocompatable magnesium alloys. *Corros. Sci*. 49, 1696–1701. doi: 10.1016/j.corsci.2007.01.001

Staiger, M. P., Pietak, A. M., Huadmai, J., and Dias, G. (2006). Magnesium and its alloys as orthopedic biomaterials: a review, *Biomaterials* 27, 1728–1734. doi: 10.1016/j.biomaterials.2005.10.003

Staroselsky, A. L. (2003). A constitutive model for hcp materials deforming by slip and twinning: application to magnesium alloy AZ31B. *Int. J. Plast*. 19, 1843–1864. doi: 10.1016/S0749-6419(03)00039-1

Thompson, C., V. (1990). Grain growth in thin films. *Annu. Rev. Mater. Sci*. 20, 245–268. doi: 10.1146/annurev.ms.20.080190.001333

Thornton, J. A. (2003). High rate thick film growth. *Annu. Rev. Mater. Sci*. 7, 239–260. doi: 10.1146/annurev.ms.07.080177.001323

Tie, D., Feyerabend, F., Hort, N., Hoeche, D., Kainer, K. U., Willumeit, R., et al. (2014). *In vitro* mechanical and corrosion properties of biodegradable Mg-Ag alloys. *Mater. Corros*. 65, 569–576. doi: 10.1002/maco.201206903

Tie, D., Feyerabend, F., Müller, W., Schade, R., Liefeith, K., and Kainer, K. U. (2013). Antibacterial biodegradable Mg-Ag alloys. *Eur. Cell Mater*. 25, 284–298. doi: 10.22203/eCM.v025a20

Witte, F., Hort, N., Vogt, C., Cohen, S., Kainer, K. U., Willumeit, R., et al. (2008). Degradable biomaterials based on magnesium corrosion. *Curr. Opin. Solid State Mater. Sci*. 12, 63–72. doi: 10.1016/j.cossms.2009.04.001

Zheng, Y. F., Gu, X. N., and Witte, F. (2014). Biodegradable metals. *Mater. Sci. Eng. R*. 77, 1–34. doi: 10.1016/j.mser.2014.01.001

Conflict of Interest: The authors declare that the research was conducted in the absence of any commercial or financial relationships that could be construed as a potential conflict of interest.

frontiers in Materials

REVIEW
published: 04 October 2019
doi: 10.3389/fmats.2019.00240

Ultrafine-Grained Magnesium Alloys for Hydrogen Storage Obtained by Severe Plastic Deformation

Eugen Rabkin[1], *Vladimir Skripnyuk*[1] *and Yuri Estrin*[2,3]*

[1] *Department of Materials Science and Engineering, Technion – Israel Institute of Technology, Haifa, Israel,* [2] *Department of Materials Science and Engineering, Monash University, Clayton, VIC, Australia,* [3] *Department of Mechanical Engineering, The University of Western Australia, Crawley, WA, Australia*

Magnesium alloys take a special place among the hydrogen storage materials, mainly due to their high gravimetric (7.6 mass %) and volumetric (110 kg m^{-3}) hydrogen storage capacity. Unfortunately, the kinetics of hydrogenation and hydrogen release are rather slow, which limits practical use of magnesium-based materials for hydrogen and heat storage. Refining the microstructure of magnesium alloys, ideally down to nanoscale, is known to accelerate the hydrogenation/dehydrogenation kinetics. A possible way to achieve that is by severe plastic deformation. Our first demonstration of this effect through processing of a Mg alloy (ZK60) by equal-channel angular pressing prompted a stream of further studies employing severe plastic deformation techniques to improve the hydrogen storage-relevant properties of Mg alloys. The present article provides an overview of the literature on the subject, with a natural focus on our own data.

Keywords: hydrogen storage, hydrogenation kinetics, magnesium alloys, magnesium-based composites, severe plastic deformation

Edited by:
Hajo Dieringa,
Helmholtz Centre for Materials and Coastal Research (HZG), Germany

Reviewed by:
Sung Bo Lee,
Seoul National University, South Korea
Claudio Pistidda,
Institute of Materials Research, Helmholtz Centre for Materials and Coastal Research (HZG), Germany

Correspondence:
Yuri Estrin
yuri.estrin@monash.edu

Specialty section:
This article was submitted to Structural Materials, a section of the journal Frontiers in Materials

Received: *25 June 2019*
Accepted: *17 September 2019*
Published: *04 October 2019*

Citation:
Rabkin E, Skripnyuk V and Estrin Y (2019) Ultrafine-Grained Magnesium Alloys for Hydrogen Storage Obtained by Severe Plastic Deformation. Front. Mater. 6:240. doi: 10.3389/fmats.2019.00240

INTRODUCTION

Hydrogen storage is a key element of hydrogen economy, and a lot of effort goes into developing viable solutions to this critical need. A particularly attractive answer to the challenging quest is solid-state storage, whereby hydrogen is embedded in the bulk of a host solid (Schlapbach and Züttel, 2001; Jena, 2011; Walker, 2011; Graetz, 2012). Magnesium could be regarded as a perfect host for hydrogen due to its high gravimetric (7.6 mass %) and volumetric (110 kg m^{-3}) hydrogen storage capacity (Shao et al., 2018), abundance in sea water and the Earth's crust, and low cost (US$2–3 per kilogram). Furthermore, hydrides it forms with hydrogen (MgH_2) are highly efficient in terms of the stored energy density (2.6 kWh/kg—about twice the energy density of liquid hydrogen) (Luo et al., 2019). Problem is that the targeted equilibrium hydrogen pressure of 1 atm (0.1 MPa) cannot be achieved at temperatures that would be acceptable for mobile (notably automotive) hydrogen storage applications. The problem is rooted in a high enthalpy of magnesium hydride formation (Huot, 2010) and is further exacerbated by a sluggish kinetics of absorption and desorption of hydrogen in magnesium-based materials (Schlapbach and Züttel, 2001; Huot, 2010; Jena, 2011; Walker, 2011; Shao et al., 2018; Luo et al., 2019; Yartys et al., 2019). In one of his last publications (Birnbaum, 2005), the nestor of research on hydrogen in metals, Prof. Howard Birnbaum, gave a rather pessimistic outlook on the prospects of overcoming the thermodynamics handicap of magnesium hydrides. He wrote: "While it is always dangerous to predict the course of science, I am not particularly optimistic about our ability to develop a hydride having the desirable properties." Despite his concerns, researchers have been exploring various pathways to outsmart the disadvantageous thermodynamics and kinetics of hydride-forming magnesium alloys, and nanostructuring appears to be one of the promising avenues to achieving that, cf. (Hardian et al., 2018; Schneemann et al., 2018; Yartys et al., 2019; Zhang et al., 2019). A popular technique for grain refinement down to nano scale is high energy ball milling (HEBM) of Mg powders which, indeed, was shown to accelerate the hydrogenation/dehydrogenation kinetics in several Mg alloys—with or without catalysts (Luo et al., 2019). Unfortunately, the cost of production of Mg alloys with sufficiently good hydrogen sorption properties by HEBM in terms of the processing time, energy input, and labor involved is prohibitively high, which limits the application of this technology at industry scale.

In 2004, we proposed an alternative route to mechanically-driven nanostructuring of hydride forming Mg alloys (Skripnyuk et al., 2004). It was a first ever attempt to employ severe plastic deformation of bulk metallic specimens to improve their hydrogen absorption/desorption properties. The term severe plastic deformation (SPD) refers to a group of techniques in which a gigantic shear deformation, combined with high hydrostatic pressure, gives rise to extreme grain refinement—down to a deep submicron scale and in some cases to nano scale [see e.g. (Valiev et al., 1999, 2016; Estrin and Vinogradov, 2013)]. Combined with a high density of crystal lattice defects generated, SPD-induced grain refinement was seen as a potent mechanism of accelerated hydrogen sorption of Mg alloys. The encouraging results of that study in terms of faster reversible hydrogenation/dehydrogenation prompted other researchers to pursue this processing route, and a significant number of publications reporting their results ensued. While these studies still constitute a niche research area, the interest in the potential of SPD as a means of combating the unfavorable thermodynamics and kinetics of hydrogenation of Mg alloys is great, and we feel that a "mini-review" of this area would be conducive for promoting it to a broader research community. In what follows, such an overview is provided.

ACCELERATED HYDROGEN SORPTION KINETICS IN MAGNESIUM ALLOYS ACHIEVED BY SEVERE PLASTIC DEFORMATION

Alloys Processed by Equal-Channel Angular Pressing

We begin by summarizing the results of the mentioned study (Skripnyuk et al., 2004), as they are representative of the research in this field heralded in that publications. The material investigated was Mg−4.95 wt% Zn−0.71 wt% Zr (ZK60)—a common commercial magnesium alloy broadly used for structural applications. The SPD technique employed was equal channel angular pressing (ECAP), in which a billet is pressed through an angular die and experiences a large shear strain when it passes through a plane at which the entry and the exit channels meet. For a 90° die, this shear strain is of the order of 100%. As in this process the cross-sectional dimensions of the billet remain unchanged, pressing can be repeated several times, so that the cumulative strain can reach levels not achievable in conventional metal forming. The outcomes of processing of many alloys in terms of microstructure variation are astounding: the grain size drops typically well below 1 μm, and in many cases reaches a 100 nm range (Valiev et al., 1999, 2016; Estrin and Vinogradov, 2013), and Mg alloys are no exception (see e.g., Orlov et al., 2011).

To compare the effect of various processing routes on the microstructure and the ensuing thermodynamic and kinetic properties of alloy ZK60, it was modified by HEBM, ECAP, or a combination of both methods. To that end, pressure-composition-temperature (PCT) diagrams and the kinetics of hydrogen desorption in a closed volume system were determined for the alloy in the initial (annealed) condition and upon mechanically-driven nanostructuring. A special ECAP schedule used involved eight passes through a 120° angular die at elevated temperatures (250 or 300°C) followed by a final pass through a 90° die at room temperature. Route A (in which the billet is not rotated between the passes) was used. Microstructure characterization by transmission electron microscopy revealed a drop in the average grain size from 46 μm in the initial condition to 0.5–2 μm in the ECAP-processed one. HEBM processing was carried out using a standard procedure described in Skripnyuk et al. (2004). Before hydrogenation tests, annealed and mechanically processed specimens were comminuted by filing with a rasp. The particles produced in this way, <1 mm in size, were hydrogenated at 300°C and hydrogen pressure of 25 atm, and then underwent desorption–absorption cycles.

Representative PCT diagrams for alloy ZK60 processed by ECAP and HEBM are shown in **Figure 1** vis-à-vis the PCT diagram for the annealed reference alloy (Skripnyuk et al., 2004). As seen from **Figure 1**, both straight ECAP and combined ECAP/HEBM processing affect the PCT diagrams. Both raise the equilibrium hydrogen pressure at the left flank of the pressure plateau and tilt the entire plateau region of the PCT diagram toward a horizontal direction. A further important observation was the disappearance of pressure hysteresis for the ECAP/HEBM processed material.

The beneficial effect of ECAP on the hydrogenation properties was enhanced when the ECAP processing temperature was raised from 250 to 300°C, causing a doubling of the hydrogen desorption pressure in the plateau region of the PC isotherm. A substantial increase of the hydrogen desorption rate was also found, especially in the low temperature range. The difference in hydrogenation behavior can be correlated with the degree of uniformity and the morphology of dehydrogenated powders. Indeed, the powders produced from the samples deformed at 300°C were more homogeneous and finely dispersed, and their morphology was less faceted than those obtained from the samples deformed at 250°C (Skripnyuk et al., 2009).

The effects observed can be associated with the ECAP-induced changes in the microstructure and the defect structure of the alloy. It is believed that a fairly uniform microstructure with a low number of twin boundaries and a large volume fraction of small grains was conducive for better hydrogenation kinetics. The chemistry, morphology and distribution of finely dispersed zinc–zirconium precipitates in the ECAP-processed alloy are further

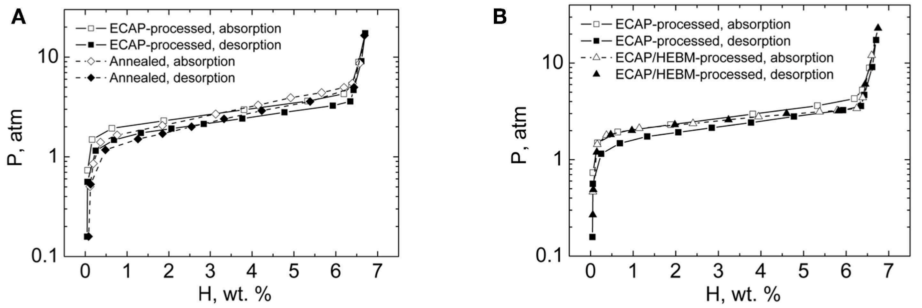

FIGURE 1 | PCT diagrams for annealed and mechanically processed alloy ZK60: **(A)** ECAP-treated vs. annealed condition; **(B)** ECAP vs. combined ECAP/HEBM conditions. The hydrogen absorption/desorption measurements were conducted in a Sievert's apparatus at 300°C. Reproduced from Skripnyuk et al. (2004) with permission from Elsevier.

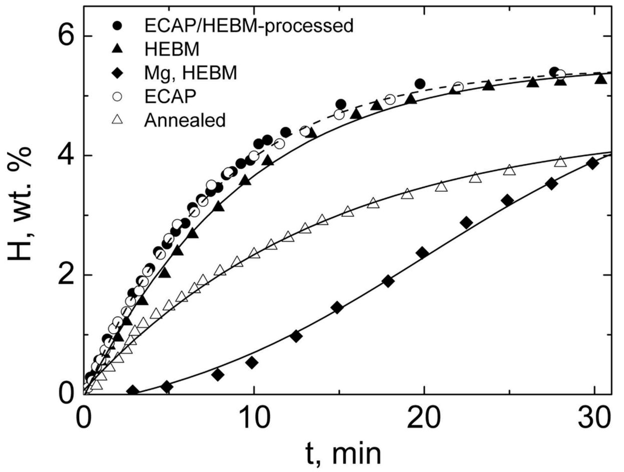

FIGURE 2 | Time dependence of hydrogen desorption from ZK60 specimens treated by ECAP, HEBM, and combined ECAP/HEBM at 300°C. The data for HEBM-processed pure Mg are included for comparison. Reproduced from Skripnyuk et al. (2004) with permission from Elsevier.

factors specific for alloy ZK60, which may have contributed to the increase of hydrogen desorption pressure.

A result of the study (Skripnyuk et al., 2004) most significant for practical hydrogen storage applications was a marked acceleration of the hydrogen desorption kinetics due to ECAP or ECAP+HEBM treatment, which is seen in **Figure 2**. The effect of ECAP conducted according to the schedule outlined above was on par with that of 15 h of HEBM. The benefits of grain refinement by any of these processing techniques in terms of the enhancement of the desorption rate are obvious. ECAP has a definite advantage over HEBM as it allows processing of bulk billets within a shorter time than HEBM. In addition to higher productivity, ECAP has an advantage of being a much safer process, as it does not require handling of potentially hazardous powder materials. More detailed data on hydrogen storage properties of ECAP-processed alloy ZK60, including the temperature dependence of the sorption kinetics were provided in Skripnyuk et al. (2009).

Encouraged by these results, other researchers have followed suit and adopted ECAP as a means to improve the hydrogenation/dehydrogenation kinetics of Mg alloys. Thus, Krystian et al. (2011) used a different schedule of ECAP processing of alloy ZK60 and were able to reduce the average grain size to 250 nm and achieve a higher hydrogen uptake and further acceleration of the desorption kinetics, cf. Figure 2 in Krystian et al. (2011). Comparison of these results with the effect of other mechanical processing routes on the hydrogenation/dehydrogenation behavior of alloy ZK60, such as cold rolling (Wang et al., 2010), shows that ECAP outperforms the latter.

Other authors (Soyama et al., 2016) using ECAP for the same purpose, yet for an alloy with a somewhat different composition (ZK60 with added 2.5% Mischmetal) were not able to achieve similar levels of improvement of hydrogen sorption kinetics by ECAP treatment, however. An important observation made by them was that by combining ECAP with cold rolling a higher hydrogen uptake and faster sorption kinetics were attained, which was associated with a favorable (002) texture produced at the cold-working stage (Crivello et al., 2016). A similar observation was made by Asselli et al. (2015) who showed that ECAP alone (6 passes using a die with a channel angle of 110°) was not efficient and that it took extra processing by Accumulated Roll Bonding (ARB), with subsequent pulverization of the billet into small platelets, to achieve reasonably high level of hydrogen uptake and accelerated hydrogenation kinetics of ZK60.

Conditioning by ECAP processing for better hydrogen sorption performance proposed in Skripnyuk et al. (2004) was adopted for a range of other Mg alloys. While in our first exercise with ZK60 an "off the shelf" alloy was used, our next approach (Skripnyuk et al., 2007) was to use a smart alloy design. The material of choice was a eutectic Mg-Ni alloy with the $Mg_{89}Ni_{11}$ composition. The motivation behind this choice was two-fold: first, Ni was known for its positive catalytic effect on hydrogen sorption properties of Mg; second, it was hoped that the fine lamellar structure of the eutectic would be conducive for further microstructure refinement by ECAP that would boost the hydrogenation/dehydrogenation kinetics. As a matter of fact, earlier work on cold rolling of Mg and Ni sheets with subsequent

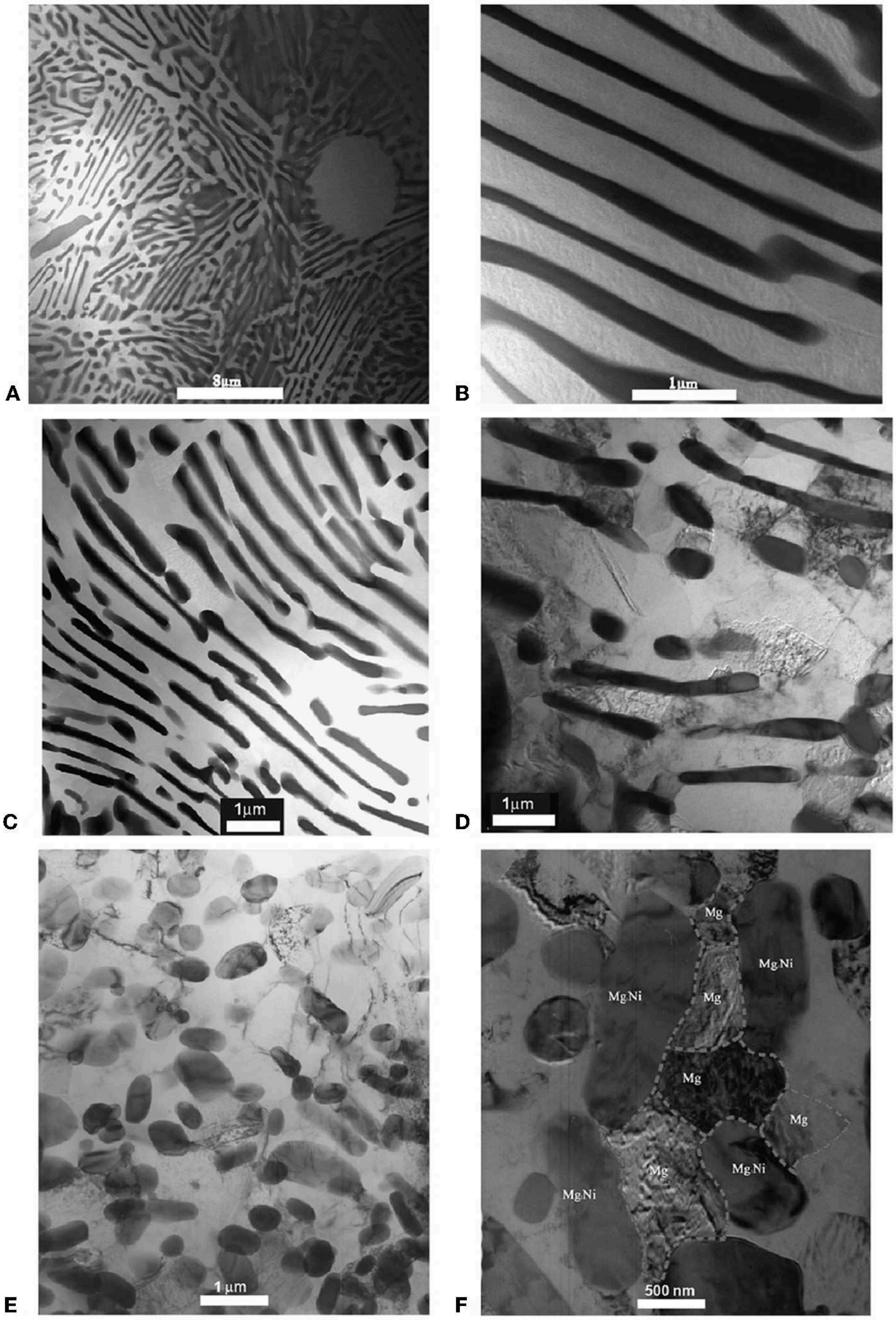

FIGURE 3 | Bright field TEM micrographs of the as cast **(A,B)** and ECAP-modified **(C–F)** $Mg_{89}Ni_{11}$ alloy: after a single ECAP pass **(C,D)** and 10 ECAP passes **(E,F)**. Reproduced from Skripnyuk et al. (2007) with permission from Elsevier.

hydrogenation produced Mg-Ni laminates containing nano scale magnesium hydrides with good electrochemical properties (Ueda et al., 2004; Pedneault et al., 2008). Our alternative ECAP-based approach (Skripnyuk et al., 2007) presumed that the lamellar eutectic structure, with brittle Mg_2Ni phase encased in ductile lamellae of Mg-based solid solution, would lead to *in situ* nanostructuring of the Mg_2Ni phase without disintegration of the alloy during processing. This effort did pay off both in terms of the extreme microstructure refinement (**Figure 3**) and the hydrogen sorption behavior. Specifically, 10 ECAP passes lifted the equilibrium pressure by about 50%. Most importantly, the desorption kinetics was improved substantially, to a larger extent than by any other known processing method. Thus, at 300°C 5% of hydrogen were desorbed within <5 min. It is interesting to note that a significantly higher level of size refinement of the Mg_2Ni phase achieved by rapid solidification of a series of Mg-rich Mg-Ni alloys did not lead to any appreciable improvement of hydrogen storage properties (Bendersky et al., 2011). This demonstrates that in addition to the grain and precipitate size refinement, intrinsic defects introduced by severe plastic straining (such as non-equilibrium grain boundaries and dislocations in the Mg matrix) play an important role in improving the hydrogenation properties.

Other authors investigated the effect of ECAP on the hydrogen sorption properties of such magnesium alloys as AZ31 (Leiva et al., 2009; Chiu et al., 2018; Skryabina et al., 2019), AZ61 (Huang et al., 2018), Mg–Mm–Ni (Mm = mischmetal) (Løken et al., 2007), and Mg-Gd-Y-Zn-Zr (Lapovok et al., 2018)—with various degrees of success. Useful summaries of the results obtained by employing ECAP as a tool for tuning the hydrogen sorption properties of Mg alloys was recently provided by Wang et al. (2017) and Huot et al. (2012).

Alloys Processed by High Pressure Torsion

While the high efficacy of equal-channel angular pressing in terms of the ease of material handling and throughput is a great benefit of this method, other SPD techniques are of interest as well. High-pressure torsion (HPT) takes a special place among these techniques, as the degree of grain refinement it provides is exceptionally high, the grain sizes attainable in metallic materials often falling in the 100 nm range, cf. (Zhilyaev and Langdon, 2008; Estrin and Vinogradov, 2013). Accordingly, several research groups hold high expectations of HPT as a technique for improving hydrogen sorption in Mg alloys. A recent review of the effect of HPT on hydrogen sorption of Mg alloys was published by Edalati et al. (2018a). This work is part of a concerted effort of Japanese researchers in the area of SPD-enabled hydrogen storage material, which started with a contribution by Kusadome et al. (2007) who successfully applied HPT to enhance the hydrogenation of a Mg_2Ni intermetallic. HPT, along with ECAP and cold rolling, was also employed in an attempt to enhance the hydrogen sorption kinetics of ball-milled nanocrystalline Mg_2Ni powders (Révész et al., 2010). The use of HPT processing for improving the hydrogen storage performance of Mg_2Ni intermetallic by Hongo et al. (2015) at Kyushu University, Fukuoka, Japan was guided by the idea that deformation-induced stacking faults may play a role similar to that of grain boundaries, thus accelerating the hydrogen sorption. To elucidate the effect of the stacking faults, the authors of Hongo et al. (2015) used two processing routes: casting and HPT (10 anvil revolutions, $N = 10$). In both cases, subsequent annealing at 673 K was used to produce a coarse-grained structure. The imprint of HPT was the presence of deformation-induced stacking faults that were retained after annealing. The superior hydrogen sorption kinetics of the material containing the HPT-induced stacking faults is evident in **Figure 4**.

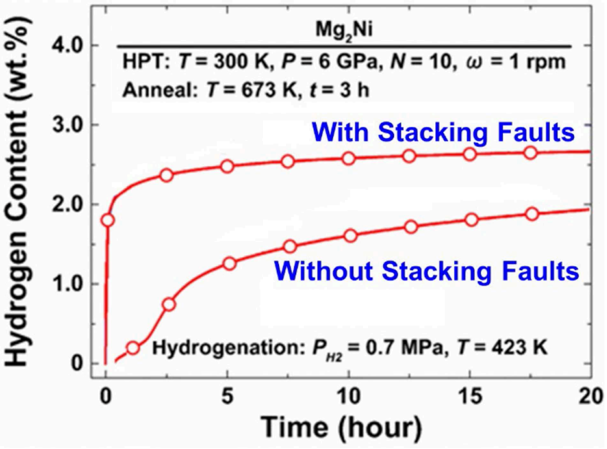

FIGURE 4 | Hydrogenation kinetics of an Mg_2Ni intermetallic with and without HPT-induced stacking faults. The processing and test conditions are indicated within the diagram. Reproduced from Hongo et al. (2015) with permission from Elsevier.

The Kyushu University group conducted a systematic study of the HPT-driven synthesis of binary and tertiary Mg-based alloys (Edalati et al., 2018a). It was shown that by mechanical mixing of Mg powders with powders of various elements and further processing these blends by means of HPT, nanograined intermetallics, metastable phases, or amorphous phases can be obtained, depending on the composition (Kusadome et al., 2007). An excellent potential of HPT for producing a broad range of Mg-based alloys and compounds for hydrogen storage applications was thus demonstrated.

A particular result of note is the successful fabrication by HPT of a Mg alloy with good hydrogen sorption properties at *room temperature* (Edalati et al., 2018b). What is quite remarkable is that the alloy was first designed *in silico* using first principle calculations and then synthesized by HPT. The compound they designed, Mg_4NiPd, is characterized by a low hydrogen binding energy, which is the reason for its favorable hydrogen storage properties. It was produced by casting and subsequent HPT to a very large number of anvil revolutions ($N = 1{,}500$) under a pressure of 6 GPa, which resulted in a homogeneous distribution of the constituent elements in a body-centered cubic lattice of the CsCl type (**Figure 5**). Also shown are the hydrogen pressure vs. hydrogen content diagrams, which demonstrate reasonably good hydrogen sorption properties of the material at room temperature (305 K).

The last decade saw a marked growth of activities in HPT processing of Mg and magnesium alloys for hydrogen storage applications, the Kyushu University group and other teams (Leiva et al., 2010; Botta et al., 2013; Panda et al., 2017) being the major drivers of this research. A report on HPT processing of Mg alloys (including hydrogen sorption results) published recently by Figueiredo and Langdon (2019) complements the review by Edalati et al. (2018a). Together they provide a comprehensive picture of research activities in this field. One can anticipate further developments in two directions: broadening the compositional base of HPT-induced synthesis of Mg-based alloys in a search for those with favorable thermodynamic and kinetic properties and perfecting the processing. A way to transcend the limitations of HPT with regard to the specimen size and the process throughput by employing its semi-continuous

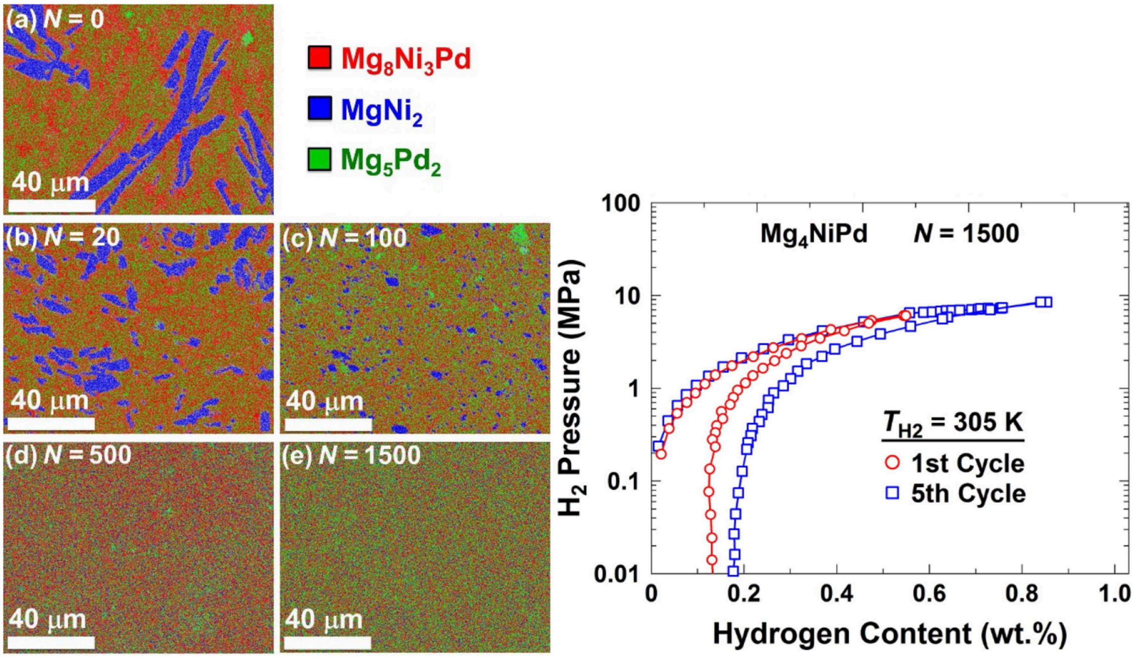

FIGURE 5 | SEM-EDS elemental mapping of HPT-processed Mg_4NiPd for different numbers of anvil revolutions [frames **(a)** to **(e)**] (left) and hydrogen pressure vs. hydrogen content diagrams at room temperature (right). Reproduced from Edalati et al. (2018b) with permission from Elsevier.

version, the so-called High-Pressure Torsion Extrusion (HPTE), was recently proposed in Omranpour et al. (2019). It was demonstrated for the case of Nb that HPTE gives rise to faster hydrogenation kinetics than ECAP. The efficacy of the process as applied to Mg based materials is yet to be evaluated.

Mg-Based Composites

One of the promising strategies to lower the reaction enthalphy of Mg-based hydrides is to combine them with other metal hydrides to composites (Dornheim et al., 2007; Crivello et al., 2016; Yartys et al., 2019). Due to their capability of enabling mixing and compaction of powders, SPD techniques are well-suited for processing composite materials targeting hydrogen storage applications. As an example, Mg-based nanocomposites were produced by HPT of stacks of disks of different materials (Figueiredo and Langdon, 2019). Another option is to produce Mg-based composites (notably, nanocomposites) with carbonaceous materials (Ruse et al., 2017; Yartys et al., 2019). With the high hydrogen storage capacity of carbon nanotubes and their expected catalytic effect on hydrogen sorption in magnesium in sight (Ruse et al., 2017), we synthesized a Mg-based composite with 2 wt.% of multiwall carbon nanotubes (MWCNT). The as-sintered composite was processed by one or two ECAP passes. The hydrogen storage properties of the as-sintered and the ECAP-processed composites were determined by volumetric method and compared with those of pure Mg. The observed effects of the addition of MWCNTs to Mg consisted in an appreciable enhancement of hydrogen desorption rate, the disappearance of the pressure hysteresis, and an increase in the slope of the pressure plateau in the PCIs measured at 573 K. Compared with pure Mg, the hydrogen desorption pressure for the as-sintered composite was by some 50% higher. Against our expectations based on earlier observations of the effect of ECAP on the hydrogen sorption/desorption, the hydrogen desorption pressure was *lowered* by ECAP processing of the as-sintered composite. Based on transmission electron microscopy observations, it was conjectured that this negative effect owes to ECAP-induced defects in MWCNTs and changes in the morphology of Mg-MWCNT interfaces.

A recently obtained insight into hydrogenation mechanisms of Mg-MWCNT composites processed by HEBM can be useful for understanding some aspects of the effect of SPD on hydrogen storage properties of Mg alloys (Popilevsky et al., 2017). It was found that prolonged milling transforms the MWCNTs into chains of carbon nanoparticles. The latter serve as preferential sites for the nucleation of hydride phase, resulting in its oblong morphology and a microstructure consisting of interpenetrating networks of metal and hydride phases (Popilevsky et al., 2017). This network allows rapid supply of hydrogen to the metal-hydride interface during the late stages of hydrogenation, since the diffusion coefficient of hydrogen in the Mg metal phase is several orders of magnitude higher than in the hydride phase. Also, a percolating network of the metal phase retained up to the late stages of the metal-hydride transformation ensures high thermal conductivity of the composite, which is essential for rapid removal of heat generated by the exothermic hydrogenation reaction. This example demonstrates that detailed studies of the microstructure of the SPD-processed Mg-based alloys at various stages of hydrogenation may hold a key to understanding the positive effects of SPD. For example, the SPD-induced crystal lattice defects may lower the barriers for nucleation of the hydride phase and change its growth morphology.

CONCLUSION

In summary, while the SPD has only a moderate effect on the thermodynamics of Mg-hydrogen interaction, its influence on the kinetics of hydrogenation is substantial and is comparable with that of HEBM. Also, the SPD-based methods can significantly shorten the time needed for initial activation of the Mg-based alloys, or eliminate it altogether (Botta et al., 2013). This is a very important factor that can significantly reduce the overall cost of a commercial hydrogen storage system. As for the thermodynamics of Mg-H interaction, realistic estimates indicate that its significant change by crystal lattice defects, surfaces, interfaces, and internal stresses is unlikely (Berube et al., 2008; Chung et al., 2012). We are of the opinion that the most promising way of improving the thermodynamics of the Mg-H system is to combine the SPD techniques with multicomponent alloying, preferably with light elements. The effect of alloying on the thermodynamics of the Mg-H system is well established (Chung et al., 2012; Skripnyuk and Rabkin, 2012), and employing the computational thermodynamics methods (such as CALPHAD) may be helpful in identifying the most promising alloying elements and alloy compositions. While the detailed mechanisms underlying the improved kinetics of hydrogen absorption and desorption of SPD-processed Mg alloys still need to be unraveled, it is undoubtable that they are associated with a high concentration of crystal lattice defects (or even partial or full amorphisation of the material), cf. (Skripnyuk et al., 2004; Edalati et al., 2018a). Dislocations and grain boundaries generated as a result of severe plastic deformation provide fast diffusion pathways for hydrogen and alloying elements that may have a catalytic effect on the hydrogen sorption properties. The role of these defects in facilitating the nucleation of the hydride phase and in optimizing its growth morphology is to be considered as well. It should also be mentioned that SPD processing may generate channels for ultra-fast diffusion, which is more rapid than what could be expected from an increased area of a grain boundary network in a grain-refined material (Divinski et al., 2010, 2011). Texture effects may also be at play (Crivello et al., 2016).

We believe that SPD processing of Mg based alloys has a great potential as a pathway to producing efficient hydrogen storage materials. Even if we are still far away from developing such materials for automotive applications, the available data show that the groundwork made so far promises breakthroughs in the realm of stationary hydrogen and heat storage facilities. The benefits of using SPD techniques over ball milling include much lower health hazards, greater amounts of material produced, relative ease of implementation at industry scale, and much higher energy efficiency (Yartys et al., 2019). Some concerns about the limited applicability of the mentioned SPD processing techniques relating to the discontinuous nature of ECAP or small quantities of material produced by HPT (Estrin and Vinogradov, 2013) could be allayed owing to some developments of SPD technology. Specifically, integration of ECAP with other processing techniques, such as Conform (Raab et al., 2004) or direct extrusion (Orlov et al., 2011), turns the process in a semi-continuous one. Similarly, a modification of the conventional HPT technique combining it with extrusion (Ivanisenko et al., 2016) makes it possible to produce long billets with ultrafine-grained structure. These upscaled SPD methods can be employed to fabricate ultrafine-grained Mg alloys targeting hydrogen storage applications. Thus, what began as a first exercise in improving hydrogen sorption properties of a Mg alloy by SPD (Skripnyuk et al., 2004) has developed to a thriving area of research with a great promise for viable industrial applications.

AUTHOR CONTRIBUTIONS

ER, VS, and YE have contributed to the development of the concept and the writing of this manuscript equally.

ACKNOWLEDGMENTS

ER and VS wish to thank the Israeli Ministry of National Infrastructures, Energy and Water Resources for partial support of this work (Project 216-11-023).

REFERENCES

Asselli, A. C., Leiva, D. R., Huot, J., Kawasaki, M., Langdon, T. G., and Botta, W. J. (2015). Effects of equal-channel angular pressing and accumulative roll-bonding on hydrogen storage properties of a commercial ZK60 magnesium alloy. *Int. J. Hydrogen Energy* 40, 16971–16976. doi: 10.1016/j.ijhydene.2015.05.149

Bendersky, L. A., Chiu, C., Skripnyuk, V. M., and Rabkin, E. (2011). Effect of rapid solidification on hydrogen solubility in Mg-rich Mg-Ni alloys. *Int. J. Hydrogen Energy* 36, 5388–5399. doi: 10.1016/j.ijhydene.2011.01.133

Berube, V., Chen, G., and Dresselhaus, M. S. (2008). Impact of nanostructuring on the enthalpy of formation of metal hydrides. *Int. J. Hydrogen Energy* 33, 4122–4131. doi: 10.1016/j.ijhydene.2008.05.083

Birnbaum, H. (2005). Fueling the 'freedom car'. *Mater. Today* 8, 64–64. doi: 10.1016/S1369-7021(05)00718-2

Botta, W. J., Jorge, A. M., Veron, M., Rauch, E. F., Ferrie, E., Yavari, A. R., et al. (2013). H-sorption properties and structural evolution of Mg processed by severe plastic deformation. *J. Alloy. Compd.* 580, S187–S191. doi: 10.1016/j.jallcom.2013.03.013

Chiu, C., Huang, S.-J., Chou, T.-Y., and Rabkin, E. (2018). Improving hydrogen storage performance of AZ31 Mg alloy by equal channel angular pressing and additives. *J. Alloys Compd.* 743, 437–447. doi: 10.1016/j.jallcom.2018.01.412

Chung, C. J., Lee, S. C., Groves, J. R., Brower, E. N., Sinclair, R., and Clemens, B. M. (2012). Interfacial alloy hydride destabilization in Mg/Pd thin films. *Phys. Rev. Lett.* 108:106102. doi: 10.1103/PhysRevLett.108.106102

Crivello, J. C., Dam, B., Denys, R. V., Dornheim, M., Grant, D. M., Huot, J., et al. (2016). Review of magnesium hydride-based materials: development and optimisation. *Appl. Phys. A* 122:97. doi: 10.1007/s00339-016-9602-0

Divinski, S., Wilde, G., Rabkin, E., and Estrin, Y. (2010). Ultra-fast atomic transport in severely deformed materials-A pathway to applications? *Adv. Eng. Mater.* 12, 779–785. doi: 10.1002/adem.200900340

Divinski, S. V., Reglitz, G., Roessner, H., Estrin, Y., and Wilde, G. (2011). Ultrafast diffusion channels in pure Ni severely deformed by equal-channel angular pressing. *Acta Mater.* 59, 1974–1985. doi: 10.1016/j.actamat.2010.11.063

Dornheim, M., Doppiu, S., Barkhordarian, G., Boesenberg, U., Klassen, T., Gutfleisch, O., et al. (2007). Hydrogen storage in magnesium-based hydrides and hydride composites. *Scripta Mater.* 56, 841–846. doi: 10.1016/j.scriptamat.2007.01.003

Edalati, K., Akiba, E., and Horita, Z. (2018a). High-pressure torsion for new hydrogen storage materials. *Sci. Techn. Adv. Mater.* 19, 185–193. doi: 10.1080/14686996.2018.1435131

Edalati, K., Uehiro, R., Ikeda, Y., Li, H.-W., Emami, H., Filinchuk, Y., et al. (2018b). Design and synthesis of a magnesium alloy for room temperature hydrogen storage. *Acta Mater.* 149, 88–96. doi: 10.1016/j.actamat.2018.02.033

Estrin, Y., and Vinogradov, A. (2013). Extreme grain refinement by severe plastic deformation: a wealth of challenging science. *Acta Mater.* 61, 782–817. doi: 10.1016/j.actamat.2012.10.038

Figueiredo, R., and Langdon, T. G. (2019). Processing magnesium and its alloys by high-pressure torsion: an overview. *Adv. Eng. Mater.* 21:1801039. doi: 10.1002/adem.201801039

Graetz, J. (2012). Metastable metal hydrides for hydrogen storage. *ISRN Mater. Sci.* 2012:863025. doi: 10.5402/2012/863025

Hardian, R., Pistidda, C., Chaudhary, A. L., Capurso, G., Gizer, G., Cao, H., et al. (2018). Waste Mg-Al based alloys for hydrogen storage. *Int. J. Hydrogen Energy* 43, 16738–16748. doi: 10.1016/j.ijhydene.2017.12.014

Hongo, T., Edalati, K., and Arita, M. (2015). Significance of grain boundaries and stacking faults on hydrogen storage properties of Mg_2Ni intermetallics processed by high pressure torsion. *Acta Mater.* 92, 46–54. doi: 10.1016/j.actamat.2015.03.036

Huang, S.-J., Chiu, C., Chou, T.-Y., and Rabkin, E. (2018). Effect of equal channel angular pressing (ECAP) on hydrogen storage properties of commercial magnesium alloy AZ61. *Int. J. Hydrogen Energy* 43, 4371–4380. doi: 10.1016/j.ijhydene.2018.01.044

Huot, J. (2010). "Metal hydrides," in *Handbook of Hydrogen Storage*, ed M. Hirscher (Weinheim: Wiley-VCH Verlag GmbH & Co. KgaA), 81–116. doi: 10.1002/9783527629800.ch4

Huot, J., Skryabina, N., and Fruchart, D. (2012). Application of severe plastic deformation techniques to magnesium for enhanced hydrogen sorption properties. *Metals* 2, 329–343. doi: 10.3390/met2030329

Ivanisenko, Y., Kulagin, R., Fedorov, V., Mazilkin, A., Scherer, T., Baretzky, B., et al. (2016). High pressure torsion extrusion as a new severe plastic deformation process. *Mater. Sci. Eng. A* 64, 247–256. doi: 10.1016/j.msea.2016.04.008

Jena, P. (2011). Materials for hydrogen storage: past, present, and future. *J. Phys. Chem. Lett.* 2, 206–2011. doi: 10.1021/jz1015372

Krystian, M., Zehetbauer, M. J., Kropik, H., Mingler, B., and Krexner, G. (2011). Hydrogen storage properties of bulk nanostructured ZK60 Mg alloy processed by equal channel angular pressing. *J. Alloys Compd.* 509, 449–455. doi: 10.1016/j.jallcom.2011.01.029

Kusadome, Y., Ikeda, K., Nakamori, Y., and Orimo, S., Horita, z. (2007). Hydrogen storage capability of $MgNi_2$ processed by high pressure torsion. *Scripta Mater.* 57, 751–753. doi: 10.1016/j.scriptamat.2007.06.042

Lapovok, R., Zolotoyabko, E., Berner, A., Skripnyuk, V., Lakin, E., Larianovsky, N., et al. (2018). Hydrogenation effect on microstructure and mechanical properties of Mg-Gd-Y-Zn-Zr alloys. *Mater. Sci. Eng. A* 719, 171–177. doi: 10.1016/j.msea.2018.02.016

Leiva, D. R., Fruchart, D., Bacia, M., Girard, G., Skryabina, N., A., et al. (2009). Mg alloys for hydrogen storage processed by SPD. *Int. J. Mat. Res.* 100, 1739–1746. doi: 10.3139/146.110225

Leiva, D. R., Jorge, A. M., Ishikawa, T. T., Huot, J., Fruchart, D., Miraglia, S., et al. (2010). Nanoscale grain refinement and H-sorption properties of MgH_2 processed by high-pressure torsion and other mechanical routes. *Adv. Eng. Mater.* 12, 786–792. doi: 10.1002/adem.201000030

Løken, S., Solberg, J. K., Maehlen, J. P., Denys, R. V., Lototsky, M. V., Tarasov, B. P., et al. (2007). Nanostructured Mg–Mm–Ni hydrogen storage alloy: structure–properties relationship. *J. Alloy. Compd. 446–447*, 114–120. doi: 10.1016/j.jallcom.2006.11.200

Luo, Q., Li, J., Li, B., Liu, B., Shao, H., and Li, Q. (2019). Kinetics in Mg-based hydrogen storage materials: enhancement and mechanism. *Magnesium J. Alloys* 7, 58–71. doi: 10.1016/j.jma.2018.12.001

Omranpour, B., Kommel, L., Sanchez, E. G., Ivanisenko, J., and Huot, J. (2019). Enhancement of hydrogen storage in Metals by using a new technique in Severe Plastic Deformations. *Key Eng. Mater.* 799, 173–178. doi: 10.4028/www.scientific.net/KEM.799.173

Orlov, D., Raab, G., Lamark, T. T., Popov, M., and Estrin, Y. (2011). Improvement of mechanical properties of magnesium alloy ZK60 by integrated extrusion and equal channel angular pressing. *Acta Mater.* 59, 375–385. doi: 10.1016/j.actamat.2010.09.043

Panda, S., Fundenberger, J.-J., Zhao, Y., Zou, J., Toth, L. S., and Grosdidier, T. (2017). Effect of initial powder type on the hydrogen storage properties of high-pressure torsion consolidated Mg. *Int. J. Hydrogen Energy* 42, 22438–22448. doi: 10.1016/j.ijhydene.2017.05.097

Pedneault, S., Huot, J., and Roué, L. (2008). Nanostructured Mg_2Ni materials prepared by cold rolling and used as negative electrode for Ni-MH batteries. *J. Power Source* 185, 566–569. doi: 10.1016/j.jpowsour.2008.06.077

Popilevsky, L., Skripnyuk, V. M., Amouyal, Y., and Rabkin, E. (2017). Tuning the thermal conductivity of hydrogenated porous magnesium hydride composites with the aid of carbonaceous additives. *Int. J. Hydrogen Energy* 42, 22395–22405. doi: 10.1016/j.ijhydene.2017.04.088

Raab, G. I., Valiev, R. Z., Lowe, T. C., Zhu, Y. T., Raab, G. J., Valiev, R. Z., et al. (2004). Continuous processing of ultrafine grained Al by ECAP–Conform. *Mater. Sci. Eng. A* 382 30–34. doi: 10.1016/j.msea.2004.04.021

Révész, Á., Kánya, Z., Verebélyi, T., Szabó, P. J., Zhilyaev, A. P., and Spassov, T. (2010). The effect of high-pressure torsion on the microstructure and hydrogen absorption kinetics of ball-milled Mg70Ni30. *J Alloys Compd.* 504, 83–88. doi: 10.1016/j.jallcom.2010.05.058

Ruse, E., Buzaglo, M., Pevsner, S., Pri Bar, I., Skripnyuk, V. M., Rabkin, E., et al. (2017). Tuning Mg hydriding kinetics with nanocarbons. *J. Alloys Compd.* 725, 616–622. doi: 10.1016/j.jallcom.2017.07.166

Schlapbach, L., and Züttel, A. (2001). Hydrogen-storage materials for mobile applications. *Nature* 414, 353–358. doi: 10.1038/35104634

Schneemann, A., White, J. L., Kang, S., Jeong, S., Wan, L. F., Cho, E. S., et al. (2018). Nanostructured metal hydrides for hydrogen storage. *Chem. Rev.* 118, 10775–10839. doi: 10.1021/acs.chemrev.8b00313

Shao, H., He, L., Lin, H., and Li, H.-W. (2018). Progress and trends in magnesium-based materials for energy-storage research: a review. *Energy Technol.* 6, 445–458. doi: 10.1002/ente.201700401

Skripnyuk, V., Buchman, E., Rabkin, E., Estrin, Y., Popov, M., and Jorgensen, S. (2007). The effect of equal channel angular pressing on hydrogen storage properties of a Mg-Ni alloy. *J. Alloy. Compd.* 436, 99–106. doi: 10.1016/j.jallcom.2006.07.030

Skripnyuk, V. M., and Rabkin, E. (2012). Mg_3Cd: a model alloy for studying the destabilization of magnesium hydride. *Int. J. Hydrogen Energy* 37, 10724–10732. doi: 10.1016/j.ijhydene.2012.04.065

Skripnyuk, V. M., Rabkin, E., Estrin, Y., and Lapovok, R. (2004). The effect of ball milling and equal channel angular pressing on the hydrogen absorption/desorption properties of Mg−4.95 wt% Zn−0.71 wt% Zr (ZK60) alloy. *Acta Mater.* 52, 405–414. doi: 10.1016/j.actamat.2003.09.025

Skripnyuk, V. M., Rabkin, E., Estrin, Y., and Lapovok, R. (2009). Improving hydrogen storage properties of magnesium based alloys by equal channel angular *pressing.Int. J. Hydrogen Energy* 35, 6320–6324. doi: 10.1016/j.ijhydene.2009.05.136

Skryabina, N., Aptukov, V., Romanov, P., Fruchart, D., de Rango, P., Girard, G., et al. (2019). Microstructure optimization of Mg-alloys by the ECAP process including numerical simulation, SPD treatments, characterization, and hydrogen sorption properties. *Molecules* 24, 89–120. doi: 10.3390/molecules24010089

Soyama, J., Floriano, R., Leiva, D. R., and Guo, Y. (2016). Severely deformed ZK60 + 2.5% Mm alloy for hydrogen storage produced by two different processing routes. *Int. J. Hydrogen Energy* 41, 11284–11292. doi: 10.1016/j.ijhydene.2016.05.031

Ueda, T. T., Tsukahara, M., Kamiya, Y., and Kikuchi, S. (2004). Preparation and hydrogen storage properties of Mg-Ni-Mg_2Ni laminate composites. *J. Alloy. Compd.* 386, 253–257. doi: 10.1016/j.jallcom.2004.04.154

Valiev, R. Z., Estrin, Y., Horita, Z., Langdon, T. G., Zehetbauer, M. J., and Zhu, Y. (2016). Producing bulk ultrafine-grained materials by severe plastic deformation: ten years later. *JOM* 68:121626. doi: 10.1007/s11837-016-1820-6

Valiev, R. Z., Islamgaliev, R. K., and Alexandrov, I. V. (1999). Bulk nanostructured materials from severe plastic deformation. *Progr. Mater. Sci.* 12:18.

Walker, G. (2011). *Solid-State Hydrogen Storage: Materials and Chemistry*. Cambridge: Woodhead Publishing Ltd.

Wang, J.-Y., Wu, C.-Y., Nieh, J.-K., Lin, H.-C., Lin, K. M., and Bor, H.-Y. (2010). Improving the hydrogen absorption properties of commercial Mg–Zn–Zr alloy. *Int. J. Hydrogen Energy* 35, 1250–1256. doi: 10.1016/j.ijhydene.2009.11.005

Wang, L., Jiang, J., Ma, A., Li, Y., and Song, D. (2017). A critical review of Mg-based hydrogen storage materials processed by equal channel. *Ang. Press. Metals* 27:324. doi: 10.3390/met7090324

Yartys, V. A., Lototskyy, M. V., Akiba, E., Albert, R., Antonov, V. E., Ares, J. R., et al. (2019). Magnesium based materials for hydrogen based energy storage: past, present and future. *Intl. J. Hydrogen Energy* 15, 7809–7859. doi: 10.1016/j.ijhydene.2018.12.212

Zhang, J., Li, Z., Wu, Y., Guo, X., Ye, J., Yuan, B., et al. (2019). Recent advances on the thermal destabilization of Mg-based hydrogen storage materials. *RSC Adv.* 9, 408–428. doi: 10.1039/C8RA05596C

Zhilyaev, A. P., and Langdon, T. G. (2008). Using high-pressure torsion for metal processing: fundamentals and applications. *Progr. Mater. Sci.* 53, 893–1024. doi: 10.1016/j.pmatsci.2008.03.002

Conflict of Interest: The authors declare that the research was conducted in the absence of any commercial or financial relationships that could be construed as a potential conflict of interest.

frontiers
in Materials

ORIGINAL RESEARCH
published: 10 October 2019
doi: 10.3389/fmats.2019.00253

Processing Effects on the Formability of Extruded Flat Products of Magnesium Alloys

Maria Nienaber, Karl Ulrich Kainer, Dietmar Letzig and Jan Bohlen*

Magnesium Innovation Centre (MagIC), Helmholtz-Zentrum Geesthacht, Geesthacht, Germany

The development of microstructure and texture during flat product extrusion of magnesium alloys differs significantly from those of rolled sheets. It has especially been shown that the range of microstructures and textures is broad in the case of extrusion which allows significant variations of the resulting textures. Three wrought magnesium–zinc alloys with texture modifying elements Nd (ZN10), Ca (ZX10), and Al (AZ31) have been used to extrude flat band profiles with varied processing parameters. This allowed a variation of grain sizes and textures of the extrudates. The impact on the mechanical properties and the forming behavior (Erichsen values IE) is revealed and discussed with respect to the microstructure and texture. It can be shown that a weak alignment of basal planes is preferred for enhanced formability over a distinct alignment of basal planes even if oriented preferentially for basal slip.

Keywords: magnesium alloys, sheets, extrusion, mechanical testing, stretch forming, Erichsen value

Edited by:
John L. Provis,
University of Sheffield,
United Kingdom

Reviewed by:
Indranil Basu,
ETH Zurich, Switzerland
Mihriban Ozden Pekguleryuz,
McGill University, Canada

***Correspondence:**
Jan Bohlen
jan.bohlen@hzg.de

Specialty section:
This article was submitted to
Structural Materials,
a section of the journal
Frontiers in Materials

Received: 08 March 2019
Accepted: 25 September 2019
Published: 10 October 2019

Citation:
Nienaber M, Kainer KU, Letzig D and
Bohlen J (2019) Processing Effects on
the Formability of Extruded Flat
Products of Magnesium Alloys.
Front. Mater. 6:253.
doi: 10.3389/fmats.2019.00253

INTRODUCTION

Making use of the full advantage of magnesium as a lightweight material also requires the production of larger thin-walled components such as sheets. However, the formability of magnesium alloys at room temperature is restricted due to their hexagonal lattice structure and the related limited number of available or easily activated slip systems (Mordike and Ebert, 2001; Beausir et al., 2009). The ability to form related parts includes the underlying manufacturing process of the sheet, e.g., rolling, as well as the sheet forming process. Conventional sheet rolling is carried out with high technical effort as the degrees of deformation per rolling pass need to remain low (Friedrich and Mordike, 2006). Processing of sheets via extrusion has also been described, which requires (and allows) a single high deformation processing step (Hsiang and Kuo, 2003; Bohlen et al., 2016, 2018a; Wang et al., 2016). This enables forming microstructures and textures that could not be produced by conventional production methods like casting or rolling (Gall et al., 2013).

Several earlier studies on the relationship between microstructure and mechanical or formability properties (Bohlen et al., 2007; Stutz et al., 2011; Suh et al., 2015) have highlighted that the formation of strong textures, i.e., with distinctly aligned basal planes parallel to the sheet plane, is one drawback for enhanced formability. Alloying with rare earth or calcium has been emphasized for texture weakening and for enhancing the formability during sheet rolling (Bohlen et al., 2007, 2015; Al-Samman and Li, 2011; Liu et al., 2016).

Typically, extruded magnesium alloys in the form of round bars develop a fiber texture with a pronounced prismatic $<10\bar{1}0>$ component parallel to the extrusion direction (ED)

(Dillamore and Roberts, 1965). Fully recrystallized materials also tend to develop a tilting component with a rotation of up to 30° around the c-axis of the lattice structure, thereby concentrating the orientations around the $<11\bar{2}0>$ pole intensity parallel to ED (Yi et al., 2010). In all cases, these textures represent a distinct preference for basal planes aligned parallel to ED. It has been shown that alloying magnesium with rare earth elements or Ca leads to distinct texture changes if the extruded profile is a round bar with a rotational symmetry around ED (Stanford and Barnett, 2008b; Stanford, 2010a). The resulting textures of these extruded alloys are also rather weak. In these cases a so-called "rare earth texture component" has been identified, often along with a $<11\bar{2}1>$ pole parallel to ED, thus tilting basal planes out of ED. Geometrically, an easier activation of basal slip during mechanical testing parallel to ED is then realized and an increase in the ductility of these materials enabled (Stanford and Barnett, 2008b; Zhou et al., 2013; Jiang et al., 2016). However, in the case of extrusion of flat profiles (without the rotational symmetry) also such alloys tend to form strong textures even if the alignment of basal planes may not preferentially be parallel to the sheet plane (Gall et al., 2013; Bohlen et al., 2018a). To give an example, extruded sheets from rare earth alloys ZE10 and ME21 in Bohlen et al. (2016) show strong textures, while extruded round bar counterparts of the same or comparable alloys showed weak textures (Bohlen et al., 2010; Nascimento et al., 2010). Flat bands (or sheets) with such strong textures can perform reasonably in deep-drawing cases or tensile testing but significantly lack formability in stretch forming cases.

In a recent work, possibilities for controlling the texture development during extrusion of flat bands (virtually representing sheets) have revealed the ability to significantly change the texture during extrusion as a result of the adjustment of the extrusion parameters (Bohlen et al., 2016). Based on an example of a magnesium alloy ZN10 (Mg+ 1 wt.% Zn+ 0.6 wt.% Nd) this corresponds directly to the dynamic recrystallization and grain growth behavior during extrusion. Especially, if the temperatures are very high during extrusion the rare earth specific texture development can even be overcome, resulting in a classical alignment of basal planes along the sheet plane. It is noteworthy, that the latter effect is also consistent with the texture development of rare earth containing round bar extrusions at high temperature (Stanford, 2010b). A similar effect like Nd on the texture development of extruded flat products has been shown for Ca-containing alloys, e.g., ZX10 (Mg+ 1 wt.%, Zn+ 0.2 wt.% Ca) in Bohlen et al. (2018b).

In this work, texture modification during direct extrusion and annealing of a flat band with different extrusion speed is investigated on two magnesium alloys with Nd (ZN10) and Ca (ZX10) in comparison to a classical benchmark magnesium alloy AZ31. It is suggested that the extrusion speed has a direct impact on the dynamic recrystallization behavior whereas annealing will cause static recrystallization. The differences in the microstructure and texture development are revealed and related to the mechanical properties from tensile tests as well as to the formability in biaxial Erichsen deepening tests.

TABLE 1 | Chemical composition of the alloys in this study; values in wt.%; Mg balance.

Alloy	Al	Zn	Ca	Nd	Mn
AZ31	2.88	0.90			0.21
ZX10		0.94	0.15		
ZN10		0.98		0.57	

MATERIALS AND METHODS

The chemical composition of the three magnesium alloys, AZ31, ZX10, and ZN10 has been measured by using spark emission spectroscopy (SPECTRO, SPECTROLAB M). Results are collected in **Table 1**. The alloys were prepared by using a modified gravity casting technique including directional solidification in a crucible. Details on this process can be found elsewhere (Elsayed et al., 2011). Billets were machined to a diameter of 49 mm to fit the 50 mm container of the extrusion press and to a length of 150 mm. Solid solution annealing of the cast billet was carried out for 16 h at 500°C (ZN10) and 16 h at 400°C (ZX10 and AZ31).

Extrusion experiments were carried out using a 2.5 MN automatic extrusion press of Müller Engineering (Müller Engineering GmbH & Co. KG, Todtenweis/Sand, Germany). The extruded bands have a width of 40 mm and a thickness of 2 mm, which corresponds to an extrusion ratio of 1:24.5. Processing temperatures were 300°C for AZ31 and ZX10 and 350°C for ZN10 in order to meet a reasonable range for material flow during extrusion. The extrusion speed (ram speed) was varied between 0.6 and 2.4 mm/s, respectively, which refers to rather low profile exit speeds of 0.9 or 3.5 m/min.

Additional annealing of the flat bands after extrusion for 10 min has been applied in order to track the microstructure development. AZ31 and ZX10 were heat treated at 400°C and ZN10 at 450°C. All bands were air-cooled after annealing.

The initial microstructure of all the materials were observed by light optical microscopy. The samples were polished with fine SiC papers (#800, #1200, and #2500), diamond suspension and OPS (oxide polishing suspension). The polished samples were etched for several seconds in standard picric acid solution of 20 ml H_2O, 7 ml acetic acid, 200 ml Ethanol, and 6 g of picric acid (as reported in Kree et al., 2004). Orientation maps on polished longitudinal sections of the extruded profiles have been measured using electron backscatter diffraction (EBSD) in a scanning electron microscope (Zeiss Crossbeam 550 L) and corresponding software to reveal grain orientations and grain characteristics. The orientation data are used to visualize the texture of the measured surface section as well as fractions of the microstructure. The nature of different grains is separated by using a grain property of the orientation distribution, the grain orientation spread (GOS). In this approach a concept from earlier works (Bohlen et al., 2015, 2016; Basu and Al-Samman, 2019) is repeated, assuming that recrystallized grains as a result of a nucleation and growth mechanism due to dynamic recrystallization will exhibit a low variation of their orientation.

However, grains which did experience active slip glide typically will show a higher orientation spread. In this work a separation of both fractions, assumed to represent a recrystallized and an unrecrystallized fraction of the microstructure, is based on a constraint of GOS = 1°. For texture measurements samples of the flat bands were ground to their midplane and polished. An X-ray diffractometer (PANalytical X'Pert PRO MRD) with Cu Kα radiation and a beam size of 2 × 1 mm² was employed to measure six pole figures up to a tilt angle of 70°. Normalized and background-corrected pole figures were completely recalculated from the orientation distribution function by using an open-source code MTEX (Bachmann et al., 2010). The recalculated (0002)- and $(10\bar{1}0)$-pole figures are used in this study to reveal the texture of the samples.

The tensile properties of the extruded alloys were measured using dog-bone-shaped specimens with a gauge length of 24 mm and a width of 5 mm. Tensile tests were carried out on a universal tensile testing machine (Zwick Z050) at room temperature with a constant initial strain rate of 10^{-3} s^{-1} parallel to the extrusion direction. The stretch forming behavior was investigated by using Erichsen tests on full sections of the extruded bands with a lubricant (OKS 352) at room temperature. The punch radius was 10 mm and the forming rate (punch displacement) 5 mm/min.

RESULT

Table 2 collects extrusion forces at the beginning, during (the middle) and the end of the extrusion experiments. As a result of the direct extrusion process the detected force includes a fraction required for the material flow (according to the flow stress) as well as a fraction for the friction between the billet and the container wall. Therefore, the force will continuously decrease during the extrusion experiment when the area of friction decreases due to the decreasing length of the remaining billet. The changing of this force in the middle range of the extrusion, i.e., the range on the flat band where samples were taken from, is averaged and it is shown that the variation is small for all six experiments.

The peak force is associated with the beginning of the material flow during the extrusion experiment. In the case of AZ31 there is a visible increase of this force with the increase of the extrusion speed, indicating that higher force is required if the deformation rate is higher. During the experiment, the gap between the force levels decreases and vanishes at the end of the extrusion, thus indicating that there is no remaining difference in the force required for material flow (i.e., the flow stress will be the same). In the case of ZX10 and ZN10 the gap in the peak force does not even exist, indicating a low rate dependence of the flow stresses. Furthermore, at the end of the extrusion experiments, the forces will be even lower if the extrusion speed is higher. If only the higher deformation rate is considered, this finding appears counterintuitive, as higher strain rate would typically be associated with a higher flow stress (Atwell and Barnett, 2007; Liu et al., 2007). A deformation related heating of the sample is hypothesized which will also affect the microstructure development of the extrudates.

TABLE 2 | Extrusion forces revealed from the extrusion experiments; peak force at the beginning of material flow (start of extrusion); force—middle of profile averaged from the center part of the profiles ranging over the part of the sample selection, and force—end of extrusion at the end of the extrusion experiment.

	Peak force (MN)	Force—middle of profile (MN)	Force—end of extrusion (MN)
AZ31 (0.6 mm/s @ 300°C)	1.86 ± 0.01	1.15 ± 0.06	0.90 ± 0.01
AZ31 (2.4 mm/s @ 300°C)	2.40 ± 0.03	1.28 ± 0.09	0.87 ± 0.01
ZX10 (0.6 mm/s @ 300°C)	2.57 ± 0.01	1.56 ± 0.07	1.20 ± 0.01
ZX10 (2.4 mm/s @ 300°C)	2.58 ± 0.03	1.45 ± 0.11	0.93 ± 0.01
ZN10 (0.6 mm/s @ 350°C)	1.93 ± 0.01	1.39 ± 0.07	1.06 ± 0.01
ZN10 (2.4 mm/s @ 350°C)	1.92 ± 0.02	1.29 ± 0.08	0.90 ± 0.01

Figure 1 shows the microstructure from the longitudinal section and the corresponding pole figures of the extruded bands. Resulting grain sizes are collected in **Table 3**. An increase of the extrusion speed leads to grain growth. The two as-extruded conditions of AZ31 (**Figures 1a,c**) are compared to their counterparts after annealing for 10 min at 400°C (**Figures 1b,d**). After slow extrusion with 0.6 mm/s (**Figure 1a**) a bimodal microstructure with non-recrystallized grains elongated parallel to extrusion direction (ED) is found. Fast extrusion with 2.4 mm/s (**Figure 1c**) qualitatively leads to an increase of the recrystallized fraction of the microstructure, however still maintaining elongated grains. The average grain size is 9 μm. The annealing of both as-extruded conditions does not show a visible effect on the microstructure, which remains mostly unchanged compared to the as-extruded condition. Furthermore, the texture of the four conditions of AZ31 also does not vary much, maintaining a strong alignment of basal planes parallel to the band surface (i.e., c-axis parallel to the normal direction ND), and a broader angular tilt of basal planes to the extrusion direction rather than to the transverse direction. A tendency to develop split peaks between ND and a tilt toward the ED is visible after fast extrusion or after annealing. Prismatic planes are randomly distributed parallel to the ND of the flat band. The variation of the intensities is small. This texture results are typical for AZ31 and compare well to those of rolled or extruded sheets of this alloy (Styczynski et al., 2004; Yi et al., 2006; Victoria-Hernandez et al., 2014; Bohlen et al., 2018a).

ZX10 was extruded and annealed with the same conditions as AZ31. Microstructure and texture results are shown in **Figures 1e–h**. After slow extrusion at 0.6 mm/s, the microstructure is homogenous and almost completely recrystallized with a small grain size of 4 μm. With fast extrusion at 2.4 mm/s, grain growth is observed, leading to an increase of the grain size to 15 μm. Additionally, an influence of the heat treatment on the microstructure is shown in both initial states of ZX10, resulting in a distinct grain growth (23 μm) after slow extrusion and a slightly lower grain size (21 μm) after fast extrusion. Obviously, the annealing procedure dominates the microstructure development rather than the initial microstructure of the as-extruded condition of this alloy. The texture is fully different compared to AZ31 but the variations are

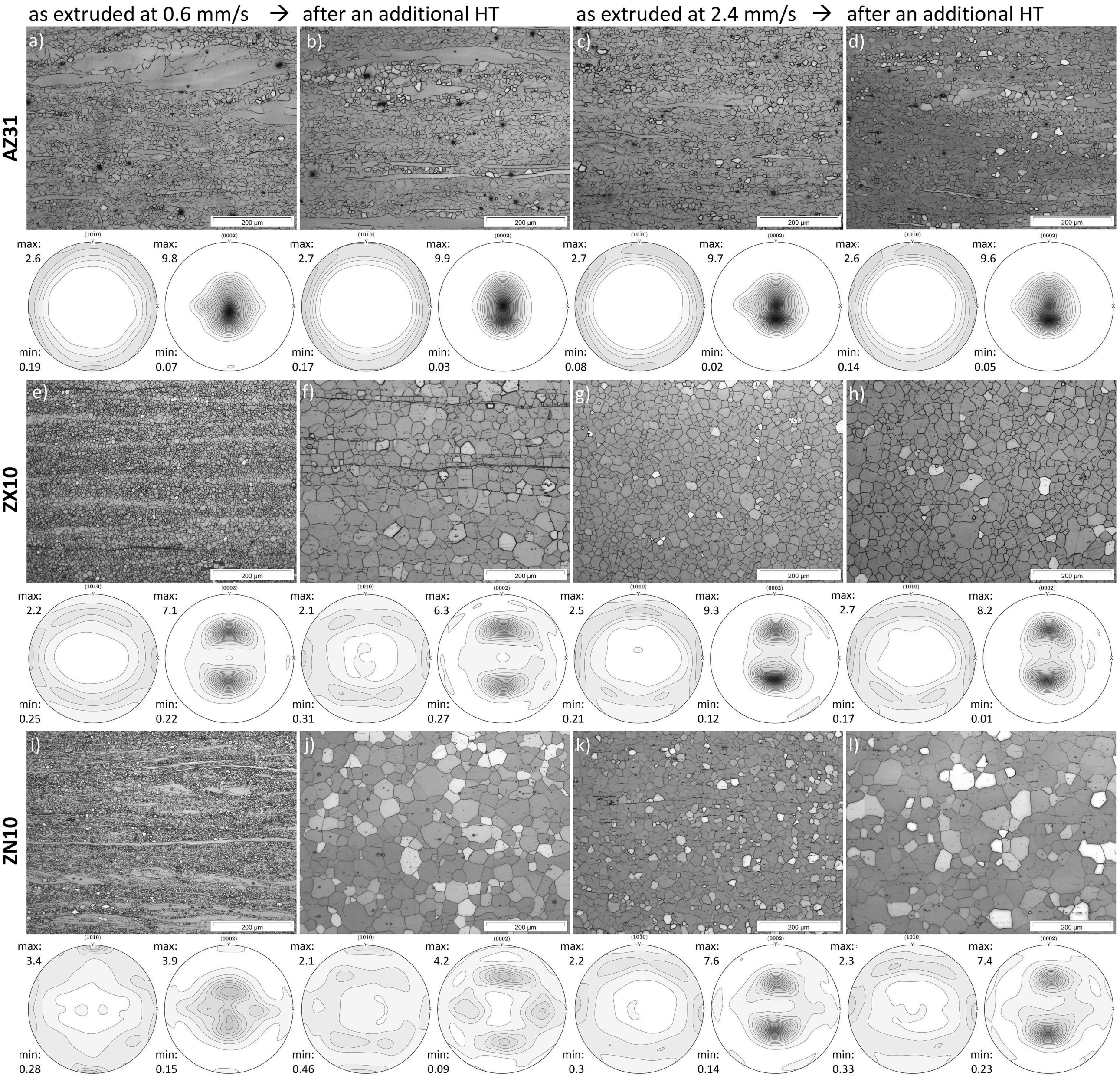

FIGURE 1 | Micrographs from longitudinal sections (ED horizontal) and pole figures (ED vertical) of the extruded flat bands of AZ31: **(a)** 300°C and 0.6 mm/s; **(b)** 300°C and 0.6 mm/s and additional heat treated (HT); **(c)** 300°C and 2.4 mm/s; **(d)** 300°C and 2.4 mm/s and additional HT; ZX10: **(e)** 300°C and 0.6 mm/s; **(f)** 300°C and 0.6 mm/s and additional HT; **(g)** 300°C and 2.4 mm/s; **(h)** 300°C and 2.4 mm/s and additional HT; ZN10: **(i)** 350°C and 0.6 mm/s; **(j)** 350°C and 0.6 mm/s and additional HT; **(k)** 350°C and 2.4 mm/s; **(l)** 350°C and 2.4 mm/s and additional HT.

also quite small. Split peaks of basal planes with a tilt toward ED are found. They are slightly more pronounced after fast extrusion but also weaken somewhat during annealing. Correspondingly, the prismatic planes are randomly distributed perpendicular to the two peak orientations of the basal poles, revealing a certain alignment parallel to ED (intensities at transverse direction TD) but no prismatic component or fiber in ED. This kind of texture of a calcium- or rare earth-containing Mg alloy has been described as a typical result for flat band extrusions and has been associated with fully recrystallized microstructures of such samples (Bohlen et al., 2018b; Brokmeier, 2018).

ZN10 (**Figures 1i–l**) exhibits a partially recrystallized microstructure after slow extrusion with a distribution of very small grains embedded into elongated unrecrystallized grains. During heat treatment, significant grain growth is observed, leading to the coarsest grained microstructure of this study with an average grain size of 29 µm. After fast extrusion, the microstructure is completely recrystallized (12 µm) but during

TABLE 3 | Grain size, Erichsen value (IE), and mechanical properties from tensile test in extrusion direction (ED) at room temperature of the extruded flat bands (TYS, tensile yield stress; UTS, ultimate tensile stress).

Alloy/condition	Grain Size (μm)	Erichsen value (mm)	TYS (MPa)	UTS (MPa)	Uniform strain (%)	Fracture strain (%)	Δ Stress = UTS-TYS (MPa)
AZ31 (0.6 mm/s @ 300°C)	6.7 ± 0.1	2.8 ± 0.2	151 ± 7	265 ± 2	18.6 ± 0.3	26.5 ± 0.1	**114**
AZ31 (0.6 mm/s @ 300°C) + HT	9.0 ± 0.7	2.8 ± 0.1	144 ± 2	256 ± 4	19.9 ± 1.1	26.5 ± 0.5	112
AZ31 (2.4 mm/s @ 300°C)	9.3 ± 0.5	2.8 ± 0.1	144 ± 6	257 ± 2	18.7 ± 1.1	25.8 ± 2.1	113
AZ31 (2.4 mm/s @ 300°C) + HT	9.9 ± 0.4	3.0 ± 0.1	153 ±10	265 ± 5	17.8 ± 1.0	25.0 ± 0.9	112
ZX10 (0.6 mm/s @ 300°C)	4.0 ± 0.1	4.9 ± 0.4	127 ±5	213 ± 4	25.1 ± 0.5	37.7 ± 2.8	**86**
ZX10 (0.6 mm/s @ 300°C) + HT	22.6 ± 1.9	**6.1 ± 0.1**	70 ±3	190 ±3	**27.8 ± 0.6**	**39.1 ± 2.1**	120
ZX10 (2.4 mm/s @ 300°C)	14.9 ± 0.2	5.3 ± 0.4	78 ± 4	195 ± 3	24.6 ± 0.4	31.8 ± 3.5	117
ZX10 (2.4 mm/s @ 300°C) + HT	20.7 ± 2.1	5.0 ± 0.2	62 ± 7	185 ± 8	25.3 ± 0.7	35.2 ± 1.4	123
ZN10 (0.6 mm/s @ 350°C)	3.5 ± 0.2	4.0 ± 0.3	188 ± 11	248 ± 4	14.2 ± 0.4	22.3 ± 2.2	**60**
ZN10 (0.6 mm/s @ 350°C) + HT	28.5 ± 3.3	**7.2 ± 0.2**	75 ± 4	189 ±4	**23.0 ± 1.0**	**34.9 ± 4.0**	114
ZN10 (2.4 mm/s @ 350°C)	12.1 ± 0.9	6.1 ± 0.3	100 ± 7	206 ± 5	21.2 ± 0.4	33.0 ± 2.7	106
ZN10 (2.4 mm/s @ 350°C) + HT	25.3 ± 1.2	5.6 ± 0.3	73 ± 5	197 ± 2	22.6 ± 1.1	32.1 ± 4.5	124

Some significant values are highlighted.

annealing grain coarsening is also found (25 μm). Although the microstructure development is generally very similar to ZX10, it appears that recrystallized grains remain smaller during extrusion, although the extrusion temperature was higher. Furthermore, the impact of the higher annealing temperature is rather small when the grain size development of ZN10 is compared to ZX10. The texture development has also many similar features, e.g., maintaining the split peaks of basal plane orientations and the distribution of prismatic planes. Especially after fast extrusion, the texture of ZN10 compares well to the same condition of ZX10. Only the maximum intensities are lower but remain unchanged during annealing. However, after slow extrusion the split peaks of basal planes remain very weak with maximum intensities of 4.2 m.r.d. and basal planes also exhibit a broader angular distribution toward TD. This transversal spread corresponds to a prismatic component in the $(10\bar{1}0)$ pole figure along with ED, which also leads to higher intensity. After the heat treatment, the prismatic component is still visible but the split peaks of basal planes with tilt to ED are stronger. Additionally (hypothetically as a result of the transversal spread of basal planes in the as-extruded condition), two weak split peaks with tilt to TD are visible. This difference of the texture development corresponds to the partly recrystallized nature of the ZN10 sample after slow extrusion.

EBSD orientation maps of the extruded profiles are collected in **Figures 2–4**. Exemplarily, results for AZ31 after slow extrusion as well as after the corresponding heat treatment are shown in **Figures 2A,B**. In the as-extruded condition (**Figure 2A**) a grain structure with a tendency in elongation along the extrusion direction (vertical) is visible, therefore repeating the finding in **Figure 1a**. The corresponding pole figures more clearly reveal an alignment of basal planes with the band plane but with a preferential tilt in the form of split peaks toward the ED. While this tilt is not clearly visible in the rather small fraction of the unrecrystallized grains (GOS > 1°), the recrystallized fraction (GOS < 1°) is consistent with this finding. A separation of these recrystallized grains into smaller (e.g., <5 μm) and larger (e.g., >10 μm) fractions does not show any change and therefore no development tendency of orientations during grain growth. The heat treated counterpart in **Figure 2B** repeats these findings in a slightly coarser grained structure but with a stronger alignment of the basal planes, e.g., the split peaks are not visible any more in the (0001) pole figure. The separation into smaller and larger grains suggests a more visible basal alignment in the larger grains rather than in the smaller recrystallized grains, aiming toward a certain growth advantage of these grains and therefore strengthening the basal alignment. Such a behavior has often been reported for rolled sheets of AZ31 (Huang et al., 2012; Victoria-Hernandez et al., 2014). **Figures 3A,B** show the EBSD results for slowly extruded ZX10 and its heat treated counterpart, respectively. Even in the as-extruded condition the microstructure appears almost fully recrystallized, leaving only a few grains exceeding a GOS of 1°. While the overall texture repeats the extended basal split peak texture from **Figure 1e**, the few unrecrystallized grains appear again with a more distinct alignment along the surface of the extruded band. For the smaller and larger recrystallized grains, again no difference in the texture is found. In **Figure 3B** very similar findings are presented for a fully recrystallized microstructure and the same split peak texture. This texture again is confirmed for all distinguished grain size fractions from the smallest grains (e.g., in the extended band of very small grains) as well as in the very large grains of this sample. The significance of the split peak texture seems stronger in the larger grains, thus corresponding to a growth advantage. **Figure 4** compares the EBSD results for the four tested samples of alloy ZN10. The slowly as-extruded condition in **Figure 4A** reveals a distinct fraction of unrecrystallized microstructure. This high fraction exhibits a texture (see GOS > 1°) with split peaks toward the TD. Furthermore, a corresponding four peak alignment in the prismatic $(10\bar{1}0)$ pole figure together with

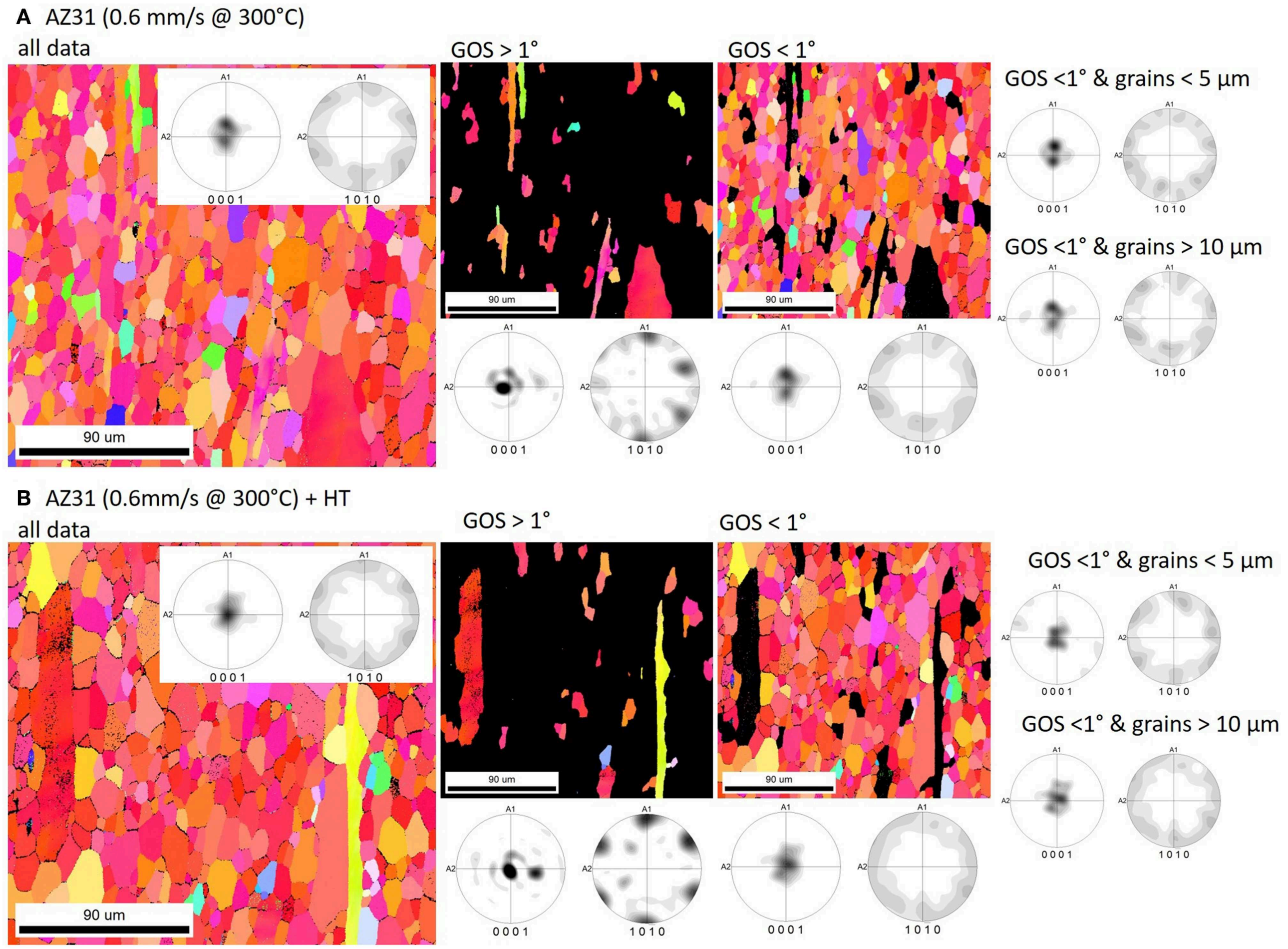

FIGURE 2 | Orientation maps from EBSD measurements on longitudinal sections of the extruded profile (ED vertical; pole figures: ED vertical, TD horizontal; color code and intensity levels see **Figure 4B**; GOS, grain orientation spread), **(A)** AZ31 after extrusion 0.6 mm/s at 300°C, **(B)** the same after heat treatment.

a strong prismatic peak in the ED is found. Obviously, an overemphasis of this fraction in the measured area leads to a clear difference of this texture compared to the one shown in **Figure 1i**. If only recrystallized grains are considered (GOS < 1°) the textures compare well, however, more distinctly showing the basal split peaks toward ED as well as a transverse spread including split peaks toward TD. A certain grain size tendency may be a higher significance of this component in the smaller recrystallized grains rather than in the larger ones. The prismatic component along ED is maintained at lower significance. The heat treatment of this sample, **Figure 4B**, allows maintaining both texture components with a certain emphasis of the ED split peak component in the larger grains. However, a clear TD spread component is not revealed any more in the fraction of the larger recrystallized grains. For the samples after fast extrusion and heat treatment, respectively, **Figures 4C,D**, again fully recrystallized microstructures are found with a possible strengthening of the ED split peak component in the larger grain fractions.

Stress–strain diagrams from tensile tests parallel to ED are shown in **Figure 5**. The corresponding mechanical properties are collected in **Table 3**. In case of AZ31 only small variations can be seen. The yield stress (TYS) varies between 144 and 153 MPa. It slightly decreases with increasing extrusion speed but during annealing there is no clear tendency. The same is found for the maximum stress (UTS) between 256 and 265 MPa and the uniform elongation which averages at about 18.7% strain. The fracture strain is also comparable at 26%. Classical strain hardening with a continuous decrease of the slope is seen in the stress–strain diagrams. ZX10 reveals a much lower TYS (62–127 MPa) and UTS (185–213 MPa). After slow extrusion the lowest grain size corresponds to the highest stress levels followed by the fast extruded condition. The annealed samples with largest grain sizes also show the lowest stress levels. It is noteworthy that only the stress–strain-curve of the slowly extruded sample exhibits a flow instability at the yield point whereas all other conditions exhibit typical strain hardening behavior, obviously higher compared to AZ31. This also results in higher uniform strains as well as fracture strains. Both properties benefit from annealing but somewhat decrease with increasing extrusion speed.

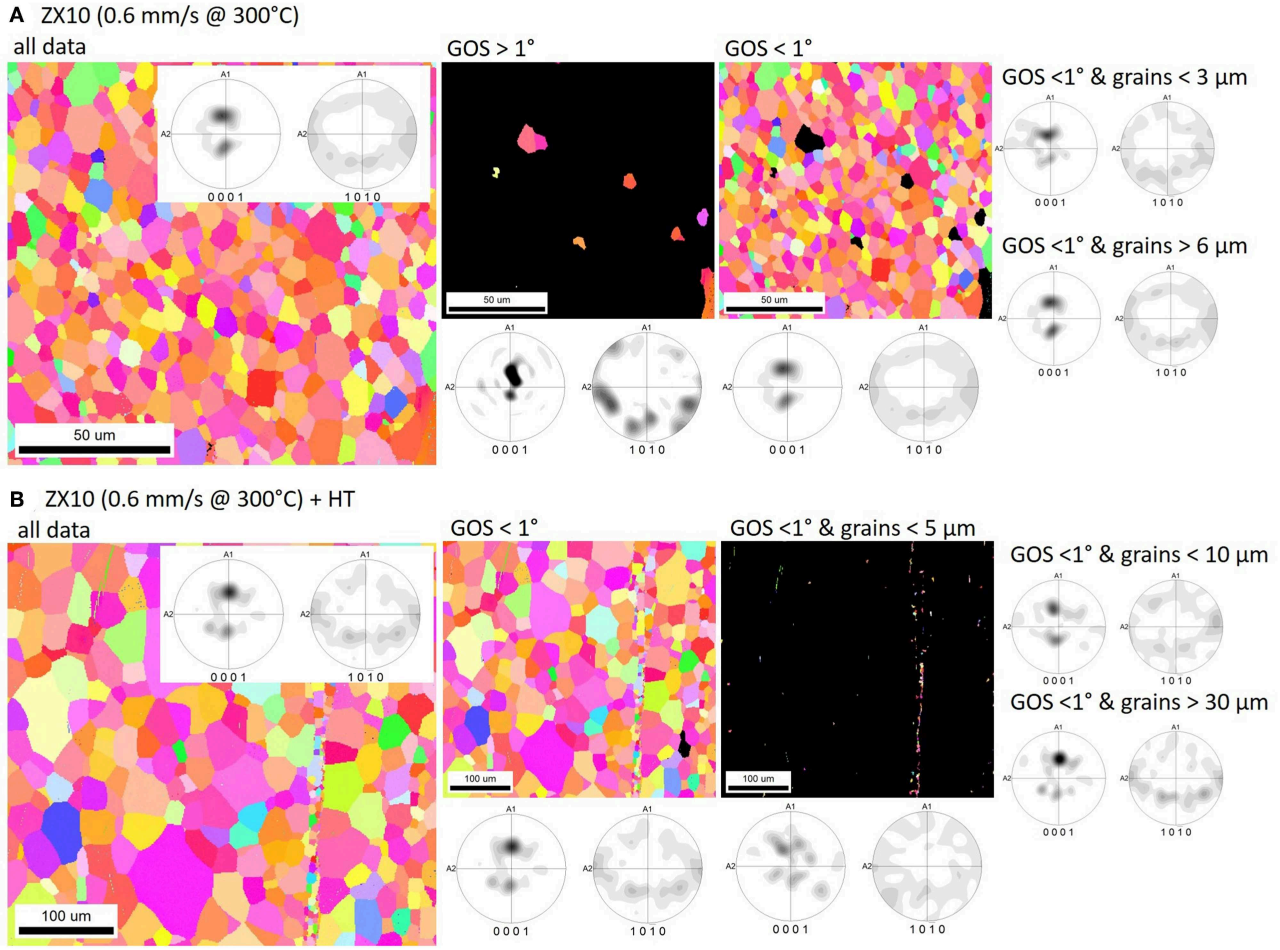

FIGURE 3 | Same as **Figure 2** but for **(A)** ZX10 after extrusion 0.6 mm/s at 300°C, **(B)** after heat treatment.

Also for ZN10, the stress levels (TYS and UTS) correspond to the grain size of the samples. They are even higher in the as-extruded conditions compared to ZX10 but comparable in the annealed condition although grain sizes are larger. This indicates an advantage of ZN10 if initial higher stress levels are envisioned at comparable grain sizes. The curves indicate a special strain hardening behavior of the slowly as-extruded samples, which corresponds well to their partly recrystallized microstructure. The increase of stress during strain hardening remains low, which also corresponds to the lowest uniform strain and fracture strain in this study. Again, uniform strains and fracture strains benefit from the annealing after extrusion. However, both values remain lower in comparison to ZX10 (but higher than for AZ31).

The results from Erichsen cupping tests are collected in **Figure 6** in the form of exemplary drawing force—drawing path curves. The presented curves reveal the increase of the force after attaching the punch to the sample surface and the beginning of the deformation while forming the cup. The drawing path is then shown as the resulting depth of the formed cup. This force increase is continued until a sudden drop due to sample cracking. The respective force level does not vary much for the four conditions of AZ31, it decreases only slightly with increasing extrusion speed but does not change due to the annealing of the samples. This finding is in good agreement to the strength considerations of this alloy as revealed from the tension tests. In the case of ZN10 and ZX10 the slowly as-extruded samples exhibit a steeper increase of the force levels compared to the other conditions, including the fast extruded samples as well as their annealed counterparts. This indicates principle strengthening of the samples as a result of the extrusion conditions. Consistently, the force levels of AZ31 remain higher than those of ZX10 and ZN10, although the maximum forces are lower due to early fracture of the samples.

The results from Erichsen cupping tests are collected in **Table 3** in the form of the Erichsen value (IE). This single value corresponds to the drawing length up to fracture of the samples, i.e., the depth of the formed cup as a result of biaxial stretching. For AZ31, the processing variations and the subsequent heat treatment show no influence on IE and remain at a very low level between 2.8 and 3.0 mm. This result compares well with the overall missing variation in the microstructure and texture development as well as with the tendency revealed for the

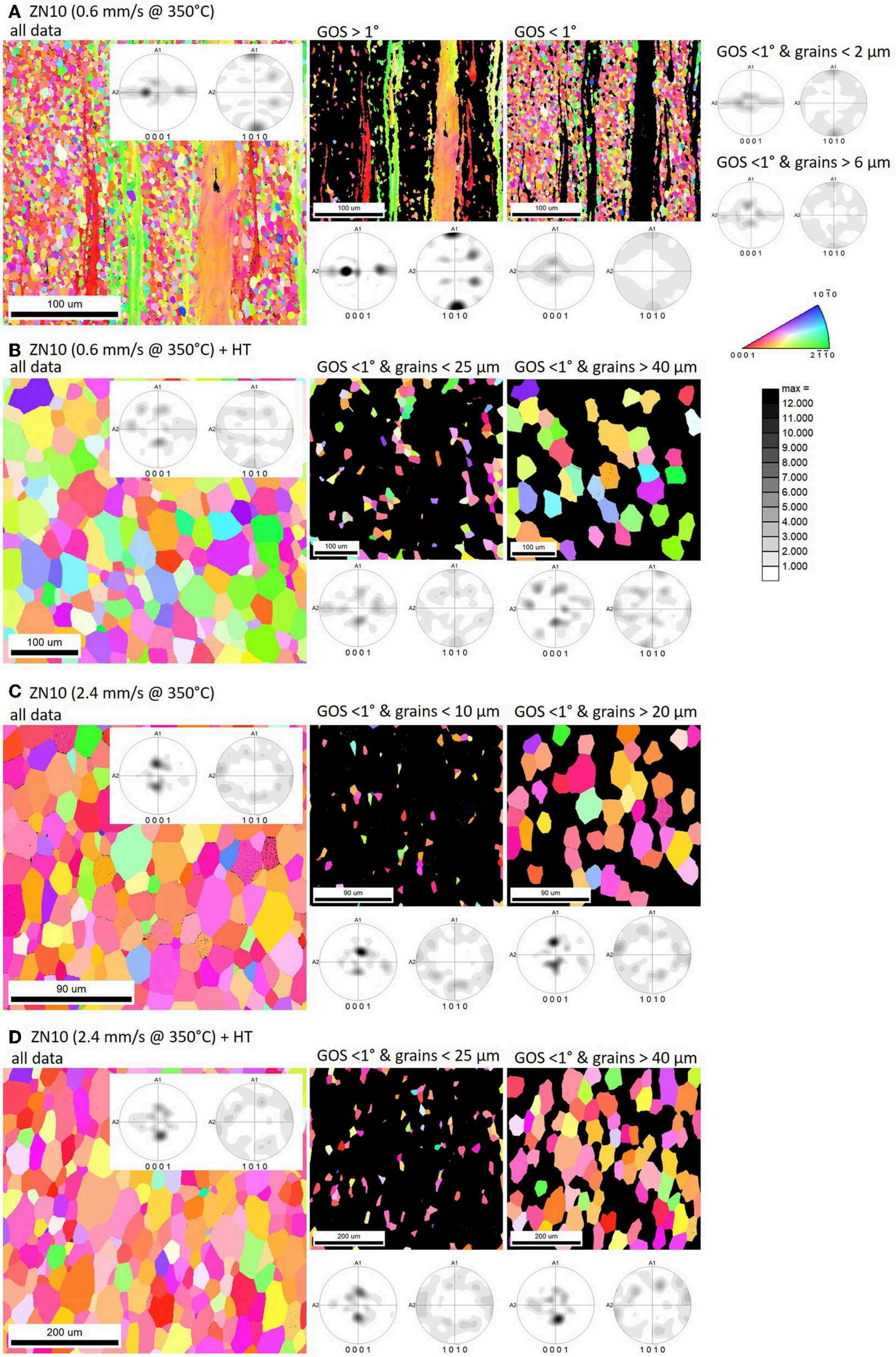

FIGURE 4 | Same as **Figure 2** but for **(A)** ZN10 after extrusion 0.6 mm/s at 350°C, **(B)** after heat treatment, **(C)** ZN10 after extrusion at 2.4 mm/s at 350°C, **(D)** after heat treatment.

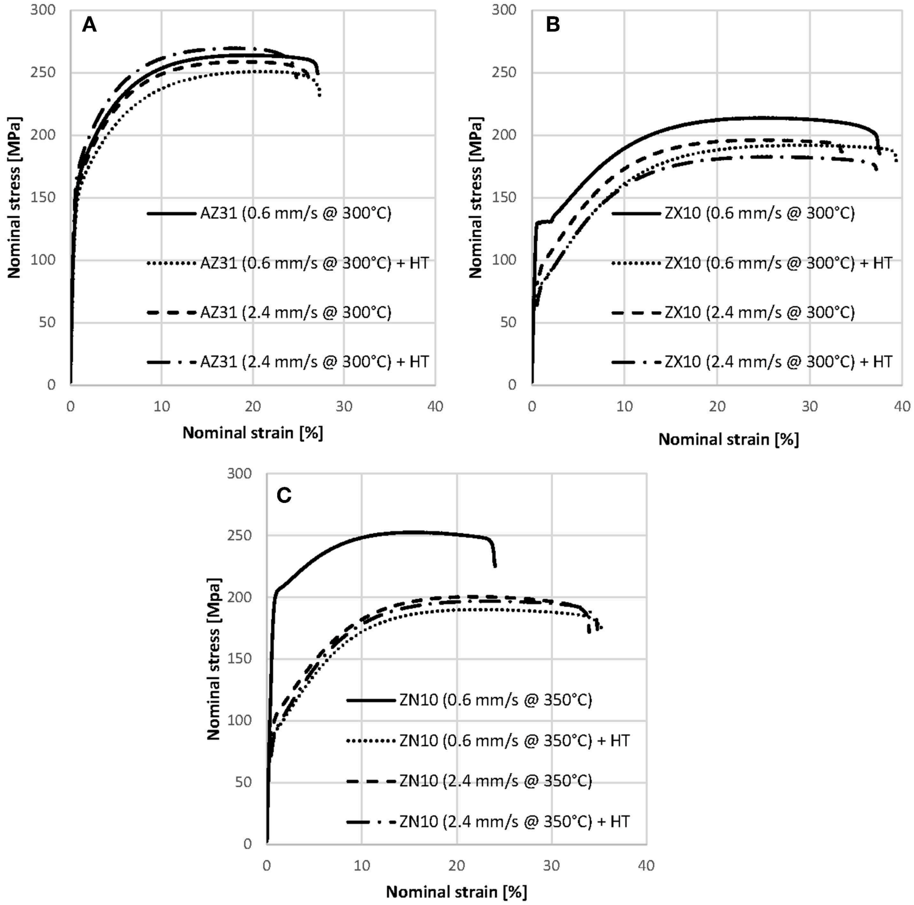

FIGURE 5 | Stress–strain diagrams in ED for the extruded bands for alloy. **(A)** AZ31. **(B)** ZX10. **(C)** ZN10.

mechanical properties. ZX10 shows a clearly higher IE between 4.9 and 6.1 mm. The maximum value is found for the annealed condition after slow extrusion and corresponds to the highest strain properties of this alloy. Interestingly, this is not associated with a fine-grained microstructure but it corresponds to the weakest texture of this alloy, which does not vary much between the four investigated conditions. In case of ZN10, the variation of the IE is larger, varying between 4.0 and 7.2 mm. Again, the highest value is found for the annealed condition of the slowly extruded band at rather large grain size but also with the highest strain levels revealed for this alloy. With the exception of the partly recrystallized condition after slow extrusion the IE are higher for ZN10 compared to ZX10. Noteworthy, in case of the strain properties from tensile tests the finding was vice versa. However, in tendency this corresponds to slightly weaker textures of ZN10. Furthermore, especially after slow speed extrusion and its annealed counterpart the textures are very weak. Thus, the highest IE corresponds to a sample with a weak and broad orientation distribution of basal planes and a fully recrystallized (not necessarily fine-grained) microstructure. In summary, these Erichsen values are among the higher levels of state of the art magnesium alloy sheets (Chino et al., 2009; Lee et al., 2014; Wang et al., 2018).

DISCUSSION

Microstructure and Texture Development

High degrees of deformation for the extrusion of profiles lead to heating during the material flow through the die. Earlier works have reported on measurements of a deformation heating, which is also influenced by the applied extrusion speed (Liu et al., 2007; Yu et al., 2013). Thus, an increase of the extrusion speed (and corresponding strain rate) leads to a steady state temperature increase due to deformation heating. The resulting change in the flow stress will then have a direct impact on the extrusion force as measured at the end of the extrusion process where it is not superimposed by a friction component. A mechanism, which has a determining influence on the resulting flow stress (and extrusion force, respectively) is the dynamic recrystallization during forming. If the tendency to recrystallization is enhanced the flow stress/extrusion force will decrease. In this regards, the data from the extrusion forces in **Table 2** show a tendency of such a decrease with the increase of the extrusion speed, from AZ31 (−0.03 MN) to ZN10 (−0.16 MN) and to ZX10 (−0.27 MN). The same alloy tendency is found in the form of an increasing average grain size in **Table 3** for AZ31 (+2.6 μm) to ZN10 (+8.6 μm) and to ZX10 (+10.9 μm). A further comparison of the microstructure

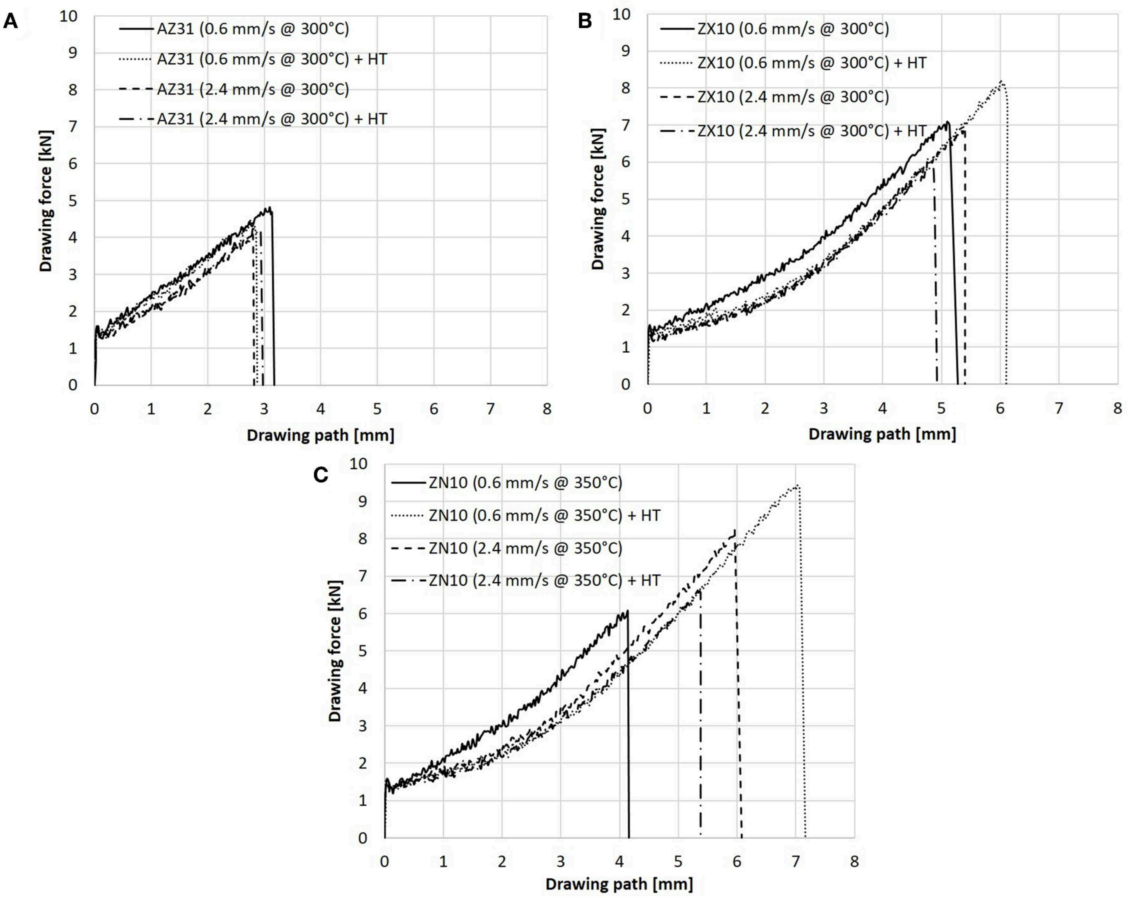

FIGURE 6 | Drawing force—drawing path curves from Erichsen cupping tests at room temperature. **(A)** AZ31. **(B)** ZX10. **(C)** ZN10.

development of the alloys does not seem appropriate as the initial extrusion temperatures needed to be varied for the different alloys in order to meet the extrusion windows. Still, the increase of the extrusion speed is associated with an enhancement of dynamic recrystallization and an alloy specific significance.

Furthermore, the resulting average grain sizes of ZN10 are lowest in this study at the highest initial billet temperatures, indicating a general retardation of recrystallization in this alloy compared to ZX10 or AZ31. The slowly extruded sample of ZN10 appears only partly recrystallized whereas both samples of ZX10 reveal fully recrystallized microstructures. For AZ31, the partly recrystallized microstructure still result in recrystallized grains grown much further than their ZN10-counterparts. This indicates a distinct difference in the recrystallization mechanisms. Such a difference has been investigated in related works, including an alloy specific change of the type of the dynamic recrystallization mechanism. A continuous type of recrystallization due to rearrangement and rotation of low angle grain boundaries toward high angle boundaries has been suggested instead of a dominating grain nucleation and growth mechanism (Barrett et al., 2017). Also particle stimulation of recrystallization is known as a specific mechanism of grain structure formation (Ball and Prangnell, 1994; Al-Samman, 2013; Liu et al., 2018).

In order to understand the impact of recrystallization on the microstructure development is appears worthwhile to compare the textures of extruded round bars of magnesium alloys with those textures obtained from shaped flat profiles. Three important texture components of round bars can be repeated as follows: A strong prismatic fiber with high intensity in the $(10\bar{1}0)$ pole figure along the ED has been associated with the remains of strong deformation textures in basically all magnesium alloy extrusions (Dillamore and Roberts, 1965; Stanford and Barnett, 2008b; Yi et al., 2010). A lattice rotation of up to 30° favors high intensity in the $(11\bar{2}0)$ pole figure along ED for recrystallized extruded bars. A component exemplarily concentrating with high intensity in a $(11\bar{2}1)$ pole figure is found in rare earth or Ca containing alloys, leading to a tilt of basal planes out of the ED. Retardation of recrystallization and corresponding new orientations developing as a result of deformation related orientation development include an impact of twins (Hantzsche et al., 2010; Al-Samman, 2013; Stanford, 2013; Minárik et al., 2019) and shear bands (Stanford and Barnett, 2008a; Zeng et al., 2019). Correspondingly, the textures of flat band extrusions from various magnesium alloys have been described with respect to the specific shape given by the profile (Brokmeier, 2018). **Figure 7** collects sketches of such alloys representing the texture components of the samples of this study. **Figure 7A** shows a texture with an alignment of basal planes parallel to the band surface, also revealing high prismatic intensity in ED in the 6 peak symmetry of the prismatic pole figure. Note, that this texture is specifically expected if a deformation texture is hypothesized which is also visible from the texture of unrecrystallized grains (GOS > 1°) of AZ31 in **Figures 2A,B**. Basically the same alignment of basal planes is found in the recrystallized fraction of the microstructure but the six peak symmetry in the prismatic pole figure vanishes toward a rotational distribution of prismatic planes. This is the same reorientation as found in round bar extrusions as a result of recrystallization and the concurrent 30° reorientation of prismatic planes. The texture component in **Figure 7B** is based on two split peaks with tilt toward ED. It reveals an orientation which is not in accordance with prismatic pole intensity in ED but tilted. Note, that the recrystallized grain fractions in **Figures 3A,B** for ZX10 and in **Figures 4C,D** for ZN10 do not exactly match with this description but again better with a 30° rotation of the prismatic planes which makes this texture component well comparable to the "rare earth texture component" described for RE containing round bar extrusions. In conclusion this ED tilted basal split peak texture component is consistent with a modified rare earth texture component and its appearance in a profile without the rotational symmetry of a round bar is confirmed.

Figure 7C shows a component with two split peaks tilted toward TD. Correspondingly, a peak intensity in the prismatic pole figure along ED is visible. This component is very comparable to the one shown in **Figure 7A** if an additional TD tilt of the basal planes is acknowledged. It is only revealed for the partly recrystallized sample of ZN10 in this study, **Figure 4A**. Interestingly, the visibility of this specific orientation requires a shaped profile and cannot be distinguished for a round bar. In such a case it is consistent with a deformation related texture component, therefore in agreement with the unrecrystallized fraction of the microstructure for ZN10. Then the origin of this texture component requires an impact of different deformation mechanisms, especially other than in the case of AZ31. Although the specification of the nature of this effect is beyond the scope of this study, it has been shown that preferential prismatic slip instead of preferential basal slip is in accordance with such effects during sheet rolling (Styczynski et al., 2004).

Mechanical Properties and Formability

Experiments with two different strain paths' were applied for the presentation of the mechanical behavior of the extruded bands. Tensile tests parallel to ED feature positive strain along the extrusion direction but corresponding free contraction along TD and ND. On the other hand, Erichsen cupping tests reveal the principal formability of the samples in operations with biaxial strain. In this condition, positive strain is enforced along ED and TD but contraction (thinning) is only freely enabled along ND. These two different procedures of plastic deformation are correlated to the microstructure and texture of the materials of this study. Both tests are not expected to meet the same microstructure requirements for enhanced formability or ductility. In a simple consideration of dislocation driven deformation the ability of strain accommodation is related to the activity of the mechanism based on their activation (e.g., the critical resolved shear stress) as well as the orientation distribution of the respective lattice planes, i.e., described by the texture (Agnew et al., 2001; Bohlen et al., 2007; Hadorn et al., 2011; Miller et al., 2016; Chaudry et al., 2019). Thus, it appears worthwhile to concentrate on the contribution of basal slip with its low CRSS value and their orientation distribution (Chapuis and Driver, 2011; Wang et al., 2011; Kim et al., 2016; Liu et al., 2017) if texture effects are addressed, but not the initial effect of alloying elements on the ability of other (non-basal) slip modes to contribute to strain accommodation (Bohlen et al., 2007). In the case of a strong alignment of basal planes in the band plane like in AZ31 there is less ability for activation of basal slip in the uni-axial-tension case as well as in the stretch forming case. Therefore, stress properties remain comparably high and strain levels low as the strain hardening ability of the samples is limited. In cases with a tilt of basal planes toward ED slip activation is enhanced in the uni-axial case and the ability for strain accommodation increases. This is typically found for ZX10 and ZN10 in this study. Interestingly, the significance of such a component does not have a distinct effect on the strain accommodation. However, the yield stress remains lower in those cases if it is not also influenced by an unrecrystallized fraction of the microstructure which hypothetically can be assumed to be a harder fraction of the microstructure as a result of dislocation hardening during extrusion (e.g., slowly as-extruded conditions of ZX10 and ZN10), see discussion below.

In case of the biaxial test positive strain enforcement in all in-plane directions leaves material flow with negative strain along ND. Accommodation of such strain may require the same orientation considerations as above, but they are especially needed homogeneously in all in-plane directions. Although sample dimensions in this study did not allow revealing the mechanical behavior along the transverse direction, it has been shown in earlier work on extruded sheets that a strong anisotropy of the mechanical behavior is often correlated to limited stretch formability (Bohlen et al., 2018a). Forming limit curves revealed low formability in stretch forming conditions on the right side of the forming limit diagram but high formability on the left side, which in the context of this study compares to a strain path of the uni-axial tension test.

The split peak texture with tilt of basal planes appears to be beneficial for the strain properties in the tension test as well as for the stretch forming Erichsen cupping test and within each material a direct correlation can be found. Only in the case of ZN10 with especially weak distribution of basal planes and a concurrent further orientation component with tilt toward TD an additional increase of strain during the Erichsen cupping test is enabled. On the other hand, the weaker alignment of basal planes is not anymore beneficial for achieving very high uniform strains (and corresponding fracture strains) which leaves the strain levels of ZN10 lower compared to ZX10 as revealed from the tensile tests. This simple texture approach allows concluding

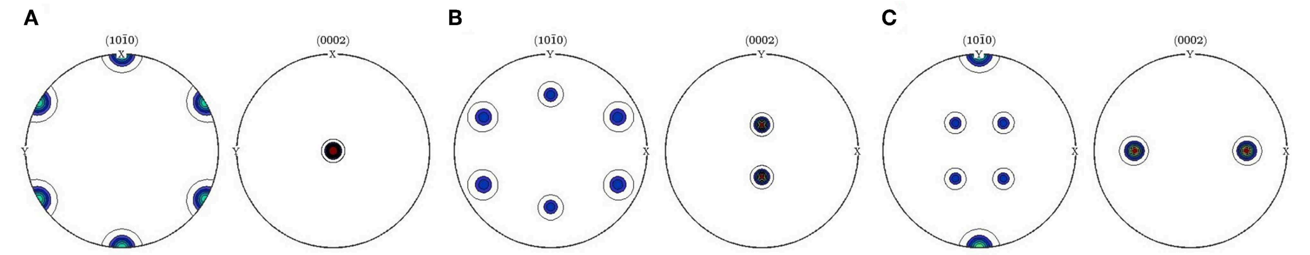

FIGURE 7 | Texture components found in flat band extrusions considering crystallographic lattice relationships, **(A)** basal component, **(B)** ED split peak component, **(C)** TD split peak component.

that weak textures with a more isotropic distribution of basal planes are required, especially to increase the stretch formability of magnesium sheets.

Such texture considerations do not include other microstructure related properties of the extruded and heat treated materials on the mechanical properties. Especially, the partly recrystallized microstructures may impose an impact on the strength properties of the samples, especially in the case of AZ31 and the slowly extruded ZN10. Together with the slowly extruded ZX10 (proven to be almost fully recrystallized in **Figure 3**) these samples exhibit high stress levels (TYS and UTS) compared to the fully recrystallized counterparts. Furthermore, if the ability to strain hardening is considered as the increase of stress from TYS to the UTS (**Table 3**) similar levels are found for AZ31 (∼113 MPa) in accordance with the unchanged nature of the microstructure. In the case of ZX10 and ZN10, however, the lowest increase is clearly found for the slowly as-extruded samples, especially low for ZN10 (∼60 MPa) with its clearly partly recrystallized microstructure. Although the quantitative fraction of the unrecrystallized microstructure cannot be directly resolved, the correlation of this strain hardening limitation to the degree of the recrystallized microstructure (and thus a partly strain hardened condition of the samples) becomes obvious. For the strain levels (uniform strain and fracture strain) this is directly confirmed for the partly recrystallized ZN10 after slow extrusion, not very distinct in case of ZX10 and again, not resolved for AZ31 based on the unchanged nature of the microstructures. Furthermore, it is also in agreement with the higher drawing forces required for Erichsen deepening in **Figure 6** as well as comparably lower Erichsen values, **Table 3**.

Figure 8 shows the TYS plotted vs. the inverse square root of the average grain size (following the Hall–Petch relationship (Mann et al., 2004). This plot has also been suggested in an earlier work (Stanford, 2013) to not only see the impact of grain boundary strengthening but also to visualize any deviation from the expected linear increase of TYS with the respective function of the grain size. In this plot, the above mentioned insignificance in the microstructure variation of AZ31 becomes visible in a very small range for the grain size function and no clear resolvable tendency for the variation of the TYS. The more pronounced broader range for the grain structures of the ZX10 and ZN10 alloys is in comprehensive agreement with a grain size related strengthening mechanism. While the variation of TYS for ZX10 and ZN10 is somewhat comparable at higher grain sizes (on the left-hand side of the diagram) the variation for both alloys at smallest grain size is significant. Again, this is in agreement with the above discussed fraction of unrecrystallized grains of this condition due to strain hardening. Furthermore, the slightly higher TYS of AZ31 in the respective grain size range in comparison to an interpolated assumption for ZX10 and ZN10 corresponds well to the strong basal textures of this alloy and the resulting limitation of slip activation.

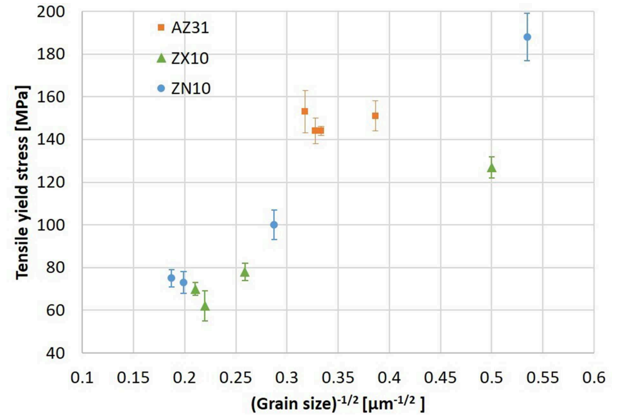

FIGURE 8 | Tensile Yield stress parallel to ED from tensile tests vs. the inverse square route of the average grain size of the results collected in **Table 3** (Hall–Petch plot).

A potential impact of precipitates as strengtheners of the extruded samples as well as their heat treated counterparts would impose a further strengthening mechanism likely to occur at least in ZX10 and ZN10. However, in the context of the solid solution annealing of the lean alloy billets prior to extrusion this effect may not be very significant for the samples of this study (Nie, 2012) and especially not resolved within the complexity of the above mentioned microstructure variations. In a consideration of the ability to design preferred mechanical properties of the alloys of this study, particle strengthening would enable a post-forming adjustment of the material strength, thereby maintaining a preferential formability after extrusion.

In combination, the enhancement of these strengthening mechanisms, orientation strengthening, partly recrystallized microstructure (and potential precipitation strengthening) counteract to an improved formability of the materials of this study. The same is concluded for a respective grain size strengthening if the corresponding microstructure development results in partly recrystallization, e.g., in the case of ZN10 compared to ZX10 after slow extrusion. Furthermore, the design of textures which lead to preferential forming properties during extrusion is based on partly recrystallized microstructures because the resulting texture needs to be weak. This is accessible if the dynamic recrystallization is retarded in a way that not only a strong recrystallization texture is obtained. Interestingly, the texture development as a result of static recrystallization during heat-treatment differs from the texture development at higher extrusion speed, a result of dynamic recrystallization. This is especially obvious in the case of ZN10. Still, annealing is required to increase the degree of recrystallization of this material, i.e., softening the samples.

CONCLUSIONS

Direct extrusion of flat bands has been used to study alloying and processing effects on the microstructure and texture development. An increase of the extrusion speed is used to induce deformation heating during extrusion and concurrently enhanced dynamic recrystallization. Besides a comprehensive behavior of increased degree of recrystallization and/or grain growth, significant variations in the texture development are found, ranking from classical strong basal textures for AZ31, strong alignments of basal planes with tilt toward ED for ZX10 and the same for the Nd containing ZN10 alloy if the samples are fully recrystallized. This texture has been associated with the typically weak textures obtained in rare earth or Ca containing round bar extrusions. A distinct texture variation becomes possible if a partly recrystallized microstructure is realized during extrusion which includes a texture component typically not visible in round bar extrusions. During heat treatment, i.e., static recrystallization, this texture component can be maintained.

The mechanical properties in tensile tests and Erichsen cupping tests reveal that for biaxial testing especially weak textures allow increasing the formability. Such weak textures are with no preferred alignment of basal planes parallel to the surface but a tilt out of this orientation. Furthermore, a rotational symmetry of this tilt around ND increases the formability. Contrary, this is not preferred for uni-axial testing where strong tilt peaks of basal planes lead to increasing ductility. Alloying elements such as Nd in ZN10 allow materials with such textures to be obtained after extrusion. In the case of the Ca containing ZX10, recrystallizations was not restricted enough to pronounce this and in the conventional magnesium alloys like AZ31 no hint for the ability to change the texture has been observed. Thus, retardation of dynamic recrystallization by alloying and adjusting the processing parameters (followed by static recrystallization during heat treatment) allows the extrusion of flat profiles with excellent forming properties. The resulting Erichsen values for flat bands (sheets) of ZX10 (6.1 mm) and ZN10 (7.2 mm) are among the higher levels revealed for magnesium sheets.

DATA AVAILABILITY STATEMENT

The datasets generated for this study are available on request to the corresponding author.

AUTHOR CONTRIBUTIONS

Experimental works were carried out by MN and JB with continuous discussion with DL and KK. All authors discussed the experimental results and the conclusion and contributed to writing the submitted manuscript.

FUNDING

The manuscript includes original work from institutional funding of the Helmholtz-Zentrum Geesthacht. The work was also related to a project proposal funded by the Deutsche Forschungsgemeinschaft. The support under Grant nos. Bo 2461/4-1, Yi 103/3-2 and BR 961/7-1 is highly appreciated.

ACKNOWLEDGMENTS

The authors would like to thank Mr. Günther Meister and Mr. Alexander Reichart for their help during casting and machining of the billets. We also appreciate the great support of Dr. Sangbong Yi during the EBSD measurements of this study.

REFERENCES

Agnew, S. R., Yoo, M. H., and Tomé, C. N. (2001). Application of texture simulation to understanding mechanical behavior of Mg and solid solution alloys containing Li or Y. *Acta Mater.* 49, 4277–4289. doi: 10.1016/S1359-6454(01)00297-X

Al-Samman, T. (2013). Modification of texture and microstructure of magnesium alloy extrusions by particle-stimulated recrystallization. *Mater. Sci. Eng. A* 560, 561–566. doi: 10.1016/j.msea.2012.09.102

Al-Samman, T., and Li, X. (2011). Sheet texture modification in magnesium-based alloys by selective rare earth alloying. *Mater. Sci. Eng. A* 528, 3809–3822. doi: 10.1016/j.msea.2011.01.080

Atwell, D. L., and Barnett, M. R. (2007). Extrusion limits of magnesium alloys. *Metallur. Mater. Trans. A* 38, 3032–3041. doi: 10.1007/s11661-007-9323-2

Bachmann, F., Hielscher, R., and Schaeben, H. (2010). Texture analysis with MTEX – free and open source software toolbox. *Solid State Phenomena* 160, 63–68. doi: 10.4028/www.scientific.net/SSP.160.63

Ball, E. A., and Prangnell, P. B. (1994). Tensile-compressive yield asymmetries in high strength wrought magnesium alloys. *Scripta Metallur. Materialia* 31, 111–116. doi: 10.1016/0956-716X(94)90159-7

Barrett, C. D., Imandoust, A., Oppedal, A. L., Inal, K., Tschopp, M. A., and El Kadiri, H. (2017). Effect of grain boundaries on texture formation during dynamic recrystallization of magnesium alloys. *Acta Mater.* 128, 270–283. doi: 10.1016/j.actamat.2017.01.063

Basu, I., and Al-Samman, T. (2019). Hierarchical twinning induced texture weakening in lean magnesium alloys. *Front. Mater.* 6:187. doi: 10.3389/fmats.2019.00187

Beausir, B., Biswas, S., Kim, D. I., Tóth, L. S., and Suwas, S. (2009). Analysis of microstructure and texture evolution in pure magnesium during symmetric and asymmetric rolling. *Acta Mater.* 57, 5061–5077. doi: 10.1016/j.actamat.2009.07.008

Bohlen, J., Cano, G., Drozdenko, D., Dobron, P., Kainer, K., Gall, S., et al. (2018a). Processing effects on the formability of magnesium alloy sheets. *Metals* 8:147. doi: 10.3390/met8020147

Bohlen, J., Cano, G., Kurz, G., Kainer, K. U., Letzig, D., Drozdenko, D., et al. (2018b). Profile shape effect on the texture and mechanical properties of extruded rare earth containing magnesium alloys. *Acta Phys. Polonica A* 134, 714–719. doi: 10.12693/APhysPolA.134.714

Bohlen, J., Nürnberg, M. R., Senn, J. W., Letzig, D., and Agnew, S. R. (2007). The texture and anisotropy of magnesium–zinc–rare earth alloy sheets. *Acta Mater.* 55, 2101–2112. doi: 10.1016/j.actamat.2006.11.013

Bohlen, J., Schlung, O., Gall, S., Müller, S., and Letzig, D. (2016). "Formability of extruded magnesium alloy sheets with different textures," in *Magnesium Technology 2016*, eds A. Singh, K. Solanki, M. V. Manuel, and N. R. Neelameggham (Hoboken, NJ: John Wiley & Sons, Inc.), 251–256.

Bohlen, J., Wendt, J., Nienaber, M., Kainer, K. U., Stutz, L., and Letzig, D. (2015). Calcium and zirconium as texture modifiers during rolling and annealing of magnesium–zinc alloys. *Mater. Character.* 101, 144–152. doi: 10.1016/j.matchar.2015.02.002

Bohlen, J., Yi, S., Letzig, D., and Kainer, K. U. (2010). Effect of rare earth elements on the microstructure and texture development in magnesium–manganese alloys during extrusion. *Mater. Sci. Eng. A* 527, 7092–7098. doi: 10.1016/j.msea.2010.07.081

Brokmeier, H.-G. (2018). Hot rectangular extrusion textures of six Mg-alloys via neutron diffraction. *Adv. Eng. Mater.* 20:1700234. doi: 10.1002/adem.201700234

Chapuis, A., and Driver, J. H. (2011). Temperature dependency of slip and twinning in plane strain compressed magnesium single crystals. *Acta Mater.* 59, 1986–1994. doi: 10.1016/j.actamat.2010.11.064

Chaudry, U. M., Kim, T. H., Park, S. D., Kim, Y. S., Hamad, K., and Kim, J.-G. (2019). Effects of calcium on the activity of slip systems in AZ31 magnesium alloy. *Mater. Sci. Eng. A* 739, 289–294. doi: 10.1016/j.msea.2018.10.060

Chino, Y., Sassa, K., and Mabuchi, M. (2009). Texture and stretch formability of a rolled Mg–Zn alloy containing dilute content of Y. *Mater. Sci. Eng. A* 513–514, 394–400. doi: 10.1016/j.msea.2009.01.074

Dillamore, I. L., and Roberts, W. T. (1965). Preferred Orientation in Wrought and Annealed Metals. *Metallur. Rev.* 10, 271–380. doi: 10.1179/mtlr.1965.10.1.271

Elsayed, F. R., Hort, N., Salgado Ordorica, M. A., and Kainer, K. U. (2011). Magnesium permanent mold castings optimization. *Mater. Sci. Forum* 690, 65–68. doi: 10.4028/www.scientific.net/MSF.690.65

Friedrich, H. E., and Mordike, B. L. (2006). *Magnesium Technology: Metallurgy, Design Data, Applications*. Heidelberg: Springer-Verlag.

Gall, S., Coelho, R. S., Müller, S., and Reimers, W. (2013). Mechanical properties and forming behavior of extruded AZ31 and ME21 magnesium alloy sheets. *Mater. Sci. Eng. A* 579, 180–187. doi: 10.1016/j.msea.2013.05.027

Hadorn, J. P., Hantzsche, K., Yi, S., Bohlen, J., Letzig, D., Wollmershauser, J. A., et al. (2011). Role of solute in the texture modification during hot deformation of Mg-rare earth alloys. *Metallur. Mater. Trans. A* 43, 1347–1362. doi: 10.1007/s11661-011-0923-5

Hantzsche, K., Bohlen, J., Wendt, J., Kainer, K. U., Yi, S. B., and Letzig, D. (2010). Effect of rare earth additions on microstructure and texture development of magnesium alloy sheets. *Scr. Mater.* 63, 725–730. doi: 10.1016/j.scriptamat.2009.12.033

Hsiang, S.-H., and Kuo, J.-L. (2003). An investigation on the hot extrusion process of magnesium alloy sheet. *J. Mater. Process. Technol.* 140, 6–12. doi: 10.1016/S0924-0136(03)00693-9

Huang, X., Suzuki, K., Chino, Y., and Mabuchi, M. (2012). Influence of initial texture on rolling and annealing textures of Mg−3Al−1Zn alloy sheets processed by high temperature rolling. *J. Alloys Compd.* 537, 80–86. doi: 10.1016/j.jallcom.2012.05.002

Jiang, M. G., Xu, C., Nakata, T., Yan, H., Chen, R. S., and Kamado, S. (2016). Development of dilute Mg–Zn–Ca–Mn alloy with high performance via extrusion. *J. Alloys Compd.* 668, 13–21. doi: 10.1016/j.jallcom.2016.01.195

Kim, S.-J., Lee, Y.-S., and Kim, D. (2016). Analysis of formability of Ca-added magnesium alloy sheets at low temperatures. *Mater. Character.* 113, 152–159. doi: 10.1016/j.matchar.2016.01.013

Kree, V., Bohlen, J., Letzig, D., and Kainer, K. U. (2004). The metallographical examination of magnesium alloys. *Pract. Metallogr.* 41, 233–246.

Lee, J.-Y., Yun, Y.-S., Suh, B.-C., Kim, N.-J., Kim, W.-T., and Kim, D.-H. (2014). Comparison of static recrystallization behavior in hot rolled Mg−3Al−1Zn and Mg−3Zn−0.5Ca sheets. *J. Alloys Compd.* 589, 240–246. doi: 10.1016/j.jallcom.2013.11.210

Liu, G., Zhou, J., and Duszczyk, J. (2007). Prediction and verification of temperature evolution as a function of ram speed during the extrusion of AZ31 alloy into a rectangular section. *J. Mater. Process. Technol.* 186, 191–199. doi: 10.1016/j.jmatprotec.2006.12.033

Liu, L., Pan, F., Chen, X., Huang, Y., Song, B., Yang, H., et al. (2018). The effect of Y addition on recrystallization and mechanical properties of Mg−6Zn−xY−0.5Ce−0.4Zr alloys. *Vacuum* 155, 445–455. doi: 10.1016/j.vacuum.2018.06.048

Liu, P., Jiang, H., Cai, Z., Kang, Q., and Zhang, Y. (2016). The effect of Y, Ce and Gd on texture, recrystallization and mechanical property of Mg–Zn alloys. *J. Magnes. Alloys* 4, 188–196. doi: 10.1016/j.jma.2016.07.001

Liu, Y., Li, N., Arul Kumar, M., Pathak, S., Wang, J., McCabe, R. J., et al. (2017). Experimentally quantifying critical stresses associated with basal slip and twinning in magnesium using micropillars. *Acta Mater.* 135, 411–421. doi: 10.1016/j.actamat.2017.06.008

Mann, G., Griffiths, J. R., and Cáceres, C. H. (2004). Hall-Petch parameters in tension and compression in cast Mg-2Zn alloys. *J. Alloys Compd.* 378, 188–191. doi: 10.1016/j.jallcom.2003.12.052

Miller, V. M., Berman, T. D., Beyerlein, I. J., Jones, J. W., and Pollock, T. M. (2016). Prediction of the plastic anisotropy of magnesium alloys with synthetic textures and implications for the effect of texture on formability. *Mater. Sci. Eng. A* 675, 345–360. doi: 10.1016/j.msea.2016.08.063

Minárik, P., Drozdenko, D., Zemková, M., Veselý, J., Capek, J., Bohlen, J., et al. (2019). Advanced analysis of the deformation mechanisms in extruded magnesium alloys containing neodymium or yttrium. *Mater. Sci. Eng. A* 759, 455–464. doi: 10.1016/j.msea.2019.05.069

Mordike, B. L., and Ebert, T. (2001). Magnesium poperties - applications - potential. *Mater. Sci. Eng. A* 302, 37–45. doi: 10.1016/S0921-5093(00)01351-4

Nascimento, L., Yi, S., Bohlen, J., Fuskova, L., Letzig, D., and Kainer, K. U. (2010). High cycle fatigue behaviour of magnesium alloys. *Procedia Eng.* 2, 743–750. doi: 10.1016/j.proeng.2010.03.080

Nie, J.-F. (2012). Precipitation and hardening in magnesium alloys. *Metall. Mater. Trans.* A 43, 3891–3939. doi: 10.1007/s11661-012-1217-2

Stanford, N. (2010a). The effect of calcium on the texture, microstructure and mechanical properties of extruded Mg–Mn–Ca alloys. *Mater. Sci. Eng. A* 528, 314–322. doi: 10.1016/j.msea.2010.08.097

Stanford, N. (2010b). Micro-alloying Mg with Y, Ce, Gd and La for texture modification—a comparative study. *Mater. Sci. Eng. A* 527, 2669–2677. doi: 10.1016/j.msea.2009.12.036

Stanford, N. (2013). The effect of rare earth elements on the behaviour of magnesium-based alloys: part 2 – recrystallisation and texture development. *Mater. Sci. Eng. A* 565, 469–475. doi: 10.1016/j.msea.2012.10.084

Stanford, N., and Barnett, M. (2008a). Effect of composition on the texture and deformation behaviour of wrought Mg alloys. *Scripta Materialia* 58, 179–182. doi: 10.1016/j.scriptamat.2007.09.054

Stanford, N., and Barnett, M. R. (2008b). The origin of "rare earth" texture development in extruded Mg-based alloys and its effect on tensile ductility. *Mater. Sci. Eng. A* 496, 399–408. doi: 10.1016/j.msea.2008.05.045

Stutz, L., Bohlen, J., Letzig, D., and Kainer, K. U. (2011). "Formability of Magnesium sheet ZE10 and AZ31 with respect to initial texture," in *Magnesium Technology 2011*, eds W. H. Sillekens, S. R. Agnew, N. R. Neelameggham, and S. N. Mathaudhu (Hoboken, NJ: John Wiley & Sons, Inc.), 373–378.

Styczynski, A., Hartig, C., Bohlen, J., and Letzig, D. (2004). Cold rolling textures in AZ31 wrought magnesium alloy. *Scripta Materialia* 50, 943–947. doi: 10.1016/j.scriptamat.2004.01.010

Suh, J., Victoria-Hernandez, J., Letzig, D., Golle, R., Yi, S., Bohlen, J., et al. (2015). Improvement in cold formability of AZ31 magnesium alloy sheets processed by equal channel angular pressing. *J. Mater. Process. Technol.* 217, 286–293. doi: 10.1016/j.jmatprotec.2014.11.029

Victoria-Hernandez, J., Yi, S., Bohlen, J., Kurz, G., and Letzig, D. (2014). The influence of the recrystallization mechanisms and grain growth on the texture of a hot rolled AZ31 sheet during subsequent isochronal annealing. *J. Alloys Compounds* 616, 189–197. doi: 10.1016/j.jallcom.2014.07.083

Wang, H., Wu, P. D., Boyle, K. P., and Neale, K. W. (2011). On crystal plasticity formability analysis for magnesium alloy sheets. *Int. J. Solids Struct.* 48, 1000–1010. doi: 10.1016/j.ijsolstr.2010.12.004

Wang, Q., Jiang, B., Chai, Y., Liu, B., Ma, S., Xu, J., et al. (2016). Tailoring the textures and mechanical properties of AZ31 alloy sheets using asymmetric composite extrusion. *Mater. Sci. Eng. A* 673, 606–615. doi: 10.1016/j.msea.2016.07.111

Wang, W., Ma, L., Chai, S., Zhang, W., and Feng, Y. (2018). Role of one direction strong texture in stretch formability for ZK60 magnesium alloy sheet. *Mater. Sci. Eng. A* 730, 162–167. doi: 10.1016/j.msea.2018.05.113

Yi, S., Brokmeier, H.-G., and Letzig, D. (2010). Microstructural evolution during the annealing of an extruded AZ31 magnesium alloy. *J. Alloys Compounds* 506, 364–371. doi: 10.1016/j.jallcom.2010.07.008

Yi, S., Davies, C. H. J., Brokmeier, H. G., Bolmaro, R. E., Kainer, K. U., and Homeyer, J. (2006). Deformation and texture evolution in AZ31 magnesium alloy during uniaxial loading. *Acta Materialia* 54, 549–562. doi: 10.1016/j.actamat.2005.09.024

Yu, H., Hyuk Park, S., Sun You, B., Min Kim, Y., Shun Yu, H., and Soo Park, S. (2013). Effects of extrusion speed on the microstructure and mechanical properties of ZK60 alloys with and without 1 wt% cerium addition. *Mater. Sci. Eng. A* 583, 25–35. doi: 10.1016/j.msea.2013.06.073

Zeng, X., Minárik, P., Dobron, P., Letzig, D., Kainer, K. U., and Yi, S. (2019). Role of deformation mechanisms and grain growth in microstructure evolution during recrystallization of Mg-Nd based alloys. *Scripta Materialia* 166, 53–57. doi: 10.1016/j.scriptamat.2019.02.045

Zhou, N., Zhang, Z., Dong, J., Jin, L., and Ding, W. (2013). High ductility of a Mg–Y–Ca alloy via extrusion. *Mater. Sci. Eng. A* 560, 103–110. doi: 10.1016/j.msea.2012.09.042

Conflict of Interest: The authors declare that the research was conducted in the absence of any commercial or financial relationships that could be construed as a potential conflict of interest.

frontiers in Materials

ORIGINAL RESEARCH
published: 23 October 2019
doi: 10.3389/fmats.2019.00262

Compressive Creep Behavior of High-Pressure Die-Cast Aluminum-Containing Magnesium Alloys Developed for Elevated Temperature Applications

Sarkis Gavras[1], Suming Zhu[2], Mark A. Easton[2], Mark A. Gibson[3] and Hajo Dieringa[1]*

[1] MagIC – Magnesium Innovation Centre, Institute of Materials Science, Helmholtz-Zentrum Geesthacht, Geesthacht, Germany, [2] School of Engineering, RMIT University, Melbourne, VIC, Australia, [3] CSIRO Manufacturing, Clayton, VIC, Australia

In addition to AZ- and AM-series magnesium alloys, which are mainly used at ambient temperature, there are also die-cast magnesium alloys developed for use at elevated temperatures. This paper examines the compressive creep resistance of several aluminum-containing magnesium high-pressure die-cast alloys, including the commercially available AE42, AE44-2, AE44-4, MRI230D alloys and newly developed DieMag series, i.e., DieMag211, DieMag422, and DieMag633. Compressive creep is the common load case for automotive powertrain components such as transmission housings, engine blocks or oil pans, which are typically mounted with steel or aluminum bolts that have lower thermal expansion than magnesium alloys. When the components heat up, there is a compressive load in the area around the bolt. The compressive creep experiments are accompanied by microstructure investigations. It is shown that MRI230D and the two high-concentrated DieMag alloys have the best creep resistance at 200°C. Similar results are also observed in the tensile tests at room temperature and 150°C, with DieMag633 showing outstanding strength.

Keywords: magnesium alloys, creep, high-pressure die casting, microstructure, density

Edited by:
Carlos Chastre,
Faculty of Sciences and Technology,
New University of Lisbon, Portugal

Reviewed by:
Pavel Lukac,
Charles University, Czechia
Ferdinand Dobeš,
Institute of Physics of Materials
(ASCR), Czechia

***Correspondence:**
Hajo Dieringa
hajo.dieringa@hzg.de

Specialty section:
This article was submitted to
Structural Materials,
a section of the journal
Frontiers in Materials

Received: *24 April 2019*
Accepted: *07 October 2019*
Published: *23 October 2019*

Citation:
Gavras S, Zhu S, Easton MA, Gibson MA and Dieringa H (2019) Compressive Creep Behavior of High-Pressure Die-Cast Aluminum-Containing Magnesium Alloys Developed for Elevated Temperature Applications. Front. Mater. 6:262. doi: 10.3389/fmats.2019.00262

INTRODUCTION

Magnesium alloys are predominantly cast (Avedesian and Baker, 1999). Only a small proportion of the alloys used are formed, e.g., rolled, extruded, or forged. The proportion of magnesium processed in high-pressure die casting (HPDC) is also comparably high compared to other casting processes such as sand-casting or gravity die casting. Magnesium high-pressure die casting alloys therefore account by far for the largest proportion of magnesium materials used. This market is divided between the common room temperature alloys AZ91 and AM50/60 and the creep-resistant alloys that can be used at higher temperatures. With very few exceptions, these alloys contain aluminum as an alloying element to assist with castability. The temperature difference between liquidus and solidus temperatures, and thus the melting range of the aluminum-containing alloys is large, which enables subsequent feeding during HPDC despite the rapid cooling. The disadvantage of an aluminum content of 3–10% is the formation of the β-phase $Mg_{17}Al_{12}$ during solidification. It has a melting point of only 437°C and is therefore responsible for the poor creep resistance of AZ and AM alloys. Since the aluminum is needed during casting, but the β-phase hinders the creep resistance, strategies have been developed to bind the aluminum in intermetallic phases with the help of further alloying elements. These phases should have the highest possible melting points and fine distribution to increase the strength of the alloys (Pekguleryuz and Celikin, 2010). For example, rare earths (AE alloys; Powell et al., 2002; Moreno et al., 2003; Kielbus and Rzychon, 2010; Zhu et al., 2012), silicon (AS alloys; Dargusch et al., 2004; Zhang, 2005; Zhu et al., 2013), strontium (AJ alloys; Kunst et al., 2009; Kielbus and Rzychon, 2010) or calcium (AX alloys, MRI; alloys; Backes et al., 2009; Xu et al., 2009; Jiang et al., 2015) are used.

Some of the creep resistant alloys investigated in this paper are die cast specimens previously investigated by Zhu et al. (2015). The alloys are AE42, AE44-2, AE44-4, and MRI230D. Usually a misch metal consisting of Ce, Nd, La, and Pr is used for the addition of rare earths. The alloy AE44-4 indeed contains these four rare earths as alloying elements. For cost reasons and because of the decreased availability of Nd, there are also variations of this alloy containing only Ce and La. This alloy (AE44-2) is cheaper and is also investigated in this study. These commercial alloys are compared with DieMag alloys, which have an aluminum-barium-calcium proportion of 2:1:1. They differ only in the absolute content of alloying elements and were produced under the same conditions and casting parameters via HPDC (Dieringa et al., 2013).

In contrast to Zhu et al. (2015), the creep tests were not carried out under tensile stress but under compressive stress. This is the loading direction which represents the more common load case for cast light metals. Typically, gearbox housings, pump housings, motor blocks, oil pans, or similar temperature-loaded components are manufactured from the alloys investigated. These components are under compressive stress in the areas where they are bolted together. When heated to operating temperature, the magnesium undergoes expansion with a coefficient of thermal expansion (CTE) of 26–32 $\times$ 10^{-6} K^{-1}. The aluminum or steel screw has a large CTE ($\sim$20–24 $\times$ 10^{-6} K^{-1} or $\sim$10–12 $\times$ 10^{-6} K^{-1}) and this leads to compressive stress in the magnesium component (Cverna, 2002). In the worst case, this can result in the area under the bolt joint experiencing significant creep at an assumed high temperature of 200°C. Additionally, after cooling to room temperature, which is associated with the same greater thermal contraction, the tightness of an oil pan or a gear part is reduced. In this paper the compressive creep resistance of all alloys at 200°C and different stresses between 60 and 100 MPa shall be investigated. These are approximately the maximum temperatures and stresses that outer areas of an engine block must withstand under a bolt load. The determination of the minimum creep rate and threshold stress with which a true stress exponent can be calculated allows for the combination of experimental creep tests with physical metallurgical models to describe the rate-determining deformation mechanisms during creep. The creep tests are accompanied by optical and electron microscopy in combination with an investigation of intermetallic phases to elucidate the mechanism of deformation.

TABLE 1 | Chemical compositions (wt.%) of die-cast alloys in this investigation analyzed by ICP-OES or Arc Sparc OES (Dieringa et al., 2013; Zhu et al., 2015).

Alloy	Al	Ba	Ca	Sr	Sn	Mn	Ce	La	Nd	Pr
AE42	3.45	–	–	–	–	0.31	1.45	0.60	0.41	0.1
AE44-2	3.95	–	–	–	–	0.15	2.82	1.32	–	–
AE44-4	3.73	–	–	–	–	0.30	2.47	1.21	0.51	0.1
MRI230D	6.49	–	2.00	0.43	0.95	0.28	–	–	–	–
DieMag211	2.01	1.01	0.97	–	–	–	–	–	–	–
DieMag422	4.05	1.82	1.79	–	–	–	–	–	–	–
DieMag633	6.54	2.76	2.71	–	–	–	–	–	–	–

MATERIALS AND METHODS

The magnesium alloys AE42, AE44-2, AE44-4, and MRI230D are commercially available. The DieMag alloys were made of pure magnesium, aluminum, barium, and calcium and were then die-cast. The composition of the alloys measured with ICP-OES or Arc Spark OES is summarized in **Table 1**. Specimen material was cast from the individual alloys in a 250 ton TOSHIBA cold chamber die casting machine. During the melting process and the holding time during casting, the molten surface was covered with HFC-134a inert gas in a CO_2 carrier gas. None of the alloys showed burning on the surface.

The castings consist of three cavities containing two "dumb-bell" and one flat test sample, the dimensions of these castings are given by Easton et al. (2008). From the dumb-bell samples, cylinders with a diameter of 6 mm and a length of 15 mm for compressive creep testing were produced by electric discharge machining. The compressive creep tests were performed at a constant temperature of 200°C and constant stresses of 60, 70, 80, 90, and 100 MPa using an ATS Lever Arm Creep Machine. The dumbbell specimens were tested at room temperature and 150°C in tensile tests. A screw-driven Instron 4505 with a 100 kN load cell was used for the tests. A cross-head speed of 5 mm/min and an extensometer with a measuring length of 25 mm were applied. Four tests were carried out for each alloy.

Density measurements according to the Archimedean principle were carried out on all alloys before and after the creep testing using a Sartorius laboratory balance, in which the sample was weighed in air and ethanol. Creep samples were used for the density measurement, both in as-cast condition and after the creep tests. At least eight samples of each alloy were tested.

Optical micrographs for grain size measurement were taken from 3 regions near the centre of each alloy to obtain the average grain sizes. A Leica DM LM optical microscope was used to capture these regions. The grain sizes were measured using the line intercept method on AnalysisPro software. Further investigation of alloy microstructures where performed on a TESCAN Vega3 SEM equipped with an EDXS detector.

RESULTS AND DISCUSSION

Density

The average densities of the alloys in the as-cast condition and after creep testing are shown in **Table 2**. The first column

TABLE 2 | Densities of as-cast and crept materials and grain size measurements of as-cast alloys.

Alloy	Gravity cast	As-cast samples			Crept samples	
	Density [g/cm^3]	Density [g/cm^3]	Porosity [%]	Grain Size [μm]	Density [g/cm^3]	Porosity [%]
AE42	1.797	1.746 ± 0.062	2.84	16.4 (±2.1)	1.763 ± 0.0264	1.89
AE44-2	1.831	1.776 ± 0.0611	3.00	16.8 (±1.7)	1.803 ± 0.0084	1.53
AE44-4	1.840	1.796 ± 0.0267	2.39	16.5 (±2.4)	1.797 ± 0.0311	2.34
MRI230D	1.809	1.745 ± 0.0516	3.54	15.5 (±0.7)	1.775 ± 0.0259	1.88
Diemag211	1.803	1.770 ± 0.0299	1.83	23.7 (±2.9)	1.759 ± 0.0187	2.44
DieMag422	1.815	1.763 ± 0.0154	2.86	24.5 (±1.7)	1.764 ± 0.0131	2.81
DieMag633	1.819	1.792 ± 0.0122	1.48	13.7 (±0.3)	1.801 ± 0.0028	0.99

TABLE 3 | Tensile properties at RT and 150°C.

Alloy	RT			150°C		
	0.2% proof [MPa]	UTS [MPa]	Elongation [%]	0.2% proof [MPa]	UTS [MPa]	Elongation [%]
AE42	121.6 ± 4.7	238.4 ± 10.8	11.8 ± 4.1	95.0 ± 1.8	130.2 ± 2.2	31.1 ± 2.0
AE44-2	127.4 ± 3.4	256.6 ± 1.5	14.2 ± 1.1	101.0 ± 1.5	151.8 ± 0.8	43.6 ± 7.1
AE44-4	129.6 ± 3.1	251.8 ± 3.7	13.2 ± 1.7	105.0 ± 2.4	152.8 ± 1.5	31.8 ± 2.8
MRI230D	179.7 ± 2.9	220.9 ± 8.8	4.1 ± 0.9	140.2 ± 3.3	181.4 ± 5.2	6.3 ± 1.2
DieMag211	140.6 ± 2.3	165.9 ± 14.6	2.5 ± 1.8	111.5 ± 5.2	144.0 ± 7.1	6.8 ± 2.1
DieMag422	172.6 ± 4.5	196.9 ± 6.5	1.4 ± 0.4	142.6 ± 1.2	182.1 ± 3.5	7.6 ± 1.6
DieMag633	202.6 ± 0.7	229.6 ± 5.8	1.6 ± 0.5	160.0 ± 1.5	196.1 ± 2.9	3.2 ± 0.7

contains density measurements from gravity castings for the respective alloys. These values are used for comparison to the density of the same alloys produced via HPDC. The density of the gravity casting samples can be regarded as a pore-free microstructure, since a laminar flow of the melt does not cause any gas inclusions and the solidification was performed without stress. We calculate the porosity as the relative difference of the densities of the materials compared to gravity casting. MRI230D shows the highest porosity with 3.5%. The AE-based alloys follow with 2.4 to 3.0%. Only DieMag211 and DieMag633 achieve porosities of <2% with the lowest value of 1.5% for DieMag633, which is a very low percentage for high-pressure die casting. The same is true for the densities of the crept samples. The pores are compressed during creep, which reduces porosity. It should be noted that DieMag633 stands out with a porosity of only 1%, which is of course also due to the lowest value in the as-cast state.

Tensile Tests

Tensile tests at room temperature and 150°C show a broad range of mechanical performance for the various alloys, as summarized in **Table 3**. At room temperature, the AE42 has the lowest yield strength with only 121.6 MPa, but good tensile strength with almost 240 MPa. The two AE44 variants are slightly higher for both values and differ only slightly to each other, but show the best ductility of all the alloys tested. With almost 180 MPa, the MRI230D has a significantly higher yield strength, but does not show much further strain hardening up to a tensile strength of 220.9 MPa and moderate ductility. The three DieMag alloys show an increasing strength with increasing content of alloying elements. DieMag422 has similar properties to MRI230D, but DieMag633 which has a yield strength of more than 200 MPa exhibits excellent properties, but at the expense of ductility.

At 150°C, AE42 again shows the lowest strength, followed by the two AE44 alloys. The MRI230D is significantly better with a yield strength of 140.2 MPa and a ductility of 6.3%. Again, DieMag422 is in the range of MRI230D and slightly exceeds it. With a yield strength of 160 MPa and a tensile strength of almost 200 MPa, DieMag633 shows the best properties, again at the expense of ductility of only 3.2%.

Compressive Creep

Creep curves of compressive creep tests at 200°C and 60, 70, 80, 90, and 100 MPa are shown in **Figures 1A–E**. **Figures 1F–J** shows the creep rates from **Figures 1A–E**, the creep strain curves. All figures show that the AE42 always has the fastest deformation rate and thus the worst creep properties. The slowest deformation

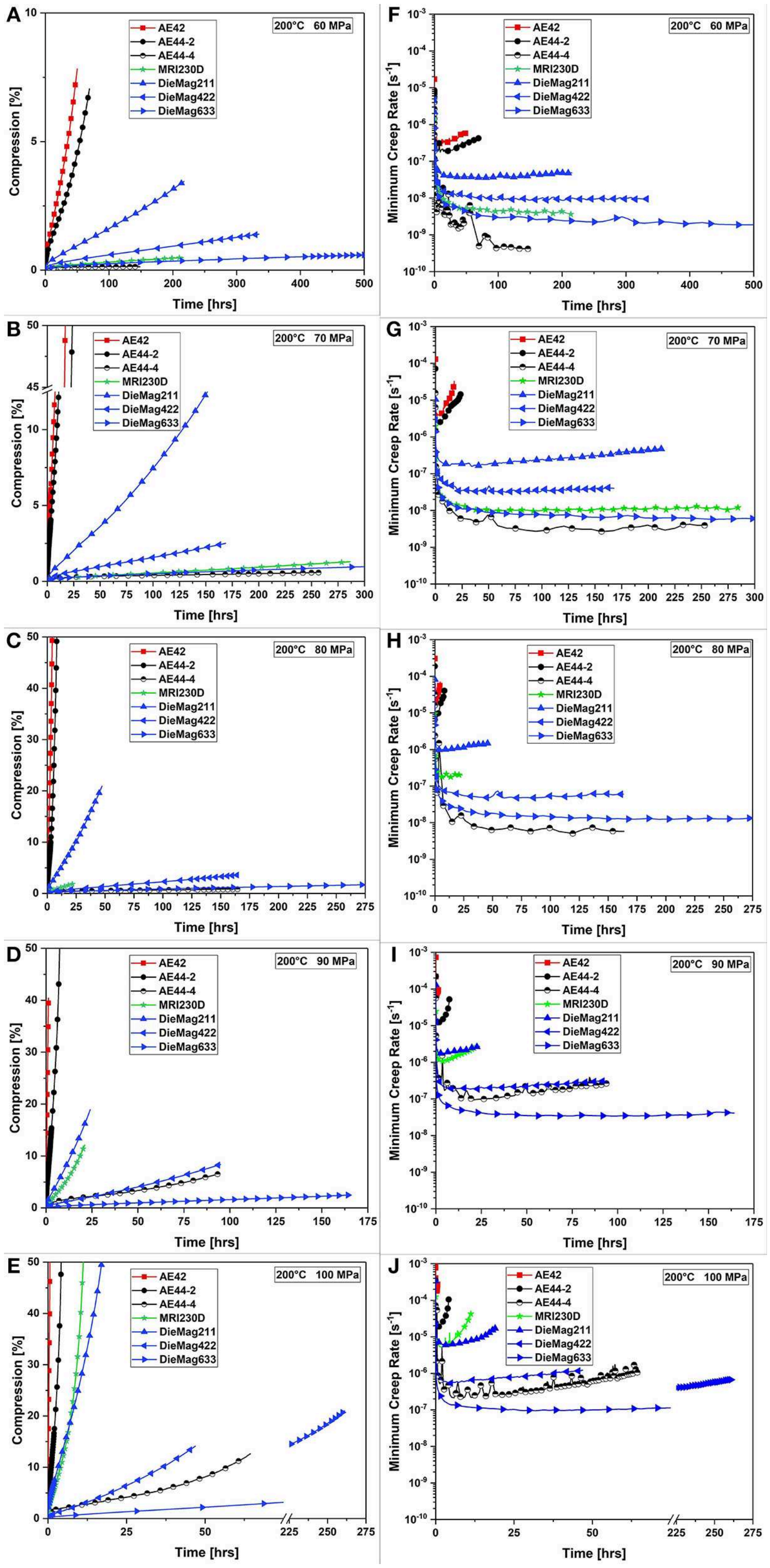

FIGURE 1 | Creep strain curves **(A–E)** and creep rate curves **(F–J)** of creep tests at 200°C and 60–100 MPa applied stress.

is shown by the AE44-4 at low stresses and the DieMag633 at higher stresses.

Equation (1) describes the dependence of the minimum creep rate on the temperature (473.15 K), and the applied stress (60–100 MPa).

$$\dot{\varepsilon}_s = \frac{ADGb}{kT}\left(\frac{\sigma}{G}\right)^n \tag{1}$$

In Equation (1), A is a material dependent constant, b is the Burgers vector, G is the shear modulus, k is the Boltzmann constant, and D is the diffusion coefficient for which Equation (2) applies.

$$D = D_0 e^{\frac{-Q_C}{RT}} \tag{2}$$

In Equation (2), D_0 is the frequency factor, Q_C is the true activation energy for creep, and R is the gas constant. From the curves in **Figures 1F–J**, the minimum creep rates $\dot{\varepsilon}_s$ are extracted and plotted according to the Norton-Arrhenius Equation (1) as plots of the minimum creep rate over the applied stress σ at constant temperature T (**Figure 2A**). It is clear that the AE42 together with the AE44-2 has the worst creep resistance at 200°C. They are followed by DieMag211, MRI230D, and DieMag422, which show lower minimum creep rates in this temperature range. The lowest values of the minimum creep rate and thus the best creep resistance at 200°C at the lower stresses of 60, 70, and 80 MPa was found to be for AE44-4 and at the higher stresses of 90 and 100 MPa was DieMag633.

The stress exponents are between 8 and 15 (**Table 4**). They appear very high according to the values expected to correlate with the rate-determining deformation mechanisms, but such high values are often reported in metal matrix composites or particle- or precipitate-strengthened alloys (Park et al., 1990; Pandey et al., 1992; Gonzalez-Doncel and Sherby, 1993). A stress exponent of $n = 1$ represents diffusion-controlled creep (Harper and Dorn, 1957; Ardell and Lee, 1986), $n = 3$ represents viscous gliding of dislocations (Weertman, 1957a; Sherby and Burke, 1968; Mohamed and Langdon, 1974; Mohamed et al., 1992), $n = 5$ represents dislocation climbing at higher temperatures (Weertman, 1957b; Sherby and Burke, 1968; Mohamed et al., 1992) and $n = 7$ represents dislocation climbing at lower temperatures (Robinson and Sherby, 1969). For these particle- or precipitation-strengthened materials, a threshold stress σ_{thr} was defined, which describes the minimum stress at which creep deformation still occurs at a certain temperature. While the existence of this threshold stress is unquestioned in literature, there are various mechanistic explanations for its origin. A common explanation of the threshold stress σ_{thr} is the existence of an additional stress needed to bend dislocations between the obstacles, the Orowan stress (Orowan, 1954). Another explanation is to associate the threshold stress with the stress needed to disconnect a dislocation from an obstacle (Arzt and Wilkinson, 1986; Arzt and Rösler, 1988). An additional back-stress for climbing over an obstacle is also considered to be the origin of the threshold stress (Arzt and Ashby, 1982).

This threshold stress can be determined by extrapolating the double-logarithmic plot of minimum creep rate over applied stress (**Figure 2A**). According to a method described by Li and Langdon (1997), the stress is extrapolated to a creep rate of 10^{-10} s^{-1}, which corresponds almost to a zero deformation (1% deformation in 3 years) and represents approximately the lowest

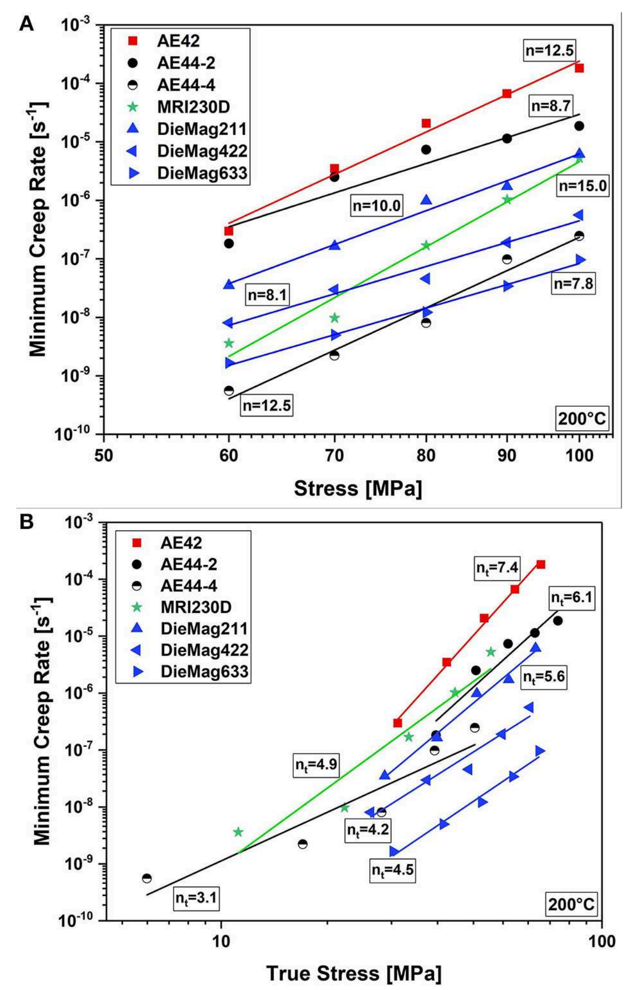

FIGURE 2 | Minimum creep rate over **(A)** stress applied during creep tests at 200°C and **(B)** true stress calculated with concept of threshold stresses at 200°C.

TABLE 4 | Stress exponent n, threshold stress σ_{thr}, and true stress exponent n_t from compressive creep tests at 200°C.

Alloy	Stress exponent n	Threshold stress σ_{thr} [MPa]	True stress exponent n_t
AE42	12.5	30.9	7.4
AE44-2	8.7	23.3	6.1
AE44-4	12.5	53.6	3.1
MRI230D	15.0	48.9	4.9
DieMag211	10.0	33.1	5.6
DieMag422	8.1	35.3	4.2
DieMag633	7.8	31.7	4.5

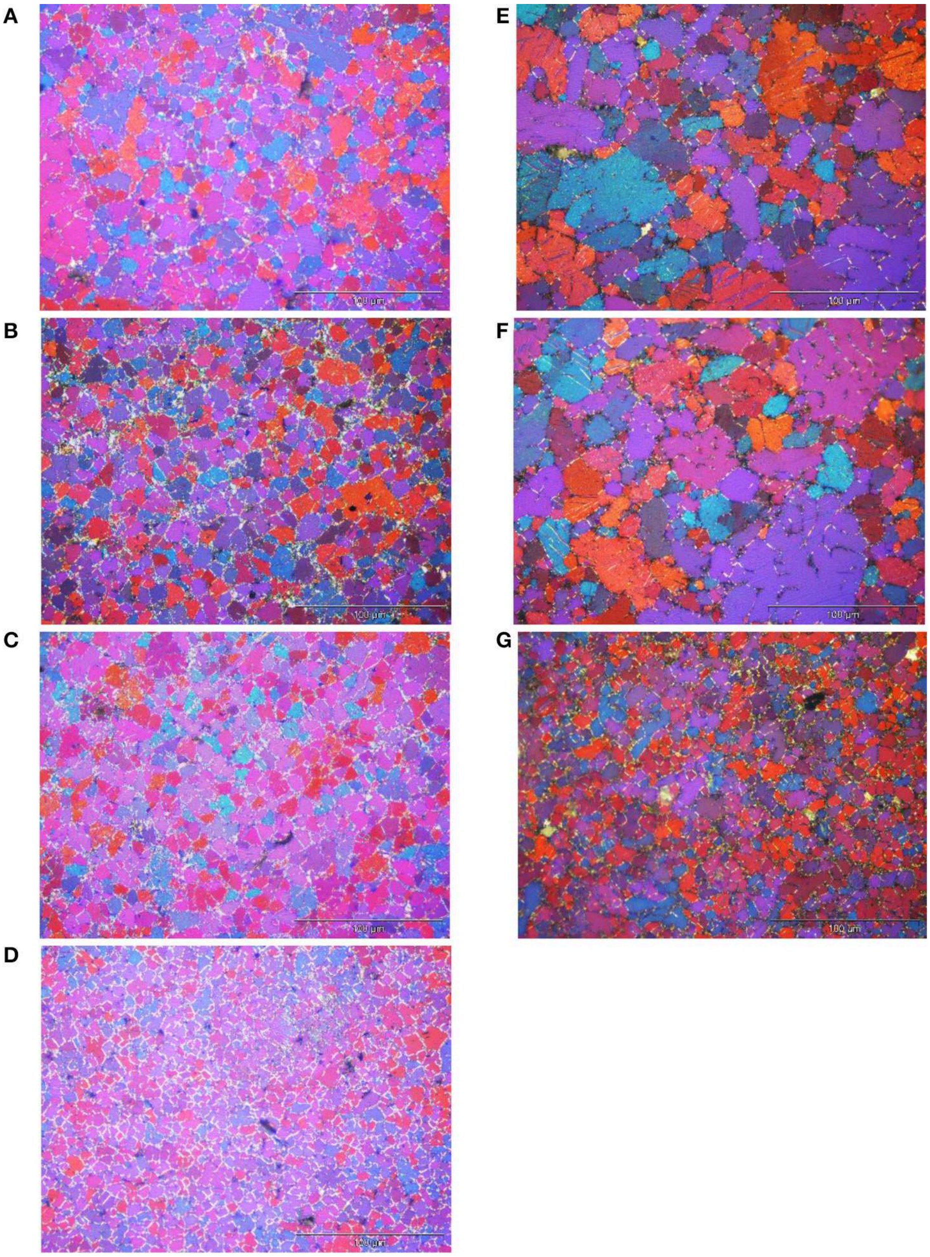

FIGURE 3 | (A–G) Micrographs of as-cast AE42, AE44-2, AE44-4, MRI230D, DieMag211, DieMag422, and DieMag633.

deformation that can be measured in creep tests. This value is the threshold stress σ_{thr} listed in **Table 4** for all alloys. With the introduction of the threshold stress, Equation (1) changes to that shown in (3):

$$\dot{\varepsilon}_s = \frac{ADGb}{kT}\left(\frac{\sigma - \sigma_{thr}}{G}\right)^n \tag{3}$$

If the true stress exponents n_t are calculated, as shown in **Figure 2B**, values between 3.1 and 7.4 are obtained, which is consistent with the rate determining deformation mechanisms during creep deformation. True stress exponents are listed in **Table 4**, as well. A stress exponent of 3.1 for the AE44-4 shows that dislocation gliding is the rate determining deformation mechanism for creep deformation at 200°C. Higher values, as seen in DieMag alloys and the MRI230D, indicate a transition to a higher proportion of dislocation climbing in combination with dislocation glide as the deformation mechanism. For the AE42 and AE44-2, with a stress exponent of 6.1 and 7.4, only dislocation climbing can be determined as the rate determining deformation mechanism.

Microstructure Analysis

The microstructures of the seven die cast alloys are shown in **Figure 3**. The optical micrographs in **Figure 3** are representative

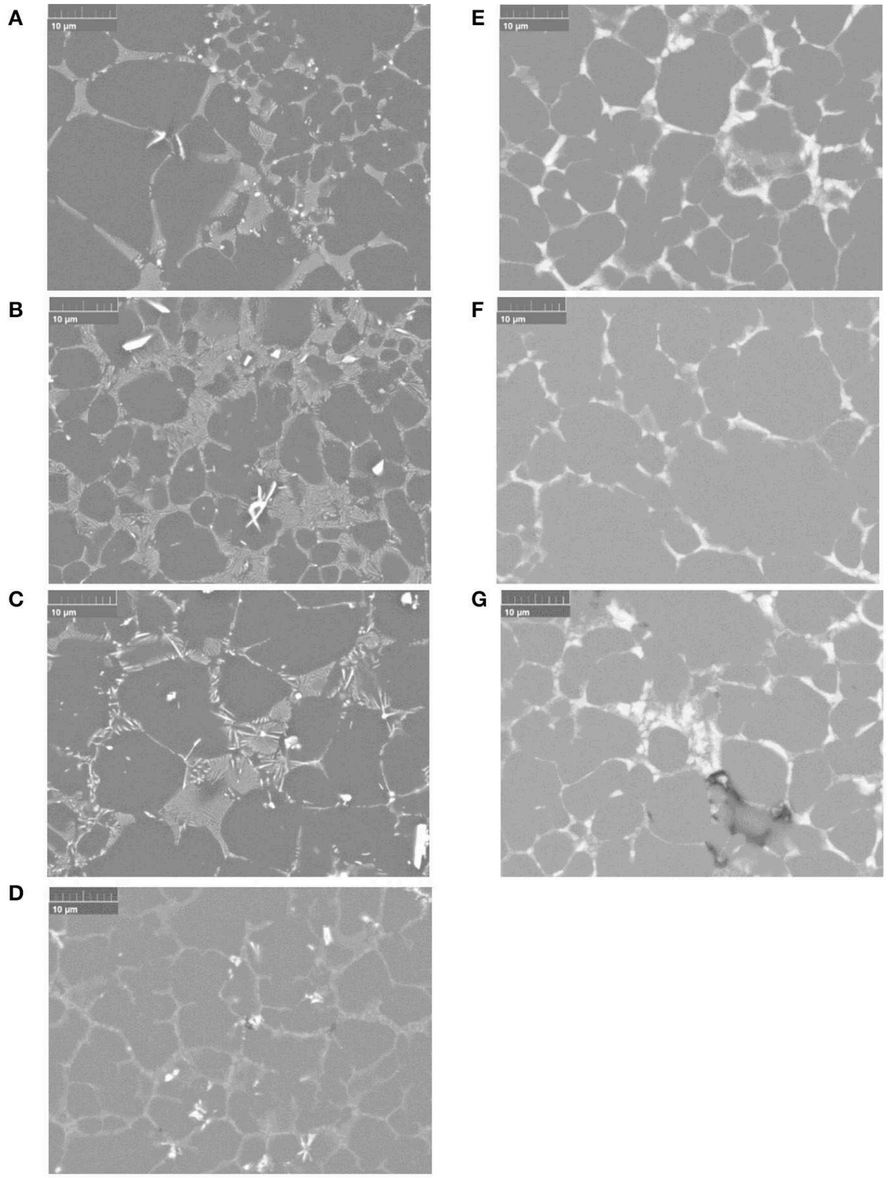

FIGURE 4 | (A–G) SEM BSE micrographs of as-cast AE42, AE44-2, AE44-4, MRI230D, DieMag211, DieMag422, and DieMag633.

of the grain morphology of each alloy. The average grain sizes are shown in **Table 2**.

A more detailed view of the microstructure of the newly developed DieMag alloys and those of the AE and MRI alloys under investigation is presented in **Figures 4A–D**. The variations of the AE alloys (**Figures 4A–C**) all have relatively similar microstructural morphologies, a lamellar eutectic at grain boundaries and a sporadically distributed (near grain boundaries) irregularly shaped intermetallic phase. Powell et al. (2002) showed that the intermetallic phase in the eutectic was $Al_{11}RE_3$ and the irregularly shaped phase was Al_2RE. Zhu et al. (2012) confirmed that the 2 intermetallic phases present in the AE44 alloys were also $Al_{11}RE_3$ and Al_2RE.

MRI230D (**Figure 4D**) has a continuous intermetallic phase and a brighter (as viewed via BSE on SEM) intermetallic phase and irregularly shaped phase present at grain boundaries. The two intermetallic phases present in MRI230D have been shown to be $(Mg,Al)_2Ca$ and CaMgSn (Zhu et al., 2015). The $(Mg,Al)_2Ca$ phase, which was shown to also have, in part, a lamellar-like appearance by Luo et al. (2002), corresponds to the continuous phase in MRI230D. The brighter irregularly shaped phase was shown to be that of CaMgSn (Zhu et al., 2015).

Figures 4E–G shows a relatively consistent morphology between DieMag211, DieMag422, and DieMag633, with exception to grain size in DieMag633. For each DieMag alloy, EDXS measurements were obtained from the intermetallic

TABLE 5 | EDXS point measurements (wt.%) of Al_2Ca or $Mg_{21}Al_3Ba_2$ intermetallic phases in DieMag alloys.

	DieMag211		DieMag422		DieMag633	
	Al_2Ca	$Mg_{21}Al_3Ba_2$	Al_2Ca	$Mg_{21}Al_3Ba_2$	Al_2Ca	$Mg_{21}Al_3Ba_2$
Mg	75.7	68.2	82.5	72.8	71.8	63.3
Al	12.4	12.3	8.1	8.6	15.0	14.7
Ca	8.5	5.6	6.4	5.6	10.1	7.1
Ba	1.6	12.0	0.9	10.7	1.4	12.9
O	1.4	1.7	1.7	1.7	1.4	1.8
Si	0.4	0.1	0.4	0.6	0.2	0.2

phases present. Representative EDXS measurements of each phase in the three DieMag alloys are given in **Table 5**. From these measurements it can be verified that the lamellar phase has little to no Ba, which correlates to the Al_2Ca phase and the white blocky continuous phase has a significant concentration of Ba, which indicates it is the $Mg_{21}Al_3Ba_2$ phase. These results match the investigation by Dieringa et al. (2013), which showed that DieMag422 contained two distinct intermetallic phases, a bulk intermetallic phase with Al_2Ca and a lamellar intermetallic phase with $Mg_{21}Al_3Ba_2$.

CONCLUSIONS

The aluminum-containing, creep-resistant magnesium alloys were successfully produced by high-pressure die casting. None of the alloys showed any noticeable burning. Compressive creep tests at 200°C, metallography, density measurements and tensile tests at RT and 150°C were carried out on the samples in as-cast condition. The following results were obtained:

- The density measurements can be seen as a measure for the die-castability of a magnesium alloy. DieMag211 and DieMag633 have the lowest porosities with only 1.8 and 1.5%, respectively.
- The alloys with the best creep resistance, displaying the lowest minimum creep rate values at 200°C, in combination with low stresses of 60, 70, and 80 MPa was AE44-4 and in combination with the higher stresses of 90 and 100 MPa was DieMag633.
- The mechanical properties at room temperature show varying results. With nearly 180 MPa, the commercial MRI230D had approximately the same yield strength as DieMag422, although its tensile strength is slightly lower. DieMag633 had the highest yield strength at over 200 MPa, and also the highest tensile strength. However, this is at the expense of ductility. It was remarkable to find DieMag633 had a significantly higher yield strength compared to an aluminum alloy A380, which is also used for engine components in automotive engineering. Their yield strength was approximately 165 MPa with a ductility of 3% (Bronfin et al., 2008).
- The mechanical properties at 150°C showed a similar trend. The MRI230D and DieMag422 showed comparably good properties and were only exceeded by DieMag633 with a yield strength and a tensile strength of 160 MPa and ∼200 MPa, respectively. The yield strength was again above that of an aluminum alloy A380, which is approximately 150 MPa (Bronfin et al., 2008).
- Microstructure as well as phase analysis of the creep-resistant magnesium alloys revealed the various intermetallic phases in the high-pressure die cast structure, which were also present in casting processes with lower cooling rates. They help to improve the creep resistance of the alloys by preferentially forming during solidification and thus avoiding the formation of the thermally unstable $Mg_{17}Al_{12}$, which has been shown to be detrimental to elevated temperature creep resistance.

DATA AVAILABILITY STATEMENT

The datasets generated for this study are available on request to the corresponding author.

AUTHOR CONTRIBUTIONS

SG contributed optical and electron microscopy including EDXS measurement. SZ contributed the evaluation of tensile properties. ME contributed alloy casting and coordination of authors. MG contributed alloy casting. HD contributed the density measurements, creep tests and evaluation thereof, idea of the paper, and coordination of authors.

REFERENCES

Ardell, A. J., and Lee, S. S. (1986). A dislocation network theory of Harper-Dorn creep I: steady state creep of monocrystalline Al. *Acta Mater*. 34, 2411–2423. doi: 10.1016/0001-6160(86)90144-6

Arzt, E., and Ashby, M. F. (1982). Threshold stresses in materials containing dispersed particles. *Scripta Metall*. 16, 1285–1290. doi: 10.1016/0036-9748(82)90484-7

Arzt, E., and Rösler, J. (1988). The kinetics of dislocation climb over hard particles-II: effects of an attractive particle-dislocation interaction. *Acta Metall*. 36, 1053–1060. doi: 10.1016/0001-6160(88)90159-9

Arzt, E., and Wilkinson, D. S. (1986). Threshold stresses for dislocation climb over hard particles: the effect of an attractive interaction. *Acta Metall*. 34, 1893–1898. doi: 10.1016/0001-6160(86)90247-6

Avedesian, M. M., and Baker, H. (1999). *ASM Specialty Handbook: Magnesium and Magnesium Alloys*. Materials Park, OH: ASM International.

Backes, B., Durst, K., Amberger, D., and Göken, M. (2009). Particle hardening in creep-resistant Mg-alloy MRI 230D probed by nanoindenting atomic force microscopy. *Metall. Mater. Trans*. 40a, 257–261. doi: 10.1007/s11661-008-9720-1

Bronfin, B., Moscovitch, N., Trostenetsky, V., Gerzberg, G., Nagar, N., and Yehuda, R. (2008). "High performance HPDC alloys as replacements for A380 aluminum alloy," in *Magnesium Technology 2008*, eds M. O. Pekguleryuz, N. R. Neelameggham, R. S. Beals, and E. A. Nyberg (TMS), 411–415.

Cverna, F. (2002). *ASM Handbook: Thermal Properties of Metals. Chapter 2: Thermal Expansion*. Materials Park, OH: ASM International.

Dargusch, M. S., Bowles, A., Pettersen, K., Bakke, P., and Dunlop, G. L. (2004). The effect of silicon content on the microstructure and creep behavior in die-cast magnesium AS alloys. *Metall. Mater. Trans.* 35A, 1905–1909. doi: 10.1007/s11661-004-0099-3

Dieringa, H., Zander, D., and Gibson, M. A. (2013). Creep behaviour under compressive stresses of calcium and barium containing Mg-Al based die casting alloys. *Mater. Sci. Forum* 765, 69–73. doi: 10.4028/www.scientific.net/MSF.765.69

Easton, M., Abbott, T., Nie, J.F., and Savage, G. (2008). "An assessment of high pressure die cast Mg-Zn-Al alloys," in *Magnesium Technology 2008,* eds M. O. Pekguleryuz, N. R. Neelameggham, R. S. Beals, and E. A. Nyberg (Warrendale, PA: TMS), 323–328.

Gonzalez-Doncel, G., and Sherby, O. D. (1993). High temperature creep behavior of metal matrix aluminum-SiC composites. *Acta Metall. Mater*. 41, 2797–2805. doi: 10.1016/0956-7151(93)90094-9

Harper, J., and Dorn, J. E. (1957). Viscous creep of aluminum near its melting temperature. *Acta Metall*. 5, 654–665. doi: 10.1016/0001-6160(57)90112-8

Jiang, Z., Jiang, B., Yang, H., Yang, Q., Dai, J., and Pan, F. (2015). Influence of the Al_2Ca phase on microstructure and mechanical properties of Mg-Al-Ca alloys. *J. Alloys Comp*. 647, 357–363. doi: 10.1016/j.jallcom.2015.06.060

Kielbus, A., and Rzychon, T. (2010). Microstructure and creep properties of AJ62 and AE44 diecasting magnesium alloys. *Mater. Sci. Forum* 638–642, 1546–1551. doi: 10.4028/www.scientific.net/MSF.638-642.1546

Kunst, M., Fischersworring-Bunk, A., L'Esperance, G., Plamondon, P., and Glatzel, U. (2009). Microstructure and dislocation analysis after creep deformation of die-cast Mg–Al–Sr (AJ) alloy. *Mat. Sci. Eng.* A510–511, 387–392. doi: 10.1016/j.msea.2008.07.078

Li, Y., and Langdon, T. G. (1997). A simple procedure for estimating threshold stresses in the creep of metal matrix composites. *Scripta Mater*. 36, 1457–1460. doi: 10.1016/S1359-6462(97)00041-9

Luo, A., Balogh, M. P., and Powell, B. R. (2002). Creep and microstructure of magnesium-aluminum-calcium based alloys. *Metall. Mat. Trans*. 33A, 567–574. doi: 10.1007/s11661-002-0118-1

Mohamed, F. A., and Langdon, T. G. (1974). The transition from dislocation climb to viscous glide in creep of solid solution alloys. *Acta Metall*. 22, 779–788. doi: 10.1016/0001-6160(74)90088-1

Mohamed, F. A., Park, K.-T., and Lavernia, E. J. (1992). Creep behavior of discontinuous SiC-Al composites. *Mater. Sci. Eng.* A150, 21–35. doi: 10.1016/0921-5093(90)90004-M

Moreno, I. P., Nandy, T. K., Jones, J. W., Allison, J. E., and Pollock, T. M. (2003). Microstructural stability and creep of rare-earth containing magnesium alloys. *Scripta Mater.* 48, 1029–1034. doi: 10.1016/S1359-6462(02)00595-X

Orowan, E. (1954). "Dislocations and mechanical properties," in *Dislocations in Metals*, ed M. Cohen (New York, NY: AIME), 69–178.

Pandey, A. B., Mishra, R. S., and Mahayan, Y. R. (1992). Stady state creep behaviour of silicon carbide particulate reinforced aluminium composite. *Acta Metall. Mater*. 40, 2045–2052. doi: 10.1016/0956-7151(92)90190-P

Park, K. T., Lavernia, E. J., and Mohammed, F. A. (1990). High temperature creep of silicon carbide particulate reinforced aluminum. *Acta Metall. Mater*. 38, 2149–2159. doi: 10.1016/0956-7151(90)90082-R

Pekguleryuz, M., and Celikin, M. (2010). Creep resistance in magnesium alloys. *Int. Mater. Rev*. 55, 197–217. doi: 10.1179/095066010X12646898728327

Powell, B. R., Rezhets, V., Balogh, M. P., and Waldo, R. A. (2002). Microstructure and creep behavior in AE42 magnesium die-casting alloy. *JOM* 8, 34–38. doi: 10.1007/BF02711864

Robinson, S. L., and Sherby, O. D. (1969). Mechanical behavior of polycrystalline tungsten at elevated temperature. *Acta Mater*. 17, 109–125. doi: 10.1016/0001-6160(69)90132-1

Sherby, O. D., and Burke, P. M. (1968). Mechanical behavior of crystalline solids at elevated temperature. *Progress Mater. Sci*. 13, 325–389. doi: 10.1016/0079-6425(68)90024-8

Weertman, J. (1957a). Steady-state creep through dislocation climb. *J. Appl. Phys*. 28, 362–364. doi: 10.1063/1.1722747

Weertman, J. (1957b). Steady-state creep of crystals. *J. Appl. Phys*. 28, 1185–1189. doi: 10.1063/1.1722604

Xu, S. W., Matsumoto, N., Yamamoto, K., Kamado, S., Honma, T., and Kojima, Y. (2009). High temperature tensile properties of as-cast Mg–Al–Ca alloys. *Mater. Sci. Eng.* A509, 105–110. doi: 10.1016/j.msea.2009.02.024

Zhang, P. (2005). Creep behavior of the die-cast Mg–Al alloy AS21. *Scr. Mater*. 52, 277–282. doi: 10.1016/j.scriptamat.2004.10.017

Zhu, S., Easton, M., Abbott, T. B., Nie, J.-F., Dargusch, M. S., Hort, N., et al. (2015). Evaluation of magnesium die casting alloys for elevated temperature applications: microstructure, tensile properties, and creep resistance. *Metall. Mater. Trans.* 46A, 3543–3554. doi: 10.1007/s11661-015-2946-9

Zhu, S. M., Easton, M. A., Gibson, M. A., Dargusch, M. S., and Nie, J. F. (2013). Analysis of the creep behaviour of die-cast Mg−3Al−1Si alloy. *Mater. Sci. Eng*. 578, 377–382. doi: 10.1016/j.msea.2013.04.100

Zhu, S. M., Nie, J. F., Gibson, M. A., Easton, M. A., and Bakke, P. (2012). Microstructure and creep behavior of high-pressure die-cast magnesium alloy AE44. *Metall. Mater. Trans*. 43A, 4137–4144. doi: 10.1007/s11661-012-1247-9

Conflict of Interest: The authors declare that the research was conducted in the absence of any commercial or financial relationships that could be construed as a potential conflict of interest.

ORIGINAL RESEARCH
published: 30 October 2019
doi: 10.3389/fmats.2019.00266

Direct Observations of Precursor Short-Range Order Clusters of Solute Atoms in a LPSO-Forming Mg-Zn-Gd Ternary Alloy

D. Egusa [1]***, K. Kawaguchi*** [1] ***and E. Abe*** [1,2]*

[1] *Department of Materials Science and Engineering, University of Tokyo, Tokyo, Japan,* [2] *Research Center for Structural Materials, National Institute for Materials Science, Tsukuba, Japan*

We have investigated short-range order (SRO) clusters of solute atoms in a $Mg_{97}Zn_1Gd_2$ alloy which forms a long-period stacking/order (LPSO) phase, based on aberration-corrected scanning transmission electron microscopy (STEM) observations and first-principles calculations. High-angle annular dark-field (HAADF) STEM provides directly the individual Gd atom positions through significant atomic-number dependent Z-contrast, and their averaged image-processing have immediately shown up the representative SRO-Gd configurations being in favor of the second-nearest networks in the *hcp*-Mg structure. Interestingly, Zn atoms seem to be essentially placed at the particular sites within the SRO-Gd configurations to form $D0_{19}$-like $ZnGd_3$ clusters, a validity of which are verified by STEM image simulations and first-principles calculations. These $D0_{19}$-like $ZnGd_3$ clusters in the *hcp*-Mg matrix are likely to be a precursor sub-structure to the $L1_2$-type Zn_6Gd_8 clusters that are embedded in the local *fcc* layers in the LPSO structure. In fact, we find that these $D0_{19}$-like $ZnGd_3$ clusters seem to form a layered atmosphere prior to the LPSO formation, providing an important clue on how the LPSO phases nucleate and grow.

Keywords: Mg alloys, long-period stacking/order (LPSO) phase, solute clusters, scanning transmission electron microscopy, first-principles calculations

OPEN ACCESS

Edited by:
Hajo Dieringa,
Helmholtz Centre for Materials and Coastal Research (HZG), Germany

Reviewed by:
Chamini Mendis,
Brunel University London, United Kingdom
Mingyi Zheng,
Harbin Institute of Technology, China

****Correspondence:***
E. Abe
abe@material.t.u-tokyo.ac.jp

Specialty section:
This article was submitted to Structural Materials, a section of the journal Frontiers in Materials

Received: *13 August 2019*
Accepted: *14 October 2019*
Published: *30 October 2019*

Citation:
Egusa D, Kawaguchi K and Abe E (2019) Direct Observations of Precursor Short-Range Order Clusters of Solute Atoms in a LPSO-Forming Mg-Zn-Gd Ternary Alloy. Front. Mater. 6:266. doi: 10.3389/fmats.2019.00266

INTRODUCTION

Since Mg has the lowest density among practical metals, it is expected to use for transportation equipment such as aircraft and automobiles for improving their energy efficiency (Egami et al., under review). Owing to a low strength and a poor ductility of Mg, it is practically alloyed with a trace amount of additive elements. Rare earth elements (hereinafter denoted as RE) have been known as one of the effective alloying elements that significantly improve the mechanical properties of Mg alloys (Homma et al., 2009; Nie, 2012; Sandlöbes et al., 2014), which are originated from such as the texture weakening by solute segregations or the age hardening due to fine precipitations of the Mg-RE compounds. However, adding a large amount of RE impairs the lightness of Mg alloys, so many studies have been conducted on alloy designs with a limited amount of RE additions.

In recent years, Mg alloys with a small addition of RE and transition metals (TM) have attracted wide attentions because they exhibit excellent mechanical properties (Kawamura et al., 2001; Itoi et al., 2004; Yamasaki et al., 2005; Honma et al., 2007; Kawamura and Yamasaki, 2007; Hagihara et al., 2010). In these ternary alloys, various kinds of precipitates form depending on the additive elements and the heat-treatment conditions (Honma et al., 2005; Matsushita et al., 2016; Fujita et al., 2018; Gu et al., 2018; Koizumi et al., 2018). In particular, Mg-Zn-RE ternary alloys have been focused as one of the candidates for next-generation lightweight alloys, which indeed show excellent mechanical properties due to the presence of the long period stacking/order (LPSO) phase (Abe et al., 2002, 2011; Kawamura and Yamasaki, 2007; Zhu et al., 2010; Egusa and Abe, 2012; Kim and Kawamura, 2013; Saal and Wolverton, 2014; Egami and Abe, 2015; Yamashita et al., 2019) as a strengthening phase via kink deformation (Kawamura and Yamasaki, 2007; Homma et al., 2009; Shao et al., 2010; Egusa et al., 2013; Yamasaki et al., 2013; Xu et al., 2015; Garcés et al., 2018; Hagihara et al., 2019; Inamura, 2019). The LPSO structures consist of stacking order as well as chemical order with respect to the hexagonal close-packed (*hcp*) Mg structure. A distinctive structural-unit represented by Intrinsic-II type stacking faults (I_2-SF) forms a local face-centered cubic (*fcc*) stacking environment, in which the additive Zn/RE elements are commonly distributed (Abe et al., 2002, 2011). The solute-enriched I_2-SF (SESF: solute-enriched stacking fault) is a basic-unit of the LPSO phases, and the isolated SESFs can be distributed randomly in the *hcp*-Mg matrix (Yamasaki et al., 2007; Nie et al., 2008; Egami et al., under review). In addition, further analysis on the LPSO structure showed that Zn and RE are ordered to form the $L1_2$-type cluster embedded within the *fcc*-SESF (Yokobayashi et al., 2011; Egusa and Abe, 2012; Ma et al., 2013; Saal and Wolverton, 2014; Okuda et al., 2015; Hosokawa et al., 2018; Nishioka et al., 2018), which indeed plays an important role for increasing thermodynamic stability of the SESF (Egami et al., under review).

It is known that these Mg-Zn-RE systems are classified into Type I (RE = Y, Dy, Ho, Er, Tm) and Type II (RE = Gd, Tb) according to formation of the LPSO phase during solidifications or aging processes (Kawamura and Yamasaki, 2007). Mg-Zn-Gd alloys, classified into Type II, precipitate the LPSO phase during an isothermal annealing, whose behaviors were experimentally summarized as a time-temperature-transformation (TTT) diagram (Yamasaki et al., 2007). Solute-enriched platelet zones (Guinier-Preston like zone) are formed at relatively low temperatures ($< \sim$500 K) (Nishijima et al., 2008; Saito et al., 2011; Koizumi et al., 2018). On the other hand, the LPSO phase and SESFs are formed in the α-Mg matrix at relatively high temperature (Jono et al., 2013; Gröbner et al., 2015). It should be noted here that Zn is essential for the formation of these various precipitates/zones, which have never been available for the Mg-Gd binary alloys (He et al., 2006; Nishijima and Hiraga, 2007).

Clustering of solute elements and the introduction of the I_2-SF are essential events for formation of the LPSO structure. Recent studies have suggested two possible formation processes of the LPSO structures; one driven by the introduction of the I_2-SF, and the other driven by spinodal-like phase separation which involves clustering of solute atoms (Yamamoto et al., 2013; Umebayashi et al., 2014; Okuda et al., 2015, 2017; Egami et al., under review). Okuda et al. investigated precipitation processes of the LPSO phase from the amorphous Mg-Zn-RE alloys in the quenched ribbon sample by *in-situ* synchrotron X-ray observations (Okuda et al., 2017). They reported that there is a short-range order (SRO) of solute element at the initial stage of the LPSO phase formation, whose sizes are corresponding to about a solute dimer in the amorphous state, and they grow in the crystalline *hcp*-Mg state. Photoemission spectroscopy investigations also supported formation of the solute SRO clusters at the initial stage of the LPSO phase formation, suggesting that the SRO is a precursor phenomenon to form the $L1_2$-type clusters (Hosokawa et al., 2018). Such precursor phenomenon significantly affects on the thermodynamics of the LPSO phase formation; however, the detailed structures and spatial distributions of such SRO clusters are not clarified yet. In the present study, we investigate the precursor SRO clusters in the *hcp*-matrix of a Mg-Zn-Gd alloy based on direct observations using advanced electron microscopy, and discuss their detailed structures and spatial distributions in terms of the LPSO phase formation.

MATERIALS AND METHODS

A nominal composition of the alloy used in the present study was $Mg_{97}Zn_1Gd_2$ (at. %). Master alloy ingots were prepared by high frequency induction melting of pure metals in an argon atmosphere. In order to control ordering and distributions of the SESF, the alloy ingots were solution treated at 793 K for 2 h, followed by water quench, and then annealed at 573 K for 10 h (Yamasaki et al., 2007). All the heat treatments were performed using a Pyrex tube in an argon atmosphere after evacuation to pressures lower than 3×10^{-3} Pa. Microstructures of the samples were observed by scanning electron microscopy (SEM, JEM-7900F) using backscattering electron (BSE) detector at the accelerating voltage of 15 kV. For atomic-resolution high-angle annular dark-field (HAADF)-scanning transmission electron microscopy (STEM) observations, we used an aberration-corrected 200 kV STEM (JEM-ARM200F) that provides a minimum probe of ∼0.8 Å with a convergence semi-angle of 22 mrad. For HAADF imaging, the annular detector was set to collect the electrons scattered at angles higher than 90 mrad, which is sufficiently high to reveal a chemical sensitive Z-contrast. Thin foils for STEM observations were prepared by standard Ar-ion milling. Image simulations were carried out using the xHREM software based on the fast-Fourier-transform multi-slice algorithm (Ishizuka, 2002). First-principles calculations were performed to evaluate formation energies of the *hcp*-Mg crystals containing solute atoms. The super cell size for calculations was $5 \times 5 \times 4$ with respect to the primitive *hcp*-Mg structure, containing 200 atoms. Structural optimizations were performed by using the Vienna Ab initio Simulation Package (VASP) code within the framework of density-functional theory (Kresse and Furthmüller, 1996), based on generalized gradient approximation (Perdew et al., 1992), and ultrasoft scalar relativistic pseudo-potentials (detailed conditions for calculations are described in the **Figure 4** captions).

RESULTS

Figure 1a shows a SEM-BSE image obtained from a heat-treated $Mg_{97}Zn_1Gd_2$ alloy. Bright-contrast regions in the image

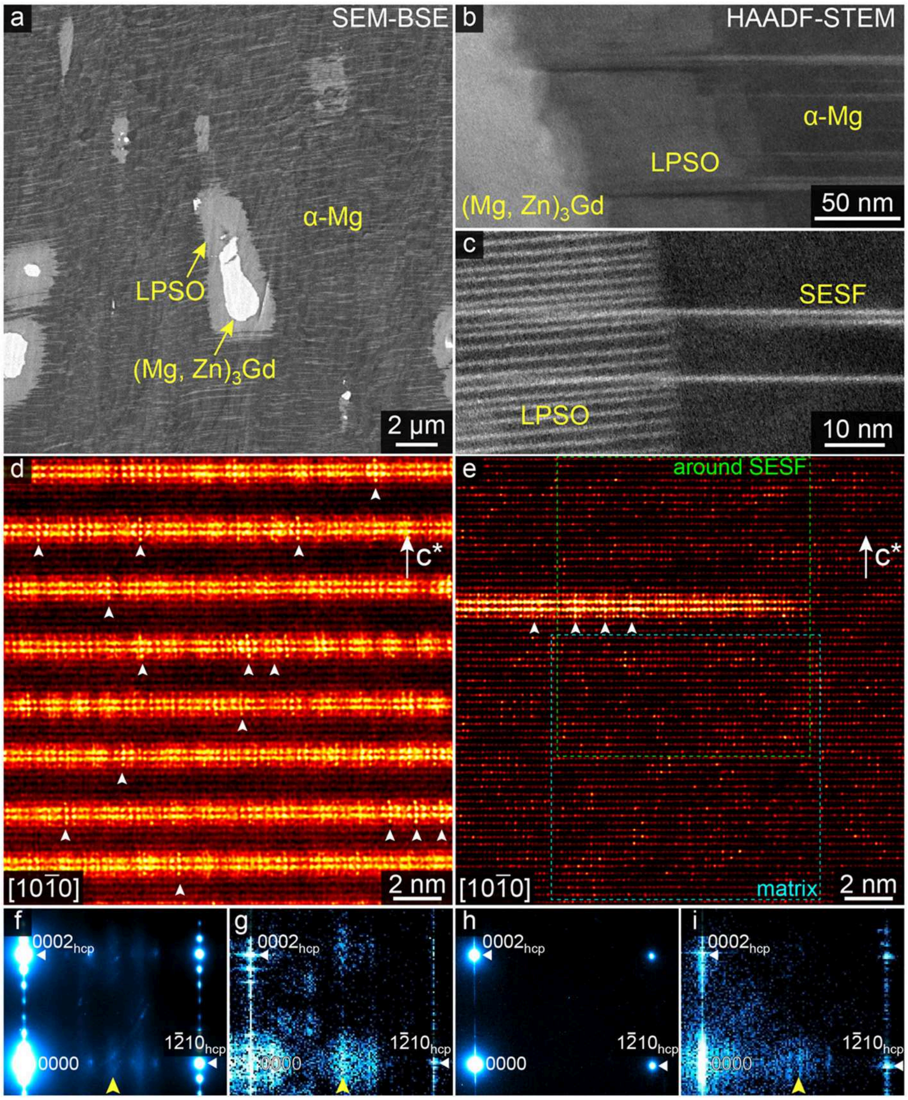

FIGURE 1 | (a) SEM-BSE image taken from a heat-treated $Mg_{97}Zn_1Gd_2$ alloy. **(b,c)** HAADF-STEM images of the multiple-phase coexisting regions of the $(Mg,Zn)_3Gd$ compound, the LPSO phase and the α-Mg phase with essential SESFs. **(d,e)** Atomic-resolution HAADF-STEM images of the 14H-type LPSO phase and the α-Mg matrix along the $[10\bar{1}0]_{hcp}$ directions, respectively. c* denotes the *c*-axis of the matrix crystals. Blue and green dotted rectangles in **(e)** correspond to the enlarged areas shown in **Figures 3a**, **7a**, respectively. **(f)** EDP and **(g)** PS calculated from the LPSO phase images of **(d)**, and **(h,i)** represent those for the α-Mg matrix image of **(e)** in the same manner, respectively. The indices of the major reflections in EDPs and PSs are given based on the *hcp*-Mg structure.

correspond to the $(Mg,Zn)_3Gd$ compound and the LPSO phase, as denoted in the image. The $(Mg,Zn)_3Gd$ compound does not fully dissolve and remains even after the solution-treatment (Jono et al., 2013). The $(Mg,Zn)_3Gd$ compounds are surrounded by the LPSO phases, suggesting that the LPSO phase has formed from the Zn/Gd-rich compound during the heat-treatment. In addition, a large number of thin bright lines in the α-Mg matrix can be seen clearly, which correspond to the SESF and/or very fine platelet LPSO precipitates. **Figure 1b** shows a HAADF-STEM image obtained around the $(Mg,Zn)_3Gd$ compound and the LPSO phase. The LPSO phase is continuously formed from the $(Mg,Zn)_3Gd$ compound, and the SESFs are grown from the edge of the LPSO phase, as clearly seen in **Figure 1c**. We below investigate details of solute arrangements in the α-Mg matrix.

Figures 1d,e show HAADF-STEM images of the 14H-type LPSO phase and the α-Mg matrix, taken along the $[10\bar{1}0]_{hcp}$ directions. The corresponding electron diffraction patterns (EDP) and the power spectra (PS) of the images of **Figures 1d,e** are shown in **Figures 1f–i**, respectively. HAADF imaging provides a significant atomic-number dependent contrast, so that bright dots in the images represent the Zn and/or Gd enriched atomic columns. White arrowheads in the LPSO structure image of **Figure 1d** indicate characteristic bright-dot configurations representing the $L1_2$-type Zn_6Gd_8 clusters, which are successfully

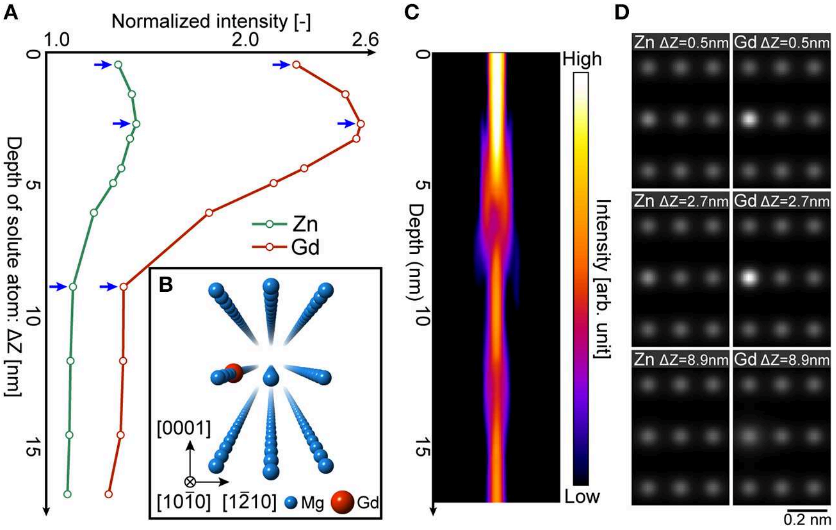

FIGURE 2 | (A) Simulated HAADF-intensity profiles of the Mg atomic columns containing single solute atom, showing solute depth-position dependent change; green and red profiles for Zn and Gd, respectively. The simulations are performed for the *hcp*-Mg crystal projected along $[10\bar{1}0]_{hcp}$, the model of which is schematically drawn in **(B)**, where the single Zn or Gd atom is placed at the left-middle column with a certain depth position. Simulation conditions are; spherical aberration coefficient Cs = 0 mm, specimen thickness = 16.8 nm, defocus = 0 nm, beam-convergent semi-angle α = 22 mrad. **(C)** Incident electron-beam propagation along the $[10\bar{1}0]_{hcp}$ direction of the *hcp*-Mg crystal, calculated with the above conditions. **(D)** Representative simulated HAADF images for the different solute Zn/Gd depth positions, each of which corresponds to the depth at those indicated by arrows in **(A)**.

imaged in the $[10\bar{1}0]_{hcp}$ projection. The $L1_2$- Zn_6Gd_8 clusters can be arrayed in an ordered manner within the SESF (i.e., in-plane order) due to inter-cluster interactions (Kimizuka et al., 2014; Yamasaki et al., 2014; Yamashita et al., 2019). For the present LPSO phase, the number of weak peaks between 0000 and $1\bar{2}10$ reflections in the EDP (**Figure 1f**) indicates 6 × $(1\bar{2}10)$ order in average. In addition, note that weak diffuse peak appears in the corresponding PS (**Figure 1g**) as indicated by the arrowhead, representing the Zn/Gd SRO due to presence of the $L1_2$-type clusters. The diffuse peak is not obvious in the EDP but significantly enhanced in the PS, since the latter has been reconstructed from the HAADF image whose information is highly weighted to heavy-atom configurations (i.e., highly sensitive to the SRO structures composed of heavy atoms).

By looking the image of **Figure 1e**, there also appears the characteristic $L1_2$-type SRO contrast within the SESF such as indicated by arrowheads, suggesting the $L1_2$-type cluster formation even in the isolated SESF (Egami et al., under review). Note that there are no significant peaks between 0000 and $1\bar{2}10$ in the DP (**Figure 1h**), but there indeed appears a diffuse peak in the PS (**Figure 1i**), as indicated by the arrowhead. This is again due to a significant atomic-number weighted Z-contrast of the HAADF imaging, which is able to enhance largely the hidden heavy-atom structures if any. Therefore, the solute SRO cluster formation can be highly anticipated within the α-Mg matrix, details of which will be discussed later.

In order to clarify the solute SRO structures, we first attempt simulations on how the single Zn/Gd atoms in the α-Mg matrix are imaged by an aberration-corrected HAADF-STEM. **Figure 2A** shows simulated HAADF-intensity profiles constructed by varying a depth position of the single solute atom in the atomic column, as schematically drawn in **Figure 2B**. Simulations are performed for the *hcp*-Mg crystal projected along the $[10\bar{1}0]_{hcp}$, and the specimen thickness is set to be 16.8 nm based on electron-energy-loss spectroscopy (EELS) log-ratio measurements (Malis et al., 1988). The image intensity is normalized with respect to that of the pure Mg atomic column. Both for the Zn and Gd atoms, the intensity profiles show the highest values when the solute atom is located at the depth of 2.7 nm from the surface, and the intensity becomes almost constant when the solute atoms are located beyond the depth of 8.9 nm. **Figure 2C** shows the focused electron-beam channeling behaviors propagated along the $[10\bar{1}0]_{hcp}$ direction in the *hcp*-Mg crystal. Due to dynamical diffraction effects with a wide convergence angle of the modern aberration-corrected STEM, the beam intensity exhibits a certain maximum at a few nanometers below the surface and oscillates along the propagating direction (Mittal and Mkhoyan, 2011). By comparing the intensity profiles (**Figure 2A**) and the beam propagations (**Figure 2C**), it immediately turns out that the column intensities show their maxima when the solute atoms are placed at the depth position relevant to the beam-flux maximum. Therefore, the column-intensity variations in the *hcp*-Mg matrix (e.g., see **Figure 1d**) are governed by the individual solute atoms placed at a certain depth range. **Figure 2D** shows the representative simulated images with the solute atoms placed at 0.5, 2.7, and 8.9 nm in depth positions, respectively, which correspond to those indicated by blue arrows in **Figure 2A**. Again, the column intensities are sufficiently strong when the solute atoms are located at the depth near the surface, and become hardly distinguishable when the solute atoms are at the deeper positions. Since the composition of the present

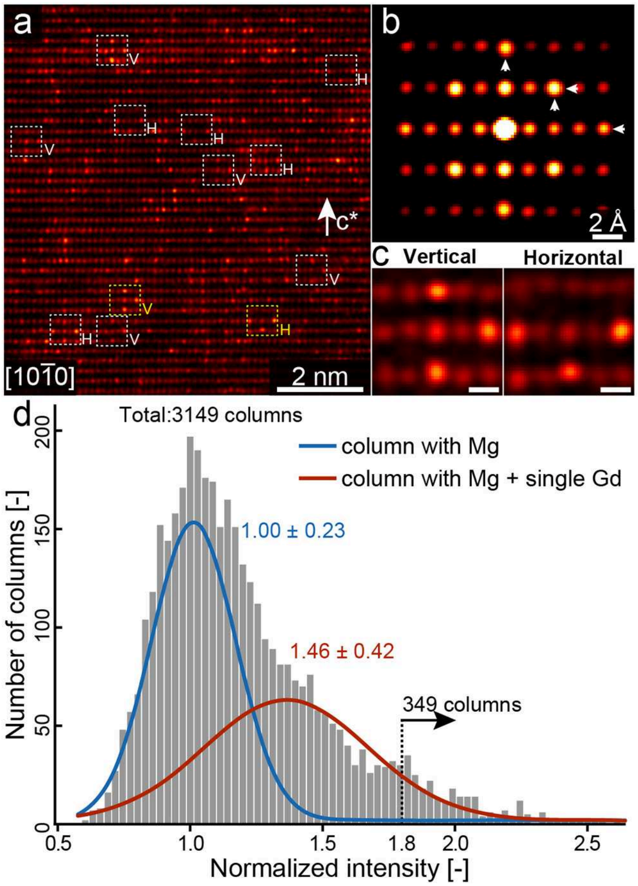

FIGURE 3 | (a) Enlarged HAADF-STEM image of the blue-box region in **Figure 1d**. c* denotes the *c*-axis of the matrix *hcp* crystal. **(b)** Auto-correlation pattern obtained from the image of **(a)**. **(c)** Representative local STEM images showing characteristic bright-dot arrangements, which are enlargements of those indicated by yellow dashed squares in **(a)**, being with scale bars of 2 Å. By using yellow-square regions as the references, the similar contrast regions indicated by white dashed squares have been selected according to cross-correlation evaluations. Details are described in the text. **(d)** Intensity distributions of the atomic columns in the image of **(a)**. Total number of the columns measured is 3,149. Blue and red lines represent gauss-fitting results; mean values, and standard deviations for each fitted-profile are 1.00 ± 0.23 and 1.46 ± 0.42, respectively.

hcp-Mg matrix is sufficiently dilute (Mg-0.3at.%Zn-0.8at.%Gd by SEM-EDS analysis), we assume that there is almost no plurality of solute atoms in the same atomic column for a thin specimen (~17.0 nm for the present case), leading that the column intensities higher than 1.8 are likely to represent the single Gd atoms in the *hcp*-Mg matrix (i.e., individual single Gd atoms placed at the depth up to 6.1 nm are detected in the experiment).

Figure 3a shows a HAADF-STEM image obtained from the α-Mg matrix at the position indicated by the dotted blue-rectangle in **Figure 1e**. Intensity variations at each of the columns in the image directly represent the distribution of individual solute atoms, as governed mostly by Gd atoms. **Figure 3b** shows an auto-correlation pattern constructed from **Figure 3a**, reflecting the spatial correlation of the bright dots in the STEM image. The strong spots indicated by white arrowheads suggest directly the SRO correlations by the solute atoms, corresponding to the second- and/or third-nearest neighbor atomic sites projected along $[1\bar{2}10]$ direction. Note that there are some characteristic configurations of the bright dots, such as indicated by the dotted rectangles in **Figure 3a** (see the figure caption for the yellow/white representations). **Figure 3c** exemplifies the two typical configurations, denoted as "vertical" and "horizontal," whose details will be discussed later. In order to evaluate the column-intensity distributions, we have extracted the intensity of the individual atomic columns and applied gaussian fitting. **Figure 3d** shows the intensity distribution measured from 3,149 atomic columns in the α-Mg matrix image. As demonstrated in **Figure 2A**, the normalized intensity of the Zn-containing column appears about 1.2 at the highest, suggesting that Zn distributions can hardly be distinguished solely by HAADF intensity. Therefore, the intensity distributions are supposed to be two groups, i.e., the most columns are with pure Mg and containing single Gd atom. The red and blue profiles in **Figure 3d** correspond to the gaussian-fitted results of the column intensity distributions, respectively. Based on the fitted result with the reasonably high R-square value of 0.987, the average intensity of the columns containing single Gd atom is estimated as 1.46 with respect to the pure Mg columns, the value of which fairly matches to the image simulations (**Figure 2**). According to the above analysis, the number of columns with the intensity higher than 1.8 turns out to be 349, which is about 11% for the total number of the measured atomic columns (3,149). The intensity level of 1.8 is relevant to the single Gd atom located up to the depth of 6.1 nm from the surface; i.e., single Gd atom per 10 Mg atoms can be roughly estimated based on the *hcp*-Mg crystal in the $[10\bar{1}0]_{hcp}$ projection (see **Figure 2**). Therefore, the solute Gd fraction in the α-Mg matrix is derived as being about 1.1at.% (11%/10), which is not largely deviated from the estimated matrix composition (0.8at.%Gd by SEM-EDS analysis) and hence support the validity of imaging individual Gd atoms.

DISCUSSION

Presence of the SRO clusters is directly indicated by STEM observations, as shown in **Figure 3c**. Here, we investigate possible SRO structures by comparing formation energies of various Gd atom arrangements using first-principles calculations. **Figure 4A** shows a model for placing two Gd atoms in the *hcp*-Mg structure. Position of the first Gd atom is fixed at the center of the polyhedron represented by orange planes, and the second Gd atom is placed at the positions denoted by capital letters from A to H. **Figure 4B** shows the calculated formation energies for the two Gd atom configurations. Energy base-line is set to the one calculated when the Gd atoms are sufficiently separated (apart more than 1 nm) and hence their interactions can be sufficiently negligible. The lowest formation energy is obtained when the second Gd atom is placed at the C site, whose configuration is inserted in **Figure 4B**. Two Gd and four Mg are located at the octahedral sites, and the Gd-Gd configuration corresponds to the

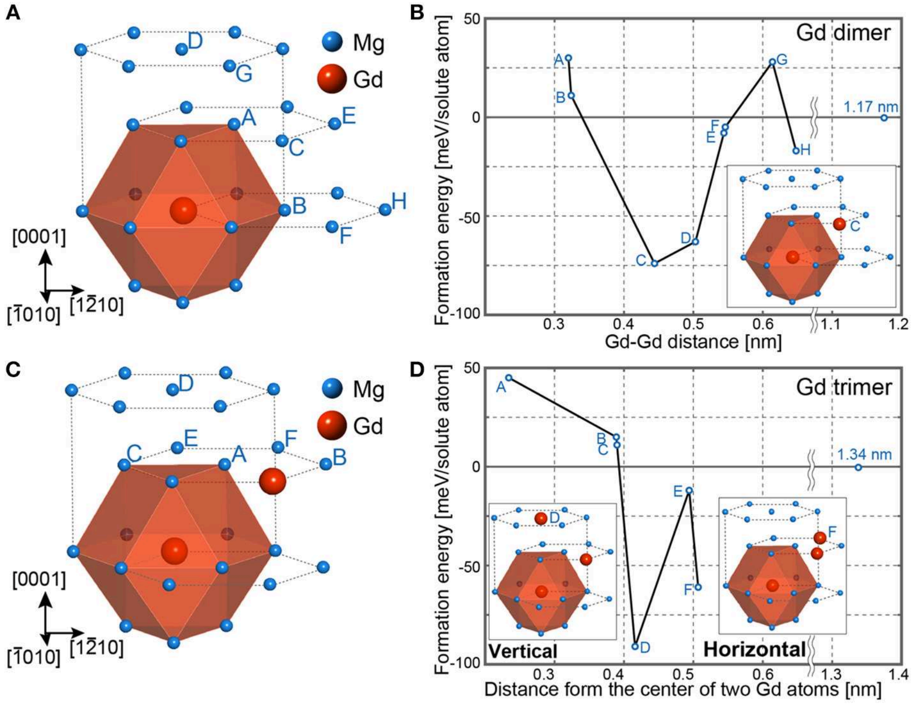

FIGURE 4 | First-principles calculations of the Gd **(A,B)** dimer and **(C,D)** trimer embedded in the *hcp*-Mg structure. Calculations were made with a *hcp*-base 5 × 5 × 4 supercell containing 200 atoms. Atom positions used for the second and the third Gd atoms are denoted by capital letters in **(A,C)**, respectively. Calculated formation energies of the Gd **(B)** dimer and **(D)** trimer at the each position in **(A,C)**, respectively. For the both cases, representative energy-minimized Gd configurations are inserted. For computations, the cut-off energy is chosen as 350 eV, with a 3 × 3 × 3 k-mesh. Calculations are performed by non-fixed conditions both for atomic positions and a unit-cell volume.

second-nearest neighbor in the *hcp*-Mg structure. Note that the second-nearest neighbor RE arrangements represents a partial structure of a $D0_{19}$-type order, which is commonly observed in various Mg-RE compounds (Nie, 2012). We termed the pair of these Gd configurations as "dimer" hereafter. In fact, dimer RE configurations appear to be frequent in the observed STEM image (**Figure 3**); though, further extended SRO configurations, such as indicated in **Figure 3c**, turn out to be also prominent in the present alloy.

Figure 4C shows a model for placing triple Gd atoms in the *hcp*-Mg structure, in which two Gd atoms are already fixed at the stable dimer environments, and the third Gd is placed at the positions denoted from A to F. **Figure 4D** shows calculated formation energies of the models. The energy-base is also set when the Gd atoms are sufficiently separated (more than 1 nm) in the super cell. There are two positions that give local minima for the formation energy, D and F, whose Gd arrangements are inserted in **Figure 4D**. We termed these Gd configurations as "vertical trimer (T_V)" and "horizontal trimer (T_H)" for the models with the third Gd atom at the D and F sites, respectively (note that the "D" site already appears as an energetically favorable position during dimer considerations; namely, the simultaneous Gd atoms both at the C and D sites in **Figure 4B** provide the Tv configuration). For the both trimers, the third Gd atom to the dimer is placed at the second-nearest neighbor to the other Gd atoms. It should be noted here that the Gd configurations in T_V and T_H are relevant to the bright-dot arrangements those frequently observed in **Figure 3a**, as indicated by dashed squares denoted with V and H, respectively. Also, the bright-dot appearances in the auto-correlation pattern (**Figure 3b**) can be explained by these two types of the Gd trimer, T_V and T_H, supporting that these trimer configurations are representative solute-atom SRO clusters in the α-Mg matrix. For the present Mg-Zn-Gd ternary alloys, it is anticipated that the T_V/T_H SRO clusters intrinsically accompany the Zn atoms, and hence we further examine the possible Zn positions that are energetically favored within the Gd trimmers.

Figure 5A shows the models placing a single Zn atom within the Gd trimer structures (T_V and T_H), and the formation energies calculated for each of the Zn positions are summarized in **Figure 5B**. For the both T_V and T_H, the Zn at the A sites appear to be the lowest formation energies with a significant energy gain about 398 and 447 meV/cell, respectively. Note that the Zn at the A sites show the energy differences larger than 100 meV/cell even compared with the next energetically-favored B sites, indicating that the Zn atoms at the A sites significantly stabilize the T_V/T_H structures. Hereafter, we denote these T_V/T_H SRO configurations of Zn/Gd atoms as a $D0_{19}$-like $ZnGd_3$ cluster. It should be noted that the atomic positions in the $ZnGd_3$ cluster are relaxed from the ideal *hcp*-Mg structure; average Gd-Gd interatomic distances in the T_V- and T_H-$ZnGd_3$ clusters are estimated to be 4.40 and 4.46 Å, respectively, which are smaller than the relevant distance

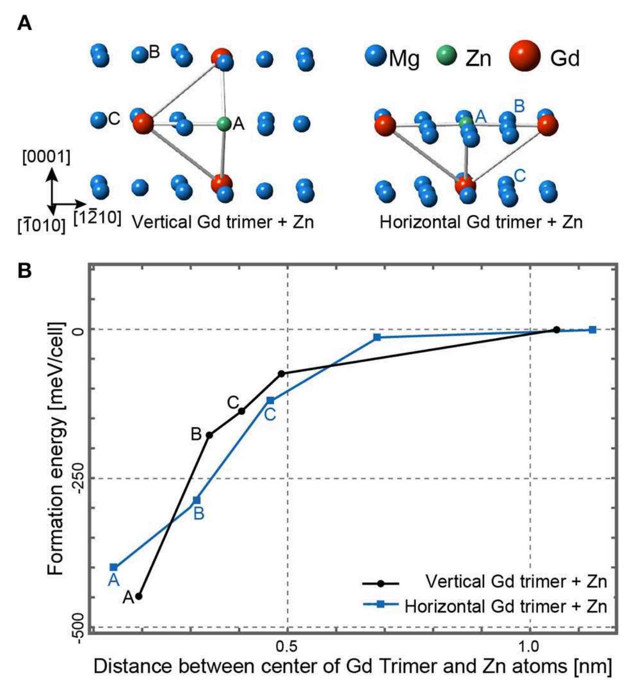

FIGURE 5 | (A) First-principles calculations of a single Zn atom effect for the Gd trimmers, $T_{V,}$ and T_H, embedded in the *hcp*-Mg structure. Calculations were made with a *hcp*-base 5 × 5 × 4 supercell containing 200 atoms. Atom positions used for the Zn atoms are denoted by (left) black and (right) blue capital letters, respectively. **(B)** Calculated formation energies of the Zn-containing Gd trimmers, black and blue lines correspond to T_V and T_H, respectively. The capital letters represent the Zn positions in accordance with **(A)**. The origin of the formation energy is set to the one when the Zn atom is placed sufficiently far from the Gd-timer centers in the super cell. Conditions for the computations are the same as those described in **Figure 4**.

of 4.50 Å in the ideal *hcp*-Mg structure. It is worth mentioning here that, for the LPSO phase, the Gd-Gd interatomic distance in the L1$_2$-type Zn$_6$Gd$_8$ cluster becomes 3.93 Å, being significantly shorter than that of the present ZnGd$_3$ clusters. This is perhaps originated from the strong condensations between the Zn/Gd atoms, causing significant relaxations whose displacements are likely to depend on a total number of the constituent solute atoms in the clusters.

The presence of the D0$_{19}$-like ZnGd$_3$ clusters can be verified from the local intensity analysis of the HAADF-STEM images. **Figure 6A** shows the experimental and the simulated images of the T_V-ZnGd$_3$ SRO clusters. The experimental image is an averaged one that has been reconstructed by searching automatically the similar T_V-SRO contrast regions over the image (**Figure 3a**), according to the cross-correlation evaluation of the local contrast variations; e.g., as shown in **Figure 3a**, given yellow-square regions as the references, the similar contrast regions of white dashed squares have been selected (*template-matching*, see for details the supplement in Egami and Abe, 2015). Note that the T_V-SRO cluster has three variants and differently appear in the <1$\bar{2}$10> projections, and hence the extracted image of **Figure 6A** represents one of the variants. The image simulations are performed for the T_V-Gd$_3$ (**Figure 4D**) and the T_V-ZnGd$_3$ (**Figure 5A**), whose intensity profiles are taken across the X-Y direction of each image and compared with that of the corresponding experiment image, as shown in **Figure 6B**. It is evident that the T_V-cluster with Zn provides significantly better fit to the observed intensity, confirming that the present T_V-SRO clusters are essentially a ternary ZnGd$_3$. We should also note that the slight peak-shift of the Gd position is also reproduced fairly well by the simulation with the Zn atom, as indicated by an arrowhead, supporting strongly the presence of the Zn atom that causes relaxation for the T_V-Gd$_3$ configurations and provides a considerable energy gain (**Figure 5B**). **Figures 6C,D** show a series of analysis for the T_H-type SRO cluster, as being made along with the same manner for the T_V-type SRO cluster described above. The experimental profiles are also reproduced significantly better by the simulation with the Zn-containing cluster, confirming that the T_H-type SRO cluster also forms as a ternary ZnGd$_3$.

Now that the SRO-ZnGd$_3$ clusters appear to be a D0$_{19}$-like configuration, which prompts the notion about structural similarity with the L1$_2$-type Zn$_6$Gd$_8$ cluster in the LPSO phase. In the both clusters, Gd atoms are placed at the second-nearest neighbor in the original *hcp*-Mg sites or the local *fcc* environment sites in the intrinsic-II type stacking fault (Egusa and Abe, 2012), and Zn occupies the first-nearest neighbor to these Gd atoms. This similarity in local structures supports an idea that the D0$_{19}$-like ZnGd$_3$ cluster can be a precursor to the L1$_2$-type SRO cluster. To complete the transformation, the D0$_{19}$-like ZnGd$_3$ clusters more than two are necessary to aggregate to form the L1$_2$-type Zn$_6$Gd$_8$ cluster, and the process must accompany the local *hcp*-*fcc* stacking change. With this in mind, we here focus on the spatial distribution of the ZnGd$_3$ clusters in the α-Mg matrix. **Figure 7a** shows an enlarged HAADF-STEM image of **Figure 1d** (green-rectangle region), where the single SESF is formed in the α-Mg matrix. A large number of bright spots clearly show up in the image, some of which indeed represent the ZnGd$_3$ clusters as described before. By carefully looking at the image, the bright spots seem to not distribute uniformly but form weak layered atmosphere. By tracing the entire intensity profile along the *c*-axis, as shown in **Figure 7b**, weak local maxima indeed appear at the positions indicated by arrowheads. Interestingly, these positions are at the distance from 7 or 14 atomic layers from the SESF, whose modulation length is equivalent to the *c*-axis correlation of the 14H-LPSO structure. As confirmed by the STEM image of the relevant region taken along the [1$\bar{2}$10] direction (**Figure 7c**), there is no change in the stacking sequences except for the single SESF. Therefore, the observed intensity modulations imply that the D0$_{19}$-like ZnGd$_3$ clusters form a layered solute atmosphere in the *hcp*-Mg matrix around the SESF, being prior to the introduction of stacking faults into the *hcp*-Mg matrix (similar phenomena was also reported for the Mg-Al-Gd system; Kishida et al., 2013). It should be noted here that the layered-atmosphere modulation across the *c*-axis is extended longer than a nanometer-scale, which may require long-range solute interactions significantly longer than those for the short-range clusters. At present, it is difficult to clarify the origin of such long-range correlations based on first-principle calculations with a limited number of solute atoms. The origin

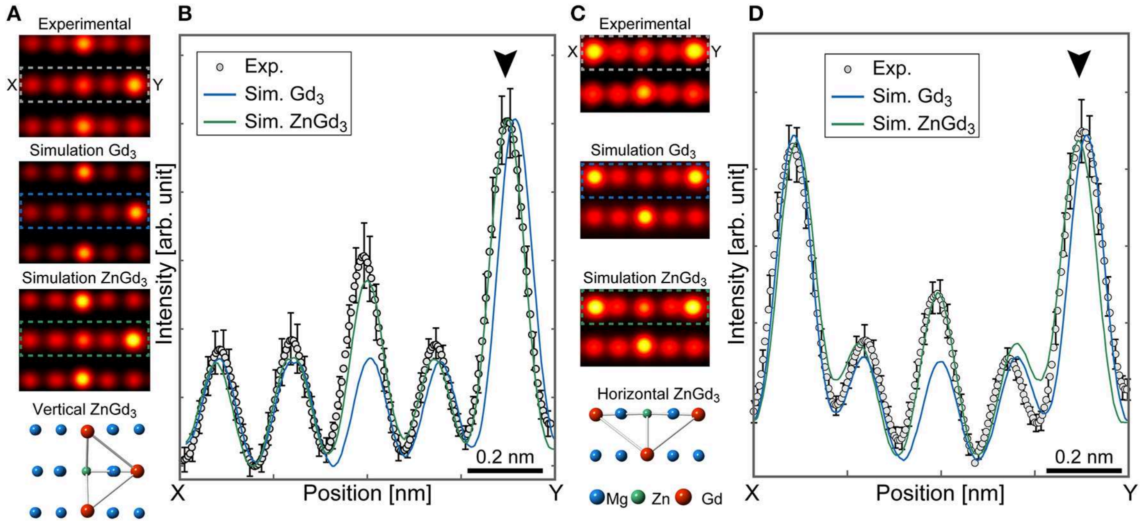

FIGURE 6 | (A) Experimental and simulated STEM images of the T_V-SRO cluster. The experimental image has been reconstructed by averaging over the 26 local images in **Figure 1d**, by automatically selecting the similar contrast regions according to the autocorrelation search. Image simulations are performed for the T_V-SRO cluster with and without Zn atom, and the T_V-SRO clusters are placed at the 4 nm in depth from the surface of the supercell. The conditions for simulations are the same as those described in **Figure 2B**. **(B)** Intensity profiles across X-Y in the dotted rectangles in the images in **(A)**. **(C)** Experimental and simulated STEM images of the T_H-SRO cluster. The 23 local images have been extracted and used for the reconstruction of the experimental image, and the averaging procedure and the simulation conditions are the same as those described in **(A)**. **(D)** Intensity profiles across X-Y in the dotted rectangles in the images in **(A)**.

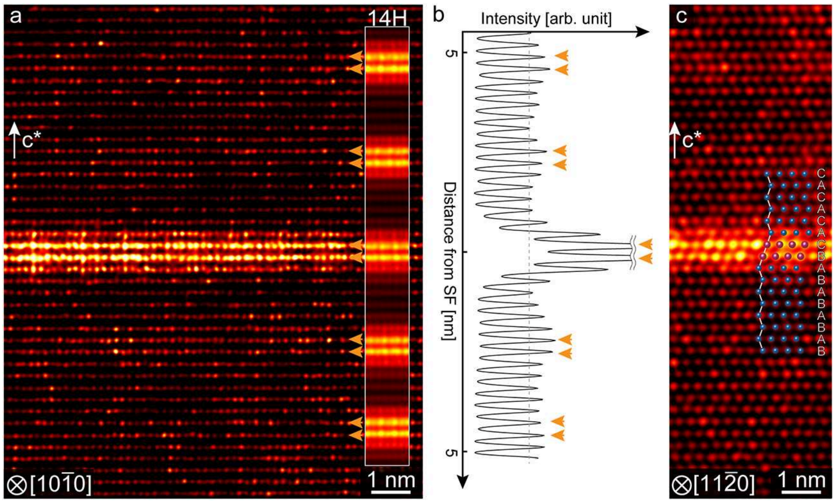

FIGURE 7 | (a) Atomic-resolution HAADF-STEM image of the α-Mg matrix with a single SESF, taken along the $[10\bar{1}0]_{hcp}$ direction. c* denotes the *c*-axis of the *hcp* crystal. A part of the 14H-type LPSO structure image is inserted for comparison, where the ordered arrays of the SESF are seen clearly. **(b)** Intensity profile of the entire image of **(a)** along the *c*-axis direction, in which weak intensity maxima are indicated by arrowheads. **(c)** HAADF-STEM image of the α-Mg matrix with a single SESF, taken along the $[1\bar{2}10]_{hcp}$ direction. Stacking sequences are unambiguously identified, as shown by the schematic model inserted.

might be interpreted by solute interactions with the multiple $L1_2$-type clusters embedded within the SESF, the details of which will be described elsewhere.

CONCLUSION

In the present study, we have investigated the possible SRO clusters of solute Zn and Gd atoms formed in the annealed $Mg_{97}Zn_1Gd_2$ alloy, based on aberration-corrected HAADF-STEM observations. The SRO structures have been successfully determined with the aid of STEM image simulations and first-principles calculations. The main results are summarized as follows.

1. HAADF-STEM imaging has confirmed presence of the solute-atom SRO clusters in the α-Mg phase as well as the LPSO phase. Quantitative image analyses with the aid of

simulations show that the observed intensity variations indeed reflect single Gd atom distributions. Characteristic SRO-related contrasts have been directly extracted from the image, emerging characteristic SRO configurations composed of three Gd atoms; vertical and horizontal trimers.

2. First-principles calculations have shown that the energetically-favored SRO configurations are the two types Gd trimer, which are represented as T_V- and T_H-SRO clusters and in good accordance with the STEM observations. Comprehensive investigations on possible Zn sites within the Gd-trimer clusters have shown that the Zn atoms are essentially involved both in the T_V- and T_H-SRO Gd clusters; $D0_{19}$-like $ZnGd_3$ clusters have emerged as significantly energy-stabilized configurations.
3. It has been found that the $D0_{19}$-like $ZnGd_3$ clusters seem to form weak layered-atmosphere around the isolated SESF. This may imply that, during the transformation from the *hcp*-Mg to the LPSO structure, the composition modulations along the *c*-axis take place prior to the introduction of the I_2-SFs.

DATA AVAILABILITY STATEMENT

All datasets generated for this study are included in the article/supplementary material.

AUTHOR CONTRIBUTIONS

EA initiated and designed the research and interpreted the data. DE and KK preformed the experiments, analyzed the data, and carried out computer simulations. DE and EA wrote the paper.

FUNDING

This study was supported by JSPS KAKENHI for Scientific Research on Innovative Areas Materials Science of a Mille-feuille Structure (Grant Numbers JP18H05475, JP18H05479), and Nanotechnology Platform of the MEXT, Japan.

REFERENCES

Abe, E., Kawamura, Y., Hayashi, K., and Inoue, A. (2002). Long-period ordered structure in a high-strength nanocrystalline Mg-1 at% Zn-2 at% Y alloy studied by atomic-resolution Z-contrast STEM. *Acta Mater.* 50, 3845–3857. doi: 10.1016/S1359-6454(02)00191-X

Abe, E., Ono, A., Itoi, T., Yamasaki, M., and Kawamura, Y. (2011). Polytypes of long-period stacking structures synchronized with chemical order in a dilute Mg–Zn–Y alloy. *Philos. Magazine Lett.* 91, 690–696. doi: 10.1080/09500839.2011.609149

Egami, M., and Abe, E. (2015). Structure of a novel Mg-rich complex compound in Mg–Co–Y ternary alloys. *Scripta Mater.* 98, 64–67. doi: 10.1016/j.scriptamat.2014.11.013

Egusa, D., and Abe, E. (2012). The structure of long period stacking/order Mg–Zn–RE phases with extended non-stoichiometry ranges. *Acta Mater.* 60, 166–178. doi: 10.1016/j.actamat.2011.09.030

Egusa, D., Yamasaki, M., Kawamura, Y., and Abe, E. (2013). Micro-kinking of the long-period stacking/order (LPSO) phase in a hot-extruded Mg97Zn1Y2 alloy. *Mater. Transac.* 54, 698–702. doi: 10.2320/matertrans.MI201216

Fujita, N., Matsushita, M., Tsukamoto, R., Yamasaki, M., Kawamura, Y., Irifune, T., et al. (2018). The structure of a novel long-period superlattice phase in $Mg_{97}Zn_1Yb_2$ alloys. *Scripta Mater.* 150, 78–81. doi: 10.1016/j.scriptamat.2018.02.043

Garcés, G., Máthis, K., Medina, J., Horváth, K., Drozdenko, D., Oñorbe, E., et al. (2018). Combination of *in-situ* diffraction experiments and acoustic emission testing to understand the compression behavior of Mg-Y-Zn alloys containing LPSO phase under different loading conditions. *Int. J. Plasticity* 106, 107–128. doi: 10.1016/j.ijplas.2018.03.004

Gröbner, J., Kozlov, A., Fang, X.-Y., Zhu, S., Nie, J.-F., Gibson, M. A., et al. (2015). Phase equilibria and transformations in ternary Mg–Gd–Zn alloys. *Acta Mater.* 90, 400–416. doi: 10.1016/j.actamat.2015.02.044

Gu, X.-F., Furuhara, T., Chen, L., and Yang, P. (2018). Study on the planar segregation of solute atoms in Mg-Al-Gd alloy. *Scripta Mater.* 150, 45–49. doi: 10.1016/j.scriptamat.2018.02.041

Hagihara, K., Kinoshita, A., Sugino, Y., Yamasaki, M., Kawamura, Y., Yasuda, H. Y., et al. (2010). Effect of long-period stacking ordered phase on mechanical properties of Mg97Zn1Y2 extruded alloy. *Acta Mater.* 58, 6282–6293. doi: 10.1016/j.actamat.2010.07.050

Hagihara, K., Li, Z., Yamasaki, M., Kawamura, Y., and Nakano, T. (2019). Strengthening mechanisms acting in extruded Mg-based long-period stacking ordered (LPSO)-phase alloys. *Acta Mater.* 163, 226–239. doi: 10.1016/j.actamat.2018.10.016

He, S. M., Zeng, X. Q., Peng, L. M., Gao, X., Nie, J. F., and Ding, W. J. (2006). Precipitation in a Mg−10Gd−3Y−0.4Zr (wt.%) alloy during isothermal ageing at 250°C. *J. Alloys Compd.* 421, 309–313. doi: 10.1016/j.jallcom.2005.11.046

Homma, T., Kunito, N., and Kamado, S. (2009). Fabrication of extraordinary high-strength magnesium alloy by hot extrusion. *Scripta Mater.* 61, 644–647. doi: 10.1016/j.scriptamat.2009.06.003

Honma, T., Ohkubo, T., Hono, K., and Kamado, S. (2005). Chemistry of nanoscale precipitates in Mg−2.1Gd−0.6Y−0.2Zr (at.%) alloy investigated by the atom probe technique. *Mater. Sci. Eng. A* 395, 301–306. doi: 10.1016/j.msea.2004.12.035

Honma, T., Ohkubo, T., Kamado, S., and Hono, K. (2007). Effect of Zn additions on the age-hardening of Mg−2.0Gd−1.2Y−0.2Zr alloys. *Acta Mater.* 55, 4137–4150. doi: 10.1016/j.actamat.2007.02.036

Hosokawa, S., Stellhorn, J., Paulus, B., Maruyama, K., Kobayashi, K., Okuda, H., et al. (2018). The seeds of Zn_6Y_8 $L1_2$-type clusters in amorphous $Mg_{85}Zn_6Y_9$ alloy investigated by photoemission spectroscopy. *J. Alloy Compd.* 764, 431–436. doi: 10.1016/j.jallcom.2018.06.012

Inamura, T. (2019). Geometry of kink microstructure analysed by rank-1 connection. *Acta Mater.* 173, 270–280. doi: 10.1016/j.actamat.2019.05.023

Ishizuka, K. (2002). A practical approach for STEM image simulation based on the FFT multislice method. *Ultramicroscopy* 90, 71–83. doi: 10.1016/S0304-3991(01)00145-0

Itoi, T., Seimiya, T., Kawamura, Y., and Hirohashi, M. (2004). Long period stacking structures observed in $Mg_{97}Zn_1Y_2$ alloy. *Scripta Mater.* 51, 107–111. doi: 10.1016/j.scriptamat.2004.04.003

Jono, Y., Yamasaki, M., and Kawamura, Y. (2013). Effect of LPSO phase-stimulated texture evolution on creep resistance of extruded Mg–Zn–Gd alloys. *Mater. Transac.* 54, 703–712. doi: 10.2320/matertrans.MI201218

Kawamura, Y., Hayashi, K., Inoue, A., and Masumoto, T. (2001). Rapidly solidified powder metallurgy $Mg_{97}Zn_1Y_2$ alloys with excellent tensile yield strength above 600 MPa. *Mater. Transac.* 42, 1172–1176. doi: 10.2320/matertrans.42.1172

Kawamura, Y., and Yamasaki, M. (2007). Formation and mechanical properties of $Mg_{97}Zn_1$ RE_2 alloys with long-period stacking ordered structure. *Mater. Transac.* 48, 2986–2992. doi: 10.2320/matertrans.MER2007142

Kim, J., and Kawamura, Y. (2013). Influence of rare earth elements on microstructure and mechanical properties of $Mg_{97}Zn_1Y_1RE_1$ alloys. *Mater. Sci. Eng.* 573, 62–66. doi: 10.1016/j.msea.2012.12.087

Kimizuka, H., Kurokawa, S., Yamaguchi, A., Sakai, A., and Ogata, S. (2014). Two-dimensional ordering of solute nanoclusters at a close-packed stacking fault: modeling and experimental analysis. *Sci. Rep.* 4:7318. doi: 10.1038/srep07318

Kishida, K., Yokobayashi, H., and Inui, H. (2013). The most stable crystal structure and the formation processes of an order-disorder (OD) intermetallic phase in the Mg–Al–Gd ternary system. *Philos. Magazine* 93, 2826–2846. doi: 10.1080/14786435.2013.790566

Koizumi, T., Egami, M., Yamashita, K., and Abe, E. (2018). Platelet precipitate in an age-hardening Mg-Zn-Gd alloy. *J. Alloy Compd.* 752, 407–411. doi: 10.1016/j.jallcom.2018.04.136

Kresse, G., and Furthmüller, J. (1996). Efficiency of ab-initio total energy calculations for metals and semiconductors using a plane-wave basis set. *Comput. Mater. Sci.* 6, 15–50. doi: 10.1016/0927-0256(96)00008-0

Ma, S.-Y., Liu, L.-M., and Wang, S.-Q. (2013). The predominant role of Zn6Y9 cluster in the long period stacking order structures of Mg–Zn–Y alloys: a first-principles study. *J. Mater. Sci.* 48, 1407–1412. doi: 10.1007/s10853-012-6890-4

Malis, T., Cheng, S., and Egerton, R. (1988). EELS log-ratio technique for specimen-thickness measurement in the TEM. *J. Electron. Micr. Tech.* 8, 193–200. doi: 10.1002/jemt.1060080206

Matsushita, M., Ingai, R., Yamasaki, M., Shinmei, T., Kawamura, Y., Irifune, T., et al. (2016). A novel long-period superlattice phase in $Mg_{97}Zn_1Yb_2$ alloys synthesized under high-pressure. *Scripta Mater.* 122, 45–49. doi: 10.1016/j.scriptamat.2016.04.022

Mittal, A., and Mkhoyan, A. K. (2011). Limits in detecting an individual dopant atom embedded in a crystal. *Ultramicroscopy* 111, 1101–1110. doi: 10.1016/j.ultramic.2011.03.002

Nie, J.-F. (2012). Precipitation and hardening in magnesium alloys. *Metal. Mater. Trans. A* 43, 3891–3939. doi: 10.1007/s11661-012-1217-2

Nie, J. F., Oh-ishi, K., Gao, X., and Hono, K. (2008). Solute segregation and precipitation in a creep-resistant Mg–Gd–Zn alloy. *Acta Mater.* 56, 6061–6076. doi: 10.1016/j.actamat.2008.08.025

Nishijima, M., and Hiraga, K. (2007). Structural changes of precipitates in an Mg-5 at%Gd alloy studied by transmission electron microscopy. *Mater. Trans.* 48, 10–15. doi: 10.2320/matertrans.48.10

Nishijima, M., Hiraga, K., Yamasaki, M., and Kawamura, Y. (2008). The structure of guinier-preston zones in an Mg-2 at%Gd-1 at%Zn alloy studied by transmission electron microscopy. *Mater. Trans.* 49, 227–229. doi: 10.2320/matertrans.MEP2007257

Nishioka, T., Yamamoto, Y., Kimura, K., Hagihara, K., Izuno, H., Happo, N., et al. (2018). In-plane positional correlations among dopants in 10H type long period stacking ordered $Mg_{75}Zn_{10}Y_{15}$ alloy studied by X-ray fluorescence holography. *Materialia* 3, 256–259. doi: 10.1016/j.mtla.2018.09.002

Okuda, H., Yamasaki, M., and Kawamura, Y. (2017). Transition to long period stacking ordered structures in $Mg_{85}Gd_9Zn_6$ alloys from amorphous ribbons examined by synchrotron radiation scattering: comparison with Mg85Y9Zn6 alloys. *Scripta Mater.* 139, 26–29. doi: 10.1016/j.scriptamat.2017.06.013

Okuda, H., Yamasaki, M., Kawamura, Y., Tabuchi, M., and Kimizuka, H. (2015). Nanoclusters first: a hierarchical phase transformation in a novel Mg alloy. *Sci. Rep.* 5:14186. doi: 10.1038/srep14186

Perdew, J., Chevary, J., Vosko, S., Jackson, K., Pederson, M., Singh, D., et al. (1992). Atoms, molecules, solids, and surfaces: applications of the generalized gradient approximation for exchange and correlation. *Phys. Rev. B* 46, 6671–6687. doi: 10.1103/PhysRevB.46.6671

Pollock, T. M. (2010). Weight loss with magnesium alloys. *Science* 328, 986–987. doi: 10.1126/science.1182848

Saal, J. E., and Wolverton, C. (2014). Thermodynamic stability of Mg-based ternary long-period stacking ordered structures. *Acta Mater.* 68, 325–338. doi: 10.1016/j.actamat.2013.10.055

Saito, K., Yasuhara, A., and Hiraga, K. (2011). Microstructural changes of Guinier–Preston zones in an Mg−1.5at% Gd−1at% Zn alloy studied by HAADF-STEM technique. *J. Alloys Compd.* 509, 2031–2038. doi: 10.1016/j.jallcom.2010.10.129

Sandlöbes, S., Pei, Z., Friák, M., Zhu, L.-F., Wang, F., Zaefferer, S., et al. (2014). Ductility improvement of Mg alloys by solid solution: Ab initio modeling, synthesis and mechanical properties. *Acta Mater.* 70, 92–104. doi: 10.1016/j.actamat.2014.02.011

Shao, X. H., Yang, Z. Q., and Ma, X. L. (2010). Strengthening and toughening mechanisms in Mg–Zn–Y alloy with a long period stacking ordered structure. *Acta Mater.* 58, 4760–4771. doi: 10.1016/j.actamat.2010.05.012

Umebayashi, T., Iikubo, S., and Ohtani, H. (2014). Thermodynamic analysis on a segregation behavior of alloying elements to stacking faults in Mg-Y-Zn based LPSO structures. *J. Jpn. Inst. Metals Mater.* 78, 117–125. doi: 10.2320/jinstmet.JBW201307

Xu, C., Zheng, M., Xu, S., Wu, K., Wang, E., Fan, G., et al. (2015). Improving strength and ductility of Mg–Gd–Y–Zn–Zr alloy simultaneously via extrusion, hot rolling and ageing. *Mater. Sci. Eng. A* 643, 137–141. doi: 10.1016/j.msea.2015.07.032

Yamamoto, Y., Sakamoto, Y., Masaki, Y., and Nishitani, S. R. (2013). First principles calculations of solute ordering in Mg–Zn–Y alloys. *Mater. Trans.* 54, 656–660. doi: 10.2320/matertrans.MI201207

Yamasaki, M., Anan, T., Yoshimoto, S., and Kawamura, Y. (2005). Mechanical properties of warm-extruded Mg–Zn–Gd alloy with coherent 14H long periodic stacking ordered structure precipitate. *Scripta Mater.* 53, 799–803. doi: 10.1016/j.scriptamat.2005.06.006

Yamasaki, M., Hagihara, K., Inoue, S., Hadorn, J., and Kawamura, Y. (2013). Crystallographic classification of kink bands in an extruded Mg–Zn–Y alloy using intragranular misorientation axis analysis. *Acta Mater.* 61, 2065–2076. doi: 10.1016/j.actamat.2012.12.026

Yamasaki, M., Matsushita, M., Hagihara, K., Izuno, H., Abe, E., and Kawamura, Y. (2014). Highly ordered 10H-type long-period stacking order phase in a Mg–Zn–Y ternary alloy. *Scripta Mater.* 78, 13–16. doi: 10.1016/j.scriptamat.2014.01.013

Yamasaki, M., Sasaki, M., Nishijima, M., Hiraga, K., and Kawamura, Y. (2007). Formation of 14H long period stacking ordered structure and profuse stacking faults in Mg–Zn–Gd alloys during isothermal aging at high temperature. *Acta Mater.* 55, 6798–6805. doi: 10.1016/j.actamat.2007.08.033

Yamashita, K., Itoi, T., Yamasaki, M., Kawamura, Y., and Abe, E. (2019). A novel long-period stacking/order structure in Mg-Ni-Y alloys. *J. Alloy Compd.* 788, 277–282. doi: 10.1016/j.jallcom.2019.02.219

Yokobayashi, H., Kishida, K., Inui, H., Yamasaki, M., and Kawamura, Y. (2011). Enrichment of Gd and Al atoms in the quadruple close packed planes and their in-plane long-range ordering in the long period stacking-ordered phase in the Mg–Al–Gd system. *Acta Mater.* 59, 7287–7299. doi: 10.1016/j.actamat.2011.08.011

Zhu, Y. M., Morton, A. J., and Nie, J. F. (2010). The 18R and 14H long-period stacking ordered structures in Mg–Y–Zn alloys. *Acta Mater.* 58, 2936–2947. doi: 10.1016/j.actamat.2010.01.022

Conflict of Interest: The authors declare that the research was conducted in the absence of any commercial or financial relationships that could be construed as a potential conflict of interest.

frontiers in Materials

ORIGINAL RESEARCH
published: 05 November 2019
doi: 10.3389/fmats.2019.00270

In-situ Investigation of the Microstructure Evolution in Long-Period-Stacking-Ordered (LPSO) Magnesium Alloys as a Function of the Temperature

Kristián Máthis[1,2]*, Daria Drozdenko[2,3], Gergely Németh[1,2], Stefanus Harjo[4], Wu Gong[5], Kazuya Aizawa[4], Michiaki Yamasaki[3] and Yoshihito Kawamura[3]

[1] Nuclear Physics Institute, Czech Academy of Sciences, Prague, Czechia, [2] Department of Physics of Materials, Faculty of Mathematics and Physics, Charles University, Prague, Czechia, [3] Department of Materials Science, Magnesium Research Center, Kumamoto University, Kumamoto, Japan, [4] J-PARC Center, Japan Atomic Energy Agency, Ibaraki, Japan, [5] Elements Strategy Initiative for Structural Materials, Kyoto University, Kyoto, Japan

Deformation behavior of two Mg–Zn–Y magnesium alloys, having a different fraction of the long-period-stacking-ordered (LPSO) phase, has been investigated at room temperature and 200°C by a combination of *in-situ* neutron diffraction (ND) and acoustic emission (AE) measurements. The results indicate that the twinning in the magnesium matrix and the kinking in the LPSO phase strongly depend on the composition of the material and the testing temperature. Further, active deformation mechanisms and particularly the load transfer from the magnesium matrix to the LPSO phase define the mechanical properties of the investigated alloys.

Keywords: twinning, kinking, neutron diffraction, acoustic emission, LPSO phase

OPEN ACCESS

Edited by:
Maria Teresa Pérez,
Instituto IMDEA Materiales, Spain

Reviewed by:
Gerardo Garces,
Centro Nacional De Investigaciones Metalurgicas (CENIM), Spain
Dong Feng Shi,
Instituto IMDEA Materiales, Spain

***Correspondence:**
Kristián Máthis
mathis@ujf.cas.cz

Specialty section:
This article was submitted to Structural Materials, a section of the journal Frontiers in Materials

Received: *28 June 2019*
Accepted: *16 October 2019*
Published: *05 November 2019*

Citation:
Máthis K, Drozdenko D, Németh G, Harjo S, Gong W, Aizawa K, Yamasaki M and Kawamura Y (2019) In-situ Investigation of the Microstructure Evolution in Long-Period-Stacking-Ordered (LPSO) Magnesium Alloys as a Function of the Temperature. Front. Mater. 6:270. doi: 10.3389/fmats.2019.00270

INTRODUCTION

Wrought magnesium (Mg) alloys belong to the most promising lightweight materials in the transportation industry. However, there are many technological challenges, including tension-compression asymmetry in yielding and low formability at ambient temperature, which have to be solved for further expansion of Mg alloys usage. The rapid degradation of the mechanical properties with increasing temperature also significantly limits the application field. These issues have been addressed recently by developing Mg alloys with long-period-stacking-ordered (LPSO) phase, which is a periodic arrangement of close-packed atomic layers enriched by rear-earth elements and transition metals in the Mg lattice (Abe et al., 2011; Egusa and Abe, 2012). The presence of the LPSO phase significantly alters the deformation behavior of the material. Consequently, this class of alloys exhibits exceptional mechanical performance at room and high-temperature tests comparing to the commercial wrought Mg alloys (Inoue et al., 2001; Kawamura et al., 2001, 2006; Yamasaki et al., 2011). Owing to their higher Young modulus, the LPSO phase can bear the majority of the applied stress. Thus, the Mg-LPSO alloys behave like short-fiber-reinforced composites. Besides the dislocation slip and twinning, additional deformation mechanism, called kinking (sharp bending of the LPSO phase) is activated during the plastic deformation. All of them significantly depends both on materials parameters (volume fraction and orientation of the LPSO phase, the grain size of Mg matrix) and experimental conditions (loading direction, temperature etc.). There are numerous works investigating deformation mechanisms of such alloys at room temperature (e.g., Kishida et al., 2014; Garcés et al., 2018). Nevertheless, an in-depth understanding of deformation mechanisms (dislocation slip, kinking, and twinning) in Mg-LPSO based alloys as a function of temperature and volume fraction of the LPSO phase is still essential.

In this work, the microstructure evolution as a result of deformation behavior during uniaxial compression of two extruded Mg–Zn–Y alloy was investigated as a function of amount of the LPSO phase and the testing temperature. The neutron diffraction (ND) and concurrently recorded acoustic emission (AE) response were used to obtain detail information about active deformation mechanism in the alloys. The novelty of this work consists in comprehensive characterization of the activity of deformation twinning, kinking, and dislocation slip by a blend of *in-situ* methods. According to our current knowledge, this is the first ND study in the literature provided at elevated temperature on Mg-LPSO alloy. The results of the *in-situ* tests are completed by microstructure observation by light and scanning electron microscopy, particularly electron-backscatter diffraction (EBSD).

EXPERIMENTAL

Mg-3 at.% Y−1.5 at.% Zn and Mg-7 at.% Y−6 at.% Zn alloys extruded at 350°C with extrusion ratio 1:10 and ram speed of 2.5 mm/s were investigated. The volume fractions of the LPSO phase in the investigated materials are 32% (Mg-3 at.% Y−1.5 at.% Zn) and 85% (Mg-7 at.% Y−6 at.% Zn), hereafter referred as S32 and S85 alloys, respectively. Both, the initial and deformed microstructures were examined by confocal light (Lasertec C-130) and scanning electron microscopes (SEM, JEOL, and JSM-7001F) equipped with EDAX/TSL EBSD system. The specimens for the light microscopy observation were prepared by grinding and polishing down to 0.25 µm diamond paste, followed by etching in picric acid for a few seconds. For EBSD measurements the final step of the preparation specimens after polishing using 0.25 µm diamond paste was ion-milling (JEOL Cross Section Polisher SM-09010). For compression deformation tests, cylindrical specimens with a gauge length of 16 mm and diameter of 8 mm were machined along extrusion direction (ED). Loading was performed at a constant strain rate of 0.1 mm/min at room temperature (RT) and 200°C. The compression direction was parallel to ED and deformation test was terminated around 12% of strain in order to maintain the specimen's integrity. ND experiments were performed *in-situ* during compression using the engineering neutron diffractometer TAKUMI at Japan Proton Accelerator Research Complex (J-PARC). The specimens were fixed horizontally to a deformation rig with its axial direction at +45° to the incident neutron beam, and two detector banks are used to collect the diffracted neutron patterns at +90° and −90° relative to the incident beam, respectively. Concurrently, the AE activity was monitored by a MICRO-II AE system (Physical Acoustics Corporation) in hit-based mode, where the threshold level was set as 32 dB. A preamplifier of 60 dB and sensors: a piezoelectric PICO S/N 7549 and a S9215 high temperature sensor for room and elevated temperature tests, respectively, were used.

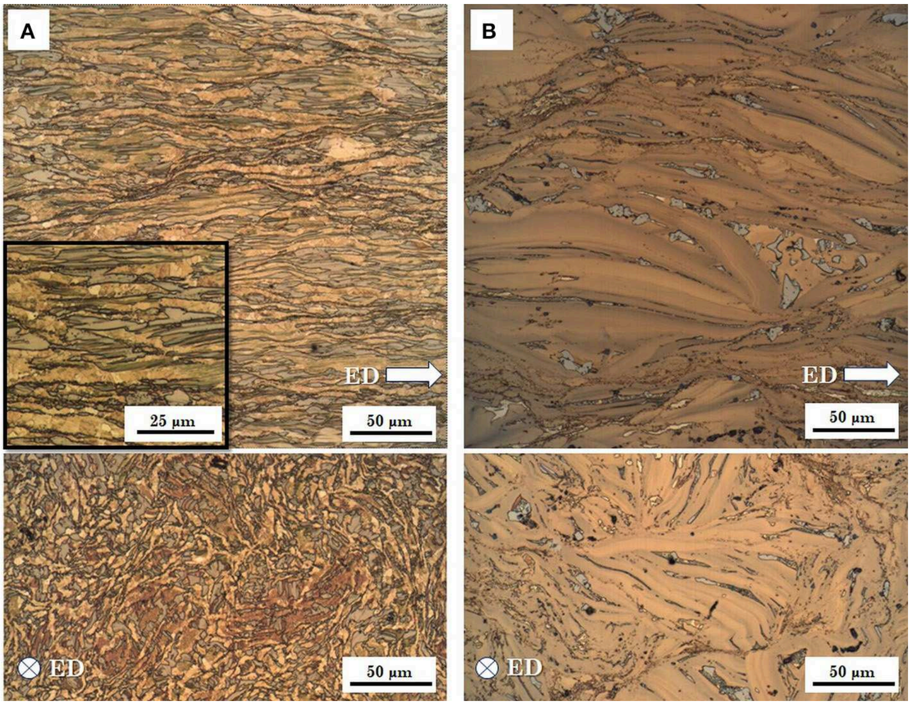

FIGURE 1 | The initial microstructure of the S32 **(A)** and S85 **(B)** alloys obtained by confocal light microscope along and perpendicular to ED.

RESULTS AND DISCUSSION

Initial Microstructure

The initial optical micrographs of the S32 and S85 alloys are presented in **Figure 1**. In both alloys the extrusion process resulted in an elongated microstructure: some non-recrystallized grains in S32 alloy and LPSO laths in both alloys are oriented parallel to ED. Nevertheless, LPSO laths are wavy and, in some cases, do not follow perfectly ED. Moreover, in the S85 alloy due to higher alloying content, i.e., higher volume fraction of a LPSO phase, LPSO laths are naturally larger comparing to one in the S32 alloy. **Figure 2** presents EBSD maps for S32 and S85 alloys, including Kernel Average Misorientation (KAM) maps for entire scan area and separated orientation maps for the α-Mg and LPSO phase together with calculated texture for each fraction. The black areas in the particular maps correspond to the other phase or unclear identification of the phase by software. The KAM maps indicate high internal strain (green color) in the LPSO laths and large non-recrystallized grains (e.g., marked by the white circle in **Figure 2A**), while the majority of α-Mg grains are characterized by low values of KAM (blue color). Therefore, it can be concluded that α-Mg grains in both alloys are mainly recrystallized one.

In general, both alloys are characterized by prismatic fiber texture, having basal planes oriented parallel to ED. From **Figure 2A** it can be seen that α-Mg grains in S32 alloy are characterized by weak texture with a distribution of intensities along the arc between the <10.0> and <11.0> poles with maximum intensity at (10.0) pole. In the case of S85 alloy, amount of α-Mg phase is dramatically reduced comparing with the S32 alloy. Therefore, presented orientation map for α-Mg grains (**Figure 2B**) has a rather informative character due to relatively small scan area caused by the small grain size of those grains in contrast to LPSO laths in this material. Nevertheless, those grains are characterized by rather random orientation similar to α-Mg grains in S32 alloy. The LPSO phase in both alloys is characterized by their prismatic {10.0} plane oriented perpendicular to the ED. Therefore, it can be seen that the major texture components for each phase are comparable for both investigated alloys. Thus, the effect of texture on mechanical

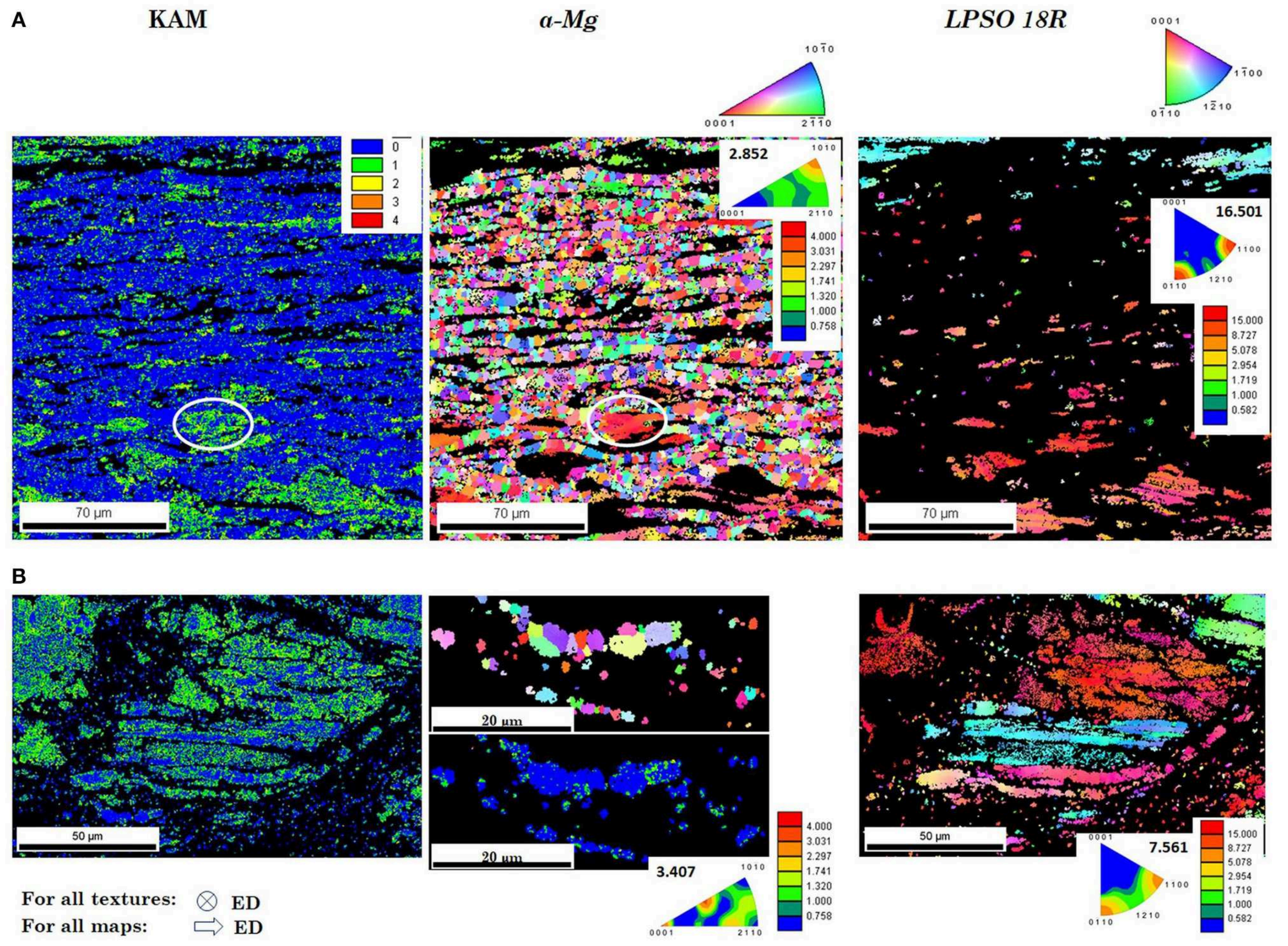

FIGURE 2 | EBSD maps for the S32 **(A)** and S85 **(B)** alloy in the as-extruded state: KAM analysis for entire map; separated orientation maps for the α-Mg and LPSO phase together with calculated texture for each fraction.

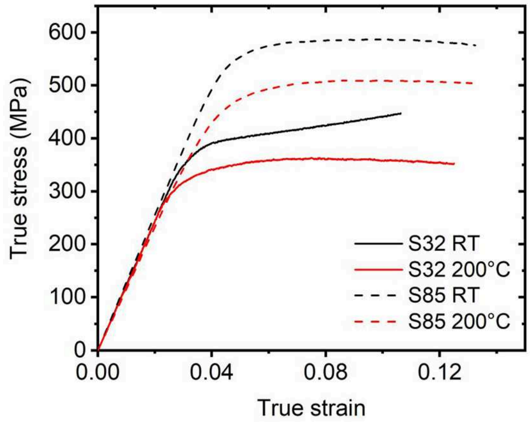

FIGURE 3 | True stress—true strain curves for S32 and S85 alloys tested in compression at room temperature and 200°C.

properties in the present study is strongly linked to the volume fraction of the respective phase.

Deformation Test

The strong influence of the LPSO content and temperature on mechanical properties is obvious from **Figure 3**. At room temperature, the yield strength (YS) of S85 specimen is more than 30% larger (525 vs. 357 MPa) than that for S32 alloy. However, the character of the deformation curve is different. The S32 specimen exhibits an S-shape curve, characteristic for wrought alloys deformed in compression along ED, when the moderate hardening region (plateau) after the yield point is followed by a secondary hardening stage. At 200°C the value of YS decreases for both alloys (S32—305 MPa, S85—420 MPa), but the degradation of mechanical properties is moderate (10 and 15%, respectively). In both materials softening occurs above 6% of strain.

Microstructure After Deformation

The microstructure of the S32 and S85 alloys after deformation at RT and 200°C is presented in **Figure 4**. In the S32 alloy after RT deformation non-recrystallized grains are highly twinned (**Figure 4A**). The S32 alloy contains low fraction of LPSO phase, which has wavy, prolonged shape owing to the extrusion process. The kinking at room temperature in S32 alloy is less developed, and it appears mostly in form of bended LPSO laths (cf. Figure 14 in Garcés et al., 2018). This can be hardly distinguished from the initial wavy form of the LPSO phase in the presented optical micrographs. In contrast, deformation of the S85 alloy at RT is characterized by significant kinking (**Figure 4B**). At higher testing temperature (at 200°C) kinking has been clearly observed also in the S32 alloy (detailed SEM image in **Figure 4C**). Moreover, with increasing deformation temperature, besides twinning and kinking, traces of the recrystallization process is observed (**Figures 4C,D**). **Figure 4D** includes a detailed EBSD map of the S85 alloys after deformation at 200°C showing small grains with low values of KAM, i.e., the DRX phenomenon for this alloy.

Acoustic Emission Testing

The acoustic emission was measured in the hit-based regime, when the raw acoustic emission signal was parametrized using a pre-set threshold level (30 dB) and hit definition time (800 μs). The evolution of the count rate (number of crossing the threshold level by signal per second) with time is plotted for the particular specimens and testing temperatures in **Figure 5**. The AE response follows the characteristic behavior in Mg alloys. Already in the elastic regime there is a steep increment of the AE signal and after reaching the YS, a significant drop of AE is observed. Closer analysis of the AE signal shows that it consists of large amplitude burst-type events. The "LPSO specific" feature is that the maximum of the AE count is reached far below the macroscopic yield. This behavior is characteristic for both investigated alloys and tested temperatures. It is obvious, that during RT loading maximum of AE count rate is higher for S32 alloy than that for S85 alloy. At 200°C the AE signal is weaker but the overall character of its behavior remains for both alloys.

Neutron Diffraction Measurements

The results of the ND experiments are presented in **Figure 6**, where for a particular specimen and temperature the stress-strain curves, stress dependence of lattice strains both for LPSO and α-Mg phases are shown in one plot. Additionally, relative intensity changes for {10.0} Mg and {01.8} LPSO peaks are shown. The reason for the selection of these peaks is given by the relationship of (00.2)-{10.0} peak pairs with twinning in α-Mg phase (Gharghouri et al., 1999) and high intensity (i.e., good statistics) and no overlapping of {10.8} LPSO peak with other Mg peaks. In S32 specimen at RT both the Mg and LPSO phase follows the line of the ideal elastic response up to 300 MPa. Above this level, a microplasticity can be observed in Mg phase, connected most probably with the onset of the extension twinning and basal slip. At 360 MPa significant relaxation of the lattice strain in Mg phase takes place. At the same time, the intensity of the {10.0} Mg peak sharply decreases, which is a clear sign of the massive twin growth. The stress dependence of the lattice strain on the LPSO planes indicates that the majority of the applied stress is bear by the LPSO phase. The behavior of the S85 specimen at RT is quite different (**Figure 6B**). Above 200 MPa the LPSO phase exhibit plastic behavior, whereas the lattice strain evaluation of Mg phase is linear up to 480 MPa. In line with these findings, the intensity of the {01.8} LPSO peak decreases above 200 MPa, which can be associated with the onset of the kinking process. At the same time, the change of relative intensity for {10.0} peak is minimal comparing to that for S32 alloy and goes along with changes of intensity of the {01.8} LPSO peak. Therefore, the decrease of the relative intensity of {10.0} Mg peak in S85 alloy can be associated with kinking rather than with twinning. It is obvious, that the intensity change caused by kinking is less sharp than that due to twinning. This is given by the gradual rotation of the lattice during the

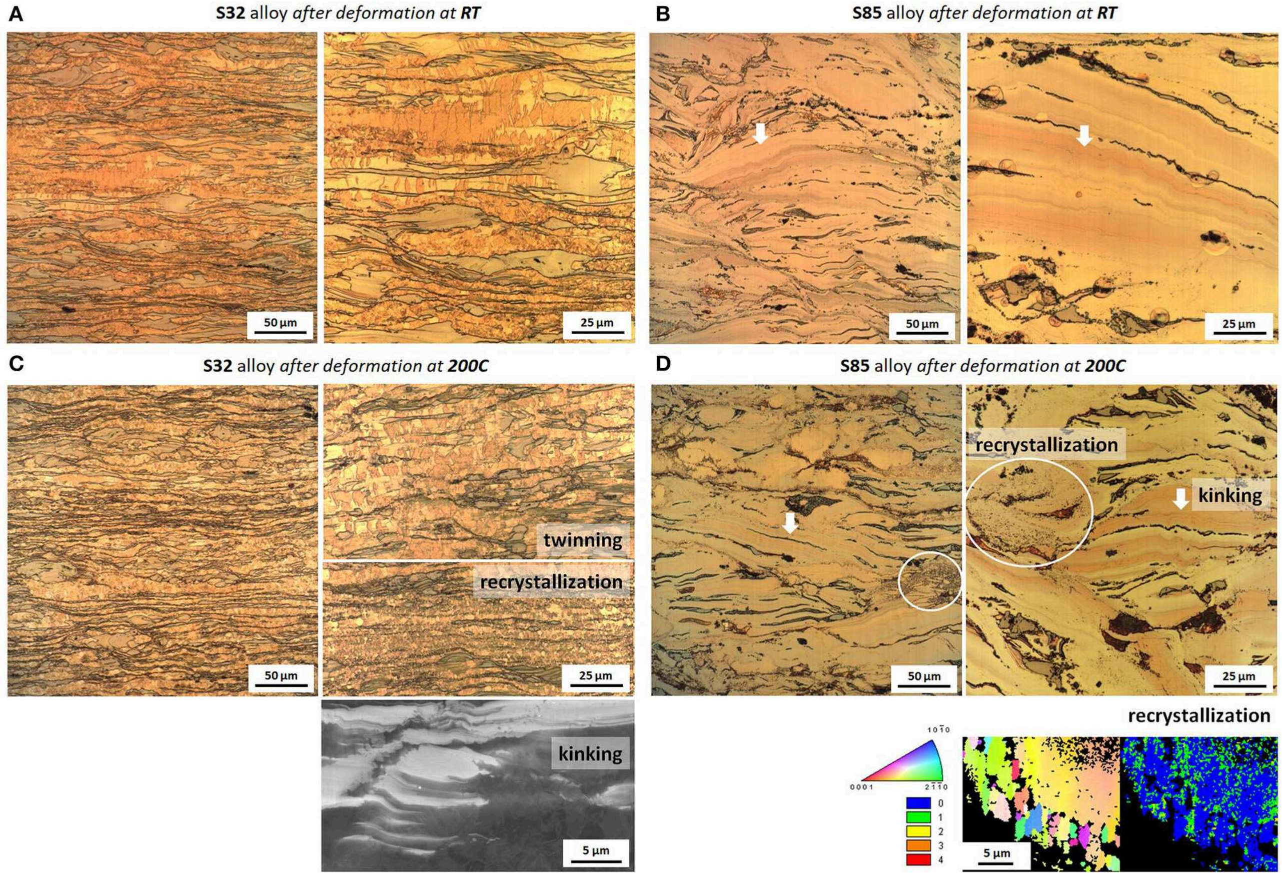

FIGURE 4 | Microstructure of the S32 **(A,C)** and the S85 **(B,D)** specimen obtained by confocal light microscope and SEM along ED after deformation at RT and 200°C, respectively. White arrows indicate kinking, white circle—recrystallization. **(C)** Includes detailed SEM image of kinking observed in the S32 alloy after deformation at 200°C. **(D)** Includes EBSD map with KAM analysis of recrystallized grains observed in the S85 alloy after deformation at 200°C.

kinking in contrast to the 86.3° lattice re-orientation during extension twinning.

At 200°C in S32 specimen the (micro)plasticity starts already below 100 MPa (**Figure 6C**), which is in good agreement with our previous results (El-Tahawy et al., 2019). The behavior of the LPSO peaks indicates temperature enhanced dislocation activity: lattice strains deviate from a linear response at lower stress comparing to RT case, what theoretically can promote kinking. Due to small amount of LPSO phase, the relative intensity of {10.8} LPSO peak does not show significant difference comparing to that at RT. At the same time, an intensity of the {10.0} Mg peak sharply decreases at yield point indicating twinning activity. Moreover, the deviation of lattice strain for LPSO and α-Mg phases from linear behavior may be affected by the recrystallization process. In the case of the S85 alloy, thermal activation also plays an important role. Gradual deviation from linearity is observed for LPSO peaks from the beginning of deformation, and for the Mg phase, a significant change for relative intensity of {10.0} peak is observed after reaching 200 MPa (**Figure 6D**). Similar to RT loading, deviation of relative intensity change of the {10.0} Mg peak is accompanied by changes of the {01.8} LPSO peak with little delay (one measuring point). Therefore, it can be concluded that changes of {10.0} Mg peak are related to the kinking process.

DISCUSSION

It is clearly seen that the volume fraction of the α-Mg (non- and recrystallized grains) decreases with the increasing volume fraction of the LPSO phase, which strongly depends on the amount of alloying elements. Both investigated alloys are characterized by prismatic fiber texture. The alignment of the (10.0) plane in the ED can be explained by the lattice rotation due to non-basal slip with the <11.0> slip direction during extrusion process (Mayama et al., 2011). Such texture is usually given by elongated worked grains having <10.0> axis parallel to ED, as it was previously reported for common wrought Mg alloys (Sillekens and Bohlen, 2012) as well as for Mg-LPSO materials (Hagihara et al., 2010a; Jono et al., 2013). In our case, most of an elongated worked grains experienced recrystallization during the extrusion process, and only a minority of non-recrystallized

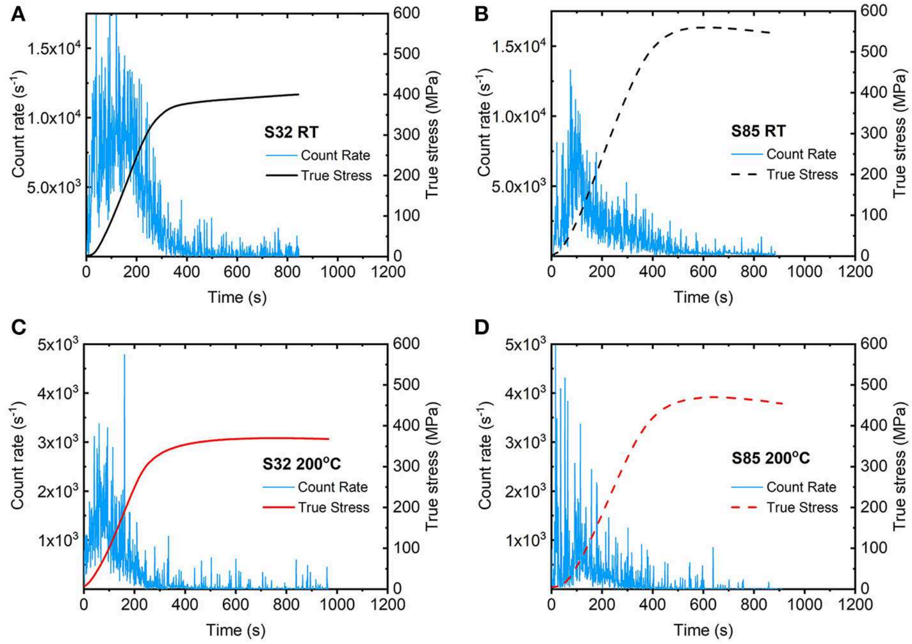

FIGURE 5 | The evolution of the AE count rate with time during compression loading of the S32 and S85 alloys at RT **(A,B)** and at 200°C (**C,D**, respectively).

grains remains in the microstructure. Despite the fact that the majority of α-Mg grains in the S32 alloy are fine recrystallized grains having preferentially a random orientation, a general characteristic of the texture persists. In the case of S85 alloy, detail EBSD maps indicate a random texture of recrystallized grains. Further, due to the concentration of high KAM values in non-recrystallized α-Mg grains and LPSO laths, S32 alloy is characterized by significantly lower overall internal stress, comparing to that in S85 alloy containing 85% of LPSO phase. The described difference in internal strain has an impact on active deformation mechanisms. The high internal strain in the grains leads to increased stress values for slip activation (Farkas et al., 2017), i.e., high yield stress can be reached as in case of S85 alloy.

The main sources of the AE in the Mg-LPSO alloys are the collective dislocation motion, twinning, kinking and failure mechanisms (cracking, delamination) and they are connected with the presence of the LPSO lath and its properties (volume, size, orientation etc.). For investigated alloys at both tested temperatures characteristic for Mg alloys AE count rate peak at the vicinity of yield point is observed. Usually, it has been explained by collective dislocation motion of dislocation (Heiple and Carpenter, 1987a) e.g., basal <a> dislocations as the easiest for activation due to lowest CRSS within deformation mechanism for Mg alloys (Bakarian and Mathewson, 1943). With the proceeding of plastic deformation, dislocation density increases and therefore, the free path of moving dislocation decreases, what leads to decrease of AE response. In the case of twinning activity, twin boundaries are also obstacles for freely dislocation movement and propagation of AE. However, it should be noted that twin nucleation itself (including propagation, i.e., growth in length) is an excellent source of AE (Toronchuk, 1977; Heiple and Carpenter, 1987b; Drozdenko et al., 2019) producing burst events with high amplitude, while twin growth (twin thickening) does not produce detectable AE (Vinogradov et al., 2016; Drozdenko et al., 2019). It was explained by the fact that the twin propagation is several order faster process than the twin growth (Vinogradov et al., 2016). At the same time, statistical analysis of AE signal in Mg-LPSO alloys has shown that kinking has similar characteristics to twinning (Garcés et al., 2018) and it can be also a source of burst high amplitudes AE events. Therefore, observed high amplitude burst AE events originate in twin nucleation and kinking. Moreover, recently Vinogradov et al. (2019) proposed a phenomenological approach for explanation the origin of AE count rate maximum around yielding through the relationship between AE power and dislocation density during dislocation-mediated plastic deformation in some face-centered cubic metals with different stacking fault energies. Thus, dislocation kinetics in investigated Mg-LPSO alloys in present work can explain the appearance of AE peak already before yielding.

The AE data analysis presented here does not allow to separate the signals from the different sources. Nevertheless, it can serve as an indicator of the onset of the particular deformation mechanisms. In the case of the S32 alloy deformed at both RT and 200°C, the strong AE at low stresses is connected with the twinning. The twin nucleation starts in the non-recrystallized grains and continues in small recrystallized one. Grain size dependence of twin nucleation studied by AE have been reported previously for Mg- (Dobron et al., 2011; Drozdenko et al., 2016) and Mg-LPSO alloys (Garcés et al., 2018). In case of S32 alloy deformed at RT, the maximum of AE count rate around 150 MPa (**Figure 5A**), whereas the lattice strain relaxation takes place in Mg phase grains above 300 MPa (**Figure 6A**). Later, a decrease

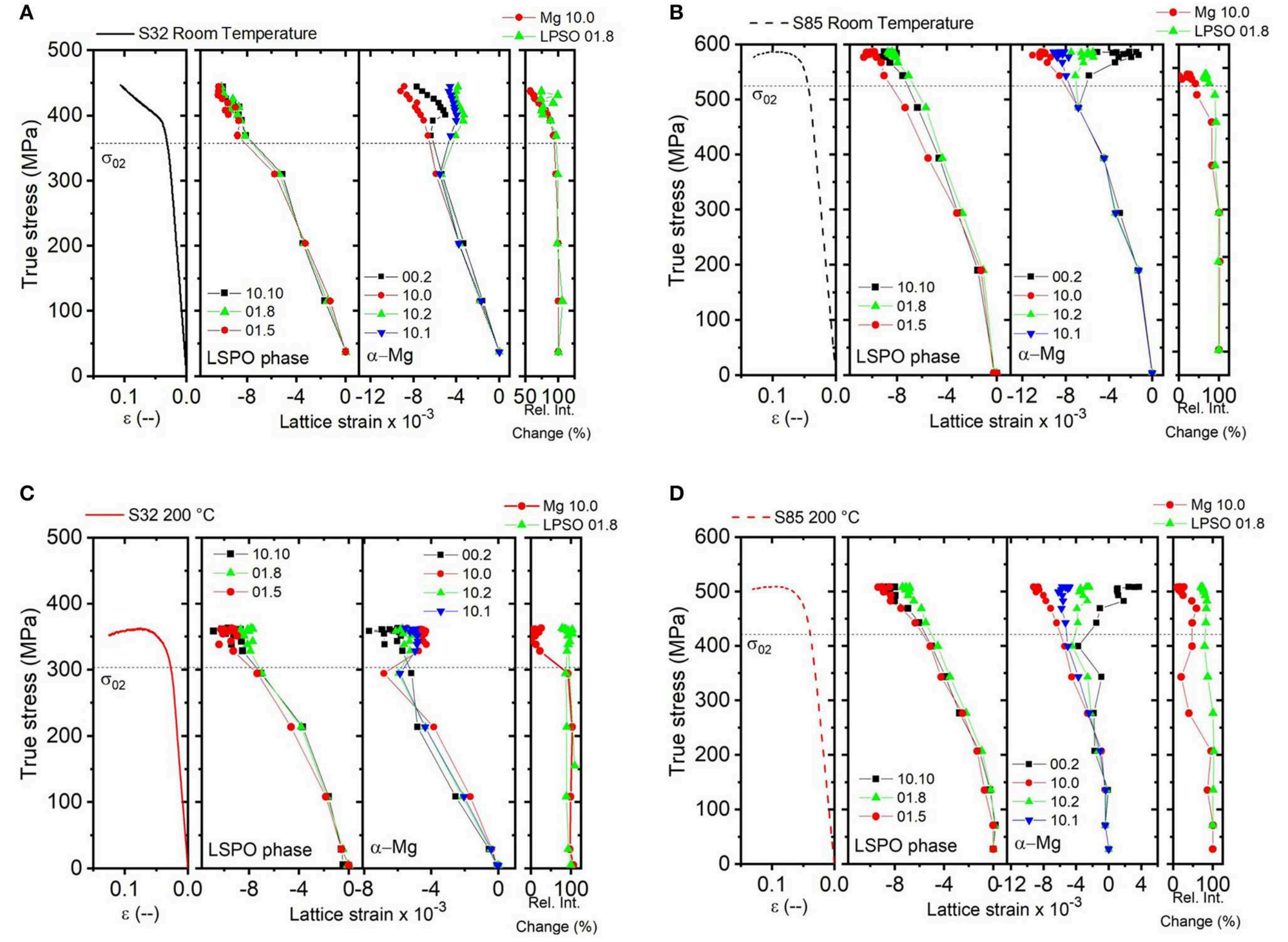

FIGURE 6 | Macroscopic stress-strain curves, the axial lattice strains as a function of the applied stress and evolution of the intensity of the major diffracted peaks of the α-Mg and LPSO phase during compression loading of the S32 and S85 alloy at RT **(A,B)** and at 200°C (**C,D**, respectively).

of AE count rate begins around 300 MPa, where the intensity of the {10.0} peak connected with the twinning starts to change. This difference in the detection of the twinning by AE and ND can be explained as follows: the AE can detect signal from a very low number of twins (2-3) even in bulk specimen. However, as it was mentioned above only the twin nucleation can be detected by AE. In contrast, the ND detect only twin growth and owing to the uncertainty in diffraction peak determination a larger specimen volume has to be twinned in order to reveal the twin growing process. Consequently, since these two methods detect the various stage of the twinning process, the appearance of its contribution in AE and ND results are shifted (AE count rate peak appears before a characteristic change in ND data). Finally, the results of AE and ND measurements are supported by microstructure observation (**Figure 4A**) showing highly twinned microstructure in S32 alloy deformed at RT.

During deformation at a higher temperature, recrystallization and twinning are active concurrently. In this case, twins can be a nucleus for the recrystallization process (Basu and Al-Samman, 2015, 2017; Guan et al., 2019). In Mg-LPSO alloys a particle-stimulated nucleation (PSN) process can control the recrystallization process (Oñorbe et al., 2012). With increasing temperature CRSS for other deformation mechanisms decreasing, therefore, twinning loses its dominance. Suppressed twining activity at higher temperature results in decreased AE count rate maximum (**Figure 5C**). Moreover, the decrease in AE response with increasing testing temperature is a commonly observed phenomenon in Mg alloys (Mathis et al., 2006) and can be explained by temperature promoted activation of other deformation mechanisms. It should be admitted, that with increasing deformation temperature, progressed kinking can be observed in S32 alloy. It is supposed that temperature promoted dislocation slip stimulates kinking.

Owing to the initial texture the basal slip is difficult for both alloys. In case of S32 alloy with majority α-Mg grains, twinning as an additional deformation mechanism plays an important role in plastic deformation. In Mg alloys with a high volume fraction of LPSO twinning is rather rarely observed (Kishida et al., 2014). Therefore, in our S85 alloy with 85% of LPSO twinning is not expected deformation mechanism. In this case, high stress concentration is necessary for another than basal slip initiation—most probably prismatic slip. The prismatic slip in S85 alloy causes crystal rotation of basal planes toward the axial detector (Mayama et al., 2011). It can explain the deviation of LPSO peaks already before yielding (**Figure 6B**). Further, the first order {10.1}<1-1.3> pyramidal slip becomes active, which causes peak shift and deviation of lattice strain of {10.10} LPSO peak. As it was shown by Matsumoto et al. (2013), the pyramidal slip activates basal slip, which finally leads to kinking. Thus, load transfer from the α-Mg matrix in S32 alloy to the LPSO phase in S85 alloy: from twinning to kinking as a dominant deformation mechanism, defines the mechanical properties of the investigated alloys, particularly higher YS in S85 comparing to S32 alloy. Kinking requires collective movement of a large number of basal dislocations (Hagihara et al., 2010b), thus it is followed by high emission of elastic waves. Consequently, kinking can explain a gradual change of lattice strain of LPSO peaks as well as concurrently recorded high amplitude AE. At the same time, owing to the kinking process, the diffracted planes come out from their Bragg position and the relative intensity of {01.8} LPSO peak decreases.

The similar tendency is observed at the deformation of S85 alloy at 200°C. However, changes in relative intensity of {10.0} Mg peak and {01.8} LPSO peak become significant at lower stress values comparing with RT test. It should be noted that the change in {10.0} Mg peak at 200 MPa does not relate to twinning activity, but to kinking. Therefore, it can be concluded that indeed temperature promoted dislocation slip stimulates kinking. Similar to S32 alloy, recrystallization also takes a place. The non-basal slip plays here an important role, and more detailed analysis of diffraction and AE data is necessary.

Obtained results show that temperature promoted changes in the dominant activity of deformation mechanisms (promoted dislocation slip and kinking, suppression of twinning) result in only moderate degradation of mechanical properties with increasing temperature. For instance, the S32 alloy with 32% of LPSO exhibits yield stress of 305 MPa, what is still acceptable value for Mg alloys. It stimulates further investigation of Mg-LPSO alloys as potential material for usage at high temperature.

CONCLUSIONS

The deformation behavior of two Mg-LPSO alloys having 32 and 85% LPSO volume content was investigated by *in-situ* neutron diffraction and acoustic emission methods. The following conclusions can be drawn:

- Temperature increase results in only moderate degradation of mechanical properties;
- load transfer from the α-Mg matrix to the LPSO phase, i.e., from twinning to kinking as a dominant deformation mechanism, defines the mechanical properties of the investigated alloys, particularly higher yield strength in alloys having 85% of LPSO comparing with alloy having 32% of LPSO;
- with increasing temperature recrystallization takes place α-Mg in both materials;
- in Mg-LPSO with 32% of LPSO twinning is the main deformation mechanisms in α-Mg, and with increasing deformation temperature other deformation mechanisms become active at the expense of twinning due to reducing their CRSS;
- kinking is the main deformation mechanism in alloy with 85% of LPSO. Neutron diffraction data indicated that thermally activated dislocation slip is supposed to promote activation of kinking at lower stress.

DATA AVAILABILITY STATEMENT

The datasets analyzed for this study is available from the corresponding author, KM, upon reasonable request.

AUTHOR CONTRIBUTIONS

KM and DD are the authors of the manuscript, performed the experiments, and evaluate the data. GN, SH, WG, and KA contributed to the ND measurements and data evaluation. MY and YK provided the materials.

FUNDING

This research was funded by Czech Science Foundation grant number 18-07140S, and by the JSPS KAKENHI Grant Nos. JP17H03431 and JP18H05476. KM acknowledges the support of the Operational Programme Research, Development and Education, The Ministry of Education, Youth and Sports of Czech Republic (OP RDE, MEYS) [CZ.02.1.01/0.0/0.0/16_013/0001794]. The neutron diffraction experiments at the Materials and Life Science Experimental Facility of the J-PARC was performed under project No. 2018A0183.

ACKNOWLEDGMENTS

The authors acknowledge the help of Dr. Gergely Farkas in ND data evaluation.

REFERENCES

Abe, E., Ono, A., Itoi, T., Yamasaki, M., and Kawamura, Y. (2011). Polytypes of long-period stacking structures synchronized with chemical order in a dilute Mg–Zn–Y alloy. *Philos. Mag. Lett.* 91, 690–696. doi: 10.1080/09500839.2011.609149

Bakarian, P. W., and Mathewson, C. H. (1943). Slip and twinning of magnesium single crystals at elevated temperatures. *Trans. AIME* 152, 226–254.

Basu, I., and Al-Samman, T. (2015). Twin recrystallization mechanisms in magnesium-rare earth alloys. *Acta Mater.* 96, 111–132. doi: 10.1016/j.actamat.2015.05.044

Basu, I., and Al-Samman, T. (2017). Competitive twinning behavior in magnesium and its impact on recrystallization and texture formation. *Mater. Sci. Eng. A* 707, 232–244. doi: 10.1016/j.msea.2017.09.053

Dobron, P., Chmelik, F., Yi, S. B., Parfenenko, K., Letzig, D., and Bohlen, J. (2011). Grain size effects on deformation twinning in an extruded magnesium alloy tested in compression. *Scr. Mater.* 65, 424–427. doi: 10.1016/j.scriptamat.2011.05.027

Drozdenko, D., Bohlen, J., Yi, S., Minárik, P., Chmelík, F., and Dobron, P. (2016). Investigating a twinning–detwinning process in wrought Mg alloys by the acoustic emission technique. *Acta Mater.* 110, 103–113. doi: 10.1016/j.actamat.2016.03.013

Drozdenko, D., Capek, J., Clausen B, Vinogradov, A., and Máthis, K. (2019). Influence of the solute concentration on the anelasticity in Mg-Al alloys: a multiple-approach study. *J. Alloy Compd.* 786, 779–790. doi: 10.1016/j.jallcom.2019.01.358

Egusa, D., and Abe, E. (2012). The structure of long period stacking/order Mg–Zn–RE phases with extended non-stoichiometry ranges. *Acta Mater.* 60, 166–178. doi: 10.1016/j.actamat.2011.09.030

El-Tahawy, M., Máthis, K., Garcés, G., Matsumoto, T., Yamasaki, M., Kawamura, Y., et al. (2019). Type and density of dislocations in a plastically deformed long-period stacking ordered magnesium alloy. *J. Alloy Compd.* 771, 629–635. doi: 10.1016/j.jallcom.2018.08.313

Farkas, G., Máthis, K., Pilch, J., Minárik, P., Lukáš P., and Vinogradov, A. (2017). Deformation behavior of Mg-alloy-based composites at different temperatures studied by neutron diffraction. *Mater. Sci. Eng. A* 685, 284–293. doi: 10.1016/j.msea.2017.01.010

Garcés, G., Máthis, K., Medina, J., Horváth, K., Drozdenko, D., Oñorbe, E., et al. (2018). Combination of in-situ diffraction experiments and acoustic emission testing to understand the compression behavior of Mg-Y-Zn alloys containing LPSO phase under different loading conditions. *Int. J. Plastic.* 106, 107–128. doi: 10.1016/j.ijplas.2018.03.004

Gharghouri, M. A., Weatherly, G. C., Embury, J. D., and Root, J. (1999). Study of the mechanical properties of Mg-7.7at.% Al by in-situ neutron diffraction. *Philos. Mag. A* 79, 1671–1695. doi: 10.1080/01418619908210386

Guan, D., Liu, X., Gao, J., Ma, L., Wynne, B. P., and Rainforth, W. M. (2019). Exploring the mechanism of "Rare Earth" texture evolution in a lean Mg–Zn–Ca alloy. *Sci. Rep.* 9:7152. doi: 10.1038/s41598-019-43415-z

Hagihara, K., Kinoshita, A., Sugino, Y., Yamasaki, M., Kawamura, Y., Yasuda, H. Y., et al. (2010a). Effect of long-period stacking ordered phase on mechanical properties of Mg97Zn1Y2 extruded alloy. *Acta Mater.* 58, 6282–6293. doi: 10.1016/j.actamat.2010.07.050

Hagihara, K., Yokotani, N., and Umakoshi, Y. (2010b). Plastic deformation behavior of Mg12YZn with 18R long-period stacking ordered structure. *Intermetallics* 18, 267–276. doi: 10.1016/j.intermet.2009.07.014

Heiple, C. R., and Carpenter, S. H. (1987a). Acoustic emission produced by deformation of metals and alloys - a review: part I. *J. Acoustic Emission* 6, 177–204.

Heiple, C. R., and Carpenter, S. H. (1987b). Acoustic emission produced by deformation of metals and alloys - a review: part II. *J. Acoust Emission* 6, 215–237.

Inoue, A., Kawamura, Y., Matsushita, M., Hayashi, K., and Koike, J. (2001). Novel hexagonal structure and ultrahigh strength of magnesium solid solution in the Mg–Zn–Y system. *J. Mater. Res.* 16, 1894–1900. doi: 10.1557/JMR.2001.0260

Jono, Y., Yamasaki, M., and Kawamura, Y. (2013). Effect of LPSO phase-stimulated texture evolution on creep resistance of extruded Mg–Zn–Gd Alloys. *Mater. Trans.* 54, 703–712. doi: 10.2320/matertrans.MI201218

Kawamura, Y., Hayashi, K., Inoue, A., and Masumoto, T. (2001). Rapidly solidified powder metallurgy $Mg_{97}Zn_1Y_2$ alloys with excellent tensile yield strength above 600 MPa. *Mater. Trans.* 42, 1172–1176. doi: 10.2320/matertrans.42.1172

Kawamura, Y., Kasahara, T., Izumi, S., and Yamasaki, M. (2006). Elevated temperature Mg97Y2Cu1 alloy with long period ordered structure. *Scr. Mater.* 55, 453–456. doi: 10.1016/j.scriptamat.2006.05.011

Kishida, K., Inoue, A., Yokobayashi, H., and Inui, H. (2014). Deformation twinning in a Mg–Al–Gd ternary alloy containing precipitates with a long-period stacking-ordered (LPSO) structure. *Scr. Mater.* 89, 25–28. doi: 10.1016/j.scriptamat.2014.06.019

Mathis, K., Chmelik, F., Janecek, M., Hadzima, B., Trojanova, Z., and Lukac, P. (2006). Investigating deformation processes in AM60 magnesium alloy using the acoustic emission technique. *Acta Mater.* 54, 5361–5366. doi: 10.1016/j.actamat.2006.06.033

Matsumoto, R., Uranagase, M., and Miyazaki, N. (2013). Molecular dynamics analyses of deformation behavior of long-period-stacking-ordered structures. *Mater. Trans.* 54, 686–692. doi: 10.2320/matertrans.MI201211

Mayama, T., Noda, M., Chiba, R., and Kuroda, M. (2011). Crystal plasticity analysis of texture development in magnesium alloy during extrusion. *Int. J. Plastic.* 27, 1916–1935. doi: 10.1016/j.ijplas.2011.02.007

Oñorbe, E., Garcés, G., Pérez, P., and Adeva, P. (2012). Effect of the LPSO volume fraction on the microstructure and mechanical properties of Mg–Y2X –Zn X alloys. *J. Mater. Sci.* 47, 1085–1093. doi: 10.1007/s10853-011-5899-4

Sillekens, W. H., and Bohlen, J. (2012). "Hydrostatic extrusion of magnesium alloys," in *Advances in Wrought Magnesium Alloys - Fundamentals of Processing, Properties and Applications*, eds C. Bettles and M. Barnett (Sawston, UK: Woodhead Publishing), 323–345.

Toronchuk, J. P. (1977). Acoustic emission during twinning of Zinc single crystals. *Mater. Eval.* 35, 51–53.

Vinogradov, A., Vasilev, E., Seleznev, M., Máthis, K., Orlov, D., and Merson, D. (2016). On the limits of acoustic emission detectability for twinning. *Mater. Lett.* 183, 417–419. doi: 10.1016/j.matlet.2016.07.063

Vinogradov, A., Yasnikov, I. S., and Merson, D. L. (2019). Phenomenological approach towards modelling the acoustic emission due to plastic deformation in metals. *Scr. Mater.* 170, 172–176. doi: 10.1016/j.scriptamat.2019.06.011

Yamasaki, M., Hashimoto, K., Hagihara, K., and Kawamura, Y. (2011). Effect of multimodal microstructure evolution on mechanical properties of Mg–Zn–Y extruded alloy. *Acta Mater.* 59, 3646–3658. doi: 10.1016/j.actamat.2011.02.038

Conflict of Interest: The authors declare that the research was conducted in the absence of any commercial or financial relationships that could be construed as a potential conflict of interest.

ORIGINAL RESEARCH
published: 20 November 2019
doi: 10.3389/fmats.2019.00288

Comparison of the Mechanical Properties and Forming Behavior of Two Texture-Weakened Mg-Sheet Alloys Produced by Twin Roll Casting

José Victoria-Hernández [1]*, ***Sangbong Yi*** [1]*, ***David Klaumünzer*** [2] ***and Dietmar Letzig*** [1]

[1] Magnesium Innovation Centre, Helmholtz-Zentrum Geesthacht, Geesthacht, Germany, [2] Volkswagen AG, Group Research, Materials and Manufacturing Processes, Wolfsburg, Germany

The influence of rolling and annealing on the resulting mechanical properties and forming behavior of Mg-Zn-RE and Mg-Zn-Ca alloys produced via twin roll casting is investigated. After hot rolling followed by an annealing treatment, both alloys develop a fine-grained microstructure with average grain sizes <10 μm. A distinctive development of a texture with a pronounced split of the basal poles in the transverse direction, so called TD-split, is observed in both alloys during the annealing. Due to the fine microstructure and weak texture, which enhances the activation of basal <a> slip, both alloys show large ductility with fracture strain higher than 30%. However, due to the TD-split texture, a high asymmetry of the yield stress is observed, where the yield stress in rolling direction is significantly higher than the yield stress along 45° and the transverse direction. Both alloys show high stretch formability at room temperature with Erichsen index around 7. Despite a low planar anisotropy and high stretch formability, the Mg-Zn-RE alloy shows undesirable earing behavior, while the Mg-Zn-Ca alloy fractures during warm deep drawing. Moreover, the deep drawing operation using the as-rolled sheet of Mg-Zn-RE alloy can be successfully done. It is observed that the earing behavior can be effectively reduced by deviating from the TD-split texture. In this regard, cold rolling was explored to reduce the anisotropy of the ductile and formable alloy.

Keywords: Mg alloys, twin roll casting, rolling, texture, formability, anisotropy

OPEN ACCESS

Edited by:
Maria Teresa Pérez,
Instituto IMDEA Materiales, Spain

Reviewed by:
Somjeet Biswas,
Indian Institute of Technology
Kharagpur, India
Xueze Jin,
Harbin Institute of Technology, China

****Correspondence:***
José Victoria-Hernández
jose.victoria-hernandez@hzg.de
Sangbong Yi
sangbong.yi@hzg.de

Specialty section:
This article was submitted to
Structural Materials,
a section of the journal
Frontiers in Materials

Received: *02 July 2019*
Accepted: *29 October 2019*
Published: *20 November 2019*

Citation:
Victoria-Hernández J, Yi S, Klaumünzer D and Letzig D (2019) Comparison of the Mechanical Properties and Forming Behavior of Two Texture-Weakened Mg-Sheet Alloys Produced by Twin Roll Casting. Front. Mater. 6:288. doi: 10.3389/fmats.2019.00288

INTRODUCTION

For the last two decades, wrought Mg alloys have been in constant development to improve their formability, corrosion resistance and recyclability. In 2001 the forecast of using Mg alloys was positive, especially in the automotive industry (Mordike and Ebert, 2001). So far, the relatively poor formability at low temperatures of wrought Mg alloy has still hindered its extensive use. Ways to improve the formability of Mg alloys, especially at temperatures lower than 200°C (i.e., "low temperature formability"), have been investigated and two approaches are of significant interest. The first approach is the utilization of different thermomechanical treatments to modify the crystallographic texture and, therefore, enhance the potential to activate more deformation modes during forming (Suh et al., 2015). In this regard, severe plastic deformation techniques are effective to enhance the ductility, strength of Mg alloys (Agnew et al., 2004; Biswas et al., 2010, 2013). For instance, it has been shown that alternative processing routes are effective for the enhancement of the microstructure, i.e., grain size and texture, resulting in a decrease anisotropy of Mg alloys (Biswas and Suwas, 2012; Han et al., 2016; Suh et al., 2016). The second approach is the design of the microstructure based on changes in the chemical composition. The use of selected alloying elements has led to significant improvements in the ductility, mechanical properties and formability of wrought Mg alloys (Chino et al., 2008; Al-Samman and Li, 2011; Sandlöbes et al., 2017). Among the elements that have shown the best effects on improving the formability are the rare-earth (RE) elements. RE elements can modify important aspects on the microstructure, e.g., changes in the stacking fault energies (Sandlöbes et al., 2011, 2017), distinctive crystallographic textures (Mackenzie and Pekguleryuz, 2008; Yi et al., 2010), and precipitation which can significantly strengthen the alloys (Liu et al., 2016; Bian et al., 2017). Crystallographic textures of rolled Mg-RE alloys are normally weak and tend to develop a broad scatter of basal poles with two peaks split toward the transverse direction (TD) in (0 0 0 1) pole figure (Mackenzie and Pekguleryuz, 2008). Such textures are linked with an improvement of the low-temperature stretch formability (Chino et al., 2010a; Yi et al., 2010; Al-Samman and Li, 2011; Stutz et al., 2011a). Nevertheless, in recent years, there is a tendency to produce RE-free Mg alloys. In this regard, Ca is an effective element, which can modify the microstructure, crystallographic texture and mechanical properties in a similar way to the Mg-RE alloys (Chino et al., 2010b, 2011; Yuasa et al., 2015; Victoria-Hernandez et al., 2019). Recently, Klaumünzer et al. (2019) showed the potential of using such RE-free alloy sheets produced by twin roll casting (TRC) for the successful production of complex automotive parts for which the forming temperature can be reduced to 160°C.

Despite the good progress in improving the forming capabilities of these alloy systems showing a TD-split texture, there are only a few works dealing with the effect of this distinctive crystallographic texture on the anisotropic forming behavior. Yi et al. (2010) have shown undesirable earing during deep drawing operations of ZE10 alloy at elevated temperature. As an important forming process, deep drawing is of industrial significance and the analysis of the effect of processing parameters on the attenuation of the undesirable earing behavior is of prime importance. In this context, we conducted experiments in order to assess the forming capabilities of the Mg-Zn-RE and Mg-Zn-Ca alloys during deep drawing. Special attention has been paid to the possible reduction of the earing phenomenon by the utilization of strain-hardened blanks used directly after hot and cold rolling, i.e., without a recrystallization heat treatment. The present work gives more insights into the potential of optimizing processing parameters to enhance the forming performance of texture-weakened Mg alloys.

MATERIALS AND METHODS

TRC strips of ZEW200 (1.81Zn-0.1Nd-0.1Ce-0.05La-0.2Y in wt.%) and ZXK (0.6Zn-0.6Ca-0.1Zr in wt.%) alloys with a thickness of 5.3 mm were hot rolled (HR) to the final gauge of 1.8 mm at 400 and 370°C, respectively. The rolling schedule consists of four rolling passes with the first one applying a degree of deformation of $\varphi = 0.25$ (true strain) and $\varphi = 0.3$ for the last three passes. Before the first rolling pass and at intermediate steps, the sheets were heated at the respective rolling temperature for 15 min. After the final rolling pass, the samples were air-cooled. A part of the ZEW200 sheets received two additional cold rolling (CR) passes at room temperature at $\varphi = 0.1$ each. In order to recrystallize the microstructure, ZEW200 samples were annealed at 350°C and ZXK samples at 370°C for 30 min.

Microstructural examination was performed by optical microscopy and electron backscatter diffraction (EBSD) on planes parallel to the normal direction (ND) and the rolling direction (RD). Samples were ground with emery paper (grit 800–2500) and polished with a water free suspension of silicon oxide (OPS 0.5 μm). The polished samples were chemically etched with a picric acid solution (150 ml of ethanol, 40 ml distilled water, 6.5 ml acetic acid and 3–4 g picric acid). The average grain size of the optical microstructures was calculated using the linear intercept method. In the case of EBSD samples, after mechanical polishing, the samples were electropolished using Struers AC2^{TM} solution at 16 V for 70 s at −25°C. EBSD measurements were performed in a field emission gun scanning electron microscope equipped with an EDAX-TSL OIM^{TM} system. An acceleration voltage of 15 kV and a step size of 0.3 μm were used. Energy-dispersive X-ray spectroscopy (EDS) was performed on the mechanically polished samples to reveal the type and chemical composition of the secondary phase particles near the fracture surface in a deep drawn cup.

Quantitative texture measurements were carried out using a Panalytical^{TM} X-ray diffractometer in reflection geometry using Cu-Kα radiation. Six pole figures (0 0 0 1), (1 0 −1 0), (1 0 −1 1), (1 0 −1 2), (1 0 −1 3), and (1 1 −2 0) were measured up to a tilt angle of 70°. The orientation distribution function (ODF) was calculated using the MTEX toolbox (Hielscher and Schaeben, 2008).

Tensile samples were machined according to the standard DIN 50125-H and were tested in a universal testing machine. The tensile tests were performed along the RD, 45° and TD at room temperature, and the Lankford parameter (r_{10}-value) were determined at $\varepsilon = 10\%$. Tensile tests were performed at 10^{-3} s^{-1} of constant strain rate to the fracture. This was ensured by employing a clip-on extensometer that allowed the continuous calibration of the strain rate during the experiment.

Room temperature stretch formability was evaluated by the Erichsen test using an Erichsen^{TM} 145–30 sheet metal testing machine according to the ISO 20482. Molykote^{TM} was used as a lubricant. The punch diameter and test speed were 20 mm and 5 mm/min, respectively. Blanks (diameter of 60 mm) cut from the as-rolled and annealed sheets were used for the tests.

Deep drawing tests were performed in the same Erichsen machine using a punch with the diameter of 50 mm at 100, 150, and 200°C. The test speed and blank holder force were set to 20 mm/min and 5 kN. Blank diameters of 85 and 100 mm were cut from the rolled sheets for two different deep drawing ratios (DR) of 1.7 and 2.0. To minimize friction between the blank, the punch, the walls of the die and the samples were coated with boron nitride spray.

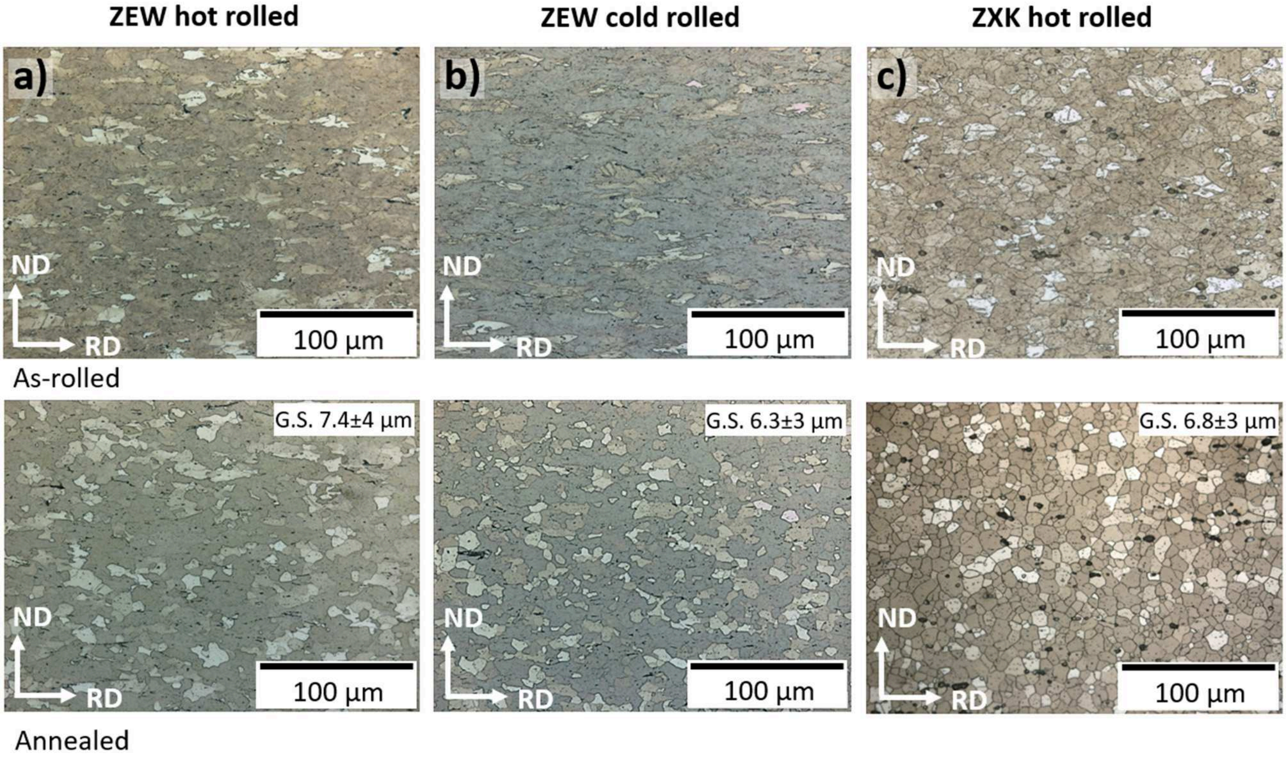

FIGURE 1 | Optical microstructures of **(a)** hot rolled ZEW200 alloy, **(b)** cold rolled ZEW200 alloy, and **(c)** hot rolled ZXK alloy in as-rolled (top) and annealed (bottom) conditions, respectively.

RESULTS AND DISCUSSION

Microstructure

The micrographs of the rolled and annealed sheets are presented in **Figure 1**. In general, the as-rolled microstructures for the three different materials, presented in **Figures 1a–c**, show deformed grains containing twins. As expected, the microstructure of the cold-rolled ZEW200 shows a more deformed grain structure. Such a microstructure is difficult to etch chemically due to the predominance of the preferred crystallographic orientations of the grains. The ZEW200 alloy in both hot and cold rolled conditions show the presence of secondary phase particles distributed homogeneously along with the microstructure. The stinger-like precipitates contain a high amount of Zn, Ce, and Y. The rolled ZXK alloy also shows coarse precipitates. They were identified as Mg_2Ca phase. They are located along grain boundaries. Some of them are fragmented and elongated toward RD, developing stinger-like structures. The microstructure of all annealed sheets show the development of a homogeneous, fine, twin-free and recrystallized microstructure with a grain size below 10 µm.

Texture

Figure 2A depicts the texture of the hot rolled ZEW200 alloy. In the as-rolled condition, the sheet shows a relatively weak deformation texture with an intensity of 4.1 multiples of random distribution (m.r.d.). As a characteristic, two main peaks representing (0 0 0 1) crystallographic planes tilted away from the ND toward RD and the <1 0 −1 0> pole parallel to RD are observed. A broad scatter of basal poles inclined toward the TD is also evident. The annealed sheet shows a weaker texture in comparison to that of the rolled one. Moreover, the transition from the RD-split of the basal pole to a TD-split texture is observed. In this condition, the basal poles are mainly tilted by ∼35° toward the TD. The texture component of <1 0 −1 0> parallel to RD is retained during the annealing. Such a tendency of the texture development, i.e., weak recrystallization texture with the basal pole split into the TD, is ascribed to the activation of non-basal slip systems and retarded recrystallization kinetics in Mg-Zn-RE and Mg-Zn-Ca alloys (Kim et al., 2017; Zeng et al., 2019). Cold rolling strengthens the texture components, which were formed after hot rolling and annealing (see **Figure 2B**). However, no qualitatively different texture development is observed in comparison to the hot rolled sheet.

The deformation texture of the ZXK alloy also shows similar peaks compared to that of the ZEW200 alloy and a broad distribution of basal planes toward TD (see **Figure 2C**). This texture is slightly stronger than the hot rolled ZEW200 alloy. A weaker texture with the basal pole split toward TD is formed after annealing, while a symmetric distribution of the basal poles is observed in a ring-like fashion around the ND, at the tilting angle of ∼37°.

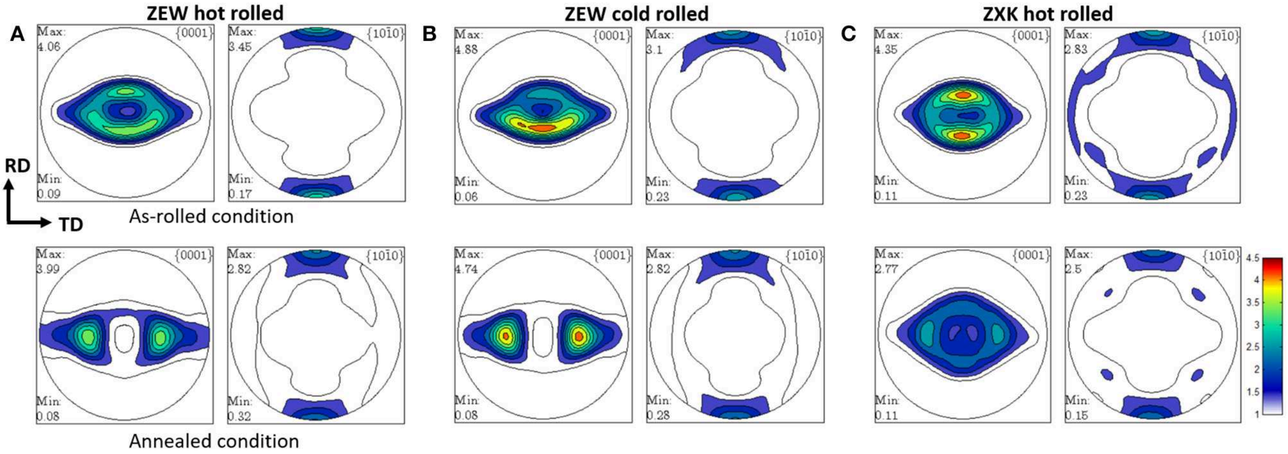

FIGURE 2 | Crystallographic textures in terms of the (0 0 0 1) and (1 0 −1 0) pole figures for the **(A)** hot rolled ZEW200 alloy, **(B)** cold rolled ZEW200 alloy, and **(C)** hot rolled ZXK alloy in as- rolled (top) and annealed (bottom) conditions, respectively.

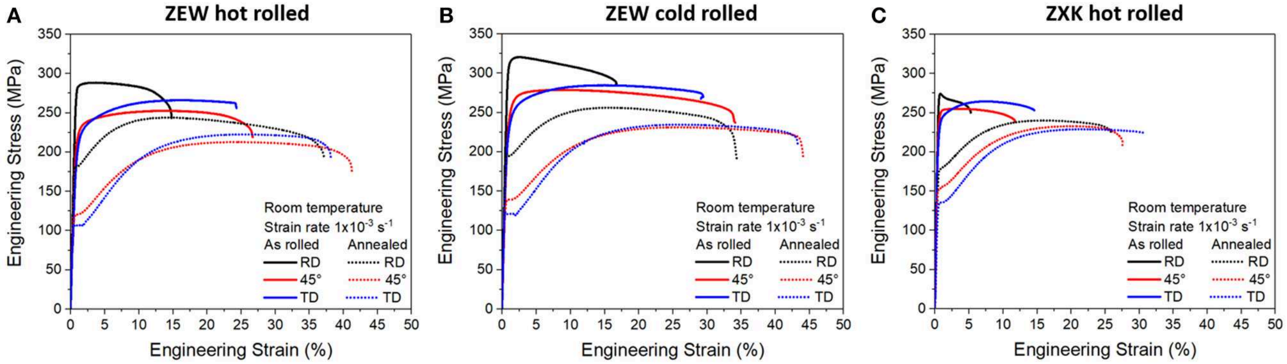

FIGURE 3 | Engineering stress-strain curves for the **(A)** hot rolled ZEW200 alloy, **(B)** cold rolled ZEW200 alloy, and **(C)** hot rolled ZXK alloy in as-rolled and annealed conditions, respectively.

Mechanical Behavior

Figure 3 plots the engineering stress-strain curves of samples in the as-rolled and annealed states. The corresponding tensile properties are listed in **Table 1**. The hot rolled ZEW200 alloy in the as-rolled condition shows an overall high strength level in all planar sheet directions. However, anisotropic behavior is observed with the strength values in the RD being the highest. Interestingly, the ductility is relatively high for a strain-hardened Mg alloy with elongations higher than 20% along both the 45° and TD, and 19% in RD (see **Figure 3A**). After annealing, the sheet shows an increase in ductility along all directions with the fracture strain higher than 35%. The annealed sheets show a distinct yield phenomenon. Various mechanisms of the occurrence of yield phenomenon in Mg alloys have been reported, e.g., twinning (Barnett et al., 2012), activity of non-basal slip (Koike et al., 2003) or dislocation interaction with solute atoms (Zhang et al., 2010). A high planar anisotropy is observed also in the annealed sheets. The sample tested parallel to the RD shows high strength and rapid work hardening in comparison to 45° and TD samples. The cold rolled samples in the as-rolled state show even higher strength, exceeding 300 MPa in the RD. Surprisingly, a drop in the ductility is not observed when contrasted to the hot rolled samples. The material remains ductile in all directions as shown in **Figure 3B**. The annealed samples after the cold rolling show a high planar anisotropy, while an increase in ductility is observed (larger than 40% along 45° and TD). The improvement of mechanical properties can be mainly attributed to the grain refinement as displayed in **Figure 1b**, since the texture is rather similar to the hot rolled sheets.

Recently Shi et al. (2019) have reported the possibility to reduce the planar anisotropy of Mg-Zn-Y-Zr alloy sheets by applying the final rolling pass with a high reduction degree. It was shown that the anisotropic effect of the TD-split texture was attenuated by increasing the deformation and controlling the post-annealing. In the present study, however, the reduction in the planar anisotropy determined by tensile tests was not observed even after cold rolling.

In contrast to the behavior of the ZEW200 alloy, the ZXK alloy shows a more moderate planar anisotropy, where the

TABLE 1 | Tensile properties at room temperature of as-rolled and annealed samples tested along RD, 45° to RD and TD (YS, tensile 0.2% yield stress; UTS, ultimate tensile stress, ε_u, uniform elongation; ε_f, elongation to fracture, r_{10} Lankford parameter).

		YS (MPa)	**UTS (MPa)**	ε_u **(%)**	ε_f **(%)**	r_{10}**-value**	$\bar{r}$	Δr
ZEW HR AR	RD	270 ± 2	288 ± 2	3	19	1.1 ± 0.1*	0.88	0.15
	45°	197 ± 3	250 ± 2	13	26	0.8 ± 0.1		
	TD	190 ± 5	266 ± 2	16	20	0.8 ± 0.1		
ZEW HR Annealed	RD	181 ± 4	244 ± 4	14	33	1.2 ± 0.1	0.85	−0.10
	45°	118 ± 4	215 ± 3	22	40	0. 9 ± 0.1		
	TD	106 ± 3	221 ± 4	24	35	0.4 ± 0.1		
ZEW CR AR	RD	298 ± 2	320 ± 4	2	16	0.6 ± 0.1*	0.88	−0.45
	45°	220 ± 3	282 ± 2	8	33	1.1 ± 0.1*		
	TD	205 ± 3	286 ± 2	14	27	0.7 ± 0.1		
ZEW CR Annealed	RD	197 ± 3	257 ± 2	15	33	0.7 ± 0.1	0.80	−0.40
	45°	134 ± 3	231 ± 2	25	43	1.0 ± 0.1		
	TD	121 ± 2	232 ± 3	26	42	0.5 ± 0.1		
ZXK AR	RD	255 ± 2	276 ± 2	1	8	1.1 ± 0.1*	1.10	−0.20
	45°	217 ± 3	255 ± 2	5	19	1.2 ± 0.1*		
	TD	200 ± 2	265 ± 2	12	23	0.9 ± 0.1		
ZXK HR Annealed	RD	174 ± 3	239 ± 3	16	25	0.9 ± 0.1	0.98	−0.25
	45°	152 ± 3	232 ± 2	19	27	1.1 ± 0.1		
	TD	135 ± 2	226 ± 2	21	31	0.8 ± 0.1		

**r-value measured at* $\varepsilon_u < 10\%$.

differences in yield stress, UTS and fracture strain are generally smaller compared to the ZEW alloy (see **Figure 3C**). The reduced anisotropy at the annealed state is to be related to the texture of the ZXK alloy and the relatively uniform scatter of basal planes, which develop a ring of basal poles around the ND.

The *r*-values strongly vary upon heat treatments. Especially for ZEW200 alloy along the TD, the *r*-value decreases after annealing, which can be related to the development of a more pronounced TD-split in the texture (see **Figures 2A,B**). The average $\bar{r}$-values and planar anisotropy Δr were calculated at each condition, according to the following relationships:

$$\bar{r} = \frac{(r_{RD} + r_{TD} + 2r_{45})}{4}$$

$$\Delta r = \frac{(r_{RD} + r_{TD} - 2r_{45})}{2}$$

where r_{RD}, r_{45}, r_{TD} are the *r*-values determined in RD, 45° to RD and TD, respectively. The calculated values are listed in **Table 1**. It is observed that the $\bar{r}$-values of the ZEW200, even after the cold rolling, are lower than those of the ZXK alloy. These results indicate that the material flow in the thickness direction is easier in the ZEW200, while the ZXK sheets with the $\bar{r}$-values close to 1 show a comparable material flow in the thickness and width directions. The uniform distribution of basal planes with a ring-fashioned texture in the ZXK sheet leads to a reduction of the anisotropy, and less pronounced earing is expected during deep drawing. Based on the magnitude of planar anisotropy (Δr), e.g., $\Delta r = -0.10$ and -0.25 in the annealed ZEW200 HR and ZXK HR sheets, respectively, the ZXK alloy would have a higher propensity of earing. However, the *r*-values of the ZEW200 sheet show a higher variation along the sheet planar direction, comparing to those measured from the ZXK sheet. Such inconsistency results from the fact that the planar anisotropy in Mg alloys is different to that in the cubic structured materials.

For example, Yi et al. (2010) reported that the earing is observed at 60° to the RD of a deep drawn cup of ZE10 sheet, such that the asymmetric deformation behavior of Mg alloy sheets would not be completely expressed by the r-values measured at the RD, TD, and 45° to the RD. It should be noted that the r-value analysis in the present study corresponds to an approximate estimate, as the r-values of some samples were determined at rather low uniform strain, e.g., samples marked with asterisk.

Formability

Erichsen Tests

To evaluate the stretch formability at room temperature, Erichsen tests were performed using blanks in as-rolled and annealed conditions. Samples after Erichsen tests are shown in **Figure 4**. Even in the as-rolled condition, the hot rolled ZEW200 alloy showed a relatively high Erichsen index (IE) of 5.1. The IE of the ZEW200 alloy increases in the annealed condition to 7.4 (see **Figure 4a**). Upon cold rolling, the stretch formability for the as-cold rolled ZEW200 alloy decreases to the IE of 3.1, which increases significantly after annealing to the IE of 8.4. This is one of the highest values recorded for conventionally rolled Mg alloys and it shows the potential to improve the sheet formability by means of altering the processing route, such as cold rolling.

For the hot rolled ZXK alloy the average IE of 3.7 and 6.2 were obtained at the as-rolled and annealed conditions, respectively. Despite the fact that the ZXK alloy showed the lowest texture intensity and a ring scatter of basal poles around the ND in

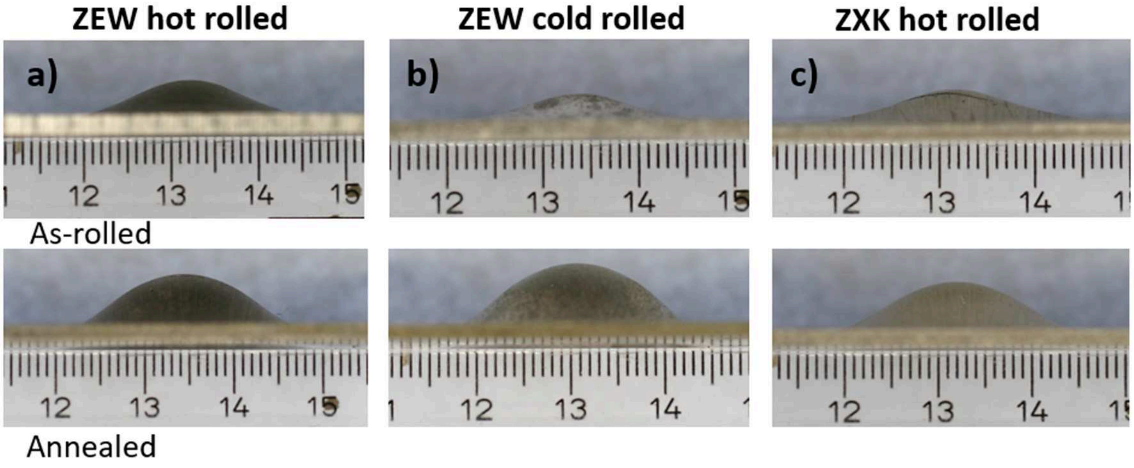

FIGURE 4 | Samples after Erichsen test **(a)** hot rolled and **(b)** cold rolled ZEW200 alloy, **(c)** hot rolled ZXK alloy. Samples tested in as-rolled (top) and annealed (bottom) conditions, respectively.

the annealed condition, the recorded IE is lower than those of annealed ZEW200 alloy. Other microstructural factors, such as the presence of Mg_2Ca particles and Mg oxides, could be related to the crack initiation or ease propagation during stretch forming. Nevertheless, the present results confirm that the stretch formability at room temperature is enhanced with the formation of the characteristic TD-split texture in the Mg-Zn-RE and Mg-Zn-Ca alloys.

Deep Drawing at Warm Temperatures

The deep drawability of the hot rolled and annealed ZEW200 and ZXK alloys was assessed at 100, 150, and 200°C and a DR of 1.7. Representative samples deformed at these conditions are displayed in **Figure 5**. In the case of the ZEW200 alloy, deep drawing can be successfully conducted at 100°C (see **Figure 5a**). There is, however, the development of fractures, which occurred at the top part of the wall of the sample. Yi et al. (2010) have attributed the development of these kinds of defects to the non-optimized process parameters, such as blank holder force or clearance. In addition, the temperature gradient in the sample during the test could affect the sample thickening toward the top area of the cup wall, leading to increased friction between the sample and the die (Ghosh et al., 2014). Yet, the present result supports that the deep drawing is feasible at 100°C, if the parameters are properly adjusted. By increasing the temperature, successfully drawn cups are obtained. There is the development of slight earing on both cups, which seem to be similar in number (4), height and position (∼63° to RD). This undesirable phenomenon seems to be independent on the forming temperature.

Despite the good stretch formability shown at room temperature by the ZXK alloy, the deep drawability is rather poor. Samples deformed at 100°C develop catastrophic failures at the shoulder of the cup, which propagates to the flange of the cup. This behavior is also observed for samples deformed at 150°C. In contrast, samples deformed at 200°C showed slightly better behavior in comparison to the previous two cases. Yet, fractures at the top of the wall are observed (see **Figure 5b**). This result is interesting, considering that both alloys have a similar initial microstructure, i.e., grain size and, in principle, crystallographic texture. It is found, however, that coarse precipitates of Mg_2Ca and oxides seem to have relationship with the brittle behavior at warm temperatures of the ZXK alloy. **Figure 6a** depicts an optical micrograph of a polished sample; it shows a fracture front of a sample drawn at 150°C. The approximate position of the analysis is marked with the white-filled arrow in **Figure 5**. The accumulation of particles is found at the crack front, marked as dotted square in **Figure 6a**. An SEM-image at this area shows the fragmentation of such particles (see **Figure 6b**). An element mapping using EDX showed that those particles mainly consist of Ca and O (see **Figures 6c,d**). The presence of those elements correlate well with high amount of hard and brittle Mg_2Ca Laves phase, in addition to the presence of MgO and/or CaO. The fragmentation and respective void formation around these particles are, therefore, related to the ease nucleation and propagation of crack during the warm deep drawing of the ZXK alloy. It was reported in Jahedi et al. (2018) that the shearing of eutectic particles and concomitant void formation lead to catastrophic failure of WE43 alloy. In such work it is discussed the more influential effect of void formation (due to particle shearing) than the texture effect during deformation. The fragmentation of particles, e.g., Mg_2Ca and oxides, and resulting void formation can be also correlated with the lower IE of ZXK alloy in the present study.

In order to gain more insight into the deformation behavior of the examined alloys, the microstructure at the wall was analyzed by means of EBSD. **Figure 7** exhibits the EBSD orientation maps of samples deformed at 100 and 200°C of the ZEW200 and ZXK alloys. The approximate position of the measurement is marked by the dotted squares in **Figure 5**. The ZEW200 sample deformed at 100°C presents a highly deformed microstructure with the presence of twins (**Figure 7A**). The

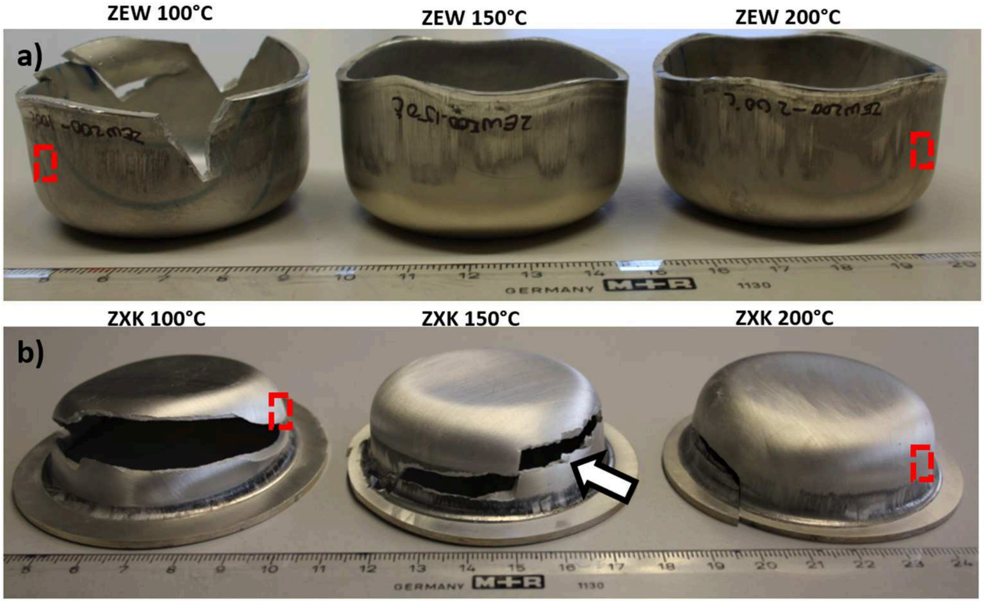

FIGURE 5 | Deep drawn cups formed at different temperatures with a DR = 1.7. **(a)** Hot rolled and annealed ZEW200 alloy and **(b)** hot rolled and annealed ZXK alloy.

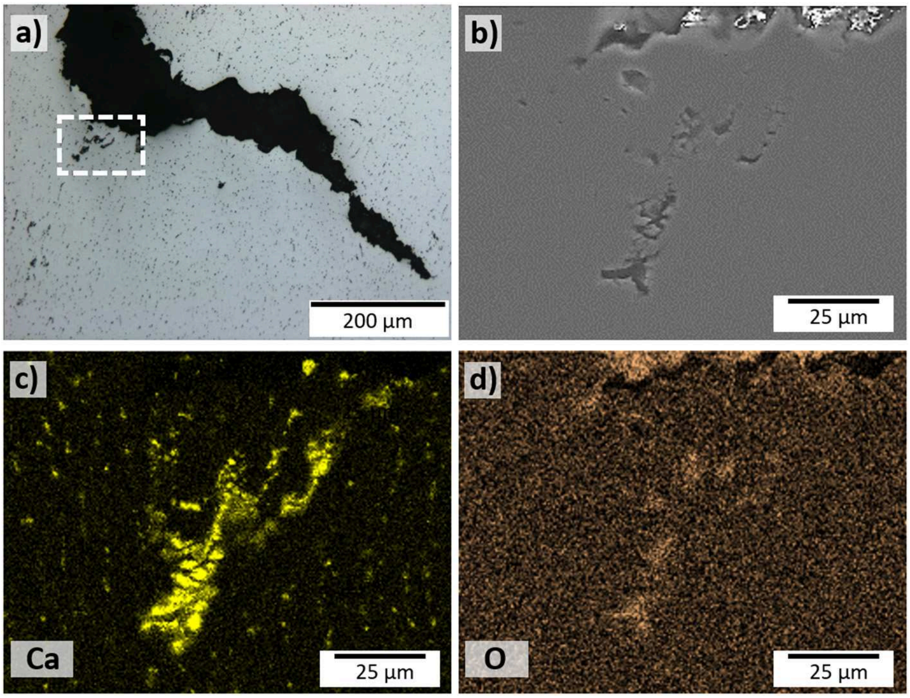

FIGURE 6 | (a) Optical micrograph showing a close up near the fracture front indicated by the white arrow in **Figure 5b**, **(b)** SEM micrograph showing an enlarged area of interest inscribed in the dashed rectangle in **(a)**, and EDX chemical element mapping of the same area for **(c)** calcium and **(d)** oxygen.

identified twinning mode mainly corresponds to {1 0 −1 2} extension twins covering an area fraction of around 7.4%. Other detected twinning modes, such as {1 0 −1 1} contraction twins and {1 0 −1 1}–{1 0 −1 2} secondary twins are seldom detected and the area fraction covered by these two systems is <1%. A strengthening of the texture toward basal type texture is also observed. Tests conducted at 200°C show similar microstructures (**Figure 7B**). The extension twin fraction is also high, covering about 6.5% of the microstructure. In this case, there is the tendency to strengthen the texture but the broad scatter of basal planes toward TD is still high. Yi et al. (2010) explained this phenomenon by the profuse activation of prismatic <a> slip.

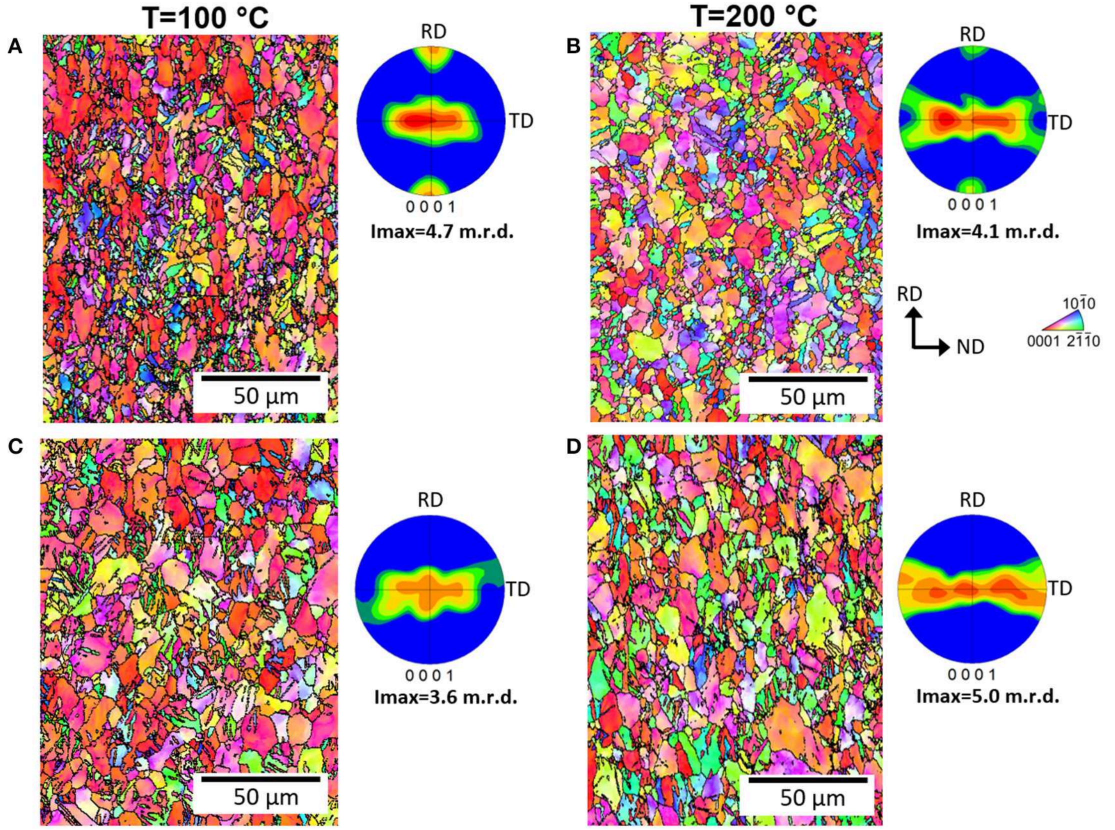

FIGURE 7 | EBSD orientation maps at the cup walls of **(A)** hot rolled and annealed ZEW200 alloy deep drawn at 100°C, **(B)** hot rolled and annealed ZEW200 alloy deformed at 200°C, **(C)** annealed ZXK alloy deformed at 100°C and **(D)** annealed ZXK alloy deformed at 200°C. Approximate positions of the EBSD measurements are indicated by dotted squares in **Figure 5**.

Despite the significantly lower deformation degree attained by the ZXK samples, a similar tendency in microstructure and texture development is observed. That is, {1 0 −1 2} extension twins are profusely activated, and a basal type texture develops at 100°C, while the broad scatter of basal planes toward TD is formed at 200°C (see **Figures 7C,D**, respectively). The present result once again shows the similarities of the involved deformation mechanisms in both alloys. Therefore, it might be feasible to improve the formability of the ZXK alloy by optimization of the alloy composition and processing parameters to control the amount, size and distribution of the brittle Mg_2Ca particles.

The earing behavior of the cold rolled ZEW200 alloy was investigated by using the blanks of 100 mm in diameter at 200°C (DR = 2) in the as-rolled and annealed conditions. Representative drawn cups are shown in **Figure 8**. Cups could be drawn fully using blanks even in the as-rolled condition. Moreover, the earing behavior is reduced by the use of the blanks in the as-rolled conditions, **Figures 8a,c**. To describe the degree of earing, the average percentage of earing height (Z) was calculated according to the following equation. This equation, which is capable of describing earing even if local asymmetry occurs, is used based on the position of the ears which are not located at 0, 45, or 90° as it normally occurs in metals with cubic structure (Yi et al., 2010).

$$\boldsymbol{Z} = \left[\left[\sum_{\boldsymbol{i}}^{\boldsymbol{n}} \left(\frac{(\boldsymbol{h}_{\boldsymbol{i}_{\max}} - \boldsymbol{h}_{\boldsymbol{i}_{\min}})}{\mathbf{0.5}(\boldsymbol{h}_{\boldsymbol{i}_{\max}} - \boldsymbol{h}_{\boldsymbol{i}_{\min}})} \right)\right] / \boldsymbol{n} \right] \times \mathbf{100}\ (\%)$$

where n is the number of ears in the drawn cup, and h is the height at the peak and valleys of each ear observed in the drawn cup. The earing degrees (Z) of the hot rolled sheet is 9.7% in the as-rolled condition and 15.9% after annealing. A similar tendency is observed in the cold rolled sheet, where Z for the as-rolled sheet is 9.9% and increases to 16.8% after annealing. This means that cold rolling can strengthen the material (as observed in **Figure 3**), and increases the anisotropic behavior after annealing, e.g., increase in the earing behavior.

Analogous to the analysis presented in **Figure 7**, the microstructures at the wall of the successfully drawn cups deformed at 200°C using hot/cold as-rolled sheets of the ZEW200 alloy are presented in **Figure 9**. The approximate positions of the EBSD measurements are marked with the red dashed rectangles in **Figure 8**. A highly deformed microstructure is found in both cases, where most of the grains are elongated parallel to the drawing direction. The formation of shear bands

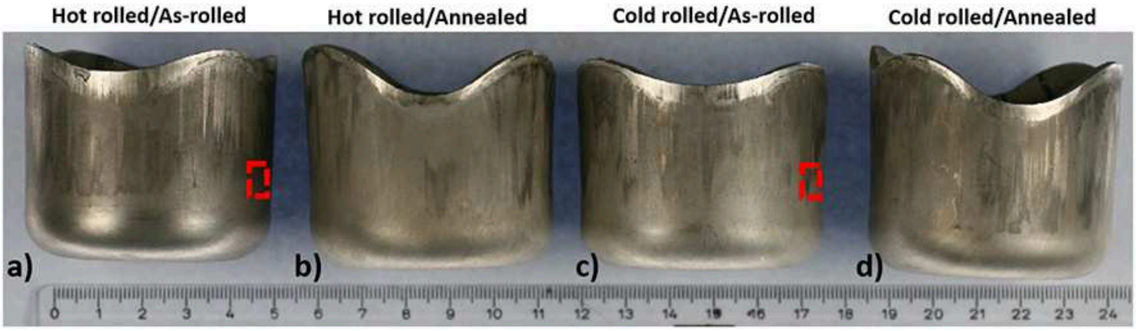

FIGURE 8 | Deep drawn cups made out ZEW200 alloy deformed at 200°C with a DR = 2.0. **(a)** hot rolled/as-rolled condition, **(b)** hot rolled/annealed condition, **(c)** cold rolled/as-rolled condition, and **(d)** cold rolled/annealed condition.

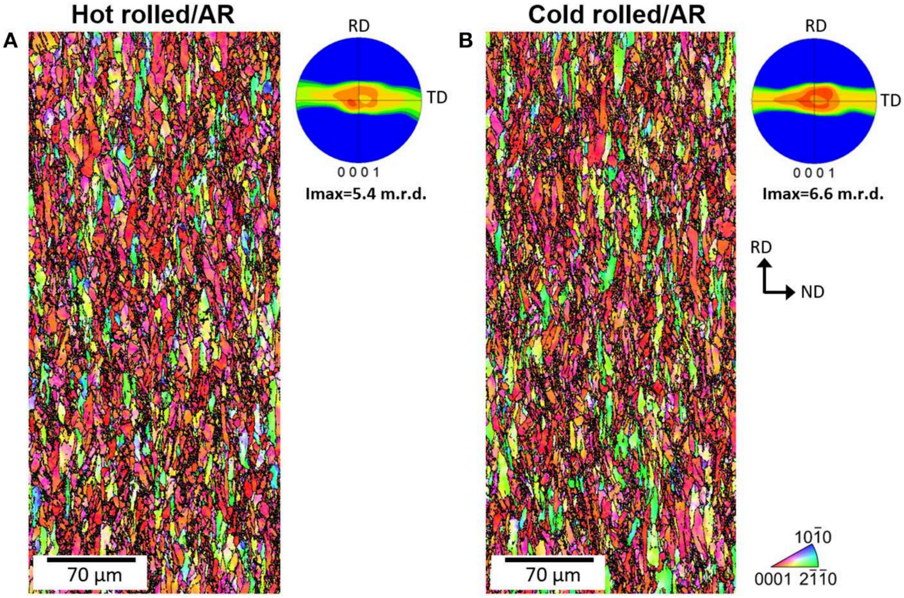

FIGURE 9 | EBSD orientation maps of deep drawn cups made out ZEW200 alloy with a DR = 2.0. **(A)** Hot rolled/as-rolled condition and **(B)** cold rolled/as-rolled condition. The approximate position of the EBSD measurement indicated by the red-dotted squares in **Figure 8**.

around the deformed grains is also evident. It is to note that the amount of recrystallized grains is maintained to a minimum despite the use of a strain hardened materials. These results indicate that the deformation is mainly accommodated by dislocation slip (in this case is hard to identify twin boundaries in the OI maps) and dynamic recovery, rather than dynamic recrystallization. This is one of the main differences compared to the deep drawing behavior of conventional AZ31 alloy, where dynamic recrystallization is an important softening mechanism that enhances the drawability at temperatures around 200°C (Yi et al., 2010; Stutz et al., 2011b). As observed in the local texture of these two as-rolled ZEW200 deformed samples, the texture is more strengthened in the as-cold rolled sheet. This could be one of the reasons for the slightly higher anisotropy as calculated by the Z factor as discussed above.

SUMMARY

A comparative study of the mechanical behavior, room temperature stretch formability and warm drawability of Mg-Zn-RE and Mg-Zn-Ca alloys with TD-split texture were carried out. Main conclusions are drawn below:

1. Upon hot rolling and subsequent annealing, both ZEW200 and ZXK alloys develop fine-grained microstructures and the so-called TD-split texture is found. By performing cold rolling in the ZEW200 the microstructure can be refined further and a stronger deformation texture than the counterpart hot rolled sheet is observed.

2. The hot/cold rolled ZEW200 alloys show high strength and high ductility. The annealing of the cold rolled sheets improves the ductility and strength in the ZEW200 alloy, whereas a high

yield stress asymmetry is observed. The ZXK alloy showed a moderate anisotropy due to its ring-fashioned texture.

3. The hot/cold rolled ZEW200 alloys show a high stretch formability, even in the as-rolled condition. The Erichsen index of 8.4 was attained for the annealed ZEW200 sheet after cold rolling. The ZXK alloy also showed good stretch formability, but IE values are lower than those of ZEW200 alloy.

4. The ZXK alloy shows a poor warm drawability. This is related to the fragmentation of hard and brittle Mg_2Ca and oxide particles with the concomitant void formation and crack propagation. On the other hand, the ZEW200 alloy shows an excellent deep drawability, even though a high anisotropy is observed. The earing behavior of this alloy was attenuated by using blanks without annealing. Analysis of the deformed microstructure indicated a profuse activity of dislocation slip during the deep drawing of the as-rolled sheets. As a softening mechanism, dynamic recovery seems to be important as the occurrence of dynamic recrystallization is not observed. It is concluded that the suppression of the TD-split texture can be an effective way to reduce anisotropic behavior of these ductile Mg alloys.

DATA AVAILABILITY STATEMENT

The datasets of this investigation cannot be shared at this moment, since they are part of an on-going investigation.

AUTHOR CONTRIBUTIONS

The study was conceived and designed by JV-H and SY. All authors took part in the discussion about the results. The manuscript was prepared by JV-H, and reviewed and edited by SY, DK, and DL. All authors approved the manuscript.

FUNDING

This work was partly financed by Volkswagen AG (Germany) and POSCO (South Korea).

ACKNOWLEDGMENTS

The technical assistance of Alexander Reichert, Guadalupe Cano-Castillo, and Deik Petersen at Helmholtz-Zentrum Geesthacht is gratefully acknowledged.

REFERENCES

Agnew, S. R., Horton, J. A., Lillo, T. M., and Brown, D. W. (2004). Enhanced ductility in strongly textured magnesium produced by equal channel angular pressing. *Scripta Mater.* 50, 377–381. doi: 10.1016/j.scriptamat.2003.10.006

Al-Samman, T., and Li, X. (2011). Sheet texture modification in magnesium based alloys by selective rare earth alloying. *Mater. Sci. Eng. A* 528, 3809–3022. doi: 10.1016/j.msea.2011.01.080

Barnett, M., Nave, M. D., and Ghaderi, A. (2012). Yield point elongation due to twinning in a magnesium alloy. *Acta Mater.* 60, 1433–1443. doi: 10.1016/j.actamat.2011.11.022

Bian, M. Z., Sasaki, T. T., Suh, B. C., Nakata, T., Kamado, S., and Hono, K. (2017). A heat treatable Mg-Al-Ca-Mn-Zn sheet alloy with good room temperature formability. *Scripta Mater.* 138, 151–155. doi: 10.1016/j.scriptamat.2017.05.034

Biswas, S., Beausir, B., Toth, L., and Suwas, S. (2013). Evolution of texture and microstructure during hot torsion of a magnesium alloy. *Acta Mater.* 61, 5263–5277. doi: 10.1016/j.actamat.2013.05.018

Biswas, S., Dhinwal, S. S., and Suwas, S. (2010). Room temperature equal channel angular extrusion of pure magnesium. *Acta Mater.* 58, 3247–3261. doi: 10.1016/j.actamat.2010.01.051

Biswas, S., and Suwas, S. (2012). Evolution of sub-micron grain size and weak texture in magnesium alloy Mg-3Al-0.4Mn by a modified multi-axial forging process. *Scripta Mater.* 66, 89–92. doi: 10.1016/j.scriptamat.2011.10.008

Chino, Y., Huang, X., Suzuki, K., and Mabuchi, M. (2010b). Enhancement of stretch formability at room temperature by addition of Ca in Mg-Zn alloy. *Mater. Trans.* 51, 818–821. doi: 10.2320/matertrans.M2009385

Chino, Y., Huang, X., Suzuki, K., Sassa, K., and Mabuchi, M. (2010a). Influence of Zn concentration on stretch formability at room temperature of Mg-Zn-Ce alloy. *Mater. Sci. Eng. A* 528, 566–572. doi: 10.1016/j.msea.2010.09.081

Chino, Y., Kado, M., and Mabuchi, M. (2008). Enhancement of tensile ductility and stretch formability of magnesium by addition of 0.2 wt% (0.035 at%) Ce. *Mater. Sci. Eng. A* 494, 343–349. doi: 10.1016/j.msea.2008.04.059

Chino, Y., Ueda, T., Otomatsu, Y., Sassa, K., Huang, X., Suzuki, K., et al. (2011). Effects of Ca on tensile properties and stretch formability at room temperature in Mg-Zn and Mg-Al alloys. *Mater. Trans.* 52, 1477–1482. doi: 10.2320/matertrans.M2011048

Ghosh, M., Miroux, A., Werkhoven, R. J., Bolt, P. J., and Kestens, L. A. I. (2014). Warm deep drawing and post drawing analysis of two Al-Mg-Si alloys. *J. Mater. Proc. Tech.* 214, 756–766. doi: 10.1016/j.jmatprotec.2013.10.020

Han, T., Huang, G., Wang, Y., Wang, G., Zhao, Y., and Pan, F. (2016). Enhanced mechanical properties of AZ31 magnesium alloy sheets by continuous bending process after V-bending. *Prog. Nat. Sci. Mater.* 26, 97–102. doi: 10.1016/j.pnsc.2016.01.005

Hielscher, R., and Schaeben, H. (2008). A novel pole figure inversion method: specification of the MTEX algorithm. *J. Appl. Crystallogr.* 41, 1024–1037. doi: 10.1107/S0021889808030112

Jahedi, M., McWilliams, B. A., and Knezevic, M. (2018). Deformation and fracture mechanisms in WE43 magnesium-rare earth alloy fabricated by direct-chill casting and rolling. *Mater. Sci. Eng. A* 726, 194–207. doi: 10.1016/j.msea.2018.04.090

Kim, Y. M., Mendis, C., Sasaki, T., Letzig, D., Pyczak, F., Hono, K., et al. (2017). Static recrystallization behavior of cold rolled Mg-Zn-Y alloy and role of solute segregation in microstructure evolution. *Scripta Mater.* 136, 41–45. doi: 10.1016/j.scriptamat.2017.04.001

Klaumünzer, D., Victoria-Hernandez, J., Yi, S., Letzig, D., Kim, S. H., Kim J. J., et al. (2019) "Magnesium process and alloy development for applications in the automotive industry," in *Magnesium Technology*, The Minerals, Metals and Materials Series, San Antonio, Texas, USA, eds V. Joshi, J. Jordon, D. Orlov, and N. Neelameggham (Cham: Springer), 15–20. doi: 10.1007/978-3-030-05789-3_3

Koike, J., Kobayashi, T., Mukai, T., Watanabe, H., Suzuki, M., Maruyama, K., et al. (2003). The activity of non-basal slip systems and dynamic recovery at room temperature in fine-grained AZ31B magnesium alloys. *Acta Mater.* 51, 2055–2065. doi: 10.1016/S1359-6454(03)00005-3

Liu, L., Chen, X., Pan, F., Gao, S., and Zhao, C. (2016). A new high strength Mg-Zn-Ce-Y-Zr magnesium alloy. *J. Alloys Compd.* 688, 537–541. doi: 10.1016/j.jallcom.2016.07.144

Mackenzie, L. W. F., and Pekguleryuz, M. O. (2008). The recrystallization and texture of magnesium-zinc-cerium alloys. *Scripta Mater.* 59, 665–668. doi: 10.1016/j.scriptamat.2008.05.021

Mordike, B. L., and Ebert, T. (2001). Magnesium poperties–applications–potential. *Mater. Sci. Eng. A* 302, 37–45. doi: 10.1016/S0921-5093(00)01351-4

Sandlöbes, S., Friák, M., Korte-Kerzel, S., Pei, Z., Neugebauer, J., and Raabe, D. (2017). A rare earth free magnesium alloy with improve intrinsic ductility. *Sci. Rep*. 7, 1–8. doi: 10.1038/s41598-017-10384-0

Sandlöbes, S., Zaefferer, S., Schestakow, I., Yi, S., and Gonzalez-Martinez, R. (2011). On the role of non-basal deformation mechanisms for the ductility of Mg and Mg-Y alloys. *Acta Mater*. 59, 429–439. doi: 10.1016/j.actamat.2010.08.031

Shi, B. Q., Xiao, Y. H., Shang, X. L., Cheng, Y. Q., Yan, H., Dong, Y., et al. (2019). Achieving ultra-low planar anisotropy and high stretch formability in a Mg-1.1Zn-0.7Y-0.56Zr sheet by texture tailoring via final-pass heavy reduction. *Mater. Sci. Eng. A* 746, 115–126. doi: 10.1016/j.msea.2018.12.116

Stutz, L., Bohlen, J., Letzig, D., and Kainer, K. U. (2011a). "Formability of magnesium sheet ZE10 and AZ31 with respect to initial texture," in *Magnesium Technology*, The Minerals, Metals and Materials Society, San Diego, California, USA, eds W. H. Sillekens, S. R. Agnew, N. R. Neelameggham, and S. N. Mathaudhu (J. Wiley and Sons, Inc.), 373–378. doi: 10.1002/9781118062029.ch6

Stutz, L., Quade, J., Dahms, M., Letzig, D., and Kainer, K. U. (2011b). Achievements in deep drawing of AZ31 magnesium alloy sheets. *Mater. Sci. Forum*. 690, 302–305. doi: 10.4028/www.scientific.net/MSF.690.302

Suh, J., Victoria-Hernandez, J., Letzig, D., Golle, R., Yi, S., Bohlen, J., et al. (2015). Improvement in cold formability of AZ31 magnesium alloy sheets processed by equal channel angular pressing. *J Mater. Proc. Tech*. 217, 286–293. doi: 10.1016/j.jmatprotec.2014.11.029

Suh, J., Victoria-Hernandez, J., Letzig, D., and Golle, Volk W. (2016). Effect of processing route on texture and cold formability of AZ31 Mg alloy sheets processed by ECAP. *Mater. Sci. Eng. A* 669, 159–170. doi: 10.1016/j.msea.2016.05.027

Victoria-Hernandez, J., Yi, S., Klaumünzer, D., and Letzig, D. (2019). Recrystallization behavior and its relationship with deformation mechanisms of a hot rolled Mg-Zn-Ca-Zr alloy. *Mater. Sci. Eng. A* 761:138054. doi: 10.1016/j.msea.2019.138054

Yi, S., Bohlen, J., Heinemann, F., and Letzig, D. (2010). Mechanical anisotropy and deep drawing behavior of AZ31 and ZE10 magnesium alloy sheets. *Acta Mater*. 58, 592–605. doi: 10.1016/j.actamat.2009.09.038

Yuasa, M., Miyazawa, N., Hayashi, M., Mabuchi, M., and Chino, Y. (2015). Effects if group II elements on the cold stretch formability of Mg-Zn alloys. *Acta Mater*. 83, 294–303. doi: 10.1016/j.actamat.2014.10.005

Zeng, X., Minárik, P., Dobron, P., Letzig, D., Kainer, K. U., and Yi, S. (2019). Role of deformation mechanisms and grain growth in microstructure evolution during recrystallization of Mg-Nd alloys. *Scripta Mater*. 166, 53–57. doi: 10.1016/j.scriptamat.2019.02.045

Zhang, J., Zhang, X., Li, W., Pan, F., and Guo, Z. (2010). Partition of Er among the constituent phases and the yield phenomenon in a semi-continuously cast Mg-Zn-Zr alloy. *Scripta Mater*. 63, 367–370. doi: 10.1016/j.scriptamat.2010.04.015

Conflict of Interest: The authors declare that the research was conducted in the absence of any commercial or financial relationships that could be construed as a potential conflict of interest.

ORIGINAL RESEARCH
published: 10 December 2019
doi: 10.3389/fmats.2019.00324

Effect of Mn Element Addition on the Microstructure, Mechanical Properties, and Corrosion Properties of Mg-3Zn-0.2Ca Alloy

Yu Yan Han[1], Chen You[1,2]*, Yun Zhao[1,2,3], Min Fang Chen[1,2,3]* and Liang Wang[1]

[1] School of Materials Science and Engineering, Tianjin University of Technology, Tianjin, China, [2] Key Laboratory of Display Materials and Photoelectric Device, Ministry of Education, Tianjin, China, [3] Tianjin Key Laboratory for Photoelectric Materials and Devices, Tianjin, China

Edited by:
Hajo Dieringa,
Helmholtz Centre for Materials and
Coastal Research (HZG), Germany

Reviewed by:
Jiangfeng Song,
Chongqing University, China
Sinan Kandemir,
Izmir Institute of Technology, Turkey

***Correspondence:**
Chen You
youchentj@126.com
Min Fang Chen
mfchentj@126.com

Specialty section:
This article was submitted to
Structural Materials,
a section of the journal
Frontiers in Materials

Received: 22 May 2019
Accepted: 25 November 2019
Published: 10 December 2019

Citation:
Han YY, You C, Zhao Y, Chen MF and
Wang L (2019) Effect of Mn Element
Addition on the Microstructure,
Mechanical Properties, and Corrosion
Properties of Mg-3Zn-0.2Ca Alloy.
Front. Mater. 6:324.
doi: 10.3389/fmats.2019.00324

Magnesium-zinc-calcium alloys have unique advantages of being used as biomedical bone implants since their mechanical properties and biocompatibility are similar to human tissues. However, insufficient strength and poor corrosion resistance have been the major problems to stunt the application. In this paper, the changes of microstructure, mechanical properties and corrosion resistance of ternary Mg-3Zn-0.2Ca (wt.%) with different contents of Mn (0.3, 0.5, 0.7, 0.9, wt.%) are studied. With the increase of Mn content, the grain size of as-cast alloy first decreases and then increases, this indicates that the amount of Mn affects the degree of subcooling of the alloy. At the 320°C/24 h homogenizing treatment, the large and uneven dendrites are transformed into uniform equiaxed grains, the mechanical properties of alloys with different Mn contents are different on the basis of Mg-3Zn-0.2Ca (wt.%) alloy. The five alloys were extruded into bar with a diameter of 8 mm through hot-extrusion process. Quaternary Mg-3Zn-0.2Ca-XMn ($X = 0.3, 0.5, 0.7, 0.9$) (wt.%) alloys are investigated and the results show that 0.5 wt.% Mn alloy has the best yield tensile strength (YS) (302 MPa) and good ultimate tensile strength (UTS) (327 MPa). The reason is that the different contents of Mn restrain the dynamic recrystallization in extrusion process, which remarkedly reduced the grain size. Moreover, each alloy is investigated by electrochemical measurements at 37°C in a simulated body fluid (SBF). The electrochemical results show that the corrosion potential of Mn-contained alloys are increased compared to ternary Mg-3Zn-0.2Ca (wt.%) alloy, and 0.5 wt.% Mn-contained alloy performs the best result.

Keywords: biomedical magnesium alloys, microstructure, mechanical properties, corrosion properties, α-Mn

INTRODUCTION

With the advancement of medical science and technology, metal implants have become an indispensable technical means in clinical medicine as an important part of bone reconstruction surgery. Some studies have shown that the use of metal implants in clinical bone reconstruction surgery has significantly improved the cure rate of large femoral fractures and bone injuries (Prins et al., 2018; Han et al., 2019).

Metal implants complete the healing process by setting the skeleton in place (Ibrahim et al., 2017). Currently, metal implant materials widely used in medicine mainly include titanium alloys, CoCr alloys and stainless steels, which cannot be absorbed by themselves and need to be permanently retained in the body or removed by secondary surgery. Permanent retention in the body will produce stress shielding after the completion of bone healing, and secondary removal will make the patient suffer from the pain of surgery again and lead to complications (Best et al., 2008; Lutz and Mändl, 2010; Arifin et al., 2014; Ibrahim et al., 2017). Therefore, we hope that there can be a material that gives sufficient strength and stiffness support during bone healing. Once the bone tissue heals, it begins to degrade and be absorbed in the body (Ibrahim et al., 2017). Magnesium and its alloys not only show excellent biocompatibility and similar mechanical properties of human bones, but also can be degraded and absorbed in the body without secondary surgery, which has received widespread attention from the scientific and medical community (Kannan and Raman, 2008; Zheng et al., 2014; Witte, 2015; Jin et al., 2019). However, owing to the insufficient mechanical properties and the rapid degradation rate, magnesium alloys have limited their applications in the medical industry (Yin et al., 2013; Tian and Liu, 2015; Bian et al., 2017). Generally, the period of bone remodeling is 3–6 months, and thus improving the mechanical properties and corrosion resistance of magnesium alloys as well as ensuring their effective service have become the focus of our current research.

Previous studies usually reported the usage of alloying or microalloying to modify the microstructures and sediments to improve their comprehensive properties. In the current studies, the main alloying elements are Ca, Sr, Zn, Si, Mn, Li, Zr, Nd, Y, RE, Al (Gu et al., 2012; Li and Zheng, 2013; Yin et al., 2013; Zhou et al., 2013; Seong and Kim, 2015; Tian and Liu, 2015; Yandong et al., 2015; Cho et al., 2016; Bian et al., 2017; Gil-Santos et al., 2017; Jiang et al., 2017; Gui et al., 2018; Abdel-Gawad and Shoeib, 2019; Guo et al., 2019; Jin et al., 2019; Liao et al., 2019; Lou et al., 2019). Based on the biosafety to the human body, the biological functional elements Ca, Sr, and the essential trace elements Zn, Si, Mn can be as the main alloying elements. Ca is the main component of human bones, which is essential for chemical signal transduction in cells. The released ions of Ca as a mineral nutrient are beneficial to bone solidification (Harkness and Darrah, 2019). Du et al. (2016) found that the addition of Ca to the Mg-6Zn alloy inhibited dynamic recrystallization and grain growth during extrusion. Meanwhile, the sediments of the alloy deposited are also increased and the alloy strength was raised by 84%. Yin et al. (2013) found that the addition of Ca into the Mg-5Zn alloy was beneficial to grain refinement. The mechanical properties and biocorrosion properties of the alloy were significantly improved. High Ca would lead to good mechanical properties and low corrosion resistance and Mg-5Zn-1.0Ca exhibited excellent corrosion resistance and good biocompatibility. Another element, Zinc, is the most common and basic nutrient element in human body. It plays an extremely important role in important physiological processes such as human growth and development, reproductive genetics, immunity, and endocrine. Zhang et al. (2011) studied the effects of different zinc contents on the mechanical, corrosion and cytotoxicity of Mg–Zn–Ca alloys. It was found that the tensile strength and corrosion rate first increased and then decreased with the increase of Zn content. When the composition is <3 wt.% Zn, the component alloy is non-toxic. Mn is a basic element of the human body and can be accepted by the human body. Some reports (Jiang et al., 2016; Ibrahim et al., 2017) indicate that Mn element can refine grains by inhibiting recrystallization growth during alloy extrusion. Further, Mn element can also be combined with impurity elements during the smelting process to form a high melting point compound precipitated at the bottom of the melt to purifying the alloy. He et al. (2018) investigated the *in vitro* corrosion and biocompatibility of extruded Mg-6Zn-Mn alloy and found that the corrosion rate of extruded alloy was only 1.01 ± 0.10 mm/year after simulated body fluid (SBF) soaking for 1 month, and the cells were non-toxic. Yandong et al. (2015) studied the effects of different Mn compositions on the microstructure and mechanical properties of Mg–Zn–Ca alloys. It was found that the strength and elongation of as-cast and heat-treated alloys decreased with the increase of Mn content. The optimum tensile strength of heat-treated Mg-2Zn-0.5Ca-1.0Mn alloy is 205 MPa and the elongation is 15.7%. Cho et al. (2017) found that the addition of Mn has an obvious grain refining effect on Mg-4Zn-0.5Ca alloy, which greatly improved the comprehensive performance of magnesium alloy. Previous studies on alloying element Mn have been reported, but the results are different, and the mechanical properties and corrosion resistance are still relatively low. Therefore, more studies are needed to fully understand the effect of Mn on magnesium alloys.

In this work, based on the previous research reports (Lin et al., 2018a,b), this work mainly focused on the effects Mn with different contents in ternary Mg-3Zn-0.2Ca alloy, and the microstructure, mechanical properties and corrosion properties are investigated systematically, which provide a more reliable basis for the further development of biomedical magnesium alloys by optimizing Mn content to enhance mechanical properties and corrosion performance of biomedical magnesium alloys.

EXPERIMENTAL MATERIALS AND METHODS

Material Preparation

Pure magnesium ingot (99.99 wt.%), pure zinc particles (99.99 wt.%), Mg-Ca master alloy (with 25 wt.% Ca), and Mg-Mn master (with 10 wt.% Mn) alloy were used to make Mg-3Zn-0.2Ca (wt.%) (MZC), Mg-3Zn-0.2Ca-0.3Mn (wt.%) (MZC0.3Mn), Mg-3Zn-0.2Ca-0.5Mn (wt.%) (MZC0.5Mn), Mg-3Zn-0.2Ca-0.7Mn (wt.%) (MZC0.7Mn), and Mg-3Zn-0.2Ca-0.9Mn (wt.%) (MZC0.9Mn) alloys. In the process of cultivating, all of alloys used vacuum induction furnace under the protection of argon atmosphere gas for melting and casting. The furnace is first heated to 720°C, then stirred for 2–3 min, kept warm for 2–3 min, cut off the power and started casting at a constant speed until the temperature drops to 690°C. The five alloy ingots were homogenized separately to eliminate dendrites, and then extruded at 315°C on a hot-extrusion molding machine. During the extrusion, the speed is set to 2–4 mm/s.

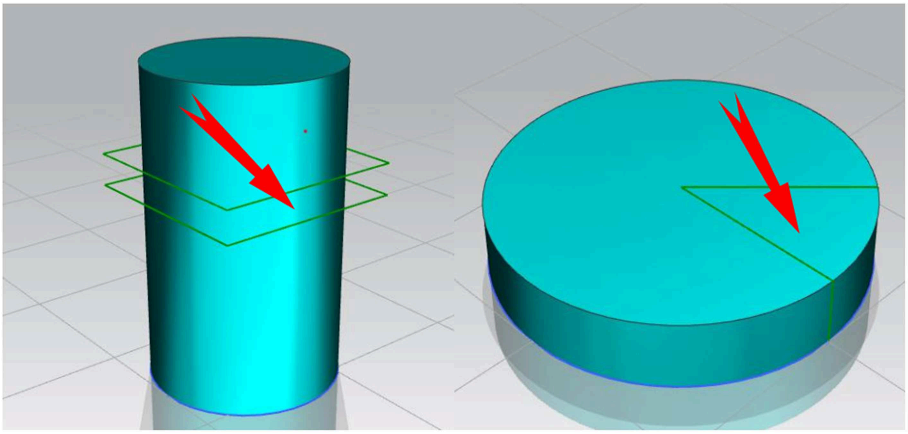

FIGURE 1 | The selected position of samples for microstructures observation.

Selection of Specimens and Observation of Microstructure

Microstructures of the as-cast alloys and homogenized alloys were observed by optical microscope (OM) and scanning electron microscopy (SEM), respectively. The grain size of five alloys are determined by GB/T 6394-2002 standards. The second phase particle size in the homogenized alloys is calculated by using the SEM ruler. Five different alloy samples must be selected at the same height and the same position for comparison. The selected position is shown in **Figure 1**.

X-Ray Diffraction and EDS Analysis

The phase composition of the detected phase was measured by X-ray diffraction at a scanning speed of 10 min, an acceleration voltage of 40 kV, a current of 100 mA and a Cu target Kα radiation (λ = 0.141618 nm). Analysis was performed by using JADE5 software to determine the presence of the second phase in the sample. The second phase in the alloy is determined by using EDS.

Mechanical Properties Test

Tensile test is carried out by using an electronic universal testing machine at room temperature. The tensile test specimens are machined according to GB/T 16865-2013 standards. The test speed is set to 0.5 mm/min. Three parallel samples are set in each group and the fracture morphology of failed specimens is analyzed by SEM.

Electrochemical Experiment

The electrochemical polarization and impedance experiments were carried out in a simulated body fluid (SBF) at 37°C by using a Zennium electrochemical workstation. The sample was used as the working electrode, graphite as the counter electrode and saturated calomel as the reference electrode to form a three-electrode assembly. Each surface exposed to the sample was smoothed by 3,000 grit water sandpaper and immersed in 37°C SBF for 30 min before the test. Three parallel samples were set in each group to ensure the accuracy. The polarization resistance (Rp) of the samples to be tested are calculated by using Equation (1) (Bakhsheshi-Rad et al., 2012).

$$R_P = \frac{\beta\alpha\beta c}{2.303\,(\beta\alpha + \beta c)\,I\mathrm{corr}} \tag{1}$$

In the Equation (1), βc represents the cathode Tafel slope, $\beta\alpha$ represents the anode Tafel slope, and Icorr represents the corrosion current density, respectively.

RESULTS AND DISCUSSION

Microstructure Observation

The microstructures of as-cast MZC, MZC0.3Mn, MZC0.5Mn, MZC0.7Mn, and MZC0.9Mn alloys are shown in **Figure 2**. Compared with the five alloys, it can be found that the addition of Mn element changed the overall solute distribution of the alloy matrix. The ellipsoidal precipitates increase and evenly disperse in the rich Mn-contained alloys. A large number of second phases are also accumulated at the grain boundaries. The morphology and distribution of these second phases may affect the subsequent mechanical properties and corrosion resistance.

The average grain sizes of as-cast MZC, MZC0.3Mn, MZC0.5Mn, MZC0.7Mn, and MZC0.9Mn alloys are shown in **Figure 3**. The average grain size of the five alloys first decreases and then increases, and the MZC0.5Mn alloy has the smallest grain size (74.2 ± 10.1 μm). The reason may be that with the addition of Mn element, the solute at the S/L interface aggregates, causing different degrees of structural overcooling. In previous reports, the effect of the addition of Mn on the supercooling of magnesium alloys was also confirmed (Cho et al., 2017).

In order to eliminate dendrites, five alloys are homogenized and the SEM photographs of five alloys are shown in **Figure 4**. Compared with the MZC alloy, the ellipsoidal second phase and elongated second phase at the grain boundary of Mn-contained alloys are significantly increased. **Figure 4F** shows the EDS data of the ellipsoidal second phase. It can be seen that the atomic ratio Mg:Zn:Ca is closed to 6:3:2, and the ellipsoidal second phase can

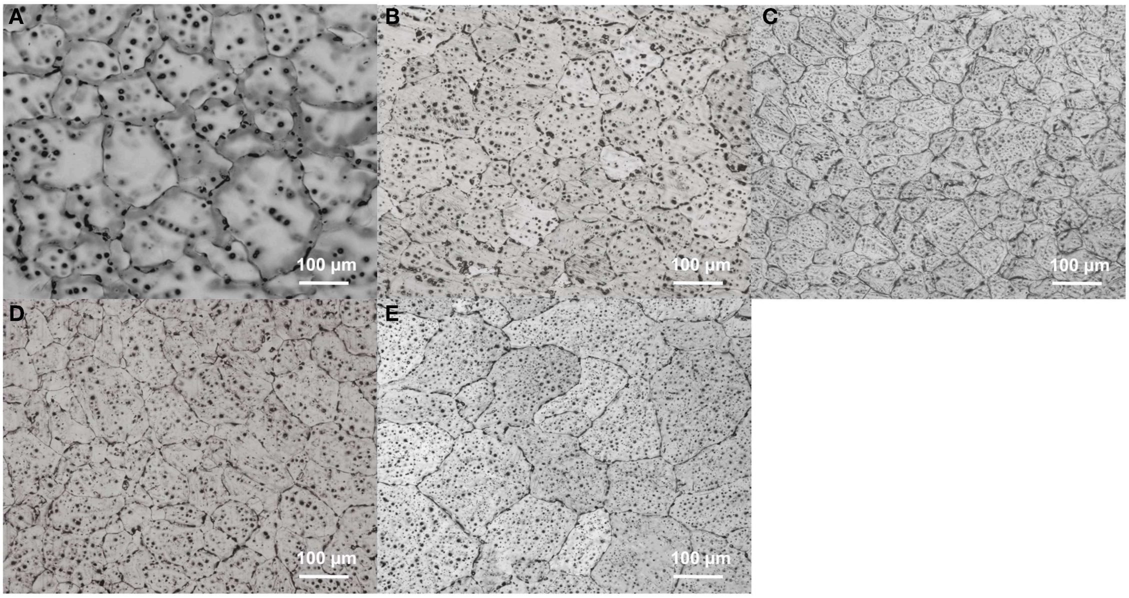

FIGURE 2 | Optical images of as-cast MZC **(A)**, MZC0.3Mn **(B)**, MZC0.5Mn **(C)**, MZC0.7Mn **(D)**, and MZC0.9Mn **(E)** alloys.

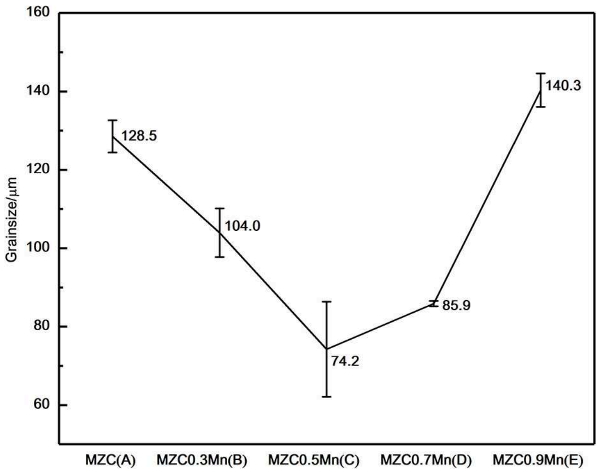

FIGURE 3 | The grain size of as-cast MZC **(A)**, MZC0.3Mn **(B)**, MZC0.5Mn **(C)**, MZC0.7Mn **(D)** and MZC0.9 Mn **(E)** alloys.

be inferred to be $Ca_2Mg_6Zn_3$ phase (Bakhsheshi-Rad et al., 2012). Previous studies (Oh-ishi et al., 2009) have shown that the long strip-shaped second phase at the grain boundary of the ternary Mg-Zn-Ca alloy is mainly $Ca_2Mg_6Zn_3$ phase. Therefore, it can conclude that the addition of Mn element greatly promotes the precipitation of the ternary $Ca_2Mg_6Zn_3$ phase.

It is also found that the difference in the content of Mn has a certain influence on the distribution of the second phase and the size of the second phase in the SEM photograph. The ellipsoidal second phase particle size measured by SEM scale is shown in **Figure 5**. The ellipsoidal second phase of MZC0.5Mn alloy is the smallest and the dispersion is more uniform.

SEM photographs of as-extruded MZC, MZC0.3Mn, MZC0.5Mn, MZC0.7Mn, and MZC0.9Mn alloys are shown in **Figure 6**. The average grain sizes of the five alloys measured by SEM scale are 3.2 ± 0.30, 3.0 ± 0.63, 1.5 ± 0.43, 2.0 ± 0.06, and 1.9 ± 0.59 μm, respectively. The Mn-contained alloys after hot extrusion deformation have smaller grain sizes compared to the MZC alloy. This may be due to the fact that the α-Mn particles dynamically precipitated during the extrusion process, inhibiting the grain growth of the alloy, resulting in a decrease in the grain size of the Mn-containing alloy (Jiang et al., 2016). It can also be seen from the SEM photographs that the volume of the second phase of the Mn-contained alloys are significantly increased compared to the MZC alloy.

Figure 7 shows the as-extruded X-ray diffraction patterns of MZC, MZC0.3Mn, MZC0.5Mn, MZC0.7Mn, and MZC0.9Mn alloys. The as-extruded MZC alloy mainly consists of α-Mg, $MgZn_2$ Mg_2Ca, and $Ca_2Mg_6Zn_3$. Compared with MZC alloy, the amount of $Ca_2Mg_6Zn_3$ in Mn-contained alloys are increased significantly. Meanwhile, the amount of Mg_2Ca in Mn-contained alloys are decreased. This is probably due to the Mn element which changes the solute element distribution and causes the solute atoms Zn and Ca to aggregate in a certain region to form more ternary phase $Ca_2Mg_6Zn_3$. In Mn-contained alloys, the Mn exists in the form of a simple substance of Mn and an α-Mn phase, and does not form a second phase with other elements.

It is also found in XRD diffraction patterns that the three strong peaks of Mg of Mn-contained alloys have a small amount of left bias at the basis of MZC alloy. MZC0.9Mn alloy has the largest offset angle, which is approximately 0.1°. This may be due to the lattice distortion caused by Mn entering the gap of Mg (HCP) cells.

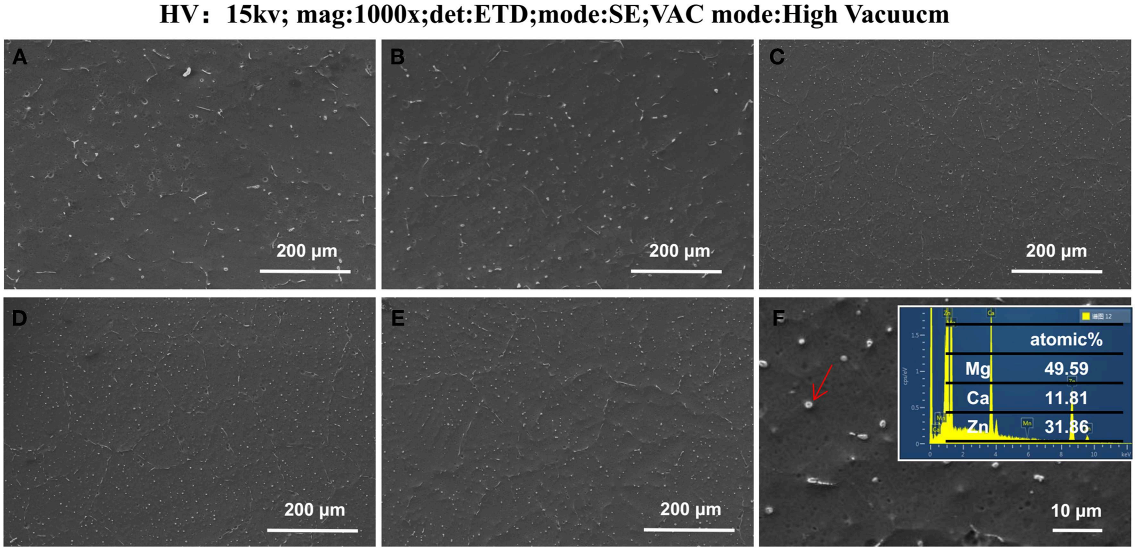

FIGURE 4 | The field-emission scanning images of as-cast homogenization MZC **(A)**, MZC0.3Mn **(B)**, MZC0.5 Mn **(C)**, MZC0.7Mn **(D)**, and MZC0.9Mn **(E)** alloys and the EDS image of ellipsoidal second phase **(F)**.

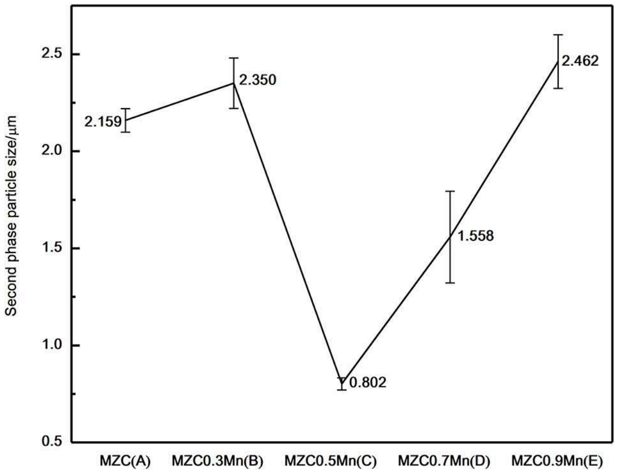

FIGURE 5 | Average particle size of spherical second phase measured by using SEM scale. **(A)** MZC, **(B)** MZC0.3Mn, **(C)** MZC0.5Mn, **(D)** MZC0.7Mn, and **(E)** MZC0.9 Mn.

Mechanical Properties Analysis

Figure 8 displays the tensile stress-strain curves of as-extruded MZC, MZC0.3Mn, MZC0.5Mn, MZC0.7Mn, and MZC0.9Mn alloys and the local stress-strain amplification curve of the MZC alloy. **Table 1** lists the room temperature mechanical properties of the five alloys. It can be seen that the MZC0.5Mn alloy exhibits the best mechanical properties. Compared with MZC alloy, the yield strength and tensile strength of MZC0.5Mn alloy are increased by 25.1 and 3.1%, respectively, and the elongation is not significantly reduced. The MZC0.5Mn alloy has the best grain refining effect, its second phase is finely dispersed and evenly distributed, and consequently the dispersion strengthening and dislocation pinning effect are obvious. Among this five alloys, MZC0.3Mn alloy has the worst mechanical properties. This is attributed to the fact that the addition of 0.3 wt.% Mn element increases the $Ca_2Mg_6Zn_3$ phase while the grains are not significantly refined, and the coarse brittle phase $Ca_2Mg_6Zn_3$ is unevenly distributed, which further exacerbates the yield and fracture of the sample.

The fracture surfaces of MZC and Mn-contained alloys are further analyzed to verify the effect of Mn on the mechanical properties of MZC alloy. The fracture morphologies of five alloys are shown in **Figure 9**. In the fracture morphology, the observation and analysis are carried out from four aspects: the macroscopic orientation of the section, the macroscopic morphology, fracture path and fracture morphology.

Macroscopic fractures of as-extruded MZC and Mn-contained alloy samples are observed with the naked eye. It can be seen that fractures are dark gray fibers with a little fine crystalline particles. It preliminarily demonstrates that the fractures are mostly ductile fracture with a small part of quasi-cleavage fracture. The SEM photographs of the fracture macro morphology of five as-extruded alloys are shown in **Figures A1–E2**. It can be seen in **Figures 9A1–E1** that the fracture section direction is at an angle of ∼45 degrees with the normal stress direction, which is consistent with the direction of the maximum shear stress and corresponding to the characteristics of shear slip fracture. The typical three-zone characteristics of the ductile fracture (fiber zone, radiation zone, shear lip zone) of five alloys can be seen in **Figures 9A2–E2**. MZC alloy has the most obvious characteristics of the three zones and performs the best toughness.

The fracture micro morphology of five as-extruded alloys SEM photographs are shown in **Figures 9A3–E5**. It is apparent in the **Figures 9A3–E3** that the cleavage step and tearing ridge

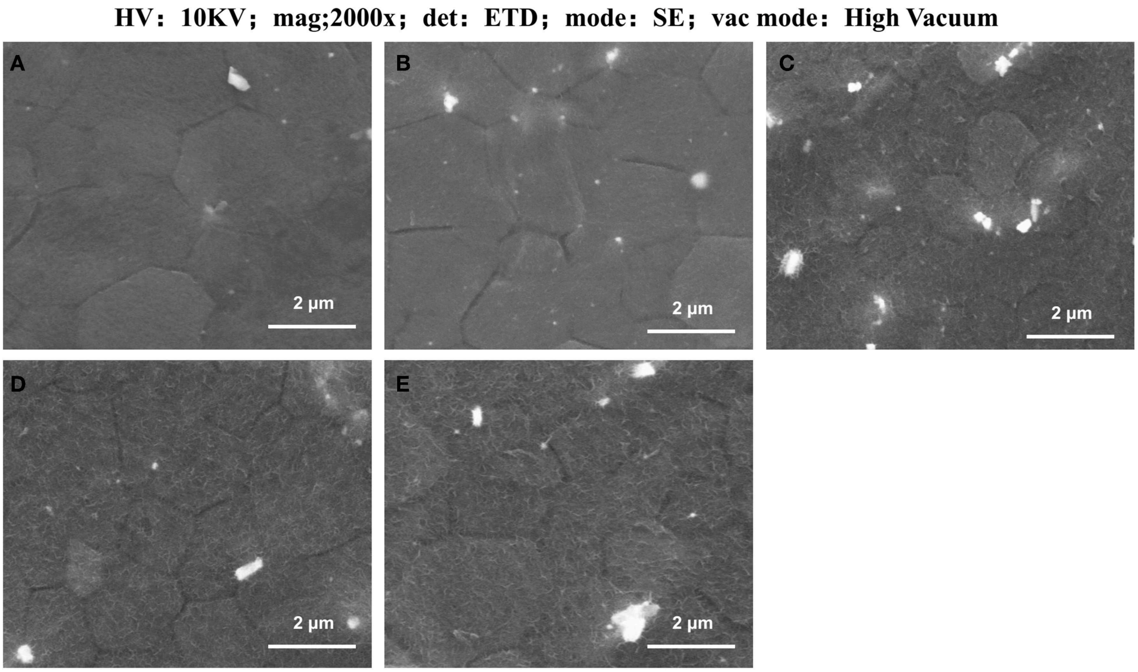

FIGURE 6 | The field-emission scanning images of as-extruded MZC **(A)**, MZC0.3Mn **(B)**, MZC0.5Mn **(C)**, MZC0.7 Mn **(D)**, and MZC0.9 Mn **(E)** alloys.

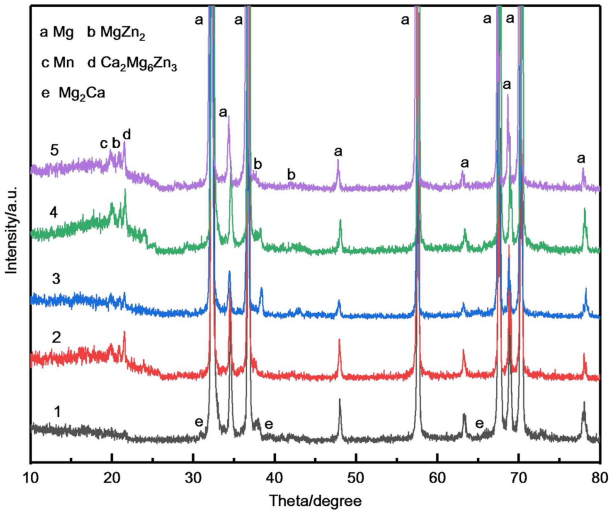

FIGURE 7 | The XRD patterns of as-extruded MZC (1), MZC0.3Mn (2), MZC0.5 Mn (3),MZC0.7Mn (4) and MZC0.9 Mn (5) alloys.

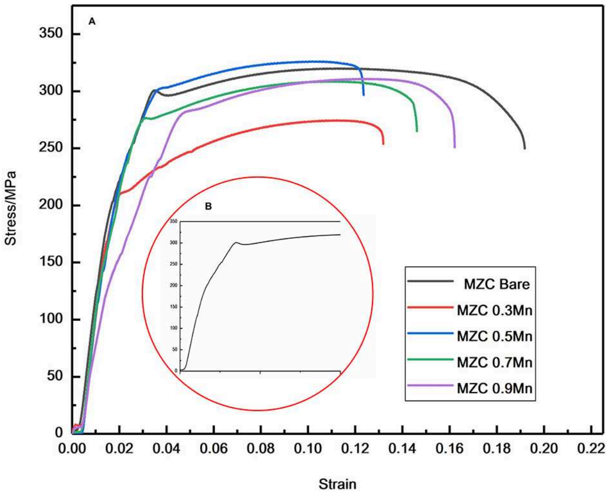

FIGURE 8 | Tensile stress-strain curve of as-extruded MZC, MZC0.3Mn, MZC0.5Mn, MZC0.7Mn and MZC0.9Mn alloys **(A)** and Local region of tensile stress-strain curve of as-extruded MZC alloy **(B)**.

are more pronounced in Mn-contained alloys than the MZC alloy. **Figures 9A4–E5** show a large number of dimples that contain obvious second phase particles, mainly corresponding to microporous aggregate fracture. From the analysis of the fracture path, it can be seen from the **Figures 9A3–E5** that the five alloys contain both transgranular and intergranular fractures. In addition, it can be clearly seen from the **Figures 9B4,5** that the quasi-cleavage fracture of MZC0.3Mn alloy is most prominent and severe, and thus exhibits poor toughness. The above fracture analysis is consistent with the tensile test results.

Electrochemical Properties Analysis

Figure 10 shows the electrochemical polarization curves of as-extruded MZC, MZC0.3Mn, MZC0.5Mn, MZC0.7Mn, and MZC0.9Mn alloys. The corrosion current densities of the five alloys are obtained by Tafel extrapolation based on the polarization curve. The specific data is shown in **Table 2**.

Figure 10 indicates that the MZC0.3Mn, MZC0.5Mn, MZC0.7Mn, and MZC0.9Mn alloys have a longer yield plateau compared to the MZC alloy, which means that a more dense passivation film is formed on the surface of the alloys with Mn than the surface of the control when the sample is immersed in the SBF. The previous XRD diffraction pattern shows that the MZC alloy is mainly composed of α-Mg, $MgZn_2$, Mg_2Ca and $Ca_2Mg_6Zn_3$ phases. The addition of Mn increases the precipitation of $Ca_2Mg_6Zn_3$ while reduces the phase of Mg_2Ca. The addition of Mn inhibits the grain growth of the alloy during the extrusion process, resulting in grain refinement of the alloy, which reduces corrosion rate compared to the MZC alloy. According to research (Bakhsheshi Rad et al., 2012), ternary $Ca_2Mg_6Zn_3$ phase behaves high standard electrode potential in $Ca_2Mg_6Zn_3$ and α-Mg, which means that $Ca_2Mg_6Zn_3$ acts as a cathode and α-Mg acts as an anode when galvanic corrosion occurs. Comparing the yielding stages of the five alloys with the short yielding stage of the MZC alloy, it can be further determined that the dense oxide film on the surface of the alloy is mainly ternary $Ca_2Mg_6Zn_3$ phase, which is consistent with the previous research (Abdel-Gawad and Shoeib, 2019).

TABLE 1 | Mechanical properties of as-extruded MZC, MZC0.3Mn, MZC0.5Mn, MZC0.7Mn, and MZC0.9Mn alloys.

Samples	YS (MPa)	UTS (MPa)	EL (%)
MZC	241.709 ± 3.22	317.793 ± 2.75	15.75 ± 1.24
MZC0.3Mn	210.879 ± 5.37	274.251 ± 0.22	14.14 ± 0.95
MZC0.5Mn	302.348 ± 2.35	327.572 ± 0.80	13.92 ± 1.6
MZC0.7Mn	275.226 ± 2.66	314.324 ± 1.53	15.736 ± 0.67
MZC0.9Mn	245.767 ± 6.49	312.217 ± 2.63	14.676 ± 1.33

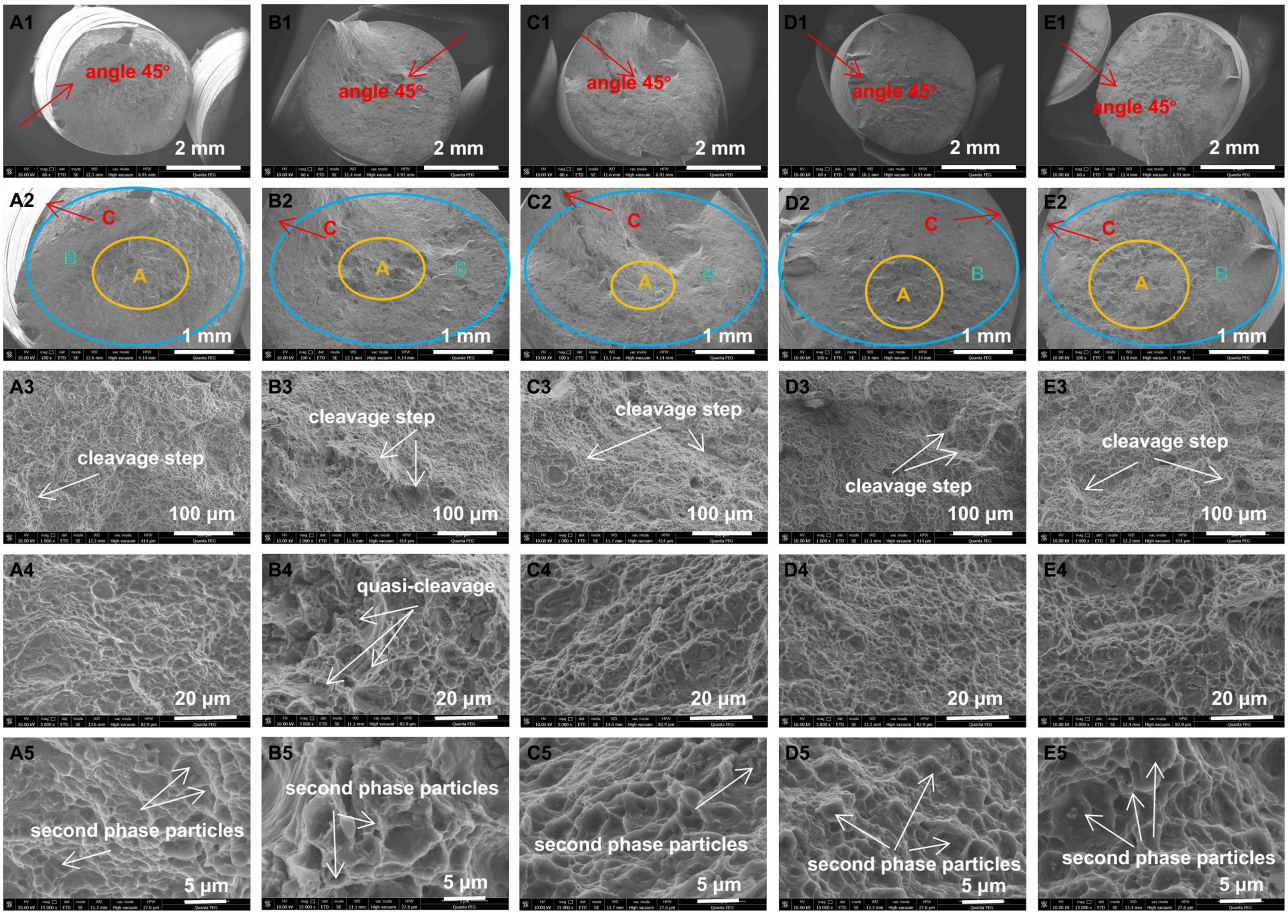

FIGURE 9 | Fracture surface morphologies of as-extruded MZC **(A)**, MZC0.3Mn **(B)**, MZC0.5Mn **(C)**, MZC0.7Mn **(D)**, and MZC0.9Mn **(E)** alloys.

Compared to four alloys with different Mn contents, it can be found that with the increment of Mn content, the polarization value of the alloy cathode decreases but the anode polarization value increases. It illustrates that the increase of Mn element

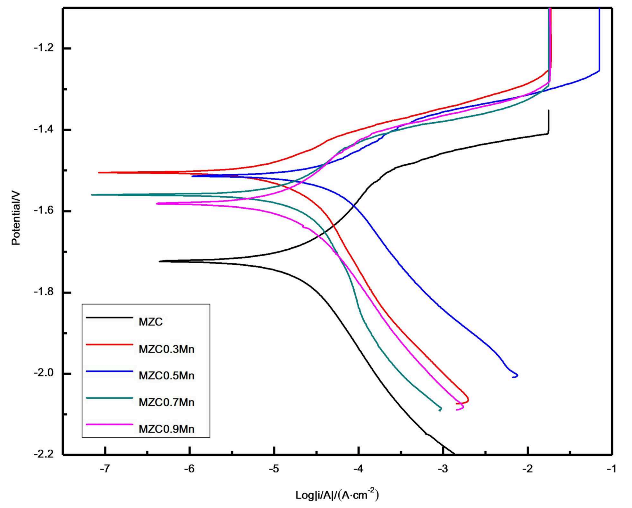

FIGURE 10 | The polarization curve of as-extruded MZC, MZC0.3Mn, MZC0.5Mn, MZC0.7Mn, and MZC0.9Mn alloys.

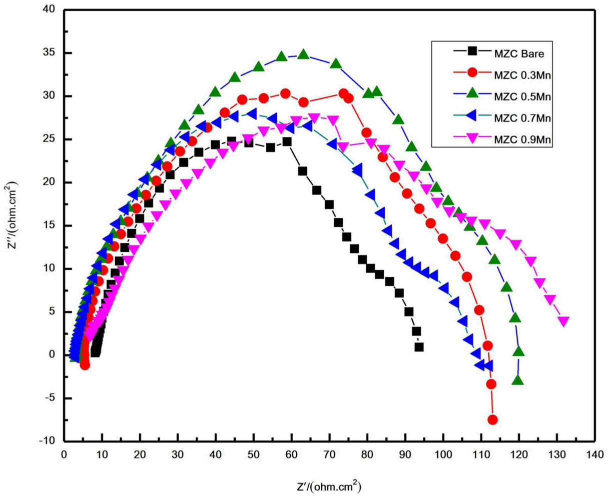

FIGURE 11 | The alternating current impedance spectra of as-extruded MZC, MZC0.3Mn, MZC0.5Mn, MZC0.7Mn, and MZC0.9Mn alloys.

TABLE 2 | Electrochemical properties of as-extruded MZC, MZC0.3Mn, MZC0.5Mn, MZC0.7Mn, and MZC0.9Mn alloys.

Sample	E_{corr} (V)	I_{corr} (μA/cm^2)	$β_c$ (v/dec)	$β_α$ (v/dec)	R_p (kΩ·cm^2)
MZC	−1.705	65.68	0.165	0.134	0.49
MZC0.3Mn	−1.502	30.65	0.239	0.092	0.94
MZC0.5Mn	−1.509	32.25	0.180	0.119	0.97
MZC0.7Mn	−1.556	48.17	0.167	0.145	0.70
MZC0.9Mn	−1.582	35.03	0.136	0.176	0.95

reduces the hydrogen evolution rate of the alloy while increasing the magnesium ion concentration.

Based on these results, the MZC0.3Mn alloy exhibited the best corrosion resistance, which may be due to the segregation of solute elements in the alloy containing Mn. As we all know, the corrosion resistance of magnesium alloys is attributed to galvanic corrosion between the second phases. In polarization curve, the degree of curve smoothness represents galvanic corrosion of the alloy. It can be seen from **Figure 10** that the MZC0.3Mn alloy curve is smoother than the other three Mn-contained alloys, indicating that the MC0.3Mn alloy has less galvanic corrosion and minimal segregation. When the Mn content in the alloy is increased, excessive Mn causes segregation of the alloy to be severe and the corrosion resistance of the alloy is lowered.

Figure 11 shows the impedance spectra of as-extruded MZC, MZC0.3Mn, MZC0.5Mn, MZC0.7Mn, and MZC0.9Mn alloys. Five alloys have two capacitor rings in the high frequency region and the low frequency region. With the addition of Mn content, the diameter of the capacitor ring in the high frequency region first increases and then decreases. MZC0.5Mn alloy has the largest capacitor ring. This is consistent with the performance of the polarization curve results. The size of the capacitor ring represents the charge transfer suppression. The larger capacitor ring display and the more obvious charge suppression effect are observed, and the formed corrosion product film layer is more stable, which ultimately leads to better protection. The reason of MZC0.5Mn alloy with good corrosion resistance is that the minimum grain size and the dispersion of the second phase particles is fine and small, which makes the galvanic corrosion less.

CONCLUSION

In this paper, the microstructures, mechanical properties and electrochemical properties were investigated to determine the effect of alloying element Mn on the ternary MZC alloy. Comparing the microstructures of the five as-cast alloys, it can be found that the alloying element Mn affected the average grain size of the alloy by changing the degree of subcooling of the alloy. Compared with as-cast MZC alloy, the average grain size of as-cast MZC0.5Mn alloy was reduced by 40.1%. Furthermore, it was found that the Mn element promoted the ellipsoidal second phase and the elongated second phase of the grain boundary, and also affected the size of the ellipsoidal second phase. The ellipsoidal second phase particle size (0.8023 μm) of MZC0.5Mn alloy was reduced by 61.9% compared with the MZC alloy. The ellipsoidal second phase was determined by EDS to be mainly ternary $Ca_2Mg_6Zn_3$ phase. The SEM of five as-extruded alloys showed that Mn element inhibited dynamic recrystallization and dynamic precipitation during extrusion, and further as heterogeneous nucleation sites promoted nucleation, resulting in the grain refinement of as-extruded alloys obviously. MZC0.5Mn alloy showed the best strength in the tensile test. The yield strength and tensile strength of MZC0.5Mn alloy were increased by 25.1 and 3.1%, respectively, while the elongation did not decrease significantly compared to MZC alloy. The addition of Mn in the electrochemical experiments resulted in a denser passivation film and a lower corrosion rate. Based on the comparison of five alloys, MZC0.5Mn alloy had the best comprehensive performance and can be further optimized as a biomedical bone implant material. The further improvement of the comprehensive performance of biomedical magnesium alloys by exploring the different heat treatment processes of Mn-contained alloys can be processed in the further studies, which provide a new basis for medical bone implant materials.

DATA AVAILABILITY STATEMENT

The datasets generated for this study are available on request to the corresponding author.

AUTHOR CONTRIBUTIONS

CY, MC, and YH contributed conception and design of the study. YH organized the database and analytic result and wrote the first draft of the manuscript. CY and MC provided the experimental resources and conducted experimental supervision. YH, CY, YZ, MC, and LW did the writing-review and editing.

FUNDING

The authors acknowledge the financial support for this work from the Joint Foundation of the National Natural Science Foundation of China (U1764254) and the National Natural Science Foundation of China (51871166), as well as Major Science and Technology projects in Tianjin (No. 15ZXQXSY00080).

REFERENCES

Abdel-Gawad, S. A., and Shoeib, M. A. (2019). Corrosion studies and microstructure of Mg–Zn–Ca alloys for biomedical applications. *Surf. Interface.* 14, 108–116. doi: 10.1016/j.surfin.2018.11.011

Arifin, A., Sulong, A. B., Muhamad, N., Syarif, J., and Ramli, M. I. (2014). Material processing of hydroxyapatite and titanium alloy (HA/Ti) composite as implant materials using powder metallurgy: a review. *Mater. Des.* 55, 167–175. doi: 10.1016/j.matdes.2013.09.045

Bakhsheshi Rad, H. R., Idris, M. H., and Kadir, M. R. A. (2012). Characterization and corrosion behavior of biodegradable Mg-Ca and Mg-Ca-Zn implant alloys. *AMM* 121–126, 568–572. doi: 10.4028/www.scientific.net/AMM.121-126.568

Bakhsheshi-Rad, H. R., Abdul-Kadir, M. R., Idris, M. H., and Farahany, S. J. C. S. (2012). Relationship between the corrosion behavior and the thermal characteristics and microstructure of Mg—0.5Ca– x Zn alloys. *Corros. Sci.* 64, 184. doi: 10.1016/j.corsci.2012.07.015

Best, S. M., Porter, A. E., Thian, E. S., and Huang, J. (2008). Bioceramics: past, present and for the future. *J. Eur. Ceram. Soc.* 28, 1319–1327. doi: 10.1016/j.jeurceramsoc.2007.12.001

Bian, D., Zhou, W., Deng, J., Liu, Y., Li, W., Chu, X., et al. (2017). Development of magnesium-based biodegradable metals with dietary trace element germanium as orthopaedic implant applications. *Acta Biomater.* 64, 422–436. doi: 10.1016/j.actbio.2017.10.004

Cho, D. H., Lee, B. W., Park, J. Y., Cho, K. M., and Park, I. M. (2017). Effect of Mn addition on corrosion properties of biodegradable Mg-4Zn-0.5Ca-xMn alloys. *J. Alloys. Compd.* 695, 1166–1174. doi: 10.1016/j.jallcom.2016.10.244

Cho, D. H., Nam, J. H., Lee, B. W., Cho, K. M., and Park, I. M. (2016). Effect of Mn addition on grain refinement of biodegradable Mg 4Zn 0.5Ca alloy. *J. Alloys Compd.* 676, 466–468. doi: 10.1016/j.jallcom.2016.03.182

Du, Y. Z., Qiao, X. G., Zheng, M. Y., Wang, D. B., Wu, K., and Golovin, I. S. (2016). Effect of microalloying with Ca on the microstructure and mechanical properties of Mg-6 mass%Zn alloys. *Mater. Des.* 98, 285–293. doi: 10.1016/j.matdes.2016.03.025

Gil-Santos, A., Marco, I., Moelans, N., Hort, N., and Van der Biest, O. (2017). Microstructure and degradation performance of biodegradable Mg-Si-Sr implant alloys. *Mater. Sci. Eng. C* 71, 26–34. doi: 10.1016/j.msec.2016.09.056

Gu, X. N., Xie, X. H., Li, N., Zheng, Y. F., and Qin, L. (2012). *In vitro* and *in vivo* studies on a Mg-Sr binary alloy system developed as a new kind of biodegradable metal. *Acta Biomater.* 8, 2363–2374. doi: 10.1016/j.actbio.2012.02.018

Gui, Z., Kang, Z., and Li, Y. (2018). Evolution of the microstructure and fracture characteristics of a Mg-Nd-Zn-Zr-Mn alloy through heat treatment and extrusion. *J. Alloys Compd.* 765, 470–479. doi: 10.1016/j.jallcom.2018.06.185

Guo, M. X., Du, J. Q., Zheng, C. H., Zhang, J. S., and Zhuang, L. Z. (2019). Influence of Zn contents on precipitation and corrosion of Al-Mg-Si-Cu-Zn alloys for automotive applications. *J. Alloys Compd.*, 778, 265–270. doi: 10.1016/j.jallcom.2018.11.146

Han, H. -S., Loffredo, S., Jun, I., Edwards, J., Kim, Y. -C., Seok, H. -K., et al. (2019). Current status and outlook on the clinical translation of biodegradable metals. *Mater. Today* 23, 59–71. doi: 10.1016/j.mattod.2018.05.018

Harkness, J. S., and Darrah, T. H. (2019). From the crust to the cortical: the geochemistry of trace elements in human bone. *Geochim. Cosmochim. Acta.* 249, 76–94. doi: 10.1016/j.gca.2019.01.019

He, R. G., Liu, R. Y., Chen, Q. B., Zhang, H. J., Wang, J. F., and Guo, S. F. (2018). *In vitro* degradation behavior and cytocompatibility of Mg-6Zn-Mn alloy. *Mater. Lett.* 228, 77–80. doi: 10.1016/j.matlet.2018.05.034

Ibrahim, H., Esfahani, S. N., Poorganji, B., Dean, D., and Elahinia, M. (2017). Resorbable bone fixation alloys, forming, and post-fabrication treatments. *Mater. Sci. Eng. C* 70, 872–888. doi: 10.1016/j.msec.2016.09.069

Jiang, H., Wang, J., Chen, M., and Liu, D. (2017). Biological activity evaluation of magnesium fluoride coated Mg-Zn-Zr alloy *in vivo*. *Mater. Sci. Eng. C*, 75, 1068–1074. doi: 10.1016/j.msec.2017.03.019

Jiang, M. G., Xu, C., Nakata, T., Yan, H., Chen, R. S., and Kamado, S. (2016). High-speed extrusion of dilute Mg-Zn-Ca-Mn alloys and its effect on microstructure, texture and mechanical properties. *Mater. Sci. Eng. A* 678, 329–338. doi: 10.1016/j.msea.2016.10.007

Jin, W., Wang, G., Qasim, A. M., Mo, S., Ruan, Q., Zhou, H., et al. (2019). Corrosion protection and enhanced biocompatibility of biomedical Mg-Y-RE alloy coated with tin dioxide. *Surf. Coat. Technol.* 357, 79–82. doi: 10.1016/j.surfcoat.2018.10.005

Kannan, M. B., and Raman, R. K. (2008). *In vitro* degradation and mechanical integrity of calcium-containing magnesium alloys in modified-simulated body fluid. *Biomaterials*. 29, 2307–2314. doi: 10.1016/j.biomaterials.2008.02.003

Li, N., and Zheng, Y. (2013). Novel magnesium alloys developed for biomedical application: a review. *J. Mater. Sci. Technol.* 29, 489–502. doi: 10.1016/j.jmst.2013.02.005

Liao, H., Kim, J., Liu, T., Tang, A., She, J., Peng, P., Pan, F., et al. (2019). Effects of Mn addition on the microstructures, mechanical properties and work-hardening of Mg-1Sn alloy. *Mater. Sci. Eng. A* 754, 778–785. doi: 10.1016/j.msea.2019.02.021

Lin, G, Chen, M. F., Zhao, Y., Sasikumar, Y., and Tie, D. (2018a). The mechanical properties and corrosion resistance of magnesium alloys with different alloying elements for bone repair. *Cryst.* 8:271. doi: 10.3390/cryst8070271

Lin, G., Liu, D., Chen, M., You, C., Li, Z., Wang, Y., et al. (2018b). Preparation and characterization of biodegradable Mg-Zn-Ca/MgO nanocomposites for biomedical applications. *Mater. Charact.* 144, 120–130. doi: 10.1016/j.matchar.2018.06.028

Lou, W. B., Xue, Z. Y., and Mao, W. M. (2019). Effect of heat treatment on the microstructure and micromechanical properties of the rapidly solidified Mg61.7Zn34Gd4.3 alloy containing icosahedral phase, *Int. J. Miner. Metall. Mater.* 26, 869–877. doi: 10.1007/s12613-019-1799-4

Lutz, J., and Mändl, S. (2010). Reduced tribocorrosion of CoCr alloys in simulated body fluid after nitrogen insertion. *Surf. Coat. Technol.* 204, 3043–3046. doi: 10.1016/j.surfcoat.2010.01.048

Oh-ishi, K., Watanabe, R., Mendis, C. L., and Hono, K. (2009). Age-hardening response of Mg−0.3at.%Ca alloys with different Zn contents. *Mater. Sci. Eng. A* 526, 177–184. doi: 10.1016/j.msea.2009.07.027

Prins, J., Donders, J. C. E., Helfet, D. L., Wellman, D. S., Klinger, C. E., Redko, M., et al. (2018). Periprosthetic femoral nonunions treated with internal fixation and bone grafting. *Injury* 49, 2296–2301. doi: 10.1016/j.injury.2018.10.019

Seong, J. W., and Kim, W. J. (2015). Development of biodegradable Mg-Ca alloy sheets with enhanced strength and corrosion properties through the refinement and uniform dispersion of the Mg(2)Ca phase by high-ratio differential speed rolling. *Acta Biomater.* 11, 531–542. doi: 10.1016/j.actbio.2014.09.029

Tian, P., and Liu, X. (2015). Surface modification of biodegradable magnesium and its alloys for biomedical applications, *Regen Biomater.*, 2, 136–151. doi: 10.1093/rb/rbu013

Witte, F. (2015). Reprint of: the history of biodegradable magnesium implants: a review. *Acta Biomater.* 23, S28–S40. doi: 10.1016/j.actbio.2015.07.017

Yandong, Y., Shuzhen, K., Teng, P., Jie, L., and Caixia, L. (2015). Effects of Mn addition on the microstructure and mechanical properties of As-cast and heat-treated Mg-Zn-Ca bio-magnesium alloy. *Metal. Micro. Anal.* 4, 381–391. doi: 10.1007/s13632-015-0224-2

Yin, P., Li, N. F., Lei, T., Liu, L., and Ouyang, C. (2013). Effects of Ca on microstructure, mechanical and corrosion properties and biocompatibility of Mg-Zn-Ca alloys. *J. Mater. Sci. Mater Med.* 24, 1367–1373. doi: 10.1007/s10856-013-4856-y

Zhang, B., Hou, Y. L., Wang, X. D., Wang, Y., and Geng, L. (2011). Mechanical properties, degradation performance and cytotoxicity of Mg–Zn–Ca biomedical alloys with different compositions. *Mater. Sci. Eng. C* 3, 1667–1673. doi: 10.1016/j.msec.2011.07.015

Zheng, Y. F., Gu, X. N., and Witte, F. (2014). Biodegradable metals. *Mater. Sci. Eng. R* 77, 1–34. doi: 10.1016/j.mser.2014.01.001

Zhou, W. R., Zheng, Y. F., Leeflang, M. A., and Zhou, J. (2013). Mechanical property, biocorrosion and *in vitro* biocompatibility evaluations of Mg-Li-(Al)-(RE) alloys for future cardiovascular stent application. *Acta. Biomater.* 9, 8488–8498. doi: 10.1016/j.actbio.2013.01.032

Conflict of Interest: The authors declare that the research was conducted in the absence of any commercial or financial relationships that could be construed as a potential conflict of interest.

frontiers
in Materials

ORIGINAL RESEARCH
published: 10 December 2019
doi: 10.3389/fmats.2019.00322

The Poisoning Effect of Al and Be on Mg—1 wt.% Zr Alloy and the Role of Ultrasonic Treatment on Grain Refinement

*Nagasivamuni Balasubramani, Gui Wang, David H. StJohn and Matthew S. Dargusch**

Centre for Advanced Materials Processing and Manufacturing (AMPAM), School of Mechanical and Mining Engineering, The University of Queensland, St. Lucia, QLD, Australia

Addition of Al—Be master alloy to a Mg—Zr alloy reduces melt oxidation, however, it has a detrimental grain coarsening effect that is believed to be caused by an unknown interaction of Be with the Zr nucleant particles. However, this study found that Al is the major cause of grain coarsening. By analysis of intermetallic phases and chemical analysis for solute Zr, it was revealed that Al reacts with the undissolved α–Zr particles forming Zr—Al intermetallic phases and reducing the amount of solute Zr both of which lead to a decrease in the grain refinement efficiency of the master alloy. Despite this negative effect of Al on grain refinement, application of ultrasonic treatment (UST) produces significant grain refinement of the Mg—Zr—Al—Be alloy demonstrating the potential for developing ignition-proof and grain refined Mg alloys.

Keywords: grain refinement, ultrasonic treatment, Mg—Zr alloy, Al—Be master alloy, nucleant poisoning

Edited by:
John L. Provis,
University of Sheffield,
United Kingdom

Reviewed by:
Wenxiang Xu,
Hohai University, China
Feng Wang,
Brunel University London,
United Kingdom

****Correspondence:***
Matthew S. Dargusch
m.dargusch@uq.edu.au

Specialty section:
This article was submitted to
Structural Materials,
a section of the journal
Frontiers in Materials

Received: *24 May 2019*
Accepted: *22 November 2019*
Published: *10 December 2019*

Citation:
Balasubramani N, Wang G,
StJohn DH and Dargusch MS (2019)
The Poisoning Effect of Al and Be on
Mg—1 wt.% Zr Alloy and the Role of
Ultrasonic Treatment on Grain
Refinement. Front. Mater. 6:322.
doi: 10.3389/fmats.2019.00322

INTRODUCTION

Ultrasonic treatment (UST) applied during alloy solidification produces excellent grain refinement which is necessary to achieve improved mechanical properties of the alloys (StJohn et al., 2005, 2013; Eskin, 2014, 2017). This attractive feature of UST facilitates opportunities to explore new alloy systems for which an appropriate grain refiner is unavailable (Nagasivamuni et al., 2018). Significant grain refinement has been reported for pure metals (Nagasivamuni et al., 2018, 2019b), binary alloys without refiners (Qian et al., 2010; Srivastava et al., 2017; Wang et al., 2017b) and in the presence of potent grain refiners (Ramirez et al., 2008; Atamanenko et al., 2010; Wang et al., 2017d; Nagasivamuni et al., 2019a). The application of UST to alloys containing elements that poison nucleation has also resulted in improved refinement. For example, the exceptional grain refinement of Al alloys by the addition of Ti is poisoned by the addition of Zr (Atamanenko et al., 2010; Sreekumar and Eskin, 2016) or Si (Wang et al., 2016b). It has been reported that UST generated cavitation enhances nucleation by reducing the poisoning effect and this results in grain refinement (Atamanenko et al., 2010; Sreekumar and Eskin, 2016; Wang et al., 2016b). Similarly, in carbon inoculated commercial Mg—Al alloys the interaction of Fe or Mn with C is reported to cause poisoning of grain refinement (Easton et al., 2006; Du et al., 2010) while the application of UST results in excellent grain refinement (Ramirez et al., 2008; Nimityongskul et al., 2010).

The interaction of impurities with the added grain refiner particles are specific to the type of alloy and the grain refiner. For instance it is well-known that additions of Zr to Mg alloys that contain Al, Fe, Si (StJohn et al., 2005, 2013) is not effective in promoting grain refinement and for Mg—Al alloys (AZ series), grain refinement by carbon inoculation is affected by the presence of Fe or Mn (StJohn et al., 2005, 2013; Easton et al., 2006; Du et al., 2010). Sometimes a complex interaction might occur in these alloys due to the formation of ternary or multi-component phases that may act as nucleant particles or degrade the nucleation potential of a potent particle (Easton et al., 2006; Du et al., 2010; Huang et al., 2010). Of all these grain refiner specific impurities, Be is an interesting element which has been reported to exhibit a poisoning effect in most of the Mg alloys (Mg—Al, Mg—RE and Mg—Zr) at trace levels of <100 ppm (i.e., 0.01 wt.%, all the compositions mentioned in this paper are in wt.%) (Cao et al., 2004). The advantage of adding Be to Mg alloys at trace levels is its tendency to reduce oxidation of the melt by the formation of a non-porous BeO + MgO oxide layer which in turn reduces the amount of greenhouse gases (such as CO_2 and SF_6) used during Mg melting and casting (Zeng et al., 2001b; Tan et al., 2016, 2018). However, the mechanism of grain coarsening and the effective methods to refine or reduce the grain coarsening tendency have not been reported for Mg alloys that contain trace amounts of Be. Investigating the application of UST to Be containing Mg-Zr alloy melts by determining the composition of dissolved solute Zr (Zr_S) and total Zr (Zr_T) by chemical analysis (Qian et al., 2003; Nagasivamuni et al., 2019a) could provide a better understanding of the underlying mechanisms behind nucleant poisoning and potentially lead to the development of grain refined Be-containing, ignition proof Mg alloys.

Therefore, the present work seeks to investigate the effect of UST on the grain refinement of Mg—1% Zr alloy with 0.01% Be by applying UST in (i) the liquid stage (Mg melt containing α-Zr particles) and (ii) during solidification (from above to below the Mg alloy liquidus temperature). This study is also focused on identifying the mechanisms responsible for poisoning the grain size.

EXPERIMENTAL PROCEDURE

Commercial purity Mg (99.91 wt.%), and Mg—25Zr and Al—5Be master alloys were used to produce Mg—1Zr alloy containing 0.01% Be under the protection of cover gas at 780°C. The use of an Al—Be master alloy is the standard practice of adding Be to commercial Mg alloys and for permanent mold castings with the maximum addition being limited to 0.01% Be (Zeng et al., 2001b; Czerwinski, 2014). The addition of the 0.01% Be from the master alloy increases the Al content of the alloy to 0.2%, therefore, in this study this alloy is referred to as a Mg—1Zr—AlBe alloy. Approximately 220–240 g of Mg was melted in a boron nitride coated clay-graphite crucible. Master alloys containing Zr and Be were added to the Mg melt together and there was no significant time difference between the addition of master alloys. The melt was stirred for 2 min and then removed from the furnace after 5 min to solidify in room temperature atmosphere for the as-cast condition. UST applied above the liquidus temperature of the Mg alloy for 1 min is referred to as UST-L (750 until 660°C) and during solidification is referred to as UST-S (690–650°C) applied for 2 min. Additional details on the methods adopted and equipment used during the casting process, UST, sample preparation, composition analysis for solute (Zr_S) and total Zr (Zr_T) and etching procedures are described elsewhere (Nagasivamuni et al., 2019a,b). **Table 1** shows the composition of the alloys investigated in the as-cast condition and after UST. All the chemical analysis samples were taken from the top region of the casting and for the as-cast alloy the composition was also analyzed from the bottom region of the sample that contains settled α-Zr particles as shown in **Figure 1A**. A Hitachi table top scanning electron microscope (TM3030) equipped with Energy Dispersive X-ray spectroscopy (EDS) at an accelerating voltage of 15keV and Bruker D8 Advance MKII X-ray diffraction were used to characterize the nucleant particles in the alloy.

RESULTS

Figures 1A–C show the macrostructures of the Mg—1Zr—AlBe alloy in the as-cast, UST-L and UST-S conditions and their respective microstructures are shown in **Figures 1D–F**. For comparison, the macro and micro structures of the Mg—1Zr alloy cast under similar conditions are shown in **Figures 1G–I** (Nagasivamuni et al., 2019a). **Figure 1D** exhibits a coarse microstructure with a smaller number of particles in the matrix due to settling of α-Zr particles to the bottom region of the casting (**Figure 1A**). However, under similar casting conditions and settling tendencies the Mg—1Zr alloy exhibits better refinement, **Figure 1G** (Nagasivamuni et al., 2019a). This settling behavior of α-Zr particles alters the alloy composition and deviates from the intended alloy composition in the as-cast condition. After UST-L and UST-S, the amount of settling is reduced in the Mg—1Zr—AlBe alloy (**Figures 1B,C**), however, the grain refinement trend lies above the refinement produced by the Mg—1Zr alloy as shown in **Figure 1J**. The best refinement conditions for the Mg—1Zr—AlBe alloy can be expressed as UST-S > UST-L > as cast.

The composition analysis shown in **Table 1** is plotted in **Figure 1K** for Zr_T against Zr_S. A significant drop in Zr_S is noted for the Mg—1Zr—AlBe alloy with respect to Zr_T when compared to the Mg—1Zr alloy under all casting conditions. **Table 1** presents the amount of Zr_S in the alloy as a percentage with respect to the equilibrium solubility limit ($Zr_S = 0.5\ wt.\%$). A noticeable reduction is observed in the amount of Zr_S and this percent remains <20% (top region) after UST for the Mg—1Zr—AlBe alloy. It is well-known that Zr_S is responsible for the activation of α-Zr particles to achieve maximum grain refinement in Mg—Zr alloys (Qian and Das, 2006; Nagasivamuni et al., 2019a). Due to the very low solute content in the Mg—1Zr—AlBe alloy the extent of refinement is significantly lower for all casting conditions (**Figure 1J**).

Figures 2A,B show the microstructures from the bottom region of the as-cast Mg—1Zr and Mg—1Zr—AlBe alloys. Despite a high Zr_T (5.3%) and 0.33% Zr_S, it is interesting to note from **Figure 2B** that the grains in the Mg—1Zr—AlBe alloy are much larger (1550 ± 350 μm) than the grains observed in the Mg—1Zr alloy in this region (**Figure 2A** with 114 ± 38 μm). **Figures 2C,D** show the X-ray diffractogram of the particles present in the bottom region (**Figures 2A,B**) separated

TABLE 1 | Chemical analysis for Zr_S, Zr_T and percentage of solute in Mg—1Zr and Mg—1Zr—AlBe alloy under different casting conditions.

Alloy	Chemical analysis area	Casting condition	Analyzed composition in wt.%						Be (ppm)	Percentage of Zr_S*	Ref
			Zr_S	Zr_T	Al	Fe	Mn	Ti			
Mg—1Zr—AlBe	Top region	As-cast	0.019	0.053	0.075	<0.002	0.012	<0.002	<10	3.80	Present work
	Bottom region		0.330	5.350	0.043	0.009	0.014	0.08	82	66.0	
	Top region	UST-L	0.049	0.270	0.045	<0.002	0.006	<0.002	<10	9.80	
		UST-S	0.083	0.820	0.032	0.002	0.005	0.002	20	16.6	
Mg—1Zr	Top region	As-cast	0.250	0.300	0.004	<0.002	0.013	0.003	–	50.0	Nagasivamuni et al., 2019a
		UST-L	0.490	0.660	0.008	0.002	0.017	0.006	–	98.0	
		UST-S	0.410	0.990	0.010	0.002	0.012	0.007	–	80.0	

Percentage of solute in the respective alloy is calculated by (Zr_S × 100)/0.5%.

for two ranges of 2θ to improve clarity. The base alloy contains predominantly Mg and Zr peaks. Due to their similar crystal structures most of the α—Zr coincides with α—Mg peaks. Since, the sample was taken from the bottom of the casting, crucible contamination such as Si peaks are identified.

Analysis of the particles in the Mg—1Zr—AlBe alloy were limited to binary phases of Zr containing Al and Be (ternary or multicomponent interactions were ignored). From **Figures 2C,D** it is observed that the intensity of prominent peaks of α–Zr at 36.68°, 57.42°, 68.69° and 90.48° in the Mg—1Zr alloy were lower for the Mg—1Zr—AlBe alloy. The possible combinations of Zr—Al phase are indicated in **Figure 2C** and other Zr-rich phases are marked as Zr_xAl_y because it is challenging to identify any specific Al—Zr phase at very low concentrations. A possible non-stoichiometric Zr—Al intermetallic compound is shown in **Figures 2C,D** because the addition of Mg—25Zr master alloy contains many α-Zr particles that can be easily affected by the dissolved Al atoms to form such phases. It should be noted at this stage (**Figure 2B**) that the interaction of Al with Zr has a tendency to decrease the excellent potency of Zr either by forming a different crystal structure or reducing the number of preferential planes for crystal nucleation on the surface of the α-Zr particles (Fan, 2013). **Figure 2B** shows a large increase in the particle size and α-Mg grain size which indicates significant growth or transformation of the α-Zr particles into Zr—Al phases. A slight enrichment of Be (0.0082%) is observed from the composition analysis in the bottom region, however, it is difficult to detect using X-ray analysis and to interpret its interaction.

Figure 3A shows the back scattered electron image of a grain (dashed line) with possible particles identified as nucleation sites (dotted circle) in the Mg—1Zr—AlBe alloy after UST-S. The elemental analysis of particles marked as A and B in **Figure 3A** are shown in **Figure 3B**. Both of these particles are rich in Zr with traces of Al. An enlarged view of Zr—Al particles in **Figure 3C** shows numerous small particles and few large white particles. The size distribution in **Figure 3D** shows that the particles present in UST-S and UST-L have an average size of 3.1 ± 1.4 μm and 2.8 ± 2.0 μm, respectively. Very fine particles <1 μm were excluded from the analysis as they are unlikely to contribute to grain refinement (Greer et al., 2000). This size distribution of particles is slightly larger than that reported for the Mg—1Zr alloy (Nagasivamuni et al., 2019a) which might be due to the formation of Zr—Al phases. Elemental mapping in **Figure 3E** shows two types of Zr—Al particles with one rich in Zr and the other rich in Al based on relative color intensity. For a better understanding, individual particles and clusters of particles from the microstructure samples (middle region) were analyzed in different fields after UST-S and UST-L and the EDS analysis is shown in **Figures 3F,G**. It is found that almost all of the Zr nucleant particles were associated with the presence of Al. Considering the limitations due to SEM-EDS interaction volumes of, for example 1–5 microns, within the sample, it is almost impossible to find a Zr particle that does not contain Al. This indicates that most of the Al is concentrated toward the vicinity of the α-Zr particles. The ratio of normalized wt.% of Al/Zr reveals that the interaction of Al varies from a ratio as low as 0.2–0.5 indicating that most of the particles are rich in Zr and only a few particles are rich in Al. Therefore, it is observed that both Zr solute and Zr nucleant particles are affected by the addition of the Al—Be master alloy.

DISCUSSION

Significant grain coarsening was reported by Cao et al. (2004) in Zr containing and Zr-free Mg alloys and suggested that nucleant poisoning occurs due to a Be coating formed on the surface of potent particles because any excess addition of Zr to Be containing Mg—Zr alloy did not refine the grains. However, the interaction of Al with Zr or the amount of the dissolved solute Zr in the Be added alloy was not reported in detail. The results of the present work imply that Al is the cause of nucleant poisoning rather than Be. Because, it is well-documented that Be segregates to the surface of a magnesium melt forming either BeO (Zeng et al., 2001a; Horst and Barry, 2006) or a complex (Mg, Be)O layer (Tan et al., 2016, 2018), it is expected that most of the Be diffuses toward the surface of the melt where it is converted into protective oxides. The composition analysis in **Table 1** supports these observations because the Be concentration remaining in the bulk of the alloy is much lower (0.002%) than the intended composition (0.01%). Although the bottom (settled) region in the

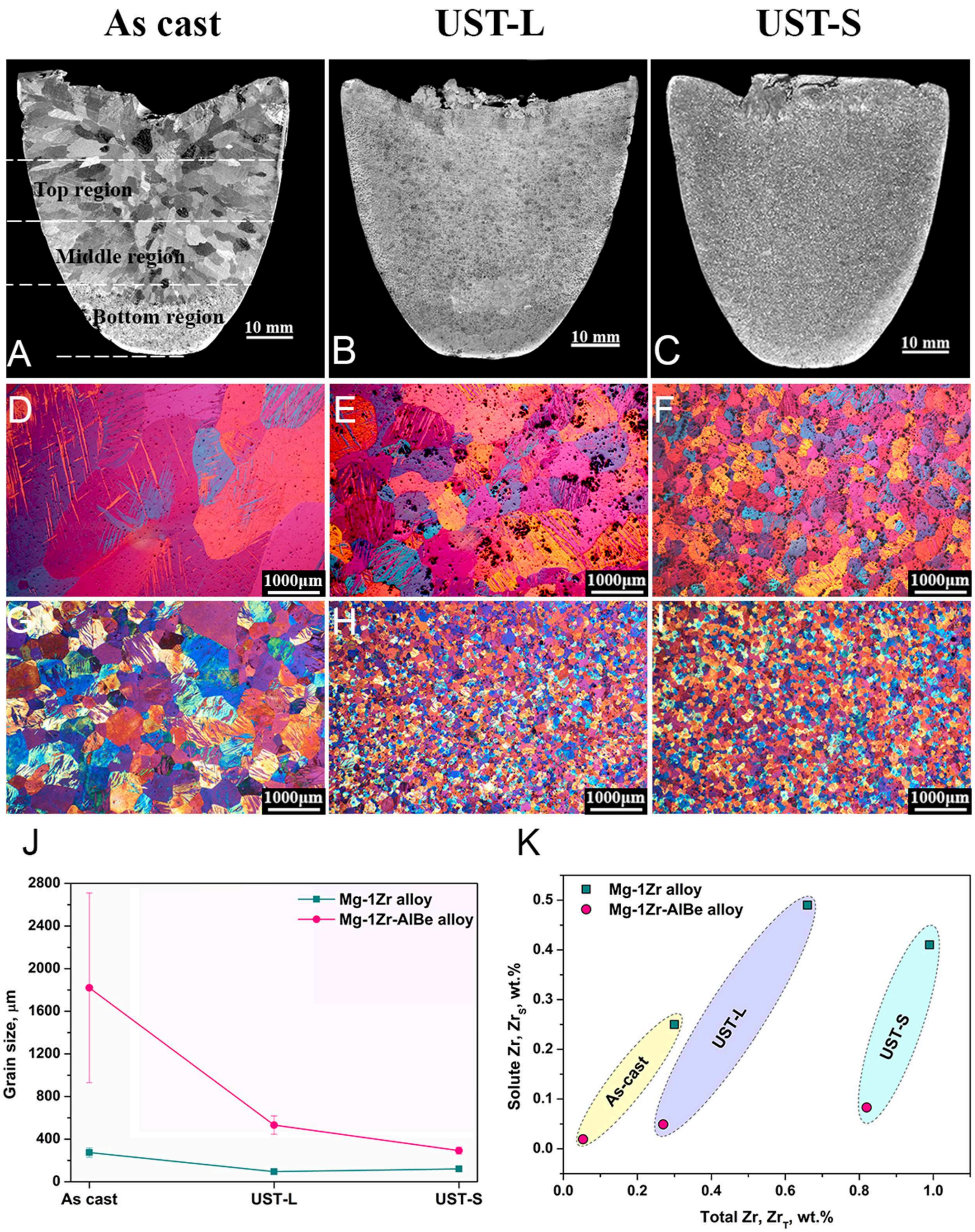

FIGURE 1 | Macrostructures of Mg—1Zr—AlBe alloy in **(A)** as-cast **(B)** UST-L and **(C)** UST-S conditions and their corresponding microstructures **(D–F)** were taken from the middle region of the casting. Under similar conditions the microstructures in **(G–I)** represent the Mg—1Zr alloy that shows excellent grain refinement. **(J)** Compares the grain size of the Mg—1Zr alloy with the Mg—1Zr—AlBe alloy. The inferior grain refinement performance is explained through the loss of solute Zr (Zr_S) plotted in **(K)**.

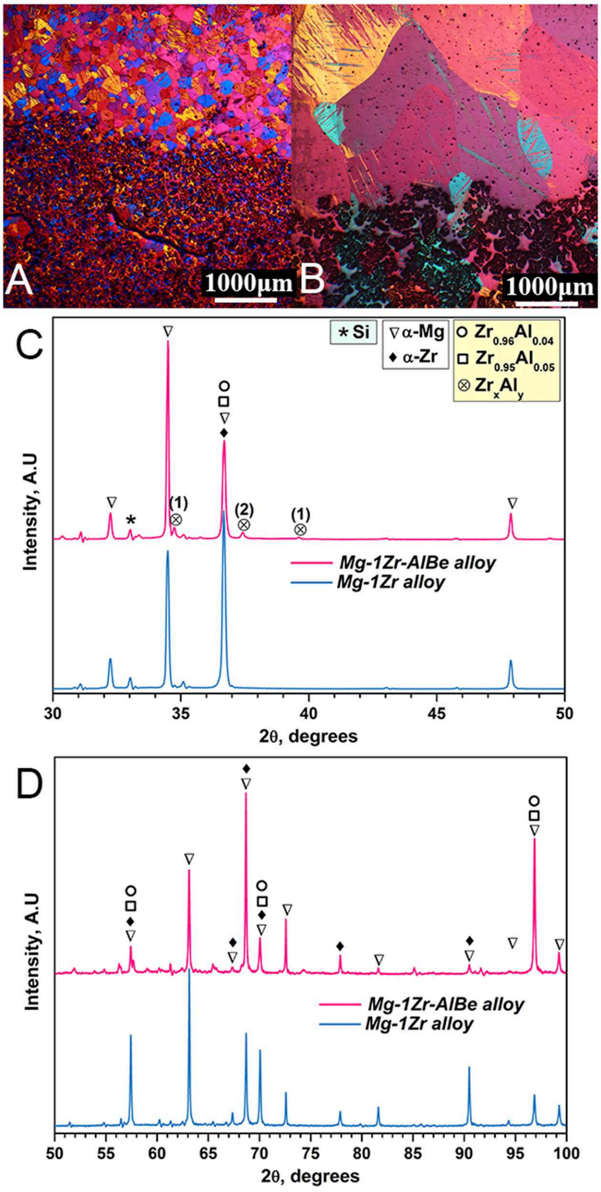

FIGURE 2 | Microstructures of as-cast **(A)** Mg—1Zr alloy and **(B)** Mg—1Zr—AlBe alloy analyzed from the bottom region of the casting exhibits different grain sizes due to the presence of potent and impotent particles (the black phase), respectively. Characterization of the Zr—Al intermetallic phases by an X-ray diffractogram of particles in the settled regions of **(A,B)**. To more clearly show the data the diffractogram is divided into the range of 2θ **(C)** from 30 to 50 degrees and **(D)** from 50 to 100 degrees.

as-cast Mg—1Zr—AlBe alloy contains 0.0082% Be, after UST-S with a reduced settling effect (**Figure 1C**) the Be concentration in the melt is only 0.0002%. The percentage ratio of Be/Zr_T essentially remains the same at 0.15% and 0.24% in as-cast and after UST-S. Therefore, the interaction of Be with Zr nucleant particles can be considered to be insignificant when compared to the effect of Al. Regarding the interaction of Be with the native nucleant particles, a grain coarsening tendency is reported as being more noticeable in commercial purity Mg than in high purity ingot (Ichikawa and Saito, 1963) and Be addition is also patented as a powerful Fe removal agent for Mg alloys (Cao et al., 2004; StJohn et al., 2005). Because the mechanism of the Fe/Mn interaction with nucleant particles is not known in Zr-free Mg alloys (StJohn et al., 2005, 2013), the grain coarsening effect of Be in those alloys needs further research.

The dissolved Al which is at a higher concentration (0.2 wt.%) than Be (0.01%), interacts with Zr in two possible ways (i) with undissolved α-Zr particles and (ii) with dissolved Zr present as solute (Zr_S). **Table 2** lists the possible Zr—Al phases reported for an equilibrium Al—Mg—Zr system after (Bochvar and Bulanova, 2005) in which it is stated that at least 0.05 % Al and 0.04 % Zr is required for the formation of $ZrAl_3$. For Al concentrations below this limit intermetallic precipitates such as Zr_2Al, Zr_2Al_3, Zr_4Al_3, and Zr rich phases are probable as shown in XRD analysis (**Figure 2C**). To compare with the chemical analysis results estimated in wt.%, the fraction of Al, Zr and the Al/Zr ratio were calculated from the molecular weight of individual intermetallic phases. The fraction of Al/Zr estimated from the normalized wt.% of EDS analysis is also included in **Table 2** where it matches with the Al/Zr ratio of some of the possible Zr—Al phases. It should be noted that this normalized wt.% from the EDS analysis is based on the concentration of elements present in that region regardless of the type of crystalline phase. Therefore, EDS quantification cannot be directly approximated for the characterization of a particular intermetallic phase.

From **Table 1**, it is found that UST can increase the amount of solute Zr to the maximum solubility level of 0.5 wt.% in the Mg—1Zr alloy. Therefore, the precipitation of the Zr—Al intermetallic phases was assumed to occur from both dissolved Al (0.2 wt.%) and solute Zr (0.5 wt.%) and the corresponding amount (in wt.%) of different Zr—Al phases are calculated by taking Al as the reaction limiting element and presented in **Table 2**. From **Table 2**, it is interesting to note that formation of one or more combinations of Zr—Al phases could lead to severe loss of both Zr as solute and total Zr in the alloy. For instance, if it is assumed that only $ZrAl_3$ intermetallic is formed in the melt because this intermetallic phase is often found in Mg—Zr alloys that contain Al (Lavernia et al., 1987; Fan, 2013), then the Mg—1Zr—AlBe alloy is still left with free solute of 0.3 wt.% Zr and total Zr of 0.8 wt.%. This level of solute Zr and unaffected α-Zr particles are sufficient to obtain significant refinement (Nagasivamuni et al., 2019a). However, in Mg alloys containing (3–10 wt.%) Al and (0.01–1.6 wt.%) Zr (Bochvar and Bulanova, 2005) and in AZ91 alloy (Kabirian and Mahmudi, 2009), $ZrAl_2$ and Zr_2Al_3 were identified and no $ZrAl_3$ phase was reported. According to **Table 2**, the formation of $ZrAl_2$ and Zr_2Al_3 could almost deplete the amount of solute Zr present in Mg—1Zr alloy (consuming 50% of total Zr). For even richer Zr phases (Al/Zr < 0.30) such as Zr_4Al_3 and Zr_3Al_2, complete consumption of Zr occurs and the melt is left with only impotent nucleation substrates of Zr—Al particles. For instance, the formation of tetragonal $ZrAl_3$ phase has a lattice misfit of 12.55% with α—Mg compared to potent α—Zr particles with a misfit of only 0.67% (Fan, 2013). Interestingly, the values of Zr_S and Zr_T become negative if one

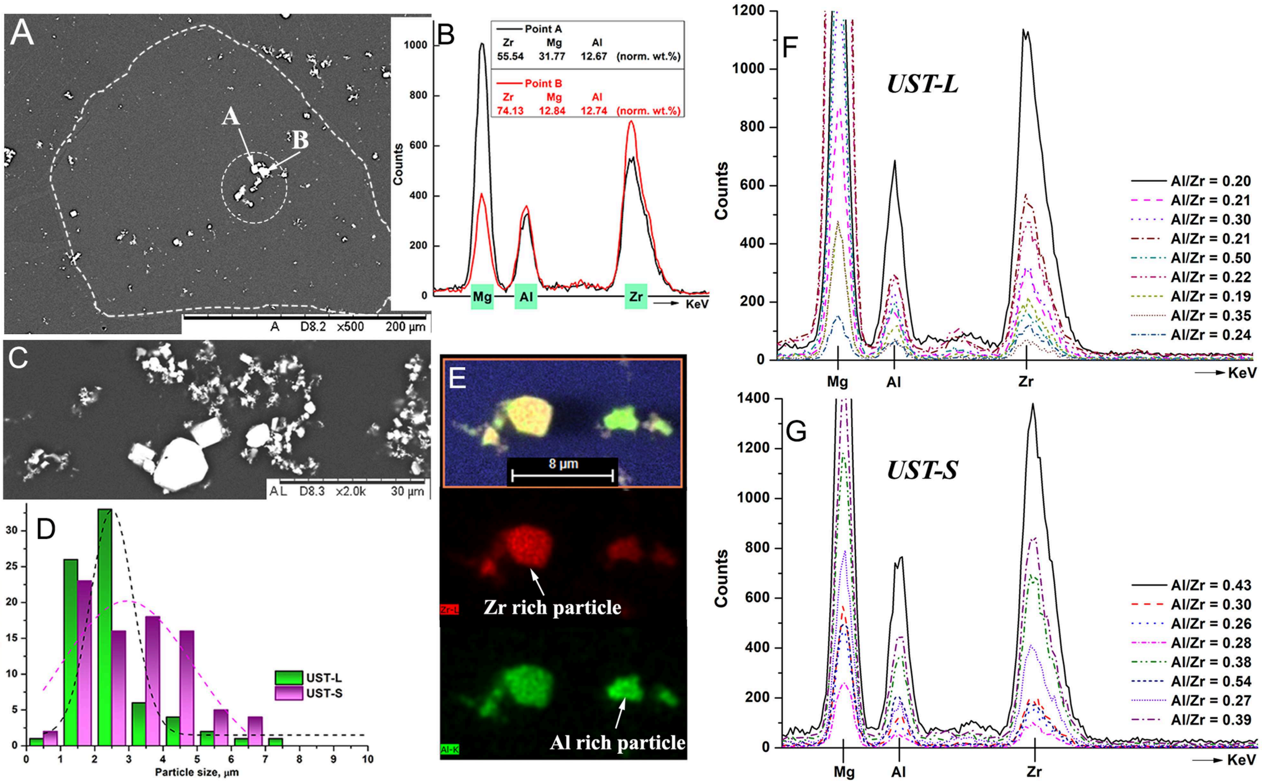

FIGURE 3 | **(A)** Back scattered electron image of Mg—1Zr—AlBe alloy after UST-S showing a grain within the dashed line and possible nucleant particles are denoted as A and B. **(B)** shows the corresponding EDS analysis. **(C)** BSD image of particles with different sizes and **(D)** shows their size distribution histograms. Two types of Zr—Al particles were identified in **(E)** with one rich in Zr and the another particle rich in Al. Almost all the α-Zr particles contain Al in **(F)** UST-L and **(G)** UST-S conditions where the Al/Zr ratio varies between 0.2 and 0.5 calculated from normalized wt.%.

TABLE 2 | Quantification of possible binary Zr—Al intermetallic phases according to the Al—Mg—Zr equilibrium diagrams (Bochvar and Bulanova, 2005) and from the XRD database.

Phases	Fraction of Al and Zr in each phase (calculated from molecular wt.%)			Al/Zr fraction from EDS measurements (norm. wt.%)	Al as rate limiting element[a]	Amount of Zr-Al phases formed[b]	Amount of Zr needed	Free solute Zr available[c]	Total Zr left unaffected[d]
	Al	Zr	Al/Zr	(wt.%)	(wt.%)	(wt.%)	(wt.%)	(wt.%)	(wt.%)
$ZrAl_3$	0.4701	0.5298	0.8873	–	0.19	0.42	0.22	0.27	0.77
$ZrAl_2$	0.3716	0.6283	0.5915	0.50–0.54	0.20	0.54	0.34	0.16	0.66
Zr_2Al_3	0.3073	0.6926	0.4436	0.26–0.43	0.19	0.65	0.45	0.05	0.54
ZrAl	0.2282	0.7717	0.2957		0.19	0.85	0.65	–0.15	0.34
Zr_4Al_3	0.1815	0.8184	0.2218		0.19	1.10	0.90	–0.40	0.09
Zr_3Al_2	0.1647	0.8352	0.1971	0.19–0.24	0.19	1.20	1.00	–0.50	0.00
Zr_5Al_3	0.1507	0.8492	0.1774		0.19	1.30	1.10	–0.60	–0.10
Zr_2Al	0.1288	0.8711	0.1478	–	0.19	1.55	1.35	–0.85	–0.35
Zr_3Al	0.0897	0.9102	0.0985	–	0.19	2.20	2.00	–1.50	–1.00
$Zr_{0.95}Al_{0.05}$	0.0153	0.9846	0.0155	–	0.20	13.0	12.80	–12.3	–11.80
$Zr_{0.96}Al_{0.04}$	0.0121	0.9878	0.0123	–	0.20	16.4	16.20	–15.7	–15.20

[a] *Addition of Al—Be master alloy increases the Al concentration in the melt to 0.2 wt.% max.*

[b] *Amount of Zr—Al phases are calculated by assuming that all dissolved Al is consumed to form the particular intermetallic phase.*

[c] *Free solute Zr left in the Mg—1Zr alloy calculated from the equilibrium solute content of 0.5 wt.%.*

[d] *Calculated from the total Zr (1.0 wt.%).*

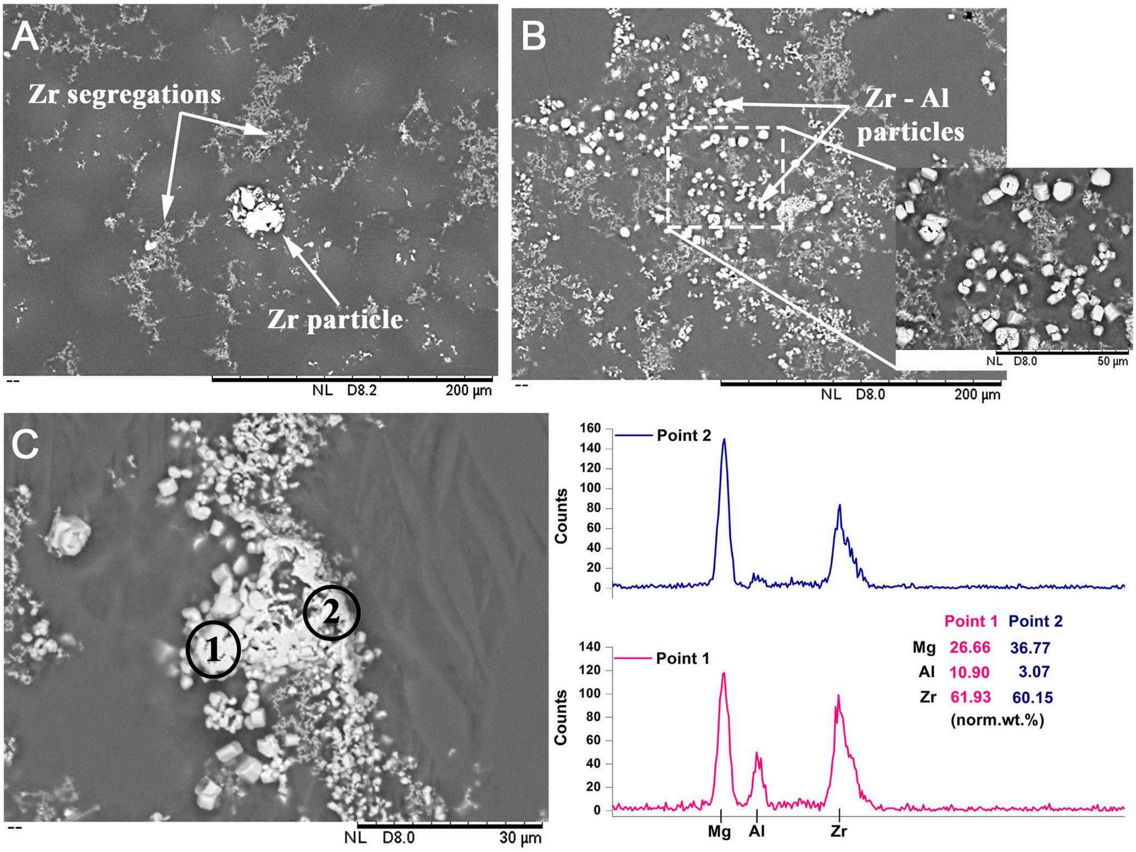

FIGURE 4 | BSD images of **(A)** the as-cast Mg—1Zr alloy showing the presence of a blocky undissolved α-Zr particle and fine Zr particle segregation and **(B)** the Mg—1Zr—AlBe alloy showing faceted Zr—Al intermetallic particles. **(C)** BSD image of a Zr particle cluster in the Mg—1Zr—AlBe alloy surrounded by fine precipitates of Zr—Al intermetallic phases. EDS analysis shows that point 1 contains Al and Zr, whereas point 2 is rich in Zr.

or more combinations of Zr rich phases occurs in the melt consuming all the Zr added to the alloy. It should be noted that the formation of more Zr-rich phases at very low concentrations of Al can consume 2–16% of Zr and this explains the important reason why any excess addition of Zr to Mg alloys containing Al is not effective in promoting significant grain refinement. The calculation indicates that most of the Zr—Al constituents in **Table 2** fall below 2% therefore, no strong peak was observed in the XRD graph to characterize a particular intermetallic other than α—Zr, $Zr_{0.95}Al_{0.05}$, and $Zr_{0.96}Al_{0.04}$. Although some possible phases based on the high intensity lines were characterized as Zr_3Al_2 and Zr_5Al_3 marked as 1 and 2, respectively in **Figure 2C**, which also matches closely with the EDS and chemical analysis results of Zr_S.

It should be noted that the above discussion is based on the assumption that dissolved Al and solute Zr results in Zr—Al phase formation. However, in order to form a Zr—Al intermetallic from dissolved constituents, a substrate is needed to facilitate nucleation and growth (Wang et al., 2017a). In the case of the Mg—1Zr—AlBe alloy, the melt initially contains numerous α-Zr particles that could readily serve as nucleation sites for the Zr—Al phases. Therefore, it is necessary to understand the interaction of the dissolved Al with undissolved α-Zr particles in the melt. **Figures 4A,B** show the BSD image of the Mg—1Zr and Mg—1Zr—AlBe alloys from the bottom region in the as-cast condition. **Figure 4A** shows Zr as bands of fine particles segregated along the grain boundary regions and a larger undissolved α-Zr particle with an approximate size of ∼25 μm. After the addition of Al—Be master alloy, several Zr—Al particles are observed within the Zr segregated regions and these particles are distinctly identified as faceted structures. The magnified insert image in **Figure 4B** shows these Zr—Al intermetallic particles more clearly. **Figure 4C** shows a typical cluster of α-Zr particles in the Mg—1Zr—AlBe alloy. EDS analysis at point 1 shows the presence of Al and Zr while at point 2 the cluster is rich in Zr with very low Al. This might be a larger Zr particle similar to that shown in **Figure 4A**, which is surrounded by numerous fine Zr—Al phases after the addition of the Al—Be master alloy. Therefore, it is more likely that the α-Zr particles act as preferential heterogeneous sites for the precipitation of fine Zr—Al phases in the melt which are then dispersed into the melt. The precipitation and growth of Zr – Al phases would lead to the significant reduction in the solute Zr content observed in the alloy. These observations would explain the coarse grain size

(1.55 mm) observed in the bottom region of the as-cast Mg—1Zr—AlBe alloy that contains 5.3 wt.% of particles (**Figure 2B**) where the growth restriction factor of the alloy is now very low and the distance between potent particles is also very large.

The liquid treatment, UST-L, produces excellent refinement when the alloy contains more potent substrates and solute (Atamanenko et al., 2010; Wang et al., 2017c; Nagasivamuni et al., 2019a). The solidification treatment UST-S, on the other hand, can produce refinement in pure metals (Wang et al., 2017d; Nagasivamuni et al., 2018) and dilute alloys (Wang et al., 2014, 2016a, 2017b; Srivastava et al., 2017) without potent substrates. The mechanism of refinement in both cases is briefly explained elsewhere (Nagasivamuni et al., 2018, 2019a,b). UST-L produces a better dispersion of particles than the as-cast condition, however, the activation of nucleation depends on the amount of solute (Zr_S) in the alloy. During UST-S, nucleation is favored by forced acoustic convection and low temperature gradients (Wang et al., 2017b; Nagasivamuni et al., 2018, 2019a,b). It is interesting to note that in either case, the presence of solute plays an important role in facilitating nucleation and the survival of grains which can be understood by comparison with the Mg—1Zr alloy (**Figure 1J**). Due to the poisoning of the α-Zr particles and the low amount of Zr solute, the extent of grain refinement is less than that of the Mg—1Zr alloy. Nevertheless, UST demonstrates the potential to refine the grains in the alloy containing low additions of Al and Be and could be beneficial for the development of ignition resistant and grain refined Mg alloys.

CONCLUSIONS

This research reveals that the grain coarsening effect of the Al—Be master alloy added to a Mg—Zr alloy mainly arises from the interaction of Al and Zr resulting in the formation of Al—Zr intermetallic phases and a reduction in the amount of Zr solute rather than an effect of Be. Together, the reduction in potency of α-Zr particles as nucleants and the amount of Zr solute due to reaction with Al cause grain coarsening. The significantly lower concentration of Be in the cast and UST processed alloy (<0.001 and 0.002%, respectively) supports the results of other research that Be has diffused to the surface of the melt forming oxides. Even at very low Zr solute contents and with impotent Zr nucleant particles, UST-S produces a greater reduction in grain size than produced by UST-L, demonstrating the potential to develop ignition proof, grain refined Mg castings with Be addition.

DATA AVAILABILITY STATEMENT

All datasets generated for this study are included in the article/supplementary material.

AUTHOR CONTRIBUTIONS

NB designed and performed the experiments, analyzed, characterized the results, designed the figures, and drafted the manuscript. GW and MD supervise the findings of the work and contributed to the final version of manuscript by evaluating the methods and procedures adopted in nucleant particle characterization. DS critically reviewed the concepts of discussion, characterization, interpretation of the results, and significantly contributed to improving the writing of the manuscript. All the authors contributed to the results and discussion section of the manuscript.

FUNDING

The authors acknowledge the funding support provided by Australian Research Council Research Hub for Advanced Manufacturing of Medical Devices IH150100024, the ARC Discovery grant DP140100702 and ARC linkage project LP150100950.

ACKNOWLEDGMENTS

NB thanks Qiyang Tan for provision of the Al—5Be master alloy. The authors also thank the scientific and technical assistance of the Australian Microscopy and Microanalysis Research Facility at the Center for Microscopy and Microanalysis, The University of Queensland.

REFERENCES

Atamanenko, T. V., Eskin, D. G., Zhang, L., and Katgerman, L. (2010). Criteria of grain refinement induced by ultrasonic melt treatment of aluminum alloys containing Zr and Ti. *Metallurgical Mater.Trans A*. 41, 2056–2066. doi: 10.1007/s11661-010-0232-4

Bochvar, N. R., and Bulanova, M. V. (2005). "Al-Mg-Zr (Aluminium - Magnesium - Zirconium): datasheet from landolt-börnstein - group IV physical chemistry volume 11A3," in *Light Metal Systems. Part 3* eds G. Effenberg and S. Ilyenko (Berlin, Heidelberg: SpringerMaterials; Springer-Verlag).

Cao, P., Qian, M., and StJohn, D. H. (2004). Grain coarsening of magnesium alloys by beryllium. *Scr. Mater*. 51, 647–651. doi: 10.1016/j.scriptamat.2004.06.022

Czerwinski, F. (2014). Controlling the ignition and flammability of magnesium for aerospace applications. *Corros. Sci*. 86, 1–16. doi: 10.1016/j.corsci.2014.04.047

Du, J., Wang, M. H., and Li, W. F. (2010). Effects of Fe addition and addition sequence on carbon inoculation of Mg-3%Al alloy. *J. Alloys Compd*. 502, 74–79. doi: 10.1016/j.jallcom.2010.04.156

Easton, M. A., Schiffl, A., Yao, J. Y., and Kaufmann, H. (2006). Grain refinement of Mg-Al(-Mn) alloys by SiC additions. *Scr. Mater*. 55, 379–382. doi: 10.1016/j.scriptamat.2006.04.014

Eskin, D. G. (2014). Ultrasonic melt processing: opportunities and misconceptions. *Aluminium Alloys* 2014 - ICAA14 794–796, 101–106. doi: 10.4028/www.scientific.net/MSF.794-796.101

Eskin, D. G. (2017). Ultrasonic processing of molten and solidifying aluminium alloys: overview and outlook. *Mater. Sci. Technol*. 33, 636–645. doi: 10.1080/02670836.2016.1162415

Fan, Z. (2013). An epitaxial model for heterogeneous nucleation on potent substrates. *Metall. Mater Trans. A* 44, 1409–1418. doi: 10.1007/s11661-012-1495-8

Greer, A. L., Bunn, A. M., Tronche, A., Evans, P. V., and Bristow, D. J. (2000). Modelling of inoculation of metallic melts: application to grain refinement of aluminium by Al-Ti-B. *Acta Mater.* 48, 2823–2835. doi: 10.1016/S1359-6454(00)00094-X

Horst, F. E., and Barry, M. L. (ed.). (2006). "Magnesium casting alloys," in *Magnesium Technology: Metallurgy, Design Data, Applications* (Berlin, Heidelberg: Springer Berlin Heidelberg), 145–218.

Huang, Y. D., Zheng, X. H., Kainer, K. U., and Hort, N. (2010). "Mechanism of grain refinement in Mg-Al alloys with carbon inoculations," in *New Frontiers in Light Metals: Proceedings of the 11th International Aluminium Conference INALCO 2010*, eds. L. Katgerman and F. Soetens (IOS Press), 451–460. doi: 10.3233/978-1-60750-586-0-451

Ichikawa, R., and Saito, R. (1963). The distribution of Be and the grain size on Mg-Al alloys containing Be. *J. Jpn Inst Metals* 27, 32–37. doi: 10.2320/jinstmet1952.27.1_32

Kabirian, F., and Mahmudi, R. (2009). Effects of zirconium additions on the microstructure of As-cast and aged AZ91 magnesium alloy. *Adv. Eng. Mater.* 11, 189–193. doi: 10.1002/adem.200800223

Lavernia, E. J., Gomez, E., and Grant, N. J. (1987). The structures and properties of Mg-Al-Zr and Mg-Zn-Zr alloys produced by liquid dynamic compaction. *Mater. Sci. Eng.* 95, 225–236. doi: 10.1016/0025-5416(87)90514-3

Nagasivamuni, B., Wang, G., StJohn, D. H., and Dargusch, M. S. (2018). The effect of ultrasonic treatment on the mechanisms of grain formation in as-cast high purity zinc. *J. Cryst. Growth* 495, 20–28. doi: 10.1016/j.jcrysgro.2018.05.006

Nagasivamuni, B., Wang, G., StJohn, D. H., and Dargusch, M. S. (2019a). Effect of ultrasonic treatment on the alloying and grain refinement efficiency of a Mg – Zr master alloy added to magnesium at hypo- and hyper-peritectic compositions. *J. Cryst. Growth* 512, 20–32. doi: 10.1016/j.jcrysgro.2019.02.004

Nagasivamuni, B., Wang, G., StJohn, D. H., and Dargusch, M. S. (2019b). *Mechanisms of Grain Formation During Ultrasonic Solidification of Commercial Purity Magnesium*. Springer International Publishing. 1579–1586.

Nimityongskul, S., Jones, M., Choi, H., Lakes, R., Kou, S., and Li, X. C. (2010). Grain refining mechanisms in Mg-Al alloys with Al4C3 microparticles. *Mater. Sci. Eng. A* 527, 2104–2111. doi: 10.1016/j.msea.2009.12.030

Qian, M., and Das, A. (2006). Grain refinement of magnesium alloys by zirconium: formation of equiaxed grains. *Scr. Mater.* 54, 881–886. doi: 10.1016/j.scriptamat.2005.11.002

Qian, M., Ramirez, A., Das, A., and StJohn, D. H. (2010). The effect of solute on ultrasonic grain refinement of magnesium alloys. *J. Cryst. Growth* 312, 2267–2272. doi: 10.1016/j.jcrysgro.2010.04.035

Qian, M., StJohn, D. H., and Frost, M. T. (2003). Effect of soluble and insoluble zirconium on the grain refinement of magnesium alloys. *Magnesium Alloys 2003* 419–4, 593–598. doi: 10.4028/www.scientific.net/MSF.419-422.593

Ramirez, A., Qian, M., Davis, B., Wilks, T., and StJohn, D. H. (2008). Potency of high-intensity ultrasonic treatment for grain refinement of magnesium alloys. *Scr. Mater.* 59, 19–22. doi: 10.1016/j.scriptamat.2008.02.017

Sreekumar, V. M., and Eskin, D. G. (2016). A new Al-Zr-Ti master alloy for ultrasonic grain refinement of wrought and foundry aluminum alloys. *Jom* 68, 3088–3093. doi: 10.1007/s11837-016-2120-x

Srivastava, N., Chaudhari, G. P., and Qian, M. (2017). Grain refinement of binary Al-Si, Al-Cu and Al-Ni alloys by ultrasonication. *J. Mater. Process. Technol.* 249, 367–378. doi: 10.1016/j.jmatprotec.2017.06.024

StJohn, D. H., Easton, M. A., Qian, M., and Taylor, J. A. (2013). Grain refinement of magnesium alloys: a review of recent research, theoretical developments, and their application. *Metall. Mater. Trans. A* 44a, 2935–2949. doi: 10.1007/s11661-012-1513-x

StJohn, D. H., Qian, M., Easton, M. A., Cao, P., and Hildebrand, Z. (2005). Grain refinement of magnesium alloys. *Metall. Mater. Trans. A* 36a, 1669–1679. doi: 10.1007/s11661-005-0030-6

Tan, Q. Y., Mo, N., Jiang, B., Pan, F. S., Atrens, A., and Zhang, M. X. (2016). Oxidation resistance of Mg-9Al-1Zn alloys micro-alloyed with Be. *Scr. Mater.* 115, 38–41. doi: 10.1016/j.scriptamat.2015.12.022

Tan, Q. Y., Mo, N., Lin, C. L., Jiang, B., Pan, F. S., Huang, H., et al. (2018). Improved oxidation resistance of Mg-9Al-1Zn alloy microalloyed with 60 wt ppm Be attributed to the formation of a more protective (Mg,Be)O surface oxide. *Corros. Sci.* 132, 272–283. doi: 10.1016/j.corsci.2018.01.006

Wang, E. Q., Wang, G., Dargusch, M. S., Qian, M., Eskin, D. G., and StJohn, D. H. (2016a). Grain refinement of an Al-2 wt%Cu alloy by Al3Ti1B master alloy and ultrasonic treatment. *IOP Conf. Ser.* 117:012050. doi: 10.1088/1757-899X/117/1/012050

Wang, F., Eskin, D., Connolley, T., and Mi, J. W. (2017a). Influence of ultrasonic treatment on formation of primary Al3Zr in Al—0.4Zr alloy. *Trans. Nonferrous Met. Soc. China* 27, 977–985. doi: 10.1016/S1003-6326(17)60115-8

Wang, G., Croaker, P., Dargusch, M., McGuckin, D., and StJohn, D. (2017b). Simulation of convective flow and thermal conditions during ultrasonic treatment of an Al-2Cu alloy. *Comput. Mater. Sci.* 134, 116–125. doi: 10.1016/j.commatsci.2017.03.041

Wang, G., Dargusch, M. S., Eskin, D. G., and StJohn, D. H. (2017c). Identifying the stages during ultrasonic processing that reduce the grain size of aluminum with added Al3Ti1B master alloy. *Adv. Eng. Mater.* 19:1700264. doi: 10.1002/adem.201700264

Wang, G., Dargusch, M. S., Qian, M., Eskin, D. G., and StJohn, D. H. (2014). The role of ultrasonic treatment in refining the as-cast grain structure during the solidification of an Al-2Cu alloy. *J. Cryst. Growth* 408, 119–124. doi: 10.1016/j.jcrysgro.2014.09.018

Wang, G., Qiang Wang, E., Prasad, A., Dargusch, M., and StJohn, D. H. (2016b). "Grain refinement Of Al-Si hypoeutectic alloys By Al3Ti1B master alloy and ultrasonic treatment," in *Shape Casting: 6th International Symposium*. John Wiley & Sons, Inc., 141–150.

Wang, G., Wang, Q., Easton, M. A., Dargusch, M. S., Qian, M., Eskin, D. G., et al. (2017d). Role of ultrasonic treatment, inoculation and solute in the grain refinement of commercial purity aluminium. *Sci. Rep.* 7:9729. doi: 10.1038/s41598-017-10354-6

Zeng, X. Q., Wang, Q. D., Lu, Y. H., Ding, W. J., Zhu, Y. P., Zhai, C. Q., et al. (2001a). Behavior of surface oxidation on molten Mg-9Al-0.5Zn-0.3Be alloy. *Mater. Sci. Eng. A* 301, 154–161. doi: 10.1016/S0921-5093(00)01798-6

Zeng, X. Q., Wang, Q. D., Lu, Y. Z., Zhu, Y. P., Ding, W. J., and Zhao, Y. H. (2001b). Influence of beryllium and rare earth additions on ignition-proof magnesium alloys. *J. Mater. Process. Technol.* 112, 17–23. doi: 10.1016/S0924-0136(00)00854-2

Conflict of Interest: The authors declare that the research was conducted in the absence of any commercial or financial relationships that could be construed as a potential conflict of interest.

frontiers in Materials

MINI REVIEW
published: 09 January 2020
doi: 10.3389/fmats.2019.00339

Texture Related Inhomogeneous Deformation and Fracture Localization in Friction-Stir-Welded Magnesium Alloys: A Review

Weijie Ren[1], Renlong Xin[1]*, Chuan Tan[1] and Dejia Liu[2]

[1] Joint International Laboratory for Light Alloys (MOE), College of Materials Science and Engineering, Chongqing University, Chongqing, China, [2] College of Materials Science and Engineering, East China Jiaotong University, Nanchang, China

Friction stir welding (FSW) is a solid-state joining technique, which can avoid surface distortion and grain coarsening, and is very suitable for the joining of magnesium (Mg) alloys. However, a pronounced and inhomogeneous deformation texture was usually formed in the stir zone (SZ) of Mg welds. This has significant effect on the joint strength and fracture behavior of FSW Mg joints. In this review, microstructure and texture evolutions in weld zone (WZ) are analyzed based on the electron backscatter diffraction (EBSD) data. Schmid factor (SF) changes for slip and extension twinning were observed and discussed. The localized plastic deformation and fracture mechanisms of Mg welds are analyzed. In addition, some methods for improving the joint strength of FSW Mg welds are tested. Finally, the research direction of FSW Mg alloys in the future is determined.

Keywords: friction stir welding, magnesium alloy, texture, localized deformation, fracture

Edited by:
Hajo Dieringa,
Helmholtz Centre for Materials and Coastal Research (HZG), Germany

Reviewed by:
Guntram Prof. Dr. Wagner,
Technische Universität Chemnitz, Germany
Sergey Mironov,
Belgorod National Research University, Russia

Correspondence:
Renlong Xin
rlxin@cqu.edu.cn

Specialty section:
This article was submitted to Structural Materials, a section of the journal Frontiers in Materials

Received: *28 June 2019*
Accepted: *10 December 2019*
Published: *09 January 2020*

Citation:
Ren W, Xin R, Tan C and Liu D (2020) Texture Related Inhomogeneous Deformation and Fracture Localization in Friction-Stir-Welded Magnesium Alloys: A Review. Front. Mater. 6:339. doi: 10.3389/fmats.2019.00339

INTRODUCTION

Mg alloys continue to receive significant interests in automotive and aerospace industries due to their obvious advantages of low density and high specific strength (Barnett et al., 2004; Suhuddin et al., 2009; Yang et al., 2010; Kainer, 2016; Dieringa, 2017). To widen their application, it is important to consider the advanced joining technology of Mg alloys (Lee et al., 2003; Xunhong and Kuaishe, 2006; Xie et al., 2007). Unfortunately, conventional fusion welding faces many challenges such as porosity, crack, intolerable distortions, emission of non-toxic fumes and evaporative loss of alloying elements (Commin et al., 2009; Cam, 2011). As a solid-state joining technique, friction stir welding (FSW) can avoid solidification problems associated with conventional fusion welding and has great potential in welding light metals such as Mg alloys (Woo et al., 2006; Lee et al., 2007; Afrin et al., 2008; Argade et al., 2012; Chen et al., 2013; He et al., 2014; Sidhar et al., 2016).

FSW was invented at the Welding Institute (TWI) of the United Kingdom in 1991, and it was initially applied to aluminum alloys (Thomas et al., 1991, 2003). During FSW, a non-consumable rotating probe is inserted into the abutting edges of the workpieces and traversed along the line of the joint (see **Figure 1**). The localized heating softens the materials around the probe. The combination of tool rotation and translation leads to movement of materials from the front to the back of the probe. Severe plastic deformation and friction heat in this process lead to dynamic recrystallization in weld zone (WZ), causing significant grain refinement (Freeney and Mishra, 2010; Xin et al., 2013b; Ni et al., 2014). Based on the basic principles of FSW, friction stir processing (FSP) technique was developed by Mishra et al. (1999) and Mishra and Mahoney (2001) mainly

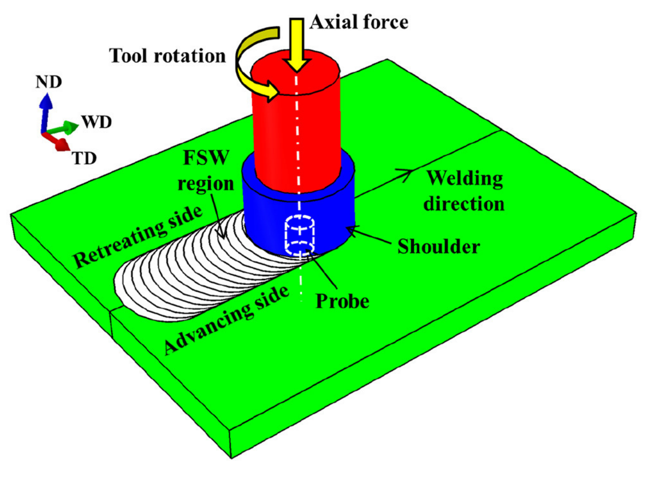

FIGURE 1 | Schematic illustration of the FSW process.

for the purpose of microstructure modification (Berbon et al., 2001; Bhargava et al., 2009; Cui et al., 2009; Yuan et al., 2011, 2013; Mansoor and Ghosh, 2012; Jain et al., 2013; Nene et al., 2018). Mohan et al. (2013) found that the average grain size of the FSP AZ91 alloy was 0.5 µm, which exhibits high strain rate superplasticity. The elongation of 1,251% was achieved at a strain rate of 1×10^{-2} s^{-1} and temperature of 330°C.

Previous studies confirmed that various series of Mg alloys, such as AZ (Mg-Al-Zn) (Afrin et al., 2007, 2008), AM (Mg-Al-Mn) (Cavaliere and De Marco, 2007), and ZK (Mg-Zn-Zr) (Mironov et al., 2007; Xie et al., 2008) have been successfully joined by FSW. However, a pronounced and inhomogeneous texture with (0001) plane roughly parallel to the probe surface was generally formed in stir zone (SZ) (Park et al., 2003a,b; Woo et al., 2008; Xin et al., 2012). As well-known that Mg alloys have strong mechanical anisotropy due to the limited number of slip systems and the large difference of critical resolved shear stress (CRSS) among the various slip and twinning systems (Song et al., 2019). Therefore, the presence of strong local texture in SZ would cause severe non-uniform plastic deformation during transverse tensile tests on the Mg joint (Ma, 2008; Xin et al., 2013a; Liu et al., 2014). This significantly deteriorates the joint strength. In addition, it was found that fracture consistently initiates in the transition region between thermal-mechanical affected zone (TMAZ) and SZ-side on advancing side (Lim et al., 2005; Yang et al., 2010; Dorbane et al., 2016).

As seen from the above descriptions, WZ is the weak place for FSW Mg alloys. In-depth understandings on its mechanical property and deformation behavior are necessary for the wide application of Mg joints. In this paper, the localized plastic deformation and fracture mechanisms of Mg welds with typical micro-texture development are discussed. In addition, some methods for improving the joint performance are tested. Finally, the research direction on FSW Mg alloys is determined.

PROPERTIES AND DEFORMATION MECHANISMS OF FSW MG JOINT

Texture and Joint Strength

Figure 2 demonstrates the evolution of complicated microtexture in the WZ of an FSP Mg alloy (Xin et al., 2010). The base material (BM) has an initial basal texture with the c-axis of most grains parallel to normal direction (ND). A localized strong basal texture is formed in SZ and it tends to tilt from transverse direction (TD) to processing direction (PD) with the position moving from SZ-side to SZ-center. This is mainly related to the shear stress generated by the rotation of the cylindrical probe surface (Park et al., 2003a). Moreover, the <0001> direction tends to tilt to ND at upper and bottom sections of SZ. The formation of <0001>//ND texture in the upper and bottom sections is attributable to the stirring effect of the tool shoulder and the probe tip, respectively. The texture in TMAZ was also affected by the stir probe, which is more diffuse compared to that in BM, and the <0001> direction was tilted toward TD. The <0001> texture in heat affected zone (HAZ) is similar to that in BM, but more diffuse. The <0001> direction in crown zone (CZ) slightly deviates from ND due to the stress from the tool shoulder.

The complicated texture distribution in Mg welds has strong influences on joint performance (Xin et al., 2013a; Liu et al., 2014; Moraes et al., 2017). As shown in **Figure 3**, the yield strength (YS) and ultimate tensile strength (UTS) of an FSP AZ31 alloy are much lower along TD than that of the as-received plate (Xin et al., 2012). Moreover, the elongation of the former is obviously decreased. The mechanical properties of several kinds of FSW Mg alloys [AZ31 (Yang et al., 2010; Xin et al., 2014; Ugender, 2018), AZ61 (Park et al., 2003b; Singh et al., 2018), ZK60 (Xie et al., 2008), ZM21 (Harikrishna et al., 2010), and Mg-Zn-Y-Zr (Xie et al., 2007)] were further summarized, as shown in **Figure 4**. It is seen that the YS and UTS of FSW Mg alloys are generally lower than that of BM. Therefore, it is desirable to understand the effects of textural variation in Mg welds on joint strength and the underlying plastic deformation mechanism.

Inhomogeneous Deformation of Joint

It is seen from **Figure 5A** that the Mg alloy joint has suffered severe non-uniform macroscopic plastic deformation (Xin et al., 2012). To estimate the inhomogeneity of plastic deformation, the thickness and width reductions in the different regions were measured and are presented in **Figure 5B**. It reveals that SZ-side experienced the largest deformation, while SZ-center and HAZ experienced the least deformation. Consequently, necking was observed in SZ-side. Xin et al. (2012) calculated the Schmid factor (SF) maps for an FSP AZ31 plate based on EBSD data, as shown in **Figure 5C**. It is seen that SZ-side has the largest mean SF (∼0.40) for basal slip, while SZ-center has the lowest (∼0.14). Considering basal slip is the most easily activated deformation mode for Mg alloy at room temperature (RT), the SF analysis indicates that SZ-side is the softest and SZ-center is the hardest during transverse tensile tests. This is consistent with the observed inhomogeneous deformation for Mg joints as shown in **Figure 5B**. The grains in SZ-center, TMAZ, and HAZ are

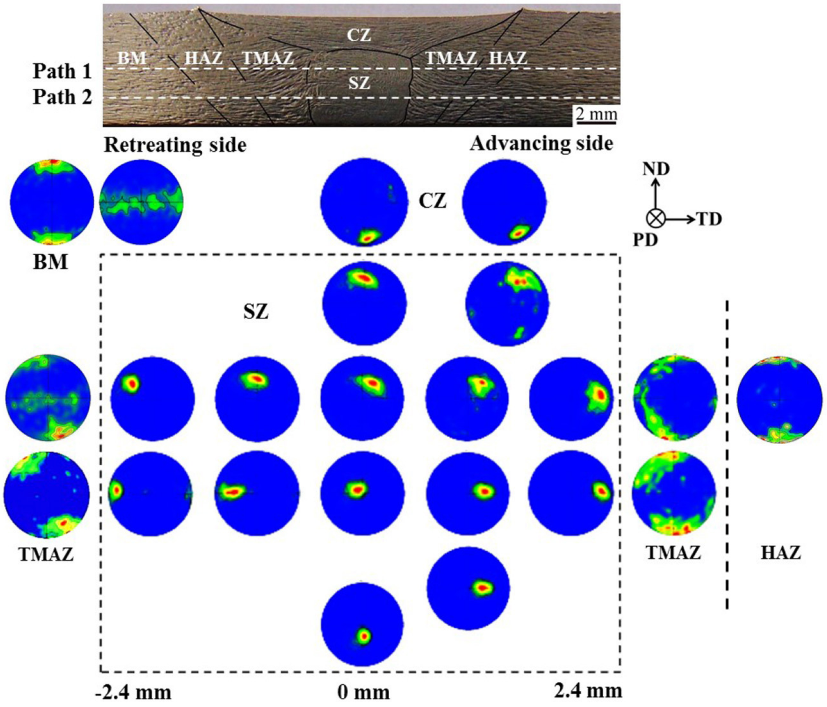

FIGURE 2 | Overall cross-sectional macrostructure of the FSP AZ31 Mg alloy and the {0002} pole figures in various regions of the joint (Xin et al., 2010) (Copyright © 2010, Trans Tech Publications Ltd.).

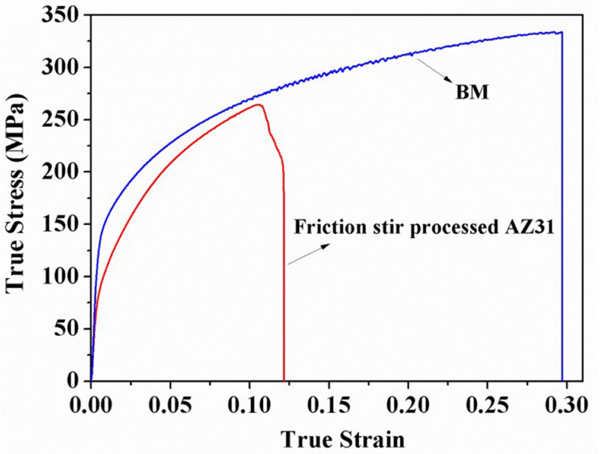

FIGURE 3 | Stress-strain curves of the transverse tensile specimen cut from the BM and the FSP AZ31 Mg alloy (Xin et al., 2012) (Copyright © 2012, Springer Nature).

oriented favorable for prismatic slip and c+a slip. However, these slip modes have high CRSS, and hence are difficult to activate at RT. Thus, the profuse activation of basal slip should be an important factor for necking in SZ-side.

It is known that {10–12} extension twinning is also an important deformation mode for Mg alloys because of its low CRSS (Barnett, 2007; Lin et al., 2016). Besides, twinning activity is highly dependent on grain orientations with respect to the loading direction. As shown in **Figure 6A**, few extension twin boundaries were observed in SZ-center and there is no obvious peak around 86° in the misorientation angle distribution. On the contrary, considerable twin boundaries are identified in SZ-side (**Figure 6B**) and the corresponding misorientation angle distribution indicates that there is a strong peak around 86°. This implies that the profuse activation of extension twinning is also responsible for the necking occurred in SZ-side. Theoretical calculation, however, indicates that the strain accommodated by extension twinning is very limited (Barnett, 2007). On the other hand, basal slip can continuously accommodate the applied plastic strain. Therefore, it is considered that the strain localization occurred in SZ is mainly attributed to basal slip. In addition, the profuse activation of basal slip and extension twinning in SZ-side is an important reason for the lower YS and UTS of the joint compared to BM.

Many studies found that an "embossed" phenomenon appears in SZ-center during the transverse tensile tests on FSW Mg joints (Xin et al., 2013a; Liu et al., 2014). Prangnell and Heason (2005) and Yang et al. (2014b) attributed this to the different sheared material layers between the two sides of the specimen. However, Xin et al. (2013a) believed that the activation of basal slip in SZ-side was a major factor for the formation of this "embossed phenomenon." The reasons for this behavior are complicated and further studies are certainly required.

It is difficult to observe the material flow in SZ during the actual welding process. Numerical simulation can help overcome

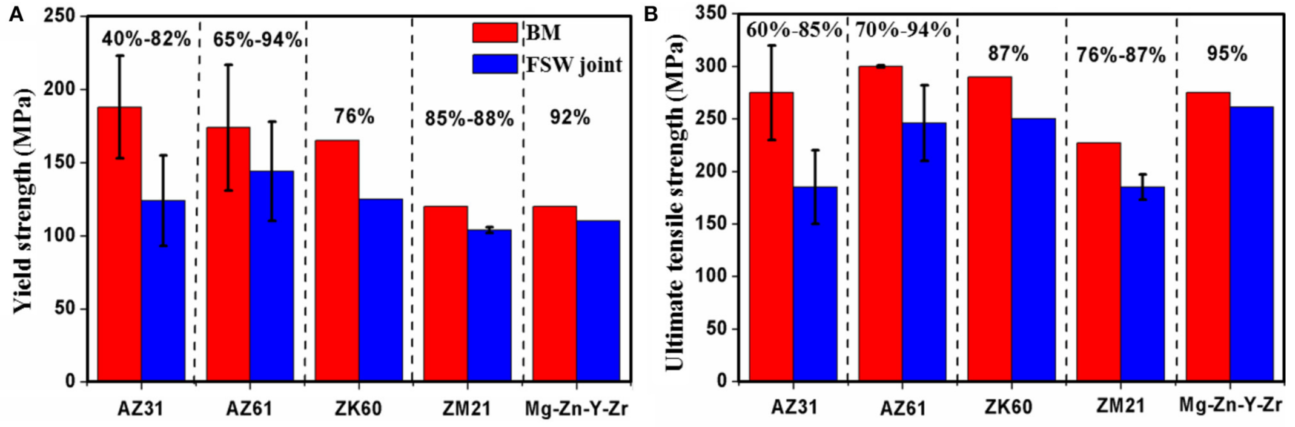

FIGURE 4 | Summary of the mechanical properties of FSW Mg alloys: **(A)** YS and **(B)** UTS.

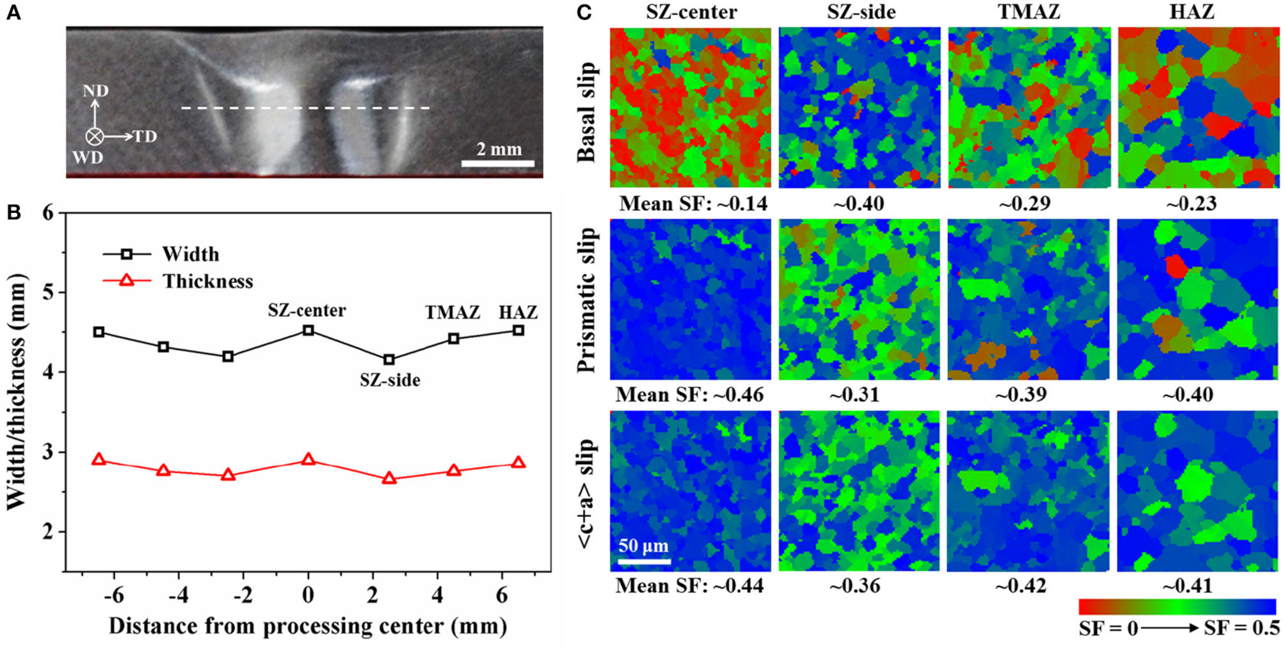

FIGURE 5 | (A) Macrograph of the Mg weld after transverse tensile test; **(B)** measured with width and thickness at different sub-regions of the FSP AZ31 Mg alloy after tensile fracture. The original width and thickness of tensile samples were 5 and 3 mm, respectively; **(C)** SF maps of the various regions of the Mg weld (Xin et al., 2012) (Copyright © 2012, Springer Nature).

this problem (Yu et al., 2012; Baffari et al., 2018; Iqbal et al., 2019). For example, the material flow and temperature field (Nandan et al., 2006) near the probe surface have been predicted and the mechanical response (Chiumenti et al., 2013) have been analyzed during FSW process. Kim et al. (2017) simulated the texture evolution in SZ of AZ31 Mg alloys during FSW process using a visco-plastic self-consistent (VPSC) polycrystal model. Ren et al. (2019) developed a crystal plasticity finite element model (CPFEM) to simulate the localized deformation of an FSW AZ31 Mg joint during bending. They confirmed that the strongly localized texture in conjunction with the different activities of slip and twinning in each sub-region cause the severe strain heterogeneity in welding direction (WD). Moreover, the localized deformation of FSW Mg alloys during transverse tensile test have been analyzed by digital image correlation (DIC) technique (Mironov et al., 2017) and surface depth measurement (Liu et al., 2014). In their study, a random ink pattern was applied on sample surface and the movement of the ink pattern during test was recorded by a high speed digital camera. Then, the in-plane Lagrangian strains can be obtained by the DIC technique.

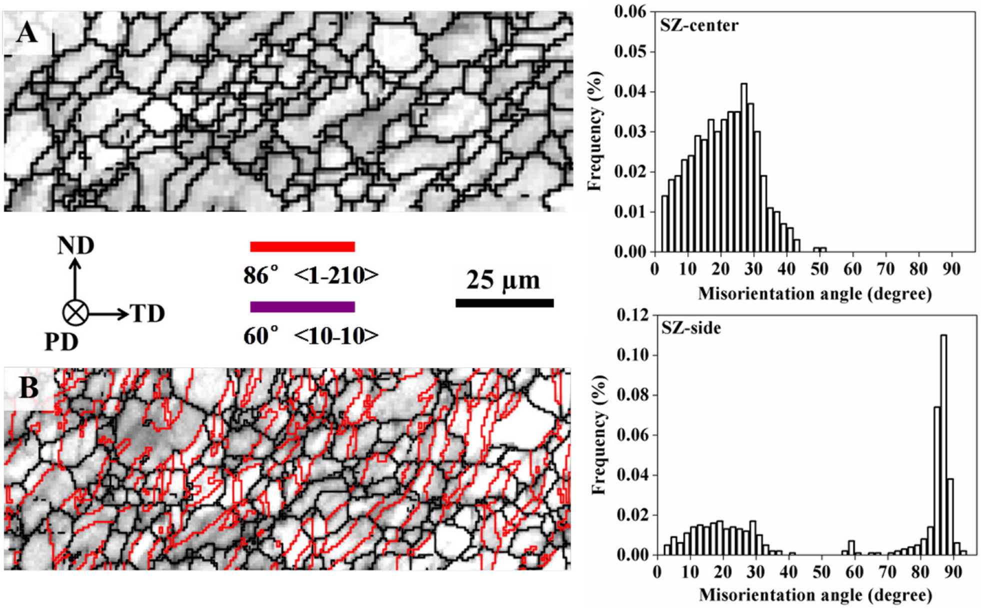

FIGURE 6 | EBSD orientation maps of the **(A)** SZ-center and **(B)** SZ-side after ∼5% strain along TD and the corresponding misorientation angle distributions (Xin et al., 2012) (Copyright © 2012, Springer Nature).

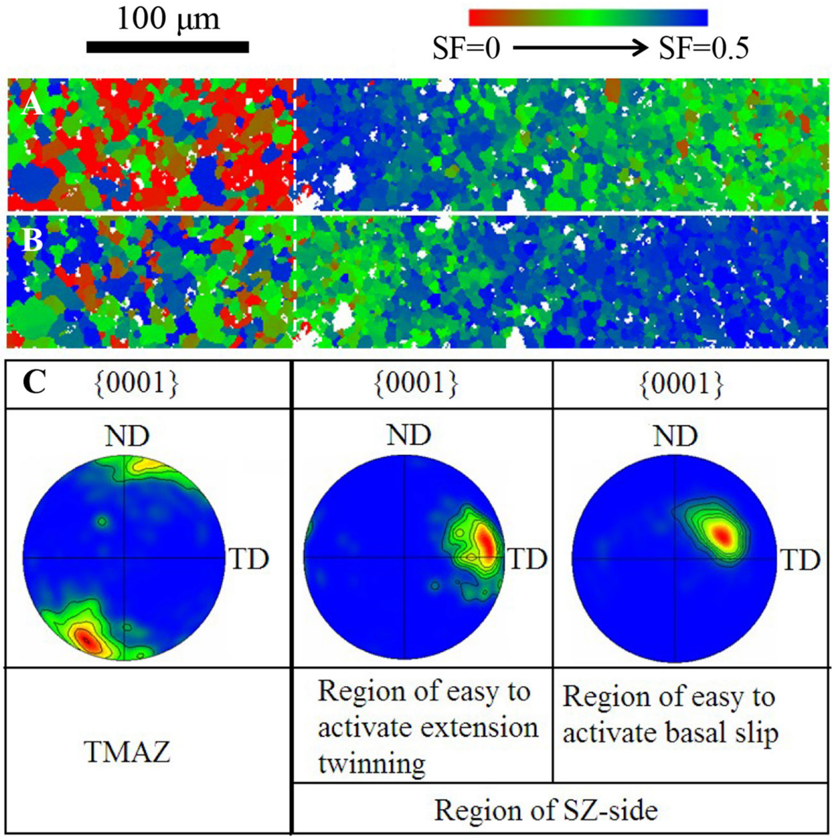

FIGURE 7 | SF maps of deformation mechanisms for tension along TD at the transition region between TMAZ and SZ-side on AS (Xin et al., 2013a): **(A)** extension twinning, **(B)** basal slip; **(C)** {0001} pole figures at the transition zone (Copyright © 2013, ELSEVIER S.A.).

Fracture Mechanisms

The fracture behavior of FSW/FSP Mg alloys is a hot topic of current research. Extensive studies indicate that fracture consistently initiates in the transition region between SZ and TMAZ on advancing side (AS) (Lim et al., 2005; Fu et al., 2012). It was found that fracture initiated in SZ where the grains were oriented favorable for basal slip (Park et al., 2003b; Woo et al., 2006). Some researchers further revealed that extension twinning activated at SZ-side can accelerate fracture (Xin et al., 2012). Some other researchers attributed fracture initiation to the incompatible plastic deformation at TMAZ/SZ interface where texture sharply changed (Xin et al., 2010, 2012; Yang et al., 2010; Shang et al., 2017a).

As seen from the above reports, the transition zone is a weak place. Therefore, it is necessary to have an in-depth understanding on the deformation behavior of this region. **Figure 7** shows the SF maps for extension twinning and basal slip based on the EBSD data in transition region on AS (Xin et al., 2013a). The SF maps were obtained by an in-house program developed by Xin. For each orientation, six twin variants were considered and the maximum SF was taken to color the maps. If the strain generated by the twin is opposite in direction to that of the imposed strain, the SF was assigned zero. **Figure 7A** reveals that a narrow region (∼100 µm) in SZ-side, close to SZ/TMAZ interface has the highest SF for extension twinning. A relatively wide region in SZ-side, slightly away from the SZ/TMAZ interface shows the highest SF for basal slip (**Figure 7B**). Based on the SF maps, SZ-side was divided into two micro-regions (Xin et al., 2013a). One is the Easy to Activate Extension Twinning (EAET) region and the other is the Easy to Activate Basal Slip (EABS) region. In addition, the SF for extension twinning in TMAZ is lower than that in EAET, showing a boundary in the transition region. {0001} pole figures of various micro-regions are presented in **Figure 7C**, indicating that the c-axis is nearly parallel to TD in EAET region, while it is inclined ∼40° toward TD in EABS region. The <0001> direction was

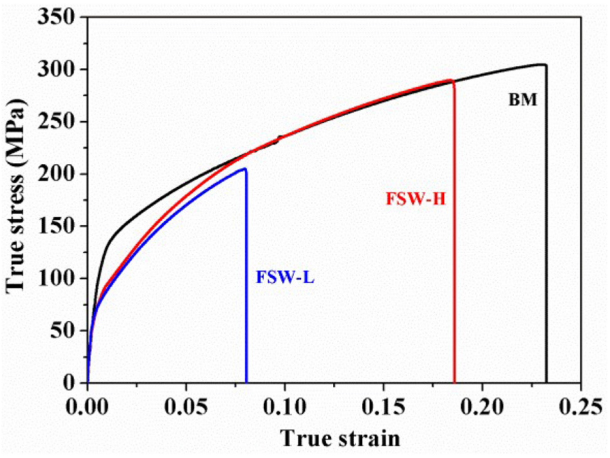

FIGURE 9 | Stress-strain curves of the as-received plate and FSW AZ31 Mg alloys (Xin et al., 2016) (Copyright © 2016, ELSEVIER BV).

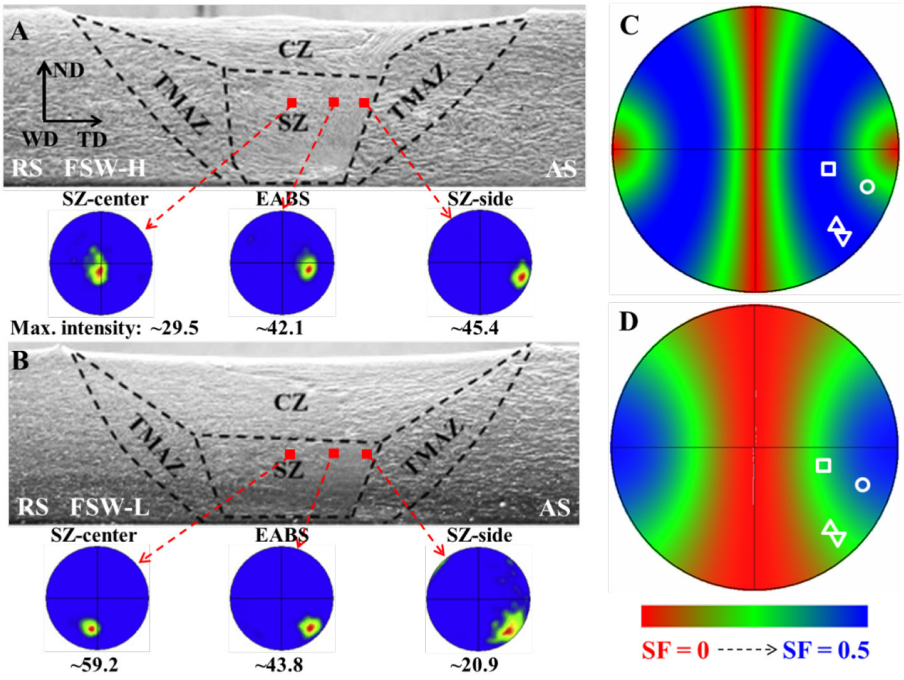

FIGURE 8 | {0001} pole figures for different regions in the SZ of **(A)** FSW-H joint and **(B)** FSW-L joint (Xin et al., 2016); (0001) pole figures showing the calculated SF for **(C)** basal slip and **(D)** extension twinning. The region close to SZ-side and SZ-side in FSW-H and FSW-L joints are superimposed on the pole figures and indicated by ☐, ○, △, and, ▽ respectively (Copyright © 2016, ELSEVIER BV).

tilted ∼25° clockwise to ND in TMAZ. This sharp texture change in each micro-region might cause deformation incompatibility and initiate fracture (Xin et al., 2010).

Recently, Liu et al. (2016a) reported that a triple junction region existed among TMAZ, CZ and SZ in AS, but it was not evident in RS. Drastic texture changes were found among the triple regions. They concluded that the significant SF differences among the different parts are the evidences for deformation incompatibility. This accelerated fracture in the triple junction region in AS. However, some researchers found that fracture also initiates in RS during transverse tensile test on FSW AZ31 Mg alloys (Liu et al., 2015). They attributed this rare situation to the easier activation of basal slip in RS than AS, which caused more severe strain localization in RS. In addition, Mironov et al. (2017) studied the tensile behaviors of FSW AZ31 alloys along TD using EBSD and DIC technique, and found that failure initiates at the weld root and originates from {10–11}–{10–12} double twinning.

WAYS TO IMPROVE THE JOINT STRENGTH

The complex texture distribution in FSW Mg joints largely deteriorates the joint strength and hinders their widespread application (Lim et al., 2005). Therefore, great efforts have been devoted to improve the joint performance. It was found that welding parameters such as weld speed and rotation rate can control heat input and modify grain size and texture of an FSW joint (Commin et al., 2009; Padmanaban et al., 2010; Yang et al., 2010, 2013; Liu et al., 2011; Chowdhury et al., 2013; Hütsch et al., 2014; Pan et al., 2016; Rao et al., 2016; Alireza Askariani et al., 2017; Richmire et al., 2018). So, it is possible to improve the joint strength by varying welding parameters. Shang et al. (2017b) indicated that the non-uniform deformation of FSW AZ31 Mg joints can be suppressed by modifying the texture distribution through increasing the tool rotation rate, which then improved the tensile strength and ductility. Xu et al. (2018) joined AZ31 plates by FSW with an extremely low welding speed and rotation rate. They found that the strong texture is randomized in the whole WZ and the strength of FSW Mg joints was enhanced without ductility loss.

Xin et al. (2016) joined AZ31 plates by FSW with two types of welding parameters, and these were referred to as FSW-H joint (rotation rate of 1,600 rpm and welding speed of 600 mm/min) and FSW-L joint (rotation rate of 800 rpm and welding speed of 90 mm/min), respectively. They found that welding parameters largely affected the texture distribution in SZ (**Figures 8A,B**). The c-axis is nearly parallel to the WD-TD plane in FSW-H joint, while it was rotated away from the WD-TD plane in FSW-L joint. Moreover, high welding speed and rotation

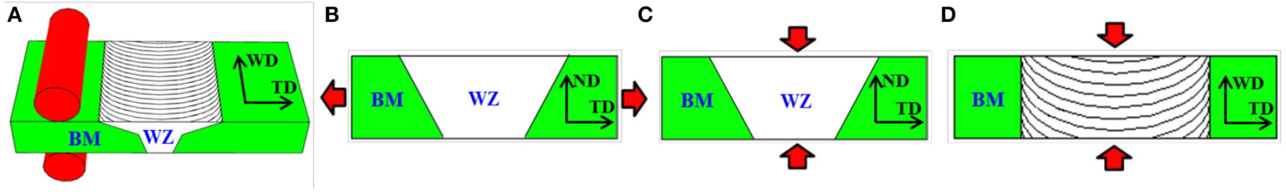

FIGURE 10 | Schematic illustration of the post-weld deformation of FSW AZ31 Mg alloys: **(A)** rolling, **(B)** tension along TD, **(C)** compression along ND, **(D)** compression along WD.

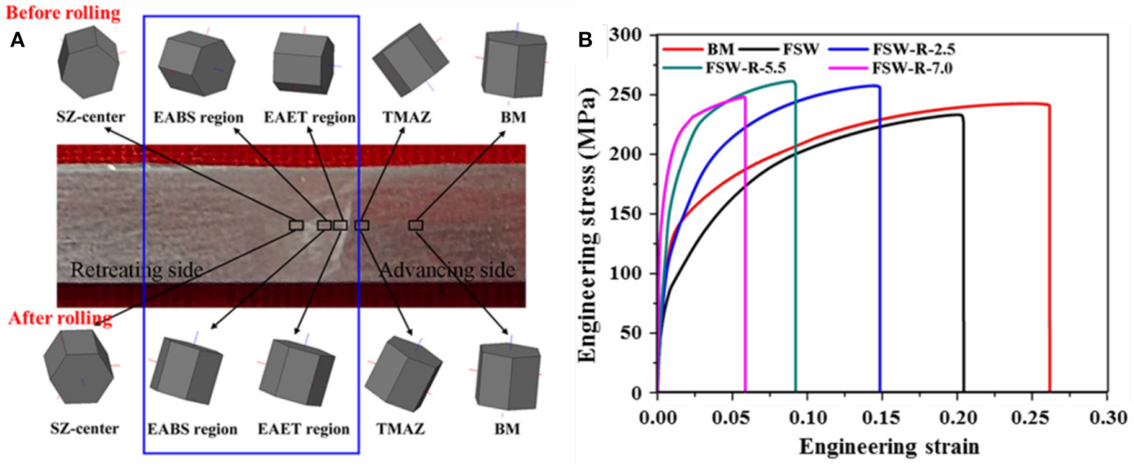

FIGURE 11 | (A) Schematic illustration of the changes of crystallographic orientation after subsequent rolling process for FSW AZ31 Mg alloy; **(B)** stress-strain curves of the transverse tensile tests (Xin et al., 2013b) (Copyright © 2013, ELSEVIER S.A.).

rate increased the size of SZ and decreased the size of CZ. The SF distributions for basal slip (**Figure 8C**) and extension twinning (**Figure 8D**) were calculated as a function of (0001) pole orientation. The tensile stress along TD was assumed for the calculation. It shows that for FSW-H joint, the grains in SZ-side are favorable for extension twinning and the grains in the region close to SZ-side are favorable for basal slip. While for FSW-L joint, the grains in both areas are more favorable for basal slip. As a consequence, the activation ability of basal slip and extension twinning was changed, which therefore influence the joint strength, inhomogeneous plastic deformation and fracture behaviors. The stress-strain curves of the as-received plate and AZ31 Mg alloy joints are displayed in **Figure 9**. It shows that the YS is almost the same for the two kinds of Mg joints, lower than that for BM. However, the elongation and UTS of the FSW-H joint increased compared to that of FSW-L joint.

Because of the strong anisotropic mechanical properties of Mg alloys, texture control post-weld deformation could be another effective way to improve the joint strength of FSW/FSP Mg alloys. Lee et al. (2007) reported that a post compressive strain of ∼6% could largely raise the YS of an FSP Mg plate, which was attributed mainly to texture strengthening. Rolling (**Figure 10A**) (Xin et al., 2013b), tension (**Figure 10B**) (Xin et al., 2014) and compression (**Figures 10C,D**) (Liu et al., 2016b) have been applied on FSW AZ31 Mg alloys to improve their joint strength. For brevity, only post-weld rolling is discussed in the following.

The change of crystallographic orientations in FSW AZ31 Mg plate during post-weld rolling is illustrated in **Figure 11A**. It is clear that drastic grain reorientation was induced by extension twinning especially in EABS and EAET regions after rolling. The twinned grains have a texture with the c-axis nearly parallel to ND, i.e., the applied stress direction. **Figures 8C,D** indicate that this c-axis//ND texture is hard for the activation of basal slip and extension twinning during tension along TD. So from texture strengthening point of view, post-rolling will greatly increase the transverse tensile strength of SZ-side. The stress-strain curves along TD before and after post-rolling are presented in **Figure 11B**. As expected, all of the specimens with subsequent rolling exhibit much larger tensile stress compared with the FSW-undeformed specimen.

Recently, Shang et al. (2019) found that the strength of FSW AZ31 Mg joints can be significantly improved by an additional pass of FSP. The YS of the joint was enhanced from 96 MPa (original FSW joint) to 122 MPa and the tensile strength increased to be roughly equal to that of BM with no reduction of elongation. The shape of the welding tool also influences the joint strength (Mishra and Ma, 2005). Yang et al. (2010) indicates that the tensile strength of FSW AZ31 Mg joints tended to increase with increasing the shoulder diameter and the elongation was significantly improved. Chen et al. (2013) joined an AZ31B Mg alloy by a double-sided FSW technique, and found that the elongation of the joint increased from 18 to 28% with similar tensile strength as the original FSW. They attributed this improved ductility to the relatively random crystallographic texture in the double-sided FSW joint. Furthermore, some researchers found that the joint strength of FSW Mg alloys can be improved by subsequent aging treatment (Yang et al., 2014a).

SUMMARY AND OUTLOOK

As a solid-state process, FSW can avoid solidification problems and therefore has great potential in welding of Mg alloys. However, strong texture is usually formed in Mg joints, which results in localized plastic deformation, and significantly deteriorates the mechanical properties of welds. This paper discussed the inhomogeneous deformation and fracture mechanisms of FSW/FSP Mg joints with typical texture distributions. In addition, some methods to improve the joint performance of FSW Mg alloys are tested.

The traditional experimental approaches are insufficient for the study of the deformation mechanism of Mg joints such as the "embossed phenomenon" in SZ-center and fracture localization. CPFEM coupled with twin reorientation, fracture criterion and grain size effect would be an effective mean for studying non-uniform plastic strain and fracture behaviors of FSW Mg joint in the future. Exploring simple and efficient methods to modify the textures in WZ, thereby improving the joint performance is also an interesting research direction.

AUTHOR CONTRIBUTIONS

WR and RX wrote the paper. CT and DL revised the paper.

FUNDING

This project was financially supported by the National Key Research and Development Program of China (2016YFB0301102) and the National Natural Science Foundation of China (Project Nos. 51571045, 51871036, and 51421001).

REFERENCES

Afrin, N., Chen, D. L., Cao, X., and Jahazi, M. (2007). Strain hardening behavior of a friction stir welded magnesium alloy. *Scr. Mater*. 57, 1004–1007. doi: 10.1016/j.scriptamat.2007.08.001

Afrin, N., Chen, D. L., Cao, X., and Jahazi, M. (2008). Microstructure and tensile properties of friction stir welded AZ31B magnesium alloy. *Mater. Sci. Eng. A* 472, 179–186. doi: 10.1016/j.msea.2007.03.018

Alireza Askariani, S., Pishbin, H., and Moshref-Javadi, M. (2017). Effect of welding parameters on the microstructure and mechanical properties of the friction stir welded joints of a Mg-12Li-1Al alloy. *J. Alloys Compd*. 724, 859–868. doi: 10.1016/j.jallcom.2017.07.071

Argade, G. R., Kandasamy, K., Panigrahi, S. K., and Mishra, R. S. (2012). Corrosion behavior of a friction stir processed rare-earth added magnesium alloy. *Corros. Sci.* 58, 321–326. doi: 10.1016/j.corsci.2012.01.007

Baffari, D., Buffa, G., Campanella, D., Lo Valvo, E., and Fratini, L. (2018). Experimental and numerical investigation on a new FSW based metal to composite joining technique. *J. Manuf. Process*. 34, 758–764. doi: 10.1016/j.jmapro.2018.03.048

Barnett, M. R. (2007). Twinning and the ductility of magnesium alloys: part II. "Contraction" twins. *Mater. Sci. Eng. A* 464, 8–16. doi: 10.1016/j.msea.2007.02.109

Barnett, M. R., Keshavarz, Z., Beer, A. G., and Atwell, D. (2004). Influence of grain size on the compressive deformation of wrought Mg−3Al−1Zn. *Acta Mater*. 52, 5093–5103. doi: 10.1016/j.actamat.2004.07.015

Berbon, P. B., Bingel, W. H., Mishra, R. S., Bampton, C. C., and Mahoney, M. W. (2001). Friction stir processing: a tool to homogenize nanocomposite aluminum alloys. *Scr. Mater*. 44, 61–66. doi: 10.1016/S1359-6462(00)00578-9

Bhargava, G., Yuan, W., Webb, S. S., and Mishra, R. S. (2009). Influence of texture on mechanical behavior of friction-stir-processed magnesium alloy. *Metall. Mater. Trans. A* 41, 13–17. doi: 10.1007/s11661-009-0079-8

Cam, G. (2011). Friction stir welded structural materials: beyond Al-alloys. *Int. Mater. Rev*. 5656, 1–48. doi: 10.1179/095066010X12777205875750

Cavaliere, P., and De Marco, P. P. (2007). Friction stir processing of AM60B magnesium alloy sheets. *Mater. Sci. Eng. A* 462, 393–397. doi: 10.1016/j.msea.2006.04.150

Chen, J., Fujii, H., Sun, Y., Morisada, Y., and Ueji, R. (2013). Fine grained Mg−3Al−1Zn alloy with randomized texture in the double-sided friction stir welded joints. *Mater. Sci. Eng. A* 580, 83–91. doi: 10.1016/j.msea.2013.05.044

Chiumenti, M., Cervera, M., Agelet De Saracibar, C., and Dialami, N. (2013). Numerical modeling of friction stir welding processes. *Comput. Method Appl. Mech. Eng*. 254, 353–369. doi: 10.1016/j.cma.2012.09.013

Chowdhury, S. H., Chen, D. L., Bhole, S. D., Cao, X., and Wanjara, P. (2013). Friction stir welded AZ31 magnesium alloy: microstructure, texture, and tensile properties. *Metall. Mater. Trans. A* 44, 323–336. doi: 10.1007/s11661-012-1382-3

Commin, L., Dumont, M., Masse, J. E., and Barrallier, L. (2009). Friction stir welding of AZ31 magnesium alloy rolled sheets: influence of processing parameters. *Acta Mater*. 57, 326–334. doi: 10.1016/j.actamat.2008.09.011

Cui, G. R., Ma, Z. Y., and Li, S. X. (2009). The origin of non-uniform microstructure and its effects on the mechanical properties of a friction stir processed Al–Mg alloy. *Acta Mater*. 57, 5718–5729. doi: 10.1016/j.actamat.2009.07.065

Dieringa, H. (2017). Influence of cryogenic temperatures on the microstructure and mechanical properties of magnesium alloys: a review. *Metals* 7:38. doi: 10.3390/met7020038

Dorbane, A., Ayoub, G., Mansoor, B., Hamade, R. F., Kridli, G., Shabadi, R., et al. (2016). Microstructural observations and tensile fracture behavior of FSW twin roll cast AZ31 Mg sheets. *Mater. Sci. Eng. A* 649, 190–200. doi: 10.1016/j.msea.2015.09.097

Freeney, T. A., and Mishra, R. S. (2010). Effect of friction stir processing on microstructure and mechanical properties of a cast-magnesium–rare earth alloy. *Metall. Mater. Trans. A* 41, 73–84. doi: 10.1007/s11661-009-0080-2

Fu, R. D., Ji, H. S., Li, Y. J., and Liu, L. (2012). Effect of weld conditions on microstructures and mechanical properties of friction stir welded joints on AZ31B magnesium alloys. *Sci. Technol. Weld. Join*. 17, 174–179. doi: 10.1179/1362171811Y.0000000056

Harikrishna, K. L., Dilip, J. J. S., Ramaswamy Choudary, K., Subba Rao, V. V., Koteswara Rao, S. R., Janaki Ram, G. D., et al. (2010). Friction stir welding of magnesium alloy ZM21. *Trans. Indian Inst. Metals* 63, 807–811. doi: 10.1007/s12666-010-0123-9

He, X., Gu, F., and Ball, A. (2014). A review of numerical analysis of friction stir welding. *Prog. Mater. Sci*. 65, 1–66. doi: 10.1016/j.pmatsci.2014.03.003

Hütsch, L. L., Hütsch, J., Herzberg, K., Dos Santos, J. F., and Huber, N. (2014). Increased room temperature formability of Mg AZ31 by high speed friction stir processing. *Mater. Des*. 54, 980–988. doi: 10.1016/j.matdes.2013.08.108

Iqbal, M. P., Jain, R., and Pal, S. K. (2019). Numerical and experimental study on friction stir welding of aluminum alloy pipe. *J. Mater. Process. Tech*. 274:116258. doi: 10.1016/j.jmatprotec.2019.116258

Jain, V., Mishra, R. S., Verma, R., and Essadiqi, E. (2013). Superplasticity and microstructural stability in a Mg alloy processed by hot rolling and friction stir processing. *Scripta. Mater*. 68, 447–450. doi: 10.1016/j.scriptamat.2012.11.009

Kainer, K. U. (2016). "Challenges for implementation of magnesium into more applications," in *Magnesium Technology 2016*, eds A. Singh, K. Solanki, M. V. Manuel, and N. R. Neelameggham (Cham: Springer International Publishing), 5–6.

Kim, M. S., Jung, J. Y., Song, Y. M., and Choi, S. H. (2017). Simulation of microtexture developments in the stir zone of friction stir-welded AZ31 Mg alloys. *Int. J. Plast*. 94, 24–43. doi: 10.1016/j.ijplas.2017.02.013

Lee, C. J., Huang, J. C., and Du, X. H. (2007). Improvement of yield stress of friction-stirred Mg–Al–Zn alloys by subsequent compression. *Scr. Mater*. 56, 875–878. doi: 10.1016/j.scriptamat.2007.01.041

Lee, W. B., Yeon, Y. M., and Jung, S. B. (2003). Joint properties of friction stir welded AZ31B– H24 magnesium alloy. *Mater. Sci. Technol*. 19, 785–790. doi: 10.1179/026708303225001867

Lim, S., Kim, S., Lee, C.-G., Kim, S. J., and Yim, C. D. (2005). Tensile behavior of friction-stir-welded AZ31-H24 Mg alloy. *Metall. Mater. Trans. A* 36, 1609–1612. doi: 10.1007/s11661-005-0252-7

Lin, J. B., Ren, W. J., and Wang, X. Y. (2016). Research on the tension-compression asymmetry of as-extruded ZK60 magnesium alloys at room temperature. *Acta. Metall. Sin*. 52, 264–270. doi: 10.11900/0412.1961.2015.00324

Liu, D., Nishio, H., and Nakata, K. (2011). Anisotropic property of material arrangement in friction stir welding of dissimilar Mg alloys. *Mater. Des*. 32, 4818–4824. doi: 10.1016/j.matdes.2011.06.020

Liu, D., Xin, R., Xiao, Y., Zhou, Z., and Liu, Q. (2014). Strain localization in friction stir welded magnesium alloy during tension and compression deformation. *Mater. Sci. Eng. A* 609, 88–91. doi: 10.1016/j.msea.2014.04.089

Liu, G., Xin, R., Li, J., Liu, D., and Liu, Q. (2015). Fracture localisation in retreating side of friction stir welded magnesium alloy. *Sci. Technol. Weld. Join*. 20, 378–384. doi: 10.1179/1362171815Y.0000000027

Liu, Z., Xin, R., Li, D., Sun, L., and Liu, Q. (2016b). Comparative study on twinning characteristics during two post-weld compression paths and their effects on joint enhancement. *Sci Rep*. 6:39779. doi: 10.1038/srep39779

Liu, Z., Xin, R., Liu, D., Shu, X., and Liu, Q. (2016a). Textural variation in triple junction region of friction stir welded Mg alloys and its influence on twinning and fracture. *Mater. Sci. Eng. A* 658, 185–191. doi: 10.1016/j.msea.2016.01.097

Ma, Z. Y. (2008). Friction stir processing technology: a review. *Metall. Mater. Trans. A* 39, 642–658. doi: 10.1007/s11661-007-9459-0

Mansoor, B., and Ghosh, A. K. (2012). Microstructure and tensile behavior of a friction stir processed magnesium alloy. *Acta Mater*. 60, 5079–5088. doi: 10.1016/j.actamat.2012.06.029

Mironov, S., Motohashi, Y., Ito, T., Goloborodko, A., Funami, K., and Kaibyshev, R. (2007). Feasibility of friction stir welding for joining and microstructure refinement in a ZK60 magnesium alloy. *Mater. Trans*. 48, 3140–3148. doi: 10.2320/matertrans.MRA2007177

Mironov, S., Onuma, T., Sato, Y. S., Yoneyama, S., and Kokawa, H. (2017). Tensile behavior of friction-stir welded AZ31 magnesium alloy. *Mater. Sci. Eng. A* 679, 272–281. doi: 10.1016/j.msea.2016.10.036

Mishra, R. S., and Ma, Z. Y. (2005). Friction stir welding and processing. *Mat. Sci. Eng. R* 50, 1–78. doi: 10.1016/j.mser.2005.07.001

Mishra, R. S., and Mahoney, M. W. (2001). Friction stir processing: a new grain refinement technique to achieve high strain rate superplasticity in commercial alloys. *Mater. Sci. Forum* 357, 507–514. doi: 10.4028/www.scientific.net/MSF.357-359.507

Mishra, R. S., Mahoney, M. W., Mcfadden, S. X., Mara, N. A., and Mukherjee, A. K. (1999). High strain rate superplasticity in a friction stir processed 7075 Al alloy. *Scr. Mater*. 42, 163–168. doi: 10.1016/S1359-6462(99)00329-2

Mohan, A., Yuan, W., and Mishra, R. S. (2013). High strain rate superplasticity in friction stir processed ultrafine grained Mg–Al–Zn alloys. *Mater. Sci. Eng. A* 562, 69–76. doi: 10.1016/j.msea.2012.11.026

Moraes, J. F. C., Rodriguez, R. I., Jordon, J. B., and Su, X. (2017). Effect of overlap orientation on fatigue behavior in friction stir linear welds of magnesium alloy sheets. *Int. J. Fatigue* 100, 1–11. doi: 10.1016/j.ijfatigue.2017.02.018

Nandan, R., Roy, G. G., Lienert, T. J., and Debroy, T. (2006). Numerical modelling of 3D plastic flow and heat transfer during friction stir welding of stainless steel. *Sci. Technol. Weld. Join*. 11, 526–537. doi: 10.1179/174329306X107692

Nene, S. S., Zellner, S., Mondal, B., Komarasamy, M., Mishra, R. S., Brennan, R. E., et al. (2018). Friction stir processing of newly-designed Mg-5Al-3.5Ca-1Mn (AXM541) alloy: microstructure evolution and mechanical properties. *Mater. Sci. Eng. A* 729, 294–299. doi: 10.1016/j.msea.2018.05.073

Ni, D. R., Chen, D. L., Yang, J., and Ma, Z. Y. (2014). Low cycle fatigue properties of friction stir welded joints of a semi-solid processed AZ91D magnesium alloy. *Mater. Des.* 56, 1–8. doi: 10.1016/j.matdes.2013.10.081

Padmanaban, G., Balasubramanian, V., and Sarin Sundar, J. K. (2010). Influences of welding processes on microstructure, hardness, and tensile properties of AZ31B magnesium alloy. *J. Mater. Eng. Perform.* 19, 155–165. doi: 10.1007/s11665-009-9389-7

Pan, F., Xu, A., Deng, D., Ye, J., Jiang, X., Tang, A., et al. (2016). Effects of friction stir welding on microstructure and mechanical properties of magnesium alloy Mg-5Al-3Sn. *Mater. Des.* 110, 266–274. doi: 10.1016/j.matdes.2016.07.146

Park, S. H. C., Sato, Y. S., and Kokawa, H. (2003a). Basal plane texture and flow pattern in friction stir weld of a magnesium alloy. *Metall. Mater. Trans. A* 34, 987–994. doi: 10.1007/s11661-003-0228-4

Park, S. H. C., Sato, Y. S., and Kokawa, H. (2003b). Effect of micro-texture on fracture location in friction stir weld of Mg alloy AZ61 during tensile test. *Scr. Mater.* 49, 161–166. doi: 10.1016/S1359-6462(03)00210-0

Prangnell, P. B., and Heason, C. P. (2005). Grain structure formation during friction stir welding observed by the 'stop action technique'. *Acta Mater.* 53, 3179–3192. doi: 10.1016/j.actamat.2005.03.044

Rao, H. M., Ghaffari, B., Yuan, W., Jordon, J. B., and Badarinarayan, H. (2016). Effect of process parameters on microstructure and mechanical behaviors of friction stir linear welded aluminum to magnesium. *Mater. Sci. Eng. A* 651, 27–36. doi: 10.1016/j.msea.2015.10.082

Ren, W., Xin, R., and Liu, D. (2019). Modeling the strongly localized deformation behavior in a magnesium alloy with complicated texture distribution. *Mater. Sci. Eng. A* 762:138103. doi: 10.1016/j.msea.2019.138103

Richmire, S., Hall, K., and Haghshenas, M. (2018). Design of experiment study on hardness variations in friction stir welding of AM60 Mg alloy. *J. Magnes. Alloy.* 6, 215–228. doi: 10.1016/j.jma.2018.07.002

Shang, Q., Ni, D. R., Xue, P., Xiao, B. L., and Ma, Z. Y. (2017a). Evolution of local texture and its effect on mechanical properties and fracture behavior of friction stir welded joint of extruded Mg-3Al-1Zn alloy. *Mater. Char.* 128, 14–22. doi: 10.1016/j.matchar.2017.03.018

Shang, Q., Ni, D. R., Xue, P., Xiao, B. L., and Ma, Z. Y. (2017b). Improving joint performance of friction stir welded wrought Mg alloy by controlling non-uniform deformation behavior. *Mater. Sci. Eng. A* 707, 426–434. doi: 10.1016/j.msea.2017.09.084

Shang, Q., Ni, D. R., Xue, P., Xiao, B. L., Wang, K. S., and Ma, Z. Y. (2019). An approach to enhancement of Mg alloy joint performance by additional pass of friction stir processing. *J. Mater. Process. Technol.* 264, 336–345. doi: 10.1016/j.jmatprotec.2018.09.021

Sidhar, H., Martinez, N. Y., Mishra, R. S., and Silvanus, J. (2016). Friction stir welding of Al–Mg–Li 1424 alloy. *Mater. Des.* 106, 146–152. doi: 10.1016/j.matdes.2016.05.111

Singh, K., Singh, G., and Singh, H. (2018). Investigation of microstructure and mechanical properties of friction stir welded AZ61 magnesium alloy joint. *J. Magnes. Alloys* 6, 292–298. doi: 10.1016/j.jma.2018.05.004

Song, B., Yang, Q., Zhou, T., Chai, L., Guo, N., Liu, T., et al. (2019). Texture control by {10-12} twinning to improve the formability of Mg alloys: a review. *J. Mater. Sci. Technol.* 35, 2269–2282. doi: 10.1016/j.jmst.2019.03.045

Suhuddin, U. F. H. R., Mironov, S., Sato, Y. S., Kokawa, H., and Lee, C. W. (2009). Grain structure evolution during friction-stir welding of AZ31 magnesium alloy. *Acta Mater.* 57, 5406–5418. doi: 10.1016/j.actamat.2009.07.041

Thomas, W. M., Johnson, K. I., and Wiesner, C. S. (2003). Friction stir welding-recent developments in tool and process technologies. *Adv. Eng. Mater.* 5, 485–490. doi: 10.1002/adem.200300355

Thomas, W. M., Nicholas, E. D., Needham, J. C., Murch, M. G., Templesmith, P., and Dawes, C. J. (1991). *Friction Stir Butt Welding*. International Patent Application No. PCT/GB92/02203, Great Britain Patent Application No. 9125978.8.

Ugender, S. (2018). Influence of tool pin profile and rotational speed on the formation of friction stir welding zone in AZ31 magnesium alloy. *J. Magnes. Alloys* 6, 205–213. doi: 10.1016/j.jma.2018.05.001

Woo, W., Choo, H., Brown, D. W., Liaw, P. K., and Feng, Z. (2006). Texture variation and its influence on the tensile behavior of a friction-stir processed magnesium alloy. *Scr. Mater.* 54, 1859–1864. doi: 10.1016/j.scriptamat.2006.02.019

Woo, W., Choo, H., Prime, M. B., Feng, Z., and Clausen, B. (2008). Microstructure, texture and residual stress in a friction-stir-processed AZ31B magnesium alloy. *Acta Mater.* 56, 1701–1711. doi: 10.1016/j.actamat.2007.12.020

Xie, G. M., Ma, Z. Y., and Geng, L. (2008). Effect of microstructural evolution on mechanical properties of friction stir welded ZK60 alloy. *Mater. Sci. Eng. A* 486, 49–55. doi: 10.1016/j.msea.2007.08.043

Xie, G. M., Ma, Z. Y., Geng, L., and Chen, R. S. (2007). Microstructural evolution and mechanical properties of friction stir welded Mg–Zn–Y–Zr alloy. *Mater. Sci. Eng. A* 471, 63–68. doi: 10.1016/j.msea.2007.03.041

Xin, R., Li, B., Liao, A., Zhou, Z., and Liu, Q. (2012). Correlation between texture variation and transverse tensile behavior of friction-stir-processed AZ31 Mg alloy. *Metall. Mater. Trans. A* 43, 2500–2508. doi: 10.1007/s11661-012-1080-1

Xin, R., Liu, D., Li, B., Sun, L., Zhou, Z., and Liu, Q. (2013a). Mechanisms of fracture and inhomogeneous deformation on transverse tensile test of friction-stir-processed AZ31 Mg alloy. *Mater. Sci. Eng. A* 565, 333–341. doi: 10.1016/j.msea.2012.12.053

Xin, R., Liu, D., Shu, X., Li, B., Yang, X., and Liu, Q. (2016). Influence of welding parameter on texture distribution and plastic deformation behavior of as-rolled AZ31 Mg alloys. *J. Alloys Compd.* 670, 64–71. doi: 10.1016/j.jallcom.2016.02.023

Xin, R., Liu, D., Xu, Z., Li, B., and Liu, Q. (2013b). Changes in texture and microstructure of friction stir welded Mg alloy during post-rolling and their effects on mechanical properties. *Mater. Sci. Eng. A* 582, 178–187. doi: 10.1016/j.msea.2013.06.005

Xin, R., Sun, L., Liu, D., Zhou, Z., and Liu, Q. (2014). Effect of subsequent tension and annealing on microstructure evolution and strength enhancement of friction stir welded Mg alloys. *Mater. Sci. Eng. A* 602, 1–10. doi: 10.1016/j.msea.2014.02.062

Xin, R. L., Li, B., and Liu, Q. (2010). Microstructure and texture evolution during friction stir processing of AZ31 Mg alloy. *Mater. Sci. Forum* 654, 1195–1200. doi: 10.4028/www.scientific.net/MSF.654-656.1195

Xu, N., Song, Q., Fujii, H., Bao, Y., and Shen, J. (2018). Mechanical properties' modification of large load friction stir welded AZ31B Mg alloy joint. *Mater. Lett.* 219, 93–96. doi: 10.1016/j.matlet.2018.02.099

Xunhong, W., and Kuaishe, W. (2006). Microstructure and properties of friction stir butt-welded AZ31 magnesium alloy. *Mater. Sci. Eng. A* 431, 114–117. doi: 10.1016/j.msea.2006.05.128

Yang, J., Ni, D. R., Wang, D., Xiao, B. L., and Ma, Z. Y. (2014a). Friction stir welding of as-extruded Mg–Al–Zn alloy with higher Al content. Part II: influence of precipitates. *Mater. Char.* 96, 135–141. doi: 10.1016/j.matchar.2014.08.001

Yang, J., Ni, D. R., Xiao, B. L., and Ma, Z. Y. (2014b). Non-uniform deformation in a friction stir welded Mg–Al–Zn joint during stress fatigue. *Int. J. Fatigue* 59, 9–13. doi: 10.1016/j.ijfatigue.2013.10.004

Yang, J., Wang, D., Xiao, B. L., Ni, D. R., and Ma, Z. Y. (2013). Effects of rotation rates on microstructure, mechanical properties, and fracture behavior of Friction Stir-Welded (FSW) AZ31 magnesium alloy. *Metall. Mater. Trans. A* 44, 517–530. doi: 10.1007/s11661-012-1373-4

Yang, J., Xiao, B. L., Wang, D., and Ma, Z. Y. (2010). Effects of heat input on tensile properties and fracture behavior of friction stir welded Mg−3Al−1Zn alloy. *Mater. Sci. Eng. A* 527, 708–714. doi: 10.1016/j.msea.2009.09.044

Yu, Z., Zhang, W., Choo, H., and Feng, Z. (2012). Transient heat and material flow modeling of friction stir processing of magnesium alloy using threaded tool. *Metall. Mater. Trans. A* 43, 724–737. doi: 10.1007/s11661-011-0862-1

Yuan, W., Mishra, R. S., Carlson, B., Mishra, R. K., Verma, R., and Kubic, R. (2011). Effect of texture on the mechanical behavior of ultrafine grained magnesium alloy. *Scripta. Mater.* 64, 580–583. doi: 10.1016/j.scriptamat.2010.11.052

Yuan, W., Panigrahi, S. K., and Mishra, R. S. (2013). Achieving high strength and high ductility in friction stir-processed cast magnesium alloy. *Metall. Mater. Trans. A* 44, 3675–3684. doi: 10.1007/s11661-013-1744-5

Conflict of Interest: The authors declare that the research was conducted in the absence of any commercial or financial relationships that could be construed as a potential conflict of interest.

frontiers in Materials

ORIGINAL RESEARCH
published: 15 April 2020
doi: 10.3389/fmats.2020.00084

Effect of Heat Treatment on the Corrosion Behavior of Mg-10Gd Alloy in 0.5% NaCl Solution

Maria del Rosario Silva Campos[1]*, Carsten Blawert[1], Chamini L. Mendis[2], Marta Mohedano[3], Tristan Zimmermann[4], Daniel Proefrock[4], Mikhail L. Zheludkevich[1,5] and Karl Ulrich Kainer[1]

[1] Magnesium Innovation Centre–MagIC, Institute of Materials Research, Helmholtz-Zentrum Geesthacht, Geesthacht, Germany, [2] BCAST, Brunel University London, Uxbridge, United Kingdom, [3] Department of Chemical and Materials Engineering, Universidad Complutense de Madrid, Madrid, Spain, [4] Institute of Coastal Research, Helmholtz-Zentrum Geesthacht, Geesthacht, Germany, [5] Faculty of Engineering, Institute for Materials Science, University of Kiel, Kiel, Germany

In 0.5 wt.% NaCl aqueous solution, Mg-10Gd alloy shows promising corrosion resistance. The microstructure of this alloy was modified via heat treatments to understand the effect of accompanying microstructural changes on the corrosion resistance. It was found that corrosion performance depends both on the amount and the distribution of the cathodic intermetallic phases. The T4 heat treatment (24 h at 540°C) caused the Gd to distribute uniformly in the matrix, which had positive effect on corrosion resistance showing a delay in the time required for the first observation of localized corrosion. The T4 heat treated specimens, specimens aged at 200°C and 300°C, showed relatively uniform degradation and thus these heat treatments are not detrimental in terms of corrosion resistance. In contrast, heat treatment at 400°C seems to increase the formation of small cuboidal particles rich in Gd, most likely to be GdH_2 particles, in the matrix, resulting in a detrimental effect on the corrosion behavior.

Keywords: Mg corrosion, rare earth – Gd, Mg_5Gd phase, Gd enrichment, EIS

Edited by:
Zuhua Zhang,
Hunan University, China

Reviewed by:
Liang Wu,
Chongqing University, China
John L. Provis,
University of Sheffield,
United Kingdom

****Correspondence:***
Maria del Rosario Silva Campos
maria.silva@hzg.de

Specialty section:
This article was submitted to
Structural Materials,
a section of the journal
Frontiers in Materials

Received: *24 May 2019*
Accepted: *20 March 2020*
Published: *15 April 2020*

Citation:
Silva Campos MR, Blawert C, Mendis CL, Mohedano M, Zimmermann T, Proefrock D, Zheludkevich ML and Kainer KU (2020) Effect of Heat Treatment on the Corrosion Behavior of Mg-10Gd Alloy in 0.5% NaCl Solution. Front. Mater. 7:84. doi: 10.3389/fmats.2020.00084

INTRODUCTION

To date several methodologies have been used to enhance the corrosion performance of Mg based materials. The most common strategies include microstructure control, reduction of impurity levels (Fe, Cu, and Ni), addition of alloying elements, and surface modifications. The majority of alloying additions have limited solid solubility in Mg and therefore either intermetallic phases form beyond the equilibrium solubility limits or due to non-equilibrium solidification processes associated with casting (Habashi, 2008). Magnesium alloys are very susceptible to localized corrosion in chloride solutions due to their inhomogeneous microstructure (Ben-Hamu et al., 2007). The existence of intermetallic phases have a pronounced influence on the corrosion behavior of Mg alloys mainly attributed to electrochemical potential differences with the matrix (Song and Atrens, 1999; Song and Atrens, 2003). Generally, these phases are nobler (i.e., have a higher redox potential) than the Mg matrix (Ambat et al., 2000) and influence the overall corrosion behavior depending on their potential relative to Mg matrix and their efficiency as cathodic sites (Silva Campos, 2016).

The alloying additions in commercial Mg alloys that influence corrosion can be categorized as:

(a) Benign or beneficial; e.g., Al, Be, Mn, rare earth (RE) elements, Si, Zn and Zr.
(b) Moderately deleterious e.g., Ag.
(c) Severely deleterious e.g., Ni, Co, Fe and Cu (Rokhlin, 2003).

In fact, generally Mg alloys could be classified into two main groups: (1) those containing Al as the primary alloying element. To increase the tensile yield strength and the castability of Mg alloys by forming the intermetallic phase $Mg_{17}Al_{12}$ (Victoria-Hernandez et al., 2013); and (2) those free of Al and containing small additions of Zr for the purpose of grain refinement (Hu et al., 2014), besides forming intermetallics with Fe and Ni in the melt (Emley, 1966). Additions of Zn are also important as Al in the magnesium alloys to increase strengthening and castability (Meza-García, 2010). In terms of corrosion, Zn increases the tolerance limits and reduces the effect of impurities on corrosion once the tolerance limit has been exceeded (Hillis, 1998). Moreover, Si is added by design to the Mg-Al-Si alloys to promote the formation of Mg_2Si, which enhance strength in the alloy and is relatively harmless to the corrosion of Mg (Carlson and Jones, 1993). Likewise, additions up to 2% Ag lead to grain refining due to formation of precipitates, increase hardness and reduce corrosion resistance in as-extruded Mg-Al-Ag alloys. In binary Mg-Ag alloys, it is mandatory to applied T4 and T6 heat treatments to maintain the general corrosion at a satisfactory level (Tie et al., 2014).

Nevertheless, additions of Ni, Fe and Cu are detrimental to corrosion resistance of Mg alloys, due to their low solid-solubility limits and their more positive potentials, which lead to formation of active/efficient cathodic sites for hydrogen evolution, thereby forming galvanic cells and enhance the corrosion rate of magnesium alloys (Hanawalt et al., 1942; NACE, 1974; Habashi, 2008). The tolerance limit of these elements depends on the alloy composition, for pure magnesium, the tolerable limits for Cu, Fe and Ni are 0.1%, 0.005, and 0.0005 wt.%, respectively. While for example, AZ91 alloy has tolerance limits of 20 ppm Fe, 12 ppm Ni and 900 ppm Cu (Hanawalt et al., 1942). In addition, these elements can be considered also as impurities if they arise from various sources; the iron from the melting crucibles and tools, copper comes from impure aluminim, while nickel is coming from the used stainless steel crucibles or traces may be contained in the used magnesium (Emley, 1966). However, additions of Mn could improve corrosion resistance of Mg alloys by reducing the effect of the impurities (Makar and Kruger, 1990, 1993; Froats et al., 1987).

It has been reported that RE additions have significant positive effects on the corrosion resistance of Mg alloys (Unsworth, 1989; Morales et al., 2003; Rosalbino et al., 2006; Takenaka et al., 2007; Birbilis et al., 2009; Hort et al., 2010; Liu et al., 2010; Nayyeri and Khomamizadeh, 2011; Silva Campos et al., 2011; Sudholz et al., 2011; Shi et al., 2013; Silva Campos, 2016). The RE elements improve the tendency of Mg to passivate and decrease the micro-galvanic effect coming from other intermetallic phases (Reichek et al., 1985; Unsworth, 1989; Zucchi et al., 2005; Liu et al., 2009).

For instance, the addition of Gd to AM50 and AZ91D alloys modified the intermetallic phases by forming Al_2Gd and Al-Mn-Gd intermetallic phases thus reducing the amount of $Mg_{17}Al_{12}$ phase (Arrabal et al., 2012a,b). As a result, the corrosion rates of these alloys decreased with additions of 0.7 and 1.0 wt.% Gd by 85% and 93%, respectively (Arrabal et al., 2012b). This is mainly due to the decreased cathodic reaction kinetics caused by the suppression of micro-galvanic corrosion between primary and secondary phases (Arrabal et al., 2012b). In another study of AZ91 based alloys in humid environments, Gd reduced the effect of micro-galvanic couples and consequently the corrosion rate (Arrabal et al., 2012a). Arrabal et al. (2011) reported the beneficial effect of Gd additions on the high temperature oxidation behavior of AZ91D alloy due to formation of Al_2Gd and Al-Mn-Gd phases, which reduced the amount of $Mg_{17}Al_{12}$. This lead to corrosion rates lower than 72–81% compared with Gd free AZ91D. This was associated to the improved surface passivity and suppression of micro-galvanic couples (Mohedano et al., 2014).

Shi et al. (2013) reported that the corrosion resistance observed in the as-cast and the heat treated Mg-5Gd alloy is comparable to other RE additions such as Ce, La, Nd and Y. This was attributed to the accelerated micro galvanic corrosion caused by Gd present in the intermetallic phases. Kainer et al. (2009) investigated binary Mg-Gd alloys, in the as-cast, T4 and T6 conditions and reported that T6 heat treated Mg-10Gd had the lowest corrosion rate in 1 wt.% NaCl due to a fine distribution of nano-sized Mg-Gd precipitates. The reduction in the solid solubility of Gd with reduced temperature makes Mg–Gd system suitable for heat treatments to adjust the mechanical properties in accordance with the requirements of the property profile of an specific application (Silva Campos, 2016).

However, the effect of heat treatments on the corrosion mechanism and kinetics on Mg-10Gd has not been fully investigated. Thus, the aim of this work is to modify the microstructure of Mg-10Gd alloy by heat treatments and evaluate their effect on the corrosion behavior using different corrosion test and electrochemical techniques to understand the mechanisms that control the corrosion behavior.

EXPERIMENTAL

Casting and Heat Treatments

Pure Mg and Gd were molten in an electrical resistance furnace under a protective gas mixture of Ar and 3% SF_6. The melt was stirred for 10 min and cast into a cylindrical steel mold of 18 mm diameter and 150 mm length. The actual chemical composition of the Mg-10Gd alloy analyzed with inductively coupled plasma mass spectrometry (ICP-MS) was found to be 10.28% Gd, 0.0026% Fe, 0.0008% Ni, and 0.0040% Cu and the balance Mg (compositions in wt.%). The as-cast Mg-10Gd was solution treated at 540°C for 24 h and quenched into water held at room temperature. Solution heat treated samples were immediately aged at 200°C, 300°C and 400°C for 24 h and then quenched in cold water ($\sim$ 8°C).

Elemental Analysis

Approx. 1 g of Mg-10Gd alloy were digested in a mixture of 30 mL Milli-Q water and 10 mL of subboiled concentrated HNO3 (65 wt.%, trace metal grade). For trace metal analysis the digests were diluted 1:100 with Milli-Q water. The determination of Gd, Fe, Ni and Cu was performed using an inductively coupled plasma tandem mass spectrometer (ICP-MS/MS) (Agilent 8800, Agilent Technologies, Tokyo, Japan). For quantification an external calibration, prepared from custom-made multi-elemental standards was used.

Microstructure Characterization

Samples for the microstructure analysis were embedded in epoxy resin (Demotec 30) and then ground with 800, 1200 and 2500 grit *SiC* paper using water. Then the samples were polished with 0.05 µm colloidal silica OPS^{TM} (Struers) suspension and soapy deionized water and rinsed with ethanol and dried with hot air.

X-Ray Diffraction (XRD)

The X-ray diffraction (XRD) analysis was conducted using a Siemens D5000 X-ray Powder Diffractometer with Cu Kα radiation operating at 40 kV and 40 mA. The diffraction peaks were recorded for 2θ between 10° and 90° with a step size of 0.010 and a dwell time of 7 s and a rotation speed of 30 rpm.

Scanning Electron Microscopy (SEM)

The microstructures were observed with a Zeiss Ultra 55 scanning electron microscope equipped with energy-dispersive X-ray spectrometer (EDX) at an accelerating voltage of 20 kV. A Cambridge Stereoscan 200 SEM with an acceleration voltage between 5–10 kV was used to examine the surface appearance of the specimens before and after corrosion experiments.

Transmission Electron Microscopy (TEM)

The precipitate microstructures were examined using a Phillips CM200 transmission electron microscope operating at 200 kV. The samples for TEM analysis were prepared by punching 3 mm disks from specimens that were ∼ 200 µm in thickness and then electropolished in a Fischione twin jet electropolishing unit using a solution of 1.5% perchloric acid in methanol at ∼−45°C, 50 V, and ∼0.8–1.2 mA to perforation.

Corrosion Evaluation

The electrochemical measurements were performed using a three electrode cell containing 330 ml of electrolyte. In this cell the sample was the working electrode (WE) with an exposed area of ∼0.5 cm^2, while reference (RE) and auxiliary (AE) electrodes were Ag/AgCl, and Pt mesh, respectively. An aerated and stirred solution of 0.5 wt.% NaCl was used as the electrolyte and the cell was connected to a Gill AC potentiostat from ACM Instruments. The experiments were conducted at 21.5 ± 0.5°C. This set up was used for open circuit potential (OCP), potentiodynamic polarization measurements and electrochemical impedance spectroscopy (EIS). Repeatability was tested by measuring at least three specimens.

Open Circuit Potential (OCP)

The open circuit potential (OCP) measurements were recorded for 30 min, directly after immersion into the electrolyte.

Potentiodynamic Polarization Measurements

The potentiodynamic polarization measurements were conducted from −150 mV vs. the open circuit potential using a scan rate of 12 mV/min and a current density limit of 0.1 mA/cm^2. The corrosion current densities were obtained with ACM Analysis software by selecting the linear part of the cathodic curve that commenced about ≈50 mV in respect to the corrosion potential (Ecorr). Subsequently the current density (icorr) was estimated from the value where the fit intercepted the vertical through the respective Ecorr (Gandel et al., 2010).

Electrochemical Impedance Spectroscopy (EIS)

Electrochemical impedance spectroscopy (EIS) measurements were performed for immersion times up to three days in the frequency range between 10^4 Hz and 10^{-2} Hz with an amplitude of ±10 mV rms. These impedance measurements were performed after different exposure periods of 1, 3, 6, 10, 16, 24, 36, 48, 60, and 72 h. The impedance spectra were fitted using Zview software.

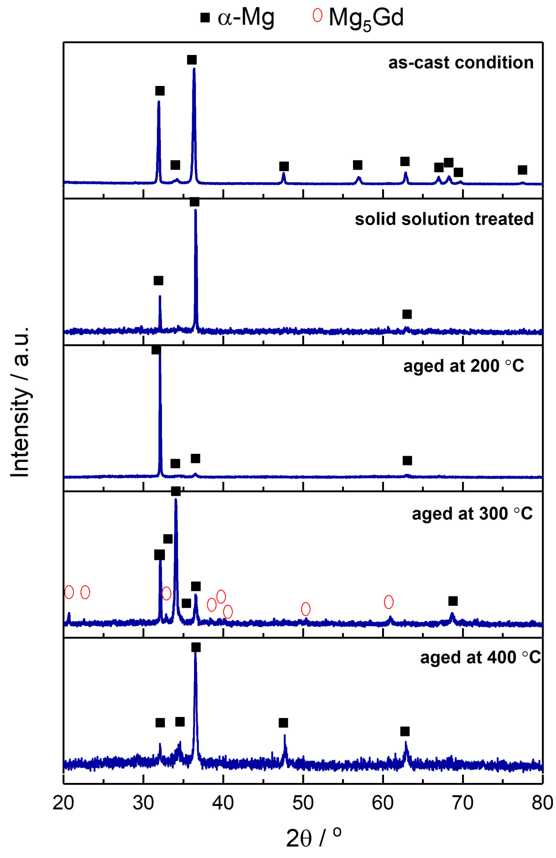

FIGURE 1 | X-ray diffraction patterns of as-cast, solution treated and heat treated at 200°C, 300°C, and 400°C conditions of Mg-10Gd alloy (Silva Campos, 2016).

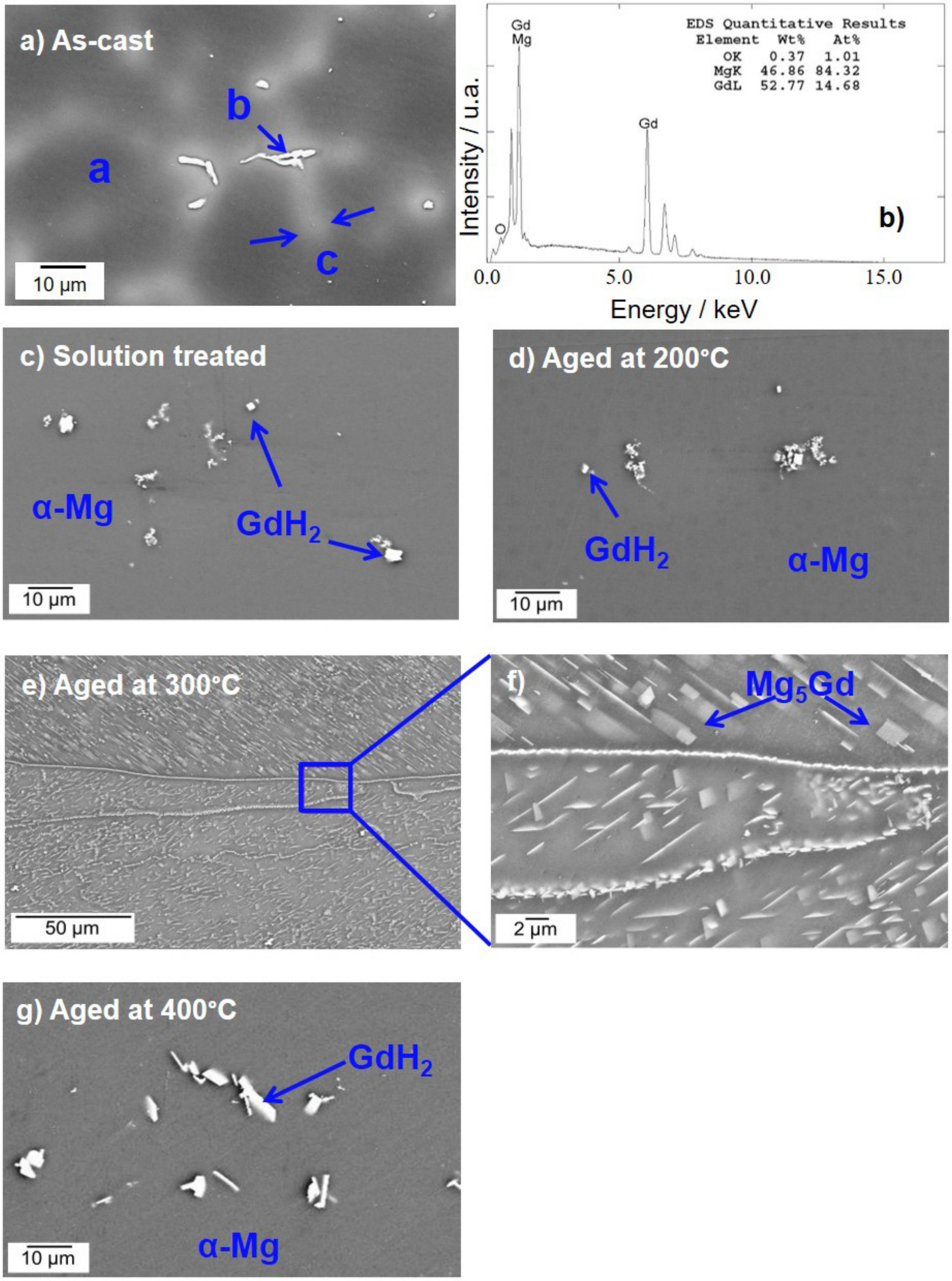

FIGURE 2 | SEM micrographs of Mg-10Gd alloy: **(a)** as-cast microstructure, letters a, b, c, corresponds to α-matrix, Mg_5Gd intermetallic phases and Gd enrichment zones, respectively, **(b)** typical EDS analysis of the "b" particles **(c)** solution treated microstructure, after 24 h at 540°C, heat treatments for 24 h **(d)** at 200°C, **(e)** at 300°C, **(f)** higher magnifications showing the precipitates of Mg_5Gd phase and **(g)** at 400°C.

Hydrogen Evolution and Weight Loss

Hydrogen evolution tests were conducted in 0.5 wt.% NaCl solution using samples with dimensions of 15 mm diameter × 4 mm thickness in standard eudiometer set-ups with a total volume of 400 ml. Details of the procedure can be found in the literature (Hort et al., 2010). The samples were

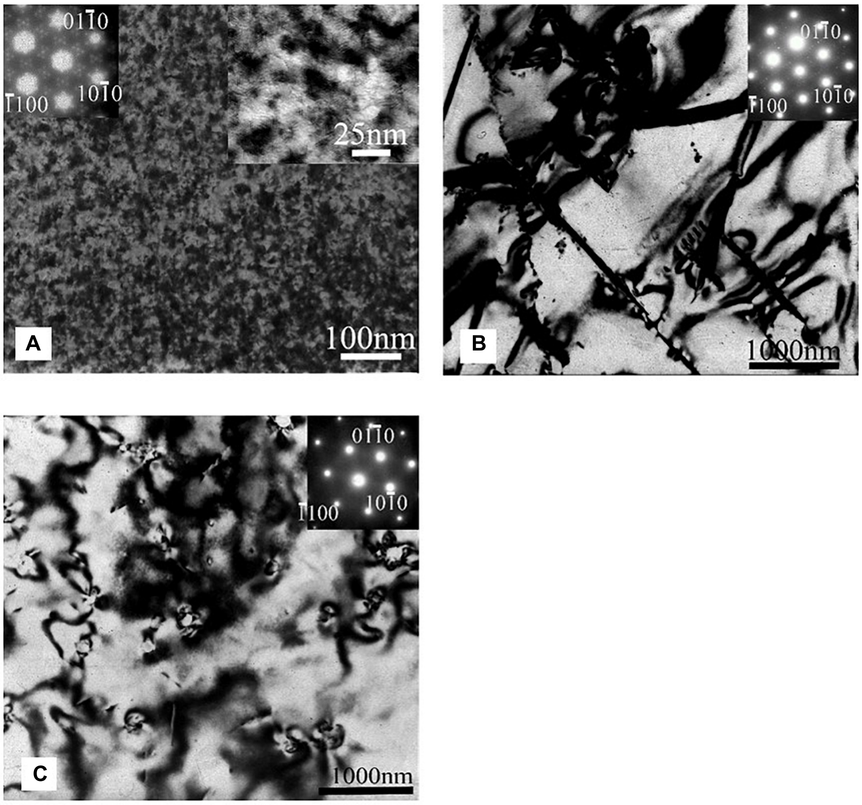

FIGURE 3 | TEM microstructures typical of Mg-10Gd alloy heat treated for 24 h at: **(A)** 200°C, **(B)** 300°C, and **(C)** 400°C. The electron beam direction is approximately parallel to [0001]Mg direction.

removed when the hydrogen has replaced the total volume of 400 ml water out the column. For the weight loss evaluations, the weight of the specimens before and after the corrosion test was cross-checked. The specimens were cleaned for 30 min in chromic acid solution (180 g/l) at room temperature then washed with ethanol and finally dried in hot air to remove the corrosion products. The corrosion rates were calculated from

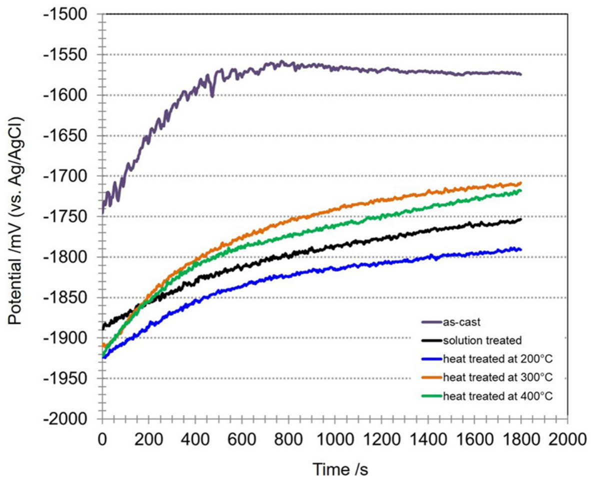

FIGURE 4 | Open circuit potentials of Mg-10Gd alloy in as-cast, solution treated, heat treated at 200°C, 300°C, and 400°C conditions in 0.5 wt.% NaCl solution for 30 min.

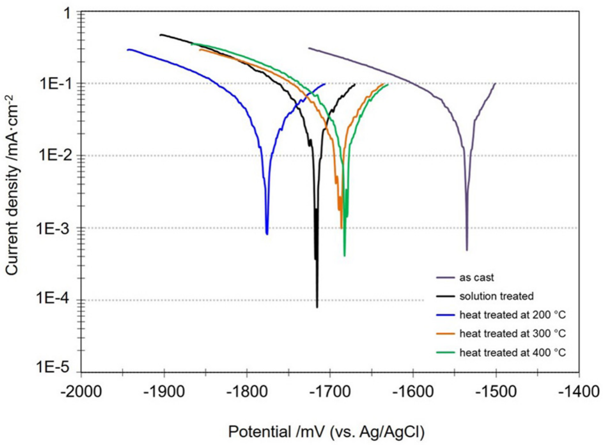

FIGURE 5 | Potentiodynamic polarization measurements of as-cast, solution treated, heat treated at 200°C, 300°C, and 400°C of Mg-10Gd alloy in 0.5 wt.% NaCl solution after 30 min OCP at room temperature.

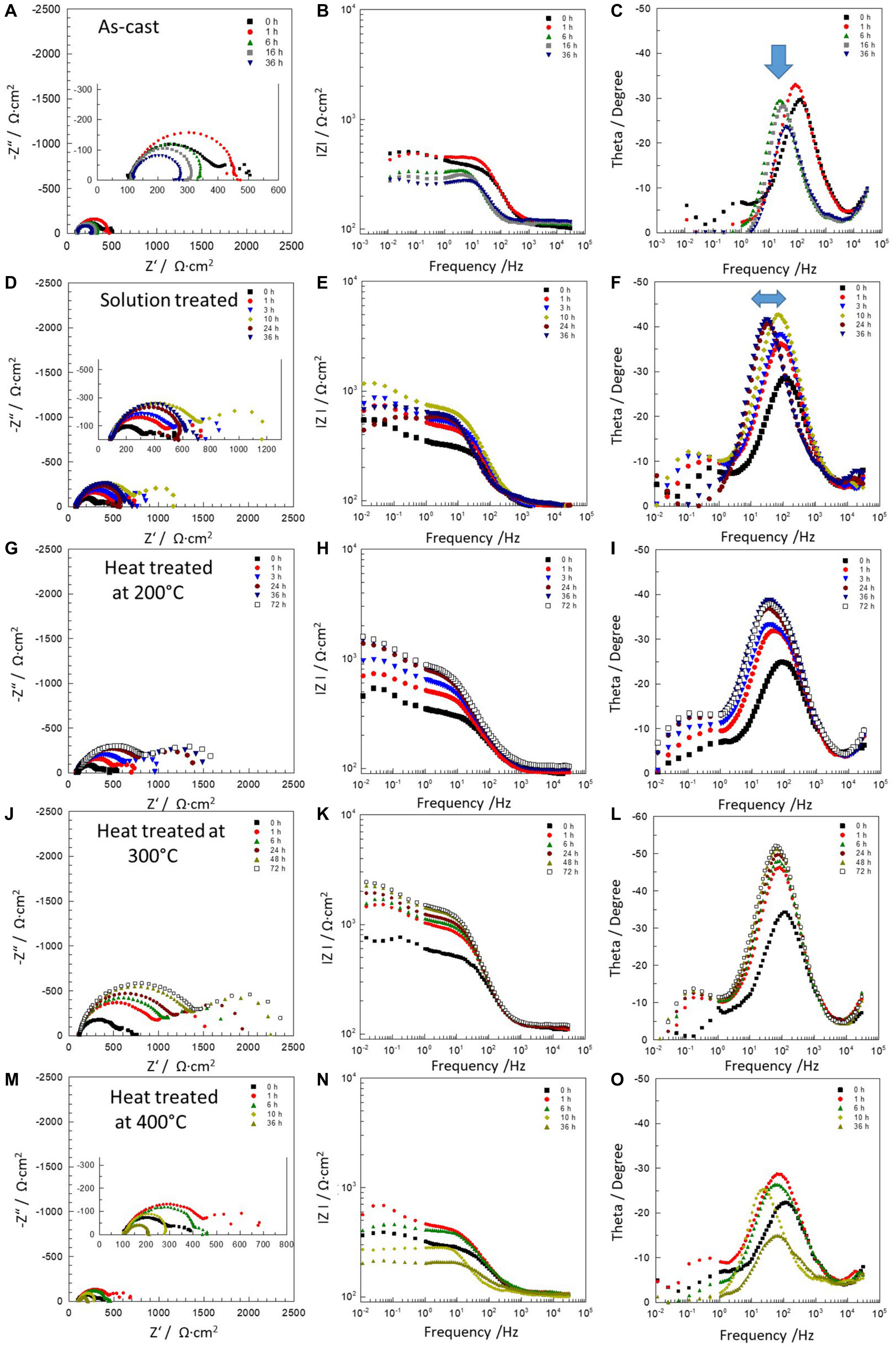

FIGURE 6 | Electrochemical impedance spectra of Mg-10Gd alloys: as-cast **(A–C)**, solution treated **(D–F)** and heat treated at 200°C **(G–I)**, 300°C **(J–L)** and 400°C **(M–O)**. Where the blue arrow indicates the displacement of the time constant from high frequencies to middle frequencies.

measurement of weight loss using the equation described in (Hort et al., 2010).

Drop Test

In order to observe the initiation and progress of corrosion process drop tests were conducted by placing drops of 0.5 wt.% NaCl solution on a polished surface of the samples for different exposure times (10 min, 30 min, 1, 3, and 5 h). After exposure, the samples were cleaned and the corrosion products removed as described above. The morphology of specimens was observed with SEM before and after the tests.

RESULTS

Microstructure

The XRD diffraction peaks did not reveal any characteristic peaks related to Mg_5Gd phase for solution treated, heat treated at 200°C and 400°C samples (Silva Campos, 2016). This is due to a lower volume fraction of the intermetallic phases and the overlapping X-ray Absorption Edges of Gd and Cu, which is described in Hort et al. (2010). However, Mg_5Gd peaks could be identified for samples heat treated at 300°C (**Figure 1**). The typical microstructures of the specimen after various process conditions are illustrated in **Figure 2**. **Figure 2a** shows the as-cast microstructure which contain Mg dendrites (a), Mg_5Gd intermetallic particles (b) and Gd segregation near the inter dendritic regions (c). The EDX spectra shows that the ratio between Mg and Gd is about 5.7 and it is likely to be Mg_5Gd (see **Figure 2b**). After solution heat treatment, **Figure 2c**, the dendritic microstructure disappears and few smaller intermetallic particles remain. Based on the morphology of the particles, these particles are likely to be GdH_2 phases, based on the SEM-EDS analysis (not shown here) the concentration of Gd in these particles is between 60 to 85 wt.%. Similar phases were reported in previous studies (Peng et al., 2011; Huang et al., 2013, 2016), without forming other Gd containing phases (Apps et al., 2003a,b). After heat treatment at 200°C and 400°C SEM micrographs show similar intermetallic phases to those observed in the solution treated alloy, see **Figures 2d,g**. The SEM micrograph did not show any solid state precipitates in the sample aged at 200°C (**Figure 2c**). The TEM analysis show the presence of a very fine distribution of prismatic plate precipitates forming on $\{10\bar{1}0\}$Mg planes in sample aged at 200°C for 24 h and as illustrated in **Figure 3A**. These precipitates were approximately 25 ± 1.5 nm in length and only few atomic layers in thickness. Examination of the diffraction patterns and information from the previous research work by Nishijima and Hiraga (2007), and Vostrý et al. (1999) are used to identify these precipitates as β' (c base centered orthorhombic structuredβ) phase (Gao et al., 2006). The alloy aged at 300°C for 24 h contained a coarse distribution of precipitates (1.12 ± 0.55 μm), see **Figures 2e,f** which could be identified as Mg_5Gd phase (**Figure 3B**; Silva Campos, 2016). The alloy aged at 400°C did not show any solid state precipitates (**Figure 2g**) but contained what was identified as GdH_2 particles (**Figure 3C**).

The heat treatment results are consistent with the observations of Vostrý et al. (1999), where they reported a decomposition of α-Mg supersaturated solid solution in Mg-9.33 wt.% Gd from a metastable β''(D019) phase to stable β'(Mg_5Gd f.c.c) phase using isochronal annealing from 20 to 500°C. Apps et al. (2003a,b) suggest that decomposition of Mg supersaturated solid solution Mg (SSSS) follows the sequence: $\beta'' \rightarrow \beta' \rightarrow \beta_1 \rightarrow \beta$, although the compositions of the β'' and β' phases are not fully characterized due to the small size of these precipitates and their close proximity to each other. However β_1 and β phases have a stoichiometry of the Mg_5RE for the Mg–7%Gd–2.25%Nd–0.6%Zr (GN72) alloy. Furthermore, they observed the presence of Mg_5Gd phase as a stable intermetallic in the binary Mg–Gd system. The Mg_5RE phase is dependent on formation temperature.

Corrosion Evaluation

Open Circuit Potential (OCP)

The heat treatments do not only influence the microstructure of the Mg-10Gd alloy but also their electrochemical properties. **Figure 4** shows the OCP curves for the Mg-10Gd alloy before and after the heat treatments. All heat treated samples showed more negative potential compared to the as-cast condition. After 500 s only the OCP of the as-cast sample reaches a plateau and for all the other conditions, the potential continues to drift to more positive potential values. This might be a result of different growth of a protective surface film (Li et al., 2011) or possibly the heat treated samples require longer immersion periods than 30 min to stabilize their OCP. After

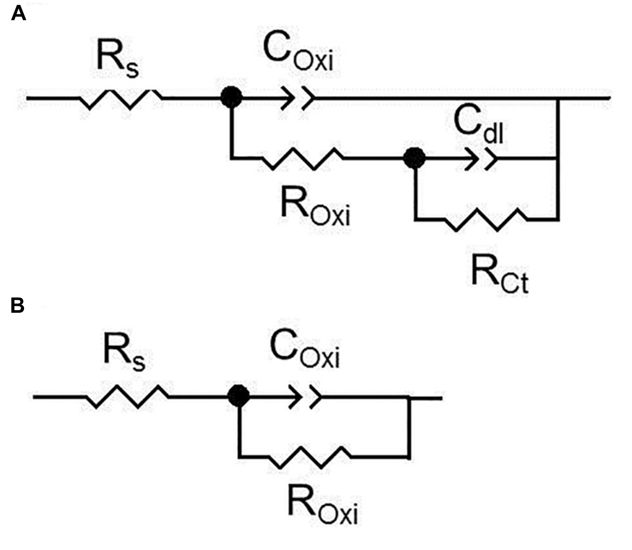

FIGURE 7 | (A,B) Equivalent electrical circuits used to simulate EIS spectra for as-cast, solution treated and heat treatments at 200°C, 300°C and 400°C conditions of Mg-10Gd alloy during different immersion time. Where, R_s is the resistance of the solution, R_{Oxi} and C_{Oxi} are the resistance and capacitance of the oxide film, respectively. R_{Ct} represents the charge transfer resistance and C_{dl} is attributed to the double-layer capacitance (Silva Campos, 2016).

TABLE 1 | Circuit parameters for as-cast condition, solution treated and heat treatments at 200°C, 300°C, and 400°C of Mg10Gd alloy.

Condition	Time (h)	R_s ($\Omega\cdot cm^2$)	C_{Pf} ($\Omega^{-1}cm^{-2}s^n$)	n_1	R_{Pf} ($\Omega\cdot cm^2$)	C_{dl} ($\Omega^{-1}cm^{-2}s^n$)	n_2	R_{Ct} ($\Omega\cdot cm^2$)	Chi-squared	Sum squared
As-cast	0	102.90	1.33E−05	0.84	297.00	4.04E−03	0.86	104.00	8.37E−04	0.12
	1	100.00	1.48E−05	0.80	363.80				2.60E−03	0.38
	3	112.30	3.26E−05	0.90	234.90				1.94E−03	0.28
	6	114.10	4.24E−05	0.99	219.20				1.89E−03	0.28
	10	119.00	5.51E−05	0.93	173.50				2.06E−03	0.30
	16	110.00	4.16E−05	0.96	182.80				1.87E−03	0.28
	24	114.50	3.49E−05	0.93	137.40				1.96E−03	0.28
	36	117.50	3.65E−05	0.96	150.40				1.47E−03	0.21
Sol. treated	0	85.29	1.81E−05	0.82	244.00	4.47E−03	0.86	115.80	5.01E−04	0.07
	1	88.73	1.78E−05	0.85	397.50	4.02E−03	0.78	287.50	4.33E−04	0.06
	3	86.30	1.69E−05	0.85	456.70	5.04E−03	0.79	390.50	3.32E−04	0.05
	6	90.21	1.62E−05	0.84	538.40	4.59E−03	0.81	418.40	4.83E−04	0.07
	10	90.54	1.56E−05	0.85	640.10	5.05E−03	0.74	601.60	4.52E−04	0.06
	16	89.12	1.43E−05	0.86	626.10	6.95E−03	0.81	359.30	7.04E−04	0.10
	24	94.39	2.72E−05	0.88	490.60				3.29E−03	0.24
	36	94.04	3.32E−05	0.84	593.70				2.14E−03	0.28
	48	93.76	2.36E−05	0.82	693.10				6.08E−03	0.10
Heat treated at 200°C	0	88.81	3.05E−05	0.74	258.20	4.59E−03	1.00	68.02	3.95E−04	0.05
	1	88.75	3.55E−05	0.76	443.30	6.20E−03	0.85	221.90	1.41E−04	0.02
	3	96.06	4.02E−05	0.73	589.90	5.56E−03	0.85	346.90	1.41E−04	0.02
	6	96.10	4.22E−05	0.73	702.40	4.78E−03	0.88	428.20	1.49E−04	0.02
	10	99.68	4.27E−05	0.72	723.20	4.97E−03	0.85	479.40	2.77E−04	0.03
	16	99.06	3.78E−05	0.74	751.80	4.72E−03	0.85	505.00	3.35E−03	0.48
	24	97.23	3.75E−05	0.74	777.60	4.74E−03	0.82	570.70	3.47E−03	0.50
	36	94.21	3.42E−05	0.76	828.30	4.40E−03	0.81	637.90	3.08E−03	0.44
	48	101.80	3.36E−05	0.75	856.80	4.70E−03	0.77	713.00	3.33E−03	0.48
	60	104.20	3.28E−05	0.75	802.50	4.72E−03	0.76	730.60	3.54E−03	0.51
	72	101.90	3.24E−05	0.75	841.40	4.66E−03	0.77	768.50	3.59E−03	0.51
Heat treated at 300°C	0	109.20	1.16E−05	0.82	466.30				7.49E−04	0.10
	1	113.20	9.33E−06	0.89	857.80	1.49E−03	0.84	594.80	1.17E−03	0.16
	3	117.20	9.01E−06	0.90	871.20	1.96E−03	0.80	656.00	9.26E−04	0.13
	6	117.30	8.88E−06	0.90	959.90	2.02E−03	0.80	781.20	1.18E−03	0.17
	10	121.80	8.67E−06	0.90	1053.00	2.05E−03	0.78	903.60	1.22E−03	0.17
	16	114.90	8.31E−06	0.91	1023.00	1.83E−03	0.78	870.90	7.84E−04	0.11
	24	113.20	8.39E−06	0.91	1058.00	1.71E−03	0.79	848.40	1.01E−03	0.14
	36	116.60	8.25E−06	0.91	1168.00	1.85E−03	0.77	1003.00	1.02E−03	0.15
	48	119.70	8.11E−06	0.91	1225.00	1.97E−03	0.73	1126.00	7.50E−04	0.11
	60	121.50	8.14E−06	0.91	1304.00	1.92E−03	0.73	1248.00	9.64E−04	0.14
	72	119.60	8.24E−06	0.91	1311.00	1.76E−03	0.77	1141.00	9.49E−04	0.14
Heat treated at 400°C	0	100.70	2.28E−05	0.78	202.30	4.80E−03	0.86	85.98	1.51E−04	0.02
	1	106.70	2.73E−05	0.78	357.70	5.35E−03	0.84	230.80	3.04E−04	0.04
	3	104.30	2.85E−05	0.77	364.00	5.74E−03	0.88	193.60	2.88E−04	0.04
	6	107.00	3.10E−05	0.75	330.70				6.53E−03	0.95
	10	105.10	6.64E−05	0.87	191.90				1.14E−03	0.06
	16	107.10	6.75E−05	0.87	168.20				1.45E−03	0.02
	24	108.50	7.97E−05	0.83	166.20				8.73E−04	0.03
	36	109.80	5.60E−05	0.78	136.60				1.04E−03	0.05

30 min immersion, the as-cast sample showed the most positive OCP of −1574 mV. The solution treated sample reached an OCP of around −1754 mV, heat treated at 200°C, 300°C, and 400°C samples shifted to OCP values of −1790 mV, −1708 mV, and −1717 mV, respectively. The comparison of the OCP of as-cast specimens with heat treated specimens decreased in the following order: as-cast > heat treated at 300°C > heat treated at 400°C > solution treated > heat treated at 200°C (Silva Campos, 2016). The heat treatments have a direct influence on the initial OCP and the way that corrosion product layers are forming during the first stage of the corrosion process.

Potentiodynamic Polarization Measurements

Figure 5 shows the potentiodynamic polarization curves for all the studied conditions. It shows that the values of corrosion potential (Ecorr) of the Mg-10Gd alloys after heat treatments became more negative than the corrosion potential of the as-cast Mg-10Gd alloy as observed during the OCP measurements. However, only slight differences in the current density values (icorr) were observed (**Supplementary Table SA**). As mention before the corrosion rates are still correlate with the volume fraction of Mg_5Gd, Gd enriched zones and in some extend with the GdH_2 phases in as-cast condition. Nevertheless, there is evidence of GdH_2 formation especially during heat treatments, a higher volume fraction was found in the solution treated and heat treated at 400°C conditions. Both solution treated specimens and heat treated at 400°C specimens revealed the relatively higher current densities (0.10 ± 0.02 and 0.095 ± 0.05 mA/cm^2, respectively) compared with 0.085 ± 0.01 mA/cm^2 for heat treated at 200°C and 0.083 ± 0.009 mA/cm^2 for heat treated at 300°C samples. Furthermore, the homogenization of Gd distribution appears to be not beneficial for the overall corrosion rate although pitting seems to be retarded. Although differences were small, but in the short term (around 20 to 60 min exposure, the heat-treatments could not significantly improve corrosion resistance. Since the current density of as-cast Mg-10Gd alloy was lowest (0.04 ± 0.004 mA/cm^2), compared with those obtained after heat treatments (Silva Campos, 2016).

Electrochemical Impedance Spectroscopy (EIS)

Figure 6 depicts the Bode and Nyquist plots for all studied materials at selected exposure times according to the heat treatment, in order to avoid any overlapping in the spectra. The impedance spectra for all specimens showed two well defined time constants. The time constant at medium frequencies ($\approx 10^1$ Hz) is related to dense oxides/hydroxides corrosion product layers formed on the alloys surface and the second time constant at low frequencies ($\approx 10^{-2}$ Hz) is attributed to the electrochemical activities at the interface metal/electrolyte. The equivalent circuits used for fitting the EIS spectra of the all materials are shown in **Figure 7** where, R_s represents the resistance of the solution. The resistance R_{Oxi} and capacitance C_{Oxi} are correlated with the oxides/hydroxides layer formed on the metal surface. The defects that formed in the oxide layers generate pathways that allow the diffusion of corrosive species to the Mg surface. Thus, the second time constant appears in the low frequency region. This is the initiation of the corrosion process and it is attributed to the existence of the double-layer capacitance at the metal/electrolyte interface, C_{dl} and the corresponding charge transfer resistance, R_{Ct} (**Figure 7A**). When the specimen starts to corrode actively, the charge transfer resistance gets very low, leading to almost complete disappearance of the respective time constant and spectra can be fitted using a simple Randles model (**Figure 7B**; Silva Campos, 2016). All simulated parameters from EIS spectra are listed in **Table 1**.

For as-cast condition after 1 h immersion one time constant remained visible related to oxide layer formation, while the second time constant is less visible due to a high dissolution activity (**Figures 6A–C**). Furthermore after 6 h immersion the high frequencies constant ($\approx 10^2$ Hz) was shifted toward middle frequencies values ($\approx 10^1$ Hz), indicating that the surface film was less protective on the alloy surface. For solution treated sample two well defined time constants were observed during the first 10 h of immersion (**Figures 6D–F**). The film improved its barrier properties and thus the resistance was increased. After 24 h, the protective layer began to fail due to localized corrosion, which was related to a slight shift of the first time constant as observed in the as-cast condition. Heat treated at 200°C sample showed two time constants during full immersion period. The impedance modulus at low frequencies increased with the exposure time indicating increase of barrier properties of corrosion products on the surface (**Figures 6G–I**). Similar behavior was observed for the heat treated at 300°C sample. Moreover at this condition Mg-10Gd alloy showed the highest impedance modulus above 2000 Ω·cm^2 at 0.01 Hz. The heat treatment at 300°C promotes formation of an oxide layer more stable and thicker with increased immersion times (**Figures 6J–L**). However, the sample heat treated at 400°C depicted strong degradation of the oxide layer already after 1 h immersion, revealing a rapid breakdown

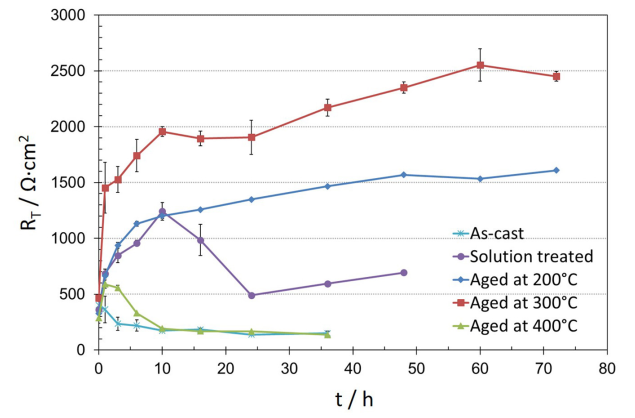

FIGURE 8 | Average evolution of total resistance (RT) values obtained after fitting EIS spectra of as-cast, solution treated and heat treatments at 200°C, 300°C and 400°C conditions of Mg-10Gd versus immersion time in 0.5 wt.% NaCl solution.

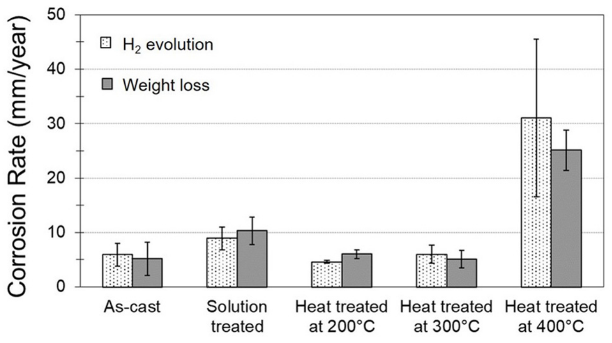

FIGURE 9 | Hydrogen evolution and weight loss of as-cast, solution treated and heat treated at 200°C, 300°C, and 400°C conditions of Mg-10Gd alloy.

of the corrosion products layer and the corrosion process was dominated by local active areas without protective film (see **Figures 6M–O**).

To compare the results, the total resistance (R_T) is displayed in **Figure 8**, as the sum of R_{Oxi} and R_{Ct}. The starting resistance values were all similar which is consistent with the polarization results. Remarkable differences are developing only with longer immersion times. Compared to the as-cast condition all heat treated specimens exhibited a better corrosion behavior. The solution treated and heat treated at 400°C specimen contained larger amounts of the GdH_2 precipitates and showed less stable passive film indicated by earlier film breakdown and active local corrosion spreading with time over the whole surface. The as-cast condition had large Mg_5Gd precipitates and no uniform solid solution distribution of Gd in the Mg matrix. Obviously, this is detrimental for a uniform film formation. A homogenized

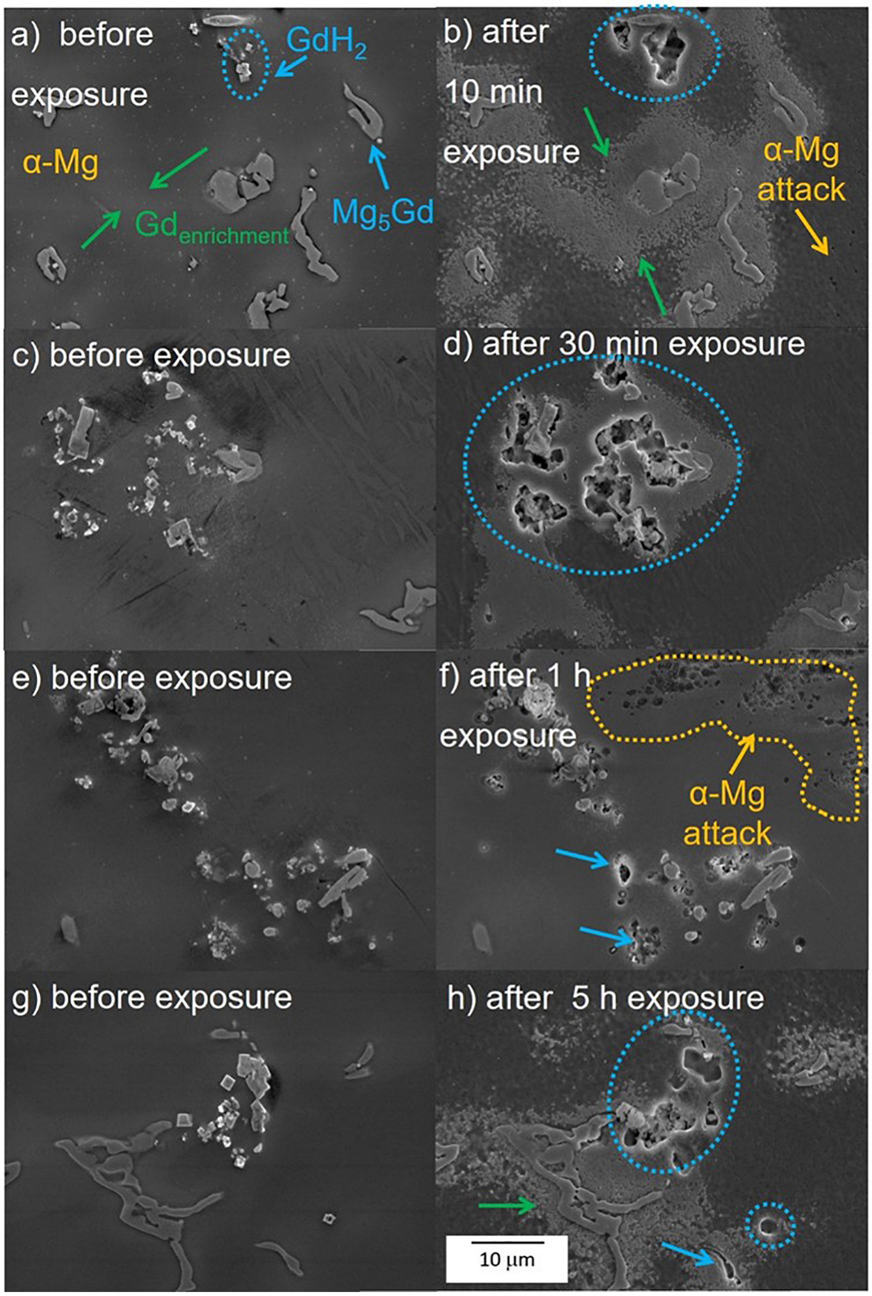

FIGURE 10 | Corrosion monitoring using drop test of as-cast Mg-10Gd alloy **(a,c,e,g)** before exposure and **(b,d,f,h)** after different exposure times in 0.5 wt. % NaCl solution. Yellow arrows/dotted areas depict the corrosion attack on the α-Mg matrix, blue arrows/dotted circles indicate corrosion process on the Mg_5Gd/GdH_2 phases and the green arrows show the corrosion degradation on the Gd enrichment areas.

Gd distribution in the matrix and uniformly distributed small Mg_5Gd precipitates are supporting obviously the passive film formation (heat treatments at 200°C and 300°C).

Hydrogen Evolution and Weight Loss

Figure 9 shows the corrosion rates determined by hydrogen evolution and weight loss measurements for samples of the as-cast and the heat treated Mg-10Gd alloy. The values calculated from hydrogen evolution measurements were comparable with those obtained from mass loss results. Similar corrosion rates of about 5 mm/y were observed for the samples of Mg-10Gd alloy in the as-cast, heat treated at 200°C and 300°C conditions. While the corrosion rate in the solution treated sample increased to almost twice the rate of the as-cast alloy. The sample heat treated at 400°C showed a corrosion rate of 31.04 and 25.11 mm/year from hydrogen evolution and mass loss measurements, respectively. This is five to six times greater than the as-cast corrosion rate. Thus, the corrosion rate of the Mg-10Gd alloy is affected not only by the amount of Mg_5Gd/GdH_2 phases present but also their distribution. The Mg_5Gd phase is found in as-cast sample and dissolves during the solid solution treatment. However, during subsequent T6 heat treatments precipitates of either Mg_5Gd or other metastable phases form in solid state with the largest particle size observed at 300°C. The corrosion rates are lower for the samples in as-cast condition and heat treated at 200°C and 300°C (Silva Campos, 2016). These results are similar to the findings of Kainer et al. (2009), where they reported that the T6 condition resulted in the lowest corrosion rate due the presence of nano-sized precipitates.

Drop Test

In this section, the results are divided into two groups, the first consisting of as-cast Mg-10Gd and the second after the all heat treatments to observe where the corrosion processes start and how they progress over time.

As-cast Mg-10Gd

Figure 10 shows the corrosion process of as-cast Mg-10Gd after different exposure times in 0.5 wt.% NaCl solution. Same selected areas before exposure were add for comparison (**Figures 10a,c,e,g**). After 10 min of exposure the sample shows slight attack in the α-Mg enriched with Gd areas (green arrows) and already visible attack around the secondary cubic phase (blue dotted circle), **Figure 10b**, which became stronger after 30 min of exposure. Cavities were generated at the base of the cubic GdH_2 and Mg_5Gd precipitates (blue dotted circles **Figure 10d**). Both phases are found close together so at the beginning of the corrosion process it is hard to define which one is more detrimental. However, some Mg_5Gd particles remained and the cubic phase disappeared most likely by undermining. From one-hour exposure, the matrix presented small pits (yellow dotted line in **Figure 10f**). The degradation in the matrix, Mg_5Gd phases and Gd enriched zones continued after 5 h exposure, in some areas severe localized corrosion was also observed (**Figure 11**).

The cubic phase (GdH_2) plays an important role in the corrosion of the as-cast alloy. GdH_2 phase causes significantly high corrosion attack, but it is not clear if this phase is removed due to the fast dissolution of the surrounding matrix or by subsequent chromic acid cleaning. However, the larger size of the region under corrosion attack compared with the original particle size is a good indicator of the severity of the galvanic attack. The Mg_5Gd phase seems to be less detrimental compared with GdH_2 phase at least during the early stages of corrosion, but it still causes dissolution of the surrounding Gd-rich α-Mg (Silva Campos, 2016).

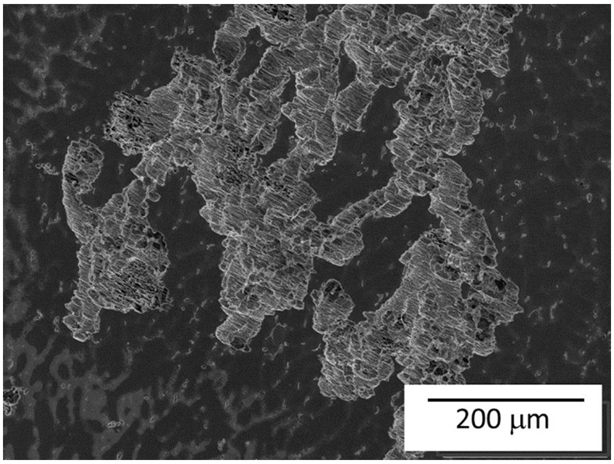

FIGURE 11 | SEM micrograph of severe localized corrosion of as-cast Mg-10Gd alloy after 5 h exposure in 0.5 wt.% NaCl solution.

Mg-10Gd after heat treatments

In this section longer immersion periods of 30, 60 min and 3 h were used as shorter exposure periods did not reveal any visible corrosion. **Figure 12** shows the corrosion process of the solution treated samples and T6 heat treated at 200°C, 300°C and 400°C samples. In the solution treated samples (**Figures 12a–d**) the attack began in the α-Mg matrix surrounding GdH_2 particles after 60 min exposure (see orange arrows, **Figure 12c**). After 3 h exposure, **Figure 12d**, only minor changes in size and number were visible. The sample heat treated at 200°C (**Figures 12e,f**) showed similar attack as in the solution treated sample but it has a more widespread localized attack after exposure for 60 min (see yellow arrows **Figures 12g,h**). However, in the sample heat treated at 300°C (**Figures 12i,j**) the size of Mg_5Gd precipitates was the highest and there was no visible corrosion attack for up to 1 h exposure (**Figure 12k**). After three hours, localized attack occurred in a comparable amount to the other conditions (**Figure 12l**). However, the treatment did not prevent the advance of severe localized corrosion in other areas of the specimen (**Figure 13**). While in heat treated at 400°C sample (**Figures 12m–p**), the first corrosion signal was also observed after 60 min of exposure (**Figure 12o**) and after 3 h immersion corrosion spread in areas close to the GdH_2 precipitates (orange dotted circles) generating more degradation in the matrix, **Figure 12p**.

The homogenization of Gd distribution in the matrix has positive effect in increasing the time required for the first observation of localized corrosion. For the solution treated, heat

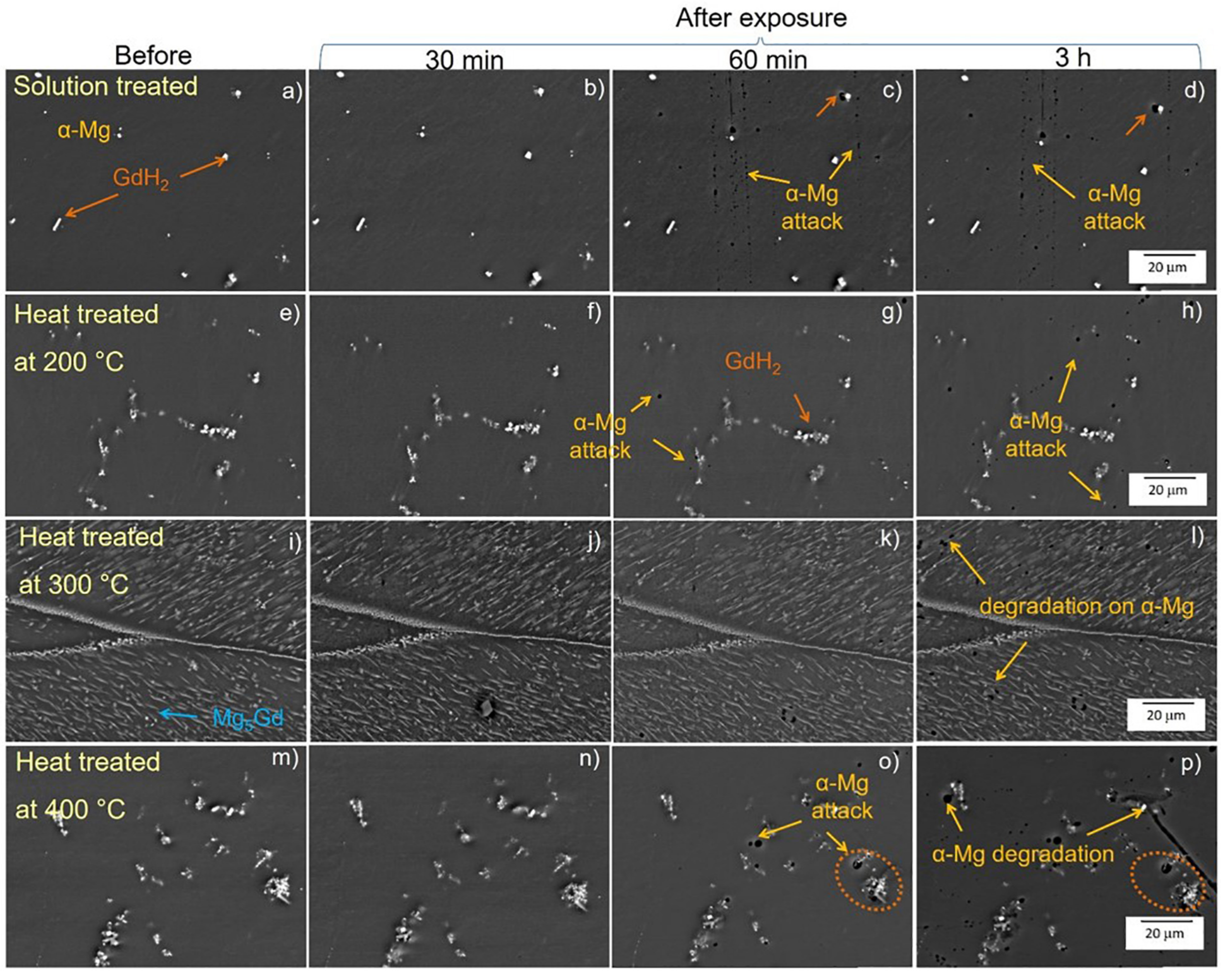

FIGURE 12 | Corrosion monitoring using drop test of solution treated **(a–d)** and heat treated at 200°C **(e–h)**, 300°C **(i–l)** and 400°C **(m–p)** of Mg-10Gd alloy after 30, 60 min and 3 h time exposure in 0.5 wt.% NaCl solution. Yellow arrows depict the corrosion attack on the α- Mg matrix, orange arrows/dotted circles indicate corrosion process on the GdH$_2$ phases.

treated at 200°C and 300°C samples, the corrosion is relatively uniform and not detrimental for the overall corrosion resistance.

In contrast, heat treatment at 400°C seems to increase the amount of GdH$_2$ precipitates in the matrix and their presence influence the localized attack with a detrimental effect on the corrosion behavior. Localized corrosion now occurs close to the agglomeration of the bright white cubic GdH$_2$ precipitates (Silva Campos, 2016).

DISCUSSION

In the current work, the Mg$_5$Gd phase has been shown to cause only minor negative effects on corrosion behavior when distributed in the following conditions:

(i) in as-cast condition with some Gd enriched zones surrounding the larger Mg$_5$Gd precipitates, reducing the local damage due to galvanic couples, (ii) if most of the Gd is in solid solution in the matrix and there is only a moderate amount of GdH$_2$ phase, and (iii) when the volume fraction of Mg$_5$Gd phase is larger but this phase is uniformly distributed and precipitates are small (aged at 200 and 300°C).

The most critical phases are not Mg$_5$Gd, but the small cubic shaped particles rich in Gd which are most likely to be GdH$_2$. The mechanism of initiation and progress of the micro-galvanic corrosion of the as-cast, T4 and T6 heat treated Mg-10Gd alloys as observed in the current investigation is presented in **Figure 14** (Silva Campos, 2016). According to this mechanism, once the specimen is exposed to the solution, two corrosion morphologies occur depending on the Gd distribution.

Firstly, formation of a Gd(OH)$_3$ layer, since Gd has a more negative electrode potential compared to Mg (Pourbaix, 1974; Bala et al., 1993). Secondly Mg(OH)$_2$ layer forms on the surface in as-cast condition due to degradation of Gd enriched areas and some α-Mg matrix, as result of metal dissolution (Pourbaix, 1974; Song et al., 1997a,b; Song and Atrens, 1999; Kainer et al., 2010), according to the reactions (1–6), **Figure 14A**. These layers are normally not continuous due to the presence of the intermetallic

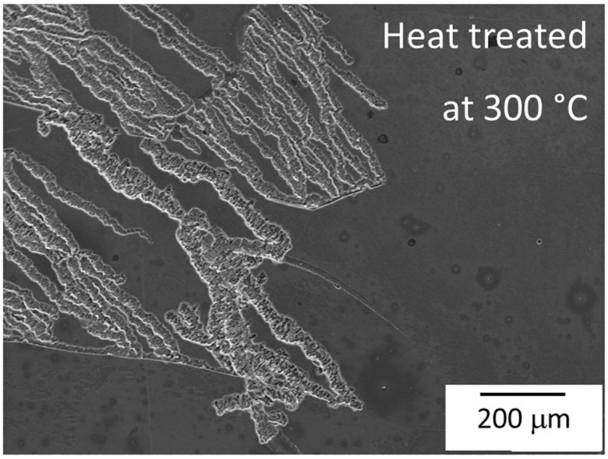

FIGURE 13 | SEM micrograph of severe localized corrosion of heat treated Mg-10Gd at 300°C after 3 h exposure in 0.5 wt.% NaCl solution.

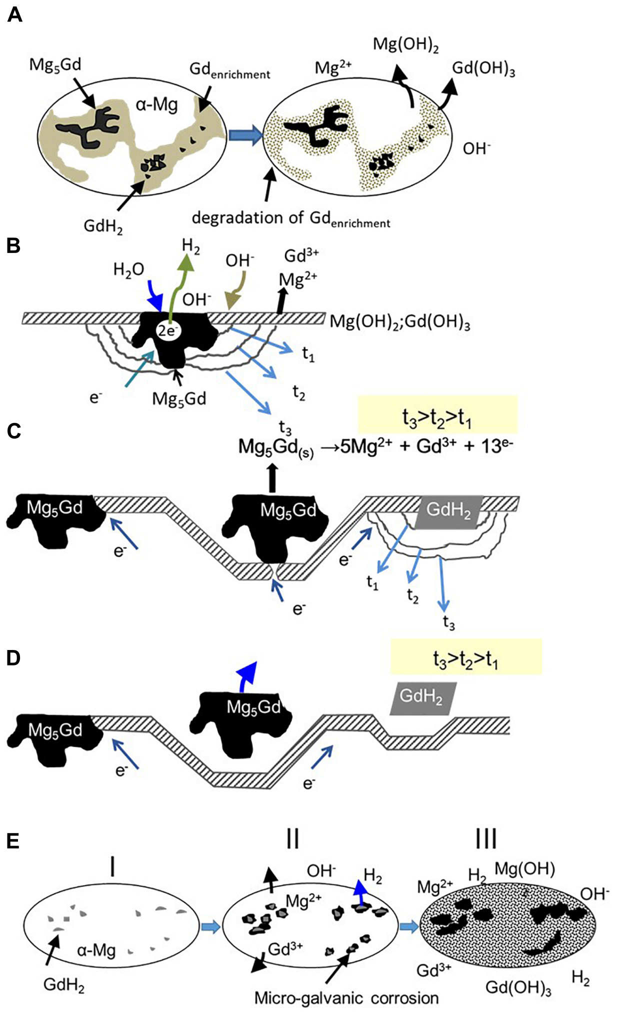

FIGURE 14 | Mechanism of micro-galvanic corrosion proposed for Mg-10Gd alloy: **(A)** formation of Gd and Mg hydroxides on the surface in as-cast condition, **(B)** degradation of the Mg matrix adjacent to Mg_5Gd phases, **(C)** higher dissolution of Mg matrix, exposing the Mg_5Gd/GdH_2 phases subsequently starts the dissolution of Mg_5Gd phase due to reducing contact area, **(D)** detachment and dissolution of Mg_5Gd/GdH_2 phases, and **(E)** localized micro-galvanic corrosion at preferential areas for samples heat treated.

(Mg_5Gd/GdH_2) phases (Song and Atrens, 2003). EDX analysis of the corrosion products layer confirmed the presence of the oxide layer, which was mainly formed by $MgO/Mg(OH)_2$ and $Gd_2O_3/Gd(OH)_3Gd$, together with some carbonates. The carbonate can form from atmospheric CO_2 dissolved in the aqueous electrolyte (**Figure 15**; Silva Campos, 2016). The noble intermetallic Mg_5Gd/GdH_2 phases are driving this process because they are the places where the cathodic partial reaction takes place, as there is no stable passive film on the intermetallics **Figure 14B**. The micro-galvanic activity continues as long as there is contact between the intermetallic Mg_5Gd/GdH_2 phases as cathodes and matrix as anode. If contact is lost in the latter stages the Mg_5Gd/GdH_2 phases are not cathodically protected anymore and starts to corrode as the phase is less stable than the matrix in NaCl solutions (Silva Campos et al., 2013). However, it is not necessary that contact is fully lost to start degradation. It is enough when the reduced contact does not allow sufficient current flow anymore to fully protect the Mg_5Gd/GdH_2 (**Figures 14C,D**).

$$Gd \rightarrow Gd^{3+} + 3e^- \qquad (\textit{anodic partial reaction}) \tag{1}$$

$$2H_2O + 2e^- \rightarrow H_2 + 2OH^- \qquad (\text{cathodic partial reaction}) \tag{2}$$

$$2Gd + 6H_2O \rightarrow 2Gd(OH)_3 + 3H_2 \qquad (\textit{overall reaction}) \tag{3}$$

$$Mg \rightarrow Mg^{2+} + 2e^- \qquad (\textit{anodic partial reaction}) \tag{4}$$

$$2H_2O + 2e^- \rightarrow H_2 + 2OH^- (\textit{cathodic partial reaction}) \tag{5}$$

$$Mg + 2H_2O \rightarrow Mg(OH)_2 + H_2 (\textit{overall reaction}) \tag{6}$$

When the specimens do not contain Gd enriched zones (heat treated samples), galvanic corrosion begins with hydrogen evolution (5) on the cathodic GdH_2 phase, while the dissolution of Mg (4) develops at the adjacent matrix areas **Figures 14E** I,II. A minor contribution to the corrosion process is added due to the presence of Mg_5Gd phase only in the heat treated at 200°C and 300°C conditions. In some cases a strong dissolution of adjacent matrix areas favors the intermetallic phase detachment (**Figure 14E** III), but also dissolution which is possible for the GdH_2 phase because of own poor stability if it is not cathodically protected anymore as also shown for Mg_5Gd phases (**Figure 14D**). Similar corrosion mechanism was proposed by Coy et al. (2010) using scanning Kelvin probe force microscopy (SKPFM) for ZE41 and WE43 alloys. They found a preferential attack of the matrix adjacent to the T-phase, after some time, Zr-rich interactions zones, including regions and intermetallic phases become the next favorable sites for corrosion in ZE41 alloy. For WE43 alloy using SKPFM evaluations a relatively higher Volta potential difference between the Mg matrix and Zr-rich precipitates was observed, which promotes localized galvanic

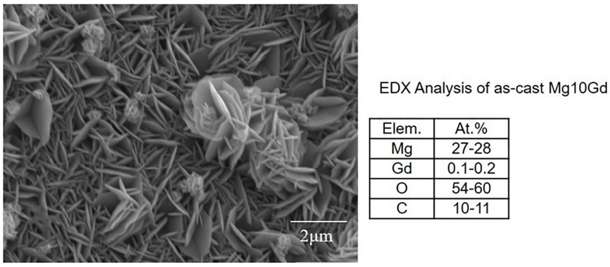

EDX Analysis of as-cast Mg10Gd

Elem.	At.%
Mg	27-28
Gd	0.1-0.2
O	54-60
C	10-11

FIGURE 15 | Surface morphology of pure as-cast Mg-10Gd and EDX analysis of the oxide layer after exposure in 0.5% NaCl solution.

attack at the adjacent areas to the cathodic micro-constituent phases. In that way the severity of the galvanic attack is related to the effectiveness of each micro-constituent as cathode (Coy et al., 2010).

In the present study, focused on Mg-10Gd modified by different heat treatments, the initiation and progress of the corrosion process was only monitoring by SEM and it was revealed that the galvanic corrosion mainly depends on the amount and distribution of the cathodic phases. In summary, a low amount of cathodic phases (GdH_2 and impurities) without Gd enrichment zones are detrimental for corrosion resistance (in solution treated condition, **Figure 14E**), while the combination of large amount of Mg_5Gd uniformly distributed and Gd enrichment zones enhance the corrosion behavior of this alloy. There is no negative influence of the grain boundaries as proposed in Coy et al. (2010) if Gd is presented. Altogether the situation is relatively complex with more noble but less chemically stable intermetallic phase in the Mg matrix and depending on the situation not only matrix dissolution and particle undermining/detachment can be observed but also dissolution of the intermetallics if not enough protecting current can be provided by the dissolving matrix. Latter is strongly influenced by the microstructure of the specimens.

It is important to notice that fine precipitates causes a more uniform attack and they have less negative effects on passive film formation. The EIS spectra corroborate the presence of an oxide layer at high frequencies. For as-cast specimen, this protective layer was only stable up to the first 60 min of immersion. The protective layer showed relatively better stability and protection after all heat treatments, but only at 200°C and 300°C, stable films can develop during immersion in chloride solutions. However, the layer formed after heat treatment at 200°C showed a C_{Oxi} of around $3–4 \times 10^{-5}$ Ω-^{1}cm^{-2}s^{n} and in the sample aged at 300°C it was $8–9 \times 10^{-6}$ Ω^{-1}cm^{-2}s^{n}. Thus, the thin protective film is thicker on the 300°C specimen, which correlates also with the overall higher resistance values. The resistance may increase not only due to increased thickness but also the layer can be more protective with the time (denser, less porous). The same is true for the heat treated at 200°C specimens, but the layer remains less protective. For solution treated and heat treated at 400°C specimens, the film is not stable. It partially dissolves or breakdown occurs and the resistance is much lower compared to the other aged specimens. This behavior also confirms the tendency observed in the hydrogen evolution and weight loss measurements. Thus, the long-term corrosion behavior is governed by the passive film formation during immersion and breakdown (Silva Campos, 2016).

CONCLUSION

The higher solid solution solubility of Gd in α-Mg matrix allows tailoring the corrosion resistance of Mg-10Gd alloy. The relatively good corrosion behavior in as-cast condition is due to formation of Gd enrichment zones, which reduce the local damage due to galvanic corrosion between the Mg_5Gd phase other noble phases (e.g., GdH_2) and α-Mg matrix.

Among the different heat treatments, the alloy shows a better corrosion resistance when the intermetallic phases are fine and/or uniformly distributed within the specimens. Galvanic corrosion depends on the amount and the distribution of the cathodic phases, small amount of larger Mg_5Gd precipitates without Gd enrichment zones is detrimental for corrosion resistance, while the combination of large amount of fine Mg_5Gd precipitates uniformly distributed in a Gd enriched matrix enhance the corrosion behavior of this alloy.

The preferential attack of the matrix adjacent to small intermetallic particles promote a uniform surface without potential differences as soon as they are detached from the matrix. Alternatively, they can be covered more easily by a growing protective film. The hydroxide films have low conductivity thus they are inhibiting the water reduction reaction on the particles by reducing the exchange current.

Protective film formation is more uniform on the heat treated alloy; because the microstructure is more uniform and the larger amount of alloying elements in solid solution are ready for oxide/hydroxide formation.

DATA AVAILABILITY STATEMENT

All datasets generated for this study are included in the article/**Supplementary Material**.

AUTHOR CONTRIBUTIONS

MS and CB conceived and designed the study. MS, CM, TZ, and DP performed the experiments. CB, TZ, DP, and MZ contributed the reagents, materials, and analysis tools. MS, CB, CM, MM, TZ, DP, and MZ analyzed and discussed the data. MS wrote the manuscript. CB, CM, MM, TZ, DP, MZ, and KK reviewed and edited the manuscript. All authors read and approved the manuscript.

FUNDING

The financial support from the CONACyT-DAAD 176552/304358-A/08/72584 for Mrs. Silva Campos's fellowship in

Helmholtz-Zentrum Geesthacht is acknowledged. M. Mohedano is grateful to MICINN (Spain) RYC-2017-21843.

ACKNOWLEDGMENTS

The authors are grateful to Mr. W. Punessen and Mr. G. Meister for the preparation of alloys, Mr. G. Wiese, Mr. V. Heitmann, and Mr. V. Kree for SEM investigations, Mr. U. Burmester for the technical support. Partial results of the presented work are based on the Ph.D. thesis of Mrs. Silva Campos http://tubdok.tub.tuhh.de/handle/11420/1321.

SUPPLEMENTARY MATERIAL

The Supplementary Material for this article can be found online at: https://www.frontiersin.org/articles/10.3389/fmats.2020.00084/full#supplementary-material

REFERENCES

Ambat, R., Aung, N. N., and Zhou, W. (2000). Studies on the influence of chloride ion and pH on the corrosion and electrochemical behaviour of AZ91D magnesium alloy. *J. Appl. Electrochem.* 30, 865–874.

Apps, P. J., Karimzadeh, H., King, J. F., and Lorimer, G. W. (2003a). Phase compositions in magnesium-rare earth alloys containing yttrium, gadolinium or dysprosium. *Scripta Mater.* 48, 475–481. doi: 10.1016/s1359-6462(02)00509-2

Apps, P. J., Karimzadeh, H., King, J. F., and Lorimer, G. W. (2003b). Precipitation reactions in Magnesium-rare earth alloys containing Yttrium. Gadolinium or Dysprosium. *Scripta Mater.* 48, 1023–1028. doi: 10.1016/s1359-6462(02)00596-1

Arrabal, R., Matykina, E., Pardo, A., Merino, M. C., Paucar, K., Mohedano, M., et al. (2012a). Corrosion behaviour of AZ91D and AM50 magnesium alloys with Nd and Gd additions in humid environments. *Corrosion Sci.* 55, 351–362. doi: 10.1016/j.corsci.2011.10.038

Arrabal, R., Pardo, A., Merino, M., Paucar, K., Mohedano, M., Casajus, P., et al. (2012b). Influence of Gd on the corrosion behavior of AM50 and AZ91D magnesium alloys. *Corrosion* 68, 398–410. doi: 10.5006/0010-9312-68.5.398

Arrabal, R., Pardo, A., Merino, M. C., Mohedano, M., Casajús, P., Paucar, K., et al. (2011). Oxidation Behavior of AZ91D Magnesium Alloy Containing Nd or Gd. *Oxidation Metals* 76, 433–450. doi: 10.1007/s11085-011-9265-3

Bala, H., Szymura, S., Pawłowska, G., and Rabinovich, Y. M. (1993). Effect of impurities on the corrosion behaviour of neodymium. *J. Appl. Electrochem.* 23, 1017–1024. doi: 10.1007/bf00266123

Ben-Hamu, G., Eliezer, D., and Shin, K. (2007). The role of Si and Ca on new wrought Mg–Zn–Mn based alloy. *Mater. Sci. Eng.* 447, 35–43. doi: 10.1016/j.msea.2006.10.059

Birbilis, N., Easton, M. A., Sudholz, A. D., Zhu, S. M., and Gibson, M. A. (2009). On the corrosion of binary magnesium-rare earth alloys. *Corrosion Sci.* 51, 683–689. doi: 10.1016/j.corsci.2008.12.012

Carlson, B. E., and Jones, J. W. (1993). "The metallurgical aspects of the corrosion behaviour of cast Mg-Al alloys," in *Proceedings of the International Symposium on Light Metals Processings and Applications*, Quebec City, 833–847.

Coy, A. E., Viejo, F., Skeldon, P., and Thompson, G. (2010). Susceptibility of rare-earth-magnesium alloys to micro-galvanic corrosion. *Corrosion Sci.* 52, 3896–3906. doi: 10.1016/j.jmbbm.2016.11.014

Emley, E. F. (1966). *Principles of Magnesium Technology*. Oxford: Pergamon Press Ltd.

Froats, A., Aune, T. K. R., Hawke, D., Unsworth, W., and Hillis, J. E. (1987). Corrosion of magnesium and magnesium alloys. *ASM Handb.* 13, 740–754.

Gandel, D., Birbilis, N., Easton, M., and Gibson, M. (2010). "Influence of manganese, zirconium and iron on the corrosion of magnesium," in *Proceedings of Corrosion & Prevention* (Preston, VIC: Australasian Corrosion Association), 875–885.

Gao, X., He, S., Zeng, X., Peng, L., Ding, W., and Nie, J. (2006). Microstructure evolution in a Mg–15Gd–0.5 Zr (wt.%) alloy during isothermal aging at 250 C. *Mater. Sci. Eng.* 431, 322–327. doi: 10.1016/j.msea.2006.06.018

Habashi, F. (2008). *Alloys: Preparation, Properties, Applications*. Hoboken, NJ: Wiley.

Hanawalt, J. D., Nelson, C. E., and Peloubet, J. A. (1942). Corrosion studies of magnesium and its alloys. *Am. Inst. Mining Metall. Eng.* 147, 273–299.

Hillis, J. E. (1998). *The Effects of Heavy Metal Contamination on Magnesium Corrosion Performance*. Warrendale, PA: SAE.

Hort, N., Huang, Y., Fechner, D., Störmer, M., Blawert, C., Witte, F., et al. (2010). Magnesium alloys as implant materials–Principles of property design for Mg–RE alloys. *Acta Biomater.* 6, 1714–1725. doi: 10.1016/j.actbio.2009.09.010

Hu, H., Nie, X., and Ma, Y. (2014). "Corrosion and surface treatment of magnesium alloys," in *Magnesium Alloys - Properties in Solid and Liquid States*, ed. F. Czerwinski (London: IntechOpen), 67–109.

Huang, Y., Yang, L., Wang, Z., Kainer, K. U., and Hort, N. (2013). "Influences of Dy content and heat treatments on the formation of hydrides in Mg-Dy alloys," in *Proceedings of the 3rd International Conference of Engineering Against Failure (ICEAF III)*, Kos.

Huang, Y., Yang, L., You, S., Gan, W., Kainer, K. U., and Hort, N. (2016). Unexpected formation of hydrides in heavy rare earth containing magnesium alloys. *J. Magn. Alloys* 4, 173–180. doi: 10.1016/j.jma.2016.08.002

Kainer, K. U., Bala Srinivasan, P., Blawert, C., and Dietzel, W. (2010). "3.09 - corrosion of magnesium and its alloys," in *Shreir's Corrosion*, eds B. Cottis, M. Graham, R. Lindsay, S. Lyon, T. Richardson, D. Scantlebury, et al. (Oxford: Elsevier), 2011–2041.

Kainer, K. U., Hort, N., Willumeit, R., and Feyerabend, F. (2009). "Magnesium alloys for the design of medical implants," in *Proceedings of the 18th International Symposium on Processing and Fabrication of Advanced Materials*, eds M. Morinaga, M. Niinomi, M. Nakai, N. Bhatnagar, and T. S. Srivatsan Sendai, 975–984.

Li, H.-Z., Liu, H.-T., Guo, F.-F., Wang, H.-J., Liang, X.-P., and Liu, C.-M. (2011). Effect of ageing time on corrosion behavior of Mg-10Gd-4.8*Y*-0.6Zr extruded-alloy. *Trans. Nonferrous Metals Soc. China* 21, 1498–1505. doi: 10.1016/s1003-6326(11)60887-x

Liu, M., Schmutz, P., Uggowitzer, P. J., Song, G., and Atrens, A. (2010). The influence of yttrium (Y) on the corrosion of Mg–Y binary alloys. *Corrosion Sci.* 52, 3687–3701. doi: 10.1016/j.corsci.2010.07.019

Liu, W., Cao, F., Zhong, L., Zheng, L., Jia, B., Zhang, Z., et al. (2009). Influence of rare earth element Ce and La addition on corrosion behavior of AZ91 magnesium alloy. *Mater. Corrosion* 60, 795–803. doi: 10.1002/maco.200805179

Makar, G. L., and Kruger, J. (1990). Corrosion studies of rapidly solidified magnesium alloys. *J. Electrochem. Soc.* 137, 414–421.

Makar, G. L., and Kruger, J. (1993). Corrosion of magnesium. *Int. Mater. Rev*. 38, 138–153.

Meza-García, E. (2010). *Influence of Alloying Elements on the Microstructure and Mechanical Properties of Extruded Mg-Zn Based Alloys*. Dissertation PhD thesis, Technische Universität Berlin, Berlin.

Mohedano, M., Arrabal, R., Pardo, A., Paucar, K., Merino, M. C., Matykina, E., et al. (2014). Galvanic corrosion of rare earth modified AM50 and AZ91D magnesium alloys coupled to steel and aluminium alloys. *Rev. Metal.* 50:e002. doi: 10.3989/revmetalm.002

Morales, E. D., Ghali, E., Hort, N., Dietzel, W., and Kainer, K. U. (2003). Corrosion behaviour of magnesium alloys with RE additions in sodium chloride solutions. *Mater. Sci. Forum* 41, 867–872. doi: 10.4028/www.scientific.net/msf.419-422.867

NACE (1974). *Localized Corrosion1974*. Houston, TX: NACE.

Nayyeri, M. J., and Khomamizadeh, F. (2011). Effect of RE elements on the microstructural evolution of as cast and SIMA processed Mg–4Al alloy. *J. Alloys Compounds* 509, 1567–1572. doi: 10.1016/j.jallcom.2010.10.147

Nishijima, M., and Hiraga, K. (2007). Structural changes of precipitates in an Mg-5 at% Gd alloy studied by transmission electron microscopy. *Mater. Trans.* 48, 10–15. doi: 10.2320/matertrans.48.10

Peng, Q., Huang, Y., Meng, J., Li, Y., and Kainer, K. U. (2011). Strain induced GdH2 precipitate in Mg–Gd based alloys. *Intermetallics* 19, 382–389. doi: 10.1016/j.intermet.2010.11.001

Pourbaix, M. (1974). *Atlas of Electrochemical Equilibria in Aqueous Solutions*. Houston, TX: National Association of Corrosion Engineers.

Reichek, K. N., Clark, K. J., Hillis, J. E., and Engineers, S. O. A. (1985). *Controlling the Salt Water Corrosion Performance of Magnesium AZ91 Alloy*. Warrendale, PA: SAE.

Rokhlin, L. L. (2003). *Magnesium Alloys Containing Rare Earth Metals: Structure and Properties*. Abignton: Taylor & Francis.

Rosalbino, F., Angelini, E., De Negri, S., Saccone, A., and Delfino, S. (2006). Electrochemical behaviour assessment of novel Mg-rich Mg–Al–RE alloys (RE=Ce. Er). *Intermetallics* 14, 1487–1492. doi: 10.1016/j.intermet.2006.01.056

Shi, Z., Cao, F., Song, G.-L., Liu, M., and Atrens, A. (2013). Corrosion behaviour in salt spray and in 3.5% NaCl solution saturated with Mg(OH)2 of as-cast and solution heat-treated binary Mg–RE alloys: RE=Ce, La, Nd, Y, Gd. *Corrosion Sci.* 76, 98–118. doi: 10.1016/j.corsci.2013.06.032

Silva Campos, M. D. R., Scharnagl, N., Blawert, C., and Kainer, K. U. (2013). "Improving corrosion resistance of Mg10Gd alloy," in *Materials Science Forum*, ed. Y. Zhao (Switzerland: Trans Tech Publication), 673–677. doi: 10.4028/www.scientific.net/msf.765.673

Silva Campos, R. (2016). *The role of Intermetallics Phases in the Corrosion of Magnesium-Rare Earth Alloys*. Dissertation PhD thesis, Hamburg University of Technology (TUHH), Hamburg HH. doi: 10.15480/882.1318

Silva Campos, R., Höche, D., Blawert, C., and Kainer, K. U. (2011). "Influence of lanthanum concentration on the corrosion behaviour of binary Mg-La alloys," in *Magnesium Technology*, ed. H. E. Friedrich (Hoboken, NJ: John Wiley & Sons, Inc), 507–511. doi: 10.1002/9781118062029.ch94

Song, G., and Atrens, A. (2003). Understanding magnesium corrosion—a framework for improved alloy performance. *Adv. Eng. Mater.* 5, 837–858. doi: 10.1002/adem.200310405

Song, G., Atrens, A., John, D. S., Wu, X., and Nairn, J. (1997a). The anodic dissolution of magnesium in chloride and sulphate solutions. *Corrosion Sci.* 39, 1981–2004. doi: 10.1016/s0010-938x(97)00090-5

Song, G., Atrens, A., Stjohn, D., Nairn, J., and Li, Y. (1997b). The electrochemical corrosion of pure magnesium in 1 N NaCl. *Corrosion Sci.* 39, 855–875. doi: 10.1016/s0010-938x(96)00172-2

Song, G. L., and Atrens, A. (1999). Corrosion mechanisms of magnesium alloys. *Adv. Eng. Mater.* 1, 11–33.

Sudholz, A. D., Gusieva, K., Chen, X. B., Muddle, B. C., Gibson, M. A., and Birbilis, N. (2011). Electrochemical behaviour and corrosion of Mg–Y alloys. *Corrosion Sci.* 53, 2277–2282. doi: 10.1016/j.corsci.2011.03.010

Takenaka, T., Ono, T., Narazaki, Y., Naka, Y., and Kawakami, M. (2007). Improvement of corrosion resistance of magnesium metal by rare earth elements. *Electrochim. Acta* 53, 117–121. doi: 10.1016/j.jmbbm.2011.12.011

Tie, D., Feyerabend, F., Hort, N., Hoeche, D., Kainer, K. U., Willumeit, R., et al. (2014). In vitro mechanical and corrosion properties of biodegradable Mg–Ag alloys. *Mater. Corrosion* 65, 569–576. doi: 10.1002/maco.201206903

Unsworth, W. (1989). The role of rare earth elements in the development of magnesium base alloys. *Int. J. Mater. Product Technol.* 4, 359–378.

Victoria-Hernandez, J., Hernandez-Silva, D., Bohlen, J., Yi, S. B., and Letzig, D. (2013). Low temperature superplasticity of hydrostatically extruded Mg-Al-Zn alloys. *Mater. Sci. Forum* 735, 307–315. doi: 10.4028/www.scientific.net/msf.735.307

Vostrý, P., Smola, B., Stulíková, I., Von Buch, F., and Mordike, B. L. (1999). Microstructure evolution in isochronally heat treated Mg–Gd alloys. *Phys. Status Sol.* 175, 491–500. doi: 10.1002/(sici)1521-396x(199910)175:2<491::aid-pssa491>3.0.co;2-f

Zucchi, F., Grassi, V., Frignani, A., Monticelli, C., and Trabanelli, G. (2005). Electrochemical behaviour of a magnesium alloy containing rare earth elements. *J. Appl. Electrochem.* 36, 195–204. doi: 10.1007/s10800-005-9053-3

Conflict of Interest: The authors declare that the research was conducted in the absence of any commercial or financial relationships that could be construed as a potential conflict of interest.

frontiers
in Materials

REVIEW
published: 17 August 2020
doi: 10.3389/fmats.2020.00198

A Review on Developments in Magnesium Alloys

*A. Arslan Kaya**

Department of Metallurgy and Materials Science and Engineering, Faculty of Engineering, Mugla Sitki Kocman University, Muğla, Turkey

In order to facilitate the understanding of the current research efforts and directions, this article first introduces the anomalous/problematic features of magnesium (Mg) and presents the recent approach of stacking fault energy (SFE)–based alloying element selection to lessen or eliminate this problem. Stacking fault energy computations *via ab initio* techniques necessitate an understanding of the free electron density distribution around atoms in a solid solution. Therefore, the assessment of the role of atoms by also considering the possibility of short range order (SRO) formation rather than a random solid solution has been revisited. Two possible types of SRO have been indicated. The relevant electronic interactions between the host Mg and the alloying element atoms are more clearly incorporated in a generally less known model by Miedema based on atomic-level thermodynamics rather than in Hume–Rothery rules. This more successful approach has also been addressed here. An evaluation founded on these premises, introducing the relatively more recent Mg alloy systems, has been given in terms of their achievements toward healing the problematic features of Mg alloys. The spectrum of alloy systems discussed ranges from doping of Mg to dilute alloy systems and to some rich alloy systems that offer remarkable properties. Among the first category, an unorthodox addition, doping with oxygen, and its implications, has been presented. The dilute alloy systems and their compositional design based on SRO and SFE together with their potentials have been reviewed. Among the rich alloy compositions, the most interesting precipitate systems, that is, the ones involving order and intermetallic formations, long-period stacking order phases, and quasi-crystals, have been discussed. Among all the alloying elements, one that deserves particular attention, calcium, with its implications such as being economical, offering environmentally friendly Mg metallurgy, and remedial effects on the shortcomings of engineering properties, and a closely related issue of calcium oxide (CaO) addition have been scrutinized. This article also makes an attempt to point out the future directions throughout the text, whenever possible.

Keywords: magnesium alloys, doping of magnesium, dilute alloys, short range order, LPSO phases, rare earth alloys, RE-free magnesium alloys

Edited by:
Hajo Dieringa,
Helmholtz Centre for Materials and Coastal Research (HZG), Germany

Reviewed by:
Mark A. Easton,
RMIT University, Australia
Ashok Kumar Mondal,
Indian Institute of Technology (BHU), India
Uma Thanu Subramonia Pillai,
Council of Scientific and Industrial Research (CSIR), India

***Correspondence:**
A. Arslan Kaya
aakaya@mu.edu.tr

Specialty section:
This article was submitted to Structural Materials, a section of the journal Frontiers in Materials

Received: *02 August 2019*
Accepted: *26 May 2020*
Published: *17 August 2020*

Citation:
Kaya AA (2020) A Review on Developments in Magnesium Alloys. Front. Mater. 7:198. doi: 10.3389/fmats.2020.00198

INTRODUCTION

Several complementary reviews to the one presented here can be found in the literature. A very detailed and fascinating history of magnesium (Mg) production and its use have been presented by Witte (2015). Elegant reviews by Nie (2012) and Pekguleryuz (2013), covering the spectrum of Mg alloys up to the beginning of this decade, and the thought-provoking strong criticism by

Abaspour and Cáceres (2015) on the conventional interpretation of solid solutions of Mg as random solutions are strongly recommended to the readers.

As Witte (2015) mentioned, the earliest use of Mg was for applications, such as ignition and photography flashes. Interestingly, its application as biomaterial also reaches as far back as 1878. Then, we see a large-scale use of Mg alloys in aviation prior to and during World War II for purely military purposes. During those years, only in the United States the production capacity would make up about a quarter of today's world production capacity of 950,000 tons (Albright et al., 2002; Pekguleryuz et al., 2002). The earlier association of the term "electron" with Mg alloys was said to be perhaps due to its bright white light when burning or as a tribute to the ancient alchemical term *electrum* (Witte, 2015). Although, this term actually originated from the geologically occurring gold and silver (Ag) alloys that were used for coinage by the inventors of money, the Lydians of the Aegean coast of Anatolia.

The review presented here does not claim to cover all aspects of alloy development efforts on Mg. For example, we will not attempt to include the consequences of alloying additions that are related to various processing methods so that the text remains within the permitted limits.

Expectations in alloying studies on Mg go beyond achieving superior engineering properties. Although such properties, if achieved, are certainly welcome, expansion of the use of Mg alloys necessitates at least lessening or, even better, remedying the anomalies/problematic attributes of Mg and its earlier commercial alloys. Without stating these issues on Mg, it would be difficult to appreciate the core aim of the efforts and the directions in the studies focusing on Mg alloys. Therefore, with the aim of serving a broader spectrum of readers, we will first introduce the problematic characteristics of Mg.

This article will next attempt to explain the current approach to recuperate those problematic properties of Mg through changing the stacking fault energy (SFE) of different planes of the hexagonal crystal. The very concept of SFE involves the changes in the free electron density distribution around atoms in solid. Thus, it also becomes necessary to evaluate how the solute atoms behave in changing this distribution in the Mg lattice. Therefore, we will, on the one hand, scrutinize the most recent approach in alloy development, that is, controlling the SFE *via* alloying element additions, and on the other hand, revisit a generally less known scheme of Miedema that assesses the atomic-level thermodynamic interactions in terms of electron exchange between different atoms of binary solid solutions using the electron gas model of atom. Based on the effects of alloying elements from these perspectives, the possibility of two different types of short range order (SRO) will be proposed here. We will then embark on reviewing some of the most outstanding Mg alloy systems. Although the atomic-level concepts of SFE or Miedema's model are introduced through binary systems, our review will extend beyond the binary systems into alloys that form long-period stacking order (LPSO) phases or quasi-crystals. This is so, mainly because these alloy systems appear to be the most successful ones in terms of their properties, and those concepts cannot be ignored for them. However, it should be emphasized that our purpose is neither to take on the task of implementation of those atomic-level concepts to multicomponent alloys, nor to present all the experimental alloy systems given in the literature in a comparative manner. Needless to say, some remedial contributions to change the problematic properties of Mg can be and have been sought through various processing routes as well. However, we will not shift the attention out of the fundamental solution, that is, alloying.

REVISITING THE FUNDAMENTAL CHARACTERISTICS OF MAGNESIUM

Magnesium is the lightest structural metal. Magnesium and its earlier commercial alloys (e.g., AZ or AM series) have more than few shortcomings that generally manifest themselves together in some combinations. Some of these properties are simply inferior properties as compared to those of aluminum alloys and steels. In this respect, it suffices to recall the low elastic modulus, yield strength, and deformation capacity; sluggish and poor aging response; and inferior creep and corrosion resistance. These constitute engineering properties that may be tackled with, at least to some degree, and with a penalty of reduced final weight saving in application, through part design. Yet, some other properties may be seen as anomalies that require in-depth understanding before seeking remedies through alloying. Those may be briefly named as the tensile/compression asymmetry, pseudoelastic behavior, deformation texture, and inefficiency of recrystallization in removing it, and peculiarities in fatigue behavior.

The slip and twinning systems in Mg are shown in **Figure 1**. Perhaps the first anomaly of Mg may be pointed out as its incompatibility with von Misses criterion due to lack of five independent slip systems. Magnesium circumvents this criterion due to twinning that operates concomitantly with the basal slip at room temperature and thus shows, although limited, some plastic deformation capacity. The other slip planes of Mg, that is, prismatic and pyramidal planes, operate sequentially, becoming active over 225°C.

Concomitant activation of twinning with slip brings about an anomaly of Mg single crystal. Magnesium displays yield strength asymmetry in compression and tensile modes (a critical assessment given in Barnett et al., 2006), the tensile yield strength being much higher than that in compression. Both the room temperature twinning and the yield asymmetry are related to the polar nature of twinning and the critical resolved shear stress (CRSS) values of different twinning planes (Agnew, 2012). It should be noted that the terminology used for the two twinning modes may be somewhat misleading. The tensile (extension) twinning simply is the one that extends an Mg single crystal along its *c*-axis, while compression twinning shortens. The low CRSS value of what is known as extension (tensile) twinning and the CRSS difference between the two twinning modes and their different Schmid factors (*m*) (Nan et al., 2012; Kim and Park, 2018) are telling why the former predominates (CRSS ratio for basal <a> slip, $\{10\bar{1}2\}$ extension twinning, prismatic <a> and pyramidal <c+a> slip: 1:0.7:2:15) (Barnett et al., 2006). The

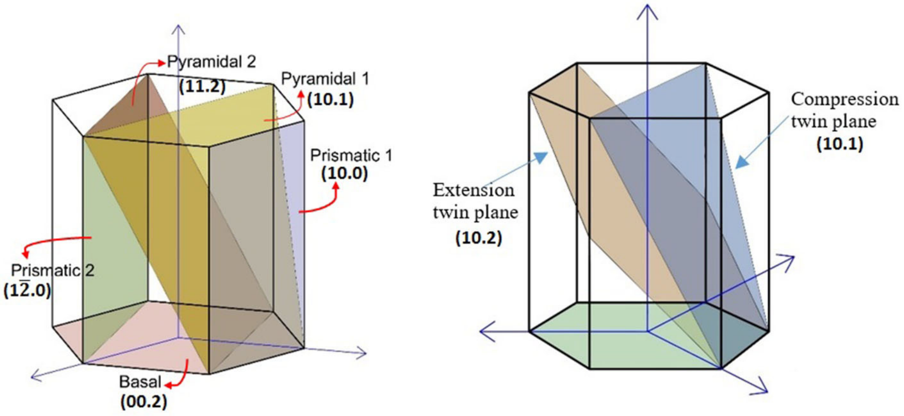

FIGURE 1 | Slip and twinning planes in magnesium crystal.

yield asymmetry of a single crystal, when coupled with texture, reveals itself once again in polycrystalline material, begetting an anisotropic material.

Twinning may appear to be a way to divide an existing α-Mg grain into several portions and create strengthening as in grain refinement. However, twinning cannot be activated in Mg when the grain size is well below 1μ (Wu et al., 2011; Zhu Y. T. et al., 2012). An additional consequence is that extensive basal slip followed by compression twinning can lead to strain softening as shown in experiments conducted on Mg micropillars (Yu et al., 2012). This is simply because the angular deviation created by compression twinning brings the basal planes, which has the highest Schmid factor, into a favorable orientation for further slip. Thus, twinning is also closely related to the crystallographic texture in deformed structures (Nie et al., 2013).

Twinning asserts itself once again and leads to pseudoelasticity. Upon reversing the stress direction, although not through an infinite number of cycles, detwinning creates what appears to be an elastic, that is, pseudoelastic, behavior. Because, at each cycle, the twinning is accompanied by slip in the same material, not all twins detwin together (Yu et al., 2011). Moreover, twinning is polarized (Christian and Mahajan, 1995), and twinning dislocations cannot behave in a military fashion with exact numbers during every reversal of the stress; thus, the pseudoelastic behavior peters out after some cycles (Wu et al., 2008; Brown et al., 2009; Yu et al., 2015).

Anomalies of Mg further extend into its fatigue behavior and complicated by twinning and detwinning (Yu et al., 2011), necessitating the interpretation of the stress- and strain-controlled fatigue tests separately (Sumitomo et al., 2003; Hasegawa et al., 2007; Mann et al., 2007). Because below a threshold grain size twinning ceases, such interpretations on fatigue should also consider the effect of grain size as well as the initial texture of the materials (Huppmann et al., 2011).

Deformation texture becomes particularly emphasized in Mg with a large contribution from its easy twinning. This leads to yet another anomaly in Mg. While texture can be lessened greatly or removed in other systems, once texture is created in Mg and many of its alloys, it becomes persistent even after the conventional remedial treatment of recrystallization. Cell formation during recovery stage does not happen, and consequently, newly forming "recrystallized" grains originate from the already textured parents, thus rendering the texture-removing function of recrystallization process futile. This feature is closely related to lack of dislocation populations on non-basal planes as well as to lower SFE of the basal plane, indicating that the remedial measure is also related to the SFE levels of different planes in Mg.

Critical resolved shear stress values for basal and prismatic planes of Mg show very different reduction rates with temperature, and non-monotonic changes for prismatic planes with temperature and alloy concentration in some systems, as well as anomalous changes with temperature in case of second-order pyramidal planes, have been reported (Akhtar and Teghtsoonian, 1969; Obara et al., 1973; Hosford, 1993; Christian and Mahajan, 1995; Balogh et al., 2009; Cipoletti et al., 2011). If we look at the room temperature values, CRSS ranges from 5 MPa for basal slip, 10 MPa for extension twinning (2.4 MPa in a report by Yu et al., 2011), 20 MPa for prismatic slip, 40 MPa for pyramidal slip, and 70–80 MPa (at 150°C) for compression twinning (Chapuis and Driver, 2011). Therefore, it should be remembered that, at the early stages of deformation, the tensile twins, because of lower CRSS value, are more likely to be observed rather than the compression twins. For details of twinning contribution to the total deformation, the reader should refer to the literature (Yoo, 1981; Brown et al., 2005).

Many studies relate the changes in CRSS values and/or in *c/a* ratio brought in by alloying additions. Indeed, *via* alloying, CRSS values can change through electronic effects (Masoumi et al., 2011), as well as by geometrically changing the *c/a* ratio of Mg crystal (Yoo, 1981; Yoo and Lee, 1991; Chen and Boyle, 2009; Wang et al., 2009). The changes in CRSS for different planes may not happen to the same extent (Kim et al., 2015) and depend on the changes incurred due to the alloying elements. Nor the changes in *c/a* ratio can simply be predetermined based on the atomic size differences of the constituent elements.

In a theoretical geometrical evaluation, *c/a* ratio undoubtedly alters the CRSS values of different slip planes as it changes the corresponding Schmid factors. Since the pioneering studies by Raynor (1959), it has come to be said that reduction in *c/a* ratio promotes non-basal slip activity in Mg. *c/a* ratio has been related to texture development as well (Styczynski et al., 2004). However, *c/a* ratio does not seem to be a factor fundamental enough to explain all the observed alloying effects in mechanical behavior in a consistent and a coherent manner. *c/a* ratio of Mg has been found to decrease for its extended solid solutions prepared *via* rapid solidification techniques for systems other than the binary Mg–gadolinium (Gd), Mg–yttrium (Y), and Mg–aluminum (Al) alloys (Hehmann et al., 1990). While modulus can change depending of *c/a* ratio, Chen and Boyle (2009) showed that the strength was not related to the modulus changes in Mg–X [X: Y, Al, zinc (Zn)]. Likewise, explanations on the ease of activation of different twinning modes based on *c/a* ratio changes in hexagonal close packed (HCP) metals, in general, are highly complex and sometimes even contradictory, creating a need to resort to the involvement of other additional mechanisms such as the ease of atomic shuffling or the ability of twin boundaries to act as sinks for dislocations (Yoo, 1981; Yoo and Lee, 1991; Wang et al., 2009). It is worth remembering that hcp titanium with a lower *c/a* ratio (c/a_{Mg}: 1.624 and c/a_{Ti} :1.58) has CRSS values lower for basal and higher for prismatic slip as compared to Mg (Raynor, 1959).

On the other hand, *ab initio* calculations do not treat CRSS values as a simple outcome of crystal geometry. The alloying effects go beyond changing the *c/a* ratio as the dislocation core structure and therefore its mobility and ability to dissociate and, in turn, to cross-slip drastically change with different solute atoms (Yasi et al., 2010; Ando et al., 2013; Liu and Li, 2015). For example, changes in *c/a* ratio can be attributed to atomic size changes, especially of Mg atoms, depending on the solute type. *Ab initio* computations by Chen and Boyle (2009) showed that *a* and *c* parameters and *c/a* reduce slightly in Mg–Zn, in which atomic volume of Mg and possibly of Zn also appeared to be reduced (as will be discussed further), whereas Y slightly increased the lattice volume by changing *a* and *c*, without changing the *c/a* ratio.

The sequential activities, based on different CRSS values and/or temperature, of different slip planes of Mg point out that some of these slip/twinning modes are "softer," whereas the others can be described as "hard." It then becomes obvious that the strategy to strengthen Mg or to increase its deformation capacity and even to lessen the propensity to generate deformation texture, as well as the ease of its removal through recrystallization, hinges on establishing the effects of alloying elements and their necessary quantities. If the differences in CRSS values are lessened, it would effectively mean either the "harder" modes becoming "softer" or *vice versa*. Another way of looking at "hard" and "soft" modes can be based on dislocation characteristics. For example, if thermal cross-slip is facilitated *via* increasing the SFE of the basal plane, and/or by lowering the SFE of nonbasal planes, a reduced anisotropy in deformation can be achieved (Moitra et al., 2014). If the prismatic and pyramidal slip systems, which do not contribute to deformation at room temperature, are activated, the former provides two and the latter five additional slip systems (Avedesian and Baker, 1999).

The relatively more recent efforts in resorting to the *ab initio* techniques together with the experimental studies focusing on dilute alloys stem from this perspective. The success of first-principles techniques (density functional theory, embedded atom model, molecular dynamics) in predicting the influences of alloying elements on dislocation behavior, and consequently on the overall mechanical behavior, lies in the fact that they allow consideration of a fundamental property, that is, free electron density distributions and the resulting bond strength and SFE changes.

In order to benefit more from the vast amount of literature involving *ab initio* techniques regarding the alloying, the reader should be well-versed on SFE and its influences on materials behavior. Therefore, it seems appropriate to remind ourselves the following:

CONCEPTS OF STACKING FAULTS AND STACKING FAULT ENERGY

It is well-known that, when stacking close packed layers of atoms to constitute an face centered cubic (FCC) or an HCP model, the difference arises by the positioning of only the third layer, thus ...ABCABCABC... stacking gives FCC, whereas ...ABABAB... stacking gives HCP. Thus, a mistake in these orders can convert one of these two crystals into the other locally. Such out-of-step stacking can be due to an extra atomic layer [named as "extrinsic stacking fault" (SF)] or, for example, because of condensation of vacancies, a missing layer ("intrinsic SF"). One can define a stacking disorder (SF) perpendicular to any crystal plane and in different directions in it, but for example, in prismatic plane of Mg, a stable SF cannot form as energetically prohibited (Uesugi et al., 2009).

If we make definitions based on the basal plane of Mg, the types of intrinsic SFs are two types, that is, the "growth type" and "deformation" types. The former is a missing layer with shear above it by $1/3[10\bar{1}0]$ (...ABABCBCB...– I_1 stacking), and the latter involving only shear by $1/3[10\bar{1}0]$ (...ABABCACACA...–I_2 stacking). Because SF involves a change in bond angles, a third type is also possible corresponding to stacking across a twin boundary (...ABABCBABABA...–*T* stacking) (Weinert, 1997). The order of increase in the energies of I_1, I_2 and extrinsic SF manifests itself in the same order in terms of the number of influenced planes neighboring the SF plane (Wang et al., 2012; Wang W. Y. et al., 2014). While I_2 SFE is directly representing an energy barrier to slip, attempt has been made also to correlate the seemingly unrelated I_1 SFE to deformation processes as will be discussed later.

Stacking fault energy, at the fundamental level, depends on the free electron density distribution, a property that changes inevitably with each alloying element, as their contribution to free electron density and/or the lattice distortion they introduce differs. Although a change in the stacking order does not change the coordination number of the atoms at and across the fault plane, at least the bond angles change. Hence, the fault plane, that is, SF, is a more energetic location compared to the planes located in the usual stacking order, in addition to being a plane where free electron density distribution in any direction from one atom to any of the neighboring atoms has also changed. An SF and its energy, as we will focus on later, not only stem from its atomic stacking configuration but also is fundamentally related to the atomic-level thermodynamics.

An SF is by definition bound by two partial dislocations, constituting a two-dimensional defect lying in between. The energy of a dislocation, being the sum of two terms, that is, the missing bond plus the strain energy due to the bent planes immediately neighboring the dislocation, also changes with SFE. Thus, dislocations on planes where SFE is low become more energetic, as the dislocation core size increases with decreasing SFE. Consequently, the ease of dissociation of a dislocation becomes closely related to SFE, getting more difficult as SFE increases, and *vice versa*. Hence, the prerequisite for creation of an SF is a low-enough SFE allowing dissociation of a full dislocation, relating the size of the SF area between the partials inversely to SFE.

These concepts, namely, the size of SF area and dislocation core size, change all of the mechanical responses of metals through changing the dislocation behavior. Stacking fault energy is related to the ease of birth, glide, cross-slip, and climb of dislocations. The sequential activation of the slip planes of Mg also manifests itself in the computed SFE values [$\mathrm{SFE}_{\mathrm{basal}} < 50$ mJ/m^2; $\mathrm{SFE}_{\mathrm{prismatic}} = 354$ mJ/m^2; $\mathrm{SFE}_{\mathrm{pyramidal}} = 452$ mJ/m^2 (Wen et al., 2009)]. These figures imply that cross-slip and climb for pyramidal slip operate more readily than those for other slip systems because of higher SFE levels (Li et al., 2013). Moreover, the initial glide of dislocations (Zhao et al., 2006), formation of twins, and movement of their boundaries (Bernstein and Tadmor, 2004; Van Swygenhoven et al., 2004) are all facilitated with lower SFEs, while climb gets slower, cross-slip restricted, and steady-state creep rate reduced (Li and Kong, 1989; Guo et al., 2006). It should also be noted that with larger core sizes, because of larger strain fields of dislocations, in a system of low SFE, while facilitating the movement of an individual dislocation, strain hardening becomes quicker, that is, dislocation movement rapidly becomes more difficult due to the larger core size of dislocations when their populations increase during deformation.

Thus, one would understand that SFE would also change whenever other players/factors are introduced. For example, if the fault plane (SF) involves foreign atoms, if near other crystal defects, when extrinsic factors such as temperature and strain are in play, we may expect SFE to change by some degree. However, all these are not to say that SFE is such an ambiguous parameter that can be ignored. On the contrary, one should remember that SFE is a relative term that can be used in a comparative way when different metals, alloys of a particular metal-base, or different planes of the same crystal are considered. Although there also exists a definition as generalized SFE (GSFE, γ surface), each crystallographic plane has, in essence, its own specific SFE value. Generalized SFEs should ideally be calculated by considering the lattice plane neighboring the SF on both sides, that is, the relaxation of the lattice perpendicular to the SF (Vitek, 1968; Yin et al., 2017). The extent of this relaxation is different when considering the SFE of different planes. Furthermore, GSFE values computed by assuming a random solid solution may contain a source of error [e.g., if SRO exists]. Thus, it becomes more useful to compare the individual SFE values of planes that are operative in slip or twinning. It should be emphasized that, in a low-symmetry system such as HCP Mg, SFE of individual crystal planes becomes more distinctive and must be considered specifically. On the other hand, GSFE values are more suitable for interpretations based on Peierls–Nabarro forces (Moitra et al., 2014).

The implications of SFE can be better interpreted through "energy change with respect to the unfaulted atomic stacking" vs. "displacement along a fault vector" plots based on *ab initio* calculations. These plots show an increase followed by a decrease over the full movement of the fault vector as shown schematically in **Figure 2**. More complex three-dimensional representations of lattice response to displacements, namely, GSFE surfaces (γ surface), are also available in the literature (Wen et al., 2009; Yasi et al., 2010; Zhang et al., 2013). In such a plot if a single curve appears, the maximum (γ_{USF}-unstable SF) (**Figure 2A**) represents the energy barrier for dislocation dissociation and implies that formation of SF is not possible. If the curve shows two maxima, the first one still shows the energy barrier for the formation of an SF, and the trough [γ_{SF}, also termed as γ_{IS} (intrinsic SF)] shows the energy of a stable SF. The second maximum in this case (**Figure 2B**) corresponds to the energy barrier for the formation of a twin. The minima in such plots, although very difficult, can be experimentally determined, while the maxima can be calculated only *via ab initio* techniques, which are also demanding tasks by any measure. The height of the peaks, that is, ratio of stable and unstable SFE levels ($\gamma_{\mathrm{SF}}/\gamma_{\mathrm{USF}}$) would indicate ease of slip, while twinning tendency diminishes as the ratio of the maxima of the two peaks ($\gamma_{\mathrm{UT}}/\gamma_{\mathrm{USF}}$) increases (Wang et al., 2011; Muzyk et al., 2012). Therefore, in order to reveal whether the birth of dislocations, dissociation into partials, or twinning is facilitated due to a particular alloying element, an evaluation of the changes in the ratios of $\gamma_{\mathrm{SF}}/\gamma_{\mathrm{USF}}$ and $\gamma_{\mathrm{UT}}/\gamma_{\mathrm{USF}}$ on specific crystallographic planes becomes critical. For example, Wen et al. (2009) showed that the unstable SFE for the prismatic plane $\{10\bar{1}10\}$ is one order of magnitude higher than the (0001) basal plane, which effectively points out that creation of <c+a> dislocations is difficult on prismatic planes. It was also shown that the γ_{USF} for the second-order prismatic plane $\{11\bar{2}0\}$ is one order of magnitude higher than the first-order prismatic plane $\{10\bar{1}0\}$.

As can be understood, developing alloys has reached to the point where assessment and adjustment of dislocation characteristics, and even phase stability in some other systems (e.g., new generation steels), in relation to SFE became imperative. In this regard, *ab initio* techniques have an exciting power in predicting the SFE changes for specific crystal planes and, in turn, all related changes for an alloy. It is obvious that ductility or strengthening considerations for Mg, in other words, adjusting the relative activities of "soft" and "hard" modes

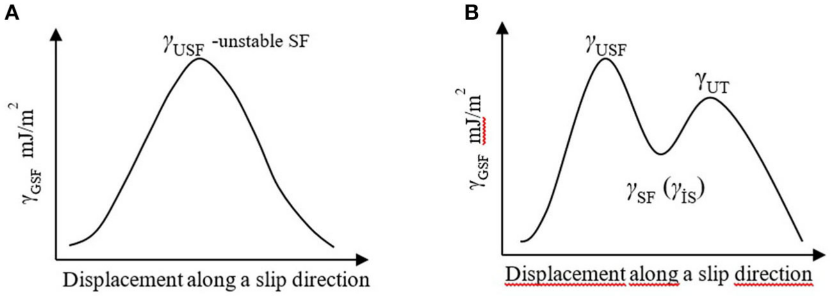

FIGURE 2 | Typical computed GSFE curves. **(A)** the maximum (γ_{USF}, unstable SF) represents the energy barrier for dislocation dissociation and implies that formation of SF is not possible; **(B)** if two maxima exist, the first one still shows the energy barrier for the formation of a stacking fault, which means dissociation of dislocation is possible, and the trough (γ_{SF}, also termed as γ_{IS}, -intrinsic SF-) shows the energy of a stable SF. The second maximum in this case corresponds to the energy barrier for the formation of a twin.

through alloying, has to involve the changes created in SFE(γ) and dislocation core properties as demonstrated in the literature (Yasi et al., 2010; Sandlöbes et al., 2011, 2012; Liu et al., 2017; Buey et al., 2018).

EFFECTS OF INDIVIDUAL ALLOYING ELEMENTS

Thermodynamic *Ab initio* Approach and *Ab initio* SFE Calculations

Because of the inherently low strength and ductility of Mg, solid solution strengthening may be regarded as the most important issue before considering the usefulness of all other strengthening mechanisms (Abaspour and Cáceres, 2015) as alloying element selection will influence all other strengthening mechanisms. Overwhelming majority of the literature is on substitutional alloying element additions, ranging in coverage from dilute systems to precipitate forming compositions. One example of much less explored area is Mg alloys containing interstitial elements, in which an interesting example now exists and will be discussed later. It is also interesting to note that those studies mostly consider the solid solutions as random solid solutions. The articles based on *ab initio* techniques, on the other hand, report the influence of alloying elements in solid solutions from the view of changing SFE values. The *ab initio* calculations, being highly important and informative, they are not exactly explaining interactions between the host and solute atoms based on atomic-level thermodynamics openly and clearly.

Therefore, we will make an attempt, by referring to the relevant literature, to point out that most of the solute elements do not form random solid solutions due to electronegativity differences, but instead they create what may be termed as *electronic effects* at the atomic level and consequently create SRO with strikingly different results. Thus, it can be argued that any calculation disregarding this concept and assuming random solid solutions would deviate, to some extent, from the reality.

The ultimate aim is to understand the behavior of each element and then expand this understanding toward designing multicomponent alloy systems. The fundamental approach attempting to explain the effects of individual elements in solid solutions has to be based on atomic-level thermodynamics. The theories on interatomic bond formations date back to Pauling (1960). Later, the geometrical method proposed by Miedema (1973a,b), Miedema et al. (1975) and Buey et al. (2018) following the work by Waber et al. (1963) showed better predictions for solubility or intermetallic formations.

These prediction methods were employing atomic-level thermodynamic parameters, for example, an electronegativity (equivalent to chemical potential) vs. atomic radius diagram (Waber et al., 1963), and chemical potential difference vs. electron density difference at the atomic Wigner–Seitz cell boundaries (Miedema, 1973a,c). As we will further discuss, the coordinates in these plots, for a host element of concern, indicate a specific area in the plot for a binary alloy, with great statistical correction over many binary systems, whether a solid solution and/or intermetallic compound is possible, and hence the term *geometrical method* is used.

On the other hand, the more recent approach in line with that of Miedema's, that is, *ab initio* techniques, so far based on relatively simple atomistic models and performed for 0 °K, has already proven invaluable in revealing the effects of alloying elements as a reference state. Some of such studies present the free electron density distributions (contour maps) around a foreign atom (Chen and Boyle, 2009; Wu et al., 2016) and also reveal the density of states (DOS) for electron orbitals involved in electron exchange (Chen and Boyle, 2009) and calculate the consequent SFE changes created (Sandlöbes et al., 2012, 2014; Zhang et al., 2013; Pei et al., 2015; Wu et al., 2016; Dong et al., 2018), including the influence of van der Waals forces (Ding et al., 2016) on SFEs in Mg. Moreover, some recent studies applied the same approach to dislocation–foreign atom (Yasi et al., 2010, 2011; Tsuru and Chrzan, 2015; Buey et al., 2018) or dislocation–dislocation (Fan et al., 2017) interactions with very interesting results.

It seems reasonable to say that the researchers have now a far better understanding on the effects of individual alloying elements as a result of *ab initio* approaches. The knowledge thus accumulated may be heralding the computer-based alloy design in some not-so-distant future. In conjunction with these efforts, experimental alloy systems started to emerge offering solutions to the shortcomings of Mg. The so-far accumulated knowledge, as Pei et al. (2015) named it, is already close to use a "theory-guided rapid alloy prototyping" approach.

Assessment of Solubility or Compound Formation

Thermodynamic assessment of solid solution hardening can be made more critically based on Miedema's model (Miedema, 1973a,b,c; Miedema et al., 1975) rather than on Hume–Rothery rules, as the former not only treats the electronegativity in physically less ambiguous way, but also takes the free electron density distribution around the atomic cells into account when calculating heat of formation. This treatment of free electron density distribution of the model also constitutes a central issue in the recent SFE calculations *via ab initio* techniques.

According to Miedema's model, when a solute atom is added (M-X binary), the system tries to smooth out free electron density distribution in the lattice at the atomic scale in addition to an electron charge transfer. The effect of the solute in these two terms is related to the electronegativity difference with the host and to the number of its valence electrons, that is, the chemical misfit. Moreover, in solid systems, additional energy terms are involved, that is, the misfit strains due to the size differences as well as the shear modulus misfit, thus making the assessment of solid state changes more complicated. Consequently, the bond energy, and in turn, SFE of a crystal plane, is also effected due to the presence of a solute. Computational techniques for solid state have been involving these concepts in calculating SFE values at atomic level with greater precision.

In the mathematical expression of Miedema, the formation enthalpy was expressed as follows:

$$\Delta H = f(c)[-Pe(\Delta\phi^*)^2 + Q(\Delta n_{WS})^2 - R]$$

(Miedema, 1973a,c)

where $f(c)$ is a function of concentration; P and Q are assumed to be constants; *e is* electronic charge; $\Delta\phi^*$ is the difference in chemical potential for electrons (equivalently the difference in electronegativity or difference between the work functions); and Δn_{WS} is the difference in the density of electrons at the boundary of the two atomic cells (i.e., Wigner–Seitz cells, which are subject to changes while atoms are changing positions from one equilibrium state to another, a point closely related to SFE; it should also be noted that Wigner–Seitz cell concept cannot be understood if one still assumes a spherical hard ball model for atoms).

The mathematical expression of the Miedema model was later modified in an empirical way for the atomic size factor (Zhang and Liu, 2002, 2005; Sun et al., 2011) and also extended to ternary systems as well (Dai et al., 2007). There may be more examples of its modifications in the literature beyond the knowledge of the author of this section.

Discrepancies in the geometrical predictions of the model when considering the case between transition and non-transition elements were attributed to a negative extra energy term R (explained to be due to hybridization of *d* and *p* orbital electrons). Unless a divalent non-transition metal is mixed with a strongly electronegative element, R was assumed to be negligible, that is, $R = 0$, for example, Mg, and a transition metal (Miedema, 1973a).

The heat of formation (ΔH) determines the nature of the binary mixture. Thus, it also dictates the general constitution of the binary phase diagram, indicating whether a random solid solution ($\Delta H = 0$), a system with limited solubilities without any formations of intermetallics ($+\Delta H$), or a system involving intermetallics (and small solubility), prevails ($-\Delta H$) (Miedema, 1973a,b,c). Let us remember that strongly electronegative metals are those with greater tendency to form negative ions, and the weakly electronegative ones are those with a greater propensity to form positive ions. It follows that as the difference in electronegativity between the constituent elements in a binary alloy increases, a greater tendency to form intermetallic compounds is observed, with an accompanying larger heat release, that is, more negative heat of formation. In such a case, formation of a solid solution is also suppressed. This assessment would also reflect itself in the phase diagram of the mixture, in which more than a single eutectic can be expected if formation of intermetallics is probable. As pointed out by Miedema (1973a), based on an earlier work of Brewr (1967); in the extreme case when the two metals have strong affinity to each other, the mixture, as in the case of Hf and Pt, can be explosive. Albeit, as emphasized by Miedema, the very concept of electronegativity is difficult to establish for metals.

As Equation (1) shows, the two intrinsic terms, namely, the electronegativities of the constituent elements (which is shown to be linearly related to the work function in the original Miedema model) and their contributions to the free electron density of the mixture, determine the enthalpy of formation. The term $\Delta\phi^*$, created through charge transfer between the two constituent elements, makes a negative contribution to the formation enthalpy of the mixture, thus reducing the total free energy of the system. The term Δn_{WS}, involves rearrangement of electron density distribution at the atomic cell boundaries (Wigner–Seitz) with the need to smooth it out. This phenomenon requires a complementary change in the Wigner–Seitz atomic cell sizes of both of the elements, therefore constituting a positive contribution term, that is, making the atoms of both elements more energetic as compared to their pure state. The most problematic issue then becomes the complication arising when also taking the size (radius) of the constituent atoms into consideration especially for systems involving the transition metals due to their compressibility levels. Possibility of the two terms, $\Delta\phi^*$ and Δn_{WS} being interdependent, was thought to be negligible and therefore ignored in the original model (Miedema, 1973a,c).

Thus, the arrived geometrical scheme is a plot of the $\Delta\phi^*$ vs. Δn_{WS}, grouping the binary systems generally into two, with a linear line having the slope of *P/Q*. Nearly all the binary systems in transition metals that have a negative enthalpy are located above this line, constituting intermetallic forming binaries, and those with positive enthalpy values remaining below the border line, representing those that cannot form compounds and show low mutual solubility. This geometrical scheme was further elaborated in the same article, taking into account the fact that

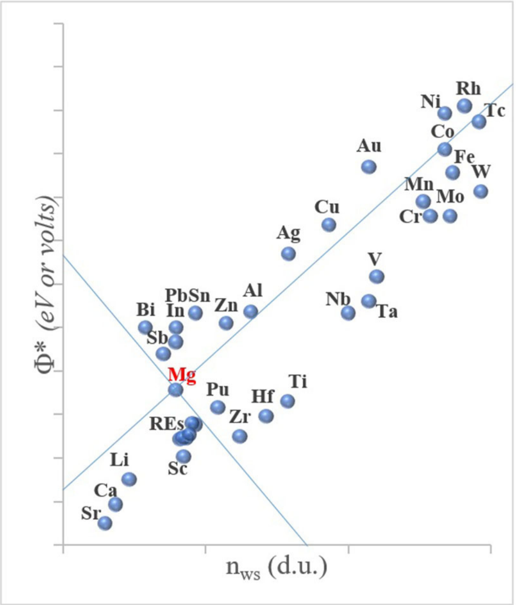

FIGURE 3 | A conceptual illustration of Φ^* (eV) the chemical potential for electrons (equivalently, electronegativity, or the work function) vs. n_{WS} (d.u., density unit) electron density at atomic cell (Wigner-Seitz) boundary (d.u., density units). The upper (north) and lower (south) sectors indicate the elements that can form intermetallics with Mg, and the left and right sectors involves the elements that do not (data adopted from the refs.: Miedema, 1973a; Abaspour and Cáceres, 2015).

such a border line can be drawn for a specific element (Mg being the one in the original article) twice by crossing each other, because the absolute values of $|\Delta\phi^*|$ and $|\Delta n_{WS}|$ (Equation 1) would mathematically necessitate it. By doing so, Miedema's scheme now presents four sectors in the ϕ^* vs. n_{WS} diagram, with the upper and lower sectors belonging to binary systems of Mg–X that would show negative enthalpy, and the left and right sectors to those with positive values. Thus, by indicating the position of any element with its own values of ϕ^* vs. n_{WS}, a crossover can be generated, which geometrically reveals a crucial information, that is, upper and lower sectors involving those elements that would form intermetallics with the reference element. The graph for Mg has been given as a conceptual plot in **Figure 3**; for quantitative information on each element in this figure, the reader should refer to Miedema (1973a) and Abaspour and Cáceres (2015).

Assessment of Solute Element Additions Based on Miedema's Scheme

The electronegativity differences between the solute and the solvent must have consequences at the atomic level and in terms of electron density distributions. Therefore, most binary systems should show some degree of resistance to form B–B bonds in a system of A–B, which may appear to be a simple solid solution on the respective phase diagram (i.e., considering the limited solubility regions at terminal sections of a phase diagram). This phenomenon was described as SRO in the early work by Cahn and Davies (1960), in which they also referred to the preceding studies of Houska and Averbach (1959) and Suzuki (1962). Short range order was also reported in earlier studies on binary Mg alloys, namely, in Mg–tin (Sn) (Henes and Gerold, 1962; van der Planken and Deruyttere, 1969), in Mg–(6.4 at%) Er and local order in Mg-(2.9 at.%) Gd (Gencheva et al., 1981), and in Mg–Zn (Akhtar and Teghtsoonian, 1969). Since then, a number of relatively recent studies on lean binary Mg alloys also focused on SRO (Blake and Cáceres, 2008; Abaspour and Caceres, 2013; Abaspour and Cáceres, 2015, 2016; Abaspour, 2014; Yang et al., 2014; Zhang et al., 2014). According to Abaspour and Caceres (2013), SRO was also claimed in previous studies (Henes and Gerold, 1962; Safranova et al., 1977) based on small-angle x-ray scattering. However, without refuting their claims, it should be borne in mind that Suzuki segregation (Suzuki, 1962) can also create similar x-ray scattering results. Many of the counter arguments on the effects of SRO were dismissed by Abaspour and Cáceres (2015). However, one that involves segregation of the solutes to dislocations does not seem to be easily dismissible. Serrated flow observed by these authors also testifies to this possibility, without going to the extreme example (Abaspour and Cáceres, 2015) of a Cottrell atmosphere.

Short range order can be viewed as a case where B–B bonds are not allowed in a binary A–B system. The phenomenon of temperature-independent flow stress in some Mg–X alloys, that is, "athermal component of solid solution strengthening," has been attributed to SRO (Akhtar and Teghtsoonian, 1969; Abaspour and Cáceres, 2015, 2016; Abaspour et al., 2016). In essence, the phenomenon is an extra strengthening mechanism that cannot be explained based on simple solid solution strengthening (van der Planken and Deruyttere, 1969). Therefore, the physical meaning of SRO requires in-depth analysis in terms of inter atomic effects. As the term implies, SRO is limited to each A–B–A (letters representing atoms, not atomic layers) sequence in an α-Mg grain and effectively constitutes stronger obstacles to dislocation motion as compared to a case where the solute atom is just a substitution in a random solid solution. Whether the interaction of such solute atoms in SRO with dislocations can be considered as a short-range or long-range interaction is debatable as it also depends on the concentration of the solute. However, such types of obstacles would be expected to be more resistant to relatively high temperatures unlike the short-range interactions of dislocations, that is, as for the dislocation–dislocation interactions, which can be overcome readily with temperature effects. Consequently, presence of SRO can become especially useful for Mg to overcome its shortcomings such as low strength and elasticity modulus and poor creep resistance. The contribution of SRO to strength with high resistance to changes in temperature was demonstrated *via* compression and stress relaxation tests conducted at various temperatures (Abaspour and Caceres, 2013; Abaspour, 2014; Abaspour et al., 2016) and *via* creep experiments (Abaspour and Cáceres, 2015).

The following experimental observations were reported by Abaspour et al. for Mg–X [X: Y, Gd, Ca, Zn, Sn, antimony (Sb), and Al] binary systems: an initial linear strengthening at constant temperature tests; for some alloys, an increasing strength at higher temperatures and little or no stress relaxations. Studies by Abaspour (2014) and Abaspour and Cáceres (2014, 2016) showed that temperature dependence of the strength of some Mg–X [X: Al, Zn, Sn, Y, Gd, neodymium (Nd)] alloys displayed an athermal regime at low strain levels up to some different temperature range and to varying levels. The same workers further claimed that there was even a strength increase within a temperature range in the case of Mg–X (X: Y, Gd, Nd) (see Figures 2, 3 in Abaspour and Cáceres, 2016). These observations, which cannot be explained based on an ordinary solid solution, were all attributed to SRO in those alloys (Abaspour and Cáceres, 2016; Abaspour et al., 2016). The potential of these alloying elements to develop SRO in Mg was given, based on Miedema's model, in the following order (Abaspour and Caceres, 2013; Abaspour and Cáceres, 2016; Abaspour et al., 2016):

> Y, Gd > Nd, calcium (Ca) > Zn, Ag, Sn > Al > Sb, strontium (Sr)… (Abaspour and Caceres, 2013; Abaspour and Cáceres, 2016)

This ranking given by Abaspour and Cáceres contradicts the implications of *ab initio* calculations of diffusion coefficients for the same binary systems:

> $D_{\mathrm{Mg-Ca}} > D_{\mathrm{Mg-Zn}} > D_{\mathrm{Mg-Sn}} > D_{\mathrm{Mg-Al}} \ldots$ (Ganeshan et al., 2011)

The apparent contradiction may be due to the assumption of "random solid solutions" employed by Ganeshan et al. (2011). However, the bond strength calculations by Chen and Boyle (2009) also contradict the experimental values given by Abaspour and Cáceres (2015) for Mg–Zn. It seems that the interpretation of SRO may not be straightforward in every case and requires more detailed insight using the available *ab initio* calculations.

Assessment of Interatomic Bonding in Solid Solutions of Mg—Two Types of SRO

Abaspour and Cáceres (2015) disagreed with the approach to explain the solid solution strengthening incurred by Y and Gd elements (the athermal strengthening effect) in Mg–X systems *via* a valence mechanism as proposed by Chen and Boyle (2009). However, their objection seems unwarranted. An *ab initio* study by Chen and Boyle (2009) on binary systems, namely, Mg–Al, Mg–Zn, and Mg–Y, and on Mg–Li (Jin et al., 2011), showed that the interatomic bonding possessed different characteristics depending on the planes and directions in pure Mg, as well as in these lean binary alloys.

Interestingly, pure Mg was found to have, although very weak, directionality in bonds within the basal plane and perpendicular to it, the latter being stronger. The DOS (local DOS) calculations of pure Mg is consistent with several other reports (Wang et al., 2007; Peng et al., 2008; Kumari and Verma, 2018). It was shown that such directionalities were also displayed in Mg–Y (Chen and Boyle, 2009) and Mg–Al (Chen and Boyle, 2009; Ganeshan et al., 2011; Jin et al., 2011) systems, the latter being weaker than the former but both being stronger than those in pure Mg to varying degrees (Chen and Boyle, 2009). It should be stated that Mg acts weakly electronegative in Mg–Y (Stanford et al., 2015) and forming hybridized bonds with Y. Likewise, although Mg behaves electropositively in Mg–Al system, the bonding is again only weakly hybridized as the DOS calculations for Al in Mg–Al showed a reduction only for its highest energy levels (Ganeshan et al., 2011).

Mg–Zn system, on the other hand, did not show directionality as also indicated in some studies (Ganeshan et al., 2011; Garg et al., 2018). Similar cases in Mg–Li (Jin et al., 2011) and in Mg–Ca (Ganeshan et al., 2011), that is, a general depletion around the solute atoms and a general homogenization in their electron densities for all energy levels, were computed for Mg–Li and Mg–Ca, where the electronegativity differences are opposite to that in Mg–Zn, that is, Mg acting electronegatively and Li and Ca acting electropositively. Moreover, Zn slightly reduced *a* and *c* parameters and *c/a* ratio, whereas Y, while slightly increasing the lattice volume by changing *a* and *c* did not alter *c/a* ratio. The former case effectively meant a reduction in atomic volume of Mg (and possibly for that of the solute atoms as discerned from their DOS calculations), and the latter, an increase (Chen and Boyle, 2009; Stanford et al., 2015).

The studies by Chen and Boyle (2009) and by Jin et al. (2011) further showed *via* computational methods that the bond strength in a solid solution dominated by the shared electrons (computed as bond order–BO–). When naming the bond types, they referred to the earlier definition by Bader (1990), who suggested that all bonding interactions fall into the following categories, as has been confirmed by the recent *ab initio* computations: (i) the shared-electron interaction, creating covalent (localized electron sharing) and metallic bonds (dilocalized electron sharing), and (ii) the closed shell interaction, leading to ionic as well as weak bonds.

An increasing BO was interpreted to mean an increasing strength through the series Mg–Zn, Mg–Al, and Mg–Y (Chen and Boyle, 2009). In Mg–Zn system, there appeared to be no covalent bond formation specific to the presence of Zn [likewise in Mg–Li (Jin et al., 2011)] as the electron localized function (ELF) maps (also known as charge density contour maps) indicated. Furthermore, DOS calculations pointed out that all electron densities (more in *p* orbital than that in *s*) around Mg atoms neighboring Zn reduced, in addition to the removal of the mild covalency within the basal plane of Mg (existed in pure Mg) around the Zn atom. However, the mild again covalency between Mg atoms in *z* direction remained unchanged. The DOS calculations for Zn in Mg–Zn (Ganeshan et al., 2011), Sn in Mg–Sn, and Li in Mg–Li also showed an overall reduction and homogenization for all energy states of the solute atoms, further indicating a possible size reduction in the atomic sizes of the solutes as well. Therefore, the atomic size reduction both for Mg and the solute atoms may be interpreted as the birth of an extra strain field around the Mg atoms surrounding each solute in these binary systems. This strain field would require consideration in addition to the one that would normally exist due to the size difference of Mg and solute atoms. This reduction in the atomic size of Mg was also pointed out by Chen and Boyle (2009). However, Chen and Boyle discerned this atomic size reduction indirectly and on the basis of crystal parameter changes, without relating to their own DOS calculations, which effectively showed the electron contribution from all orbitals of Mg in Mg–Zn. The proposed extra lattice straining due to large electronegativity difference between Mg and the solute atoms was also foreseen for the system of Mg–Sn in another study (van der Planken and Deruyttere, 1969), constituting another example of SRO without covalency (hybridization).

Regarding the Mg–Y system, Chen and Boyle (2009) showed that no significant DOS change occurred in *s* and *d* orbitals of Mg, whereas its *p* orbital showed some increase, which was interpreted as hybridization between Mg and Y atoms, involving *p* and *d* orbitals, respectively (the calculated DOS of *d* orbital of Y in Mg–Y being strikingly dominant), as well as stronger directionality in the bond structure. They further confirmed through Cauchy pressure evaluation that in one direction the value was negative, also indicating directionality in the bond strength.

The proposed two SRO mechanisms also comply with the expected SFE changes in two different cases. Zn should increase $I1_{SFE}$ due to reduced average atomic size (Pei et al., 2015), while Y showing an opposite trend, and indeed reported to be so (Sandlöbes et al., 2014). It may further be expected that the influence of hybridized bonds would not be uniform on the SEFs of different crystal planes, whereas the non-hybridized type would create more uniform changes, that is, either increase or decrease to similar extents. A critical evaluation of SFEs for elements representing two different SRO types showed that the expectation is largely fulfilled (Moitra et al., 2014; Shang et al., 2014; Zhang et al., 2014a; Dong et al., 2018). It seems that the implications of atomic size changes in terms of changes in *a*, *c*, and *c/a* ratio are also worth considering.

In one case, based on the DOS reductions in all orbitals of Mg and the consequent change in its atomic size, as in Mg–Zn and Mg–Sn, it may be interpreted that Mg behaved as a strong donor (more electropositive) as compared to the case of Mg in Mg–Y. Thus, in this SRO case, if the electronegativity difference is large enough between Mg and solute atoms, the charge transfer is stronger, leading to homogenization and an accompanying reduction in all DOS levels. Hence, the consequence is a reduction in atomic sizes, without resorting to hybridization. Such Wigner–Seitz atomic cell size changes were said to be large in Miedema's model (1973c). This can be envisaged to lead to an extra strain field (in addition to the atomic size difference of the solute) involving both the Mg and the solute atoms whenever they are neighbors and consequently additional strengthening as compared to the one expected from a random solid solution, whereas if hybridization of electron orbitals takes place, this extra strain field is absent or negligible. In this case, the SRO and accompanying strengthening are only due to the increased bond strength (covalency) between Mg and solute element.

Thus, it may be concluded that the strengthening mechanism of individual elements may depend on the way the electrons are shared. In both non-hybridized and hybridized cases, SRO forms. However, the degree of effectiveness in increasing strength differs, being stronger if hybridization exists. This view should also be taken to emphasize the importance of the purity of the alloys prepared for experimental comparisons (van der Planken and Deruyttere, 1969). In the case of Mg–Y, that is, hybridization, while increased covalency increases strength, the alloy may be expected to become more brittle according to the criteria (brittleness: $R_{G/B} > 0.5$) by Pugh (1954). However, Chen and Boyle (2009) showed that the strengthening effects in case of Al, Zn, and Y did not seem to be related to the changes in bulk moduli, and therefore despite the modulus-based criteria of Pugh, brittleness did not prevail in Mg–Y ($R_{G/B} > 0.605$).

To the best knowledge of the author, DOS calculations and ELF maps are unfortunately not available in the literature for all Mg–X binary systems to firmly conclude the presence or absence of covalency. The atomic size change is a complex phenomenon as it may be necessary to consider more than the immediate neighbors of the solute atom, in addition to the original atomic radii and concentrations. The DOS calculations and constructions of ELF maps seem indispensable for each binary system for a more complete understanding.

The phenomenon of SRO elegantly indicates the possibility for an approach to design alloy systems in a subtle and economical way. For example, α-Mg solid solutions containing only 1% addition of Y, rare earth (elements) (RE), or Ca were shown to be competitive in flow behavior with the traditional alloys, such as QE22 and ZE41, and be better than AE42 and AS21 (Abaspour and Cáceres, 2016). Abaspour and Cáceres, with reference to the studies by Zhang et al. (2014), pointed out the importance of SRO and, in turn, the selection of the alloying element, especially for cast structures showing inherent coring. The overall strength levels of such cast parts were said to dependent on the strength level of the weakest regions of what was described as percolated structures that were made up of weak solid solution regions (interiors of the cored grains) and interconnected strong grain boundary intermetallics.

When accounting for their observations, Abaspour and Cáceres (2015) disputed any role of the mechanisms, such as pinning of edge dislocations with mobile solute atoms, atomic size effect on the diffusivity, or dynamic precipitation of thermally stable precipitates. However, there exist atomic resolution imaging studies, explaining the temperature resistance of the strength on the basis of solute segregation (said to be driven by the need to reduce the twin boundary strain energy minimization) to mechanical twin boundaries in Mg–Gd, Mg–Gd–Zn (Nie et al., 2019), Mg–Y (Somekawa et al., 2017), Mg–Ca, and Mg–Zn (Somekawa et al., 2014) systems. Such solute segregations themselves were shown to be ordered along the twin boundaries and to have occurred in short annealing times. If one treats the coherent twin boundary planes as SFs, a justifiable likeness as only the bond angles change across the plane, then this segregation may be regarded as Suzuki segregation. There has been suggestions in the literature to use this type of segregation as an alloy design criterion based on *ab initio* calculations (Zhang et al., 2014b).

Whether this order accompanying segregation to the twin boundaries can be described as a local SRO is a subject for discussion. However, the very existence of the alloying element segregation along the twin boundaries effectively means that they diffused from the nearby matrix regions to these boundaries. Whereas, the original claim (Abaspour and Cáceres, 2015) was that SRO-forming solutes were stable to the extent that temperature changes had little effect, if at all, on their mobility. Hence was the athermal nature of the strengthening effect of SRO. However, this way of questioning is not meant to dismiss the reality of SRO. Examinations of regions away from the twin boundaries in the same α-Mg grains were not given in those reports that presented segregation to twin boundaries. Seeking the presence of SRO away from such twin boundaries would reveal if this segregation and resulting stabilization of the twins were solely responsible for the observed strengthening or were an additional contribution to an already existing SRO effect.

The explanations based on SRO alone in Mg alloys can also be strengthened *via* conducting some advanced imaging techniques. In such a study on Mg–Zn and Mg–Y systems (Stanford et al., 2015), the alloys were defined as random solid solutions based on tomographic atom probe maps. However, those alloys had very rich solute concentrations, and even then, the majority of solute atoms were a few atomic distance apart rather than presenting a readily noticeable solute–solute neighboring. Moreover, despite the larger atomic size of Y and much richer concentrations of Mg–Y, perhaps due to the extra strain field created by Zn in Mg–Zn, the average nearest neighbor distance between Zn–Zn was almost double compared to that of Y–Y. It is fair to say that further elaborate imaging studies would contribute to our understanding greatly.

SFE-Based Assessment on the Effects of Alloying Elements in Mg–X Systems

First, it should be recalled that SFE for a given crystal plane is strongly influenced by the interatomic electron density distribution and therefore influenced by all atomic scale parameters. It is not a priori that all the SFE values of different planes in a system will follow the suit of change in the SFE of a particular plane under the influence of a particular solute (Yin et al., 2017). As to the GSFE calculations, an important assumption in the currently employed *ab initio* techniques is that a random solid solution is assumed (Equation 4 in Yin et al., 2017). Considering the small size of the atomic models used in calculations, whether this makes a great difference or not is debatable but not unlikely. In this respect, individual SFE calculations may be considered more reliable than those for GSFE.

Several studies on SFE calculations are particularly comprehensive in terms of the number of alloying elements considered (Moitra et al., 2014; Shang et al., 2014; Yuasa et al., 2015; Dong et al., 2018). Pei et al. (2015), in an attempt to devise a practical guide to alloying, plotted qualitative relationships between the $I_{1\text{SFE}}$ in Mg–X and the relative atomic volume, atomic number, $I_{1\text{SFE}}$ of the solute, bulk modulus, and electronegativity of the solute for 18 elements. Similar reports can also be found in the literature (Wen et al., 2009).

Among the SF types, $I_{1\text{SFE}}$ has been said, although not unanimously, to be indicative of the deformation capacity of the Mg–X systems based on computations as well as observations on Mg–Y (Sandlöbes et al., 2011, 2014; Agnew et al., 2015). Although, $I_{1\text{SFE}}$ does not reveal an energy barrier to slip, its formation is regarded as a source for generation of nonbasal, <c+a>, dislocations, providing a step for slip at room temperature. Therefore, if $I_{1\text{SFE}}$ is low I_1-type SFs form, the proposed mechanism is assumed to work and explain the ductility imparted by Y (and REs for that matter). A strong criticism to this proposal came from Yin et al. (2017), indicating that necessary number of I_1 type cannot be generated by slip, and a large population of I_1 SF prior to deformation is necessary to render the mechanism feasible. An alternative mechanism was also put forward by Kim et al. (2015) who, by using molecular dynamics simulation, suggested different level of changes in CRSS values associated with Peierls potentials for pyramidal plane and a very complex movement of leading and trailing partials in a comparative study on Mg–Y and Mg–Al.

According to the findings of Yin et al. (2017), Zn was the least effective element in reducing both basal and pyramidal I_1 and I_2 SFEs (no effect on basal types), and Al moderately reduced the basal SFEs while not changing the pyramidal types; Y created the most effective reductions as compared to Al and Zn. These findings, when considered together with the previously mentioned results by Chen and Boyle (2009), may be indicating that SFE reduction becomes more effective as the ranking of interatomic bond between the solute and Mg goes from lack of covalency, that is, Mg–Zn, to weak covalency, that is, Mg–Al, and finally to strong covalency (hybridized bonds) as in Mg–Y.

As to the computed GSFE values, the reports for a wide range of alloying elements for binary Mg alloys are unfortunately not free from contradictions, for some elements even giving opposite trends as can be seen by comparing the values given in Wang et al. (2013), Moitra et al. (2014), Shang et al. (2014), Wang W. Y. et al. (2014), Zhang et al. (2014), Yuasa et al. (2015) and Dong et al. (2018). Having summarized the effects of individual alloying elements in Mg–X systems based on the existing literature that relies on atomic scale thermodynamics, or on first-principles calculations revealing SFE values, we will now attempt to indicate the relationship between the atomic number, size, and $\Delta\Phi^*$, Δn_{WS}, and SFE in the periodic table. While Miedema's model considers all the elements in a single plot collectively, we will consider the elements along individual periods of the table.

In order to understand the general trend in the periodic table, several relevant plots have been given in **Figures 4–6**. The well-known electronegativity change by atomic number has been given in **Figure 4** as a reminder that there is an overall trend of increase within each period. The intensity of increase appears to reduce as the period number increases. On the other hand, the plots of atomic number (**Figure 5A**) or size (**Figures 5B,C**) vs. n_{WS} or Φ^* showed clear modulations, each "inverted parabola" belonging to a period. An inverted parabolic increase in the plots of $I_{1\text{SFE}}$ (SFE values from Wang W. Y. et al., 2014; Dong et al., 2018) vs. atomic number (**Figure 6A**) or size (**Figure 6B**) for each period also exists. **Figure 7** shows the changes in in Φ^* (**Figure 7A**) and in n_{WS} (**Figure 7A**) vs. $I_{1\text{SFE}}$ (Φ^* and n_{WS} values are from Miedema (1973a), Abaspour and Cáceres (2015), Buey et al. (2018); SFE values from Wang T. et al., 2014 and Dong et al., 2018). Although a graphical illustration has not been given here, it was found that $I_{2\text{SFE}}$ also showed a similar relationship with Φ^* and n_{WS}, whereas GSFE did not show any specific trend (perhaps due to insufficient data). The increase in SFE as the Φ^* increased may be interpreted due to an increasing binding force between the solvent and solute atoms. On the other hand, the increase in SFE vs. n_{WS} plots may be attributed to a relatively more polarized electron density distribution at Wigner–Seitz atomic cell boundaries.

The parallelism between n_{WS} and Φ^* against the atomic number and radii further testifies Miedema's original hypothesis regarding the interdependency of the two terms. The linear relationship between the n_{WS} and Φ^* was already known due to Miedema. These trends also indicate the relationship between the $I_{1\text{SFE}}$ and the values of n_{WS} and Φ^* as atomic scale thermodynamic parameters. Pei et al. (2015) have shown, for presumably a single period (elements were not stated), that $I_{1\text{SFE}}$ in Mg–X increased as the electronegativity of the solute increased.

The inflection points in **Figure 6** as well as in **Figure 7** correspond to about the middle position in each period, that is, about the midrange in transition metals. This intriguing feature requires further evaluation. If compared with Miedema's plot (**Figure 3**), it can readily be noticed that all the elements of the upper (north) sector are located in the second half, namely, the decreasing part, in the Φ^*, n_{WS}, $I_{1\text{SFE}}$ vs. atomic number plots, and reverse their side in plots vs. atomic size, whereas the elements located in the lower (south) sector of the Miedema plot reside on the reverse half of the same plot in each case. By taking into account the findings of *ab initio* studies (DOS calculations and the contour maps), it may be deduced that the elements that are likely to form the non-hybridized type SRO with Mg and those that form hybridized type SRO reside on the opposite sides in these "inverted parabolic" plots for each period. As such, it appears to be logical to suggest that the question of what type of SRO forms can be answered depending on the position of the candidate solute element on any of these plots involving the n_{WS}, Φ^* or $I_{1\text{SFE}}$. It may be suggested that if the size difference is relatively smaller and electronegativity is larger, the tendency to form non-hybridized bond type is greater, and *vice versa*.

Based on the interpretation of these plots, the possibility of using a currently available measurement technique, that is, Kelvin probe force microscopy (KPFM), may be suggested when assessing the SFE changes especially in studies involving multicomponent alloys (Φ^* was said to change linearly with Φ, the work function, of the constituent atoms) and that the electronegativity and chemical potential for electrons in an atomic cell were equivalent (Miedema, 1973c; Abaspour and Cáceres, 2015). *Ab initio* computations are rather difficult (Pei et al., 2015) and currently not capable of computing SFE in models involving several different solute atoms [few studies considered two solute atoms together (Kimizuka and Ogata, 2013)]. Kelvin probe force microscopy, because it measures work function (Φ), that is, the equivalent (Miedema, 1973c) of Φ^* in Equation (1), may be useful in understanding the SFE changes indirectly as compared to some reference materials, be it pure Mg and/or a binary alloy of known SFE. Because SFE changes are invaluable in selecting alloying elements, this practical measurement technique may prove useful in designing multicomponent alloy systems.

Relationship between electron work function (EWF) and material properties, such as strength and elastic modulus for metals and alloys, was demonstrated (Halas, 2006; Hua and Li, 2011; Lu et al., 2018). Liu and Li (2015), *via ab initio* calculations, showed that both I_1 and I_2 SFEs increased with EWF and that alloying Mg with the elements having lower EWF compared to Mg would impart strengthening as well as ductility and with the other elements, while increasing strength, and lower ductility.

It is thus reasonable to suggest that an understanding of alloying effects has already been established in relation to EWF, which can be measured *via* KPFM. Admittedly, this knowledge basis currently stems from the *ab initio* calculations rather than KPFM as a practical method. One impediment when employing KPFM may be the inevitable surface oxide on samples. However, if relative values are to be considered rather than seeking absolute values, KPFM readings may be promising for comparison purposes between different systems.

DOPING MAGNESIUM WITH OXYGEN

As a counterintuitive alloying approach, intentional addition of oxygen into Mg has been arguably the most interesting attempt in the history of Mg alloys. Doping Mg with oxygen results in many interesting properties and may also be taken to indicate the potential of dilute systems involving interstitial atoms.

A recent study (Kang et al., 2016) showed that dilute concentrations of oxygen, as an interstitial element, yielded highly surprising remedial effects on the problematic properties of Mg, namely, an increased strength and deformation capacity, removal of the yield asymmetry, and even improved corrosion resistance. It has been postulated that, as a non-metallic addition, oxygen would form interatomic bonds that may be strongly ionic/covalent in character and increase strength (Kang et al., 2016).

Kang et al. (2016) succeeded in mono atomic oxygen addition to Mg by employing the dissociation tendency of nanosized TiO_2 over 400°C when in molten Mg and detected ~0.3% at. oxygen at a depth of 15–18 μ in solidified state after removing the surface oxide layer. Their first report covered pure Mg, Mg–Al, and Mg–Zn systems with oxygen additions. Among them, Mg–Zn–O system showed additional extraordinary features, such as more than 50% elongation to failure without apparent twinning, a yield drop phenomenon akin to simple low carbon steels, and, strikingly, non-basal slip in submicron-sized grains. Thermal conductivities of all oxygen containing alloys were also shown to have increased.

Two of their following studies on Mg−9Al-O alloy also reported a higher oxygen content in β-phase (~3.86% at. in $Mg_{17}Al_{12}$) than in α-Mg (~0.79%), leading to increased *d*-spacings in both phases and consequently a better match (Kang et al., 2017, 2018) and stability at the β/α interface, disappearance of the β/α eutectic, and refinement of β-phase. Presence of oxygen brought about benefits in the mechanical properties as compared to Mg−9Al, namely, 30% improved yield strength, 41% increased UTS, doubled elongation to failure, ~10% increase in elastic modulus, and fracture toughness. Albeit, their claim regarding

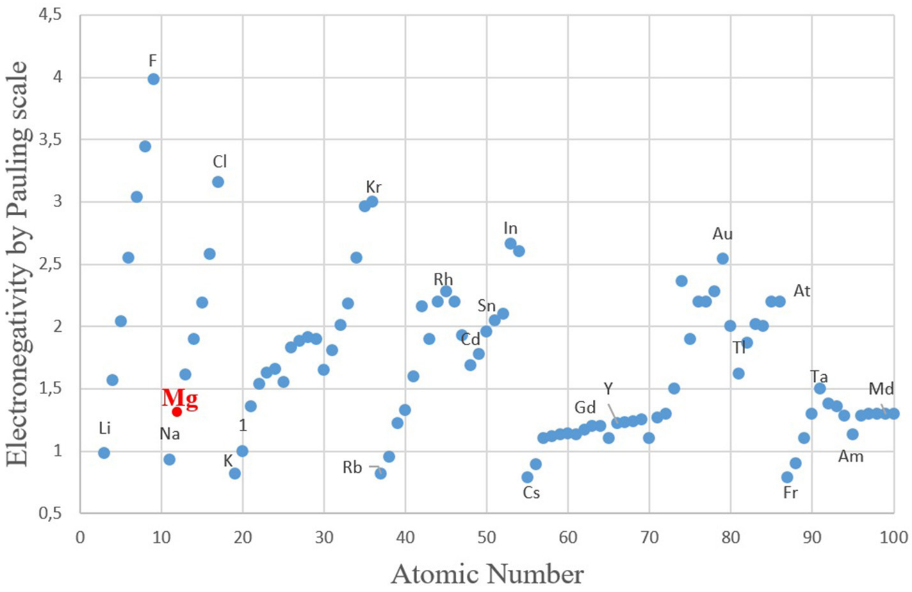

FIGURE 4 | The relationship between the Pauling scale electronegativity values with atomic numbers (data set from: https://en.wikipedia.org/wiki/Electronegativities_of_the_elements_(data_page) with reference to: L. Pauling, *The Chemical Bond*, Cornell University Press, Ithaca, New York, 1967).

the formation of so-called "reticular" phase during annealing treatments (Kang et al., 2018), due to lack of verification *via* an irrefutable method, needs substantiation. This reticular phase may turn out to be nothing more than an oxide phase.

To our best knowledge, there exist no studies yet as to the changes incurred in SFE by dissolved oxygen atoms in Mg matrix or an evaluation with actual figures of formation enthalpy of such a solid solution, although based on the evaluations by Pei et al. (2015), due to the very high electronegativity value of oxygen, a large increase at least in I_1 SFE value of Mg–O can be expected. This foreseen increase would conform to the plot given by Pei et al. (2015) that shows an increase at least in I_1 SFE with average atomic size reduction in Mg–X (Mg–O system should have a decrease in average atomic size according to Figure 3 in Pei et al. (2015). The experimental observation as to lack of twinning (Kang et al., 2016) seems to support these expectations.

Furthermore, because of the large electronegativity difference between Mg and oxygen, a dilute system of Mg–O is highly likely to form SRO. Based on the discussions earlier, directionality in bonding around oxygen atoms would not be expected. It may also be thought that, through binding, more of the available free electrons of Mg that would otherwise contribute to the corrosion potential may also be the reason for the observed (Kang et al., 2016) improvement of the corrosion resistance in Mg–O system. Such interpretations may render all the beneficial effects of this dilute binary alloy system understandable, but a demonstrated explanation through *ab initio* techniques could prove highly useful.

The potential beneficial effects of dissolved oxygen deserve exploration at fundamental level and in different alloy systems, be it Mg or other metals. In essence, the effect of oxygen in solid solution has long manifested its potential also in other well-known metallic systems. CP (commercial purity) titanium serves as an engineering material owing its strength level to oxygen in solid solution at ppm levels. Yet another commercially available example is oxygen-free copper, a material that would otherwise be hard and brittle. Even just these two materials clearly point out that addition of oxygen in trace amounts has the potential to create striking changes in metals including Mg. Perhaps the down side to the idea is the inherent difficulty in producing bulk quantities of materials containing controlled and dilute amounts of oxygen. Coupled with this difficulty, the highly problematic issue of finding an economical monoatomic oxygen source may continue to stand on the way to utilization of this approach. Formerly, addition of nitrogen into Mg was also attempted (Kaya et al., 2003). Despite the disappearance of the eutectic morphology in the microstructure as in oxygen addition, the attempt was probably a failure in terms of supplying monoatomic nitrogen into the molten metal due to employment of simple gas purging.

ULTRASTRONG MAGNESIUM ALLOYS

Because comparable to the high-strength steels, the strength levels achieved in some Mg alloys deserve the definition of "ultra." For example, owing to nanocrystalline structures containing LPSO phases, yield strength level as high as 600 MPa was reported in rapidly solidified powder metallurgy products (Inoue et al., 2001; Kawamura et al., 2001). More complex but again Y- and RE-containing, a composition [Mg−1.8 Gd−1.8 Y−0.7 Zn−0.2 zirconium (Zr) at.%] also showed a high yield strength of 473 MPa in aged condition (Homma et al., 2009).

A hot-rolled Mg−8.5 Gd−2.3 Y−1.8 Ag−0.4 Zr (wt%) with a yield strength of ∼575 MPa (Wang et al., 2010; Jian et al.,

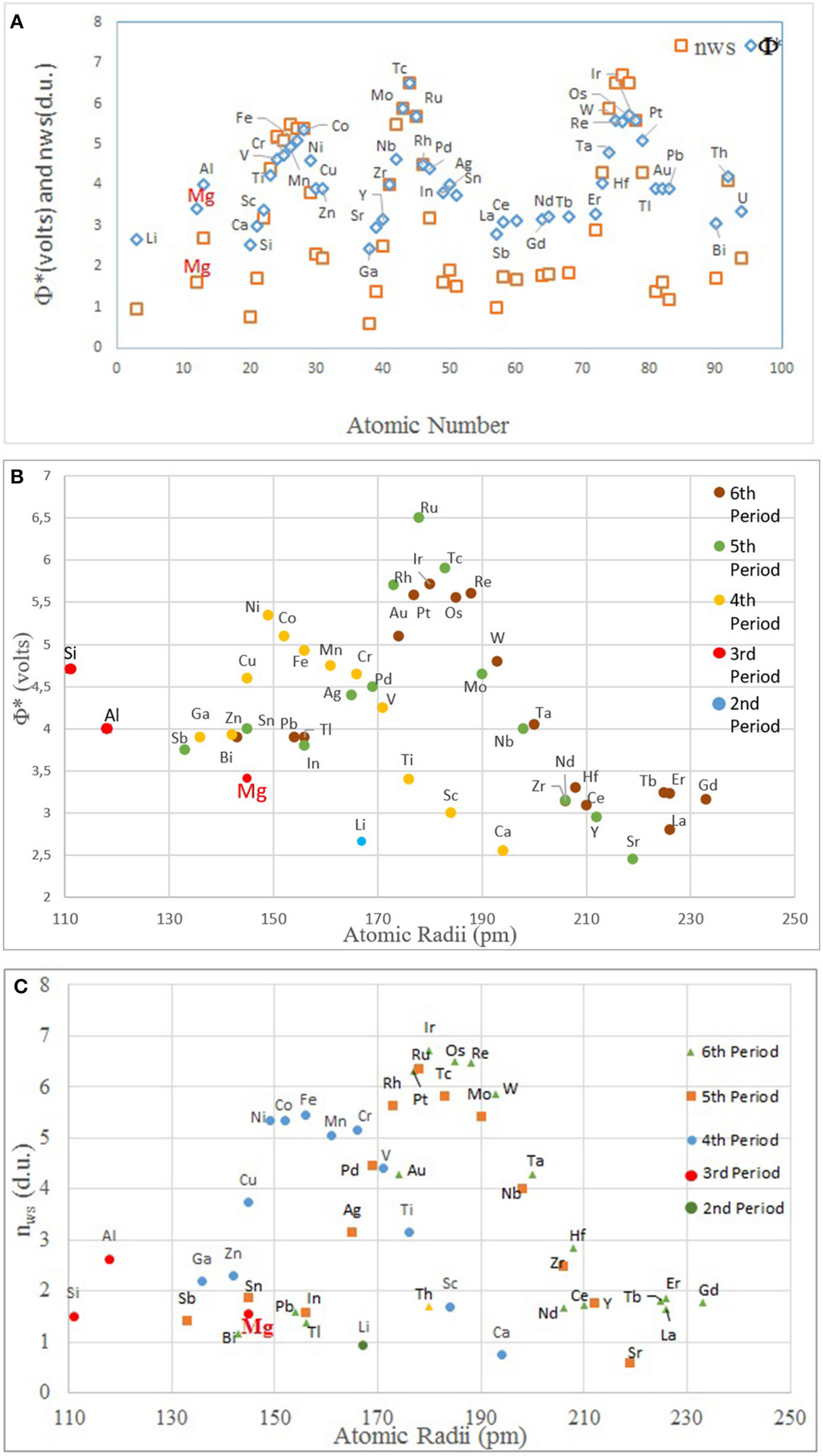

FIGURE 5 | The plots of **(A)** atomic number vs. n_{WS} and Φ^* (for clarity, the element names are only given for one data set, Φ^*); **(B)** atomic size vs. Φ^*; and **(C)** atomic size vs. n_{WS}. Note that the modulations correspond to individual periods in the periodic table (n_{WS} and Φ^* values are from Miedema, 1973a; Abaspour and Cáceres, 2015).

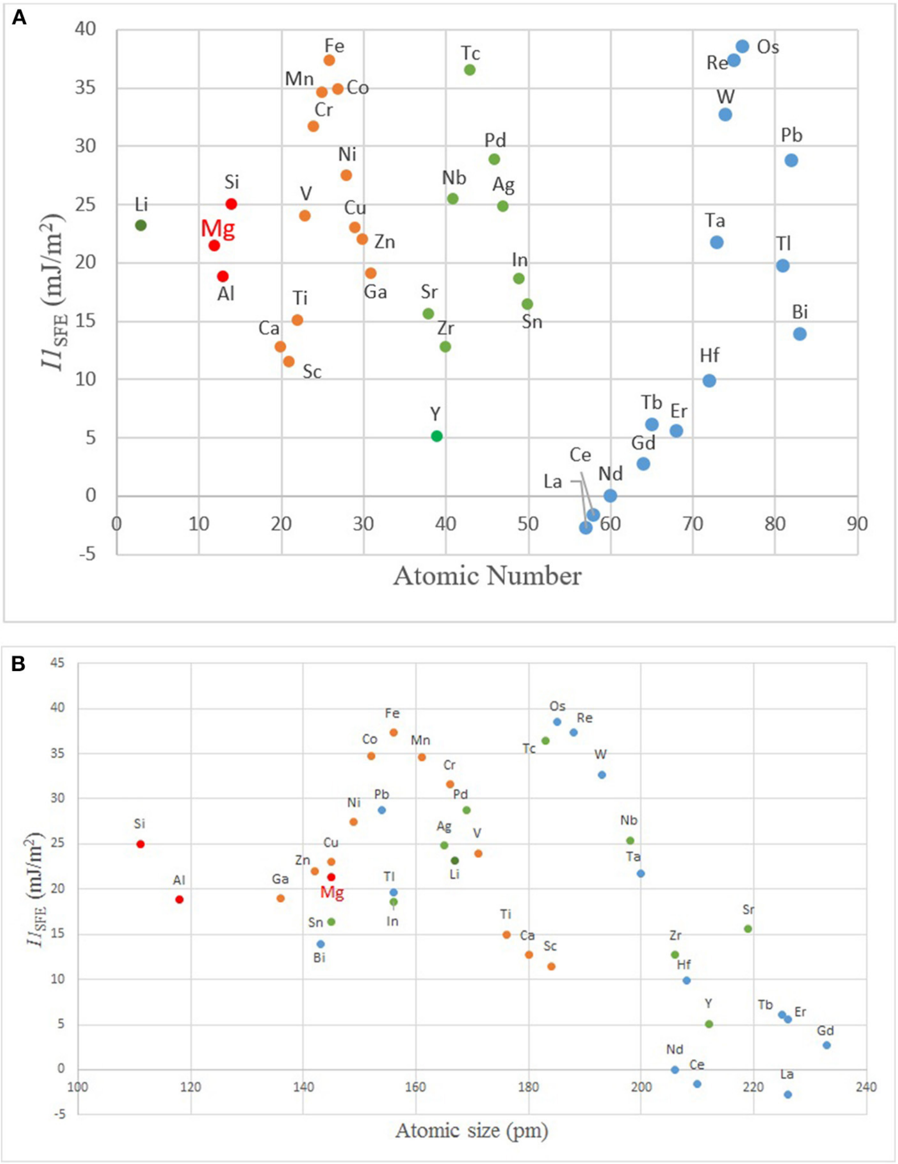

FIGURE 6 | The plots of $I1_{SFE}$ vs. **(A)** atomic number, and **(B)** size showing modulations (SFE values from Wang T. et al., 2014; Dong et al., 2018).

2013) and Mg−8.2 Gd−3.8 Y−1.0 Zn−0.4 Zr alloy with a proof stress of 426 MPa (Xu et al., 2012) and an earlier example of alloy extrusions in the Mg–Al–Zn–Si–RE system with yield strength levels of >500 MPa (Chang et al., 1986, 1987) can also be considered in the ranks of the ultra-strength alloys, albeit these high strength levels were not accompanied by high deformation capacities, which were typically <10%.

One study, among those that reported ultrastrong levels, is particularly interesting because of its implications toward developing high-strength Mg alloys. The achieved strength level (σ_y ∼575 MPa, UTS ∼600 MPa, and 5.2% uniform elongation) was attributed to finely spaced SFs by Jian et al. (2013). As such, because the alloys contain abundant SFs to start with, this alloy system may also serve as a test case to show if *I1*-type SFs really play an important part in increasing deformation capacity as suggested in Sandlöbes et al. (2011), Sandlöbes et al. (2014), and Agnew et al. (2015). In this alloy, presence of such nanospaced SFs was proposed as an effective means to increase strength without losing the modest level of ductility even after multipass rolling. It appears that the achieved properties simply depend on the adjustment of SFE. The same study also suggested an interesting deformation mechanism, supporting the findings of an earlier work (Liao et al., 2004). The deformation was said to have changed mode and became SF-mediated instead of slip-dominated after reaching a total deformation range of 30–50% reduction as the SF widening started to operate (Jian et al., 2013). The foundation of this explanation is none other than Suzuki segregation.

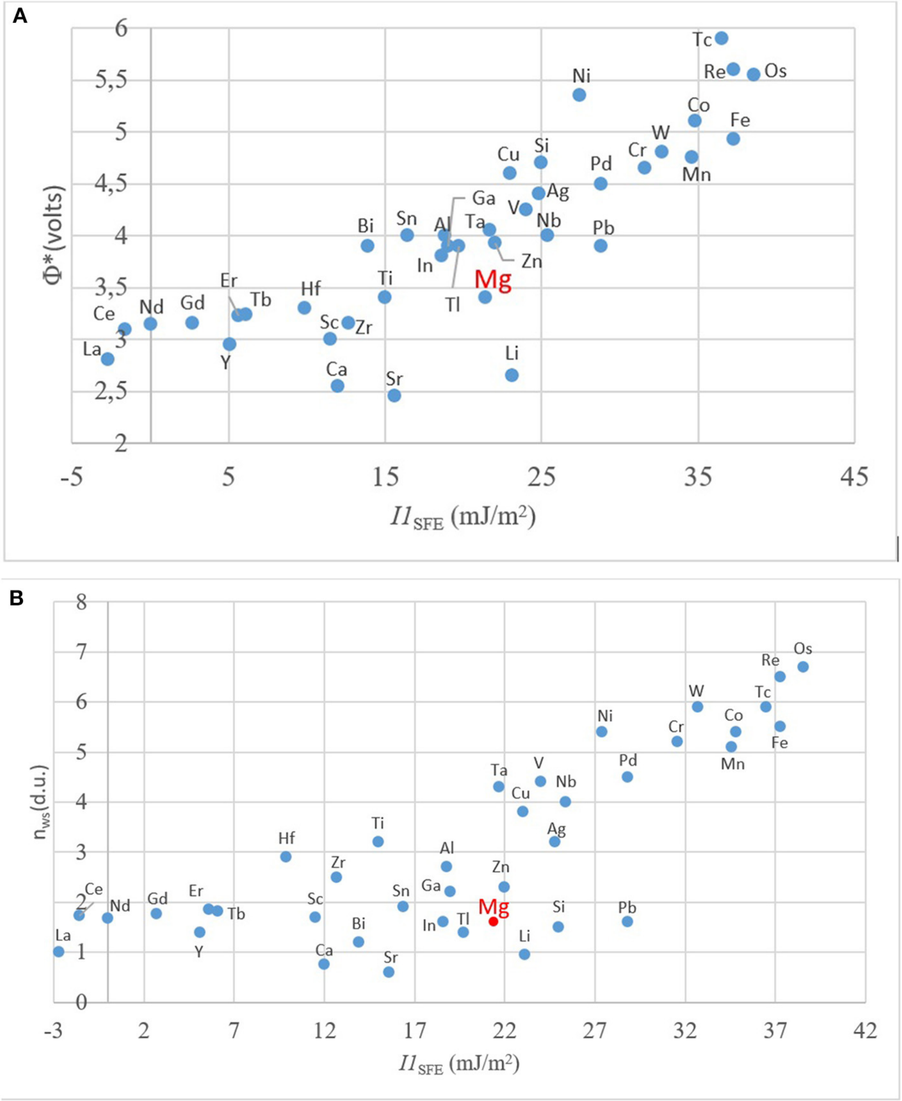

FIGURE 7 | The relationship between the computed values of $I1_{SFE}$ with **(A)** Φ^*; and **(B)** n_{WS}. (Φ^* and n_{WS} values are from Miedema, 1973a,b; Abaspour and Cáceres, 2015; SFE values from Wang T. et al., 2014 and Dong et al., 2018).

The composition of this interesting alloy is akin to those that generate LPSO phases as discussed below. However, it is also worth noticing that despite the proliferation of SFs and presence of the main player elements in LPSO formation, perhaps due to the level of SFEs not being at a necessary critical range, the alloy composition with nanospaced SFs did not create LPSO phases. Considering the fact that the strength level of this structure is as high as those that contain LPSO phases leads to an intriguing question. Is the ultrastrength level achieved in composition with LPSO phases really due to these so-called strengthening particles or only a result of presence of multitude of SFs in the same structures? This view is admittedly simplifying the comparison; however, it appears that with or without LPSO phases, so long as the SFs proliferated the strength can reach to ultra levels.

A category of Mg alloys with outstanding strength levels is found within Mg–Zn–RE [or Mg–TM (*transition metal*)–RE] system involving LPSO phases. These may be viewed as the succession of those structures that involve nanospaced SFs without forming another phase as mentioned above. We will now embark on their discussion next.

Systems Containing LPSO Phases

The earliest observation on LPSO in Mg alloys may be ascribed to the report by Luo et al. (1994) on Mg–Zn–Zr–RE system. Many studies also refer to the report by Kawamura et al. (2001) as the precursor study on LPSO phases. Although neither the term LPSO was mentioned nor their morphology presented in that study, superior room and high temperature strengths, relatively good deformation capacity, and high strain rate superplasticity were reported for Mg–Zn–Y system. Later on, the alloys forming LPSO phases proliferated and generally expressed as Mg–TM (transition metal)–RE systems (Zhiping et al., 1994; Yokobayashi et al., 2011a,b; Kishida et al., 2012, 2013; Xu et al., 2016). Existing literature on alloys involving LPSO phases collectively reports high strength (Kawamura et al., 2001; Hagihara et al., 2010a,b) and improvement in deformation capacity, as well as in creep (Hu et al., 2016; Xu et al., 2016) and corrosion resistance as common characteristics, as compared to AZ31, WE43, ZK60, and ZX60 (Xu et al., 2016) alloys. These improved mechanical properties were generally achieved with small additions of Zn and RE, for example, 1 at.% Zn−2 at.% RE (Nie et al., 2005; Liu et al., 2008; Gao et al., 2009; Egusa and Abe, 2012).

Long-period stacking order precipitates that can exist at the grain boundaries, as well as intragranularly, are classified into two types, one that forms during solidification, and the other upon annealing (Kawamura and Yamasaki, 2007; Li et al., 2018; Sato et al., 2018). It should be noted that, alloy composition permitting, the entire grains are composed of lamella of LPSO together with bands of α-Mg, while LPSO precipitates along the grain boundaries can also be present. Thus, the material, due to formation of LPSO structures, carries many FCC layers in each grain (Kim et al., 2016). Building blocks of LPSO phases should be envisaged as SFs located between Shockley partial dislocations of α-Mg phase (Zhu et al., 2009, 2010a,b; Kim et al., 2016, 2017).

The classification of the crystal repetition of such layered structures goes back to the earlier work by Ramsdell (1947). In earlier classification of LPSO phases, the 10H (Matsuda et al., 2005; Abe et al., 2011; Hagihara et al., 2016), 18R (Kawamura et al., 2006), 14H (Itoi et al., 2004; Hagihara et al., 2010b; Abe et al., 2011; Egusa and Abe, 2012; Zhu Y. M. et al., 2012; Jin et al., 2013; Nie et al., 2014), and 24R (Abe et al., 2011) polytypes emerged, corresponding to 5, 6, 7, and 8 layers in structural blocks, each being a close-packed plane stacked in the direction of the c-axis of α-Mg crystal. Recently, an extended series have been expressed (Li et al., 2018) as 6H (now known as a building block of 18R) (Abe et al., 2002; Ping et al., 2002; Amiya et al., 2003), 10H, 14H, 15R (Mi and Jin, 2013), 18R, and 24R. Some metastable LPSO phases were also revealed by the work of Kim et al. (2016). In this notation, H stands for hexagonal, and R for rhombohedral symmetries of the Bravais systems, whereas the number refers to the number of repetitions of the structural blocks (SB) (Kim et al., 2016), each of which essentially may also be seen as having HCP stacking involving SFs. The 4 polytypes can essentially be described by a structural unit composed of AB stacking followed by a C fault layer. This fault layer is enriched in Zn and RE atoms (Egusa and Abe, 2012; Kim et al., 2017). Thus, the final ordered stacking, including the fault layer, makes up a local FCC, that is, ABCA stacking, and also shows chemical ordering perpendicular to the fault, that is, basal planes in α-Mg. As such, the workings of the system are reminiscent of Suzuki segregation and ordered segregation of the solute elements to twin boundaries as previously discussed.

The precise deciphering of the stacking sequences in 4 major types of LPSO phases in materials prepared *via* rapid solidification techniques has been given by Matsuda et al. (2005) and Egusa and Abe (2012) as follows: The 10H and 14H, both carrying mirror symmetry with respect to the basal plane, show stacking sequence of ABACBCBCAB and ACBCBABABABCBC, respectively. 18R and 24R, not carrying mirror symmetry with respect to the basal plane, have stacking sequence of ABABABCACACABCBCBC and ABABABABCACACACABCBCBCBC, respectively. It has been shown that 18R and 14H are stable at high and low temperatures, respectively, whereas 10H and 24R phases are not stable in every alloy system (Kim et al., 2018a). Furthermore, 14H and 18R are the most frequently observed ones (Lv et al., 2014), with the 18R showing a tendency to transform into 14H upon heat treatment or hot deformation (Oñorbe et al., 2012; Zhu Y. M. et al., 2012), as 14H appears to be energetically preferable one among the others (Kim et al., 2016). This transformation from 18R to 14H was reported to be accompanied by a decrease in SFE (Fan et al., 2011; Lv et al., 2014; Kim et al., 2016).

Long-period stacking order phases are further complicated by in-plane ordering in 14H and 18R types (Kishida et al., 2015; Kim et al., 2018b). This complication manifests itself with the presence of $L1_2$ type clusters, and the order is violated in one dimension, leading to the definition of order-disordered crystallographic structure in some Mg–TM-RE alloys (Yokobayashi et al., 2011a; Okamoto et al., 2014; Iwatake et al., 2015; Kishida et al., 2015, 2017). The in-plane order may be a long-range type as in Mg–Al–Gd system (Kimizuka et al., 2013; Tane et al., 2015; Kim et al., 2018b) or may be composition dependent as in Mg–Y–Zn system, being present more locally in relatively dilute alloys, and long-range type in richer Mg–Y–Zn alloys (Egusa and Abe, 2012). It has been suggested that LPSO formation is essentially governed by formation of Zn6RE8 clusters, with Mg atoms being substitutes for RE atoms (Egusa and Abe, 2012). This in-plane ordered clusters were reported to have an important effect in determining the elastic properties of the LPSO structure and, in turn, influence the properties of the alloy (Kimizuka et al., 2013; Tane et al., 2015; Kim et al., 2018b). Another important effect of LPSO phases is inhibition of the dynamic recrystallization toward maintaining small grain size. This has been attributed to the suppression of dislocation numbers due to creation of many SFs on the basal planes (Lv et al., 2014). 14H LPSO has been reported to be more effective in this regard as compared to 18R (Lv et al., 2014).

The formation and growth mechanism of LPSO structures were investigated incorporating *ab initio* calculations (Zhu Y. M. et al., 2012; Kim et al., 2016). Kim et al. (2017) suggested a coupled diffusional and displacive transformation mechanism involving formation of GP zones and their transformation to LPSO structures as opposed to the formerly proposed spinodal decomposition model (Iikubo et al., 2013; Narita et al., 2013). According to their model, a Zn/Y-enriched layer was defined as the precursor of LPSO structure in lean Mg–Y–Zn system and termed as GP zones. Indeed, the term fits well as these zones fulfill the criteria of being chemically ordered and coherent with the matrix. At the stage of GP zones, it was shown that no stacking alterations in the HCP arrangement of the basal planes of α-Mg took place (Kim et al., 2017). This primary step constituted the diffusional part of their suggested "coupled diffusional-displacive transformation" mechanism. In the following displacive step, LPSO structure is formed by generation and propagation of Shockley partials. Although in the original model the coherency strains were not mentioned explicitly, one can assume that the existence of such strains at precipitate–matrix interface, as in conventional GP zones, is inherent and facilitating the process. Formation of GP zones lowers the SFE paving the way for the formation of Shockley partials, at which stage the coherency stresses are substituted by the shear strains due to the partial dislocations (Kim et al., 2016). Different types of these GP zones were said to lead to different LPSO structures, in terms of both chemical and structural ordering, and to be composition dependent (Kim et al., 2017). Several other studies also reported GP zones in Mg alloys (Ping et al., 2003; Oh et al., 2005; Nishijima et al., 2007; Saito et al., 2010; Lee et al., 2011).

QUASI-CRYSTAL FORMING SYSTEMS

Formation of quasi-crystals in Mg alloys may be viewed as an extension of the assessment of the potential for intermetallics through Miedema's scheme.

Quasi-crystals were discovered by Shechtman et al. (1984) in a rapidly solidified Al–manganese alloy. This discovery in 1984 was later awarded with Nobel Prize in 2011. Since then, other systems also have been found to exhibit quasi-crystal formations.

Quasi-crystals are essentially topologically closely packed intermetallics, also known as Frank–Kasper phases. Thermodynamically stable (Abe et al., 2000) icosahedral (i-) (Kounis et al., 2000) and decagonal (d-) phases were obtained. However, they are different from the true topologically close pack structures as they do not comply with the space-filling Bravais lattices. Instead, they possess a long-range quasi-periodic order without the translational periodicity in three dimensions, showing forbidden rotational symmetry in diffraction, that is, 5-, 10-fold, and so on.

The first quasi-crystal forming Mg system, Mg–Zn–(Y, RE), was reported by Luo et al. (1993). It is now known that Mg–Zn–Al, Mg–Al–Cu/Ag/Au, Mg–Al– Zn–Cu, Mg–Al–Pd, and Mg–Cd–Yb alloy systems can form quasi-crystal phases (Yadav and Mukhopadhyay, 2018). Quasi-crystalline phases themselves have interestingly low frictional properties, high hardness and oxidation resistance, low thermal conductivity, and so on (Dubois, 2012).

It is interesting to note that once again Mg–TM–RE system, as for LPSO structures, is at the forefront in the case of quasi-crystal forming alloys. The icosahedral *i*-phase was obtained in Mg–Zn–Y system through normal casting conditions. Formation of quasi-crystalline phases in this system has been said to exhibit a relatively large compositional range, as well as casting process parameters (Zhang et al., 2008). Zhao and Wang (2016) reported quasi-crystalline formations with 22 kinds of different morphologies obtained through different cooling processes in Mg–Zn–Y system. High strength values up to 450 MPa were reported for this system (Bae et al., 2001).

An important outcome of their properties is that, because of their low interfacial energy, quasi-crystals are stable strengthening particles in Mg alloys (Bae et al., 2002). Therefore, we may expect to see an increasing trend in their use.

A COMPETITOR TO RARE EARTH ELEMENTS? CALCIUM CONTAINING ALLOYS

The effect of Ca in Mg is similar to REs according to Miedema's model. Benefit of Ca may be summarized as follows: reduces the tension/compression asymmetry, refines grain size (Jiang et al., 2015), increases creep resistance (Ninomiya et al., 1995; Terada et al., 2005; Amberger et al., 2009), and reduces stress relaxation (Abaspour et al., 2016) and deformation texture (Stanford, 2010; Wang T. et al., 2014). An important issue is that all these benefits of Ca addition work in AM and AZ series commercial alloys. By combined addition of Ca and Sr, some commercial alloys were also developed such as ACX or AXJ series (Suzuki et al., 2004, 2008; Luo et al., 2007; Zhu et al., 2015).

Reported *ab initio* calculations of GSFE due to Ca addition are again not in unison as expressed before. For example, according to the majority of the literature (Wang et al., 2013; Shang et al., 2014; Zhang et al., 2014; Yuasa et al., 2015; Dong et al., 2018), Ca decreased γ_{USF} of Mg. Yet, in one study (Moitra et al., 2014), Ca increased the $\mathrm{GSFE}_{\mathrm{basal}}$ of Mg (γ_{USF}) in $<11\bar{2}0>$ slip indicating a strengthening effect equal to that of Gd, while Ce reducing it as RE elements. Whereas for another slip direction in basal plane, although lowering the SFE of pure Mg (γ_{SF}) and allowing for formation of an SF, Ca is more prohibitive as compared to Gd and Ce, for dislocation dissociation with much higher $\mathrm{GSFE}_{\mathrm{basal}}$ in $<10\bar{1}0>$ slip. Reported trends were in better agreement on the effect of Ca in lowering the $\mathrm{GSFE}_{\mathrm{prismatic}}$ of Mg (γ_{USF}) in the $\{10\bar{1}0\}$ $<11\bar{2}0>$ slip system, being almost equal to those of Gd and Ce, indicating facilitation of dislocation generation. As to the pyramidal slip, Zhang et al. (2014) reported a decrease in GSFE of $\{11\bar{2}2\}<11\bar{2}3>$ due to Ca, Gd, and Y to varying degrees.

From the above given account based on GSFE values, Ca falls no short of RE elements. The solid solution effect of Ca may also be viewed from the perspective of SRO effects. Calcium with its low electronegativity difference with Mg is likely to form a type of SRO similar to that in Mg–Y(RE), that is, hybridized bonds. Such elements are evidently more potent in improving the strength (Abaspour et al., 2016).

When added to AZ series, it was said that Ca in the $Mg_{17}Al_{12}$ eutectic phase increased the melting temperature of this otherwise insufficient-for-creep-strength phase, enhancing the strength of the Mg–Al bond (Min, 2003). Depending on Al/Ca ratio, Ca addition also leads to formation of Laves phases, namely, Al_2Ca, Mg_2Ca, and $(Mg, Al)_2Ca$ (Chai et al., 2018; Zubair et al., 2019). Among the Mg17Al12-, Al2Ca-, Mg2Sn-, and Mg2Ca-type intermetallics, based on the calculated enthalpy of formation and binding energies, Al2Ca was found to be the most stable one (Wang et al., 2016).

RE elements are expensive, and therefore, it is desirable to find alloy compositions that can perform at least to the same level as those involving REs. Calcium is the best economic alloying element that can compete with the good-for-all-illnesses-of-Mg, the RE elements, as it seems to provide remedies for a number of shortcomings and anomalies of Mg alloys (Abaspour et al., 2016; Guan et al., 2019). Furthermore, it has been shown that Ca addition conferred arguably the most attractive property to Mg, that is, protection of the melt against atmospheric corrosion, eliminating the need for a protective gas cover (Kim, 2011) during secondary melting. In fact, calcium oxide (CaO) addition for this purpose, as an easier, and if not more, equally successful metallurgical option, may further compel researchers to examine the effects of Ca in a wider spectrum of Mg alloys as CaO would open the way to Ca entry into the melts. Therefore, as one of the highlights of the past two decades, we will also scrutinize the topic of CaO addition next.

CaO Addition to Mg—Improvements in Melt Protection and Corrosion of Mg Alloys

CaO addition may just be taken as one of the most important advancements over the past two decades regarding melt protection and imparting corrosion resistance to the conventional Mg alloys. It was shown that CaO addition by 0.3–0.7 wt%, without changing the basic microstructure except for grain refinement, singlehandedly conferred perhaps the most attractive property to Mg and to its conventional alloys in the AZ series, that is, protection of the melt against burning (Kim, 2011).

Figure 8 (Rafiei et al., 2018) shows the surface of a cast Mg without any protection during melting. Without CaO addition, a severe burning and oxidation would be imminent within a matter of seconds, now resulted in a surface with silvery metallic shine, as was observed in a number of AZ series alloys (Kim, 2011). This ecologically friendly metallurgical practice, as emphasized by the foremost proponent of this method, Kim (2011), further encompasses many other additional benefits, for example, metal cleanliness, grain refinement, and, consequently, improved mechanical properties and recyclability. The outcomes of CaO addition are expected to be particularly beneficial for the wrought Mg alloys, for which the processing route starts with billet or ingot castings (Kim et al., 2007).

Exploration of the possibility of using CaO addition can be traced back to the preceding work by Sakamoto et al. (1997), reporting that Ca in pure Mg was increasing the flammability resistance. However, handling Ca industrially is a difficult and expensive operation. Moreover, Ca addition as a means for melt protection, although successful, has been reported to alter both the material properties, as well as the processing parameters employed, whereas CaO was doing the same job equally well arguably without releasing substitutional Ca into the solid solution (Kim, 2011; Lee and Kim, 2011a). Other already foreseen difficulties in Ca addition were mentioned as decreased in metal fluidity, increased die sticking, and problems related to utilization of Ca-containing scrap (Kim, 2011; Lee and Kim, 2011b).

The initial addition of CaO to Mg melt is a rather slow process, during which melt protection using a protective gas cover would still be needed (Kim et al., 2007; Lee and Kim, 2011a,b). Once added, otherwise an insufficient N_2 gas cover (Holtzer and Bobrowski, 2008) was claimed to do the job effectively in the secondary melting operations.

FIGURE 8 | Photomicrograph showing the effect of CaO addition on melt protection. Silvery surface shine of a cast Mg-0.4Al-1CaO (wt%) alloy piece solidified without protective gas (reproduced with permission from Rafiei et al., 2018; https://www.civilica.com/Paper-IMES12-IMES12_010.html).

Initially, there was a contradiction, not on the outcomes of CaO addition but as to what happens to CaO in molten metal. First, CaO was supposed to be more stable than MgO according to Ellingham diagrams (Brain and Knacke, 1973). Second, in some reports, it was stated that CaO dispersed in pure Mg and AZ series alloys (Huang et al., 2004; Ha et al., 2008; Kondoh et al., 2011; Nam et al., 2012). It was also claimed that CaO was not to survive during solidification but to transform into Mg_2Ca phase in pure Mg (Ha et al., 2006) and into Al_2Ca, and/or $(Mg,Al)_2Ca$, if added to AZ series (Kim, 2011; Lee and Kim, 2011b). The first issue was resolved by a thermodynamic analysis, showing the possibility of CaO dissociation against the formation of Mg_2Ca Laves phase (Kondoh et al., 2011). The second issue, *via* a TEM study on AZ31 (Jeong et al., 2013), was also resolved, showing that survival of CaO particles could be attributed to the solidification rate and that the difference between Ca and CaO additions lies in the agglomeration tendency of the intermetallics in CaO-added cases. A following *in situ* study (Wiese et al., 2015) also confirmed CaO dissolution that even started in solid state and increased until melting.

CaO addition was also proven useful in increasing the ignition temperatures of pure Mg and AZ series alloys, lessening concerns about safe handling of machining chips (You et al., 2000; Lee and Kim, 2009a,b, 2011b; Kim, 2011), as well as paving the way for use in aviation applications. An earlier study also reported this improvement in Ca-added Mg. Although the ignition temperature decreases with increasing Al content with a corresponding decrease in melting temperatures for AZ alloys, it was shown that CaO addition in all AZ series, MRI153, MRI230, and AS21 alloys, led to increasing ignition temperatures. A noteworthy example was the remarkable figure of 1,177°C for AZ31 with 1.22 wt% CaO (Kim, 2011). In addition to the flammability findings, general corrosion resistance of Mg and AZ series alloys was also reported to have benefited greatly from the addition of CaO (You et al., 2000; Lee and Kim, 2009a,b; Kim, 2011). The conclusion arrived was that the Al content had an adverse effect, and the total amount of Ca-bearing phases was the determining figure for the ignition temperature (Lee and Kim, 2011b).

The oxide film forming on the CaO-added Mg and Mg alloys was said not to conform to the Pilling–Bedworth (Pilling and Bedworth, 1923) theory that requires no volumetric change between the unit metal and the oxide phase replacing it for formation of a protective oxide film. According to the Pilling–Bedworth theory, pure Mg forms an unprotective MgO as the related R value is less than unity, being only 0.83, whereas CaO has even a worse figure of 0.78. It appears that these figures, as they may not represent the case for a mixed oxide, are counterintuitive to explain the improvement in the case CaO addition. Although a dense oxide film formation (Lee and Kim, 2011b) was assumed to explain the protective effect of CaO addition, the nature of this phenomenon in terms of structure of the surface oxide requires further exploration.

It is fair to say that much work is still needed to understand whether such use of CaO is universally applicable for all, and especially for the potentially useful novel Mg alloys of the future, and in terms of suitability to different popular production methods. For example, a twin-roll-casting study (Li et al., 2010) showed that both Al and Ca contents deteriorated the surface quality of the product in AZ series alloys. The fact that Ca-containing complex intermetallics were found in CaO-added structures should also be taken to indicate this necessity for a more comprehensive research on alloys involving elements having the potential to form precipitates with Ca.

CONCLUSIONS AND SUGGESTIONS FOR FUTURE WORK

Stacking fault energy changes due to addition of solute atoms into a host system are not straightforward to understand. On the other hand, Miedema's model leads to a better understanding of the free electron density distribution and the consequent SFE changes presented by the *ab initio* calculations. The fundamental terms of the atomic-level thermodynamic expression given by Miedema, that is, n_{WS} (density of electrons at the boundary of the two atomic cells, Wigner–Seitz cells) and Φ^* (the difference in chemical potential for electrons or equivalently the difference in electronegativity, or difference between the work functions), have been shown to be related to SFE in binary systems.

The qualitative relationship of those terms in Miedema's model with SFE shows that the employment of work function measurements (e.g., Kelvin Probe Force Microscopy) is possible to, at least, qualitatively assess the influence of the extra alloying elements into an alloy system with reference to a pure or binary system. Thus, a qualitative assessment of the changes in SFE in multicomponent systems can be undertaken readily when experimentally developing new alloys. This point may be appreciated better when considering the fact that *ab initio* calculations in multicomponent systems are currently not feasible.

Furthermore, it seems reasonable to indicate the need to extend the atomic-level thermodynamic assessment according to Miedema's approach to multicomponent systems. This difficult task would then facilitate a more complete evaluation and allow predictions in terms of precipitate forming multicomponent alloy systems, especially in terms of those that form LPSO phases or quasi-crystals.

The concept of SRO indicates the possibility of designing dilute alloy systems with desirable engineering properties. This concept also indicates the possibility to alter the freezing range of alloys with dilute additions; that is, strong SRO may expand the freezing range, as a critical parameter for casting operations such as twin roll casting. There appears to be sufficient literature that warrants further studies to explore the types of SRO through first-principles calculations, which include DOS computations. Our evaluation of the existing literature has indicated that two types of SRO can be expected depending on whether hybridization occurs in electron sharing between neighboring atoms. Miedema's geometric scheme also shows such categorization for binary alloys of Mg in terms of upper (north) and lower (south) sectors in a plot of n_{WS} vs. Φ^*.

The case of dilute levels of oxygen in Mg, or in other metals, presents a particularly interesting example in this regard. Presence of trace amounts of oxygen in different Mg alloy systems deserves attention.

The highly useful addition of Ca/CaO needs to be examined in a broader perspective in terms of its melt protection and the probable concomitant precipitation effects, as well as influences on castability or other processing techniques.

It should be indicated that some Mg alloy systems, such as those involving LPSO phases or quasi-crystals, and those containing Ca or dilute amount of oxygen have been developed, which offer superior engineering properties and solutions to the relatively problematic features of Mg. A steady increase in the use of Mg alloys can therefore be expected.

AUTHOR CONTRIBUTIONS

The author confirms being the sole contributor of this work and has approved it for publication.

ACKNOWLEDGMENTS

I would like to thank to my students Sevcan Arslan, Talha Cakmak, and Ugurcan Ozogut for their help in preparation of the figures. I also extend my special thanks to my friend Prof. Dr. Ahmet Oral of Middle East Technical University for conducting the KPFM measurements at Nanomagnetics Instruments Co. The author also thankfully acknowledges the financial support provided by Scientific Research Projects (BAP) office of Mugla Sitki Kocman University toward the production of microscopy and KPFM work within the Project no: 16/070.

REFERENCES

Abaspour, S. (2014). *Thermodynamics-based design of creep resistant mg solid solutions using the miedema scheme* (Ph.D. thesis). Queensland: The University of Queensland, Australia.

Abaspour, S., and Caceres, C. H. (2013). "Creep beha viour of Mg binary solid solutions," in *Magnesium Technology 2013*, eds N. Hort, S. N. Mathaudhu, N. R. Neelameggham, and M. Alderman [San Antonio, TX: The Minerals, Metals & Materials Society (TMS)], 17–20. doi: 10.1007/978-3-319-72332-7

Abaspour, S., and Cáceres, C. H. (2014). "The athermal component of the strength of binary mg solid solutions," in *International Conference on Magnesium Technology 2014,* eds N. R. Alderman, M. Manuel, M. V. Hort, and N. Neelameggham (San Diego, CA: The Minerals, Metals & Materaisl Society), 73–75.

Abaspour, S., and Cáceres, C. H. (2015). Thermodynamics-based selection and design of creep-resistant cast mg alloys. *Metall. Mater. Trans. A Phys. Metall. Mater. Sci.* 46, 5972–5988. doi: 10.1007/s11661-015-3128-5

Abaspour, S., and Cáceres, C. H. (2016). High temperature strength and stress relaxation behavior of dilute binary Mg alloys. *Metall. Mater. Trans. A Phys. Metall. Mater. Sci.* 47, 1313–1321. doi: 10.1007/s11661-015-3292-7

Abaspour, S., Zambelli, V., Dargusch, M., and Cáceres, C. H. (2016). Atomic size and local order effects on the high temperature strength of binary Mg alloys. *Mater. Sci. Eng. A* 673, 114–121. doi: 10.1016/j.msea.2016.07.019

Abe, E., Kawamura, Y., Hayashi, K., and Inoue, A. (2002). Long-period ordered structure in a high-strength nanocrystalline Mg-1 at% Zn-2 at% Y alloy studied by atomic-resolution Z-contrast STEM. *Acta Mater.* 50, 3845–3857. doi: 10.1016/S1359-6454(02)00191-X

Abe, E., Ono, A., Itoi, T., Yamasaki, M., and Kawamura, Y. (2011). Polytypes of long-period stacking structures synchronized with chemical order in a dilute Mg-Zn-Y alloy. *Philos. Mag. Lett.* 91, 690–696. doi: 10.1080/09500839.2011.609149

Abe, E., Sato, T. J., and Tsai, A. P. (2000). Structure and phase transformation of the Zn-Mg-rare-earth quasicrystals. *Mater. Sci. Eng. A* 294–296, 29–32. doi: 10.1016/S0921-5093(00)01312-5

Agnew, S. R. (2012). "Advances in wrought magnesium alloys," in *Fundamentals of Processing, Properties and Applications*, eds C. Bettles and M. Barnett (Pittsburgh, PA: Woodhead Publishing), 63–104.

Agnew, S. R., Capolungo, L., and Calhoun, C. A. (2015). Connections between the basal I1 "growth" fault and <c+a> dislocations. *Acta Mater.* 82, 255–265. doi: 10.1016/j.actamat.2014.07.056

Akhtar, A., and Teghtsoonian, E. (1969). Solid solution strengthening of magnesium single crystals-I alloying behaviour in basal slip. *Acta Metall.* 17, 1339–1349. doi: 10.1016/0001-6160(69)90151-5

Albright, D. L., Bergeron, F., Neelameggham, R., Luo, A., Kaplan, H., and Pekguleryuz, M. O. (2002). Magnesium technology 2002, part II: wrought products, alloy processing, R&D strategies, corrosion, welding. *JOM* 54, 22–24. doi: 10.1007/BF02711862

Amberger, D., Eisenlohr, P., and Göken, M. (2009). Microstructural evolution during creep of Ca-containing AZ91. *Mater. Sci. Eng. A* 510–511, 398–402. doi: 10.1016/j.msea.2008.04.115

Amiya, K., Ohsuna, T., and Inoue, A. (2003). Long-period hexagonal structures in melt-spun Mg(97)Ln(2)Zn(1) (Ln=lanthanide metal) alloys. *Mater. Trans.* 44, 2151–2156. doi: 10.2320/matertrans.44.2151

Ando, S., Kodera, A., Yagi, T., and Tsushida, M. (2013). "Alloying effects on non-basal slips in magnesium single crystals," in *Materials Science and Technology Conference and Exhibition* (Montreal, CA), 1449–1454.

Avedesian, M., and Baker, H. (1999). *Magnesium and Magnesium Alloys, Handbook*. Cleveland, OH: ASM International.

Bader, R. F. W. (1990). *Atoms in Molecules: A Quantum Theory*. Oxford: Oxford University Press.

Bae, D. H., Kim, S. H., Kim, D. H., and Kim, W. T. (2002). Deformation behavior of Mg-Zn-Y alloys reinforced by icosahedral quasicrystalline particles. *Acta Mater.* 50, 2343–2356. doi: 10.1016/S1359-6454(02)00067-8

Bae, D. H., Kim, S. H., Kim, W. T., and Kim, D. H. (2001). High strength Mg-Zn-Y alloy containing quasicrystalline particles. *Mat. Transact.* 42, 2144–2147.

Balogh, L., Tichy, G., and Ungár, T. (2009). Twinning on pyramidal planes in hexagonal close packed crystals determined along with other defects by X-ray line profile analysis. *J. Appl. Crystallogr.* 42, 580–591. doi: 10.1107/S0021889809022936

Barnett, M. R., Keshavarz, Z., and Ma, X. (2006). A semianalytical Sachs model for the flow stress of a magnesium alloy. *Metall. Mater. Trans. A Phys. Metall. Mater. Sci.* 37, 2283–2293. doi: 10.1007/BF02586147

Bernstein, N., and Tadmor, E. B. (2004). Tight-binding calculations of stacking energies and twinnability in fcc metals. *Phys. Rev. B* 69, 1–10. doi: 10.1103/PhysRevB.69.094116

Blake, A. H., and Cáceres, C. H. (2008). Solid-solution hardening and softening in Mg-Zn alloys. *Mater. Sci. Eng. A* 483–484, 161–163. doi: 10.1016/j.msea.2006.10.205

Brain, I., and Knacke, O. (1973). *Thermochemical Properties of Inorganic Substances*. Berlin; New York, NY: Springer-Verlag.

Brewr, L. (1967). A most striking confirmation of engel metallic correlation. *Acta Metall.* 15, 553–560. doi: 10.1016/0001-6160(67)90088-0

Brown, D. W., Agnew, S. R., Bourke, M. A. M., Holden, T. M., Vogel, S. C., and Tom, C. N. (2005). Internal strain and texture evolution during deformation twinning in *magnesium. Mater. Sci. Eng. A* 399, 1–12. doi: 10.1016/j.msea.2005.02.016

Brown, D. W., Jain, A., Agnew, S. R., and Clausen, B. (2009). Twinning and detwinning during cyclic deformation of Mg alloy AZ31B. *Mater. Sci. Forum.* 539–543, 3407–3413. doi: 10.4028/www.scientific.net/MSF.539-543.3407

Buey, D., Hector, L. G., and Ghazisaeidi, M. (2018). Core structure and solute strengthening of second-order pyramidal <c+a> dislocations in Mg-Y alloys. *Acta Mater.* 147, 1–9. doi: 10.1016/j.actamat.2017.12.066

Cahn, R. W., and Davies, R. G. (1960). X-ray evidence for segregation of solute to stacking faults in a copper-aluminium alloy. *Philos. Mag.* 5, 1119–1126. doi: 10.1080/14786436008238320

Chai, Y., Jiang, B., Song, J., Wang, Q., He, J., Zhao, J., et al. (2018). Role of Al content on the microstructure, texture and mechanical properties of Mg-3.5Ca based alloys. *Mater. Sci. Eng. A* 730, 303–316. doi: 10.1016/j.msea.2018.06.011

Chang, C. F., Das, S. K., and Raybould, D. (1987). Rapidly solidified Mg-Al-Zn-rare earth alloys. *J. Mater. Eng.* 9, 141–146. doi: 10.1007/BF02833703

Chang, C. F., Das, S. K., Raybould, D., and Brown, A. (1986). Corrosion resistant high strength magnesium alloys by Rsp. *Metal. Powder Rep.* 41, 302–305.

Chapuis, A., and Driver, J. H. (2011). Temperature dependency of slip and twinning in plane strain compressed magnesium single crystals. *Acta Mater.* 59, 1986–1994. doi: 10.1016/j.actamat.2010.11.064

Chen, K., and Boyle, K. P. (2009). Elastic properties, thermal expansion coefficients, and electronic structures of Mg and Mg-based alloys. *Metall. Mater. Trans. A Phys. Metall. Mater. Sci.* 40, 2751–2760. doi: 10.1007/s11661-009-9954-6

Christian, J. W., and Mahajan, S. (1995). Deformation twinning. *Progr. Mater. Sci.* 39, 1–157. doi: 10.1016/0079-6425(94)00007-7

Cipoletti, D. E., Bower, A. F., and Krajewski, P. E. (2011). A microstructure-based model of the deformation mechanisms and flow stress during elevated-temperature straining of a magnesium alloy. *Scr. Mater.* 64, 931–934. doi: 10.1016/j.scriptamat.2010.12.033

Dai, X. D., Li, J. H., and Liu, B. X. (2007). Molecular statics calculation of the formation enthalpy for ternary metal systems based on the long-range empirical interatomic potentials. *Appl. Phys. Lett.* 90, 6–9. doi: 10.1063/1.2716361

Ding, Z., Liu, W., Li, S., Zhang, D., Zhao, Y., Lavernia, E. J., et al. (2016). Contribution of van der waals forces to the plasticity of magnesium. *Acta Mater.* 107, 127–132. doi: 10.1016/j.actamat.2016.01.026

Dong, Q., Luo, Z., Zhu, H., Wang, L., Ying, T., Jin, Z., et al. (2018). Basal-plane stacking-fault energies of Mg alloys: a first-principles study of metallic alloying effects. *J. Mater. Sci. Technol.* 34, 1773–1780. doi: 10.1016/j.jmst.2018.02.009

Dubois, J. M. (2012). Properties- and applications of quasicrystals and complex metallic alloys. *Chem. Soc. Rev.* 41, 6760–6777. doi: 10.1039/c2cs35110b

Egusa, D., and Abe, E. (2012). The structure of long period stacking/order Mg-Zn-RE phases with extended non-stoichiometry ranges. *Acta Mater.* 60, 166–178. doi: 10.1016/j.actamat.2011.09.030

Fan, H., Tang, J., Tian, X., Wang, Q., Tian, X., and El-Awady, J. A. (2017). Core structures and mobility of ⟩*c*⟨ dislocations in magnesium. *Scr. Mater.* 135, 37–40. doi: 10.1016/j.scriptamat.2017.03.012

Fan, T. W., Tang, B. Y., Peng, L. M., and Ding, W. J. (2011). First-principles study of long-period stacking ordered-like multi-stacking fault structures in pure magnesium. *Scr. Mater.* 64, 942–945. doi: 10.1016/j.scriptamat.2011.01.039

Ganeshan, S., Hector, L. G., and Liu, Z. K. (2011). First-principles calculations of impurity diffusion coefficients in dilute Mg alloys using the 8-frequency model. *Acta Mater.* 59, 3214–3228. doi: 10.1016/j.actamat.2011.01.062

Gao, Y., Wang, Q., Gu, J., Zhao, Y., Tong, Y., and Yin, D. (2009). Comparison of microstructure in Mg-10Y-5Gd-0.5Zr and Mg-10Y-5Gd-2Zn-0.5Zr alloys by conventional casting. *J. Alloys Compd.* 477, 374–378. doi: 10.1016/j.jallcom.2008.10.003

Garg, P., Adlakha, I., and Solanki, K. N. (2018). Effect of solutes on ideal shear resistance and electronic properties of magnesium: a first-principles study. *Acta Mater.* 153, 327–335. doi: 10.1016/j.actamat.2018.05.014

Gencheva, D. S., Katsnelson, A. A., Rokhlin, L. L., Silonov, V. M., and Khavadzha, F. A. (1981). Investigation of short-range order in magnesium alloys with erbium and gaolinium. *Fiz. Metal.* 51, 788–793.

Guan, D., Liu, X., Gao, J., Ma, L., Wynne, B. P., and Rainforth, W. M. (2019). Exploring the mechanism of "Rare Earth" texture evolution in a lean Mg–Zn–Ca alloy. *Sci Rep.* 9:7152. doi: 10.1038/s41598-019-43415-z

Guo, Z., Miodownik, A. P., Saunders, N., and Schillé, J. P. (2006). Influence of stacking-fault energy on high temperature creep of alpha titanium alloys. *Scr. Mater.* 54, 2175–2178. doi: 10.1016/j.scriptamat.2006.02.036

Ha, S.-H., Lee, J.-K., and Kim, S. K. (2008). Effect of CaO on oxidation resistance and microstructure of pure Mg. *Mater. Trans.* 49, 1081–1083. doi: 10.2320/matertrans.MC200786

Ha, S. H., Lee, J. K., Jo, H. H., Jung, S. B., and Kim, S. K. (2006). Effect of CaO addition on ignition behavior in molten AZ31 and AZ91D Magnesium alloys. *Rare Metals* 25, 150–154. doi: 10.1016/S1001-0521(08)60071-6

Hagihara, K., Kinoshita, A., Sugino, Y., Yamasaki, M., Kawamura, Y., Yasuda, H. Y., et al. (2010a). Effect of long-period stacking ordered phase on mechanical properties of Mg97Zn1Y2 extruded alloy. *Acta Mater.* 58, 6282–6293. doi: 10.1016/j.actamat.2010.07.050

Hagihara, K., Okamoto, T., Izuno, H., Yamasaki, M., Matsushita, M., Nakano, T., et al. (2016). Plastic deformation behavior of 10H-type synchronized LPSO phase in a Mg-Zn-Y system. *Acta Mater.* 109, 90–102. doi: 10.1016/j.actamat.2016.02.037

Hagihara, K., Yokotani, N., and Umakoshi, Y. (2010b). Plastic deformation behavior of Mg12YZn with 18R long-period stacking ordered structure. *Intermetallics* 18, 267–276. doi: 10.1016/j.intermet.2009.07.014

Halas, S. (2006). 100 years of work function. *Mater. Sci. Poland* 24, 20–31.

Hasegawa, S., Tsuchida, Y., Yano, H., and Matsui, M. (2007). Evaluation of low cycle fatigue life in AZ31 magnesium alloy. *Int. J. Fatigue* 29, 1839–1845. doi: 10.1016/j.ijfatigue.2006.12.003

Hehmann, F., Sommer, F., and Predel, B. (1990). Extension of solid solubility in magnesium by rapid solidification. *Mater. Sci. Eng. A* 125, 249–265. doi: 10.1016/0921-5093(90)90175-3

Henes, S., and Gerold, V. (1962). "Roentgenographic investigation of the separation process in magnesium-lead and magnesium-zinc alloys. II," in *The Separation of the Stable Equilibrium Phase (in German)*, ed Z. Metallk. 53, 46–51.

Holtzer, M., and Bobrowski, A. (2008). Magnesium melt protection by covering gas. *Arch. Found. Eng.* 8, 131–136.

Homma, T., Kunito, N., and Kamado, S. (2009). Fabrication of extraordinary high-strength magnesium alloy by hot extrusion. *Scr. Mater.* 61, 644–647. doi: 10.1016/j.scriptamat.2009.06.003

Hosford, W. F. (1993). *The Mechanics of Crystals and Textured Polycrystals. Materials Characterization*, Vol. 34. Oxford: Oxford University Press.

Houska, C. R., and Averbach, B. L. (1959). Neutron irradiation effects in a copper aluminum alloy. *J. Appl. Phys.* 81, 1525–1532. doi: 10.1063/1.1734994

Hu, W., Yang, Z., Liu, J., and Ye, H. (2016). "Creep of A Mg-Zn-Y alloy at elevated temperatures," in *Magnesium Technology* (Hoboken, NJ: John Wiley & Sons), 169–174.

Hua, G., and Li, D. (2011). Generic relation between the electron work function and young's modulus of metals. *Appl. Phys. Lett.* 99, 2011–2014. doi: 10.1063/1.3614475

Huang, Y. B., Chung, I. S., You, B. S., Park, W. W., and Choi, B. H. (2004). Effect of be addition on the oxidation behavior of mg-ca alloys at elevated temperature. *Met. Mater. Int.* 10, 7–11. doi: 10.1007/BF03027357

Huppmann, M., Lentz, M., Chedid, S., and Reimers, W. (2011). Analyses of deformation twinning in the extruded magnesium alloy AZ31 after compressive and cyclic loading. *J. Mater. Sci.* 46, 938–950. doi: 10.1007/s10853-010-4838-0

Iikubo, S., Hamamoto, S., and Ohtani, H. (2013). Thermodynamic analysis of the Mg–RE–Zn (RE = Y, La) ternary hcp phase using the cluster variation method. *Mater. Trans.* 54, 636–640. doi: 10.2320/matertrans.MI201222

Inoue, A., Kawamura, Y., Matsushita, M., Hayashi, K., and Koike, J. (2001). Novel hexagonal structure and ultrahigh strength of magnesium solid solution in the Mg–Zn–Y system. *J. Mater. Res.* 16, 1894–1900. doi: 10.1557/JMR.2001.0260

Itoi, T., Seimiya, T., Kawamura, Y., and Hirohashi, M. (2004). Long period stacking structures observed in Mg97Zn 1Y2 alloy. *Scr. Mater.* 51, 107–111. doi: 10.1016/j.scriptamat.2004.04.003

Iwatake, Y., Okamoto, N. L., Kishida, K., Inui, H., Ishida, J., Kai, T., et al. (2015). New crystal structure of Nd2Ni7 formed on the basis of stacking of block layers. *Int. J. Hydrogen Energ.* 40, 3023–3034. doi: 10.1016/j.ijhydene.2015.01.007

Jeong, J., Im, J., Song, K., Kwon, M., Kim, S. K., Kang, Y. B., et al. (2013). Transmission electron microscopy and thermodynamic studies of CaO-added AZ31 Mg alloys. *Acta Mater.* 61, 3267–3277. doi: 10.1016/j.actamat.2013.02.015

Jian, W. W., Cheng, G. M., Xu, W. Z., Yuan, H., Tsai, M. H., Wang, Q. D., et al. (2013). Ultrastrong Mg alloy via nano-spaced stacking faults. *Mater. Res. Lett.* 1, 61–66. doi: 10.1080/21663831.2013.765927

Jiang, Z., Jiang, B., Yang, H., Yang, Q., Dai, J., and Pan, F. (2015). Influence of the Al2Ca phase on microstructure and mechanical properties of Mg-Al-Ca alloys. *J. Alloys Compd.* 647, 357–363. doi: 10.1016/j.jallcom.2015.06.060

Jin, Q. Q., Fang, C. F., and Mi, S. B. (2013). Formation of long-period stacking ordered structures in Mg 88M5Y7 (M = Ti, Ni and Pb) casting alloys. *J. Alloys Compd.* 568, 21–25. doi: 10.1016/j.jallcom.2013.03.061

Jin, Z. H., Han, J., Su, X. M., and Zhu, Y. T. (2011). Basal-plane stacking-fault energies of Mg: a first-principles study of Li- and Al-alloying effects. *Scr. Mater.* 2, 121–128. doi: 10.1002/9781118062142.ch15

Kang, H., Choi, H. J., Kang, S. W., Shin, S. E., Choi, G. S., and Bae, D. H. (2016). Multi-functional magnesium alloys containing interstitial oxygen atoms. *Sci. Rep.* 6:23184. doi: 10.1038/srep23184

Kang, S. W., Kang, H., and Bae, D. H. (2017). Strengthening and toughening behaviors of a Mg-9Al alloy containing oxygen atoms. *J. Alloys Compd.* 725, 441–448. doi: 10.1016/j.jallcom.2017.07.190

Kang, S. W., Kang, H., Choi, H. J., and Bae, D. H. (2018). Phase boundary sliding of a reticular-structured Mg-O-9Al alloy. *J. Alloys Compd.* 750, 729–740. doi: 10.1016/j.jallcom.2018.04.039

Kawamura, Y., Hayashi, K., Inoue, A., and Masumoto, T. (2001). Rapidly solidified powder metallurgy Mg97Zn1Y2Alloys with excellent tensile yield strength above 600 MPa. *Mater Trans.* 42, 1172–1176. doi: 10.2320/matertrans.42.1172

Kawamura, Y., Kasahara, T., Izumi, S., and Yamasaki, M. (2006). Elevated temperature Mg97Y2Cu1 alloy with long period ordered structure. *Scr. Mater.* 55, 453–456. doi: 10.1016/j.scriptamat.2006.05.011

Kawamura, Y., and Yamasaki, M. (2007). Formation and mechanical properties of alloys with long-period stacking ordered structure. *Mater. Trans. Jpn Inst. Met.* 48, 2986–2992. doi: 10.2320/matertrans.MER2007142

Kaya, A. A., Yucel, O., Eliezer, D., and Aghion, E. (2003). "An electron microscopy investigation on as-cast AZ91D alloy modified with nitrogen," in *Magnesium, The 6th International Conference on Magnesium Alloys and Their Application,* ed K. U. Kainer (Wolfsburg: Wiley-VCH), 150–157.

Kim, H., Ross, A. J., Shang, S. L., Wang, Y., Kecskes, L. J., and Liu, Z. K. (2018a). First-principles calculations and thermodynamic modelling of long periodic stacking ordered (LPSO) phases in Mg-Al-Gd. *Materialia* 4, 192–202. doi: 10.1016/j.mtla.2018.09.013

Kim, H., Wang, W. Y., Shang, S. L., Kecskes, L. J., Darling, K. A., and Liu, Z. K. (2018b). Elastic properties of long periodic stacking ordered phases in Mg-Gd-Al alloys: a first-principles study. *Intermetallics* 98, 18–27. doi: 10.1016/j.intermet.2018.04.009

Kim, J. K., Jin, L., Sandlöbes, S., and Raabe, D. (2017). Diffusional-displacive transformation enables formation of long-period stacking order in magnesium. *Sci. Rep.* 7:4046. doi: 10.1038/s41598-017-04343-y

Kim, J. K., Ko, W. S., Sandlöbes, S., Heidelmann, M., Grabowski, B., and Raabe, D. (2016). The role of metastable LPSO building block clusters in phase transformations of an Mg-Y-Zn alloy. *Acta Mater.* 112, 171–183. doi: 10.1016/j.actamat.2016.04.016

Kim, K. H., Jeon, J. B., Kim, N. J., and Lee, B. J. (2015). Role of yttrium in activation of "c + a" slip in magnesium: an atomistic approach. *Scr. Mater.* 108, 104–108. doi: 10.1016/j.scriptamat.2015.06.028

Kim, S. H., and Park, S. H. (2018). Underlying mechanisms of drastic reduction in yield asymmetry of extruded Mg-Sn-Zn alloy by Al addition. *Mater. Sci. Eng. A* 733, 285–290. doi: 10.1016/j.msea.2018.07.063

Kim, S. K. (2011). "Design and development of high-performance eco-mg alloys," in *Design, Processing and Properties*, ed Czerwinski, F. IntechOpen. Available online at: https://www.intechopen.com/books/magnesium-alloys-design-processing-and-properties/design-and-development-of-high-performance-eco-mg-alloys (accessed January 14, 2011).

Kim, S. K., Lee, J. K., Yoon, Y. O., and Jo, H. H. (2007). Development of AZ31 Mg alloy wrought process route without protective gas. *J. Mater. Process. Technol.* 187–188, 757–760. doi: 10.1016/j.jmatprotec.2006.11.172

Kimizuka, H., Fronzi, M., and Ogata, S. (2013). Effect of alloying elements on in-plane ordering and disordering of solute clusters in Mg-based long-period stacking ordered structures: a first-principles analysis. *Scr. Mater.* 69, 594–597. doi: 10.1016/j.scriptamat.2013.07.003

Kimizuka, H., and Ogata, S. (2013). Predicting atomic arrangement of solute clusters in dilute Mg alloys. *Mater. Res. Lett.* 1, 213–219. doi: 10.1080/21663831.2013.838705

Kishida, K., Nagai, K., Matsumoto, A., Yasuhara, A., and Inui, H. (2015). Crystal structures of highly-ordered long-period stacking-ordered phases with 18 R, 14 H and 10 H -type stacking sequences in the Mg–Zn–Y system. *Acta Mater.* 99, 228–239. doi: 10.1016/j.actamat.2015.08.004

Kishida, K., Yokobayashi, H., and Inui, H. (2013). The most stable crystal structure and the formation processes of an order-disorder (OD) intermetallic phase in the Mg-Al-Gd ternary system. *Philos. Mag.* 93, 2826–2846. doi: 10.1080/14786435.2013.790566

Kishida, K., Yokobayashi, H., and Inui, H. (2017). A formation criterion for order-disorder (OD) phases of the long-period stacking order (LPSO)-type in Mg-Al-RE (Rare Earth) ternary systems. *Sci. Rep.* 7:12294. doi: 10.1038/s41598-017-12506-0

Kishida, K., Yokobayashi, H., Inui, H., Yamasaki, M., and Kawamura, Y. (2012). The crystal structure of the LPSO phase of the 14H-type in the Mg-Al-Gd alloy system. *Intermetallics* 31, 55–64. doi: 10.1016/j.intermet.2012.06.010

Kondoh, K., Fujita, J., Umeda, J., Imai, H., Enami, K., Ohara, M., et al. (2011). Thermo-dynamic analysis on solid-state reduction of CaO particles dispersed in Mg-Al alloy. *Mater. Chem. Phys.* 129, 631–640. doi: 10.1016/j.matchemphys.2011.05.017

Kounis, A., Miehe, G., and Fuess, H. (2000). Investigation of icosahedral phases in the Zn-Mg-(Y, Er) system by high resolution transmission electron microscopy. *Mater. Sci. Eng. A* 294–296, 323–326. doi: 10.1016/S0921-5093(00)01182-5

Kumari, M., and Verma, U. P. (2018). Full potential study of HoMg. *J. Magnes. Alloy* 6, 189–196. doi: 10.1016/j.jma.2018.03.002

Lee, J.-K., and Kim, S. K. (2011b). Effect of CaO addition on the ignition resistance of Mg-Al alloys. *Mater. Trans.* 52, 1483–1488. doi: 10.2320/matertrans.M2010397

Lee, J. B., Sato, K., Konno, T. J., and Hiraga, K. (2011). Complex precipitates with long periodic stacking (LPS) phase and precipitation behaviors in the Mg97Zn1Y 1.5Nd0.5 alloy by age-annealing. *Intermetallics* 19, 1096–1101. doi: 10.1016/j.intermet.2010.12.003

Lee, J. K., and Kim, S. K. (2009a). Development of novel environment-friendly magnesium alloys. *Adv. Mater. Res.* 47–50, 940–943. doi: 10.4028/www.scientific.net/AMR.47-50.940

Lee, J. K., and Kim, S. K. (2009b). Thermodynamic consideration of CaO added Mg alloys in recycling process. *Mater. Sci. Forum.* 620–622, 615–618. doi: 10.4028/www.scientific.net/MSF.620-622.615

Lee, J. K., and Kim, S. K. (2011a). Effect of CaO composition on oxidation and burning behaviors of AM50 Mg alloy. *Trans. Nonferr. Metals Soc. China* 21, s23–s27. doi: 10.1016/S1003-6326(11)61054-6

Li, N., Huang, G., Zhong, X., and Liu, Q. (2013). Deformation mechanisms and dynamic recrystallization of AZ31 Mg alloy with different initial textures during hot tension. *Mater. Des.* 50, 382–391. doi: 10.1016/j.matdes.2013.03.028

Li, X. K., Jiang, B., and Liao, J. C. (2010). Effects of Al and Ca on microstructure and surface defect of magnesium alloy thin strip. *Trans. Nonferr. Metals Soc. China* 20, s361–s365. doi: 10.1016/S1003-6326(10)60498-0

Li, Y., and Kong, Q. P. (1989). Creep rate and stacking fault energy. *Phys. Stat. Sol. A* 113, 345–351. doi: 10.1002/pssa.2211130212

Li, Y., Yang, C., Zeng, X., Jin, P., Qiu, D., and Ding, W. (2018). Microstructure evolution and mechanical properties of magnesium alloys containing long period stacking ordered phase. *Mater. Charact.* 141, 286–295. doi: 10.1016/j.matchar.2018.04.044

Liao, X. Z., Srinivasan, S. G., Zhao, Y. H., Baskes, M. I., Zhu, Y. T., Zhou, F., et al. (2004). Formation mechanism of wide stacking faults in nanocrystalline Al. *Appl. Phys. Lett.* 84, 3564–3566. doi: 10.1063/1.1734689

Liu, G., Zhang, J., Xi, G., Zuo, R., and Liu, S. (2017). Designing Mg alloys with high ductility: reducing the strength discrepancies between soft deformation modes and hard deformation modes. *Acta Mater.* 141, 1–9. doi: 10.1016/j.actamat.2017.09.006

Liu, X. B., Chen, R. S., and Han, E. H. (2008). Effects of ageing treatment on microstructures and properties of Mg-Gd-Y-Zr alloys with and without Zn additions. *J. Alloys Compd.* 465, 232–238. doi: 10.1016/j.jallcom.2007.10.068

Liu, Z. R., and Li, D. Y. (2015). The electronic origin of strengthening and ductilizing magnesium by solid solutes. *Acta Mater.* 89, 225–233. doi: 10.1016/j.actamat.2015.01.051

Lu, H., Li, L., Huang, X., and Li, D. (2018). An electron work function based mechanism for solid solution hardening. *J. Alloys Compd.* 737, 323–329. doi: 10.1016/j.jallcom.2017.12.065

Luo, A. A., Powell, B. R., and Balogh, M. P. (2007). Creep and microstructure of magnesium-aluminum-calcium based alloys. *Metall. Mater. Trans. A* 33, 567–574. doi: 10.1007/s11661-002-0118-1

Luo, Z., Zhang, S., Tang, Y., and Zhao, D. (1993). Quasicrystals in as-cast Mg-Zn-RE alloys. *Scr. Metall. Mater.* 28, 1513–1518. doi: 10.1016/0956-716X(93)90584-F

Luo, Z. P., Zhang, S. Q., Tang, Y. L., Zhao, D. S. (1994). Microstructures of Mg-Zn-Zr-RE alloys with high RE and low ZN contents. *J. Alloy. Compd.* 209, 275–278.

Lv, B. J., Peng, J., Zhu, L., Wang, Y. J., and Tang, A. T. (2014). The effect of 14H LPSO phase on dynamic recrystallization behavior and hot workability of Mg-2.0Zn-0.3Zr-5.8Y alloy. *Mater. Sci. Eng. A* 599, 150–159. doi: 10.1016/j.msea.2014.01.079

Mann, G. E., Sumitomo, T., and Griffiths, J. R. (2007). Reversible plastic strain during cyclic loading – unloading of Mg and Mg – Zn *alloys. Mater. Sci. Eng. A* 456, 138–146. doi: 10.1016/j.msea.2006.11.160

Masoumi, M., Hoseini, M., and Pekguleryuz, M. (2011). The influence of Ce on the microstructure and rolling texture of Mg-1%Mn alloy. *Mater. Sci. Eng. A* 528, 3122–3129. doi: 10.1016/j.msea.2010.12.096

Matsuda, M., Ii, S., Kawamura, Y., Ikuhara, Y., and Nishida, M. (2005). Variation of long-period stacking order structures in rapidly solidified Mg97Zn1Y2 alloy. *Mater. Sci. Eng. A* 393, 269–274. doi: 10.1016/j.msea.2004.10.040

Mi, S. B., and Jin, Q. Q. (2013). New polytypes of long-period stacking ordered structures in Mg-Co-Y alloys. *Scr. Mater.* 68, 635–638. doi: 10.1016/j.scriptamat.2012.12.025

Miedema, A. R. (1973a). A simple model for Alloys-I. rules for the alloying behaviour of transition metals. *Philips Techn. Rev.* 33, 149–160.

Miedema, A. R. (1973b). A simple model for Alloys- II. the influence of ionicity on the stability and other physical properties of alloys. *Philips Tech. Rev.* 33, 196–202.

Miedema, A. R. (1973c). The electronegativity parameter for transition metals: heat of formation and charge transfer in alloys. *J. Less-Common Metals* 32, 117–136. doi: 10.1016/0022-5088(73)90078-7

Miedema, A. R., Boom, R., and de Boer, F. R. (1975). On the heat of formations of solid alloys. *J. Less Common Metals* 41, 283–298. doi: 10.1016/0022-5088(75)90034-X

Min, X. (2003). Analysis of EET on Ca increasing the melting point of Mg17Al12 phase. *Chin. Sci. Bull.* 47, 1082–1086. doi: 10.1360/02tb9243

Moitra, A., Kim, S. G., and Horstemeyer, M. F. (2014). Solute effect on basal and prismatic slip systems of Mg. *J. Phys. Condensed Matter*. 26:445004. doi: 10.1088/0953-8984/26/44/445004

Muzyk, M., Pakiela, Z., and Kurzydlowski, K. J. (2012). Generalized stacking fault energy in magnesium alloys: density functional theory calculations. *Scr. Mater.* 66, 219–222. doi: 10.1016/j.scriptamat.2011.10.038

Nam, N. D., Bian, M. Z., Forsyth, M., Seter, M., Tan, M., and Shin, K. S. (2012). Effect of calcium oxide on the corrosion behaviour of AZ91 magnesium alloy. *Corros. Sci.* 64, 263–271. doi: 10.1016/j.corsci.2012.07.026

Nan, X. L., Wang, H. Y., Zhang, L., Li, J. B., and Jiang, Q. C. (2012). Calculation of schmid factors in magnesium: analysis of deformation behaviors. *Scr. Mater.* 67, 443–446. doi: 10.1016/j.scriptamat.2012.05.042

Narita, K., Koyama, T., and Tsukada, Y. (2013). Phase-field simulation of spinodal decomposition on metastable hexagonal close-packed phase in magnesium–Yttrium–Zinc Alloy. *Mater. Trans.* 54, 661–667. doi: 10.2320/matertrans.MI201212

Nie, A. J. F., Zhu, Y. M., Liu, J. Z., and Fang, X. Y. (2019). Periodic segregation of solute atoms in fully coherent twin boundaries. *Science* 340, 957–960.

Nie, J. F. (2012). Precipitation and hardening in magnesium alloys. *Metall. Mater. Trans. A Phys. Metall. Mater. Sci.* 43, 3891–3939. doi: 10.1007/s11661-012-1217-2

Nie, J. F., Gao, X., and Zhu, S. M. (2005). Enhanced age hardening response and creep resistance of Mg-Gd alloys containing Zn. *Scr. Mater.* 53, 1049–1053. doi: 10.1016/j.scriptamat.2005.07.004

Nie, J. F., Zhu, Y. M., Liu, J. Z., and Fang, X. Y. (2013). Periodic segregation of solute atoms in fully coherent twin boundaries. *Science* 340, 957–960. doi: 10.1126/science.1229369

Nie, J. F., Zhu, Y. M., and Morton, A. J. (2014). On the structure, transformation and deformation of long-period stacking ordered phases in Mg-Y-Zn alloys. *Metall. Mater. Trans. A Phys. Metall. Mater. Sci.* 45, 3338–3348. doi: 10.1007/s11661-014-2301-6

Ninomiya, R., Ojiro, T., and Kubota, K. (1995). Improved heat resistance of Mg-Al alloys by the Ca addition. *Acta Metall. Mater.* 43, 669–674. doi: 10.1016/0956-7151(94)00269-N

Nishijima, M., Hiraga, K., Yamasaki, M., and Kawamura, Y. (2007). The structure of guinier-preston zones in an Mg-2 at%Gd-1 at%Zn alloy studied by transmission electron microscopy. *Mater. Trans.* 49, 227–229. doi: 10.2320/matertrans.MEP2007257

Obara, T., Yoshinga, H., and Morozumi, S. (1973). Pyramidal slip system in magnesium. *Acta Metall.* 21, 837–1028. doi: 10.1016/0001-6160(73)90141-7

Oh, J. C., Ohkubo, T., Mukai, T., and Hono, K. (2005). TEM and 3DAP characterization of an age-hardened Mg-Ca-Zn alloy. *Scr. Mater.* 53, 675–679. doi: 10.1016/j.scriptamat.2005.05.030

Okamoto, N. L., Yasuhara, A., and Inui, H. (2014). Order-disorder structure of the δ1kphase in the Fe-Zn system determined by scanning transmission electron microscopy. *Acta Mater.* 81, 345–357. doi: 10.1016/j.actamat.2014.08.025

Oñorbe, E., Garcés, G., Pérez, P., and Adeva, P. (2012). Effect of the LPSO volume fraction on the microstructure and mechanical properties of Mg-Y 2X -Zn X alloys. *J. Mater. Sci.* 47, 1085–1093. doi: 10.1007/s10853-011-5899-4

Pauling, L. (1960). *The Nature of the Chemical Bond, 3rd Edn.* Ithaca, NY: Cornell University Press.

Pei, Z., Friák, M., Sandlöbes, S., Nazarov, R., Svendsen, B., Raabe, D., et al. (2015). Rapid theory-guided prototyping of ductile Mg alloys: from binary to multi-component materials. *N. J. Phys.* 17:93009. doi: 10.1088/1367-2630/17/9/093009

Pekguleryuz, M. (2013). "Alloying behavior of magnesium and alloy design," in *Fundamentals of Magnesium Alloy Metallurgy, 1st Edn.*, eds A. A. Pekgleryuz, M. Kainer, and K. U. Kaya (Philadelphia: Woodhead Publishing), 152–196.

Pekguleryuz, M. O., Kaplan, H., Neelameggham, R., Hryn, J., Nyberg, E., Powell, B., et al. (2002). Magnesium technology 2002, part I: primary production, environmental issues, high-temperature alloys. *JOM* 54, 18–21. doi: 10.1007/BF02711861

Peng, J. Z., Wang, Y. F., and Gray, M. F. (2008). First-principles study of structural stabilities and electronic properties of Mg-Nd intermetallic compounds. *Phys. Condensed Matter.* 403, 2344–2348. doi: 10.1016/j.physb.2007.12.016

Pilling, N. B., and Bedworth, R. E. (1923). The oxidation of metals at high temperatures. *J. Inst. Metals.* 29, 529–582.

Ping, D.-H., Hono, K., and Nie, J. F. (2003). Atom probe characterization of plate-like precipitates in a Mg–RE–Zn–Zr casting alloy. *Scri. Mater.* 48, 1017–1022. doi: 10.1016/S1359-6462(02)00586-9

Ping, D. H., Hono, K., Kawamura, Y., and Inoue, A. (2002). Local chemistry of a nanocrystalline high-strength Mg97Y2Zn1 alloy. *Philos. Mag. Lett.* 82, 543–551. doi: 10.1080/0950083021000018652

Pugh, S. F. (1954). XCII. Relations between the elastic moduli and the plastic properties of polycrystalline pure metals. *Lond Edinburgh Dublin Philos. Mag. J. Sci.* 45, 823–843. doi: 10.1080/14786440808520496

Rafiei, S., Habibollahzadeh, A., and Wiese, B. (2018). "An insight into environment-conscious (ECO) magnesium : a review 1- introduction 2- CaO dissolution," in *IMAT 2018, 7th International Conference on Materials Engineering and Metallurgy* (Tehran: MDRO), 1–10.

Ramsdell, L. S. (1947). Studies on silicon carbide. *Am. Min.* 32:64.

Raynor, G. V. (1959). *The Physical Metallurgy of Magnesium and its Alloys,* Vol. 5. New York, NY: Pergamon Press.

Safranova, L. A., Kastnelson, A. A., Sveshnikov, S. V., L'Vov, S. V., and Yu, M. (1977). Short-range order in Mg-In solid solutions. *Fiz. Metall.* 43, 76–80.

Saito, K., Nishijima, M., and Hiraga, K. (2010). Stabilization of guinier-preston zones in hexagonal close-packed Mg-Gd-Zn alloys studied by transmission electron microscopy. *Mater. Trans.* 51, 1712–1714. doi: 10.2320/matertrans.M2010173

Sakamoto, M., Akiyama, S., and Ogi, K. (1997). Suppression of ignition and burning of molten Mg alloys by Ca bearing stable oxide film. *J. Mater. Sci. Lett.* 16, 1048–1050. doi: 10.1023/A:1018526708423

Sandlöbes, S., Friák, M., Zaefferer, S., Dick, A., Yi, S., Letzig, D., et al. (2012). The relation between ductility and stacking fault energies in Mg and Mg-Y alloys. *Acta Mater.* 60, 3011–3021. doi: 10.1016/j.actamat.2012.02.006

Sandlöbes, S., Pei, Z., Friák, M., Zhu, L. F., Wang, F., Zaefferer, S., et al. (2014). Ductility improvement of Mg alloys by solid solution: Ab initio modeling, synthesis and mechanical properties. *Acta Mater.* 70, 92–104. doi: 10.1016/j.actamat.2014.02.011

Sandlöbes, S., Zaefferer, S., Schestakow, I., Yi, S., and Gonzalez-Martinez, R. (2011). On the role of non-basal deformation mechanisms for the ductility of Mg and Mg-Y alloys. *Acta Mater.* 59, 429–439. doi: 10.1016/j.actamat.2010.08.031

Sato, K., Tashiro, S., Matsunaga, S., Yamaguchi, Y., Kiguchi, T., and Konno, T. J. (2018). Evolution of long-period stacking order (LPSO) in Mg97Zn1Gd2 cast alloys viewed by HAADF-STEM multi-scale electron tomography. *Philos. Mag.* 98, 1945–1960. doi: 10.1080/14786435.2018.1468940

Shang, S. L., Wang, W. Y., Zhou, B. C., Wang, Y., Darling, K. A., Kecskes, L. J., et al. (2014). Generalized stacking fault energy, ideal strength and twinnability of dilute Mg-based alloys: a first-principles study of shear deformation. *Acta Mater.* 67, 168–180. doi: 10.1016/j.actamat.2013.12.019

Shechtman, D., Blech, I., Gratias, D., and Cahn, J. W. (1984). Metallic phase with longrange orientational order and no translational symmetry. *Phys. Rev. Lett.* 53, 1951–1953. doi: 10.1103/PhysRevLett.53.1951

Somekawa, H., Singh, A., Inoue, T., and Tsuzaki, K. (2014). Crack propagation behaviour in magnesium binary alloys. *Philos. Mag.* 94, 3317–3330. doi: 10.1080/14786435.2014.956840

Somekawa, H., Watanabe, H., Basha, D. A., Singh, A., and Inoue, T. (2017). Effect of twin boundary segregation on damping properties in magnesium alloy. *Scr. Mater.* 129, 35–38. doi: 10.1016/j.scriptamat.2016.10.019

Stanford, N. (2010). The effect of calcium on the texture, microstructure and mechanical properties of extruded Mg-Mn-Ca alloys. *Mater. Sci. Eng. A* 528, 314–322. doi: 10.1016/j.msea.2010.08.097

Stanford, N., Marceau, R. K. W., and Barnett, M. R. (2015). The effect of high yttrium solute concentration on the twinning behaviour of magnesium alloys. *Acta Mater.* 82, 447–456. doi: 10.1016/j.actamat.2014.09.022

Styczynski, A., Hartig, C., Bohlen, J., and Letzig, D. (2004). Cold rolling textures in AZ31 wrought magnesium alloy. *Scr. Mater.* 50, 943–947. doi: 10.1016/j.scriptamat.2004.01.010

Sumitomo, T., Veidt, M., and Ca, C. H. (2003). Pseudoelastic behaviour of cast magnesium AZ91 alloy under cyclic loading – *unloading. Acta Mater*. 51, 6211–6218. doi: 10.1016/S1359-6454(03)00444-0

Sun, S. P., Yi, D. Q., Jiang, Y., Zang, B., Xu, C. H., and Li, Y. (2011). An improved atomic size factor used in miedema's model for binary transition metal systems. *Chem. Phys. Lett.* 513, 149–153. doi: 10.1016/j.cplett.2011.07.076

Suzuki, A., Saddock, N. D., Jones, J. W., and Pollock, T. M. (2004). Structure and transition of eutectic (mg,al)2ca laves phase in a die-cast mg-al-ca base alloy. *Scr. Mater.* 51, 1005–1010. doi: 10.1016/j.scriptamat.2004.07.011

Suzuki, A., Saddock, N. D., TerBush, J. R., Powell, B. R., Jones, J. W., and Pollock, T. M. (2008). Precipitation strengthening of a Mg-Al-Ca - based AXJ530 die-cast alloy. *Metall. Mater. Trans. A Phys. Metall. Mater. Sci.* 39, 696–702. doi: 10.1007/s11661-007-9455-4

Suzuki, H. (1962). Segregation of solute atoms to stacking faults. *J. Phys. Soc. Jpn.* 17, 322–325. doi: 10.1143/JPSJ.17.322

Tane, M., Kimizuka, H., Hagihara, K., Suzuki, S., Mayama, T., Sekino, T., et al. (2015). Effects of stacking sequence and short-range ordering of solute atoms on elastic properties of Mg-Zn-Y alloys with long-period stacking ordered structures. *Acta Mater.* 96, 170–188. doi: 10.1016/j.actamat.2015.06.005

Terada, Y., Ishimatsu, N., Mori, Y., and Sato, T. (2005). Eutectic phase investigation in a Ca-added AM50 magnesium alloy produced by die casting. *Mater. Trans.* 46, 145–147. doi: 10.2320/matertrans.46.145

Tsuru, T., and Chrzan, D. C. (2015). Effect of solute atoms on dislocation motion in Mg: an electronic structure perspective. *Sci. Rep.* 5:8793. doi: 10.1038/srep08793

Uesugi, T., Kohyama, M., Kohzu, M., and Higashi, K. (2009). Generalized stacking fault energy and dislocation properties for various slip systems in magnesium: a first-principles study. *Mater. Sci. Forum.* 419–422, 225–230. doi: 10.4028/www.scientific.net/MSF.419-422.225

van der Planken, J., and Deruyttere, A. (1969). Solution hardening of magnesium single crystals by tin at room temperature. *Acta Metall.* 17, 451–454. doi: 10.1016/0001-6160(69)90026-1

Van Swygenhoven, H., Derlet, P. M., and Frøseth, A. G. (2004). Stacking fault energies and slip in nanocrystalline metals. *Nat. Mater.* 3, 399–403. doi: 10.1038/nmat1136

Vitek, V. (1968). Intrinsic stacking faults in body-centered cubic. *Acta Metall. Sinica* 18, 773–786. doi: 10.1080/14786436808227500

Waber, J. T., Gschneidner, K. Jr., Larson, A. C., Prince, M. Y. (1963). Prediction of solid solubility in metallic alloys. *Trans. Metal. Soc. AlME* 227, 717–723.

Wang, C., Zhang, H. Y., Wang, H. Y., Liu, G. J., and Jiang, Q. C. (2013). Effects of doping atoms on the generalized stacking-fault energies of Mg alloys from first-principles calculations. *Scr. Mater.* 69, 445–448. doi: 10.1016/j.scriptamat.2013.05.026

Wang, F., Sun, S. J., Yu, B., Zhang, F., Mao, P. L., and Liu, Z. (2016). First principles investigation of binary intermetallics in Mg-Al-Ca-Sn alloy: stability, electronic structures, elastic properties and thermodynamic properties. *Trans. Nonferr. Metals Soc. China* 26, 203–212. doi: 10.1016/S1003-6326(16)64107-9

Wang, H. Y., Zhang, N., Wang, C., and Jiang, Q. C. (2011). First-principles study of the generalized stacking fault energy in Mg-3Al-3Sn alloy. *Scr. Mater.* 65, 723–726. doi: 10.1016/j.scriptamat.2011.07.016

Wang, J., Hirth, J. P., and Tomé, C. N. (2009). (1 0 1 2) Twinning nucleation mechanisms in hexagonal-close-packed crystals. *Acta Mater.* 57, 5521–5530. doi: 10.1016/j.actamat.2009.07.047

Wang, Q., Chen, J., Zhao, Z., and He, S. (2010). Microstructure and super high strength of cast Mg-8.5Gd-2.3Y-1.8Ag-0.4Zr alloy. *Mater. Sci. Eng. A* 528, 323–328. doi: 10.1016/j.msea.2010.09.004

Wang, T., Jiang, L., Mishra, R. K., and Jonas, J. J. (2014). Effect of Ca addition on the intensity of the rare earth texture component in extruded magnesium alloys. *Metall. Mater. Trans. A Phys. Metall. Mater. Sci.* 45, 4698–4709. doi: 10.1007/s11661-014-2371-5

Wang, W. Y., Shang, S. L., Wang, Y., Darling, K. A., Mathaudhu, S. N., Hui, X. D., et al. (2012). Electron localization morphology of the stacking faults in Mg: a first-principles study. *Chem. Phys. Lett.* 551, 121–125. doi: 10.1016/j.cplett.2012.09.028

Wang, W. Y., Shang, S. L., Wang, Y., Mei, Z. G., Darling, K. A., Kecskes, L. J. et al. (2014). Effects of alloying elements on stacking fault energies and electronic structures of binary Mg alloys: a first-principles study. *Mater. Res. Lett.* 2, 29–36. doi: 10.1080/21663831.2013.858085

Wang, Y. F., Zhang, W. B., Wang, Z. Z., Deng, Y. H., Yu, N., Tang, B. Y., et al. (2007). First-principles study of structural stabilities and electronic characteristics of Mg-La intermetallic compounds. *Comput. Mater. Sci.* 41, 78–85. doi: 10.1016/j.commatsci.2007.03.003

Weinert, N. C. M. (1997). Stacking fualts in magnesium. *Phys. Rev. B* 56, 844–851. doi: 10.1103/PhysRevB.56.10844

Wen, L., Chen, P., Tong, Z. F., Tang, B. Y., Peng, L. M., and Ding, W. J. (2009). A systematic investigation of stacking faults in magnesium via first-principles calculation. *Eur. Phys. J. B* 72, 397–403. doi: 10.1140/epjb/e2009-00365-2

Wiese, B., Mendis, C. L., Tolnai, D., Stark, A., Schell, N., Reichel, H. P., et al. (2015). CaO dissolution during melting and solidification of a Mg-10 wt.% CaO alloy detected with *in situ* synchrotron radiation diffraction. *J. Alloys Compd.* 618, 64–66. doi: 10.1016/j.jallcom.2014.08.151

Witte, F. (2015). Reprint of: the history of biodegradable magnesium implants: a review. *Acta Biomater.* 23, S28–S40. doi: 10.1016/j.actbio.2015.07.017

Wu, L., Jain, A., Brown, D. W., Stoica, G. M., Agnew, S. R., Clausen, B., et al. (2008). Twinning-detwinning behavior during the strain-controlled low-cycle fatigue testing of a wrought magnesium alloy, ZK60A. *Acta Mater.* 56, 688–695. doi: 10.1016/j.actamat.2007.10.030

Wu, X. L., Youssef, K. M., Koch, C. C., Mathaudhu, S. N., Kecskés, L. J., and Zhu, Y. T. (2011). Deformation twinning in a nanocrystalline hcp Mg alloy. *Scr. Mater.* 64, 213–216. doi: 10.1016/j.scriptamat.2010.10.024

Wu, Y. F., Li, S., Ding, Z. G., Liu, W., Zhao, Y. H., and Zhu, Y. T. (2016). Effect of charge redistribution factor on stacking-fault energies of Mg-based binary alloys. *Scr. Mater.* 112, 101–105. doi: 10.1016/j.scriptamat.2015.09.023

Xu, C., Zheng, M. Y., Xu, S. W., Wu, K., Wang, E. D., Kamado, S., et al. (2012). Ultra high-strength Mg-Gd-Y-Zn-Zr alloy sheets processed by large-strain hot rolling and ageing. *Mater. Sci. Eng. A* 547, 93–98. doi: 10.1016/j.msea.2012.03.087

Xu, D., Han, E. H., and Xu, Y. (2016). Effect of long-period stacking ordered phase on microstructure, mechanical property and corrosion resistance of Mg alloys: a review. *Progr. Nat. Sci. Mater. Int.* 26, 117–128. doi: 10.1016/j.pnsc.2016.03.006

Yadav, T. P., and Mukhopadhyay, N. K. (2018). Quasicrystal: a low-frictional novel material. *Curr. Opin. Chem. Eng.* 19, 163–169. doi: 10.1016/j.coche.2018.03.005

Yang, K. V., Cáceres, C. H., and Easton, M. A. (2014). Strengthening micromechanisms in cold-chamber high-pressure Die-Cast Mg-Al alloys. *Metall. Mater. Trans. A Phys. Metall. Mater. Sci.* 45, 4117–4128. doi: 10.1007/s11661-014-2326-x

Yasi, J. A., Hector, L. G., and Trinkle, D. R. (2010). First-principles data for solid-solution strengthening of magnesium: from geometry and chemistry to properties. *Acta Mater.* 58, 5704–5713. doi: 10.1016/j.actamat.2010.06.045

Yasi, J. A., Hector, L. G., and Trinkle, D. R. (2011). Prediction of thermal cross-slip stress in magnesium alloys from direct first-principles data. *Acta Mater.* 59, 5652–5660. doi: 10.1016/j.actamat.2011.05.040

Yin, B., Wu, Z., and Curtin, W. A. (2017). First-principles calculations of stacking fault energies in Mg-Y, Mg-Al and Mg-Zn alloys and implications for<c+a> activity. *Acta Mater.* 136, 249–261. doi: 10.1016/j.actamat.2017.06.062

Yokobayashi, H., Kishida, K., Inui, H., Yamasaki, M., and Kawamura, Y. (2011a). Enrichment of Gd and Al atoms in the quadruple close packed planes and their in-plane long-range ordering in the long period stacking-ordered phase in the Mg-Al-Gd system. *Acta Mater.* 59, 7287–7299. doi: 10.1016/j.actamat.2011.08.011

Yokobayashi, H., Kishida, K., Inui, H., Yamasaki, M., and Kawamura, Y. (2011b). Structure analysis of a long period stacking ordered phase in Mg-Al-Gd alloys. *Mater. Res. Soc. Symp. Proc.* 1295, 267–272. doi: 10.1557/opl.2011.36

Yoo, M. H. (1981). Slip, twinning and fracture in hexagonal close-packed metals. *Metall. Trans. A* 12A, 409–418. doi: 10.1007/BF02648537

Yoo, M. H., and Lee, J. K. (1991). Deformation twinning in h.c.p. metals and alloys. *Phil. Mag. A* 5, 987–1000. doi: 10.1080/01418619108213931

You, B. S., Park, W. W., and Chung, I. S. (2000). Effect of calcium additions on the oxidation behavior in magnesium alloys. *Scr. Mater.* 42, 1089–1094. doi: 10.1016/S1359-6462(00)00344-4

Yu, Q., Jiang, Y., and Wang, J. (2015). Cyclic deformation and fatigue damage in single-crystal magnesium under fully reversed strain-controlled tension-compression in the [1010] direction. *Scr. Mater.* 96, 41–44. doi: 10.1016/j.scriptamat.2014.10.020

Yu, Q., Qi, L., Chen, K., Mishra, R. K., Li, J., and Minor, A. M. (2012). The nanostructured origin of deformation twinning. *Nano Lett.* 12, 887–892. doi: 10.1021/nl203937t

Yu, Q., Zhang, J., and Jiang, Y. (2011). Direct observation of twinning-detwinning-retwinning on magnesium single crystal subjected to strain-controlled cyclic tension-compression in [0 0 0 1] direction. *Philos. Mag. Lett.* 91, 757–765. doi: 10.1080/09500839.2011.617713

Yuasa, M., Miyazawa, N., Hayashi, M., Mabuchi, M., and Chino, Y. (2015). Effects of group II elements on the cold stretch formability of Mg-Zn alloys. *Acta Mater.* 83, 294–303. doi: 10.1016/j.actamat.2014.10.005

Zhang, B., Gavras, S., Nagasekhar, A. V., Cáceres, C. H., and Easton, M. A. (2014). The strength of the spatially interconnected eutectic network in HPDC Mg-La, Mg-Nd, and Mg-La-Nd alloys. *Metall. Mater. Trans. A Phys. Metall. Mater. Sci.* 45, 4386–4397. doi: 10.1007/s11661-014-2416-9

Zhang, J., Dou, Y., and Dong, H. (2014a). Intrinsic ductility of Mg-based binary alloys: a first-principles study. *Scr. Mater.* 89, 13–16. doi: 10.1016/j.scriptamat.2014.06.035

Zhang, J., Dou, Y., and Zheng, Y. (2014b). Twin-boundary segregation energies and solute-diffusion activation enthalpies in Mg-based binary systems: a first-principles study. *Scr. Mater.* 80, 17–20. doi: 10.1016/j.scriptamat.2014.02.004

Zhang, Q., Fu, L., Fan, T. W., Tang, B. Y., Peng, L. M., and Ding, W. J. (2013). Ab initio study of the effect of solute atoms Zn and y on stacking faults in Mg solid solution. *Phys. B Condensed Matter* 416, 39–44. doi: 10.1016/j.physb.2013.02.013

Zhang, R. F., and Liu, B. X. (2002). Proposed model for calculating the standard formation enthalpy of binary transition-metal systems. *Appl. Phys. Lett.* 81, 1219–1221. doi: 10.1063/1.1499510

Zhang, R. F., and Liu, B. X. (2005). Thermodynamic criterion for the formation of laves phases in binary transition-metal systems. *Philos. Mag. Lett.* 85, 283–287. doi: 10.1080/09500830500197385

Zhang, Y., Yu, S., Zhu, X., and Luo, Y. (2008). Study on as-cast microstructures and solidification process of Mg-Zn-Y alloys. *J. Non-Cryst. Solids* 354, 1564–1568. doi: 10.1016/j.jnoncrysol.2007.08.049

Zhao, Y. H., Zhu, Y. T., Liao, X. Z., Horita, Z., and Langdon, T. G. (2006). Tailoring stacking fault energy for high ductility and high strength in ultrafine grained Cu and its alloy. *Appl. Phys. Lett.* 89, 89–91. doi: 10.1063/1.2356310

Zhao, Z., and Wang, W. (2016). Mg-based Quasicrystals. *Intech Open.* doi: 10.5772/57353

Zhiping, L., Shaoqing, Z., Yali, T., and Dongshan, Z. (1994). Microstructures of Mg-Zn-Zr-RE alloys with high RE and low ZN contents. *J. Alloys Compd.* 209, 275–278. doi: 10.1016/0925-8388(94)91113-4

Zhu, S., Easton, M. A., Abbott, T. B., Nie, J. F., Dargusch, M. S., Hort, N., et al. (2015). Evaluation of magnesium die-casting alloys for elevated temperature applications: microstructure, tensile properties, and creep resistance. *Metall. Mater. Trans. A Phys. Metall. Mater. Sci.* 46, 3543–3554. doi: 10.1007/s11661-015-2946-9

Zhu, Y. M., Morton, A. J., and Nie, J. F. (2010a). The 18R and 14H long-period stacking ordered structures in Mg-Y-Zn alloys. *Acta Mater.* 58, 2936–2947. doi: 10.1016/j.actamat.2010.01.022

Zhu, Y. M., Morton, A. J., and Nie, J. F. (2012). Growth and transformation mechanisms of 18R and 14H in Mg-Y-Zn alloys. *Acta Mater.* 60, 6562–6572. doi: 10.1016/j.actamat.2012.08.022

Zhu, Y. M., Morton, A. J., Weyland, M., and Nie, J. F. (2010b). Characterization of planar features in Mg-Y-Zn alloys. *Acta Mater.* 58, 464–475. doi: 10.1016/j.actamat.2009.09.025

Zhu, Y. M., Weyland, M., Morton, A. J., Oh-ishi, K., Hono, K., and Nie, J. F. (2009). The building block of long-period structures in Mg-RE-Zn alloys. *Scr. Mater.* 60, 980–983. doi: 10.1016/j.scriptamat.2009.02.029

Zhu, Y. T., Liao, X. Z., and Wu, X. L. (2012). Deformation twinning in nanocrystalline materials. *Progr. Mater. Sci.* 57, 1–62. doi: 10.1016/j.pmatsci.2011.05.001

Zubair, M., Sandlöbes, S., Wollenweber, M. A., Kusche, C. F., Hildebrandt, W., Broeckmann, C., et al. (2019). On the role of Laves phases on the mechanical properties of Mg-Al-Ca alloys. *Mater. Sci. Eng. A* 756, 272–283. doi: 10.1016/j.msea.2019.04.048

Conflict of Interest: The author declares that the research was conducted in the absence of any commercial or financial relationships that could be construed as a potential conflict of interest.

frontiers
in Materials

MINI REVIEW
published: 23 April 2021
doi: 10.3389/fmats.2021.575530

Novel Magnesium Based Materials: Are They Reliable Drone Construction Materials? A Mini Review

***Daniel Höche*[1,2]*, *Wolfgang E. Weber*[3], *Eugen Gazenbiller*[1,2], *Sarkis Gavras*[2,4], *Norbert Hort*[2,4] and *Hajo Dieringa*[2,5]**

[1] Institute of Surface Science, HELMHOLTZ-Zentrum Geesthacht, Zentrum für Material-und Küstenforschung GmbH, Geesthacht, Germany, [2] MagIC - Magnesium Innovation Centre, HELMHOLTZ-Zentrum Geesthacht, Zentrum für Material-und Küstenforschung GmbH, Geesthacht, Germany, [3] Chair of Structural Analysis, Faculty of Mechanical Engineering, HELMUT-SCHMIDT-University/University of the Federal Armed Forces, Hamburg, Germany, [4] Institute of Metallic Biomaterials, HELMHOLTZ-Zentrum Geesthacht, Zentrum für Material-und Küstenforschung GmbH, Geesthacht, Germany, [5] Institute of Materials and Process Design, HELMHOLTZ-Zentrum Geesthacht, Zentrum für Material-und Küstenforschung GmbH, Geesthacht, Germany

Novel magnesium-based materials are ideal candidates for use in future aviation vehicles because they are extremely light and can therefore significantly increase the range of these vehicles. They show very good castability, are easy to machine and can be shaped into profiles or forgings to be used as components for next generation aerial vehicle construction. In the case of a large number of identical components, high-pressure die casting of magnesium alloys is clearly superior to high-pressure die casting of aluminum alloys. This is due to the lower solubility of iron in magnesium and thus tool/casting life is significantly longer. In addition, the die filling times for magnesium high-pressure die casting are approximately 30% shorter. This is due to the lower density: aluminum alloys are approximately 50% heavier than magnesium alloys, which is a significant disadvantage for aluminum alloys especially in the aerospace industry. There are cost-effective novel die casting alloys, besides AZ91 or AM50/60 such as DieMag633 or MRI230D, which show very good specific strength at room and elevated temperatures. In the case of magnesium-based wrought alloys, the choice is smaller, a typical representative of these materials is AZ31, but some new alloys based on Mg-Zn-Ca are currently being developed which show improved formability. However, magnesium alloys are susceptible to environmental influences, which can be eliminated by suitable coatings. Novel corrosion protection concepts for classical aerial vehicles currently under development might suitable but may need adaption to the construction constraints or to vehicle dependent exposure scenarios. Within this mini-review a paradigm change due to utilization of new magnesium materials as drone construction material is briefly introduced and future fields of applications within next-generation aerial vehicles, manned or unmanned, are discussed. Possible research topics will be addressed.

Keywords: ultra-lightweight construction, hybrid design, magnesium alloy, aerial vehicle, urbane mobility

OPEN ACCESS

Edited by:
Xiangming Zhou,
Brunel University London,
United Kingdom

Reviewed by:
Guosong Wu,
Hohai University, China
Faruk Mert,
Ankara Yıldırım Beyazıt University,
Turkey

***Correspondence:**
Daniel Höche
daniel.hoeche@hzg.de

Specialty section:
This article was submitted to
Structural Materials,
a section of the journal
Frontiers in Materials

Received: *23 June 2020*
Accepted: *30 March 2021*
Published: *23 April 2021*

Citation:
Höche D, Weber WE, Gazenbiller E, Gavras S, Hort N and Dieringa H (2021) Novel Magnesium Based Materials: Are They Reliable Drone Construction Materials? A Mini Review. Front. Mater. 8:575530. doi: 10.3389/fmats.2021.575530

INTRODUCTION

Lightweight materials such as magnesium and its alloys are of great interest for the industrial sector. Potential applications can be found in the automobile industry and in civil engineering as structural components (Dieringa and Kainer, 2013), in batteries as anode material (Deng et al., 2018; Höche et al., 2018) and in medical engineering as biocompatible, resolvable implants (Kirkland, 2012; Luthringer et al., 2014). The aspects of applying magnesium based materials in vehicle concepts have been widely discussed (Dieringa et al., 2007; Dieringa and Kainer, 2009; Dieringa and Bohlen, 2016) with the result that functionalizations of magnesium alloys are feasible (Xianhua et al., 2016). Thus, it is reasonable to think about application of novel magnesium based materials to construct additional vehicle components e.g., for a quadcopter or other next generation aerial vehicles, if they meet technical and economic constraints.

Typically, drones are classified according to weight or flight range (Weibel and Hansman, 2004; Arjomandi et al., 2006; Brooke-Holland, 2012; Dalamagkidis, 2015). Of these weight or flight range classifications, improvements to ultra-light-weight drones is an ultimate goal to achieve. Presently drone materials are very often composites as sandwich panels applying fiberglass, graphite fiber or aramid based systems as skin and reinforcement materials, and foams mostly based on polymers as panel core materials (Fahlstrom and Gleason, 2012). Such systems are already established within aviation sector and just need to be applied. For example, the City-Airbus, the Lilium-Jet (Lilium, 2018) or Volocopter aiming to conquer the air taxi sector construct their vehicles with CFRP concepts. Generally lightweight vehicle constructions require a high strength to weight ratio with the ability to adapt shapes onto aero- and flight dynamical requirements. In this context, morphing materials are of great interest and might bring constructional aspects to the limit (Sun et al., 2016; Goh et al., 2017). Despite this trend there is a lot of space to use new magnesium alloys, such as DieMag633, MRI230D (Gavras et al., 2019; Tu et al., 2019), Mg-Zn-Ca based (Pan et al., 2016; You et al., 2017; Tu et al., 2019), magnesium based foams (Kucharczyk et al., 2017) or high strength AM60 + 1AlN nanocomposites (Dieringa et al., 2017; Malaki et al., 2019). Particularly with regards to manned aerial vehicles (MAV's) or even air-taxis which might become very expensive and not environmental benign if they are conventionally designed. The application of magnesium in recent aerial vehicles is a first step. For example, the commercially available DJI Inspire 2 unmanned aerial vehicle (UAV), has an AZ91 housing. The DJI Mavic Air applies brackets based on AZ91. The Phantom 4 Pro V2.0 quadcopter applies a titanium magnesium hybrid structure to achieve maximal rigidity of the airframe for excellent maneuverability[1]. Obviously, based on this existing experience, there is a lot of potential in conceptional design approaches using magnesium materials. Possibilities going beyond this need to be further explored.

AERIAL VEHICLE COMPONENTS

Design of unmanned aerial vehicles and manned aerial vehicles follow the well-established construction criteria of aircraft industry. However, this does not mean that there is no space for innovation and novel thinking. Considering the price developments (Q4/2020 at 2.55–2.70 $/kg Source: Platts Metals Week) but also enhanced manufacturing capabilities Mg based components might replace vehicle components and attachments (e.g., camera housings) but also on structural level.

The structure of a typical UAV consists of basic subsystems. All those components typically do not mainly differ in their function from conventional aircraft concepts but might be adapted. The most important are listed:

- The fuselage including stringers, the skin (coated), longerons (longitudinal structural members reinforcing the skin), and some bulkheads can be made from many lightweight engineering materials.
  This can be impregnated fabrics, standard AA2024 structures or many other composites (CFRP, GLARE, etc.). Components for the fuselage can be made of magnesium alloys. These are, for example, sheets for the outer skin made of AZ31 or aluminum-free ZE10. The latter shows excellent forming properties and a reduced texture. Frames and cross members can be made of AM60 by high-pressure die casting. Any further fairings (and filets) can still be made of Al alloys or respective foils.
- The wings including the spars (mono and multi), ribs, stiffeners, and the skin in 2, 3, or 4 rotor systems (sheathed and unsheathed) are structural parts as well and critical loads are transferred to the fuselage by a topological designed beam or truss structure. Materials in use must be light but also stiff and limit vibrations. However, using current lightweight materials such as CFRP leads to structures being more flexible than desired. Thus, additional effort is necessary to limit the deformations—one example for that are truss braced wings (see e.g., Scott et al., 2016). Instead, extruded profiles of wrought magnesium alloys could be used here for the load-bearing structures; they show yield strengths of up to 300 MPa. Cast components for wing and spar construction made of AZ91 or AM60 could be used as ultralight structural components here as well.
- The tails (horizontal and vertical) very often are made of carbon- or glass fiber materials applying resins, wax and hardeners with foam cores.
- The rotor blades are mostly made of composite materials involving impregnated fabrics. Especially for UAV's which are used for civil applications in urban areas, an outer ring housing the rotor blades is necessary in order to prevent people and animals from accidental collisions and to reduce noise. This ring might be made of magnesium or magnesium alloys because this material may better withstand collisions with both the built environment and moving objects such as other UAV's. Additionally, the damping properties of such Mg based systems are excellent.

---

[1] www.dji.com

- The engine/powertrain group consisting of for example pylons, inlet, supports, etc. does not follow the classical turbine design with Ti- or Ni based alloys. For UAV's like quadcopters electrical engines depending on battery power are required, where it should be mentioned that battery mass is a problem. Casings or heads of piston engines are often made of cast aluminum but might be replaced by Mg based materials. Ti alloys or steels are other options if the situation (temperature, etc.) requires countermeasures. Magnesium alloys for higher temperatures are available, as well, although they are often more costly (AE-series, DieMag-series, AJ-series) (Gavras et al., 2019).
- The landing gear (and if required, its bay door) can also be part of the structure especially for MAV's. It has to take up high loads and can already be made of carbon composites or simply AISI 300M steels.
- It should be noted that the dies for applying the forming processes mentioned above may also be made from ultra-high performance concrete (UHPC) (see e.g., Kleiner et al., 2008), which may lead to economic gains. This holds especially for low and medium contoured part shapes. For producing parts with small radii, the UHPC dies should be additionally confined or reinforced (see also Kleiner et al., 2008).

DRONE CONSTRUCTION MATERIAL REQUIREMENTS

Material selection especially for aerospace vehicles has been introduced by Arnold et al. (2012) based on Ashby (2010). The structure and its materials have to ensure the functionality of the drone. They have to keep the aerodynamics of the UAV and carry the occurring loads at any time. Thus, structural components are constructed following the lightweight design rules (e.g., high Youngs modulus/density ratio E/ρ, etc.; Arnold et al., 2012) as shown in **Figure 1**, whereas safe design in c) has special emphasis for manned vehicles. Here the most common material is aluminum, followed by composite materials, such as glass/epoxy and carbon fiber. Surprisingly, magnesium based materials such as magnesium based metal matrix nanocomposites (MMNC's) are yet not in use despite their very good potential. Some of these Mg-MMNC's show excellent properties caused by only small additions of ceramic nanoparticles. The great advantage of these materials is that the nanoparticles not only increase mechanical strength (by grain refinement or Orowan strengthening), but also increase ductility (Dieringa, 2011; Dieringa et al., 2017).

The structural members are designed to carry the flight loads or to handle stress without failure. In designing the structure, the entirety of the wing and fuselage must be considered in relation to the physical characteristics of the material of which it is made. Every part of the structure is engineered to carry the load which is applied on it. The structural designer has to determine flight loads (including bird strikes) and other loads, calculate stresses, and design the structural elements such as to allow the UAV components to perform their aerodynamic functions and durability requirements efficiently. This goal will be considered simultaneously with the objective of the lowest structural weight.

The entire airframe and its components are joined by rivets, bolts, screws, and other fasteners. Welding, adhesives, and special bonding techniques are also employed. In order to enhance the delamination toughness of e.g., CFRP laminates, techniques such as z-pinning are investigated (cf. Mouritz, 2007). Additionally, composite materials with enhanced delamination toughness such as GLARE are of scientific interest (see Rittmeier et al., 2018). The most common design of UAV structure is semi- monocoque (single shell) which implies that the respective skin is stressed and thus needs to be reinforced.

Structural parts of UAV's are subjected to: (1) tension, (2) compression, (3) torsion, (4) shear, and (5) bending. Typically, a single member of the structure is often subjected to a combination of the resulting stresses. It is worth mentioning that the UAV is subjected to time-harmonic loads (i.e., due to vibrations induced by the engine) and impact loads (e.g., during the landing phase, due to bird strikes or impacts such as the Hudson River landing in 2009). Additionally, fluttering as well as limit-cycle oscillations due to wind loads is a major issue. Hence, the design principles known from e.g., aeronautical applications or wind power plants are a good starting point when designing UAV's. A major issue in designing lightweight-structures from composite materials is that these structures tend to delaminate. Although there are substantial contributions to prevent structural elements from delamination, this problem is not yet solved. Promising approaches to increase delamination toughness can be found in the literature (e.g., Mouritz, 2007; Rittmeier et al., 2018). However, by suggesting magnesium based construction materials for e.g., quadcopter drones, the authors believe that the potential problem of delamination can be circumvented. This advantage holds for the drone's skin and bulkhead, which are also subjected to lateral loads. Structural members such as frames and longerons are mainly loaded longitudinally and consequently can be treated as rods in most cases (cf., Rothert and Gensichen, 1987). Using lightweight configurations made of composite materials mentioned above has another effect: the respective structures are getting more flexible. Thus, scientific effort is necessary in order to reduce the resulting deformations. For example, this led to the development of the so-called truss braced wing (see Scott et al., 2016). Again, the authors of the current contribution believe that the rigidity of structural members made of magnesium or magnesium alloys is sufficient to ensure moderate deformations and might improve acoustic emission profiles. Concerns about corrosion issues are not appropriate due to the existence of novel corrosion protection concepts (Lamaka et al., 2016; Dieringa et al., 2018) and the expected uncritical corrosive in-service exposure conditions.

Besides these mechanical and design aspects, the ecological footprint (Ehrenberger, 2020) and the social acceptance of the materials used in drone design is also of interest. Many contributions show the positive effect on fuel/energy consumption when using CFRP for MAV's (see Timmis et al., 2015). The authors expect that similar conclusions hold for UAV's and other lightweight materials such as magnesium or

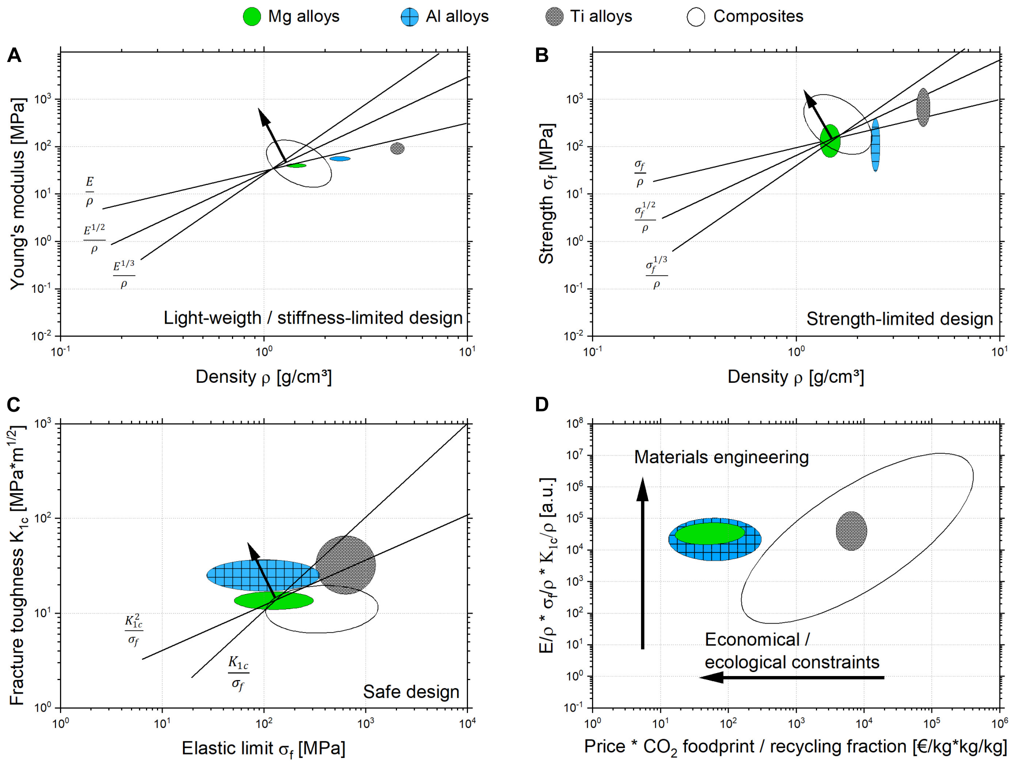

FIGURE 1 | Materials selection following Ashby for aerospace applications (based on Granta-design data). **(A)** Stiffness limited, **(B)** strength limited, and **(C)** safe design as proposed by standard structural design concepts, whereas the bottom-right diagram **(D)** shows the product of previous mechanical parameters vs. the product of non-physical properties like the material price, the carbon dioxide footprint and the reciprocal of recycling fraction.

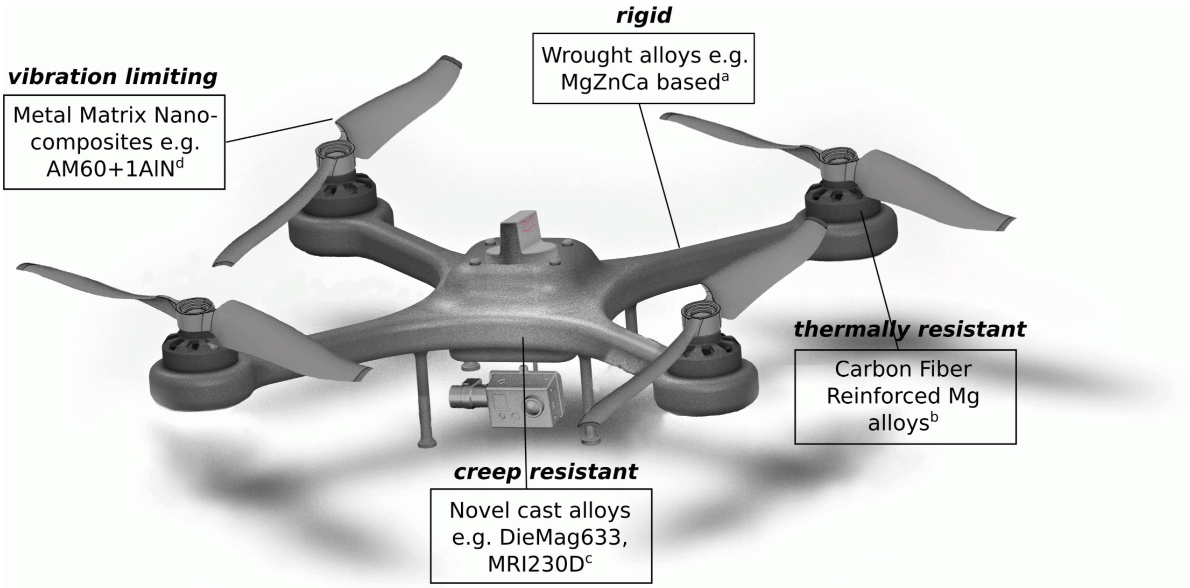

FIGURE 2 | Possible Mg-based alloys/hybrid materials for application in aerial vehicle construction like a quadcopter. Exemplified sources for further information about the materials are a: Naghdi et al. (2016), b: Dieringa et al. (2004), c: Gavras et al. (2019), d: Dieringa et al. (2017).

magnesium alloys. However, recycling of lightweight materials such as CFRP is challenging (Dong et al., 2018). In comparison, recycling of magnesium and magnesium alloys is quite well-understood. Additionally, magnesium and magnesium alloys can be separated easily from the other materials which is not the case for carbon in CFRP. Thus, from an ecological but also from an economical point of view the use of magnesium and magnesium alloys seems to be promising since the price and CO_2 fingerprint are on the same level as aluminum. In a life cycle assessment study (Ehrenberger et al., 2013; Ehrenberger, 2020), it was shown that magnesium, which is primarily produced by electrolysis, has a better carbon footprint than aluminum from the production stage. Over the service life of a component, this advantage increases continuously due to its lower weight. In a comparison of aircraft components made of magnesium or aluminum, the slightly higher greenhouse gas emissions caused by the production of magnesium are compensated for after only a few flights by the fuel savings during flight.

The utilization of Mg based materials generally launches a fire risk discussion. A dedicated study on flammability of the material within aircraft fire tests (Marker, 2013) indicates that for example the behavior of the Mg alloy E21 does not significantly differ to aluminum alloys. Nowadays the SAE standard AS8049D paves the way toward utilization of novel Mg based materials (Czerwinski, 2014) at commercial cabin interiors.

THE MAGNESIUM BASED URBANE AVIATION VEHICLE—DESIGN

The use of magnesium in the aircraft industry has been an important topic since the beginning of aircraft construction. Even before the Second World War, a large number of magnesium parts were used in aircraft construction, including propellers and sheet metal for the outer skin (Reed, 1925; Beck, 1939; Hallion, 2017). During the Second World War, however, a great amount of magnesium was used to build aircrafts in Germany. Both the Messerschmidt Bf 110 and the Junkers Ju 88 used both die-cast and forged magnesium parts (small bell cranks, engine cowl flaps, large dive brake forgings) (DOW, 1941). The first all-magnesium aircraft was described in 1954 (American Aviation, 1955). The F-80C was characterized by a simpler construction of the wings, because considerably fewer components were needed, the number was reduced from 1,644 to only 508, which corresponds to a decrease of 69%. The lighter construction led to an increase of the maximum speed by 5 mph. After the war, the United States built the Convair B-36 bomber, an aircraft that was made of 10% magnesium (Jenkins, 2001) large parts of the outer skin and the control parts were made of magnesium alloys. In 1950 the Sikorsky S-56 Helicopter from Westland Aircraft Ltd., applied 115 kg magnesium. Furthermore, in the Sovjet Union in 1963 the TU-134 from Tupolev already had 1,325 parts made of Mg (Ostrowsky and Henn, 2007).

The operating flight loads limits on a UAV are usually presented in the form of a V-n diagram (airspeed and load variation diagram). Structural designers selecting Mg based materials will construct this diagram with the cooperation of the flight dynamics group. The diagram will determine the failure areas, and area of structural damage/failure. The UAV should not be flown out of the flight envelope, since it is not safe for the structures. The UAV structural design is out of scope of this mini-review. Detailed information can be found elsewhere (Megson, 2016).

Figure 2 shows the principles and an idea to design a hypothetical quadcopter mainly based on Mg-materials. The different requirements for the respective construction parts can be fulfilled by the materials in the boxes. They are:

- **Rigid—**such as MgZnCa wrought alloys with 306 MPa YS and 11% elongation (You et al., 2017).
- **Vibration limiting**—AM60 based nano composites with high ductility of 15.4% at RT (Dieringa et al., 2017).
- **Creep resistant**—such as novel DieMag alloys without rare-earth elements showing better creep resistance compared to commercial alloys and better high temperature yield strength than even aluminum alloy A380 (Gavras et al., 2019).
- **High strength and thermally resistant**—such as carbon fiber reinforced Mg MMCs up to 300°C (Dieringa et al., 2004).

Considering production and design aspects, it becomes obvious that besides efficient manufacturing- and surface technologies (computational based), topological design but also efficient joining technologies for Mg based parts are key enablers for this technology. It will require a concerted research effort and might also be a future market for additive manufactured parts made out of Magnesium.

CONCLUSION

Magnesium based materials can become an essential part of design concepts of UAV's, especially if flight maneuvers require high rigidity and noise pollution become critical decision criteria. Also crash-worthiness is an aspect where magnesium has benefits. The authors are convinced that the economic advantages of using magnesium based materials in drone construction may be further increased if promising techniques such as e.g., performing sheet metal hydroforming by means of UHPC dies are applied. As compared to CFRP and related composite materials, magnesium based materials can be easier separated and recycled once the UAV's reached the end of its service-life.

With respect to the title of this contribution and based on the precedent sections the authors thus are convinced that: Magnesium is—A drone construction material!

AUTHOR CONTRIBUTIONS

DH wrote the main part of the manuscript. EG performed the visualization. HD and SG contributed to the historical aspects.

WW and NH contributed to the mechanical and historical aspects. All authors contributed to the manuscript revision, read and approved the submitted version.

ACKNOWLEDGMENTS

This article is a personal acknowledgement to K. U. Kainer.

REFERENCES

American Aviation (1955). *American Aviation. 14, 58–60*.

Arjomandi, M., Agostino, S., Mammone, M., Nelson, M., and Zhou, T. (2006). *Classification of Unmanned Aerial Vehicles*. Report for Mechanical Engineering class. Adelaide: University of Adelaide.

Arnold, S. M., Cebon, D., and Ashby, M. (2012). *Materials Selection for Aerospace Systems*. Tech. Rep. 2012-217411, NASA/TM. Washington, D.C: NASA.

Ashby, M. F. (2010). *Materials Selection in Mechanical Design*. Oxford: Butterworth-Heinemann.

Beck, A. (1939). *Magnesium Und Seine Legierungen (in German)*, 2 Edn. Berlin: Springer.

Brooke-Holland, L. (2012). *Unmanned Aerial Vehicles (drones): an Introduction*. London: House of Commons Library.

Czerwinski, F. (2014). Overcoming barriers. *Adv. Mat. Proc.* 5, 28–31.

Dalamagkidis, K. (2015). "Classification of UAVs," in *Handbook of Unmanned Aerial Vehicles*, eds K. P. Valavanis and G. J. Vachtsevanos (Berlin: Springer), 83–91. doi: 10.1007/978-90-481-9707-1_94

Deng, M., Höche, D., Lamaka, S. V., Snihirova, D., and Zheludkevich, M. L. (2018). Mg-Ca binary alloys as anodes for primary Mg-air batteries. *J. Power Sourc.* 396, 109–118. doi: 10.1016/j.jpowsour.2018.05.090

Dieringa, H. (2011). Properties of magnesium alloys reinforced with nanoparticles and carbon nanotubes: a review. *J. Mater. Sci.* 46, 289–306. doi: 10.1007/s10853-010-5010-6

Dieringa, H., and Bohlen, J. (2016). Magnesiumlegierungen im Leichtbau. *Nachhaltige Konstruktion* 10, 24–25.

Dieringa, H., and Kainer, K. (2009). Technologische Eigenschaften und Potential von Magnesium-legierungen (in German). *Gießerei-Rundschau* 56, 114–119.

Dieringa, H., and Kainer, K. U. (2013). *Die Leichtbauwerkstoffe für den Fahrzeugbau (in German)*. Wiesbaden: Springer Fachmedien Wiesbaden, 199–442.

Dieringa, H., Bohlen, J., Hort, N., Letzig, D., and Kainer, K. U. (2007). "Advances in manufacturing processes for Magnesium alloys," in *Magnesium Technology 2007 (TMS)*, eds R. S. Beals, A. A. Luo, N. R. Neelameggham, and M. O. Pekguleryuz (TMS The Minerals, Metals and Materials Society), 3–8.

Dieringa, H., Hort, N., and Kainer, K.-U. (2004). Magnesium based MMCss reinforced with C-fibers. *Adv. Tehnol. Mater. Mater. Process. J.* 6, 136–141.

Dieringa, H., Hort, N., Letzig, D., Bohlen, J., Höche, D., Blawert, C., et al. (2018). "Mg Alloys: Challenges and Achievements in Controlling Performance, and Future Application Perspectives," in *Magnesium Technology 2018. TMS 2018. The Minerals, Metals & Materials Series*, eds D. Orlov, V. Joshi, K. Solanki, and N. Neelameggham (Cham: Springer).

Dieringa, H., Katsarou, L., Buzolin, R., Szakacs, G., Horstmann, M., Wolff, M., et al. (2017). Ultrasound assisted casting of an AM60 based metal matrix nanocomposite, its properties, and recyclability. *Metals* 7:388. doi: 10.3390/met7100388

Dong, P. A. V., Azzaro-Pantel, C., and Cadene, A.-L. (2018). Economic and environmental assessment of recovery and disposal pathways for cfrp waste management. *Resour. Conserv. Recycl.* 133, 63–75. doi: 10.1016/j.resconrec.2018.01.024

DOW (1941). *Application of Magnesium Alloys on the Junckers ju-88 Bomber*. The DOW chemical report. Midland, MI: The DOW Chemical Company, 11373.

Ehrenberger, S. (2020). Carbon Footprint of Magnesium Production and its Use in Transport Applications, Update of Life Cycle Assessment of Magnesium Components in Vehicle Construction. Available online at: https://elib.dlr.de/140926/1/2020-10-30_IMA_LCA-Study_Report_Update.pdf (accessed March 8, 2021).

Ehrenberger, S., Dieringa, H., and Fridrich, H. (2013). *Life Cycle Assessment of Magnesium Components in Vehicle Construction*. Available online at: https://elib.dlr.de/87332/1/2013-12_IMA_LCA-Study_Report_Part-I-and-II_incl-summary.pdf (accessed June 22, 2020).

Fahlstrom, P., and Gleason, T. (2012). *Introduction to UAV systems*. Hoboken, NJ: John Wiley & Sons.

Gavras, S., Zhu, S., Easton, M. A., Gibson, M. A., and Dieringa, H. (2019). Compressive creep behavior of high-pressure die-cast aluminum-containing magnesium alloys developed for elevated temperature applications. *Front. Mater.* 6:262. doi: 10.3389/fmats.2019.00262

Goh, G., Agarwala, S., Goh, G., Dikshit, V., Sing, S. L., and Yeong, W. Y. (2017). Additive manufacturing in unmanned aerial vehicles (uavs): challenges and potential. *Aerosp. Sci. Technol.* 63, 140–151. doi: 10.1016/j.ast.2016.12.019

Hallion, R. P. (2017). "Germany and the invention of the all-metal cantilever airplane, 1915–1925: a historical review," in *Proceedings of the 55th AIAA Aerospace Sciences Meeting*, (Reston, VA: AIAA).

Höche, D., Lamaka, S. V., Vaghefinazari, B., Braun, T., Petrauskas, R. P., Fichtner, M., et al. (2018). Performance boost for primary magnesium cells using iron complexing agents as electrolyte additives. *Sci. Rep.* 8:7578.

Jenkins, D. R. (2001). *Magnesium Overcast: The Story of the Convair B-36*. Thurgoona: Specialty Press.

Kirkland, N. T. (2012). Magnesium biomaterials: past, present and future. *Corros. Eng. Sci. Technol.* 47, 322–328. doi: 10.1179/1743278212y.0000000034

Kleiner, M., Curbach, M., Tekkaya, A. E., Ritter, R., Speck, K., and Trompeter, M. (2008). Development of ultra-high performance concrete dies for sheet metal hydroforming. *Prod. Eng.* 2, 201–208. doi: 10.1007/s11740-008-0099-z

Kucharczyk, A., Naplocha, K., Kaczmar, J. W., Dieringa, H., and Kainer, K. U. (2017). Current Status and Recent Developments in Porous Magnesium Fabrication. *Adv. Eng. Mater.* 20:1700562. doi: 10.1002/adem.201700562

Lamaka, S. V., Höche, D., Petrauskas, R. P., Blawert, C., and Zheludkevich, M. L. (2016). A new concept for corrosion inhibition of magnesium: suppression of iron re-deposition. *Electrochem. Commun.* 62, 5–8. doi: 10.1016/j.elecom.2015.10.023

Lilium (2018). *Simplicity was Our Most Complicated Goal. Lilium—Technology*. Available online at: https://lilium.com/technology/ (accessed June 22, 2020).

Luthringer, B. J., Feyerabend, F., and Willumeit-Romer, R. (2014). ¨Magnesium-based implants: a mini-review. *Magnes. Res.* 27, 142–154. doi: 10.1684/mrh.2015.0375

Malaki, M., Xu, W., Kasar, A. K., Menezes, P. L., Dieringa, H., Varma, R. S., et al. (2019). Advanced metal matrix nanocomposites. *Metals* 9:330. doi: 10.3390/met9030330

Marker, T. (2013). *Evaluating the Flammability of Various Magnesium Alloys During Laboratory-and Full-Scale Aircraft Fire Test*. New Jersey, NY: US Department of Transportation. .

Megson, T. H. G. (2016). *Aircraft Structures for Engineering Students*. Oxford: Butterworth-Heinemann.

Mouritz, P. A. (2007). Review of z-pinned composite laminates. *Compos. Part A Appl. Sci. Manuf.* 38, 2383–2397. doi: 10.1016/j.compositesa.2007.08.016

Naghdi, F., Kang, J., and Kim, H. (2016). Microstructure and high-temperature mechanical properties of the mg-4zn-0.5ca alloy in the as-cast and aged conditions. *Mater. Sci. Eng. A* 649, 441–448. doi: 10.1016/j.msea.2015.10.011

Ostrowsky, I., and Henn, Y. (2007). "Present state and future of magnesium application in aerospace industry," in *Proceeding of the International Conference "New Challenges in Aeronautics"*, (India: ASTEC).

Pan, H., Ren, Y., Fu, H., Zhao, H., Wang, L., Meng, X., et al. (2016). Recent developments in rare-earth free wrought magnesium alloys having high strength: a review. *J. Alloys Compd.* 663, 321–331. doi: 10.1016/j.jallcom.2015.12.057

Reed, S. A. (1925). *Aeronautical Propeller*. US Patent, No. 1,542,412.

Rittmeier, L., Losch, T., Sinapius, M., and Lammering, R. (2018). Investigation on the influence of material interfaces and impedance changes on the propagation of guided waves in laminated steel layers. *Procedia Manuf.* 24, 196–202. doi: 10.1016/j.promfg.2018.06.039

Rothert, H., and Gensichen, V. (1987). *Nichtlineare Stabstatik (in German)*. Berlin: Springer.

Scott, R. C., Bartels, R. E., Funk, C. J., Allen, T. J., Sexton, B. W., Dykman, J. R., et al. (2016). Aeroservoelastic test of the subsonic ultra-green aircraft research truss-braced wing model. *J. Guid. Control Dyn.* 39, 1820–1833. doi: 10.2514/1.g000265

Sun, J., Guan, Q., Liu, Y., and Leng, J. (2016). Morphing aircraft based on smart materials and structures: a state-of-the-art review. *J. Intell. Mater. Syst. Struct.* 27, 2289–2312. doi: 10.1177/1045389x16629569

Timmis, A. J., Hodzic, A., Koh, L., Bonner, M., Soutis, C., Schafer, A. W., et al. (2015). Environmental¨ impact assessment of aviation emission reduction through the implementation of composite materials. *Int. J. Life Cycle Assess.* 20, 233–243. doi: 10.1007/s11367-014-0824-0

Tu, T., Chen, X.-H., Chen, J., Zhao, C.-Y., and Pan, F.-S. (2019). A high-ductility Mg–Zn–Ca magnesium alloy. *Acta Metall. Sin.* 32, 23–30.

Weibel, R., and Hansman, R. J. (2004). "Safety considerations for operation of different classes of UAVs in the nas," in *Proceedings of the AIAA 4th Aviation Technology, Integration and Operations (ATIO) Forum* (Reston, VA: AIAA).

Xianhua, C., Yuxiao, G., and Fusheng, P. (2016). Research progress in magnesium alloys as functional materials. *Rare Metal Mater. Eng.* 45, 2269–2274. doi: 10.1016/s1875-5372(17)30015-2

You, S., Huang, Y., Kainer, K. U., and Hort, N. (2017). Recent research and developments on wrought magnesium alloys. *J. Magnes. Alloys* 5, 239–253. doi: 10.1016/j.jma.2017.09.001

Conflict of Interest: The authors declare that the research was conducted in the absence of any commercial or financial relationships that could be construed as a potential conflict of interest.

Advantages of publishing in Frontiers

OPEN ACCESS
Articles are free to read
for greatest visibility
and readership

FAST PUBLICATION
Around 90 days
from submission
to decision

HIGH QUALITY PEER-REVIEW
Rigorous, collaborative,
and constructive
peer-review

TRANSPARENT PEER-REVIEW
Editors and reviewers
acknowledged by name
on published articles

Frontiers
Avenue du Tribunal-Fédéral 34
1005 Lausanne | Switzerland

Visit us: www.frontiersin.org
Contact us: frontiersin.org/about/contact

REPRODUCIBILITY OF RESEARCH
Support open data
and methods to enhance
research reproducibility

DIGITAL PUBLISHING
Articles designed
for optimal readership
across devices

FOLLOW US
@frontiersin

IMPACT METRICS
Advanced article metrics
track visibility across
digital media

EXTENSIVE PROMOTION
Marketing
and promotion
of impactful research

LOOP RESEARCH NETWORK
Our network
increases your
article's readership